D 2022

U.PORTO
FEUP FACULDADE DE ENGENHARIA
UNIVERSIDADE DO PORTO

CO_2 METHANATION OVER BIMETALLIC CATALYSTS SUPPORTED ON CARBON MATERIALS WITH TAILORED SURFACE PROPERTIES

LILIANA P. L. GONÇALVES

TESE DE DOUTORAMENTO APRESENTADA
À FACULDADE DE ENGENHARIA DA UNIVERSIDADE DO PORTO EM
ENGENHARIA QUÍMICA E BIOLÓGICA

CO_2 Methanation over bimetallic catalysts supported on carbon materials with tailored surface properties

Liliana P. L. Gonçalves

Dissertation presented to obtain the Doctor of Philosophy (PhD) degree in Chemical and Biological Engineering

Supervisor | Professor M. Fernando R. Pereira
Co-Supervisors | Doctor Yury V. Kolen'ko
Doctor O. Salomé G. P. Soares
Doctor Juliana P. S. Sousa

Nanochemistry Research Group – International Iberian Nanotechnology Laboratory (INL), Braga, Portugal
Laboratory of Separation and Reaction Engineering – Laboratory of Catalysis and Materials (LSRE-LCM), Faculty of Engineering of University of Porto, Porto, Portugal

2022

This work was financially supported by Fundação para a Ciência e Tecnologia (FCT) through the PhD grant SFRH/BD/128986/2017.

Additional funding was provided by: Base-UIDB/50020/2020 and Programmatic-UIDP/50020/2020 Funding of LSRE-LCM, funded by national funds through FCT/MCTES (PIDDAC).

Preface

The PhD thesis presented herein is submitted for the degree of Doctor in Chemical and Biological Engineering. It was written based on the research carried out at the Nanochemistry Research Group in the International Iberian Nanotechnology Laboratory (INL) and at the Catalysis and Carbon Materials group of the Associate Laboratory LSRE – LCM (Laboratory of Separation and Reaction Engineering – Laboratory of Catalysis and Materials), hosted in the Department of Chemical Engineering, Faculty of Engineering of the University of Porto. The research was supervised by Professor M. Fernando R. Pereira and Doctor O. Salomé G. P. Soares, from LSRE-LCM, and Doctor Yury V. Kolen'ko and Doctor Juliana P. S. Sousa, from INL. Furthermore, two research internships were accomplished along the PhD in the Technical University of Denmark (Denmark), under the supervision of Doctor Søren Kegnæs, and in CRISMAT at the École Nationale Supérieure d'Ingénieurs de Caen (ENSICAEN) (France), under the supervision of Doctor Oleg I. Lebedev.

It all started with the intent for me to gather the knowledge characteristic of each Research Group in order to develop, evaluate and characterize improved catalysts for the CO_2 methanation reaction. Therefore, this thesis describes the relevance of tailoring the surface of supporting carbon materials to develop efficient catalyst supports for CO_2 methanation reaction. The thesis presents the results obtained along this four-year journey, and it is organized in 8 Chapters.

Chapter 1 describes the motivation of the work, the state-of-the-art on CO_2 methanation reaction, and the objectives as well as the thesis outline. Chapter 2 describes the methods for the synthesis, characterization, and catalytic evaluation of the materials. Chapters 3–7 present the main core of the thesis that is based on a compilation of the research results from 5 scientific publications, 2 of which are already published and 3 are currently under revision. And, finally, Chapter 8 explains the main conclusions and suggestions for further work.

Acknowledgements

First and foremost, I would like to express my gratitude to my supervisors Professor Fernando Pereira, Dr. Yury Kolen'ko, Dr. Salomé Soares and Dr. Juliana Sousa, for the opportunity to embark on this project and for their constant support, encouragement and for believing in me along this path.

I would like to thank Prof. Fernando for the fruitful and enlightening discussions and encouraging words along these four years as well as for his availability every time I needed, to Yury for the opportunity to start my research career at the Nanochemistry group and for everything he taught me along the line with the useful brainstorm meetings as well as for the ideas and opportunities that emerged, to Salomé for her availability to assist me in everything I needed in all aspects, including laboratory work, new ideas, and encouragement when things were not perfect (thank you for helping me remotely with the setup when Afonso was born), and to Juliana for all the help in the beginning of my research career and for connecting me to the LCM group and also, for the fruitful discussions and support given along this time.

To Dr. Søren Kegnæs for the opportunity to join his group at the Technical University of Denmark for the development of part of the work of the thesis. To him and Dr. Jerrik Mielby I would like to thank the great welcoming in Denmark, all the knowledge they provided me during this stay and all the help in the performance of the proposed experiments. To Dr. Oleg I. Lebedev, for the opportunity to learn about Transmission Electron Microscopy in CRISMAT laboratory, in France. I would like to thank him for the great welcoming in France and for all the knowledge he provided me in microscopy during this stay. To Dr. Dmitri Y. Petrovykh, for the assistance and knowledge sharing in, not only, but especially XPS data treatment.

To all my co-authors, thank you for your cooperation; without it, the work presented in this thesis would not have been possible.

I could not forget to acknowledge all my colleagues and friends from Nanochem group and from LCM group, without their support, encouragement, and cooperation this path would not have been the same. To all my Nanochem colleagues, the new ones and the ones that had left already, in special to Soraia, and Natália. From the LCM group, a special thank you to the E324 people for the fun breaks and all the words of encouragement and to the coffee break people also for the fun moments as well as fruitful discussions.

I would like to express my sincere gratitude to my parents for believing in me, for all the encouragement and support given along the years, as well as for trying to always be involved and try to understand what I was doing on my work. Also, to my sister for all the support given and for listening and advising me even though I'm the oldest: thank you for your patience and support.

Finally, to Gonçalo, thank you for the encouragement, patience, and for the discussions about the typical problems of a PhD student. Thank you for understanding and supporting me.

Abstract

The rising of the CO_2 emissions to the atmosphere, allied to the need to find a solution to store the energy produced through renewable energy sources, has led to the increasing interest in the CO_2 methanation reaction. This reaction can be applied in the Power-to-Gas technology as a way to mitigate CO_2 emissions and store energy in the form of methane fuel. In this thesis, the possibility to prepare catalysts for CO_2 methanation with enhanced performance by using advanced carbon materials as supporting material was investigated.

Four sets of catalysts were successfully synthesized, and their performance for CO_2 methanation was evaluated in a laboratory scale setup in order to develop new high performing catalysts. The materials were extensively characterized, in order to gather properties-performance relationships, by the conventional characterization techniques, such as N_2 physisorption at −196 °C, elemental analysis, point of zero charge (pH_{PZC}), X-ray photoelectron spectroscopy (XPS), transmission electron microscopy (TEM), high-angle annular dark-field scanning transmission electron microscopy (HAADF-STEM), electron diffraction (ED), and energy-dispersive X-ray spectroscopy in STEM mode (STEM−EDX), X-ray diffraction (XRD), H_2 temperature programmed reduction (H_2–TPR), H_2–chemisorption, and temperature Ppogrammed desorption (TPD). Additionally, emerging characterization techniques, such as *in situ* TEM and modulation excitation–phase sensitive detection–diffuse reflectance infrared Fourier transform spectroscopy (ME–PSD–DRIFTS), were used to gather more insightful knowledge on the catalyst behavior under reaction conditions and on the reaction mechanism.

The research was started by evaluating the influence of different surface chemistries of activated carbon (AC) as support for Ni-based CO_2 methanation catalysts. For that, activated carbon was successfully functionalized with O through wet oxidation, N groups by a solid-state ball milling procedure and also with O-free Lewis basic sites through thermal reduction, and Ni and NiFe

nanoparticles were successfully deposited through incipient wetness impregnation (IWI) followed by thermal reduction. The catalytic experiments demonstrated that reduced activated carbon (AC−R) with O-free Lewis basic sites showed the best performance with a CO_2 conversion of 76% and selectivity to methane of 97%, at 450 °C. These results suggested that methanation reaction is highly dependent on the basicity of the supporting material for Ni catalysts, since the best-performing support was also the one with more basic character. Following this study, the promotion with 5% Fe of the best-performing Ni catalyst led to a favorable decrease of the optimal reaction temperature and significantly improved the stability of the catalyst.

Taking these results into consideration, further work was conducted with a different type of carbon supporting material, namely, carbon nanotubes (CNTs). In this case, pristine and N-doped CNTs, successfully prepared with the same solid-state ball milling procedure used with AC, were investigated since N-doping of CNTs proved to be an effective way to enhance the catalytic performance of Ni catalysts for CO_2 methanation. The study aimed for an in-depth understanding of the properties of N-doped CNTs that afforded enhanced performance in CO_2 methanation. The Ni catalysts on N-doped CNT, prepared by IWI, achieved a higher CO_2 conversion of 81% with selectivity to methane of 99% at a lower temperature of 400 °C, compared to Ni on non-doped CNT, exhibiting excellent stability over 48 h time-on-stream testing. The study demonstrated that the N-doped CNT support exhibited a better distribution of the Ni sites that were strongly interacting with the support, even with atomically dispersed Ni being observed. Such a high dispersion was expected to be enabled by the anchoring sites provided by the N functional groups on N-doped CNT and was confirmed to be one of the main reasons for the enhanced performance of Ni on N-doped CNT compared to Ni on non-doped CNT, since it markedly increases the H_2 uptake capacity.

The good performance of reduced activated carbon and N-doped CNT led to the idea to investigate the performance of the state-of-the-art carbon-supported Ni-based electrocatalysts, that are used for hydrogen oxidation and

evolution reactions, as CO_2 methanation catalysts. Accordingly, commercially available Ni, NiMo and NiRe electrocatalysts supported on carbon were probed for the first time as catalysts for CO_2 methanation. The monometallic Ni on carbon material demonstrates the best CO_2 methanation properties from this set of catalysts, achieving an excellent CO_2 conversion of 83% at 400 °C with nearly complete selectivity to CH_4 of ≈100%, and intact performance during 90 h of time-on-stream testing. These catalytic properties are among the topmost reported to date for carbon-supported Ni-based methanation catalysts, and it was established that their excellent performance is originated from the good dispersion of the Ni catalytically active phase over the N-containing advanced carbon support.

In the quest to develop a novel supporting material for CO_2 methanation catalysts, a composite of reduced activated carbon and CeO_2 was developed since CeO_2 is known to improve the low-temperature catalytic performance of the catalysts in CO_2 methanation, although it is composed of a rare-earth metal. Hence, a set of Ni catalysts on pure CeO_2 and composite of reduced activated carbon and CeO_2 was successfully synthesized through IWI and investigated in CO_2 methanation. The supports were prepared through precipitation of the Ce precursor, in the absence or presence of reduced activated carbon. The resultant materials afforded an excellent conversion of around 87% with almost complete selectivity to methane and excellent stability at a favorably low reaction temperature of 370 °C. The composite of carbon with CeO_2 in the supporting material allowed for an efficient reduction in the usage of the expensive rare-earth CeO_2 while affording not only a cost-effective but also a high-performing methanation catalyst.

The next effort of the thesis was to understand the behavior of the catalysts under reaction conditions. Firstly, taking into account the development of a Ni@NiO core-shell nanostructure observed in Ni on reduced activated carbon, an *in situ* transmission electron microscopy (TEM) study was performed on this high-performing catalyst. This study provided direct insights into the formation of a NiO shell around the metallic Ni core during the catalytic reaction. This

structure played an important role in the CO_2 methanation, evidenced by their dynamic behavior under the reaction conditions. Coke formation over the catalyst nanoparticles was not observed; however, a slight increase in particle size of the catalyst was observed, which could be a reason for the slight deactivation observed for this catalyst.

Finally, in order to understand the reaction mechanism, the topmost-performing Ni supported on carbon-CeO_2 composite and Ni supported on CeO_2 catalysts were investigated using the emerging ME-PSD-DRIFTS technique. The study determined the rate of formation/consumption of the various intermediates demonstrating that the CO_2 methanation reaction follows both CO and formate pathways in Ni/CeO_2, while in Ni/ACR−CeO_2, it only follows the formate pathway. Importantly, it was found that a partial modification in the supporting material of the catalysts can lead to different mechanisms of CO_2 methanation.

Resumo

O aumento crescente das emissões de CO_2, aliado à emergente procura por uma solução para armazenar a energia obtida de fontes renováveis tem originado um crescente interesse pela reação de metanação de CO_2. Esta reação pode ser utilizada na chamada tecnologia "Power-to-Gas" como forma de mitigar as emissões de CO_2 e de armazenar energia na forma de metano. Nesta tese, foi investigada a possibilidade de preparar catalisadores para metanação de CO_2 com propriedades catalíticas melhoradas, utilizando materiais de carbono avançados como suporte.

Quatro conjuntos de catalisadores foram sintetizados com sucesso e o seu desempenho para a metanação de CO_2 foi avaliado numa instalação à escala laboratorial de forma a desenvolver novos catalisadores com elevado desempenho. Os materiais foram caracterizados extensivamente, de forma a estabelecer relações entre as propriedades e o desempenho catalítico, através de técnicas de caracterização convencionais como fisissorção de N_2 a −196 °C, análise elementar, ponto de carga zero (pH_{PZC}), espectroscopia de fotoeletrões excitados por raios X (XPS), microscopia eletrónica de transmissão (TEM), microscopia eletrónica de transmissão de varrimento de campo escuro anular de alto ângulo (HAADF-STEM), difração de eletrões (ED), e espectroscopia de raios X com dispersão de energia em modo STEM (STEM-EDX), difração de raios X (XRD), redução a temperatura programada em H_2 (H_2−TPR), quimisorção de H_2 e dessorção a temperatura programada (TPD). Adicionalmente, foram utilizadas técnicas de caracterização emergentes como TEM *in situ* e espectroscopia de infravermelhos de reflectância difusa por transformada de Fourier com recurso a modulação-excitação e deteção sensível à fase (ME–PSD–DRIFTS), de forma a adquirir um conhecimento mais profundo do comportamento do catalisador sob condições de reação e ainda do mecanismo de reação.

A investigação foi iniciada avaliando a influência da química superficial do carvão ativado (AC) como suporte para catalisadores de Ni para metanação

de CO_2. Para tal, o carvão ativado foi funcionalizado com sucesso com grupos de O, através de oxidação líquida, e de N, através de um método de reacção em fase sólida recorrendo a um moinho de bolas, assim como centros básicos de Lewis através de redução térmica; finalmente, nanopartículas de Ni e NiFe foram depositadas com sucesso através de impregnação incipiente, seguida de redução térmica. Os ensaios catalíticos com estes materiais demonstraram que o material com centros básicos de Lewis apresentou o melhor desempenho com uma conversão de CO_2 de 76%, e seletividade para metano de 97%, a 450 °C. Estes resultados sugerem que a reação de metanação é altamente dependente da basicidade do suporte em catalisadores de Ni, uma vez que o suporte com melhor desempenho foi aquele com uma superfície mais básica. No seguimento deste estudo, foi adicionado 5% Fe ao catalisador de Ni com melhor desempenho, o que levou a uma diminuição favorável na temperatura ótima de reação e melhorou significativamente a sua estabilidade.

Considerando estes resultados, foi avaliado o desempenho de outro tipo de material de carbono, os nanotubos de carbono (CNT). Neste caso, foram avaliados CNT originais e dopados com N, que foram preparados através do mesmo método utilizado no AC (recorrendo ao moinho de bolas), uma vez que é conhecido que a dopagem com N é uma forma eficiente de melhorar o desempenho catalítico de catalisadores de Ni para metanação de CO_2. O estudo pretendia obter um conhecimento aprofundado das propriedades dos CNT dopados com N que lhes conferem um melhor desempenho nesta aplicação. O catalisador de Ni em CNT dopado com N, preparado por impregnação incipiente, obteve uma conversão de CO_2 mais alta, de 81%, com seletividade para metano de 99%, a uma temperatura mais baixa, de 400 °C, comparando com o catalisador de Ni nos CNT originais, demonstrando ainda uma excelente estabilidade ao longo de 48 h. O estudo demonstrou que o suporte de CNT dopado com N apresentou uma melhor distribuição das nanopartículas de Ni que demonstraram interagir fortemente com o suporte, apresentando ainda Ni atomicamente disperso. Esta melhor dispersão deve-se provavelmente à disponibilidade de sítios de ancoragem

para as nanopartículas, providenciados pelos grupos azotados nos CNT dopados com N, confirmando uma das razões principais para o desempenho melhorado do Ni nos CNT dopados com N comparando com Ni nos CNT originais, uma vez que este facto leva a uma melhor capacidade de adsorção de H_2.

O bom desempenho do carvão ativado reduzido e dos CNT dopados com N, levou à ideia de investigar o desempenho de eletrocatalisadores de Ni suportados em materiais de carbono (C) comerciais que são usados para reações de oxidação e evolução de hidrogénio. Assim, foram avaliados pela primeira vez eletrotacalisadores comerciais de Ni, NiMo e NiRe suportados num material de carbono (C), na reação de metanação de CO_2. O catalisador monometálico, Ni em C, demonstrou o melhor desempenho deste conjunto de catalisadores, obtendo uma excelente conversão de CO_2 de 83% a 400 °C com seletividade quase completa para metano (≈100%), permanecendo com o desempenho intacto ao fim de 90 h. Estas propriedades catalíticas são semelhantes às mais elevadas reportadas na literatura para catalisadores de Ni suportados em materiais de carbono e foi estabelecido que este desempenho excelente é originado pela elevada dispersão da fase ativa de Ni no material de carbono avançado contendo N.

Com o objetivo de desenvolver um novo suporte para catalisadores de metanação de CO_2, foi desenvolvido um compósito de carvão ativado reduzido e CeO_2, uma vez que o CeO_2 é conhecido por melhorar o desempenho a baixas temperaturas de catalisadores para metanação de CO_2, apesar de ser composto por um metal raro. Desta forma, um conjunto de catalisadores de Ni suportados em CeO_2 e no compósito de AC reduzido e CeO_2 foram sintetizados através e impregnação incipiente, e foram avaliados para metanação de CO_2. Os suportes foram preparados através da precipitação do precursor de Ce, na presença ou ausência de carvão ativado. Os materiais resultantes atingiram uma excelente conversão de CO_2 de 87% com seletividade quase completa para metano a uma baixa temperatura de 370 °C. O compósito do material de carbono com o CeO_2 permitiu uma

redução eficiente no uso do metal raro e dispendioso – Ce, oferecendo assim uma alternativa menos dispendiosa, mas com alto desempenho enquanto suporte de catalisadores de metanação de CO_2.

O objetivo seguinte da tese era o estudo do comportamento dos catalisadores desenvolvidos sob as condições de reação. Primeiro, tendo em conta o desenvolvimento de uma estrutura núcleo-"casca" Ni@NiO, observado no catalisador de Ni em AC reduzido, foi realizado um estudo *in situ* de microscopia eletrónica de transmissão neste catalisador. Este estudo revelou uma prova direta da formação da "casca" de NiO, envolvendo o núcleo de Ni, durante a reação catalítica. Esta estrutura demonstrou ter um papel importante na reação de metanação de CO_2, o que foi evidenciado pelo seu comportamento dinâmico sob condições de reação. Não foi observada formação de *coke* nas nanopartículas do catalisador; contudo, foi observado um ligeiro aumento no tamanho das mesmas, o que pode ser a razão da ligeira desativação observada.

Finalmente, de forma a perceber o mecanismo da reação, os melhores catalisadores de Ni suportado no compósito de AC reduzido e CeO_2 e de Ni em CeO_2 foram investigados utilizando a técnica emergente de ME-PSD-DRIFTS. Este estudo permitiu avaliar a velocidade de formação/consumo dos vários intermediários da reação, demonstrando que a reação de metanação de CO_2 segue tanto a via conhecida como via de formato, como a via em que o CO é um intermediário da reação no caso do Ni/CeO_2, enquanto que no caso no Ni/ACR−CeO_2, a via observada é apenas a via de formato. Desta forma, foi demonstrado que modificações parciais no material de suporte dos catalisadores podem levar a diferenças no mecanismo da reação de metanação de CO_2.

Table of Contents

Preface i

Acknowledgements iii

Abstract v

Resumo ix

Table of Contents xiii

List of Figures xix

List of Tables xxxi

List of Abbreviation and Variables xxxv

Chapter 1 1

Motivation 2

1. Carbon dioxide – A greenhouse gas 2

2. Carbon dioxide capture and utilization 3

3. Power-to-Gas (PtG) Technology 6

State of the art 9

4. CO_2 methanation reaction 9

4.1. CO_2 methanation catalysts 10

4.2. CO_2 methanation mechanism 15

5. Carbon Materials as Catalyst supports 16

5.1 Activated carbon 17

5.2 Carbon nanotubes 17

5.3 Carbon xerogels 18

5.4 Modification of surface chemistry of the carbon materials 18

6. *In situ* characterization 20

Objectives and Thesis Outline 22

References 26

Chapter 2.....33

1. Preparation of the supporting materials.....34

1.1 Materials 34

1.1 Preparation of the Activated Carbon (AC) supporting materials with different surface functionalities 34

1.2 Preparation of the Carbon Nanotubes (CNT) supporting materials with different surface functionalities 35

1.3 Preparation of CeO_2 and ACR−CeO_2 composite 35

1.4 Preparation of N-containing Carbon Xerogel 36

2. Preparation of the monometallic and bimetallic supported metal catalysts 37

2.1 Materials 37

2.2 Incipient Wetness Impregnation 37

2.3 Impregnation – Precipitation 38

3. Characterization Techniques 38

3.1 N_2 adsorption-desorption isotherms at −196 ºC 38

3.2 Elemental analysis 40

3.3 Thermogravimetric Analysis.....40

3.4 Point of Zero Charge (pH_{PZC}) 40

3.5 X-ray photoelectron spectroscopy (XPS).....40

3.6 Transmission electron microscopy (TEM).....41

3.7 Powder X-ray diffraction (XRD) 41

3.8 H_2 temperature programmed reduction (H_2–TPR) 42

3.9 H_2 pulse chemisorption 42

3.10 Temperature programmed desorption (TPD).....43

4. CO_2 Methanation Catalytic Experiments 43

5. Simulation of Thermodynamic Equilibrium of CO_2 Methanation.....45

6. *In situ* Studies 46

6.1 Steady-state diffuse reflectance infrared Fourier transform spectroscopy 46

6.2 Modulation excitation–phase sensitive detection–diffuse reflectance infrared Fourier transform spectroscopy 47

6.3 *In situ* TEM 49

References 50

Chapter 3 51

Abstract 52

1. Introduction 53

2. Experimental 55

3. Results 57

3.1 Topmost performance of Ni catalyst supported on reduced AC. 57

3.2 Similar materials characteristics but distinct surface properties of the synthesized Ni catalysts. 58

3.3 Lowering the temperature of methanation and increasing the stability of Ni catalyst by Fe promotion 62

3.5 Formation of Ni@NiO core-shell nanostructure after TOS testing 64

4. Discussion 65

4.1 Role of the surface chemistry 66

4.2 Role of the promotion by Fe 68

5. Conclusions 70

6. Supplementary information 71

6.1 Characterization of supporting carbon materials 71

6.2 Characterization of the as-synthesized Catalysts 74

6.3 Simulation of Thermodynamic Equilibrium of CO_2 Methanation 77

6.4 Catalysts Characterization after prolonged catalytic testing 77

6.5 Characterization of the Ni/AC−R before and after TOS 78
References 81
Chapter 4 85
Abstract 86
1. Introduction 87
2. Experimental 89
3. Results 90
3.1 Characterization of the synthesized catalysts 90
3.2 Catalytic performance in CO_2 methanation 96
3.3 Characterization of the catalysts after TOS 98
4. Discussion 100
5. Conclusions 102
6. Supplementary Information 103
6.1 Loading Study 103
6.2 N_2 Physisorption 104
6.3 Transmission Electron Microscopy 105
6.4 X-ray photoelectron spectroscopy 106
6.5 Tables 109
References 111
Chapter 5 115
Abstract 116
1. Introduction 117
2. Experimental 120
3. Results 121
3.1 CO_2 methanation 121
3.2 Characterization of the catalysts before methanation 124

3.3 Characterization of the catalysts after TOS testing 129
4. Discussion 131
5. Conclusions 136
6. Supplementary Information 137
6.1 Characterization Results 137
References 145
Chapter 6 149
Abstract 150
1. Introduction 151
2. Experimental 153
3. Results and Discussion 153
4. Conclusions 159
5. Supplementary material 160
5.1 Additional TEM images 160
5.2 Experiments Conditions 163
References 164
Chapter 7 167
Abstract 168
1. Introduction 169
2. Experimental 171
3. Results 172
3.1 CO_2 methanation over Ni/CeO_2 and Ni/ACR–CeO_2 172
3.2 Characterization of the catalysts 174
3.3 Probing the mechanism of CO_2 methanation by *in situ* DRIFTS 182
4. Discussion 189
5. Conclusions 197

6. Supplementary Information 199
6.1 Composite loading study 199
6.2 Characterization 199
6.3 Steady-state *in situ* DRIFTS 205
6.4 ME-PSD-DRIFTS 206
References 208
Chapter 8 211
1. Main Conclusions 212
1.1 Carbon materials as catalyst supports 212
1.2 Bimetallic catalysts 214
1.3 *In situ* studies 215
1.4 Developed catalysts 217
2. Future Work 218
Appendices 221
Appendix 1 – Calibration Curves and Calculation Example 222
Calibration Curves 222
Calculation Example 224
Appendix 2 – Influence of the Ni and Fe loading 226
Appendix 3 – CNT with different surface chemistries 229
Appendix 4 – N-doped Carbon Materials 230
Appendix 5 – NiFe bimetallic catalysts on different supports 231
Appendix 6 – CeO_2 vs MgO as composite material with AC−R 232
Appendix 7 – Bimetallic Catalysts for CO_2 methanation – Performance evaluation of the use of different second metals on Ni catalysts supported on AC−R 233
References 236
Appendix 8 – Published Articles 237

List of Figures

Figure 1.1. World and Portuguese CO_2 emissions from fuel combustion by sector, 2019 [5,9]. 3

Figure 1.2. Main approaches for CO_2 capture [13]. 4

Figure 1.3. Schematic representation of the Power-to-Gas (PtG) technology.. 6

Figure 1.4. Capacities of Power-to-X projects in Europe, (A) between 2016 and 2020, (B) planned for 2021–2025 [26]. 7

Figure 1.5. CO_2 conversion (X_{CO2}), and CH_4 (S_{CH4}) and CO (S_{CO}) selectivities at the thermodynamic equilibrium (a), together with molar composition of CO_2, CH_4 and CO at the thermodynamic equilibrium (b). The thermodynamic equilibrium values were calculated using a model based on the minimization of Gibbs free energy of the existing species, with a CO_2:H_2 ratio of 1:4, P = 1 bar (See Chapter 6-5). 9

Figure 1.6. CO_2 associative (A) and dissociative (B) methanation scheme. 16

Figure 2.1. Schematic representation of the reactor setup……..44

Figure 2.2. Schematic representation of the *in situ* DRIFTS setup. 48

Figure 3.1. Comparison of the catalytic properties of the synthesized Ni catalysts supported on ACs with different surface functionalities: X_{CO2} (a), S_{CH4} (b) and Y_{CH4} (c) as a function of temperature, together with the respective thermodynamic equilibrium curves. Reaction conditions: P = 1 bar; $WHSV$ = 60 000 mL g^{-1} h^{-1};
CO_2 : H_2 = 1 : 4…….....58

Figure 3.2. Comparison of XRD patterns (a) and H_2–TPR profiles (b) for Ni/AC, Ni/AC–N, Ni/AC–O, Ni/AC–R, and bimetallic NiFe/AC–R catalysts for CO_2 methanation..... 61

Figure 3.3. High-resolution XPS data for Ni $2p_{3/2}$ region collected from Ni/AC, Ni/AC–N, Ni/AC–O, Ni/AC–R, and bimetallic NiFe/AC–R catalysts. Symbols: raw

data; black lines: overall fits; coloured lines: fits of individual components; dashed lines: background. 62

Figure 3.4. Comparison of the catalytic properties of the best Ni catalyst Ni/AC–R and the same promoted by Fe NiFe/AC–R: X_{CO2} and S_{CH4} as a function of temperature (a, b) as well as time-on-stream (TOS) at 450 °C (c). Reaction conditions: P = 1 bar; $WHSV$ = 60 000 mL g^{-1} h^{-1}; CO_2 : H_2 = 1 : 4. 63

Figure 3.5. Low magnification bright field TEM images and selected [110] HRTEM images of single NP of as-synthesized (a) and spent (b) Ni/AC–R catalyst after long time-on-stream CO_2 methanation at 450 °C for 90 h, which evidences the development of core-shell Ni NPs. 64

Figure 3.6. HAADF-STEM image of core-shell NP (left upper panel) and their noise filtered image (right upper panel). The core of the NP is depicted with white arrows. The magnified HAADF-STEM filtered image marked by a white box in the filtered image and the corresponding intensity scan line profile perpendicular to lattice planes direction (double head arrows) confirm different d-spacing and evidence that core is Ni (A) while the shell is NiO (B). 65

Figure 3S.1. Comparison of N_2 adsorption–desorption isotherms measured at −196 °C for the pristine AC, N-doped AC–N, oxidized AC–O and reduced AC–R supporting materials..... 71

Figure 3S.2. High-resolution XPS data for C 1s region (left) and O 1s region (right) for pristine AC, N-doped AC–N, oxidized AC–O and reduced AC–R supporting materials. Symbols: raw data; black lines: overall fits; colored lines: fits of individual components; dashed lines: background. $C_{ar,al}$, C–NH_2: aromatic and aliphatic carbon; COH, CN: hydroxyl groups, CN; C=O: carbonyl groups; COOH: carboxylic groups; $C_{shake\text{-}up}$: plasmon loss. O1: C=O; O2: hydroxyls, ethers and C=O in esters, amides, anhydrides; O3: C–O in esters and anhydrides; O4: carboxylic groups. 73

Figure 3S.3. High-resolution XPS data for N 1s region for AC–N. Symbols: raw data; black lines: overall fits; colored lines: fits of individual components;

dashed lines: background. N-6: Pyridinic groups; N-5: Pyridonic or pyrrolic groups; N-Q: Quaternary groups; N-X: Nitrogen oxides or nitrates. 73

Figure 3S.4. Comparison of N_2 adsorption–desorption isotherms measured at −196 °C for the as-synthesized CO_2 methanation catalysts Ni/AC, Ni/AC–N, Ni/AC–O, Ni/AC–R, and NiFe/AC–R. 74

Figure 3S.5. Low-magnification TEM images of AC (a) Ni/AC (b), Ni/AC–N (c), Ni/AC–O (d), Ni/AC–R (e), and bimetallic NiFe/AC–R catalysts for CO_2 methanation. 75

Figure 3S.6. Comparison of the size distribution of Ni NPs in Ni/AC, Ni/AC–N, Ni/AC–O, Ni/AC–R, and bimetallic NiFe/AC–R, estimated from TEM images. 75

Figure 3S.7. TPD profiles of Ni/AC, Ni/AC–N, Ni/AC–O, Ni/AC–R, and bimetallic NiFe/AC–R, showing the CO (left) and CO_2 (right) evolution. The CO evolution peak was deconvoluted in three peaks: (1) carboxylic anhydrides; (2) phenols; (3) carbonyl/quinones. 76

Figure 3S.8. Thermodynamic equilibrium composition as a function of the temperature. 77

Figure 3S.9. X_{CO2} and S_{CH4} as a function of a prolonged time on stream (90 h) at 450 °C for Ni/AC−R. Reaction conditions: P = 1 bar; $WHSV$ = 60 000 mL g^{-1} h^{-1}; CO_2 : H_2 = 1 : 4. 77

Figure 3S.10. HAADF−STEM images of Ni NPs in as-synthesized Ni/AC–R catalyst, together with elemental maps for Ni, O, C and their mixture. Inset in top panel is the corresponding ED pattern. 79

Figure 3S.11. TEM and HAADF−STEM images of Ni NPs in spent Ni/AC–R catalyst after 90 h on stream experiment, together with elemental maps for Ni, O, C and their mixture. Inset in top panel is the corresponding ED pattern. . 79

Figure 3S.12. Particle size distribution of the Ni NPs in as-synthesized Ni/AC−R and the same catalyst after the long time on stream experiment (90 h), calculated using the TEM images (spent Ni/AC−R). 80

Figure 3S.13. High-resolution XPS data for Ni $2p_{3/2}$ region of as-synthesized Ni/AC−R and the same catalyst after the long time on stream reaction experiment (90 h) (Ni/AC−R spent). 80

Figure 4.1. XRD patterns of the Ni/CNT, and Ni/CNT−N catalysts, indicating the presence of graphitic carbon, metallic Ni and NiO. 92

Figure 4.2. Comparison of the H_2−TPR profiles for Ni/CNT and Ni/CNT−N catalysts. The grey lines are the deconvolution of the peaks. 93

Figure 4.3. Representative low-magnification (a,e) and high-resolution (b,f,g) HAADF−STEM images and Fourier transform (FT) pattern [inset in panel (f)], together with high-resolution (c) ADF−STEM image and the corresponding STEM–EDX O and Ni mixture maps of the Ni/CNT (a–d) and Ni/CNT−N (e–h). 95

Figure 4.4. High-resolution XPS data for the Ni $2p_{3/2}$ region collected from the as-synthesized Ni/CNT and Ni/CNT−N catalysts (top) and after their time-on-stream (TOS) testing for 2 days (bottom). Dots: raw data; black lines: overall fits; colored lines: fits of individual components; dashed lines: background. 96

Figure 4.5. Comparison of the CO_2 conversion X_{CO2} (a) and CH_4 selectivity S_{CH4} (b) as a function of temperature for the Ni/CNT and Ni/CNT−N catalysts. Results of the isothermal TOS testing for 48 h in terms of X_{CO2} (c) and S_{CH4} (d). The thermodynamic equilibrium lines are shown in the graphics and were calculated using a model based on the minimization of Gibbs free-energy of the existing species. Reaction conditions: P = 1 bar; $WHSV$ = 60 000 $cm^3\ g^{-1}\ h^{-1}$; $CO_2 : H_2 = 1 : 4$ 98

Figure 4.6. Representative high-resolution HAADF−STEM images (a,b,d,e,) and Fourier transform (FT) pattern [inset in panel (b)] of the resultant catalyst particles in TOS-tested Ni/CNT (a,b) and Ni/CNT−N (d,e) catalysts, together with the respective STEM−EDX Ni and O mixture maps, confirming the Ni@NiO core-shell nanostructure of the catalyst particles in spent Ni/CNT (c) and Ni/CNT−N (f). 100

Figure 4S.1. Comparison of the CO_2 conversion X_{CO2} (a) and CH_4 selectivity S_{CH4} (b) as a function of temperature for the 5Ni/CNT−N, 15Ni/CNT−N, and 25Ni/CNT−N catalysts with different Ni loadings of 5%, 15% and 25%, respectively. The catalytic data indicate that the optimal loading of Ni onto N-doped CNTs is 15%. The thermodynamic equilibrium curves are shown in the graphics and were calculated using a model based on the minimization of Gibbs free-energy of the existing species. Methanation conditions: P = 1 bar; $WHSV$ = 60 000 $cm^3\ g^{-1}\ h^{-1}$; $CO_2 : H_2 = 1 : 4$ 103

Figure 4S.2. Comparison of N_2 adsorption–desorption isotherms measured for the pristine CNTs and N-doped CNTs supporting materials, as well as for the derivative Ni/CNT and Ni/CNT−N methanation catalysts with 15% Ni loading. 104

Figure 4S.3. Pore size distribution obtained using the non-local density functional theory (NLDFT), where a cylindrical-pore model is assumed, for the pristine CNTs and N-doped CNTs supporting materials, as well as for the derivative Ni/CNT and Ni/ CNT−N methanation catalysts with 15% Ni loading. 104

Figure 4S.4. Representative low-magnification TEM images of the as-synthesized Ni/CNT (a–c) and Ni/CNT−N (d–f) methanation catalysts. 105

Figure 4S.5. Comparison of the catalyst particle size distribution in the as-synthesized Ni/CNT and Ni/CNT−N, estimated by the analysis of the TEM images. 105

Figure 4S.6. Representative low-magnification TEM images of the spent Ni/CNT (a–c) and Ni/CNT−N (d–f) methanation catalysts after their TOS testing for 48 h. 106

Figure 4S.7. Comparison of the catalyst particle size distribution in the spent Ni/CNT and Ni/CNT−N after TOS testing for 48 h, estimated by the analysis of the TEM images. 106

Figure 4S.8. High-resolution XPS data for C 1s region for pristine CNTs and N-doped CNTs, as well as for the as-synthesized and TOS-tested Ni/CNT and

Ni/CNT−N catalysts. Symbols: raw data; black lines: overall fits; colored lines: fits of individual components; dashed lines: background. C1: aromatic and aliphatic carbon; C2: phenols, and CN groups; C3: keto-groups; C4: carboxylic groups; $C_{shake\text{-}up}$: plasmon loss. 107

Figure 4S.9. High-resolution XPS data O 1s region for pristine CNTs and N-doped CNTs, as well as for the as-synthesized and TOS-tested Ni/CNT and Ni/CNT−N catalysts. Symbols: raw data; black lines: overall fits; colored lines: fits of individual components; dashed lines: background. MO: O in metal oxides; O1: C=O; O2: hydroxyls, ethers and C=O in esters, amides, anhydrides; O3: C–O in esters and anhydrides; O4: carboxylic groups. 108

Figure 4S.10. High-resolution XPS data N 1s region for N-doped CNTs, as well as for the as-synthesized and TOS-tested Ni/CNT−N catalysts. Symbols: raw data; black lines: overall fits; colored lines: fits of individual components; dashed lines: background. N-6: pyridinic groups; N-5: pyridonic or pyrrolic groups; N-Q: quaternary groups. 108

Figure 4S.11. Thermogravimetric analysis (TGA) of the Ni/CNT and Ni/CNT−N catalysts until 900 °C with a heating rate of 10 °C min^{-1} under Argon, with an isothermal step of 7 min and a final isothermal step at 900 °C under air for 13 min. 109

Figure 4S.12. Results of the isothermal TOS testing for 90 h in terms of X_{CO2} (a) and S_{CH4} (b) for the Ni/CNT−N catalyst. Methanation conditions: T = 400 °C; P = 1 bar; $WHSV$ = 60 000 $cm^3\ g^{-1}\ h^{-1}$; $CO_2 : H_2$ = 1 : 4 109

Figure 5.1. CO_2 conversion X_{CO2} (a) and CH_4 selectivity S_{CH4} (b) in 200–500 °C temperature range for Ni/C, NiMo/C and NiRe/C catalysts, together with the evolution of X_{CO2} (c) and S_{CH4} (d) during long-term time-on-stream (TOS) testing. Reaction conditions: P = 1 bar; $WHSV$ = 60 000 $cm^3\ g^{-1}\ h^{-1}$; CO_2:H_2 = 1:4 123

Figure 5.2. XRD patterns of the Ni/C, NiMo/C and NiRe/C catalysts, showing the presence of the peaks corresponding to Carbon, Ni and NiO in all catalysts. 125

Figure 5.3. High-resolution XPS data for the Ni $2p_{3/2}$ region collected from as-received and TOS-tested Ni/C (a), NiMo/C (b), and NiRe/C (c) catalysts, together with Mo 3d region collected from NiMo/C (d) and Re 4f region collected from NiRe/C (d). Symbols: raw data; black lines: overall fits; coloured lines: fits of individual components; dashed lines: background. 126

Figure 5.4. HRTEM images of the NPs in Ni/C (a, b), NiMo/C (c, d) and NiRe/C (e, f), evidencing no shell being present over Ni NPs (b) in Ni/C, an epitaxially grown MoO_2 shell with few atomic layers (d), as well as ultrasmall Mo NPs (c) over Ni NPs in NiMo/C; and a carbon shell around Ni NPs (f) in NiRe/C. 128

Figure 5.5. Low magnification bright field TEM images, low magnification HAADF–STEM images and simultaneously acquired STEM–EDX elemental mappings for Ni/C (a), NiMo/C (b), and NiRe/C (c) catalysts. 130

Figure 7.1. Comparison of X_{CO2} (a) and S_{CH4} (b) as a function of reaction temperature, together with the stability testing results in terms of X_{CO2} (c) and S_{CH4} (d) over 90 h TOS of the new Ni/CeO_2 and Ni/ACR-CeO_2 catalysts in comparison with previously reported ceria-free Ni/ACR[2]. The thermodynamic equilibrium curves were calculated using a model based on the minimization of Gibbs free-energy of the existing species. Methanation conditions: P = 1 bar; $WHSV$ = 60 000 $cm^3\ g^{-1}\ h^{-1}$; CO_2 : H_2 (V:V) = 1 : 4.....174

Figure 7.2. High-resolution XPS data for the Ni $2p_{3/2}$ and Ce 3d region collected from as-synthesized and TOS-tested Ni/CeO_2 and Ni/ACR−CeO_2. Symbols: raw data; black lines: overall fits; colored lines: fits of individual components; dashed lines: background. 178

Figure 7.3. TEM images of Ni nanoparticles dispersed on CeO_2 (a) and ACR–CeO_2 (e) supporting materials, together with the representative HRTEM images of Ni and CeO_2 nanoparticles in the Ni/CeO_2 (b,c) and Ni/ACR–CeO_2 (f,g) catalysts. Low-magnification STEM images of the Ni/CeO_2 (d) and Ni/ACR–CeO_2 (h) catalysts, together with the respective STEM–EDX maps for Ni, Ce, O and their mixture. 180

Figure 7.4. HRTEM imaging of the surface of a single Ni nanoparticle in the as-synthesized Ni/ACR–CeO_2 catalyst (a) and zoom-in (white rectangle) image (b) and in the same catalyst after its TOS testing for 90 h (c,d), revealing the core-shell appearance of the nanoparticles. The insets in (b,d) show the FT patterns from the corresponding regions. The white arrows mark the NiO shell and the white arrow heads depict the twinning within the Ni nanoparticles. 182

Figure 7.5. Steady-state *in situ* DRIFTS studies of CO_2 adsorption and methanation over Ni/CeO_2 (a,b) and Ni/ACR–CeO_2 (c,d) catalysts. Experimental conditions for CO_2 adsorption: P = 1 bar; CO_2 flowrate of 2.5 $cm^3\ min^{-1}$; N_2 flowrate of 100 $cm^3\ min^{-1}$; m_{cat} = 15 mg. Experimental conditions of CO_2 methanation: P = 1 bar; CO_2 flowrate of 2.5 $cm^3\ min^{-1}$; 10%H_2/N_2 gas mixture flowrate of 100 $cm^3\ min^{-1}$; m_{cat} = 15 mg. The dashed lines indicate the positions of the observed peaks. 184

Figure 7.6. Phase-resolved spectra of the modulation excitation *in situ* DRIFTS studies conducted for the Ni/CeO_2 catalyst at 250, 300 and 350 °C. Experimental conditions: P = 1 bar; flowrate A: CO_2 = 2.5 $cm^3\ min^{-1}$ and 10% H_2/N_2 = 100 $cm^3\ min^{-1}$; flowrate B: CO_2 = 2.5 $cm^3\ min^{-1}$ and N_2 = 100 $cm^3\ min^{-1}$; m_{cat} = 15 mg. The dashed lines indicate the positions of the peaks. 186

Figure 7.7. Phase-resolved spectra of the modulation excitation *in situ* DRIFTS studies conducted for the Ni/ACR–CeO_2 catalyst at 250, 300 and 350 °C. Experimental conditions: P = 1 bar; flowrate A: CO_2 = 2.5 $cm^3\ min^{-1}$ and 10% H_2/N_2 = 100 $cm^3\ min^{-1}$; flowrate B: CO_2 = 2.5 $cm^3\ min^{-1}$ and N_2 = 100 $cm^3\ min^{-1}$; m_{cat} = 15 mg. The dashed lines indicate the positions of the peaks. 188

Figure 7S.1. Comparison of the CO_2 conversion X_{CO2} (a) and CH_4 selectivity S_{CH4} (b), as a function of temperature for the Ni/ACR–CeO_2 catalysts having different weight percentage ratios of AC−R to CeO_2: 90 : 10, 70 : 30 and 50 : 50. The thermodynamic equilibrium lines are shown in the graphics and were calculated using a model based on the minimization of Gibbs free-energy of

the existing species. Methanation conditions: P = 1 bar; $WHSV$ = 60 000 $cm^3\,g^{-1}\,h^{-1}$; $CO_2 : H_2 = 1 : 4$. 199

Figure 7S.2. Comparison of N_2 adsorption–desorption isotherms measured at −196 °C for the synthesized CeO_2 and ACR–CeO_2 supporting materials, as well as for the respective Ni/CeO_2 and Ni/ACR–CeO_2 catalysts with 15 wt% Ni loading. 199

Figure 7S.3. Comparison of pore size distributions for the synthesized CeO_2 and ACR–CeO_2 supporting materials, as well as for the respective Ni/CeO_2 and Ni/ACR–CeO_2 catalysts with 15 wt% Ni loading..... 200

Figure 7S.4. Comparison of the (a) H_2−TPR profiles for Ni/CeO_2 and Ni/ACR–CeO_2 catalysts, as well as comparison with the (b) H_2−TPR profiles of the catalysts and the respective CeO_2 and ACR–CeO_2 supports. 200

Figure 7S.5 XRD patterns of the CeO_2 and ACR–CeO_2 supporting materials and the respective Ni/CeO_2 and Ni/ACR–CeO_2 catalysts with 15 wt% Ni loading. Bragg reflections corresponding to cubic CeO_2 (ICDD #04-006-1932) and metallic Ni (ICDD #04-016-4761) are marked by * and +, respectively..... 201

Figure 7S.6. High-resolution XPS data for C 1s region for fresh Ni/ACR−CeO_2, and after TOS Ni/ACR−$CeO_{2\,TOS}$. Symbols: raw data; black lines: overall fits; colored lines: fits of individual components; dashed lines: background. $C_{ar,al}$: aromatic and aliphatic carbon; COH: hydroxyl groups; COOH: carboxylic groups; $C_{shake\text{-}up}$: plasmon loss. 202

Figure 7S.7. High-resolution XPS data O 1s region for fresh Ni/CeO_2 and Ni/ACR−CeO_2, and after TOS Ni/$CeO_{2\,TOS}$ and Ni/ACR−$CeO_{2\,TOS}$. Symbols: raw data; black lines: overall fits; colored lines: fits of individual components; dashed lines: background. O1: lattice O species (O^{2-}) binding to Ce^{3+} and Ce^{4+}, O2: surface OH groups, O vacancies in CeO_2; O3: O vacancies in CeO_2, and hydroxyls, ethers and C=O in esters, amides, anhydrides in AC−R; O4: C–O in esters and anhydrides in AC−R; O5: carboxylic groups in AC−R. 202

Figure 7S.8. Comparison of the microstructure and elemental distribution for the TOS tested Ni/$CeO_{2\,TOS}$ and Ni/ACR–$CeO_{2\,TOS}$ catalysts. Showing TEM

images of Ni nanoparticles dispersed on CeO_2 support in $Ni/CeO_{2\ TOS}$ (a), together with the representative HRTEM images of particles (b), and Ni nanoparticles (c) on this sample and STEM-EDX mapping (d); and TEM images TOS tested $Ni/ACR–CeO_{2\ TOS}$ catalyst (e), together with the representative HRTEM images of CeO_2 particles (f), and Ni nanoparticles (g), presenting a carbon shell, on this sample and STEM-EDX mapping (h).....204

Figure 7S.9. Steady-state *in situ* DRIFTS studies of CO_2 adsorption and CO_2 methanation over Ni/CeO_2 (a,b) and $Ni/ACR–CeO_2$ (c,d) catalysts. Experimental conditions for CO_2 adsorption: P = 1 bar; CO_2 flowrate of 2.5 $cm^3\ min^{-1}$; N_2 flowrate of 100 $cm^3\ min^{-1}$; m_{cat} = 15 mg. Experimental conditions for CO_2 methanation: P = 1 bar; CO_2 flowrate of 2.5 $cm^3\ min^{-1}$; 10%H_2/N_2 gas mixture flowrate of 100 $cm^3\ min^{-1}$; m_{cat} = 15 mg. 205

Figure 7S.10. Phase-resolved spectra of the modulation excitation *in situ* DRIFTS studies for Ni/CeO_2 conducted at 250, 300 and 350 °C. Experiment conditions: P = 1 bar; flowrate A: CO_2 = 2.5 $cm^3\ min^{-1}$ and N_2 = 100 $cm^3\ min^{-1}$; flowrate B: CO_2 = 2.5 $cm^3\ min^{-1}$ and 10% H_2/N_2 = 100 $cm^3\ min^{-1}$; m_{cat} = 15 mg. The dashed lines indicate the peak positions.....206

Figure 7S.11. Phase-resolved spectra of the modulation excitation *in situ* DRIFTS studies for $Ni/ACR–CeO_2$ conducted at 250, 300 and 350 °C. Experiment conditions: P = 1 bar; flowrate A: CO_2 = 2.5 $cm^3\ min^{-1}$ and N_2 = 100 $cm^3\ min^{-1}$; flowrate B: CO_2 = 2.5 $cm^3\ min^{-1}$ and 10% H_2/N_2 = 100 $cm^3\ min^{-1}$; m_{cat} = 15 mg. The dashed lines indicate the peak positions.....206

Figure 7S.12. Phase-resolved spectra of the modulation excitation *in situ* DRIFTS studies for pure CeO_2 supporting material conducted at 250, 300 and 350 °C. Experiment conditions: P = 1 bar; flowrate A: CO_2 = 2.5 $cm^3\ min^{-1}$ and N_2 = 100 $cm^3\ min^{-1}$; flowrate B: CO_2 = 2.5 $cm^3\ min^{-1}$ and 10% H_2/N_2 = 100 $cm^3\ min^{-1}$; m_{cat} = 15 mg. The dashed lines indicate the peak positions.....206

Figure 7S.13. Phase-resolved spectra of the modulation excitation *in situ* DRIFTS studies for the composite $ACR–CeO_2$ supporting material conducted

at 250, 300 and 350 °C. Experiment conditions: P = 1 bar; flowrate A: CO_2 = 2.5 cm^3 min^{-1} and N_2 = 100 cm^3 min^{-1}; flowrate B: CO_2 = 2.5 cm^3 min^{-1} and 10% H_2/N_2 = 100 cm^3 min^{-1}; m_{cat} = 15 mg. The dashed lines indicate the peak positions. 207

Figure 8.1. Comparison of the CO_2 conversion (X_{CO2}) as a function of the optimal temperature ($T_{optimal}$) for the topmost performing catalysts…….217

List of Tables

Table 1.1. Industrial Power to gas Projects (Adapted from [22]). 8

Table 1.2. Comparison of monometallic and multimetallic catalysts in CO_2 methanation in terms of conversion of CO_2 (X_{CO2}) and selectivity to methane (S_{CH4}). 14

Table 3.1. Textural properties, mean Ni NPs diameter (d_p), TPD, and H_2-chemisorption results of the as-synthesized Ni-based CO_2 methanation catalysts Ni/AC, Ni/AC–N, Ni/AC–O, Ni/AC–R, and NiFe/AC–R, together with pH_{PZC} of the respective support (AC, AC–N, AC–O and AC–R). 59

Table 3S.1. Elemental composition and textural properties of pristine AC and as-synthesized AC–N, AC–O and AC–R. 71

Table 3S.2. Surface elemental composition of pristine AC and synthesized AC–N, AC–O, and AC–R supporting materials, determined by XPS. 72

Table 3S.3. Relative percentage of each peak, corresponding to the different groups ((1) carboxylic anhydrides, (2) phenols, and (3) carbonyl/quinones) in the CO evolution graphic. 76

Table 3S.4. Relative atomic percentage (at%) of Ni^0, NiO and $Ni(OH)_2$ phases in as-synthesized Ni/ AC−R and the same catalyst after the long time on stream experiment (90 h) (spent Ni/AC−R), as estimated by XPS analysis. 80

Table 4.1. Selected textural, morphological and catalytic properties (T_{50} – temperature at which the sample reaches 50% X_{CO2} and $Y_{CH4,MAX}$ – maximum methane yield) for pristine CNT, synthesized N-doped CNT as well as Ni/CNT and Ni/CNT−N catalysts for CO_2 methanation. 92

Table 4.2. Comparison of the catalytic performance in terms X_{CO2}, S_{CH4}, and activity (r) for Ni/CNT and Ni/CNT−N catalysts at 400 °C and 430 °C, together with the temperature at which the sample reaches 50% X_{CO2} (T_{50}) and the maximum methane yield ($Y_{CH4,MAX}$), that occurs at 430 °C and 400 °C for Ni/CNT and Ni/CNT−N, respectively. 97

Table 4S.1. Elemental composition of pristine CNT and the synthesized CNT−N. 109

Table 4S.2. Relative atomic percentage (at%) of Ni^0 and Ni^{2+} in the as-synthesized and TOS-tested Ni/CNT and Ni/CNT−N catalysts, as quantified by XPS analysis. 110

Table 4S.3. Relative atomic percentage (at%) of C, N, and O in the CNT and CNT−N supports, as well as the as-synthesized and TOS-tested Ni/CNT and Ni/CNT−N catalysts, as quantified by XPS analysis. 110

Table 4S.4. Comparison of the catalytic properties of the catalysts of the present work (Ni/CNT and Ni/CNT−N) with similar catalysts already reported in the literature, including the conditions used in the catalytic system and the reaction experiment in each case. 110

Table 5.1. Textural properties, H_2 uptake, mean nanoparticle diameter, temperature at which X_{CO2} = 50% (T_{50}), and maximum X_{CO2} for Ni/C, NiMo/C and NiRe/C catalysts 122

Table 5.2. XPS relative atomic percentage (at%) of Ni^0 and Ni^{2+} from Ni $2p_{3/2}$ spectra, Mo^0, Mo^{4+} and Mo^{6+} from Mo 3d spectra and Re^0, Re^{4+} and Re^{7+} from Re 4f spectra in Ni/C, NiMo/C and NiRe/C catalysts and after their TOS testing. 127

Table 5S.1. Elemental composition of ECS (Engineered Catalyst Support™) carbon supporting material from Pajarito Powder 137

Table 5S.2. XPS atomic percentage (at%) of Ni^0, Ni^{2+} and O from metal oxide in Ni/C, NiMo/C and NiRe/C catalysts and the same catalyst after TOS testing. 138

Table 7.1. Textural properties [specific surface area (S_{BET}), and total pore volume (V_p)], average size of CeO_2 crystallites ($d_{c,CeO2}$), and Ni crystallites ($d_{c,Ni}$), metallic Ni surface area (S_M), temperature at which X_{CO2} = 50% (T_{50}), and maximum X_{CO2}, attained at 450 °C for Ni/ACR[2] and 370 °C for Ni/CeO_2 and Ni/ACR−CeO_2 176

Table 7.2. Assignment of the bands observed during steady-state DRIFTS and ME–PSD–DRIFTS experiments: hydroxyl groups (OH^-), gaseous methane (CH_4), gaseous carbon dioxide (CO_2), bridged carbon monoxide (br−CO), formyl groups (CHO), bi-dentate carbonates (b−CO_3), poly-dentate carbonates (p−CO_3), formates (HCOO), carboxylate ($CO_2^{-\delta}$), and methoxy groups (OCH_3). 185

Table 7S.1. Binding energies (BE) and assignment of the peaks positions identified in C 1s, O 1s, Ni 2p and Ce 3d spectra of fresh Ni/CeO_2 and Ni/ACR−CeO_2, and after TOS Ni/$CeO_{2\ TOS}$ and Ni/ACR−$CeO_{2\ TOS}$. 203

Table 7S.2. Relative atomic percentage (at%) of Ni^0, Ni^{2+}, Ce^{3+}, and Ce^{4+} phases, determined by XPS, in fresh Ni/CeO_2 and Ni/ACR−CeO_2, and after TOS Ni/$CeO_{2\ TOS}$ and Ni/ACR−$CeO_{2\ TOS}$. 204

List of Abbreviation and Variables

AC – activated carbon

a_m – area of the cross section of a molecule of adsorbate

At% - atomic percentage

BE – binding energy

BET – Brunauer-Emmett-Teller

BJH – Barrett–Joyner–Halenda

CCS – carbon capture and storage

CCU – carbon capture and utilization

CNT – carbon nanotubes

CX – carbon xerogel

d_c – crystallite diameter

DRIFTS – Diffuse reflectance infrared Fourier transform spectroscopy

ED – electron diffraction

EDX – energy-dispersive X-ray spectroscopy

EPR – electron paramagnetic resonance

ETEM – environmental transmission electron microscopy

EU – European Union

f – fugacity at the operating conditions

f^0 – fugacity at the standard state

$F_{CO2,in}$ – molar flowrate of CO_2 in the inlet gas flow,

$F_{CO2,out}$ – molar flowrate of CO_2 in the outlet gas flow

$F_{CH4,out}$ – molar flowrate of CH_4 in the outlet gas flow

$F_{CO,out}$ – molar flowrate of CO in the outlet gas flow

FT – Fourier transform

FU – functional unit: Utilization of 1 kg hydrogen for CO_2-based processes

G_0 – standard Gibbs free energy

G_s – Gibbs free energy of solid carbon at the operating conditions

G^t – Gibbs energy

GHG – greenhouse gases

HAADF−STEM – high-angle annular dark-field scanning transmission electron microscopy

HP-STM – high-pressure scanning tunnelling microscopy

ICDD – International Centre for Diffraction Data

IFT – inverse Fourier transform

IR – infrared spectroscopy

K – Scherrer constant

LCA – life cycle assessment

m_{cat} – catalyst mass

ME–PSD–DRIFTS – modulation-excitation – phase-sensitive-detection Diffuse reflectance infrared Fourier transform spectroscopy

MS – mass spectrometer

MWCNT – multi walled carbon nanotubes

N – Avogadro's number

n – number of metal atoms

n^a – total amount of adsorbed gas

n^a_m – monolayer capacity

NLDFT – non-local density functional theory method

NMR – nuclear magnetic resonance

NP – nanoparticle

n_s – number of atoms in the surface per unit of area

P – Pressure

P_a – atmospheric pressure

pH_{PZC} – pH at point of zero charge

PSD – Phase sensitive detection

PtG – Power to Gas

PtX – Power to X

R – ideal gas constant

S_{BET} – specific surface area

S_{CH4} – selectivity to CH_4

S_{CO} – selectivity to CO

S_M – metallic surface area

S_{meso} – mesopore surface area

STEM – scanning transmission electron microscopy

SWCNT – single walled carbon nanotubes

T - temperature

T_{50} – temperature at which X_{CO2} = 50% is attained

TCD – thermal conductivity detector

TGA – thermogravimetric analysis

TEM – transmission electron microscopy

TOS – time on stream

TPD – Temperature programmed desorption

TPR – Temperature programmed reduction

UV-Vis – ultraviolet–visible spectroscopy

V_{ads} – amount of vapor adsorbed at relative pressure close to unity P/P_0 = 0.95

V_{liq} – volume of liquid adsorbate

V_M – molar volume

V_{micro} – micropore volume

V_P – specific pore volume

$WHSV$ – weight hourly space velocity

X_{CO2} – CO_2 conversion

XPS – X-ray photoelectron spectroscopy

XRD – X-Ray diffraction

Y_{CH4} – yield in CH_4

Y_{CO} – yield in CO

β – full width at half maximum (FWHM)

λ – X-ray wavelength

ϕ_k^{PSD} – modulation phase angle

φ – phase delay

θ – Bragg angle

ω – angular modulation frequency

Chapter 1

Motivation, State of the art, Objectives and Thesis Outline

Motivation

1. Carbon dioxide – A greenhouse gas

Carbon dioxide (CO_2) is considered the main contributor to the greenhouse effect and consequently one of the major causes of global warming; thus, it is well known that action should be taken in order to reduce its emissions to the atmosphere before we reach the known warming limit of 2 °C relative to pre-industrial levels [1].

The concentration of this greenhouse gas (GHG) in the atmosphere has risen from ca. 280 ppm before the industrial revolution to ca. 403 ppm in 2016 [2,3]. Interestingly, the global CO_2 emissions declined by 5.8% in 2020 due to the pandemic. Nonetheless, despite this decline, the CO_2 average annual concentration in the atmosphere in 2020 was 412.5 ppm, around 50% higher than before the industrial revolution [4].

Interestingly, this increase in the emissions of carbon dioxide is attributed to the high consumption of carbon-based fuels for transport and energy production, which is expected to increase in the future – CO_2 emissions from energy account for the largest share of global anthropogenic GHG emissions, representing about 43.9% of global emissions [5]. It can be observed in Figure 1.1 that the major contributor to the world CO_2 emissions is the energy sector, being responsible for 43.9% of the emissions in 2019, followed by the transport sector, responsible for 25.7% of the emissions [5]. In the case of Portugal, the energy sector is also among the major responsible sectors (ca. 30%); however, it presents similar values as the industry and transport sectors (25−28%), in 2019 [9].

These facts lead to two important points that are going to be discussed herein: (i) the actual concern of transitioning from a fossil fuel-based energy society to a society more based on renewable energy resources, and (ii) the major concern in recent years in trying to develop carbon-neutral closed cycles as an attempt to reduce these emissions[2,3,6–8].

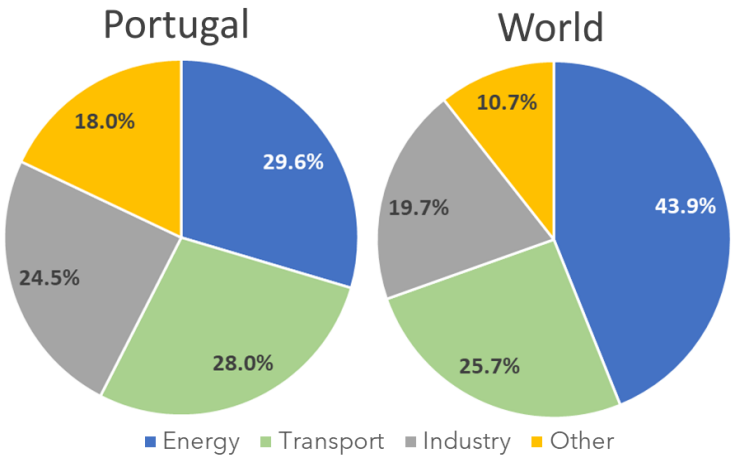

Figure 1.1. World and Portuguese CO_2 emissions from fuel combustion by sector, 2019 [5,9].

In the last decades, the European Union (EU) have made efforts to decrease the CO_2 emissions by (i) promoting the use of renewable energy sources, (ii) implementing measures of energy saving, and (iii) developing carbon capture and storage (CCS) projects. This fact led to the rapid development of CCS technologies, which is now an efficient and relatively well-established method for CO_2 capture; however, in the developed technologies, the main options for the CO_2 storage are geological and ocean storage, meaning that, in this case, the carbon cycle is not closed and the consequences for the geosphere in the long term may not be controllable. On the contrary, in the carbon capture and utilization (CCU) technologies, which have only received large attention in the recent years, the captured CO_2 is used as a carbon source to produce bulk chemicals, fuels, and materials [6–8,10]. Therefore, the CCU technologies appear as a way to develop carbon-neutral closed cycles since, for example, the CO_2 emitted by fuel consumption can be used to produce new fuels. On the other hand, CCU technologies are also a key role in the transition from fossil fuel to renewable-based energy sources since they can present a way to store the intermittent energy from renewable energy sources, which will be discussed in the following section.

2. Carbon dioxide capture and utilization

Carbon dioxide capture is a process in which CO_2 from point emitting (localized) industrial and energy related sources is captured and separated

from the other flue gases in order to avoid its disposal in the atmosphere [8,11]. It is worth to refer that localized CO_2 sources account for 70% of the total CO_2 emissions to the atmosphere [12]. Specifically, combustion systems from industrial or energy production plants are the main contributors to the anthropogenic CO_2 emissions; thus, the development of CO_2 capture technologies is of extreme importance [11].

CO_2 is emitted during combustion and the type of combustion process influences the type of CO_2 capture technology to be used. Basically, there are three main approaches for CO_2 capture (Figure 1.2): (i) as a pure or almost pure CO_2 stream (pre-combustion separation, oxyfuel combustion or chemical looping combustion); (ii) by concentration of the discharge from an industrial stream to a pure or almost pure CO_2 stream (Post-combustion separation); or (iii) direct capture from air into a pure CO_2 stream [11,13].

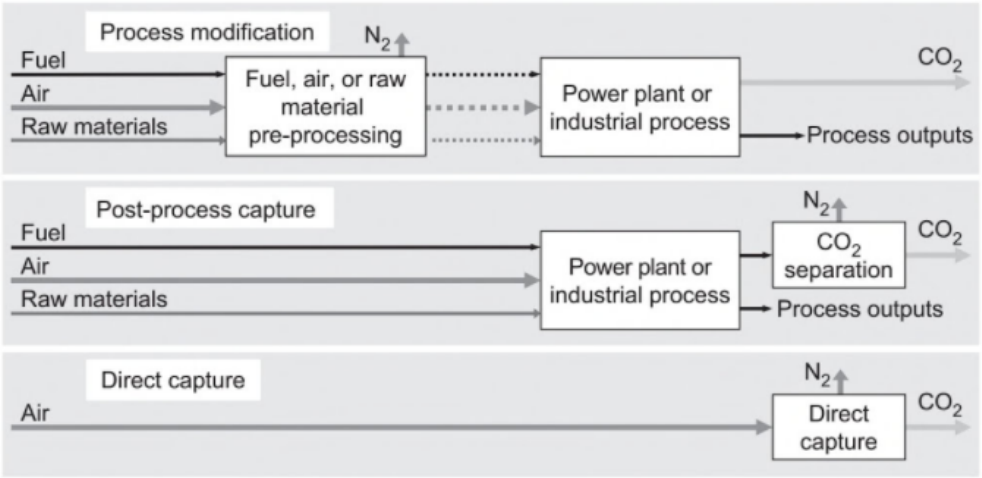

Figure 1.2. Main approaches for CO_2 capture [13].

As referred before, after the capture process, the captured CO_2 can be either stored or valorized by being used as a carbon source – specifically, CO_2 can be used as C_1 building block for bulk chemicals, polymers, materials, and fuels, which, besides avoiding its emission to the atmosphere, adds value to this molecule [14–16].

CO_2 utilization, or as commonly referred to, conversion can be performed through three different main approaches: (i) chemical conversion (thermocatalytic, electrochemical, and photocatalytic), (ii) enzymatic

conversion and (iii) technological utilization [17,18]. Each of these approaches presents its advantages and disadvantages, but herein the focus will be given to the chemical conversion of CO_2.

In theory, the chemical conversion of CO_2 to either chemicals or fuels can be achieved through the use of renewable energy sources either to supply the energy demanded for electrochemical conversion, to achieve the high temperatures required for thermocatalytic processes, or even to produce the hydrogen (through water electrolysis) needed for the thermocatalytic hydrogenation of CO_2. On the one hand, this approach results in a carbon-neutral industrial process, and, on the other hand, it can store renewable energy in the form of a liquid or gaseous fuel.

Interestingly, a recent life cycle assessment (LCA) study [19] demonstrated that a reduction in environmental impacts is achieved with the production of carbon monoxide, methanol, and methane if hydrogen is supplied by water electrolysis with renewable electricity. Even though formic acid production gives the highest environmental impact reductions (11.8 to 12.6 kg CO_2-eq per FU[1]), the CO_2-based methane production process is also a viable option in terms of impact reduction, as it presents a global warming impact that varies from 7.7–8.9 kg CO_2-eq.

Importantly, methane is an interesting product for CO_2 conversion technologies since it is considered a fundamental element of modern economies. It is an energy carrier of significant importance to the industry, energy, and transportation sectors worldwide. Additionally, it owns a developed distribution infrastructure in several countries, allowing its efficient distribution, meaning that the methane produced through CO_2 hydrogenation can be directly injected into the existing gas grids and distributed efficiently.

[1] FU – functional unit: Utilization of 1 kg hydrogen for CO_2-based processes

3. Power-to-Gas (PtG) Technology

As previously mentioned, the attempt to reduce fossil fuel consumption has led to the consequent effort to increase renewable energy utilization; however, the renewable energy sources present mismatches between demand and supply since their production is intermittent. This fact leads to the need to find a solution to store this energy and balance these mismatches to avoid losing the produced energy.

Therefore, the store of this energy in the form of liquid or gaseous fuels emerges as an interesting approach since the present solutions with storage devices such as batteries cannot be scaled-up in order to be used for an entire electrical system [20]. Specifically, the Power-to-Gas (PtG) technology (Figure 1.3) uses the electricity produced through renewable sources to produce H_2 through water electrolysis. The H_2 itself can be injected into the existing gas grids; however, regulations in the different countries limit the amount of H_2 that can be injected into the gas grid to 0−12% vol [21]. On the other hand, a different approach on PtG technologies is to further convert this H_2 to methane by the hydrogenation of CO_2 from point emitting sources.

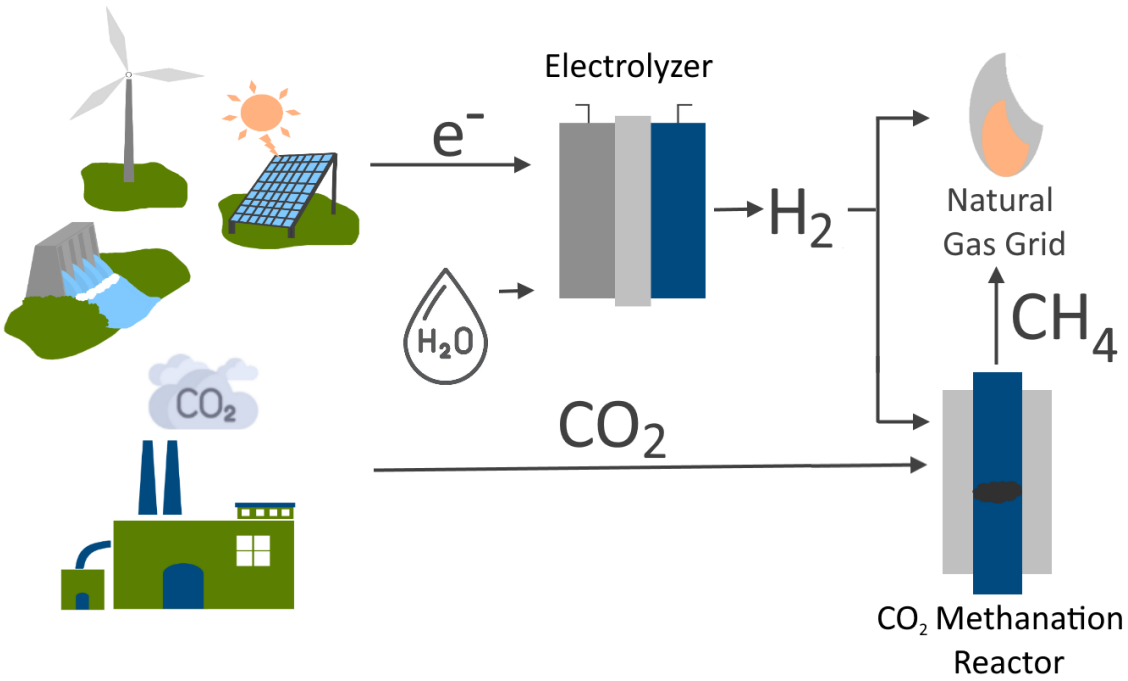

Figure 1.3. Schematic representation of the Power-to-Gas (PtG) technology.

In this case, methane can also be injected into the gas grid, but without the H_2 limitations, and also, it can be used, for example, in transportation in natural gas motors [22,23]. Even though CO_2 methanation is a widely studied reaction, comprehensive studies on the reaction mechanisms and key steps that control the activity and selectivity using *in situ* techniques at experimental reaction conditions are still limited [24]; thus, there is the need to perform additional studies on this area.

Interestingly, the first pilot projects of PtG were launched between 2004 and 2009, although the first pilot project of Power-to-Methane with catalytic methanation was launched later in 2009 in Germany [25]. Several European countries are investing in Power to X (PtX) projects, being X the possible products of the facilities, and Figure 1.4 shows the PtX projects in Europe, between 2016 and 2020, and planned for 2021–2025 [26]. It is evident that Germany has demonstrated the highest capacity over the past five years, and it is expected to increase in the next five years. Additionally, several other countries, such as France, the Netherlands, Belgium, and Denmark are planning to increase their capacities in PtX technologies over the next 5 years.

Table 1.1 describes some examples of existing industrial Power to gas projects, and some technical aspects of the methanation reaction, showing that this process requires high temperatures and pressures.

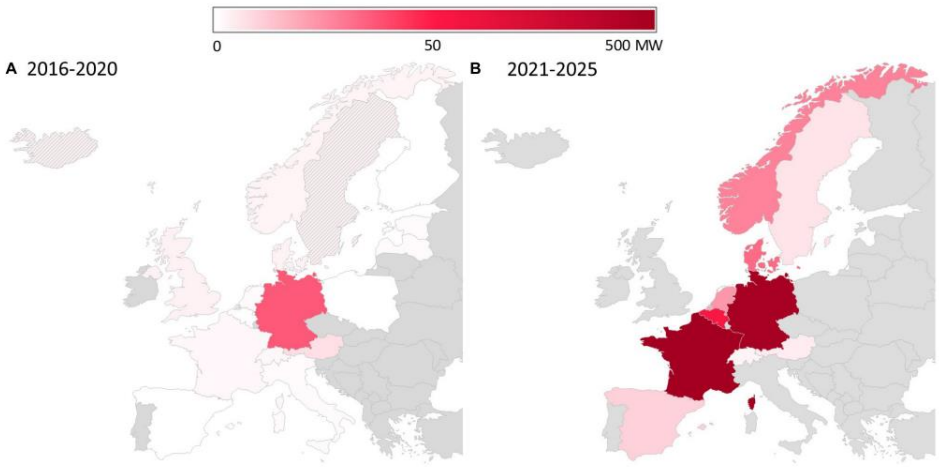

Figure 1.4. Capacities of Power-to-X projects in Europe, (A) between 2016 and 2020, (B) planned for 2021–2025 [26].

Table 1.1. Industrial Power to gas Projects (Adapted from [22]).

Project Name	*Location*	*Period*	*Methanation Conditions*			*Reference*
			Reactor type	Temperature (°C)	Pressure (bar)	
Audi e-gas	Germany	2013	Isothermal fixed bed	--	--	[27,28]
HELMETH	N/A	2014−2017	--	300	30	[29,30]
Technical assumptions, technology demonstration and results P2G project	Netherlands	2013−2015	Fixed Bed	150−700	8−15	[31,32]
CO_2 recycling via reaction with hydrogen	US	2009	Fixed Bed	300−350	--	[33,34]
CO_2 Conversion to Methane Project	Thailand	2012−2016	Fixed Bed	200	--	[35,36]
EE-Methane from CO_2	Austria	2013−2016	Honeycomb	<350	1−20	[37,38]

4. CO_2 methanation reaction

CO_2 methanation, also called Sabatier reaction (1), since it was first reported by Paul Sabatier, is the hydrogenation of CO_2 to CH_4 [39]. This reaction is exothermic; thus, thermodynamically, high CO_2 conversion (X_{CO2}) values can be obtained at relatively low temperatures (25 – 400 °C), with selectivity to CH_4 (S_{CH4}) close to 100% at stoichiometric flow composition of CO_2:H_2 = 1:4 (Figure 1.5). However, at temperatures higher than 400 °C, the X_{CO2} decreases as the increased energy input shifts the equilibrium to favor the reverse reaction, as it is demonstrated in Figure 1.5. Furthermore, as the temperature rises above 450 °C, the formation of CO starts to appear due to the reverse water gas shift reaction (2).

$$CO_2 + 4H_2 \leftrightarrow CH_4 + 2H_2O \qquad \Delta H_{298K} = -165\ kJ\ mol^{-1} \qquad (1)$$

$$CO_2 + H_2 \leftrightarrow CO + H_2O \qquad \Delta H_{298K} = +40.6\ kJ\ mol^{-1} \qquad (2)$$

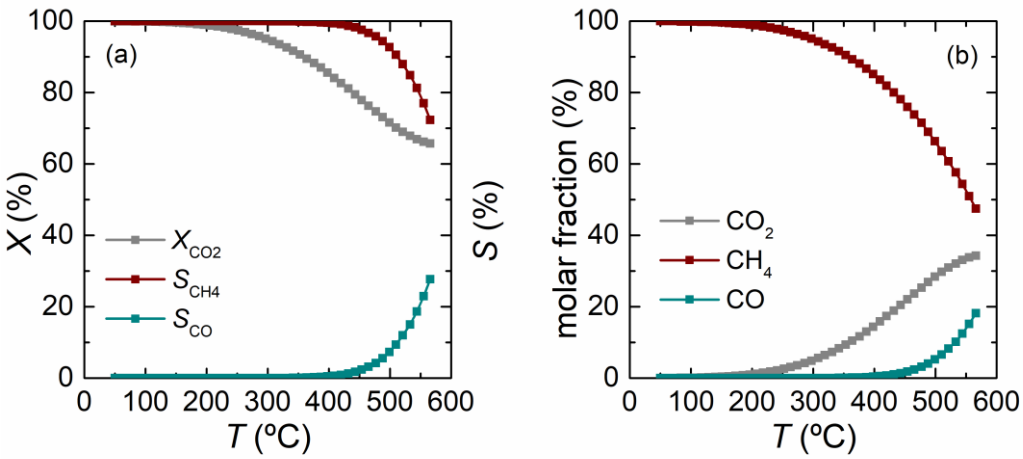

Figure 1.5. CO_2 conversion (X_{CO2}), and CH_4 (S_{CH4}) and CO (S_{CO}) selectivities at the thermodynamic equilibrium (a), together with molar composition of CO_2, CH_4 and CO at the thermodynamic equilibrium (b). The thermodynamic equilibrium values were calculated using a model based on the minimization of Gibbs free energy of the existing species, with a CO_2:H_2 ratio of 1:4, P = 1 bar (See Chapter 2 (5)).

Despite being a thermodynamically favorable reaction, the Sabatier reaction has significant kinetic barriers since the reduction of the fully oxidized carbon to methane is an eight-electron process, requiring a catalyst to reduce reaction barriers and to achieve considerable activity and selectivity [40]. Importantly, the catalysts require a high activation temperature; thus, taking into consideration the thermodynamic equilibrium results, it is important to optimize the reaction conditions and use a catalyst in order to be able to operate at temperatures that allow for an optimal X_{CO2} with increased S_{CH4}.

4.1. CO_2 methanation catalysts

Several studies have been conducted on metal-based catalysts for CO_2 methanation, and many group VIII transition metals, such as Co [41–43], Ni [44-55], Ru [56–58], Rh [59,60] and Pd [61,62] have been found to be active.

The activity and selectivity of the different metals have been ordered, based on previous research works, and the activity of these metals follows the order [63]:

Ru > Rh > Ni > Fe > Co > Os > Pt > Ir > Mo > Pd > Ag > Au

while the selectivity was found to decrease in the following order [63]:

Pd > Pt > Ir > Ni > Rh > Co > Fe > Ru > Mo > Ag > Au.

Even though Ni is not the most active or selective metal, supported Ni-based catalysts are the most commonly used, owing to its good combination of activity, selectivity and price [44-55]. However, there is still plenty of room for improvement since it is still difficult to achieve high CO_2 conversion at low temperatures with Ni catalysts due to the high activation energy [44]. Furthermore, Ni catalysts also feature low stability at higher temperatures due to sintering of the catalyst nanoparticles, degradation via formation of volatile $Ni(CO)_4$, and coke build-up on active Ni sites under severe reaction conditions [64,65].

Nonetheless, the active phase of a metal catalyst is not the only important factor to take into consideration when selecting a good catalyst. The support used can significantly influence the activity and selectivity of the catalysts, as it can have different properties that can affect the performance, such as pore size [66], structure [42,67], surface chemistry [68] and metal-support interaction (MSI) [69,70].

Different supports have been tested, mainly metal oxides, such as Al_2O_3, SiO_2 and TiO_2 [44]. Recently, new types of supports are being tested, such as zeolites [45], carbon nanofiber-reinforced foams [71], and metal-organic frameworks [46], for example.

Still, despite the large number of catalysts studied, most of the available commercial catalysts are Ni/Al_2O_3 based [47], since they can achieve high selectivities and activities. However, these good performances are only achieved with high Ni loads on the catalysts, relatively high temperatures, or high H_2:CO_2 ratios, which leaves plenty of room for further improvement [48–50]. Interestingly, the use of supports with different properties is an interesting toolbox to try to solve this problem, obtaining catalysts capable of operating with lower metal loads, lower temperatures, and lower H_2:CO_2 ratios.

For example, Cheng *et al.* [72] demonstrated that Ni supported on rice husk ash (RHA) achieved better methane selectivity than silica-supported catalysts, due to the stronger MSI. Furthermore, Aziz *et al.* [67] demonstrated that the methanation activity increased with an increase in the basic sites of the support by testing γ-Al_2O_3, SiO_2, protonated Y zeolite (HY), MCM-41 and mesostructured silica nanoparticles (MSN) as supports. Also, the ability of the support to adsorb CO_2 was found to be crucial in the performance of the catalyst in a study performed by Pandey and Deo [73] in Ni-Fe catalysts using Nb_2O_5, SiO_2, TiO_2, ZrO_2 and Al_2O_3 as supports. They demonstrated that Nb_2O_5 achieved the highest yield to methane.

Regarding carbon materials, they have been less extensively tested as supporting material for this reaction, since a study in 1985 from Guerrero-Ruiz [74] demonstrated that supporting Ni on saran carbon reduces CH_4 selectivity by

increasing CO selectivity compared to bulk Ni. Furthermore, it is believed that carbon materials present lower thermal stability than metal oxides. However, recent studies have been proving that carbon materials are in fact interesting options. For example, Wang *et al.* [75] compared Ni-supported on multiwalled carbon nanotubes (CNTs) with Al_2O_3 and obtained better results with the CNTs, which were attributed to the extent of reduction of Ni that was higher on CNT-supported catalysts. However, these results were only good in the initial stage of the reaction. Nevertheless, the stability, as well as the activity of the catalyst, were increased by introducing ceria on the CNTs surface.

Interestingly, the particle size of the metal phase is extremely important to the behavior of the catalyst. Millet *et al.* [76] recently reported the successful synthesis of single atom Ni catalysts for CO_2 activation. They demonstrated that single atom Ni catalysts were active for the activation of CO_2; however, their selectivity was restricted to CO. Meanwhile, with the formation of Ni clusters with few nanometers, the formation of CH_4 was observed. This study concluded that to catalyze multielectron reactions, the formation of Ni clusters is needed; it obtained insights on the differences in reactivity regimes that occur before and after particle formation[76].

Another approach for tailoring the catalyst performance for CO_2 methanation is the addition of promoters. Hu *et al.* [77] and Fan *et al.* [78] demonstrated that MgO as promoter was capable of increasing carbon resistance and thermal stability of alumina-supported Ni catalysts. Cobalt was studied as promoter by Wang *et al*. [79] to modify the surface structure of Mo catalysts in order to improve the sulfur resistance. CeO_2-doped Ni/Al_2O_3 catalysts were studied by Liu *et al.* [80] and showed higher reducibility and stability. Other promoters like La_2O_3 and V_2O_3 were also found to improve the performance of Ni catalysts [81,82]. However, for example, in the case of potassium, Campbell and Falconer [83] demonstrated that its effect depended on the support used: on $Ni/SiO\text{-}Al_2O_3$ catalyst, potassium at low coverage increased the rate for CO_2 hydrogenation with only small amounts of C_2 hydrocarbons produced. However, on Ni/SiO_2 catalyst, potassium rapidly decreased the hydrogenation rate.

Besides the use of different supports or promoters to try to increase the performance of metallic catalysts, the addition of a second metal is also an interesting approach.

Bimetallic catalysts can exhibit higher catalytic activity than monometallic ones, since the interaction between two metal surfaces can change the electronic and geometric structure of the catalyst, increasing its activity [84].

Table 1.2 presents some examples of comparisons between multimetallic catalysts and their monometallic counterparts. For example, Ocampo *et al.* [85] reported a synergetic effect of Ni with Ru and Rh that enabled an improvement in activity and catalyst lifetime, when compared with the monometallic Ni catalyst. They attributed these improvements to a better Ni dispersion induced by Ru or Rh promotion, which enhanced the Ni^0 surface/volume ratio. Ren *et al.* [55] compared the addition of Co, Cu and Fe to Ni/ZrO_2 catalysts and concluded that Fe is a better second metal to add to this catalyst than Co or Cu. They claimed that the strong electron-donating ability of Fe^{2+} promoted the reduction of both Ni and ZrO_2, leading to higher Ni dispersion and sufficient reduction of NiO, which produced more active sites on the catalyst surface to adsorb H_2. Additionally, the partial reduction of the ZrO_2 support promoted the CO_2 dissociation at lower temperatures. Other works demonstrated that the addition of Fe improves the dispersion and reduction degree of Ni, improving the catalyst activity and stability on CO_2 methanation [53,55,86].

Table 1.2. Comparison of monometallic and multimetallic catalysts in CO_2 methanation in terms of conversion of CO_2 (X_{CO2}) and selectivity to methane (S_{CH4}).

T (°C)	*P* (bar)	Reactor used	Monometallic catalysts	X_{CO2} (%)	S_{CH4} (%)	Multimetallic catalysts	X_{CO2} (%)	S_{CH4} (%)	Ref
125	2	Fixed-bed tubular flow microreactor	1 wt% Ni/AC	0	--	1 wt% Ni/AC + 1 wt% Rh/Al_2O_3	8	100	[87]
350-400	1	Fixed-bed tubular reactor	Ni/CDC	≈25	≈20	Ni-Ce/CDC Ni-Mg/CDC Ni-Mg-Ce/CDC	78 70 ≈80	100 100 100	[88]
450	1	Fixed-bed reactor	Pd/SiO_2 Ni/SiO_2 Mg/SiO_2	40.8 36.8 0.8	10.4 81.8 10.3	$Pd-Fe/SiO_2$ $Pd-Ni/SiO_2$ $Pd-Mg/SiO_2$	44.7 50.5 59.2	2.8 89 95	[61]
400	1	Fixed-bed reactor	Rh/Al_2O_3	55	94	$Rh-K/Al_2O_3$ $Rh-Ba/Al_2O_3$	25 43	0 95	[89]
380	1	Fixed-bed reactor	Ni/Al_2O_3-HT	82	99.2	$K-Ni/Al_2O_3$-HT	86	99.8	[90]
400	1	Fixed-bed down-flow reactor	$5Ni/CeO_2/ZrO_2$	71.5	98.5	$5Ni-0.5Rh/CeO_2/ZrO_2$	77.8	99.2	[85]
250	1	Down-flow tubular reactor	Fe/Al_2O_3	11.4	96.5	$Fe-Ni/Al_2O_3$	22.1	99.5	[91]
250	5	High pressure fixed-bed reactor	Ni/ZrO_2	90	90	$Co-Ni/ZrO_2$ $Fe-Ni/ZrO_2$ $Cu-Ni/ZrO_2$	93 96 50	90 92 70	[55]

4.2. CO_2 methanation mechanism

Although CO_2 methanation is an extensively studied reaction, the reaction mechanism is still under debate, and there is no consent with respect to the intermediates of the reaction. However, the proposed mechanisms can be grouped in two different categories: (A) the associative pathway, and (B) the dissociative pathway (Figure 1.6).

In the proposed associative pathway, CO_2 is molecularly adsorbed associatively with a H atom previously adsorbed on the surface, forming formate as an intermediate, i.e., without CO formation.[92]

Regarding the dissociative pathway, the CO_2 is dissociated into CO, which acts as the main intermediate; the way that the C-O bond is broken after that is also subject of discussion: it can be either associative (assisted by an adsorbed H atom) or it can occur in a dissociative scheme, directly on the catalyst surface [63,92]

The reaction pathway is highly dependent on the catalytic system, as it depends on the active metal and support used, as well as on their interactions. However, the discrepancies between proposed reaction mechanisms on similar catalytic systems can be attributed to different reaction conditions used [63,92].

Westermann *et al.* [45] reported that the CO route was followed in the catalytic system of Ni supported on USY zeolites, while Solis-Garcia *et al.* [93] proposed the formate route as the pathway for CO_2 methanation in ZrO_2 supported Ni catalysts. Regarding Ru based catalysts, Akamaru et al. [94] proposed, with density functional theory (DFT) calculations, that the reaction mechanism on a Ru/TiO_2 system was dissociative, forming CO as intermediate, which was proved by isotopic and infrared experiments [94,95]. However, Prairie et al. [96] observed from diffuse reflectance infrared Fourier transform spectroscopy (DRIFTS) that, over Ru/Al_2O_3 and Ru/TiO_2 catalysts, formate was formed on the support, and carbonyl on Ru and Ru-oxide sites.

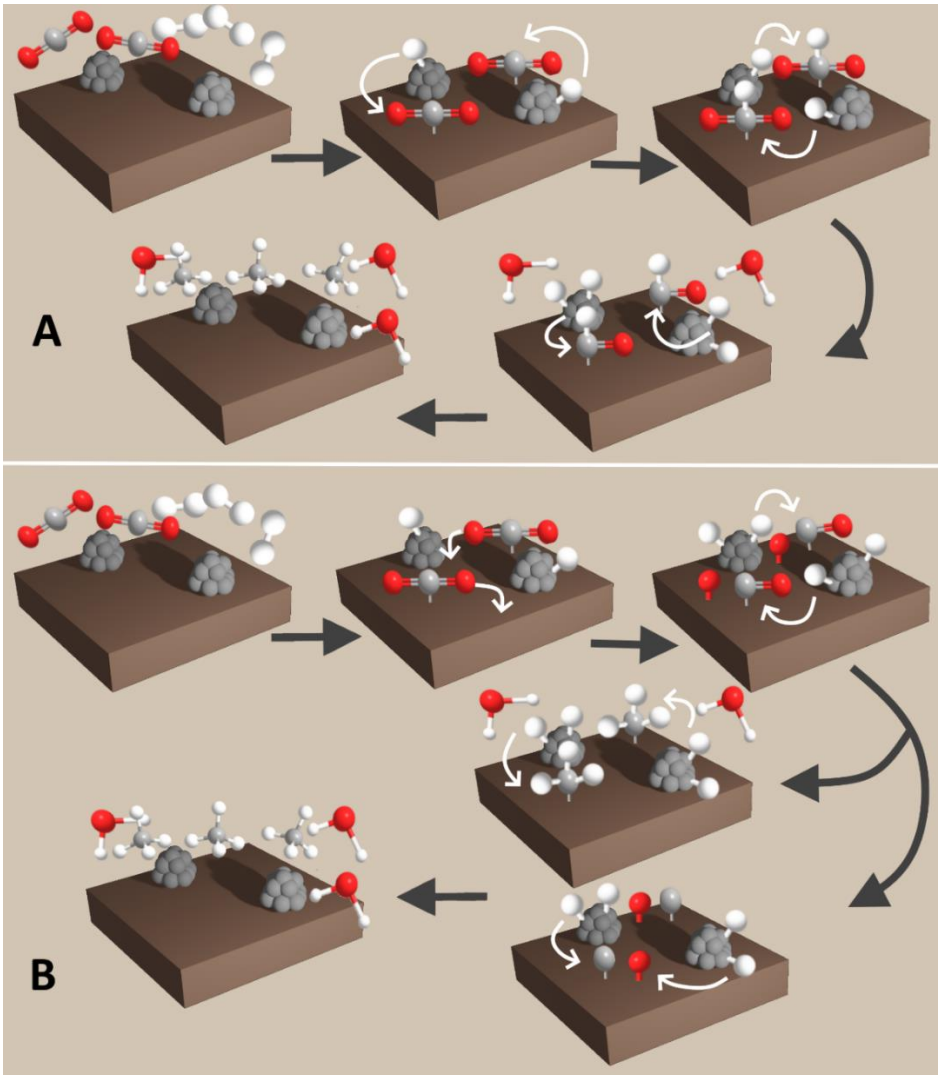

Figure 1.6. CO_2 associative (A) and dissociative (B) methanation scheme.

5. Carbon Materials as Catalyst supports

Carbon materials have been used in the last years for diversified areas of application, such as gas separation, water and air purification, fuel cells, adsorption and catalysis. These materials possess interesting properties that are advantageous for their use as catalyst supports. Their high surface area, high pore volume, good mechanical and thermal stability, and the fact that it is possible to modify their surface chemistry, are fundamental properties that make carbon attractive supporting material in catalysis [97]. Besides the textural properties, the nature of the surface groups of these materials is also important. Based on the application, they can be easily modified through chemical and/or thermal treatments, as it is explained below.

5.1 Activated carbon

Activated carbon (AC) is a class of carbon materials widely used as adsorbents and catalyst supports or as catalysts by themselves, due to their large surface areas and well-developed porous structures, comprised of hydrophobic graphene layers and hydrophilic surface functional groups [97,98].

This material is produced by chemical or physical activation of vegetable or mineral matter: the chemical activation is performed by low temperature (400−700 °C) carbonization of the material in the presence of a dehydrating agent ($ZnCl_2$, KOH or H_3PO_4, for example), while the physical activation is performed, usually at high temperatures (600−900 °C), by the carbonization of the carbon precursor followed by the activation of the obtained charcoal with oxidation gases, such as CO_2 or H_2O [97,98].

Activated carbon has specific surface areas in the range of 500−1500 $m^2\ g^{-1}$, which can vary, based on different factors, such as nature of the raw material and type of activation. They are mainly composed of micropores; however, the pore size distribution (proportion of micro, meso- and macropores) can also vary with the precursor and synthesis method [97,98].

5.2 Carbon nanotubes

Carbon nanotubes (CNTs), another class of carbon materials, have exceptional mechanical and electronic properties, which make them suitable for numerous applications, such as polymer reinforcements for composites, energy storage, electronics, and catalysis. Also, it has been shown that when used in catalysis, these conductive supports demonstrate clear differences with respect to activated carbon. CNTs can be divided in two classes: single-wall nanotubes (SWNTs), with surface areas between 400 and 900 $m^2\,g^{-1}$ and multi-wall nanotubes (MWNTs), with surface areas between 200 and 400 $m^2\,g^{-1}$. This class of carbon materials presents advantages compared to activated carbon, since CNTs do not exhibit microporosity, which prevents the intraparticle diffusional

limitations and also, they display excellent thermal and electronic conductivity [99,100].

5.3 Carbon xerogels

Carbon xerogels (CXs) also have good properties that make them suitable as catalysts supports. They have high surface areas, between 400 and 1200 $m^2 g^{-1}$, high porosity, high density (0.6−0.8 g cm^{-3}), good conductivity, a controllable pore size that can be tuned during synthesis and also, they can be prepared in the desired form (i.e., monoliths, thin-film or powder) [101]. These materials are prepared by sol-gel polycondensation of benzene derivatives (phenol, catechol, resorcinol, hydroquinone) and aldehydes (formaldehyde and furfural) in a solvent, followed by drying and carbonization. The most common precursors are resorcinol and formaldehyde, using water as solvent and sodium hydroxide as catalyst [102,103].

Furthermore, it is possible to prepare carbon xerogels with nitrogen in their structure by introducing a nitrogen precursor in the organic xerogel. As it will be explained later, the presence of nitrogen on the structure of the carbon material can be important for the desired application [104]. However, the introduction of nitrogen grants an additional challenge: the porous structure of the materials has to be maintained after the carbonization treatment; thus, the precursor used has to be present in the formation of the xerogel structure through the polycondensation of resorcinol and formaldehyde [104].

5.4 Modification of surface chemistry of the carbon materials

Carbon materials have the advantage that it is possible to modify their surface chemistry in order to tailor their properties for the desired application. When used as supports for heterogeneous catalysts, the role of surface modification on the final metal dispersion has been clearly demonstrated [99].

As referred before, carbon materials have been studied only to some extent as supports for CO_2 methanation catalysts. Multiwalled CNTs, when used as Ni

support, allow a higher reduction of Ni than Al_2O_3 [75]. Also, the mixture of Rh/γ-Al_2O_3 and Ni/AC catalysts prepared separately shows a significant collaborative catalytic effect in the methanation of CO_2 due to the synergy between the good adsorption of CO_2 by Rh/γ-Al_2O_3 and the efficient adsorption of hydrogen by Ni/AC [87]. If carbon materials are to be used as supports for CO_2 methanation, studies on the influence of their surface properties on the reaction performance should be performed, since the surface chemistry can be modified to satisfy the requirements for the catalytic performance.

Due to the acidic role of CO_2 (weak Lewis acid), it is expected that the introduction of Lewis bases onto the carbon surfaces may favor the CO_2 capture performance of these materials [105]. It has also been shown that the introduction of nitrogen groups into the carbon surface can increase the CO_2 adsorption capacity of activated carbons [105]. The treatment with nitrogen precursors with thermal treatments at temperatures higher than 600 °C can result in an increase in quaternary nitrogen, pyridinic, and pyrrole-type structures, which are considered basic; specifically, the N-groups incorporated in the graphene structure provide additional electrons, which increases the basicity of the material [97,106]. Figure 1.7 describes the N-groups that can be incorporated on the surface of the carbon materials.

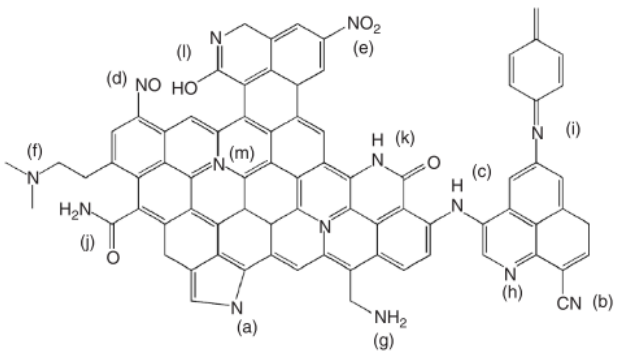

Figure 1.7. Types of nitrogen-containing functionalities on the carbon materials: (a) pyrrole-like group; (b) nitrile; (c) secondary amine; (d) nitro group; (e) nitroso group; (f) tertiary (g) amine; (h) pyridine-like group; (i) imine; (j) amide; (k) lactam; (l) pyridone; (m) quaternary amine [97].

Oxygen basic groups can also be formed on the surface of the carbon materials (Figure 1.8). In this case, the nature of the oxygen groups can be either basic or acidic. It has been demonstrated that gas phase oxidation of activated carbon is capable of increasing mainly the concentration of carbonyl and hydroxyl groups, which have a neutral to basic nature, which, as referred before, can enhance the CO_2 coverage of the material [97,107]. On the other hand, the introduction of acidic groups (e.g., carboxylic acid, lactone, phenol groups) on the surface of the material, which can be performed through the oxidation in liquid phase, can have beneficial effects on the catalyst preparation, since the increase of the acidity of the surface leads to an enhancement on the adsorption capacity for the metal ions, increasing the dispersion of the metal phase [108].

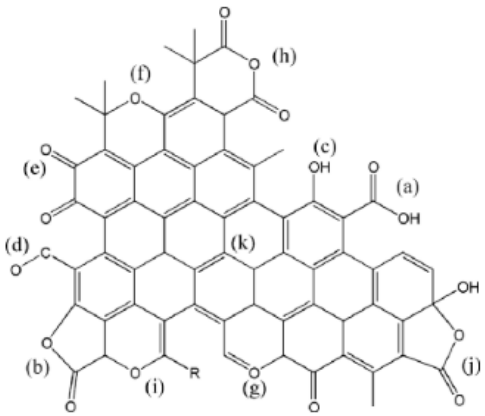

Figure 1.8. Acidic and basic oxygen-containing functionalities of carbon surface: (a) carboxyl groups, (b) lactone, (c) hydroxyl, (d) carbonyl, (e) quinone, (f) ether, (g) pyrone, (h) carboxylic anhydride, (i) chromene, (j) lactol, and (k) π electron density on carbon basal planes [97].

6. *In situ* characterization

The elucidation of the mechanisms involved in a catalytic reaction and the characterization of active sites under the reactive conditions is of great interest since it allows to obtain and understand structural information of the functioning active sites. Traditionally, the development of new catalysts to be used in industry is based on empirical testing of different materials; however, recently, the use of *in situ* studies has been recognized with increasing interest for the development of new catalysts [109].

In situ studies, such as ambient pressure *in situ* X-ray photoelectron spectroscopy (XPS), *in situ* transmission electron microscopy (TEM), and *in situ* spectroscopic methods (infrared spectroscopy (IR), nuclear magnetic resonance (NMR), electron paramagnetic resonance (EPR) and ultraviolet–visible spectroscopy (UV-Vis)) are among the techniques that can be used to obtain comprehensive knowledge on the catalyst behavior and on the intermediate species present under reaction conditions [109].

For example, *in situ* XPS studies of the catalysts allow to establish correlations between the catalytic activity and the electronic state of the active sites on the surface of the catalyst through the clarification of the chemical composition and electronic structure of the catalyst. *In situ* IR spectroscopy can be used to understand the reaction intermediates and the formation mechanism of active centers and their in-depth structural description. *In situ* TEM allows the investigation of the changes in the catalyst morphology during reaction, responsible, for example, for the catalyst deactivation [110].

In particular, the *in situ* diffuse reflectance infrared fourier transform spectroscopy (DRIFTS) is a technique widely used to understand the reaction mechanism in heterogeneous catalysis since it allows the investigation of the adsorbed species on the catalysts under reaction conditions. However, this technique presents drawbacks since it detects not only the intermediate species, but also the sample's background, noise and the spectator species, making it difficult to separate and understand which are the real intermediates of the reaction [111,112]. Furthermore, the intermediate species are short living, making it even more difficult to differentiate them from the remaining species present under steady-state conditions. Interestingly, the Modulation-Excitation (ME) technique appears as a possible solution to overcome this problem since it is based on the introduction of a rapid periodic perturbation on the system to which only the intermediate species of the reaction respond. The resultant spectroscopic signal is usually analyzed by phase sensitive detection (PSD) technique in order to enhance the signal-to-noise ratio and extract information

about intermediate species that respond to the modulation signal, avoiding the spectator species signal [111–116].

Additionally, imaging of catalysts with a spatial resolution down to ca. 1 Å is nowadays possible, with the developments achieved in transmission electron microscopy (TEM) and scanning transmission electron microscopy (STEM). The major *in situ*/operando techniques for catalyst structure identification are high-pressure scanning tunnelling microscopy (HP-STM) and environmental transmission electron microscopy (ETEM) [117–120].

Objectives and Thesis Outline

The main goal of the present thesis is the development of novel efficient and stable catalysts for the CO_2 methanation reaction. The proposed approach for the design of efficient catalysts is based on the investigation and understanding of the catalysts' supporting material. Thus, the focus was placed on the extraordinary properties of carbon materials, including their high surface area, high porosity and, importantly, tunable surface properties and developed Ni-based catalysts with tuned properties. Therefore, several catalytic materials were prepared, characterized, and tested in a laboratory scale CO_2 methanation reactor setup. Furthermore, *in situ* studies on the developed materials were performed to gather properties-performance insights on the synthesized materials. The thesis is organized in 8 Chapters, as follows:

Chapter 1 describes the motivation of the work, where the major concerns and available technologies that lead to the present work are identified, as well as a state-of-the-art review about CO_2 methanation reaction, catalysts and also carbon materials as catalyst supports. At the end of the chapter, the Objectives and Thesis Outline are presented, where the main goals of the thesis are described, together with a description of the thesis organization. In Chapter 2, the experimental techniques used in this work are described in detail.

Chapters 3−7 are based on published or submitted articles:

- Chapter 3 addresses the tuning of the surface properties of activated carbon as catalyst support for Ni based catalysts, including the study on monometallic and bimetallic Ni-Fe catalysts.

  Gonçalves, L. P. L.; Sousa, J. P. S.; Soares, O. S. G. P.; Bondarchuk, O.; Lebedev, O. I.; Kolen'ko, Y. V.; Pereira, M. F. R. *The Role of Surface Properties in CO_2 Methanation over Carbon-Supported Ni Catalysts and Their Promotion by Fe*. Catal. Sci. Technol. **2020**, 10 (21), 7217

  In this work, I was responsible for the materials' synthesis, characterization (including some of the TEM experiments), and catalytic evaluation, as well as for the writing of the original manuscript.

- Chapter 4 describes the property performance insights on Ni catalysts supported on pristine CNT and N-doped CNT on CO_2 methanation.

  Gonçalves, L. P. L.; Meledina, M.; Meledin, A.; Petrovykh, D. Y.; Sousa, J. P. S.; Soares, O. S. G. P.; Kolen'ko, Y. V.; Pereira, M. F. R. *Understanding the importance of N-doping for CNT-supported Ni catalysts for CO_2 methanation*. Carbon **2022**, 195, 35-43.

  In this work, I was responsible for the materials' synthesis, characterization (including some of the TEM experiments), and catalytic evaluation, as well as for the writing of the original manuscript.

- Chapter 5 presents the opportunity of using commercial carbon-based electrocatalysts as catalysts for CO_2 methanation, based on the previous findings regarding the enhanced performance of carbon materials as supports for this reaction.[121]

  Gonçalves, L. P. L.; Serov, A.; McCool, G.; Dicome, M.; Sousa, J. P. S.; Soares, O. S. G. P.; Bondarchuk, O.; Petrovykh, D. Y.; Lebedev, O. I.; Pereira, M. F. R.; Kolen'ko, Y. *New Opportunity for Carbon-Supported Ni-based Electrocatalysts: Gas-phase CO_2 Methanation*. ChemCatChem **2021**, 13, 1–11

In this work, I was responsible for the materials' characterization (including TEM), catalytic evaluation, as well as for the writing of the original manuscript.

- Chapter 6 focuses on the microstructural transformations that the catalyst present in Chapter 3 undergoes under catalytic reaction in an attempt to understand the behavior of the catalyst under reaction conditions.

MacArthur, K. E.; Basak, S.; Gonçalves, L. P. L.; Sousa, J. P. S.; Soares, O. S. G. P.; Pereira; M. F. R.; Eichel, R. A.; Kolen'ko, Yu. V. *In situ study of CO_2 methanation over carbon-supported Ni nanoparticles: formation and role of a NiO shell*. Submitted. **2022**.

In this work, I was responsible for the materials' synthesis, the writing of the introduction and part of the discussion in the original manuscript, as well as for the mechanism scheme conception.

- Chapter 7 presents a detailed *in situ* DRIFTS study on two different catalysts, which led to the hypothesis of a possible mechanism for the reaction on the developed catalysts.

Gonçalves, L. P. L.; Mielby, J.; Soares, O. S. G. P.; Sousa, J. P. S.; Petrovykh, D. Y.; Lebedev, O. I.; Pereira, M. F. R.; Kegnæs, S.; Kolen'ko, Yu. V. *In situ investigation of the CO_2 methanation on carbon/ceria-supported Ni catalysts using modulation-excitation DRIFTS.* Appl. Catal. B Environ. **2022**, 312, 121376.

In this work, I was responsible for the materials' synthesis, ex situ characterization (including TEM), catalytic evaluation, and in situ studies, as well as for the writing of the original manuscript.

Finally, Chapter 8 explains the main conclusions of the work, together with suggestions for future work.

It is worth to refer that the work was started by trying to develop new catalysts based on Covalent Organic Frameworks (COFs), a new type of materials that has been explored in the recent years; however, the thermal stability of these materials hindered their use for the CO_2 methanation reaction. Nonetheless,

this fact encouraged us to perform a stability study on this material to understand which type of applications it could be used for, which led to a publication that is in preparation. And also, in a partnership with the Technical University of Denmark, we performed a study on this material for a different catalytic application that led to a published article (Gonçalves, L. P. L.; Christensen, D. B.; Meledina, M.; Salonen, L. M.; Petrovykh, D. Y.; Carbó-Argibay, E.; Sousa, J. P. S.; Soares, O. S. G. P.; Pereira, M. F. R.; Kegnæs, S.; Kolen'ko, Y. V. *Selective Formic Acid Dehydrogenation at Low Temperature over a RuO_2/COF Pre-Catalyst Synthesized on the Gram Scale*. Catal. Sci. Technol. **2020**, 10 (7), 1991–1995).[122]

References

(1) Rogelj, J.; Schaeffer, M.; Friedlingstein, P.; Gillett, N. P.; Van Vuuren, D. P.; Riahi, K.; Allen, M.; Knutti, R. Differences between Carbon Budget Estimates Unravelled. *Nat. Clim. Chang.* **2016**, *6* (3), 245–252. https://doi.org/10.1038/nclimate2868.

(2) International Energy Agency. CO_2 Emissions from Fuel Combustion: Overview. *IEA Stat.* **2017**, 14.

(3) Rahman, F. A.; Aziz, M. M. A.; Saidur, R.; Bakar, W. A. W. A.; Hainin, M. R.; Putrajaya, R.; Hassan, N. A. Pollution to Solution: Capture and Sequestration of Carbon Dioxide (CO_2) and Its Utilization as a Renewable Energy Source for a Sustainable Future. *Renew. Sustain. Energy Rev.* **2017**, *71* (January), 112–126. https://doi.org/10.1016/j.rser.2017.01.011.

(4) Interntional energy agency. Global Energy Review 2021 - CO_2 emissions https://www.iea.org/reports/global-energy-review-2021/co2-emissions (accessed Dec 10, 2021).

(5) International Energy Agency. Greenhouse Gas Emissions from Energy: Overview https://www.iea.org/reports/greenhouse-gas-emissions-from-energy-overview/emissions-by-sector (accessed Dec 9, 2021).

(6) Wang, W.; Wang, S.; Ma, X.; Gong, J. Recent Advances in Catalytic Hydrogenation of Carbon Dioxide. *Chem. Soc. Rev.* **2011**, *40* (7), 3703. https://doi.org/10.1039/c1cs15008a.

(7) Baraj, E.; Vagaský, S.; Hlinčik, T.; Ciahotný, K.; Tekáč, V. Reaction Mechanisms of Carbon Dioxide Methanation. *Chem. Pap.* **2016**, *70* (4), 395–403. https://doi.org/10.1515/chempap-2015-0216.

(8) Zhang, J.; Sewell, C. D.; Huang, H.; Lin, Z. Closing the Anthropogenic Chemical Carbon Cycle toward a Sustainable Future via CO_2 Valorization. *Adv. Energy Mater.* **2021**, 2102767. https://doi.org/10.1002/aenm.202102767.

(9) Agência Portuguesa do Ambiente. Emissões de Gases com Efeito de Estufa https://rea.apambiente.pt/content/greenhouse-gas-emissions?language=en (accessed Dec 9, 2021).

(10) Patricio, J.; Angelis-Dimakis, A.; Castillo-Castillo, A.; Kalmykova, Y.; Rosado, L. Region Prioritization for the Development of Carbon Capture and Utilization Technologies. *J. CO_2 Util.* **2017**, *17*, 50–59. https://doi.org/10.1016/j.jcou.2016.10.002.

(11) Intergovernmental Panel on Climate Change. *Carbon Dioxide Capture and Storage*; 2005.

(12) Vogt, C.; Monai, M.; Kramer, G. J.; Weckhuysen, B. M. The Renaissance of the Sabatier Reaction and Its Applications on Earth and in Space. *Nat. Catal.* **2019**, *2* (3), 188–197. https://doi.org/10.1038/s41929-019-0244-4.

(13) Rackley, S. A. *Carbon Capture and Storage*; Elsevier Science, 2017.

(14) Olajire, A. A. Valorization of Greenhouse Carbon Dioxide Emissions into Value-Added Products by Catalytic Processes. *J. CO_2 Util.* **2013**, *3–4*, 74–92. https://doi.org/10.1016/j.jcou.2013.10.004.

(15) Prieto, G. Carbon Dioxide Hydrogenation into Higher Hydrocarbons and Oxygenates: Thermodynamic and Kinetic Bounds and Progress with Heterogeneous and Homogeneous Catalysis. *ChemSusChem* **2017**, *10* (6), 1056–1070. https://doi.org/10.1002/cssc.201601591.

(16) Yang, H.; Zhang, C.; Gao, P.; Wang, H.; Li, X.; Zhong, L.; Wei, W.; Sun, Y. A Review of the Catalytic Hydrogenation of Carbon Dioxide into Value-Added Hydrocarbons. *Catal. Sci. Technol.* **2017**, *7* (20), 4580–4598. https://doi.org/10.1039/C7CY01403A.

(17) Zheng, Y.; Zhang, W.; Li, Y.; Chen, J.; Yu, B.; Wang, J.; Zhang, L.; Zhang, J. Energy Related CO_2 conversion and Utilization: Advanced Materials/Nanomaterials, Reaction Mechanisms and Technologies. *Nano Energy* **2017**, *40* (April), 512–539. https://doi.org/10.1016/j.nanoen.2017.08.049.

(18) Saravanan, A.; Senthil Kumar, P.; Vo, D. V. N.; Jeevanantham, S.; Bhuvaneswari, V.; Anantha Narayanan, V.; Yaashikaa, P. R.; Swetha, S.; Reshma, B. A Comprehensive Review on Different Approaches for CO_2 Utilization and Conversion Pathways. *Chem. Eng. Sci.* **2021**, *236*, 116515. https://doi.org/10.1016/j.ces.2021.116515.

(19) Sternberg, A.; Jens, C. M.; Bardow, A. Life Cycle Assessment of CO_2-Based C1-Chemicals. **2017**, 2244–2259. https://doi.org/10.1039/c6gc02852g.

(20) Schlögl, R. Renewable Energy Put the Sun in the Tank:Future Developments in Sustainable Energy Systems. **2019**, *58*, 43–348. https://doi.org/10.1002/ange.201808799.

(21) Götz, M.; Lefebvre, J.; Mörs, F.; McDaniel Koch, A.; Graf, F.; Bajohr, S.; Reimert, R.; Kolb, T. Renewable Power-to-Gas: A Technological and Economic Review. *Renew. Energy* **2016**, *85*, 1371–1390. https://doi.org/10.1016/j.renene.2015.07.066.

(22) Bailera, M.; Lisbona, P.; Romeo, L. M.; Espatolero, S. Power to Gas Projects Review: Lab, Pilot and Demo Plants for Storing Renewable Energy and CO_2. *Renew. Sustain. Energy Rev.* **2017**, *69* (November 2016), 292–312. https://doi.org/10.1016/j.rser.2016.11.130.

(23) Schaaf, T.; Grünig, J.; Schuster, M. R.; Rothenfluh, T.; Orth, A. Methanation of CO_2 - Storage of Renewable Energy in a Gas Distribution System. *Energy. Sustain. Soc.* **2014**, *4* (1), 1–14. https://doi.org/10.1186/s13705-014-0029-1.

(24) Kattel, S.; Liu, P.; Chen, J. G. Tuning Selectivity of CO_2 Hydrogenation Reactions at the Metal/Oxide Interface. *J. Am. Chem. Soc.* **2017**, *139* (29), 9739–9754. https://doi.org/10.1021/jacs.7b05362.

(25) Ajanovic, A.; Haas, R. On the Long-Term Prospects of Power-to-Gas Technologies. **2019**, No. April 2018, 1–16. https://doi.org/10.1002/wene.318.

(26) Wulf, C.; Zapp, P.; Schreiber, A. Review of Power-to-X Demonstration Projects in Europe. *Front. Energy Res.* **2020**, *8* (September), 1–12. https://doi.org/10.3389/fenrg.2020.00191.

(27) Otten, R. The First Industrial PtG Plant - Audi e-Gas as Driver for the Energy Turnaround. *CEDEC Gas Day 2014* **2014**, No. May.

(28) Rieke, S. Catalytic Methanation – the Audi e-Gas Project as an Example of Industrialized Technology for Power to Gas. In *REGATEC 2015*; **2015**.

(29) *Programme Review Report 2014 - Fuel Cells and Hydrogen Joint Undertaking*; 2015. https://doi.org/10.2843/443072.

(30) Landgraf, M. Power to Gas: Storing the Wind and Sun in Natural Gas. *Karlsruhe: Press Release - Karlsruhe Institute of Technology*. **2014**.

(31) Holstein, J.; Vlap, H.; Steen, A. van der; Grond, L.; Bos, K. Experiences with One Year Operation of Power-to-Gas in Rozenburg, NL. In *Conference Proceedings of the 2nd International Conference on Renewable Energy Gas Technology, Barcelona, Spain: Renewable Energy Technology International AB*; **2015**.

(32) Vlap, H.; Steen, A. van der; Knijp, J.; Holstein, J.; Grond, L. *Power-to-Gas Project in Rozenburg, The Netherlands (Report No.; GCS.15.R24613, Rev. 0). DNV GL Oil & Gas*; **2015**.

(33) Hoekman, S. K.; Broch, A.; Robbins, C.; Purcell, R. CO_2 Recycling by Reaction with Renewably-Generated Hydrogen. *Int. J. Greenh. Gas Control* **2010**, *4* (1), 44–50. https://doi.org/https://doi.org/10.1016/j.ijggc.2009.09.012.

(34) Robbins, C.; Hoekman, S.; Broch, A. CO_2 Recycling by Reaction with Renewable- Generated Hydrogen. In *NHA Conference, Desert Research Institute*; **2009**.

(35) Weerawong, A. CO_2 Conversion to Methane Project. In *PTT Exploration and Production PCL*; **2015**.

(36) Demonstration of a New CO_2-Methanation Process. *Chem Eng* **2014**, *121*, 16.

(37) Biegger, P.; Felder, A. H.; Lehner, M. Entwicklung Eines Katalytischen Prozesses Zur Methanisierung von CO_2 Aus Industriellen Quellen. *Chemie Ing. Tech.* **2014**, *86* (9), 1430–1431. https://doi.org/https://doi.org/10.1002/cite.201450250.

(38) Biegger, P.; Felder, A.; Lehner, M. Methan Als Speicher Für Erneuerbare Energien Und Zur CO_2-Verwertung. In *DepoTech 2014 - Abfallwirtschaft, Abfallverwertung und Recycling, Deponietechnik und Altlasten*; **2014**.

(39) Sabatier, P., & Senderens, J. B. Nouvelles Synthèses Du Mèthane. *Comptes Rendus Hebd. des Séances l'Académie des Sci.* **1902**, *134*, 514–516.

(40) Wang, W.; Gong, J. Methanation of Carbon Dioxide: An Overview. *Front. Chem. Eng. China* **2011**, *5* (1), 2–10. https://doi.org/10.1007/s11705-010-0528-3.

(41) Janlamool, J.; Praserthdam, P. Ti-Si Composite Oxide-Supported Cobalt Catalysts for CO_2 Hydrogenation. *J. Nat. Gas Chem.* **2011**, *20* (5), 558–564. https://doi.org/10.1016/S1003-9953(10)60213-7.

(42) Zhou, G.; Wu, T.; Xie, H.; Zheng, X. Effects of Structure on the Carbon Dioxide Methanation Performance of Co-Based Catalysts. *Int. J. Hydrogen Energy* **2013**, *38* (24), 10012−10018. https://doi.org/10.1016/j.ijhydene.2013.05.130.

(43) Xie, H.; Feng, Y. Carbon Dioxide Methanation on Ordered Mesoporous Co/KIT-6 Catalyst. *Chem. Eng. Comm.* **2014**, *201*, 233–240. https://doi.org/10.1080/00986445.2013.766881.

(44) Rönsch, S.; Schneider, J.; Matthischke, S.; Schlüter, M.; Götz, M.; Lefebvre, J.; Prabhakaran, P.; Bajohr, S. Review on Methanation - From Fundamentals to Current Projects. *Fuel* **2016**, *166*, 276–296. https://doi.org/10.1016/j.fuel.2015.10.111.

(45) Westermann, A.; Azambre, B.; Bacariza, M. C.; Graça, I.; Ribeiro, M. F.; Lopes, J. M.; Henriques, C. Insight into CO_2 Methanation Mechanism over NiUSY Zeolites: An Operando IR Study. *Appl. Catal. B Environ.* **2015**, *174*−*175*, 120−125. https://doi.org/10.1016/j.apcatb.2015.02.026.

(46) Zhen, W.; Li, B.; Lu, G.; Ma, J. Enhancing Catalytic Activity and Stability for CO_2 Methanation on Ni@MOF-5 via Control of Active Species Dispersion. *Chem. Commun.* **2015**, *51*, 1728−1731. https://doi.org/10.1039/C4CC08733J.

(47) Garbarino, G.; Riani, P.; Magistri, L.; Busca, G. A Study of the Methanation of Carbon Dioxide on Ni/Al_2O_3 Catalysts at Atmospheric Pressure. *Int. J. Hydrogen Energy* **2014**, *39* (22), 11557−11565. https://doi.org/10.1016/j.ijhydene.2014.05.111.

(48) Rahmani, S.; Rezaei, M.; Meshkani, F. Preparation of Promoted Nickel Catalysts Supported on Mesoporous Nanocrystalline Gamma Alumina for Carbon Dioxide Methanation Reaction. *J. Ind. Eng. Chem.* **2014**, *20* (6), 4176–4182. https://doi.org/10.1016/j.jiec.2014.01.017.

(49) Shashidhara, G. M.; Ravindram, M. A Kinetic Study of the Methanation of CO_2 over $Ni\text{-}Al_2O_3$ Catalyst. *React. Kinet. Catal. Lett.* **1988**, *37* (2), 451–456.

(50) Jia, C.; Gao, J.; Li, J.; Gu, F.; Xu, G.; Zhong, Z.; Su, F. Nickel Catalysts Supported on Calcium Titanate for Enhanced CO Methanation. *Catal. Sci. Technol.* **2013**, *3* (2), 490–499. https://doi.org/10.1039/C2CY20542D.

(51) Chang, F.-W.; Tsay, M.-T.; Liang, S.-P. Hydrogenation of CO_2 over Nickel Catalysts Supported on Rice Husk Ash Prepared by Ion Exchange. *Appl. Catal. A Gen.* **2001**, *209* (1), 217–227. https://doi.org/10.1016/S0926-860X(00)00772-9.

(52) Chang, F.; Kuo, M.; Tsay, M.; Hsieh, M. Hydrogenation of CO_2 over Nickel Catalysts on Rice Husk Ash-Alumina Prepared by Incipient Wetness Impregnation. *Appl. Catal. A Gen.* **2003**, *247*, 309–320. https://doi.org/10.1016/S0926-860X(03)00181-9.

(53) Hwang, S.; Hong, U. G.; Lee, J.; Baik, J. H.; Koh, D. J.; Lim, H.; Song, I. K. Methanation of Carbon Dioxide over Mesoporous Nickel-M-Alumina (M = Fe, Zr, Ni, Y, and Mg) Xerogel Catalysts: Effect of Second Metal. *Catal. Letters* **2012**, *142* (7), 860–868. https://doi.org/10.1007/s10562-012-0842-0.

(54) Hwang, S.; Lee, J.; Hong, U. G.; Baik, J. H.; Koh, D. J.; Lim, H.; Song, I. K. Methanation of Carbon Dioxide over Mesoporous $Ni\text{-}Fe\text{-}Ru\text{-}Al_2O_3$ Xerogel Catalysts: Effect of Ruthenium Content. *J. Ind. Eng. Chem.* **2013**, *19* (2), 698–703. https://doi.org/10.1016/j.jiec.2012.10.007.

(55) Ren, J.; Qin, X.; Yang, J.-Z.; Qin, Z.-F.; Guo, H.-L.; Lin, J.-Y.; Li, Z. Methanation of Carbon Dioxide over Ni–M/ZrO_2 (M=Fe, Co, Cu) Catalysts: Effect of Addition of a Second Metal. *Fuel Process. Technol.* **2015**, *137* (August), 204–211. https://doi.org/10.1016/j.fuproc.2015.04.022.

(56) Kuśmierz, M. Kinetic Study on Carbon Dioxide Hydrogenation over Ru/ɣ-Al_2O_3 Catalysts. *Catal. Today* **2008**, *137* (2–4), 429–432. https://doi.org/10.1016/j.cattod.2008.03.003.

(57) Sci E, S.; Crisafulli, C.; Maggiore, R.; Mini O, S.; Galvagno, S. Influence of the Support on CO_2 Methanation over Ru Catalysts: An FT-IR Study. *Catal. Letters* **1998**, *51*, 41–45. https://doi.org/10.1023/A:1019028816154.

(58) Toemen, S.; Abu Bakar, W. A. W.; Ali, R. Effect of Ceria and Strontia over $Ru/Mn/Al_2O_3$ Catalyst: Catalytic Methanation, Physicochemical and Mechanistic Studies. *J. CO_2 Util.* **2016**, *13*, 38–49. https://doi.org/10.1016/j.jcou.2015.11.005.

(59) Kohl, A.; Linsmeier, C.; Taglauer, E.; Knözinger, H. Influence of Support and Promotor on the Catalytic Activity of Rh/VO_x/SiO_2 Model Catalysts. Phys. *Chem. Chem. Phys.* **2001**, *3*, 4639–4643.

(60) Karelovic, A.; Ruiz, P. CO_2 Hydrogenation at Low Temperature over Rh/γ-Al_2O_3 Catalysts : Effect of the Metal Particle Size on Catalytic Performances and Reaction Mechanism. *Appl. Catal. B, Environ.* **2012**, *113–114*, 237–249. https://doi.org/10.1016/j.apcatb.2011.11.043.

(61) Park, J. N.; McFarland, E. W. A Highly Dispersed Pd-Mg/SiO_2 Catalyst Active for Methanation of CO_2. *J. Catal.* **2009**, *266* (1), 92–97. https://doi.org/10.1016/j.jcat.2009.05.018.

(62) Kwak, J. H.; Kovarik, L.; Szanyi, J. Heterogeneous Catalysis on Atomically Dispersed Supported Metals: CO_2 Reduction on Multifunctional Pd Catalysts. *ACS Catal.* **2013**, *3* (9), 2094–2100. https://doi.org/10.1021/cs4001392.

(63) Li, W.; Wang, H.; Jiang, X.; Zhu, J.; Liu, Z.; Guo, X. A Short Review of Recent Advances in CO_2 Hydrogenation to Hydrocarbons over Heterogeneous Catalysts. *RSC Adv.* **2018**, *8*, 7651–7669. https://doi.org/10.1039/c7ra13546g.

(64) Shen, W. M.; Dumesic, J. A.; Hill, C. G. Criteria for Stable Ni Particle Size under Methanation Reaction Conditions: Nickel Transport and Particle Size Growth via Nickel Carbonyl. *J. Catal.* **1981**, *68* (1), 152–165. https://doi.org/https://doi.org/10.1016/0021-9517(81)90048-8.

(65) Strucks, P.; Failing, L.; Kaluza, S. A Short Review on Ni-Catalyzed Methanation of CO_2 : Reaction Mechanism, Catalyst Deactivation, Dynamic Operation. *Chemie Ing. Tech.* **2021**, No. 10, 1–12. https://doi.org/10.1002/cite.202100049.

(66) Liu, Y.; Fang, K.; Chen, J.; Sun, Y. Effect of Pore Size on the Performance of Mesoporous Zirconia-Supported Cobalt Fischer–Tropsch Catalysts. *Green Chem.* **2007**, *9* (6), 611–615. https://doi.org/10.1039/B614266D.

(67) Aziz, M. A. A. A.; Jalil, A. A.; Triwahyono, S.; Mukti, R. R.; Taufiq-Yap, Y. H.; Sazegar, M. R. Highly Active Ni-Promoted Mesostructured Silica Nanoparticles for CO_2 Methanation. *Appl. Catal. B Environ.* **2014**, *147*, 359–368. https://doi.org/10.1016/j.apcatb.2013.09.015.

(68) Pan, Q.; Peng, J.; Sun, T.; Wang, S.; Wang, S. Insight into the Reaction Route of CO_2 Methanation: Promotion Effect of Medium Basic Sites. *Catal. Commun.* **2014**, *45*, 74–78. https://doi.org/10.1016/j.catcom.2013.10.034.

(69) Li, S.; Xu, Y.; Chen, Y.; Li, W.; Lin, L.; Li, M.; Deng, Y.; Wang, X.; Ge, B.; Yang, C.; Yao, S.; Xie, J.; Li, Y.; Liu, X.; Ma, D. Tuning the Selectivity of Catalytic Carbon Dioxide Hydrogenation over Iridium/Cerium Oxide Catalysts with a Strong Metal–Support Interaction. *Angew. Chemie - Int. Ed.* **2017**, *56* (36), 10761–10765. https://doi.org/10.1002/anie.201705002.

(70) An, B.; Zhang, J.; Cheng, K.; Ji, P.; Wang, C.; Lin, W. Confinement of Ultrasmall Cu/ZnO x Nanoparticles in Metal-Organic Frameworks for Selective Methanol Synthesis from Catalytic Hydrogenation of CO_2. *J. Am. Chem. Soc.* **2017**, *139*, 3834–3840. https://doi.org/10.1021/jacs.7b00058.

(71) Frey, M.; Édouard, D.; Roger, A. C. Optimization of Structured Cellular Foam-Based Catalysts for Low-Temperature Carbon Dioxide Methanation in a Platelet Milli-Reactor. *Comptes Rendus Chim.* **2015**, *18* (3), 283–292. https://doi.org/10.1016/j.crci.2015.01.002.

(72) Chang, F.-W.; Hsiao, T.-J.; Chung, S.-W.; Lo, J.-J. Nickel Supported on Rice Husk Ash -Activity and Selectivity in CO_2 Methanation. *Appl. Catal. A Gen.* **1997**, *164*, 225–236. https://doi.org/10.1021/acs.joc.8b01672.

(73) Pandey, D.; Deo, G. Effect of Support on the Catalytic Activity of Supported Ni-Fe Catalysts for the CO_2 methanation Reaction. *J. Ind. Eng. Chem.* **2016**, *33*, 99–107. https://doi.org/10.1016/j.jiec.2015.09.019.

(74) Guerrero-Ruiz, A.; Rodríguez-Ramos ,I. Hydrogenation of CO_2 on Carbon-Supported Nickel and Cobalt. *React. Kinet. Catal. Lett.* **1985**, *29* (1), 93–99.

(75) Wang, W.; Chu, W.; Wang, N.; Yang, W.; Jiang, C. Mesoporous Nickel Catalyst Supported on Multi-Walled Carbon Nanotubes for Carbon Dioxide Methanation. *Int. J. Hydrogen Energy* **2016**, *41* (2), 967–975. https://doi.org/10.1016/j.ijhydene.2015.11.133.

(76) Millet, M.-M.; Algara-Siller, G.; Wrabetz, S.; Mazheika, A.; Girgsdies, F.; Teschner, D.; Seitz, F.; Tarasov, A.; Levchenko, S. V.; Schloegl, R.; Frei, E. Ni Single Atom Catalysts for CO_2 Activation. *J. Am. Chem. Soc.* **2019**,

jacs.8b11729. https://doi.org/10.1021/jacs.8b11729.

(77) Hu, D.; Gao, J.; Ping, Y.; Jia, L.; Gunawan, P.; Zhong, Z.; Xu, G.; Gu, F.; Su, F. Enhanced Investigation of CO Methanation over Ni/Al_2O_3 Catalysts for Synthetic Natural Gas Production. *Ind. Eng. Chem. Res.* **2012**, *51* (13), 4875–4886. https://doi.org/10.1021/ie300049f.

(78) Fan, M. T.; Miao, K. P.; Lin, J. D.; Zhang, H. Bin; Liao, D. W. Mg-Al Oxide Supported Ni Catalysts with Enhanced Stability for Efficient Synthetic Natural Gas from Syngas. *Appl. Surf. Sci.* **2014**, *307*, 682–688. https://doi.org/10.1016/j.apsusc.2014.04.098.

(79) Wang, B.; Yao, Y.; Jiang, M.; Li, Z.; Ma, X.; Qin, S.; Sun, Q. Effect of Cobalt and Its Adding Sequence on the Catalytic Performance of MoO_3/Al_2O_3 toward Sulfur-Resistant Methanation. *J. Energy Chem.* **2014**, *23* (1), 35–42. https://doi.org/10.1016/S2095-4956(14)60115-7.

(80) Liu, H.; Zou, X.; Wang, X.; Lu, X.; Ding, W. Effect of CeO_2 Addition on Ni/Al_2O_3 catalysts for Methanation of Carbon Dioxide with Hydrogen. *J. Nat. Gas Chem.* **2012**, *21* (6), 703–707. https://doi.org/10.1016/S1003-9953(11)60422-2.

(81) Liu, Q.; Gu, F.; Lu, X.; Liu, Y.; Li, H.; Zhong, Z.; Xu, G.; Su, F. Enhanced Catalytic Performances of Ni/Al_2O_3 Catalyst via Addition of V_2O_3 for CO Methanation. *Appl. Catal. A Gen.* **2014**, *488*, 37–47. https://doi.org/10.1016/j.apcata.2014.09.028.

(82) Qin, H.; Guo, C.; Wu, Y.; Zhang, J. Effect of La_2O_3 Promoter on NiO/Al_2O_3 Catalyst in CO Methanation. *Korean J. Chem. Eng.* **2014**, *31* (7), 1168−1173. https://doi.org/10.1007/s11814-014-0013-7.

(83) Campbell, T. K.; Falconer, J. L. Carbon Dioxide Hydrogenation on Potassium-Promoted Nickel Catalysts. *Appl. Catal.* **1989**, *50* (1), 189−197. https://doi.org/https://doi.org/10.1016/S0166-9834(00)80835-0.

(84) Hammer, B.; Nørskov, J. K. Theoretical Surface Science and Catalysis—Calculations and Concepts. *Adv. Catal.* **2000**, *45*, 71−129. https://doi.org/10.1016/S0360-0564(02)45013-4.

(85) Ocampo, F.; Louis, B.; Kiwi-Minsker, L.; Roger, A. C. Effect of Ce/Zr Composition and Noble Metal Promotion on Nickel Based $Ce_xZr_{1-x}O_2$ Catalysts for Carbon Dioxide Methanation. *Appl. Catal. A Gen.* **2011**, *392* (1–2), 36–44. https://doi.org/10.1016/j.apcata.2010.10.025.

(86) Hwang, S.; Hong, U. G.; Lee, J.; Seo, J. G.; Baik, J. H.; Koh, D. J.; Lim, H.; Song, I. K. Methanation of Carbon Dioxide over Mesoporous Ni-Fe-Al_2O_3 Catalysts Prepared by a Coprecipitation Method: Effect of Precipitation Agent. *J. Ind. Eng. Chem.* **2013**, *19* (6), 2016–2021. https://doi.org/10.1016/j.jiec.2013.03.015.

(87) Swalus, C.; Jacquemin, M.; Poleunis, C.; Bertrand, P.; Ruiz, P. CO_2 Methanation on Rh/γ-Al_2O_3 Catalyst at Low Temperature: "In Situ" Supply of Hydrogen by Ni/Activated Carbon Catalyst. *Appl. Catal. B Environ.* **2012**, *125*, 41–50. https://doi.org/10.1016/j.apcatb.2012.05.019.

(88) Tarifa, P.; Megías-Sayago, C.; Cazaña, F.; González-Martín, M.; Latorre, N.; Romeo, E.; Delgado, J. J.; Monzón, A. Highly Active Ce-And Mg-Promoted Ni Catalysts Supported on Cellulose-Derived Carbon for Low-Temperature CO_2 Methanation. *Energy and Fuels* **2021**. https://doi.org/10.1021/acs.energyfuels.1c01682.

(89) Büchel, R.; Baiker, A.; Pratsinis, S. E. Effect of Ba and K Addition and Controlled Spatial Deposition of Rh in Rh/Al_2O_3 catalysts for CO_2 hydrogenation. *Appl. Catal. A Gen.* **2014**, *477*, 93−101. https://doi.org/10.1016/j.apcata.2014.03.010.

(90) He, L.; Lin, Q.; Liu, Y.; Huang, Y. Unique Catalysis of Ni-Al Hydrotalcite Derived Catalyst in CO_2 Methanation: Cooperative Effect between Ni Nanoparticles and a Basic Support. *J. Energy Chem.* **2014**, *23* (5), 587–592. https://doi.org/10.1016/S2095-4956(14)60144-3.

(91) Pandey, D.; Deo, G. Effect of Support on the Catalytic Activity of Supported Ni-Fe Catalysts for the CO_2 Methanation Reaction. *J. Ind. Eng. Chem.* **2016**, *33*, 99−107. https://doi.org/10.1016/j.jiec.2015.09.019.

(92) Miao, B.; Ma, S. S. K.; Wang, X.; Su, H.; Chan, S. H. Catalysis Mechanisms of CO_2 and CO Methanation. *Catal. Sci. Technol.* **2016**, *6* (12), 4048–4058. https://doi.org/10.1039/C6CY00478D.

(93) Solis-garcia, A.; Louvier-hernandez, J. F.; Almendarez-camarillo, A.; Fierro-gonzalez, J. C. Participation of Surface Bicarbonate , Formate and Methoxy Species in the Carbon Dioxide Methanation Catalyzed by ZrO_2 -Supported Ni. *"Applied Catal. B, Environ.* **2017**, *218*, 611–620. https://doi.org/10.1016/j.apcatb.2017.06.063.

(94) Akamaru, S.; Shimazaki, T.; Kubo, M.; Abe, T. Density Functional Theory Analysis of Methanation Reaction of CO_2 on Ru Nanoparticle Supported on TiO_2 (1 0 1). *"Applied Catal. A, Gen.* **2014**, *470*, 405–411. https://doi.org/10.1016/j.apcata.2013.11.016.

(95) Eckle, S.; Anfang, H. G.; Behm, R. J. Reaction Intermediates and Side Products in the Methanation of CO and CO_2 over Supported Ru Catalysts in H_2-Rich Reformate Gases. *J. Phys. Chem. C* **2011**, *115* (4), 1361−1367. https://doi.org/10.1021/jp108106t.

(96) Prairie, M. R.; Renken, A.; Highfield, J. G.; Thampi, K. R.; Grätzel, M. A Fourier Transform Infrared Spectroscopic Study of CO_2 Methanation on Supported Ruthenium. *J. Catal.* **1991**, *129* (1), 130−144. https://doi.org/https://doi.org/10.1016/0021-9517(91)90017-X.

(97) Serp, P.; Figueiredo, J. L. *Carbon Materials for Catalysis*; Serp, P., Figueiredo, J. L., Eds.; Wiley: New Jersey, 2009.

(98) Yin, C. Y.; Aroua, M. K.; Daud, W. M. A. W. Review of Modifications of Activated Carbon for Enhancing Contaminant Uptakes from Aqueous Solutions. *Sep. Purif. Technol.* **2007**, *52* (3), 403–415. https://doi.org/10.1016/j.seppur.2006.06.009.

(99) Serp, P.; Corrias, M.; Kalck, P. Carbon Nanotubes and Nanofibers in Catalysis. *Appl. Catal. A Gen.* **2003**, *253* (2), 337–358. https://doi.org/10.1016/S0926-860X(03)00549-0.

(100) Serp, P.; Castillejos, E. Catalysis in Carbon Nanotubes. *ChemCatChem* **2010**, *2* (1), 41–47. https://doi.org/10.1002/cctc.200900283.

(101) Mahata, N.; Silva, A. R.; Pereira, M. F. R.; Freire, C.; de Castro, B.; Figueiredo, J. L. Anchoring of a [Mn(Salen)Cl] Complex onto Mesoporous Carbon Xerogels. *J. Colloid Interface Sci.* **2007**, *311* (1), 152−158. https://doi.org/10.1016/j.jcis.2007.02.080.

(102) Job, N.; Théry, A.; Pirard, R.; Marien, J.; Kocon, L.; Rouzaud, J. N.; Béguin, F.; Pirard, J. P. Carbon Aerogels, Cryogels and Xerogels: Influence of the Drying Method on the Textural Properties of Porous Carbon Materials. *Carbon N. Y.* **2005**, *43* (12), 2481–2494. https://doi.org/10.1016/j.carbon.2005.04.031.

(103) Job, N.; Pirard, R.; Marien, J.; Pirard, J. P. Porous Carbon Xerogels with Texture Tailored by PH Control during Sol-Gel Process. *Carbon N. Y.* **2004**, *42* (3), 619–628. https://doi.org/10.1016/j.carbon.2003.12.072.

(104) Gorgulho, F.; Gonc, F.; Fernando, M.; Pereira, R. Synthesis and Characterization of Nitrogen-Doped Carbon Xerogels. *Carbon N. Y.* **2009**, *7*. https://doi.org/10.1016/j.carbon.2009.03.050.

(105) Shafeeyan, M. S.; Daud, W. M. A. W.; Houshmand, A.; Shamiri, A. A Review on Surface Modification of Activated Carbon for Carbon Dioxide Adsorption. *J. Anal. Appl. Pyrolysis* **2010**, *89* (2), 143−151. https://doi.org/10.1016/j.jaap.2010.07.006.

(106) Figueiredo, J. L. Functionalization of Porous Carbons for Catalytic Applications. *J. Mater. Chem. A* **2013**, *1*, 9351–9364. https://doi.org/10.1039/c3ta10876g.

(107) Figueiredo, J. L.; Pereira, M. F. R. R.; Freitas, M. M. A. A.; Órfão, J. J. M. Modification of the Surface Chemistry of Activated Carbons. *Carbon N. Y.* **1999**, *37* (9), 1379−1389. https://doi.org/10.1016/S0008-6223(98)00333-9.

(108) Wang, S.; Lu, G. Q. Effects of Acidic Treatments on the Pore and Surface Properties of Ni Catalyst Supported on Activated Carbon. *Carbon N. Y.* **1998**, *36* (3), 283–292. https://doi.org/10.1016/S0008-6223(97)00187-5.

(109) Hunger, M.; Weitkamp, J. *In Situ* IR , NMR , EPR , and UV/Vis Spectroscopy: Tools for New Insight into the Mechanisms of Heterogeneous Catalysis. *Angew. Chem. Int. Ed.* **2001**, *40*, 2954–2971.

(110) Rodriguez, J. A.; Hanson, J. C.; Chupas, P. J. *In-Situ Characterization of Heterogeneous Catalysts*; Wiley, 2013.

(111) Srinivasan, P. D.; Patil, B. S.; Zhu, H.; Bravo-Suárez, J. J. Application of Modulation Excitation-Phase Sensitive Detection-DRIFTS for: *In Situ*/Operando Characterization of Heterogeneous Catalysts. *React. Chem. Eng.* **2019**, *4* (5), 862–883. https://doi.org/10.1039/c9re00011a.

(112) Urakawa, A.; Bürgi, T.; Baiker, A. Sensitivity Enhancement and Dynamic Behavior Analysis by Modulation Excitation Spectroscopy : Principle and Application in Heterogeneous Catalysis. *Chem. Eng. Sci.* **2009**, *63* (2008), 4902–4909. https://doi.org/10.1016/j.ces.2007.06.009.

(113) Hemmingsson, F.; Schaefer, A.; Skoglundh, M.; Carlsson, P. A. CO_2 Methanation over Rh/CeO_2 Studied with

Infrared Modulation Excitation Spectroscopy and Phase Sensitive Detection. *Catalysts* **2020**, *10* (6), 601. https://doi.org/10.3390/catal10060601.

(114) Aguirre, A.; Collins, S. E. Selective Detection of Reaction Intermediates Using Concentration- Modulation Excitation DRIFT Spectroscopy. *Catal. Today* **2013**, *205*, 34–40. https://doi.org/10.1016/j.cattod.2012.08.020.

(115) Baurecht, D.; Fringeli, U. P. Quantitative Modulated Excitation Fourier Transform Infrared Spectroscopy. *Rev. Sci. Instrum.* **2001**, *72* (10), 3782–3792. https://doi.org/10.1063/1.1400152.

(116) Srinivasan, P. D.; Khivantsev, K.; Tengco, J. M. M.; Zhu, H.; Bravo-Suárez, J. J. Enhanced Ethanol Dehydration on γ-Al_2O_3 Supported Cobalt Catalyst. *J. Catal.* **2019**, *373*, 276–296. https://doi.org/10.1016/j.jcat.2019.03.024.

(117) Tao, F.; Crozier, P. A. Atomic-Scale Observations of Catalyst Structures under Reaction Conditions and during Catalysis. *Chem. Rev.* **2016**, *116* (6), 3487–3539. https://doi.org/10.1021/cr5002657.

(118) Helveg, S. An Industrial Perspective of the Impact of Haldor Topsøe on (*in situ*) Electron Microscopy in Catalysis. *J. Catal.* **2015**, *328*, 102−110. https://doi.org/10.1016/j.jcat.2014.12.017.

(119) Li, X.; Yang, X.; Zhang, J.; Huang, Y.; Liu, B. *In Situ*/Operando Techniques for Characterization of Single-Atom Catalysts. *ACS Catal.* **2019**, *9*, 2521–2531. https://doi.org/10.1021/acscatal.8b04937.

(120) Jinschek, J. R. Advances in the Environmental Transmission Electron Microscope (ETEM) for Nanoscale in Situ Studies of Gas–Solid Interactions. *Chem. Commun.* **2014**, *50*, 2696–2706. https://doi.org/10.1039/c3cc49092k.

(121) Gonçalves, L. P. L.; Serov, A.; McCool, G.; Dicome, M.; Sousa, J. P. S.; Soares, O. S. G. P.; Bondarchuk, O.; Petrovykh, D. Y.; Lebedev, O. I.; Pereira, M. F. R.; Kolen'ko, Y. New Opportunity for Carbon-Supported Ni-based Electrocatalysts: Gas-phase CO_2 Methanation. *ChemCatChem* **2021**, *13*, 1−11. https://doi.org/10.1002/cctc.202101284.

(122) Gonçalves, L. P. L.; Christensen, D. B.; Meledina, M.; Salonen, L. M.; Petrovykh, D. Y.; Carbó-Argibay, E.; Sousa, J. P. S.; Soares, O. S. G. P.; Pereira, M. F. R.; Kegnæs, S.; Kolen'Ko, Y. V. Selective Formic Acid Dehydrogenation at Low Temperature over a RuO_2/COF Pre-Catalyst Synthesized on the Gram Scale. *Catal. Sci. Technol.* **2020**, *10* (7), 1991−1995. https://doi.org/10.1039/d0cy00145g.

Chapter 2

Experimental Techniques

1. Preparation of the supporting materials

1.1 Materials

All the chemicals were purchased from commercial sources and used as received, without further purification, unless stated otherwise.

Activated carbon (AC) NORIT GAC 1240 PLUS was obtained from CABOT, and NC3100™ CNTs were obtained from Nanocyl; Melamine (≥99%) was purchased from Fluka; Ultrapure water (18.2 MΩ cm^{-2}) was generated using a Milli-Q Advantage A10 system (Millipore). HNO_3 (65%, AnalaR NORMAPUR®) was purchased from VWR, NaOH (98.5% for analysis, pellets) was purchased from Acros Organics, $Ce(NO_3)_3 \cdot 6H_2O$ (≥ 99.0%), Formaldehyde solution (37 wt% in H_2O), and Resorcinol (ACS reagent, ≥99.0%) were purchased from Sigma-Aldrich.

1.1 Preparation of the Activated Carbon (AC) supporting materials with different surface functionalities

Three different treatments were performed on a commercial AC (Norit GAC 1240Plus) in order to obtain materials with different surface chemistries.

To prepare oxidized AC (AC−O), 7 g of AC was placed in a 100 mL extraction Soxhlet. In the attached 250 mL round bottom flask, 5 M HNO_3 was heated until its boiling point and the system was maintained under reflux for 6 h. After that, the material was washed with distilled water until neutral pH and finally dried at 120 °C [1].

To prepare N-doped AC (AC−N), 1.8 g of AC and 1.17 g of melamine were ball milled in a closed pot for 2 h at 15 vibrations s^{-1} using a Retsch MM200 ball-milling equipment. After that, the mixture was annealed at 600 °C for 1 h under 100 cm^3 min^{-1} flowrate of N_2 [2].

To obtain an oxygen-free surface with Lewis base sites (AC−R), 3 g of AC was heated to 900 °C at 10 °C min^{-1} in a quartz tube reactor, under a N_2 flowrate of 100 cm^3 min^{-1}. When 900 °C was reached, the flowrate was changed to 50 cm^3 min^{-1} of H_2 and the system was maintained at 900 °C for 1 h [3].

1.2 Preparation of the Carbon Nanotubes (CNT) supporting materials with different surface functionalities

To obtain N-doped CNTs (referred to as CNT−N), 0.6 g of CNTs and 0.39 g of melamine (N source) were co-ball-milled in a closed pot at 15 vibrations s^{-1} for 4 h using a MM200 ball-milling (Retsch). After that, the resultant fine powdered mixture was heated at 10 °C min^{-1} and annealed at 600 °C for 1 h under a flowrate of N_2 of 100 cm^3 min^{-1} [2].

To obtain an oxygen-free surface with Lewis base sites (CNT−R), 1 g of CNT was heated to 900 °C at 10 °C min^{-1} in a quartz tube reactor, under a N_2 flowrate of 100 cm^3 min^{-1}. When 900 °C was reached, the flowrate was changed to 50 cm^3 min^{-1} of H_2 and the system was maintained at 900 °C for 1 h [3].

1.3 Preparation of CeO_2 and ACR−CeO_2 composite

Ceria (CeO_2) and a composite of reduced activated carbon with ceria (ACR–CeO_2) were prepared by the precipitation method adapted from elsewhere.[4] In the case of pure CeO_2, 100 mL of 3 M NaOH aqueous solution was added dropwise to a solution of 7.5 g of $Ce(NO_3)_3{\cdot}6H_2O$ in 50 mL of Mili-Q water under vigorous stirring at room temperature. After that, the resultant slurry was centrifuged, and the obtained precipitate was then washed by Mili-Q water until neutral pH was reached. Next, the resultant solid was dried at 120 °C overnight. Finally, the material was calcined at 450 °C for 3 h in an air flowrate of 100 cm^3 min^{-1}.

ACR–CeO_2 composites were prepared by a similar protocol, but in this case, 1 g of AC−R was firstly dispersed in the $Ce(NO_3)_3{\cdot}6H_2O$ aqueous solution with

the amount of $Ce(NO_3)_3 \cdot 6H_2O$ calculated to obtain the desired composite ratio and left stirring for 1 h. After that, the 3 M NaOH aqueous solution was added dropwise to the ACR/$Ce(NO_3)_3 \cdot 6H_2O$ suspension under vigorous stirring at room temperature, and the resultant slurry was left shaking for 5 h. The amount of 3 M NaOH aqueous solution added was calculated in order to have 6 times excess to $Ce(NO_3)_3 \cdot 6H_2O$ used for each composite. The amount of water used to prepare the $Ce(NO_3)_3 \cdot 6H_2O$ aqueous solution was determined in order to have a final volume of 45 mL.

Then, the precipitate was centrifuged and washed with Mili-Q water until neutral pH was reached. Next, the solid was dried at 120 °C overnight, and finally calcined at 450 °C for 3 h under a N_2 flowrate of 100 $cm^3\ min^{-1}$.

1.4 Preparation of N-containing Carbon Xerogel

For the synthesis of xerogels with nitrogen groups, resorcinol (15 g) and melamine (3 g) (as nitrogen precursor) were mixed in 18 mL of distilled water. The solution was heated under agitation until the temperature of 90 °C is reached and was kept at this temperature until complete dissolution of melamine. After cooling down to room temperature, 20 mL of formaldehyde (37%) were added to the solution under agitation and few drops of NaOH 2 M were also added to obtain a pH of 6. The gel formation was performed at 85 °C for 3 days, and after that, the gel was dried in an oven for 4 days (1st day at 60 °C, 2nd day at 80 °C, 3rd day at 100 °C and 4th day at 120 °C). Finally, the gel was carbonized with the following steps, using a heating rate of 2 °C min^{-1}: (1) 2 h at 200 °C; (2) 1 h at 300 °C; and (3) 2 h at 900 °C.

2. Preparation of the monometallic and bimetallic supported metal catalysts

2.1 Materials

$Ni(NO_3)_2 \cdot 6H_2O$ (≥ 97.0%), $Fe(NO_3)_3 \cdot 6H_2O$ (≥ 98.0%), $Mg(NO_3)_2 \cdot 6H_2O$ (≥ 99.0%), $Y(NO_3)_3 \cdot 6H_2O$ (99.8% trace metals basis), $Cr(NO_3)_3 \cdot 9H_2O$ (99%), and $Al(NO_3)_3 \cdot 9H_2O$ (≥ 98%), $AgNO_3$ (≥ 99.0%) were purchased from Sigma Aldrich and $SnCl_2 \cdot 2H_2O$ (98%) was purchased from Alfa Aesar.

2.2 Incipient Wetness Impregnation

Supported Ni nanocatalysts were prepared by the incipient wetness impregnation (IWI) method. 0.5 g of the respective supporting material was placed under ultrasonic vibration and an aqueous solution of $Ni(NO_3)_2 \cdot 6H_2O$ was added to obtain the desired Ni loading. The sample was left under ultrasonic vibration for 90 min, and after that was dried at 120 °C overnight.

The bimetallic catalysts were prepared similarly, by sequential impregnation. 0.5 g of supporting material was placed under ultrasonic vibration and an aqueous solution of $Ni(NO_3)_2 \cdot 6H_2O$ was added first to obtain the desired Ni loading. The sample was left under ultrasonic vibration for 90 min and after that was dried at 120 °C overnight. Next, the Ni-containing sample was placed under ultrasonic vibration again and an aqueous solution of the desired metal precursor was added to obtain the desired loading of the second metal.

Finally, all samples are annealed under N_2 and reduced under H_2 at the respective temperature determined by H_2 temperature programmed reduction (H_2–TPR). The samples were placed in a quartz tube reactor and heated to the desired temperature at 10 °C min^{-1} under a N_2 flowrate of 100 cm^3 min^{-1} and annealed for 1 h. After that, the flowrate was switched to 50 cm^3 min^{-1} of H_2 and the sample was reduced for 3 h.

2.3 Impregnation – Precipitation

Commercially available monometallic Ni/C and bimetallic NiMo/C and NiRe/C electrocatalysts supported on ECS-4601 carbon material (Engineered Catalyst Support™, Pajarito Powder, LLC) were synthesized by thermal reduction of metal precursors: nickel nitrate, ammonium molybdate and ammonium perrhenate. Calculated amount of ECS-4601 carbon support was added to the respective metal solution, in the amount to obtain 50% of Ni loading in the final Ni/C catalyst, 50% of NiMo with 85:15 at% ratio in the NiMo/C catalyst, as well as 50% of NiRe with 87:13 at% ratio in the NiRe/C catalyst. After 1 h of stirring, the pH of the solution was adjusted to 13 using 5 M NaOH, followed by the precipitation of metal compounds. The precipitate was washed with DI water until pH ≈ 6.5. Washed precipitate was then dried at 85 °C for 12 h. The dry mixture was ground with mortar and pestle, and the resultant fine powder was reduced at 450 °C for 1 h under 100 $cm^3\ min^{-1}$ flowrate of 7%H_2/N_2 gas mixture. Finally, the catalyst was passivated in a flow of 0.1%O_2/He at room temperature for 8 h.

3. Characterization Techniques

3.1 N_2 adsorption-desorption isotherms at −196 ºC

The N_2 adsorption-desorption isotherms at −196 °C were collected using a Quantachrome NOVA 4200e multi-station apparatus. Before the physisorption analysis, the samples (c.a. 100 mg) were degassed at 170 °C for 3 h. The surface area (S_{BET}) was calculated by determining the amount of adsorbed vapor needed to cover the surface with a monolayer using the linearized Brunauer-Emmett-Teller (BET) equation (1) in the interval $0.05 < P/P_0 < 0.3$ [5].

$$\frac{P/P_0}{n^a\left(1 - P/P_0\right)} = \frac{1}{Cn_m^a} + \frac{C-1}{Cn_m^a} \times P/P_0 \qquad (1)$$

Where C is a constant, $n^a{}_m$ is the amount of adsorbed vapor needed to cover the surface with a monolayer (monolayer capacity (mol g^{-1})), and n^a is the total amount of adsorbed gas.

Specifically, the S_{BET} is calculated with equation (2),

$$S_{BET} = n_m^a N a_m \ (m^2\ g^{-1}) \tag{2}$$

Where N is the Avogadro's number (6.02×10^{23} mol^{-1}) and a_m is the area of the cross section of a molecule of adsorbate (0.162 nm^2 for N_2).

The BET equation was originally deducted for non-porous solids; however, it is usually applied (between certain limits) to the textural characterization of macro or mesoporous materials.

The mesopore surface area (S_{meso}) and the micropore volumes (V_{micro}) were calculated by the t-method, which determines the microporous volume and the specific surface area of a sample by comparison with a reference adsorption isotherm of a nonporous material having a similar surface chemistry [5].

The total specific pore volume (V_P) was calculated by equation (3) using the amount of vapor adsorbed at relative pressure close to unity $P/P_0 = 0.95$ (V_{ads}) by assuming that the pores were filled with liquid adsorbate (V_{liq}), and thus, converting the adsorbed volume in volume of liquid nitrogen [5].

$$V_{liq} = \frac{P_a V_{ads} V_M}{RT} \tag{3}$$

Where P_a is the atmospheric pressure (atm), T is 273.15 K, R is the ideal gas constant ($R = 82.057$ cm^3 atm K^{-1} mol^{-1}), and V_M is the molar volume of N_2 ($V_M = 34.7$ cm^3 mol^{-1}).

Pore size distribution was determined either using the Barrett–Joyner–Halenda (BJH) analysis of the desorption branch of the isotherms or the non-local density functional theory (NLDFT) method.

3.2 Elemental analysis

Elemental analysis was carried out on a vario MICRO cube and a rapid OXY cube analyzer from Elemental. Each element (CHNS/O) was determined by combustion of the sample at 1050 °C and calculated by the mean of three independent measurements, using a per-day calibration with a standard compound.

3.3 Thermogravimetric Analysis

Ash content was determined by thermogravimetric analysis (TGA) using a Mettler-Toledo TGA/DSC 1 STAR equipment, by heating the samples under Ar flow from 50 to 900 °C, at a heating rate of 10 °C min^{-1}, while performing two isothermal steps: 7 min under Ar and 13 min under air.

3.4 Point of Zero Charge (pH_{PZC})

The point of zero charge (pH_{PZC}) was determined by placing 20 mg of the sample in closed Erlenmeyer flasks with 20 mL of 0.01 M NaCl solution, to which the pH was adjusted to a value between 2 and 12 by adding either 0.1 M HCl or 0.1 M NaOH solutions. The Erlenmeyer flasks with different pH were left for 24 h under stirring at room temperature. The final pH was measured for each sample, as well as for a blank experiment (without material, $pH_{initial}$). The pH_{PZC} is the point where the curve pH_{final} versus $pH_{initial}$ crosses the line $pH_{initial}=pH_{final}$.

3.5 X-ray photoelectron spectroscopy (XPS)

X-ray photoelectron spectroscopy (XPS) measurements were performed in a ESCALAB 250Xi (Thermo Scientific) using a monochromated microfocused Al K_α X-ray source. Powdered samples were pressed into carbon tape, which was directly attached to the sample holder. Charge neutralization was provided by a flood gun producing low-energy (≤ 1 eV) beams of Ar^+ ions and electrons. Fitting of the XPS spectra was performed using the Avantage

software from Thermo Fisher Scientific, in which the peaks were fitted with a Gaussian–Lorentzian function.

3.6 Transmission electron microscopy (TEM)

Transmission electron microscopy (TEM) studies were conducted using a JEOL 2100 microscope operated at 200 kV.

In Chapters 3, 5 and 7, TEM, high-angle annular dark-field scanning transmission electron microscopy (HAADF-STEM), electron diffraction (ED), and energy-dispersive X-ray spectroscopy in STEM mode (STEM−EDX) were performed using JEM-ARM200F cold FEG probe and image aberration corrected microscope, operated at 200 kV and equipped with large angle CENTURIO EDX detector and QUANTUM GIF. The samples were dispersed in ethanol and placed onto a copper grid. The particle size distribution was obtained by measuring at least 100 particles using ImageJ software.

In chapter 4, high-angle annular dark-field scanning TEM (HAADF–STEM) and energy dispersive X-ray spectroscopy in STEM mode (STEM–EDX) using a Titan electron microscope (FEI), equipped with a Super-X EDX system, and operated at 200 kV.

3.7 Powder X-ray diffraction (XRD)

Powder X-ray diffraction (XRD) analysis was performed using a PANanalytical X'Pert PRO diffractometer with Ni filtered Cu K_α radiation and a PIXcel detector. The sample was grounded to a fine powder and placed in the sample holder. A Bragg Brentano configuration was used in a 2θ range from 20° to 80° with step size of 0.01° and a time per step of 300 s. Collected data was analyzed using PANanalytical High Score software. The diameter of crystallites (d_c) was calculated using Scherrer equation (4) from the XRD data.

$$d_C = \frac{K \times \lambda}{\beta \times \cos(\theta)} \quad (4)$$

Where K is Scherrer constant, λ is the X-ray wavelength, β is the full width at half maximum (FWHM) of the peak and θ is the Bragg angle.

3.8 H_2 temperature programmed reduction (H_2–TPR)

H_2 temperature programmed reduction (H_2–TPR) analysis was performed using an AMI–200 Catalyst Characterization apparatus from Altamira Instruments, equipped with a thermal conductivity detector (TCD), high precision mass flow controllers and adjustable furnace with air cooling. Approximately 100 mg of sample was placed in a U-shaped quartz tube in a furnace. Before the heating phase, Ar (25 $cm^3\ min^{-1}$) was used for flushing the tube, and then H_2 diluted in Ar (5% H_2/Ar) was used as reducing atmosphere. While the reducing gas was going through the tube, the temperature was raised until 1000 °C with a heating rate of 10 °C min^{-1}.

3.9 H_2 pulse chemisorption

H_2 pulse chemisorption analysis was performed using an AMI–200 catalyst characterization setup (Altamira Instruments), equipped with a thermal conductivity detector (TCD), high precision mass flow controllers and a furnace with air cooling. Approximately 100 mg of sample was placed in a U-shaped quartz tube in a furnace. The sample was pre-treated *in situ* under H_2 for 30 min at 450 °C, then cooled down to 35 °C and flushed with Ar. After that, pulses of 58 µL of H_2 were injected in the carrier gas (Ar at 25 $cm^3\ min^{-1}$ flowrate) until the area of the hydrogen peak on the chromatograph was identical. The metallic Ni surface area (S_M) was calculated assuming two metal atoms are needed for the adsorption of a molecule of H_2, using the following equation (5):

$$S_M = \frac{n_m^a N n}{n_S} \tag{5}$$

Where S_M is the metal specific surface area ($m^2\ g_{cat}^{-1}$), n_m^a is the quantity of adsorbed hydrogen (mol g_{cat}^{-1}), N the Avogadro's number, n is the number of metal atoms needed to adsorb a H_2 molecule, and n_s the number of atoms in the surface per unit of area.

3.10 Temperature programmed desorption (TPD)

Temperature programmed desorption (TPD) analysis was performed using an AMI–300 Catalyst Characterization apparatus from Altamira Instruments, equipped with a thermal conductivity detector (TCD) and a Mass Spectrometer (MS), high precision mass flow controllers and adjustable furnace with air cooling.

Approximately 100 mg of catalyst was placed in a U-shaped quartz tube in a furnace. The sample was pretreated *in situ* under H_2 for 30 min at the reduction temperature and cooled down to 40 °C under He. After that, the temperature was increase until 1050 °C under He (25 $cm^3\ min^{-1}$). The amount of CO and CO_2 released by the sample was analyzed by MS.

4. CO_2 Methanation Catalytic Experiments

The catalytic experiments were carried out in a Microactivity XS15 system from PID Eng & Tech, using a fixed bed quartz reactor (d_{int} = 1 cm), and the products in the outflow were analyzed online by a gas chromatograph (GC 1000 from DANI) equipped with a thermal conductivity detector (TCD) and a GS-CarbonPLOT capillary column, with He as carrier gas, using a continuous flow of N_2 as internal standard (Figure 2.1). A condenser in the Microactivity XS15 system condensates the water formed before the gas was injected in the GC. The catalyst (100 mg) was mixed with inert SiC (to assure a significant bed height and a good space velocity) and placed in a fixed bed quartz reactor. Each catalyst was pre-treated *in situ* under H_2 flowrate (40 $cm^3\ min^{-1}$) at the reduction temperature for 30 min, at 1 bar. After that, the reactor temperature was decreased to 200 °C under He (50 $cm^3\ min^{-1}$), and then, the reactor was

fed with 10% CO_2, 40% H_2 (the stoichiometric composition) and 50% He. A temperature ramping from 200 °C to 500 °C, with a heating rate of 5 °C min^{-1}, was performed under reaction conditions in order to evaluate the performance of each sample at various temperatures.

To evaluate the stability of the best performing sample, the experiment was performed under the same conditions referred before; however, under isothermal conditions at the established optimal temperature.

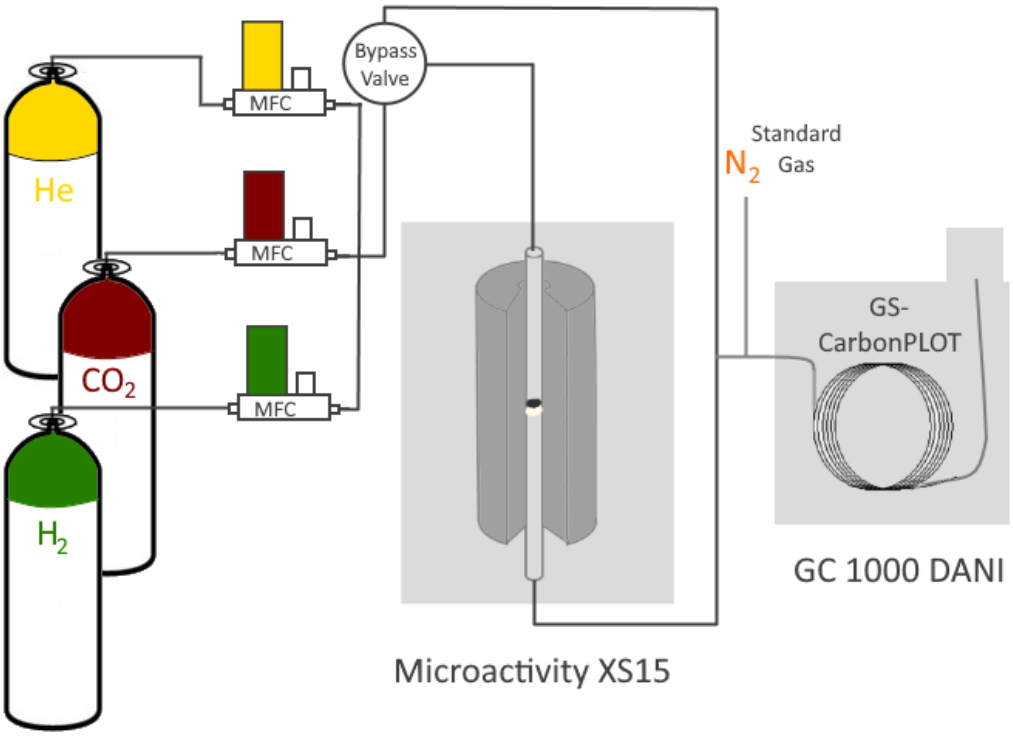

Figure 2.1. Schematic representation of the reactor setup.

Conversion of CO_2 (X_{CO2}), selectivity to methane (S_{CH4}) and CO (S_{CO}), and yield to methane (Y_{CH4}) were calculated as following, considering CO as the only by-product:

$$X_{CO_2}\,(\%) = \frac{\mathrm{F}_{CO_2,in} - \mathrm{F}_{CO_2,out}}{\mathrm{F}_{CO_2,in}} \times 100 \quad (6)$$

$$S_{\mathrm{CH_4}} = \frac{\mathrm{F}_{CH_4,out}}{\mathrm{F}_{CH_4,out} + \mathrm{F}_{CO,out}} \times 100 \quad (7)$$

$$S_{CO} = \frac{\mathrm{F}_{CO,out}}{\mathrm{F}_{CH_4,out} + \mathrm{F}_{CO,out}} \times 100 \quad (8)$$

$$Y_{CH_4} = \frac{X \times S_{CH_4}}{100} \quad (9)$$

Where $F_{CO2,in}$ and $F_{CO2,out}$ are the molar flowrate of CO_2 in moles min^{-1} in the inlet and outlet gas flow, respectively. $F_{CH4,out}$ and $F_{CO,out}$ are the molar flowrate of CH_4 and CO in moles min^{-1} in the outlet gas flow, respectively. Due to variations in the total exit flowrate, N_2 is used as internal standard in the GC to determine the total exit flowrate. A detailed example of calculation is described in Appendix 1.

5. Simulation of Thermodynamic Equilibrium of CO_2 Methanation

Thermodynamic equilibrium analysis was performed by the simulation software HSC Chemistry®. The equilibrium compositions of the system were determined at specified operating conditions (temperature, pressure and feed composition) using a model based on the minimization of Gibbs free energy of the existing species (CH_4, H_2O, CO_2, CO, H_2, solid carbon). This method does not require the indication of chemical reactions that are taking place in the system, since it is based on the hypothesis that at chemical equilibrium, for a given temperature and pressure, the total Gibbs energy of the system minimum and its differential is zero. The total Gibbs energy is given by [6]

$$G^t = \sum_{i=1}^{N} n_i \mu_i = \sum_{i=1}^{N} n_i \left(G_i^0 + RTln \frac{f_i}{f_i^0} \right) \quad (10)$$

Where N is the number of compounds of i species, n is the number of moles, μ is the chemical potential, G_0 is the standard Gibbs free energy, R is the molar gas constant, T is the temperature of the system, f is the fugacity at the operating conditions and f^0 is the fugacity at the standard state.

In the gas phase, for the reaction equilibrium, the equation is

$$G^t = \sum_{i=1}^{N} n_i \left(\Delta G_{fi}^0 + RTln \frac{y_i \phi_i P}{P^0} \right) \quad (11)$$

Where ΔG^0_f is the standard function of formation, y is the gas phase molar fraction, Φ is the fugacity coefficient, P is the pressure of the system and P^0 is the standard-state pressure of 101.3 kPa.

Therefore, the minimum Gibbs free energy of the total system can be expressed as:

$$\sum_{i=1}^{N} n_i \left(\Delta G_{fi}^0 + RTln \frac{y_i \phi_i P}{P^0} + \sum_k \lambda_k a_i k \right) + n_s G_S = 0 \quad (12)$$

where λ_k is the Lagrange multiplier and α_{ik} is the number of atoms of the k^{th} element present in each molecule of species I, n_s is the number of solid carbon molecules (accounting for coke deposition), and G_s is the Gibbs free energy of solid carbon at the operating conditions.

6. *In situ* Studies

6.1 Steady-state diffuse reflectance infrared Fourier transform spectroscopy

In situ diffuse reflectance infrared Fourier transform spectroscopy (DRIFTS) was performed under CO_2 adsorption and CO_2 methanation steady-state conditions in a Nicolet™ iS50 FTIR spectrometer (Thermo Scientific), equipped with a Mercury-Cadmium-Telluride (MTC) detector and a Praying Mantis™ high temperature reaction chamber. The catalyst (15 mg) was diluted in 135 mg of KBr in order to increase the transmissivity. Similarly to the catalytic experiments, each catalyst was pre-treated *in situ* under 10%H_2/N_2 flowrate of 100 cm^3 min^{-1} at 400 °C for 30 min. After that, the temperature was decreased to the desired temperature, and after 30 min of stabilization, the DRIFTS

background was collected with resolution of 128 cm^{-1}. In the case of CO_2 adsorption experiments, the flowrate was switched to 2.5 cm^3 min^{-1} CO_2 plus 100 cm^3 min^{-1} N_2, and after 30 min of stabilization, a spectrum with a resolution of 256 cm^{-1} was acquired. For CO_2 methanation experiments, the flowrate was switched to 2.5 cm^3 min^{-1} CO_2 plus 100 cm^3 min^{-1} 10%H_2/N_2, and after 30 min of stabilization, a spectrum was acquired with a resolution of 256 cm^{-1}. Steady-state DRIFTS experiments of CO_2 adsorption and CO_2 methanation were conducted at 250, 300 and 350 °C.

6.2 Modulation excitation–phase sensitive detection–diffuse reflectance infrared Fourier transform spectroscopy

In situ modulation excitation–phase sensitive detection–diffuse reflectance infrared Fourier transform spectroscopy (ME–PSD–DRIFTS) was carried out using the same spectrometer as in steady-state experiments above. Similarly, 15 mg of catalyst were diluted by 135 mg of KBr in order to increase the transmissivity and each catalyst was pre-treated *in situ* under 10% H_2/N_2 flowrate of 100 cm^3 min^{-1} at 400 °C for 30 min. After that, the temperature was decreased under N_2 flow to the desired temperature and stabilized for 30 min. The background was collected with a resolution of 128 cm^{-1}, and the sample was subjected to a continuous flowrate of 2.5 cm^3 min^{-1} CO_2 plus 100 cm^3 min^{-1} 10%H_2/N_2 for 30 min for the stabilization. Finally, the experiment was started by switching the flow periodically, using a VALCO valve controlled by Labview software, from flowrate A [2.5 cm^3 min^{-1} CO_2 plus 100 cm^3 min^{-1} 10%H_2/N_2] to flowrate B [2.5 cm^3 min^{-1} CO_2 plus 100 cm^3 min^{-1} N_2] with a period of 120 s for 20 cycles. The spectra were collected every 4 s with a resolution of 4 cm^{-1}. Figure 2.2 presents a scheme of the ME-PSD-DRIFTS setup.

The intermediate species of the reaction should be the only species responding to the perturbation frequency *f*. The response of the spectra to this perturbation was processed via Fourier transform (FT) to obtain the spectra in

the frequency domain that was subjected to a filter leaving only the species that responded to the modulation perturbation.

The method commonly used for phase sensitive detection of IR data was established by Baurecht and Fringeli [7] and combines the FT and inverse Fourier transform (IFT) by solving:

$$A_k^{\phi_k^{PSD}}(\tilde{\nu}) = \frac{2}{T}\int_0^T A(\tilde{\nu},t)\sin(k\omega t + \phi_k^{PSD})dt \tag{13}$$

where $A_k^{\phi_k^{PSD}}(\tilde{\nu})$ is the IFT (i.e., phase-resolved absorbance spectrum) of absorbance in the time domain, $A(\tilde{\nu},t)$, T is the time of one period, ω is the angular modulation frequency, k is a positive integer (where k=1 corresponds to the fundamental frequency – modulation frequency), ϕ_k^{PSD} is the modulation phase angle.

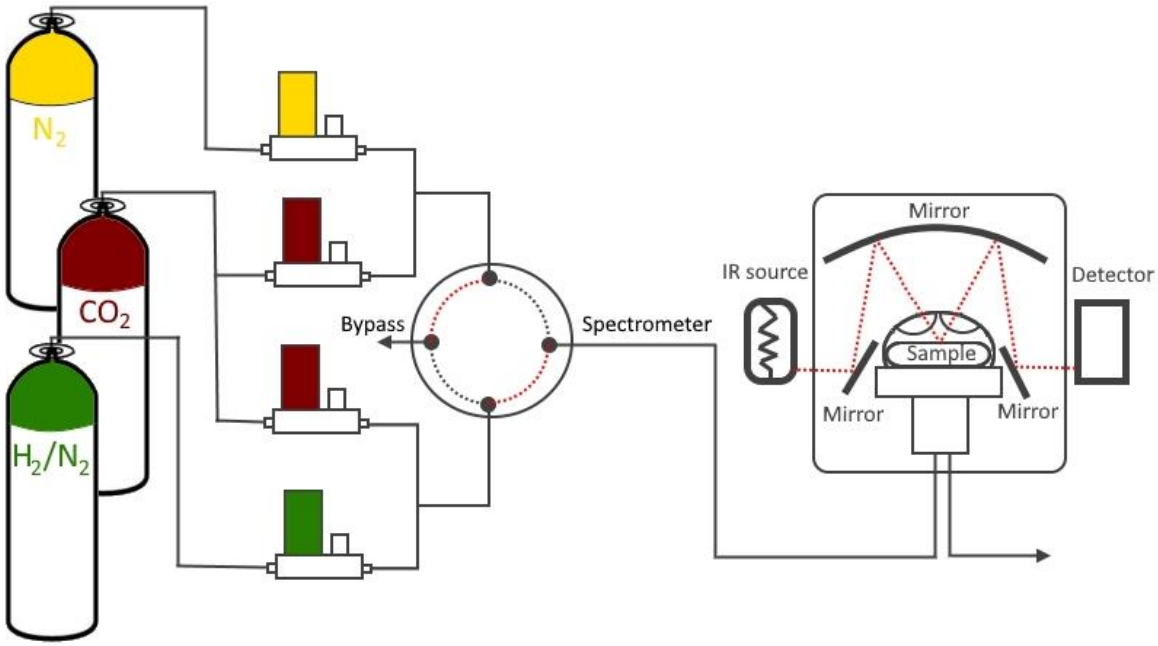

Figure 2.2. Schematic representation of the in situ DRIFTS setup.

In this work, a similar method was used, established by Srinivasan et al. [8,9] by solving $X(\tilde{\nu},\omega)$, the (complex) continuous FT of the function $x(\tilde{\nu},t)$:

$$F(\tilde{\nu},\omega) = \frac{1}{2\pi}\int_{-\infty}^{\infty} f(\tilde{\nu},t)e^{-i\omega t}dt \quad (14)$$

With the data in the frequency domain, a filter was applied to restrict signals to the frequency of modulation. And after that, the IFT was applied.

Where $x(\tilde{\nu},t)$ is transformed in $X(\tilde{\nu},\omega)$ by the IFT equation was applied:

$$f(\tilde{\nu},t) = \int_{-\infty}^{\infty} F(\tilde{\nu},\omega)e^{i\omega t}d\omega \quad (15)$$

This way, the spectroscopic data, in the phase domain, contained only the species that respond to the feed modulation frequency.

The discrete FT (DFT) and the inverse DFT (IDFT) to a discrete sequence of time-domain spectra were applied.

Furthermore, the phase delay (φ) was determined as the in-phase angle value of ϕ^{PSD} at which the amplitude reaches a maximum. [10]

The data was processed, solving numerically these equations with a Python software code (www.python.org).

6.3 *In situ* TEM

The catalyst powder was drop cast directly on the bottom MEMS chip into the center of the heating spiral for a DENSsolutions Climate gas and heating holder. The holder was then assembled in air and leak tested before loading into an image corrected Titan-300 operating at 300 kV. Once inside the column, Ar gas was used to purge the system of any air. Three separated *in situ* experiments were performed: first, a replication of external conditions with a pre-treatment under H_2 in Ar ratio 4:96 before observing the particles under various ratios of CO_2:H_2; second, the particle behavior with the reduction treatment beforehand, finally the particle behavior in CO_2 alone. Heating was carried out at various temperatures, including 400 °C, 450 °C and 500 °C.

References

(1) Figueiredo, J. L.; Pereira, M. F. R. R.; Freitas, M. M. A. A.; Orfao, J. J. M. Modification of the Surface Chemistry of Activated Carbons. *Carbon N. Y.* **1999**, *37* (9), 1379–1389. https://doi.org/10.1016/S0008-6223(98)00333-9.

(2) Soares, O. S. G. P.; Rocha, R. P.; Gonçalves, A. G.; Figueiredo, J. L.; Órfão, J. J. M.; Pereira, M. F. R. Easy Method to Prepare N-Doped Carbon Nanotubes by Ball Milling. *Carbon N. Y.* **2015**, *91*, 114–121. https://doi.org/10.1016/j.carbon.2015.04.050.

(3) Menéndez, J. A.; Xia, B.; Phillips, J.; Radovic, L. R. On the Modification and Characterization of Chemical Surface Properties of Activated Carbon: Microcalorimetric, Electrochemical, and Thermal Desorption Probes. *Langmuir* **1997**, *13* (13), 3414–3421. https://doi.org/10.1021/la9602022.

(4) Faria, P. C. C.; Órfão, J. J. M.; Pereira, M. F. R. A Novel Ceria – Activated Carbon Composite for the Catalytic Ozonation of Carboxylic Acids. *Catal. Commun.* **2008**, *9*, 2121–2126. https://doi.org/10.1016/j.catcom.2008.04.009.

(5) Figueiredo, J. L.; Ribeiro, F. R. *Catálise Heterogénea*; Fundação Calouste Gulbenkian: Lisboa, 1989.

(6) Vita, A.; Italiano, C.; Previtali, D.; Fabiano, C.; Palella, A.; Freni, F.; Bozzano, G.; Pino, L.; Manenti, F. Methanol Synthesis from Biogas: A Thermodynamic Analysis. *Renew. Energy* **2018**, *118*, 673–684. https://doi.org/10.1016/j.renene.2017.11.029.

(7) Baurecht, D.; Fringeli, U. P. Quantitative Modulated Excitation Fourier Transform Infrared Spectroscopy. *Rev. Sci. Instrum.* **2001**, *72* (10), 3782–3792. https://doi.org/10.1063/1.1400152.

(8) Srinivasan, P. D.; Patil, B. S.; Zhu, H.; Bravo-Suárez, J. J. Application of Modulation Excitation-Phase Sensitive Detection-DRIFTS for: *In Situ*/Operando Characterization of Heterogeneous Catalysts. *React. Chem. Eng.* **2019**, *4* (5), 862–883. https://doi.org/10.1039/c9re00011a.

(9) Srinivasan, P. D.; Khivantsev, K.; Tengco, J. M. M.; Zhu, H.; Bravo-Suárez, J. J. Enhanced Ethanol Dehydration on γ-Al_2O_3 Supported Cobalt Catalyst. *J. Catal.* **2019**, *373*, 276–296. https://doi.org/10.1016/j.jcat.2019.03.024.

(10) Aguirre, A.; Collins, S. E. Selective Detection of Reaction Intermediates Using Concentration- Modulation Excitation DRIFT Spectroscopy. *Catal. Today* **2013**, *205*, 34–40. https://doi.org/10.1016/j.cattod.2012.08.020.

Chapter 3

The Role of the Surface Properties in CO_2 Methanation over Carbon-Supported Ni Catalysts and their Promotion by Fe

Gonçalves, L. P. L.; Sousa, J. P. S.; Soares, O. S. G. P.; Bondarchuk, O.; Lebedev, O. I.; Kolen'ko, Y. V.; Pereira, M. F. R. *The Role of Surface Properties in CO_2 Methanation over Carbon-Supported Ni Catalysts and Their Promotion by Fe*. Catal. Sci. Technol. **2020**, 10 (21), 7217

Abstract

The surface chemistry of the activated carbon supporting material was tailored to investigate the influence of O and N groups as well as O-free Lewis basic sites on the performance of the Ni-based catalysts for CO_2 methanation. Catalytic experiments demonstrated that 15% Ni on carbon with O-free Lewis basic sites showed the best performance (X_{CO2} = 76%, S_{CH4} = 97%, T = 450 °C, P = 1 bar), suggesting that methanation reaction is highly dependent on the basicity of the support. Promotion with 5% Fe enabled the decrease of the optimal reaction temperature while improving the stability of the catalyst. Microstructural and compositional studies of the catalyst after prolonged time on stream experiment suggested that the slight but gradual catalyst deactivation during methanation is associated with the sintering of Ni nanoparticles and the development of distinct Ni@NiO core-shell nanostructure.

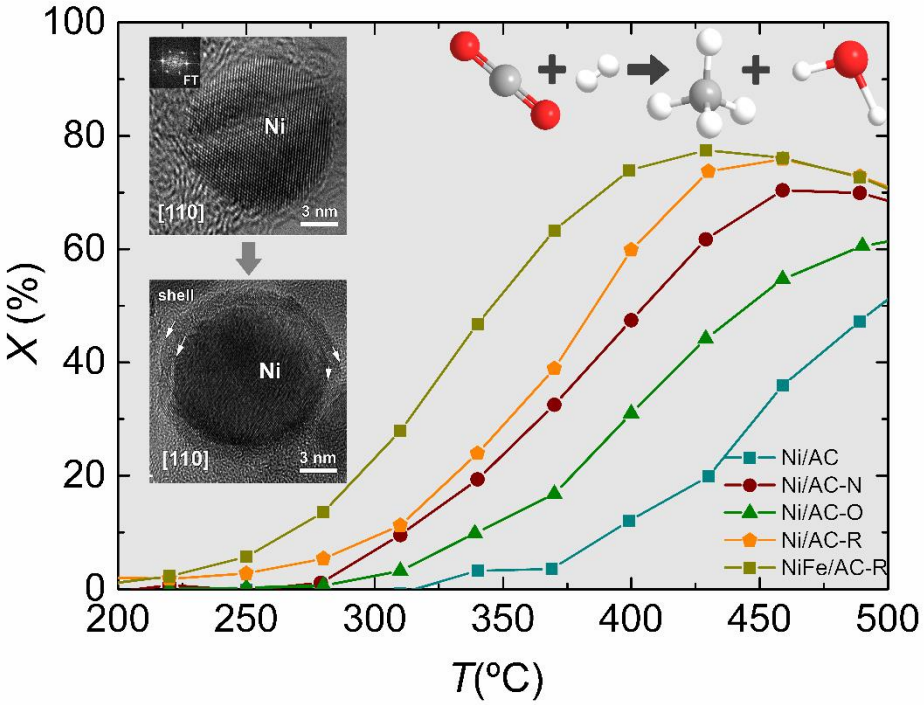

1. Introduction

Sabatier reaction of CO_2 methanation is the reaction of CO_2 hydrogenation to CH_4 ($CO_2 + 4H_2 \leftrightarrow CH_4 + 4H_2O$, $\Delta H_{298K} = -165$ kJ mol^{-1}).[1] This widely studied reaction presents a great interest since it can be used as a solution to combat CO_2 emissions by converting it into CH_4 gas fuel with the help of H_2 produced using renewable energy. Although CO_2 methanation is a thermodynamically favorable reaction, it has significant kinetic barriers, requiring a catalyst to achieve good CO_2 conversion and selectivity to CH_4. The reaction can occur through two pathways in the different catalysts: (*i*) CO_2 is adsorbed associatively with a former adsorbed H atom, forming formate as an intermediate, without CO formation (associative scheme), or (*ii*) CO_2 adsorbs dissociatively on the catalyst and CO acts as an intermediate of the reaction (dissociative scheme).[2,3]

Several studies have been conducted on metal-based catalysts for CO_2 methanation, and mainly group VIII transition metals, such as Ni,[4–13] Co,[14,15] Ru,[16,17] Rh,[12,18] and Pd,[19,20] have been found to be active. From this set, Ni-based catalysts are the most commonly used, owing to the optimal combination of activity, selectivity and cost.[4–12] For instance, a typical industrial Ni/Al_2O_3 catalyst can achieve a CO_2 conversion $X_{CO2} \approx$ 80–90% at 400 °C with selectivity towards CH_4 $S_{CH4} \approx 100\%$.

Notably, it is still challenging to achieve high X_{CO2} at low temperatures with Ni catalysts due to the high activation energy involved in this process. Ni catalysts also feature low stability at higher temperatures due to sintering of the catalyst nanoparticles, degradation *via* formation of volatile $Ni(CO)_4$, as well as coke building-up on active Ni sites under severe reaction conditions.[9]

An interesting way to improve the performance of Ni catalysts is to use an appropriate supporting material. The properties of the supporting materials, such as surface area, pore size, hierarchical structure, surface chemistry, and metal-support interaction (MSI), have been reported to be an excellent tool-

box for tailoring the performance of the catalyst and its stability.[5,8,9,11] Specifically, mainly metal oxide supporting materials have been investigated, such as Al_2O_3, SiO_2, TiO_2, and CeO_2, [4–8] but recently, new types of supports have emerged, such as zeolites[10] and metal-organic frameworks.[11] By contrast, the investigation of activated carbon (AC) supporting materials for CO_2 methanation catalysts remain remarkably scarce.[9,12,21–23] Drawing on our extended experience in catalytically-relevant carbon materials, we decided to investigate AC as support for Ni-based catalysts for CO_2 methanation.[24–26]

AC is a cost-effective class of carbon materials exhibiting high surface area, controlled pore size distribution and degree of graphitization. Moreover, AC can be doped with non-metal N, O and other elements, providing access to interesting supporting materials with tailored surface properties.[27]

Furthermore, AC has been extensively studied as CO_2 adsorbent, demonstrating a high efficiency at low pressure,[28] which has been implicated in CO_2 methanation.[22]

Cam *et al.*[23] investigated the CO_2 methanation reaction on AC−supported Ni with different metal loadings. They attributed the good performance of the catalyst to the high reducibility of Ni species on the AC support. Furthermore, Li *et al.*[9] studied Ni-based catalysts supported on coconut shell carbon and concluded that the high surface area of this type of support promoted a better dispersion of the Ni nanoparticles (NPs), exhibiting better performance when compared to those supported on Al_2O_3 and ZrO_2. Despite these insights, a systematic study of the role of the surface properties in CO_2 methanation over AC−supported Ni catalysts has not been conducted.

Another interesting approach to improve the performance of a catalyst, in this case working on the active metal side, is the addition of a second active metal. The resultant bimetallic catalyst can present higher catalytic activity than the monometallic counterpart, since the interaction between the surfaces of two metals can change the electronic and geometric structure of the catalyst, increasing its activity and selectivity.

Fe has been often studied as a co-metal for Ni methanation catalysts, and it has been shown that it can improve both activity and stability of the catalyst, due to several factors. Specifically, the formation of the Ni–Fe alloy potentially increases the reducibility of Ni, due to the distinct redox properties of Fe, reducing the MSI.[29–32] Fe can also improve the stabilization of the Ni phase, allowing a better distribution of the metal phase and preventing sintering under reaction conditions. Furthermore, the formation of the alloy can facilitate CO dissociation on the catalyst due to an optimal CO dissociation energy at the surface of the alloy, which is considered as the rate-determining step of the reaction in the dissociative mechanism.[30–39]

Notably, there is no study of NiFe catalysts on AC support materials, and therefore we decided to address this in the current study.

We modified the surface of AC in order to study the influence of different surface chemistry properties on the performance of Ni/AC catalysts for CO_2 methanation. AC with oxygen functional groups, N-doped AC, and reduced AC with increased base Lewis sites were prepared and Ni nanoparticles were supported on each material, and compared with Ni supported on pristine AC. Furthermore, a bimetallic NiFe catalyst was prepared with the best performing support, in order to evaluate the influence of Fe addition on the performance of the catalyst. The materials were fully characterized and their activity and selectivity for CO_2 methanation reaction were evaluated. The results of this study provide new insights on the influence of the surface chemistry of the support, as well as on the addition of Fe on the catalyst performance for CO_2 methanation. Our results demonstrate that an increase in the basicity of the support leads to higher CO_2 methanation activity, while the addition of Fe leads to higher catalyst activity at lower temperatures as well as better stability.

2. Experimental

In the present work, we modified the surface of commercial AC to investigate the influence of different surface chemistries on the catalyst performance. AC

was oxidized with 5 M HNO_3 in a Soxhlet to obtain a sample with an extended amount of oxygen functional groups (AC−O).[24] N-doped AC (AC−N) was synthesized by mixing AC with melamine as N source in a ball milling, followed by heat treatment at 600 °C under N_2.[40] Finally, a reduced AC with increased number of Lewis basic sites (AC−R) was prepared by heat treatment in H_2 at 900 °C.[41]

Next, Ni NPs were anchored on the resultant supports, as well as on pristine AC, while NiFe NPs were anchored on the best performing support. For this, we leveraged on the convenient incipient wetness impregnation (IWI) method, using $Ni(NO_3)_2{\cdot}6H_2O$ and $Fe(NO_3)_3{\cdot}9H_2O$ as Ni and Fe precursors, respectively, followed by the reduction in H_2 at temperatures established by H_2 temperature programmed reduction (H_2–TPR), which were 400 °C in the case of Ni/AC, Ni/AC−O, Ni/AC−R, and NiFe/AC−R and 300 °C in the case of Ni/AC−N. Based on preliminary catalytic testing, the optimal Ni loading was found to be 15% and Fe loading 5% (Appendix 2).

The resultant supports and catalysts, namely AC, AC−N, AC−O, and AC−R, and Ni/AC, Ni/AC−N, Ni/AC−O, Ni/AC−R, and NiFe/AC−R were characterized by N_2 physisorption at −196 °C, elemental analysis, point of zero charge (pH_{PZC}), X-ray photoelectron spectroscopy (XPS), transmission electron microscopy (TEM), high-angle annular dark-field scanning transmission electron microscopy (HAADF-STEM), electron diffraction (ED), and energy-dispersive X-ray spectroscopy in STEM mode (STEM−EDX), X-ray diffraction (XRD), H_2 temperature programmed reduction (H_2–TPR), H_2–Chemisorption, and Temperature Programmed Desorption (TPD).

Their activity, selectivity, and stability in CO_2 methanation were evaluated in a Microactivity XS15 system (PID Eng & Tech), using a fixed bed quartz reactor (d_{int} = 1 cm). The products in the outflow were analyzed online by a GC 1000 gas chromatograph (DANI), equipped with a thermal conductivity detector (TCD) and a GS-CarbonPLOT capillary column, using He as carrier gas and a continuous flow of N_2 as internal standard. Each catalyst (100 mg) was pre-treated *in situ* under H_2 flow (40 cm^3 min^{-1}) at the reduction temperature for

30 min, at 1 bar. After that, the reactor temperature was decreased to 200 °C under He (50 $cm^3\ min^{-1}$), and then, the reactor was fed with 10% CO_2, 40% H_2 (the stoichiometric composition) and 50% He, with a total flow rate of 100 $cm^3\ min^{-1}$. A temperature ramping from 200 °C to 500 °C was performed under reaction conditions to evaluate the performance of each sample at various temperatures. Additionally, the isothermal time on stream (TOS) experiments were conducted under the same reaction conditions to evaluate the stability of the best performing samples.

More experimental details for the synthesis of the catalysts and their detailed characterization are summarized in Chapter 2.

3. Results

3.1 Topmost performance of Ni catalyst supported on reduced AC.

We began by performing a light-off experiment for CO_2 methanation reaction over 200-500 °C temperature range using the synthesized Ni catalysts (Figure 3.1). All carbon materials without Ni (AC, AC−N, AC−O, AC−R) were initially tested and their activities were found to be null (data not shown). For the Ni-containing catalysts, the conversion of CO_2 increases with the temperature until it reaches a maximum at 450 °C for Ni/AC−N (X_{CO2} = 70%) and Ni/AC−R (X_{CO2} = 76%) catalysts (Figure 3.1). The other two catalysts, Ni/AC (X_{CO2} = 54%) and Ni/AC−O (X_{CO2} = 62%), achieve their maximum conversion only at 500 °C (Figure 3.1). A similar behavior was observed in terms of the selectivity (S_{CH4}) and yield (Y_{CH4}) towards CH_4 and it is important to note that the only other product formed was CO. A further increase above the optimal temperature resulted in a decrease of activity due to thermodynamic reasons, wherein higher temperature favors methane steam reforming and the reverse water gas shift (RWGS) reaction.[42]

Comparing to the calculated thermodynamic equilibrium curves (Figure 3.1), the X_{CO2} remains below the thermodynamic limits; especially at low

temperatures. This is most likely due to the kinetic barrier for the full reduction of C^{+4} in CO_2 to C^{-4} in CH_4, an 8 e^- process that requires a high activation energy. When looking at the Y_{CH4}, one can assume that at low temperatures (200–450 °C) the methanation reaction over our catalysts was probably a kinetic controlled reaction. Thermodynamically, Y_{CH4} should decrease with temperature, in contrast, our experiments show an increasing trend.

The catalysts with modified surface properties (Ni/AC−N, Ni/AC−O, Ni/AC−R) demonstrate significantly improved performance in comparison to the Ni catalyst supported on pristine AC (Ni/AC). Accounting for the highest X_{CO2}, S_{CH4} and Y_{CH4}, the catalytic performance order was established to be Ni/AC−R > Ni/AC−N > Ni/AC−O >> Ni/AC. Notably, from all the prepared catalysts with different surface functionality, Ni/AC−R exhibits the topmost performance, achieving X_{CO2} = 76% and S_{CH4} = 97% at 450 °C, approaching the thermodynamic limit at this temperature.

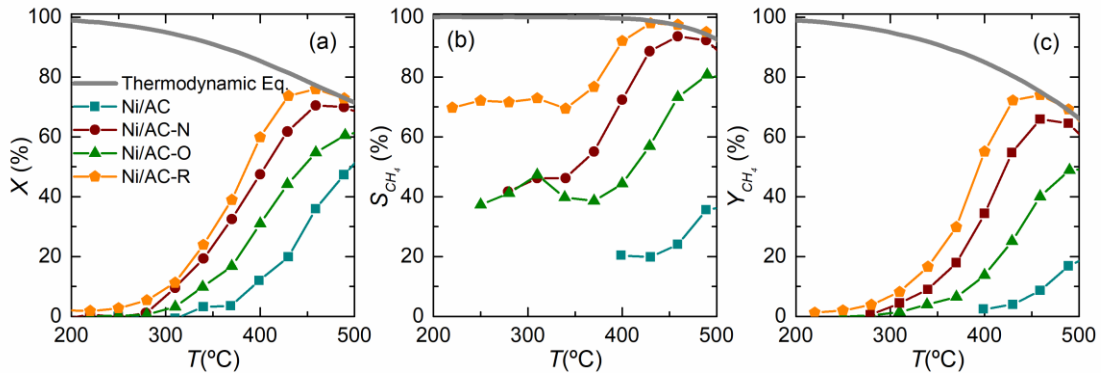

Figure 3.1. Comparison of the catalytic properties of the synthesized Ni catalysts supported on ACs with different surface functionalities: X_{CO2} (a), S_{CH4} (b) and Y_{CH4} (c) as a function of temperature, together with the respective thermodynamic equilibrium curves. Reaction conditions: P = 1 bar; $WHSV$ = 60 000 mL g^{-1} h^{-1}; CO_2 : H_2 = 1 : 4.

3.2 Similar materials characteristics but distinct surface properties of the synthesized Ni catalysts.

To understand the activity trend, the catalysts were extensively characterized. N_2 adsorption–desorption isotherms indicate that both the supports (Figure 3S.1, Table 3S.1) and the catalysts (Figure 3S.4, Table 3.1) exhibit similar

textural properties, with the catalysts showing high S_{BET} of ca. 650 $m^2\ g^{-1}$ (except Ni/AC−N, which has slightly lower S_{BET} of 480 $m^2\ g^{-1}$).

The elemental composition results (Table 3S.1) confirm the higher amount of O in AC−O support (9.6% cf. 7.0% in AC) as a result of the oxidation treatment; the lower amount of O in AC−R (3.8%), caused by the reduction treatment, and the higher amount of N in AC−N (5.8% cf. 0.0% in AC) compared to the results obtained in pristine AC. These results are in good agreement with the XPS data obtained for the supporting materials (Figure 3S.2, Figure 3S.3 and Table 3S.2).

Furthermore, temperature-programmed desorption (TPD) (Figure 3S.7, Table 3.1), allowed to quantify the amount of oxygen containing groups in the samples, which are directly correlated with the acidity/basicity of the Ni/AC, Ni/AC−O, and Ni/AC−R samples.[43] Generally, the acidity of a sample increases with the increase of surface oxygen groups that decompose as CO_2 (ie. carboxylic acids and anhydrides). It can be observed in Table 3.1 that the amount of CO_2 evolved from the samples' decomposition follows the order Ni/AC−O > Ni/AC >> Ni/AC−R.

Table 3.1. Textural properties, mean Ni NPs diameter (d_p), TPD, and H_2-chemisorption results of the as-synthesized Ni-based CO_2 methanation catalysts Ni/AC, Ni/AC−N, Ni/AC−O, Ni/AC−R, and NiFe/AC−R, together with pH_{PZC} of the respective support (AC, AC−N, AC−O and AC−R).

Sample	S_{BET} ($m^2\ g^{-1}$)	$V_{P,P/P0=0.95}$ ($cm^3\ g^{-1}$)	V_{micro} ($cm^3\ g^{-1}$)	d_p (nm)[a]	pH_{PZC} (support)	*CO Peak 3*[b] *(Relative %)*[c]	CO_2 ($\mu mol\ g^{-1}$)[c]	H_2 chemisorbed ($\mu mol\ g^{-1}$)[d]	*Ni Surface Area* ($m^2\ g_{cat}^{-1}$)[d]
Ni/AC	653	0.40	0.27	12±5	7.9	30	519	19.1	1.49
Ni/AC−N	480	0.30	0.20	10±9	7.1	20	673	15.2	1.18
Ni/AC−O	634	0.39	0.26	10±8	2.1	28	555	19.5	1.53
Ni/AC−R	656	0.41	0.27	10±6	9.4	34	417	34.9	2.73
NiFe/AC−R	659	0.42	0.25	10±5	9.4	30	551	23.6	--

[a] Determined by TEM; [b] Peak 3 of CO evolution graphic, relative to carbonyl-quinone groups; [c] Determined by TPD; [d] Determined by H_2-chemisorption.

Additionally, from the oxygen-containing groups present in a carbon material, those that contribute more to the basicity of a sample are carbonyl-quinone groups, which decompose as CO at high temperatures during TPD. It can be observed in Table 3.1 that the relative percentage of these groups (Peak 3),

analyzed by the CO evolution from TPD (Figure 3S.7), compared to the others that decompose as CO, is higher in the case of Ni/AC−R. Thus, we can conclude that the basicity of these samples follows the order Ni/AC−R >> Ni/AC > Ni/AC−O, which is confirmed by pH_{PZC} (Table 3.1). Regarding Ni/AC−N, the basicity of this sample is related to the amount of N-groups, and both elemental composition analysis and XPS confirmed the increased amount of N-groups in this sample.

TEM results (Table 3.1, Figure 3S.5, Figure 3S.6) indicate that the mean size of Ni NPs and their spatial dispersion over functionalized ACs are quite similar, with $d_p \approx 10$ nm; though, NPs supported on pristine AC present a slightly higher $d_p \approx 12$ nm. However, observing H_2-chemisorption results (Table 3.1), the best performing sample, Ni/AC−R present higher metallic Ni surface area, comparing to the other samples, which have similar values.

The phase composition of the NPs was studied by XRD analysis, which demonstrated that all Ni catalysts were composed of metallic Ni NPs (Figure 3.2a), as reflected by the presence of Ni(111) peak at $2\theta = 44.4°$, Ni(200) peak at $2\theta = 51.8°$, and Ni(220) peak at $2\theta = 76.4°$.[5,6] Interestingly, peaks corresponding to the NiO oxide phase were not detected in any catalysts.[13]

Ni/AC, Ni/AC−O and Ni/AC−R show similar reducibility profiles (Figure 3.2b) with two main peaks: (*i*) at ca. 330 °C due to the reduction of the Ni species that are weakly interacting with the carbon support, and (*ii*) at ca. 380 °C, related to the reduction of Ni species that interact more strongly with the carbon support. Ni catalyst on N-doped AC (Ni/AC−N) demonstrates a slightly distinct profile from the other catalysts, with three main peaks at lower temperatures (ca. 280 °C, 315 °C, and 340 °C).

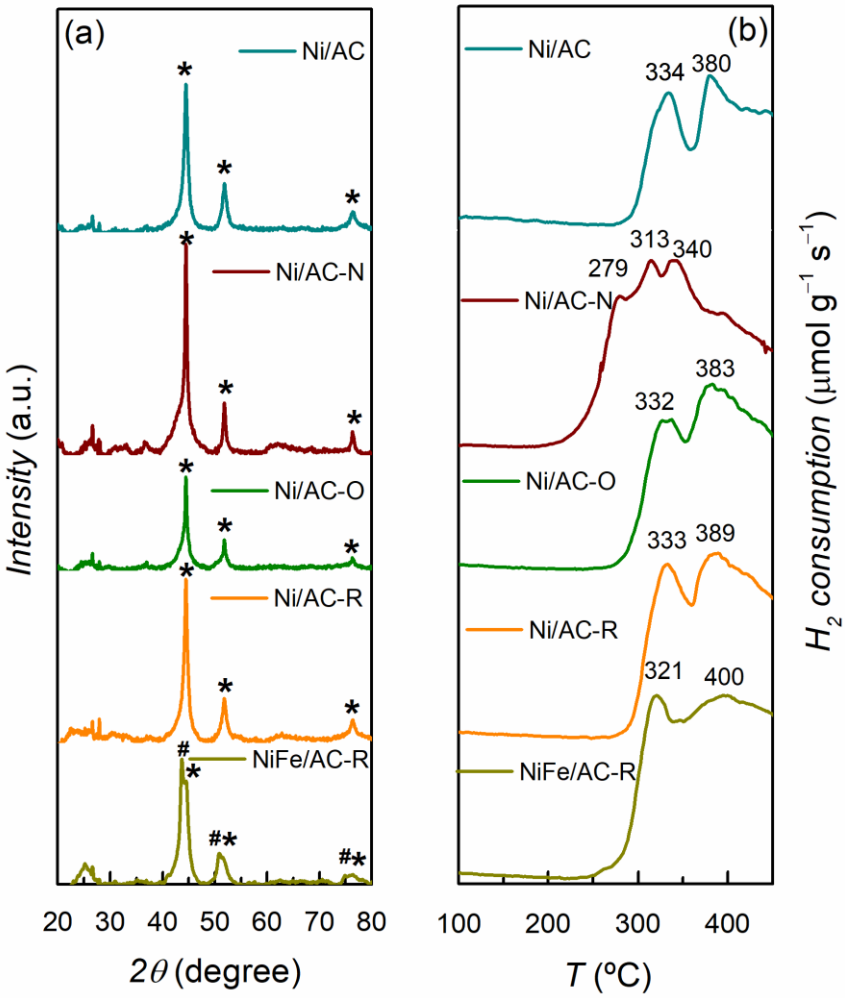

Figure 3.2. Comparison of XRD patterns (a) and H_2–TPR profiles (b) for Ni/AC, Ni/AC−N, Ni/AC−O, Ni/AC−R, and bimetallic NiFe/AC−R catalysts for CO_2 methanation.

For all the catalysts, three different components are observed from the deconvolution of the XPS data on the Ni $2p_{3/2}$ (Figure 3.3). The lower energy component (852.8 eV) is assigned to Ni^0 species, while the component at 854.2 ± 0.2 eV is assigned to NiO phase, and the one at 856.0 ± 0.1 eV to $Ni(OH)_2$ phase. [13,44-47] Even though all the samples were reduced under H_2 at the respective temperatures established by H_2–TPR experiments, it is reasonable to expect the presence of NiO and $Ni(OH)_2$ phases due to inevitable oxidation of metallic Ni surface upon the exposure to ambient conditions.

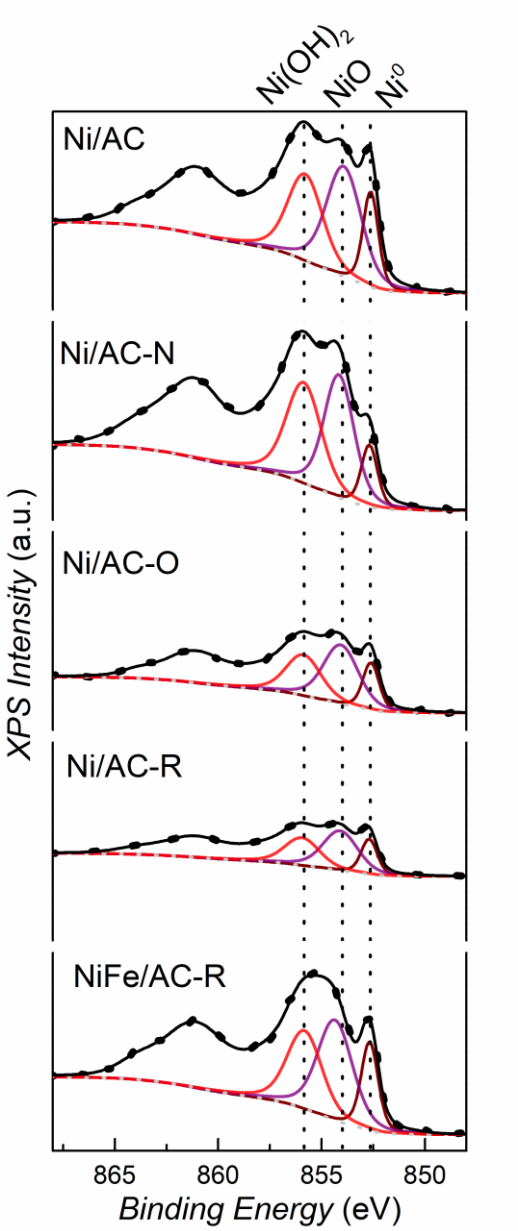

Figure 3.3. High-resolution XPS data for Ni $2p_{3/2}$ region collected from Ni/AC, Ni/AC−N, Ni/AC−O, Ni/AC−R, and bimetallic NiFe/AC−R catalysts. Symbols: raw data; black lines: overall fits; coloured lines: fits of individual components; dashed lines: background.

3.3 Lowering the temperature of methanation and increasing the stability of Ni catalyst by Fe promotion

We examined whether the catalytic performance of the best Ni/AC−R material could be improved by adding Fe as second active metal. For this purpose, several Ni–Fe bimetallic catalysts were prepared. After the catalytic screening of the synthesized materials with different loadings (Appendix 2), the optimal Ni and Fe co-loading was established to be 15% of Ni and 5% of Fe.

The XRD analysis of this bimetallic NiFe/AC−R catalyst indicates the formation of a NiFe alloy. Specifically, the broadening of the diffraction peaks and their shift towards lower 2θ, namely, 43.7 °, 50.8 ° and 74.8 °, suggest the presence of a phase mixture of metallic Ni and Ni-Fe alloy (Figure 3.2a).[31,32,48] According to the TEM, the bimetallic NiFe/AC−R exhibits a mean particle size of $d_p \approx 10$ nm, which is similar to monometallic Ni/AC−R (Figure 3S.5, Figure 3S.6). H_2–TPR profile of NiFe/AC−R shows two main peaks at 321 °C and 400 °C. Comparing these temperatures with those of the monometallic Ni/AC−R, the reduction of the Ni species in NiFe/AC−R occurs at lower temperature: thus, the addition of Fe leads to weaker MSI.

Regarding catalytic properties, the resultant NiFe/AC−R exhibits higher conversion and selectivity at lower temperatures (250-450 °C) in comparison to the monometallic Ni/AC−R counterpart (Figure 3.4a,b). In particular, the bimetallic catalyst demonstrates excellent X_{CO2} = 77% and S_{CH4} = 98%, which are similar to those of the best monometallic Ni/AC−R, however, obtained at a lower temperature (430 °C cf. 450 °C). We compared further the stability of monometallic Ni/AC−R and bimetallic NiFe/AC−R catalysts by testing them at 450 °C for 48 h. Remarkably, while Ni/AC−R demonstrates a loss in X_{CO2} by 8% and in S_{CH4} by 6%, the promoted NiFe/AC−R shows only a marginal loss in X_{CO2} of 3% and in S_{CH4} of 2% (Figure 3.4c).

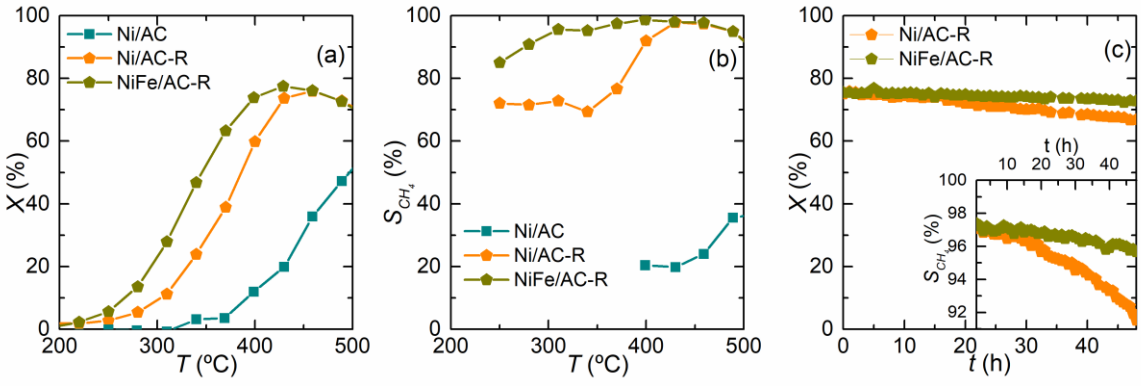

Figure 3.4. Comparison of the catalytic properties of the best Ni catalyst Ni/AC−R and the same promoted by Fe NiFe/AC−R: X_{CO2} and S_{CH4} as a function of temperature (a, b) as well as time-on-stream (TOS) at 450 °C (c). Reaction conditions: P = 1 bar; $WHSV$ = 60 000 mL g^{-1} h^{-1}; CO_2 : H_2 = 1 : 4.

3.5 Formation of Ni@NiO core-shell nanostructure after TOS testing

Since we observed a slight deactivation of the Ni/AC−R catalyst with time (Figure 3.4c), we suspected that the deactivation might be related to the microstructural changes in the catalyst. Therefore, we subjected Ni/AC−R to prolonged time-on-stream (TOS) methanation at 450 °C for 90 h (Figure 3S.9), and then compared the catalyst appearance and chemical composition before and after this testing through electron microscopy.

TEM (Figure 3.5a) and HAADF−STEM (Figure 3S.10) observations of the as-synthesized Ni/AC−R catalyst indicate that the Ni NPs are well-anchored and quite uniformly distributed over the AC−R support. This is also highlighted by the corresponding STEM−EDX elemental maps for Ni and C (Figure 3S.10).

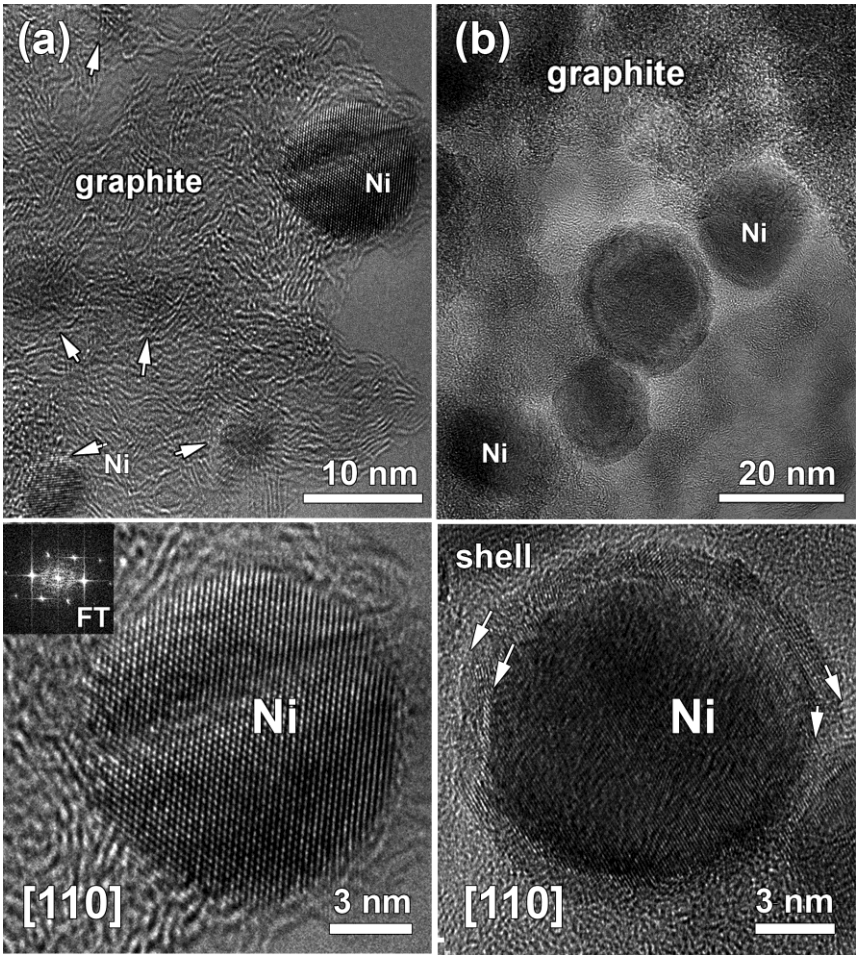

Figure 3.5. Low magnification bright field TEM images and selected [110] HRTEM images of single NP of as-synthesized (a) and spent (b) Ni/AC−R catalyst after long time-on-stream CO_2 methanation at 450 °C for 90 h, which evidences the development of core-shell Ni NPs.

On the other hand, TEM and HAADF−STEM imaging of the spent Ni/AC−R catalyst after 90 h of TOS experiment reveals the growth of Ni NPs from original 10 ± 6 nm to 13 ± 6 nm (Figure 3S.11, Figure 3S.12), while the NPs remain to be well-dispersed over AC−R (Figure 3S.11). Interestingly, our high-resolution TEM and HAADF−STEM investigations of the spent Ni/AC−R after 90 h of methanation at 450 °C evidence the formation of NPs with distinct Ni@NiO core-shell nanostructure (Figure 3.5b, Figure 3.6). Also, XPS analysis of the as-synthesized and spent Ni/AC−R catalyst indicates that the methanation induces a change in the chemical composition of the surface of Ni catalyst. Specifically, the relative amount of Ni^0 and $Ni(OH)_2$ increase while the amount of NiO decreases after TOS testing (Figure 3S.13, Table 3S.4).

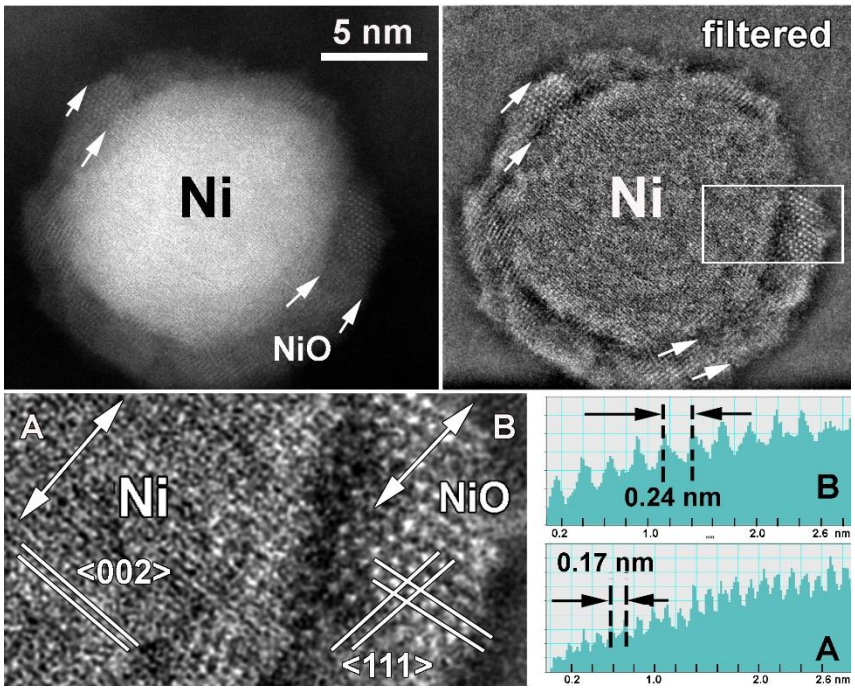

Figure 3.6. HAADF-STEM image of core-shell NP (left upper panel) and their noise filtered image (right upper panel). The core of the NP is depicted with white arrows. The magnified HAADF-STEM filtered image marked by a white box in the filtered image and the corresponding intensity scan line profile perpendicular to lattice planes direction (double head arrows) confirm different d-spacing and evidence that core is Ni (A) while the shell is NiO (B).

4. Discussion

Here we present the investigation of the influence of the surface chemistry of activated carbon supporting materials of Ni-based catalysts for CO_2

methanation. We prepared, characterized, and tested Ni nanocatalysts supported on oxidized AC, N-doped AC, and reduced AC possessing basic Lewis sites. Furthermore, we studied the influence of the addition of Fe to the best performing monometallic Ni catalyst and compared the catalytic properties of the monometallic and bimetallic catalysts.

4.1 Role of the surface chemistry

From the combination of catalytic and characterization results, we assume that the performance trend of the catalysts (Ni/AC−R > Ni/AC−N > Ni/AC−O >> Ni/AC) can be correlated with the surface properties of AC supports. This claim is supported by the fact that the catalysts exhibit similar (*i*) textural properties, (*ii*) mean size of Ni NPs, (*iii*) phase and surface compositions of the active Ni NPs, and (*iv*) reducibility profiles. We thus inferred that the observed catalytic performance trend most likely corresponds to the surface chemistry of the carbon materials.

The better performance of the functionalized supports compared to the pristine one is related to two factors: (*i*) good Ni dispersion, and (*ii*) better CO_2 adsorption. Due to the lack of any specifically designed surface functionality, pristine AC demonstrates worse dispersion of the Ni NPs (bigger NPs observed by TEM) and, consequently, low performance of the respective Ni/AC catalyst.

AC−O support has a higher amount of O-groups when compared to the other supports, as well as a higher degree of oxidation, (determined by the ratio of total oxygen to total carbon, O_t/C_t, Table 3S.2),[24] which leads to a good dispersion of the Ni NPs (smaller NPs observed by TEM), responsible for the better performance of Ni/AC−O than Ni/AC (Figure 3.1).

Regarding to AC−N, the presence of N-groups has two benefits: (*i*) they improve the Ni dispersion (smaller NPs observed by TEM) by providing binding sites that facilitate the Ni stabilization on the support, but also (*ii*) improve the CO_2 adsorption capacity of the sample.[49–51] These two factors lead

to the better performance of Ni/AC−N, when compared to Ni/AC and Ni/AC−O (Figure 3.1), regardless that Ni/AC− N has slightly lower S_{BET} than the other samples.

Ni/AC−R showed the best performance of all tested catalysts (Figure 3.1), which can be attributed to (*i*) the good Ni dispersion and higher metallic Ni surface area of all samples, and to (*ii*) the basicity of this support. The higher metallic Ni surface area can be related to the fact that the AC−R support presents a higher amount of oxygen-free Lewis basic sites on the graphene layers, with resonating π-electrons of carbon aromatic rings. These resonating π-electrons attract protons, which might be the reason for higher dispersion of the Ni nanoparticles on this support since the metal protons dispersion is enhanced during impregnation.[50] Furthermore, as shown in Table 3.1, AC−R exhibits the highest basicity (highest pH_{PZC} = 9.4, lowest total amount of oxygen surface groups (amount of CO_2 released during TPD), and higher relative amount of carbonyl-quinone groups, compared to the other oxygen containing groups) due to the presence of a large number of O-free Lewis basic sites and carbonyl-quinone groups, since most of the acidic O groups were removed during the thermal treatment at 900 °C in H_2. The basicity improves the CO_2 adsorption capacity over Ni/AC−R and, as shown by recent investigations,[50,51] high basicity enables gradients of CO_2 concentration close to the Ni active sites, thus boosting its performance.

Other carbon materials have been studied for CO_2 methanation. Hu *et al.*[52] studied Ni catalysts supported on reduced graphene oxide (RGO), which was more active and selective than Ni/AC and Ni/γ-Al_2O_3. Interestingly, Ni/RGO catalyst obtained a similar CO_2 conversion (X_{CO2} = 78.4% at 350 °C) to our best performing Ni/AC−R catalyst, although at lower weight hourly space velocity (*WHSV*). They attributed the better performance of the catalyst to the RGO high surface area that favors the formation of fine Ni NPs, as well as to the O-containing functional groups on RGO that promote the stable anchoring of the NPs.

Li *et al.*[9] studied Ni catalysts supported on coconut shell carbon (CSC), which also obtained a conversion (X_{CO2} = 77.1% at 450 °C) similar to our best Ni/AC−R, but again at lower *WHSV*. They also attributed the better performance of the catalyst, compared to other supports (Al_2O_3 and ZrO_2), to the large specific surface area of the CSC, promoting a better Ni dispersion. Additionally, they showed that adding Mg to the catalyst improved its performance due to the increase in the catalyst's basicity, which is consistent with our results.

Romero-Sáez *et al.*[44] investigated Ni catalysts supported on carbon nanotubes (CNT), and the Ni/CNT catalyst showed $X_{CO2} \approx 50\%$ with $S_{CH4} \approx 30\%$ at 450 °C. They could drastically improve the S_{CH4} by adding ZrO_2 to Ni/CNT catalyst, achieving $S_{CH4} \approx 97\%$. In another study, Wang *et al.*[51] demonstrated that Ni catalyst supported on N-doped CNT exhibited high basicity, and accordingly showed good performance with X_{CO2} = 80% and S_{CH4} = 99% at 360 °C.

For several decades, ACs were known to be interesting supporting materials for catalysis, but here we demonstrated that the surface modification of these readily available materials is a convenient strategy to boost the catalytic properties: by increasing the surface basicity of the supporting material (Ni/AC−R), we increased the *X* by 22% and the S_{CH4} by 60% cf. Ni/AC. Our results allow to conclude that the basicity of the support plays a major role on the performance of the catalyst since the most basic catalyst (Ni/AC−R) presented the best performance.

4.2 Role of the promotion by Fe

The bimetallic NiFe/AC−R exhibits higher conversion and selectivity than the monometallic Ni/AC−R at lower temperatures. These results are consistent with the reported literature, where it has been shown that the formation of a Ni–Fe alloy is of great importance since it can facilitate CO dissociation on the catalyst due to an optimal CO dissociation energy at the surface of the alloy, as revealed by DFT calculations, and also confirmed experimentally.[31,33–35] Furthermore, the weaker MSI in NiFe/AC−R cf. Ni/AC−R (Figure 3.2b) is an

additional reason for the better performance of the bimetallic catalyst, since it is closely related to the CO dissociation energy.[31–33]

Moghaddam *et al.*[53] studied the addition of different metal promoters to Ni/Al_2O_3 catalysts. They concluded that among the tested metals, Fe was the most promising promoter, allowing to achieve X_{CO2} of 78% and S_{CH4} of 99% at 350 °C. Notably, the *WSHV* was lower than that we used in the current study (9 000 cf. 60 000 mL g^{-1} h^{-1}), and when it was increased to 30 000 mL g^{-1} h^{-1}, the obtained X_{CO2} was significantly lower. However, regarding other supports, the same effect was not so apparent. Pandey *et al.*[54] studied the influence of Fe addition to Ni catalysts supported on various supporting materials, such as Al_2O_3, ZrO_2, TiO_2, SiO_2 and Nb_2O_5. They concluded that Al_2O_3 exhibited a higher enhancement in activity as a consequence of Fe addition compared to the other supporting materials, and these results were attributed to the enhanced ability of Al_2O_3 for CO_2 adsorption.

The results obtained from the long TOS experiment evidence that the addition of Fe leads to an increase in the stability of the Ni/AC−R methanation catalyst, which is most likely due to the stabilization of Ni by Fe, preventing the sintering of Ni NPs.

Based on the characterization results of Ni/AC−R after prolonged TOS, we observed microstructural and compositional changes; however, we are uncertain whether these occur owing to the oxidation of the spent catalyst under exposure to ambient conditions, or they are due to sintering-induced *in situ* restructuring of the Ni surface under methanation reaction. Therefore, our ongoing research is directed towards *in situ* TEM investigation of the Ni/AC−R and NiFe/AC−R catalysts under reaction conditions to piece together fine microstructure and chemical composition for understanding the exact reasons behind their weak but gradual deactivation.

5. Conclusions

A convenient strategy leveraging on fine-tuning the surface functionality of the activated carbon supporting materials can be used to prepare highly active and selective Ni catalysts for the CO_2 methanation. We observed that the basicity of the support plays a major role on the performance of the catalyst since the most basic catalyst (Ni/AC−R) presented the best performance. Importantly, enhancing the catalytic performance of the Ni catalyst while simultaneously reducing the temperature of methanation reaction is possible through judicious Fe promotion. Slight but gradual deactivation of the monometallic catalyst during prolonged time-on-stream CO_2 methanation is primarily associated with Ni NPs sintering, which can be prevented by the addition of Fe. Interestingly, post-reaction *ex situ* analysis of spent Ni catalyst evidenced distinct changes in its chemical composition and microstructure.

6. Supplementary information

6.1 Characterization of supporting carbon materials

6.1.1 N_2 physisorption

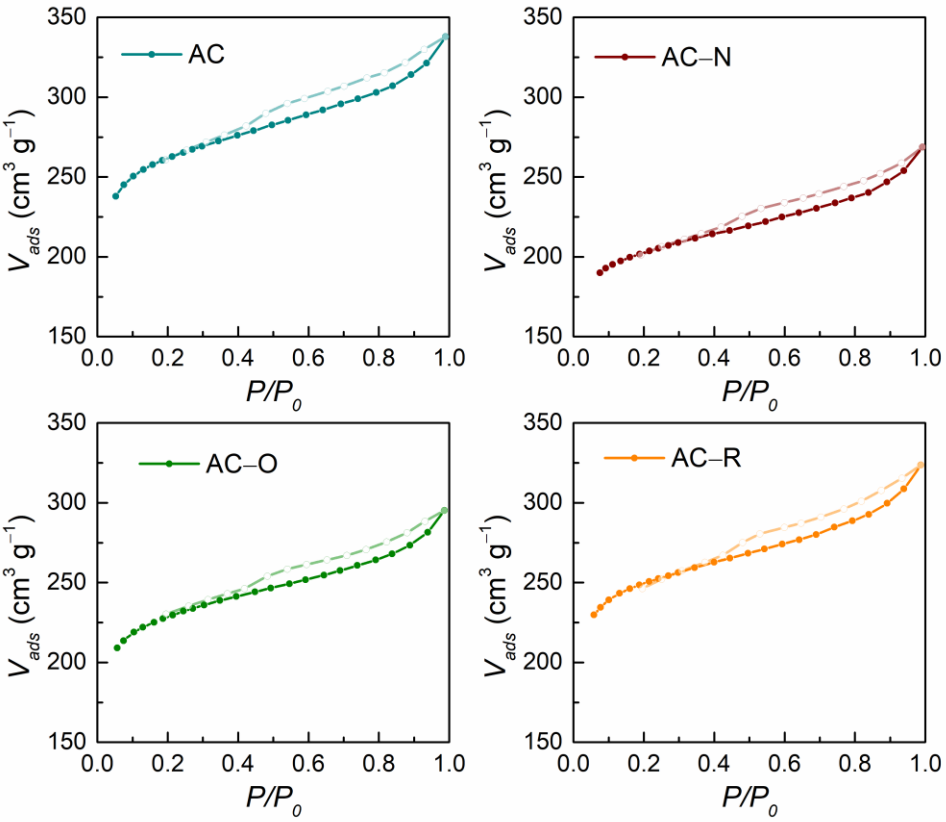

Figure 3S.1. Comparison of N_2 adsorption–desorption isotherms measured at −196 °C for the pristine AC, N-doped AC−N, oxidized AC−O and reduced AC−R supporting materials.

Table 3S.1. Elemental composition and textural properties of pristine AC and as-synthesized AC−N, AC−O and AC−R.

Sample	N (%)	C (%)	H (%)	S (%)	O (%)	S_{BET} (m^2 g^{-1})	$V_{p,p/p0=0.95}$ (cm^3 g^{-1})	V_{micro} (cm^3 g^{-1})
AC	0.0	85.4	2.1	0.4	7.0	784	0.50	0.34
AC−N	5.8	79.7	2.4	0.1	6.9	622	0.39	0.26
AC−O	0.2	82.7	2.4	0.2	9.5	720	0.44	0.30
AC−R	0.0	88.5	2.1	0.0	3.8	768	0.48	0.33

6.1.2 X-ray photoelectron spectroscopy

Five peaks were identified in the C 1s region (Figure 3S.2, left), which correspond to the aromatic and aliphatic carbon, as well as C–NH_2 ($C_{ar,al}$,C–NH_2) at 284.6 eV, the hydroxyl groups and C–N (COH, CN) at 286.0 ± 0.2 eV, carbonyl groups (C=O) at 287.8 ± 0.2 eV, carboxylic groups (COOH) at 289.5 ± 0.2 eV, and the plasmon loss ($C_{shake\text{-}up}$) at 291.2 ± 0.2 eV.[49]

Regarding O 1s region (Figure 3S.2, right), five peaks were identified, which correspond to oxygen in C=O groups (O1) at 531.3 ± 0.1 eV; hydroxyls, ethers and C=O in esters, amides, anhydrides (O2) at 532.2 ± 0.1 eV, C–O groups in esters and anhydrides (O3) at 533.4 ± 0.1 eV; carboxylic groups (O4) at 534.5 ± 0.1 eV, and water at 536.3 ± 0.1 eV. Furthermore, the N content is null in all samples, except AC−N, which presents majorly pyridinic groups (N-6) at 398.3 eV, but also pyrrolic (N-5) at 400.0 eV, quaternary (N-Q) at 401.4 eV and also nitrogen–oxygen complexes (NX) at 403.4 eV (Figure 3S.3).[49]

Table 3S.2. Surface elemental composition of pristine AC and synthesized AC−N, AC−O, and AC−R supporting materials, determined by XPS.

Sample	N_{XPS} (at%)	C_{XPS} (at%)	O_{XPS} (at%)	Total oxygen to total carbon O_t/C_t
AC	0	95.7	4.3	0.045
AC−N	8.1	88.6	3.4	0.038
AC−O	1.3	90.6	8.1	0.089
AC−R	0	96.6	3.4	0.035

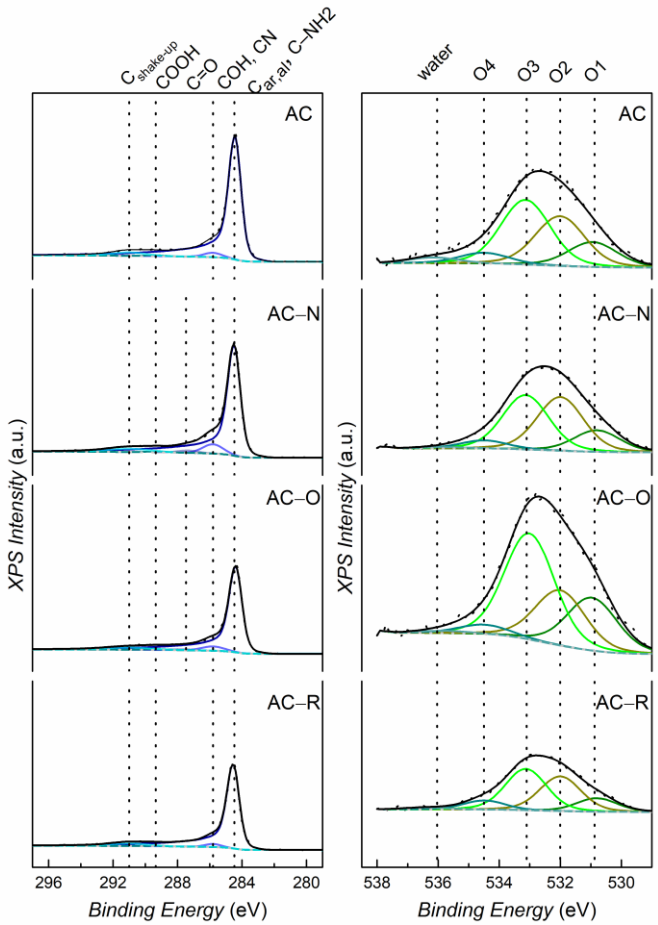

Figure 3S.2. High-resolution XPS data for C 1s region (left) and O 1s region (right) for pristine AC, N-doped AC−N, oxidized AC−O and reduced AC−R supporting materials. Symbols: raw data; black lines: overall fits; colored lines: fits of individual components; dashed lines: background. $C_{ar,al}$, $C–NH_2$: aromatic and aliphatic carbon; COH, CN: hydroxyl groups, CN; C=O: carbonyl groups; COOH: carboxylic groups; $C_{shake-up}$: plasmon loss. O1: C=O; O2: hydroxyls, ethers and C=O in esters, amides, anhydrides; O3: C–O in esters and anhydrides; O4: carboxylic groups.

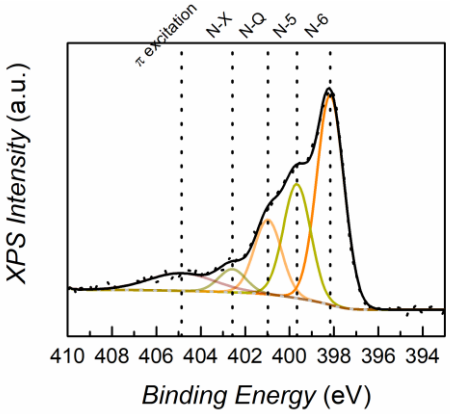

Figure 3S.3. High-resolution XPS data for N 1s region for AC−N. Symbols: raw data; black lines: overall fits; colored lines: fits of individual components; dashed lines: background. N-6: Pyridinic groups; N-5: Pyridonic or pyrrolic groups; N-Q: Quaternary groups; N-X: Nitrogen oxides or nitrates.

6.2 Characterization of the as-synthesized Catalysts

6.2.1 N_2 physisorption

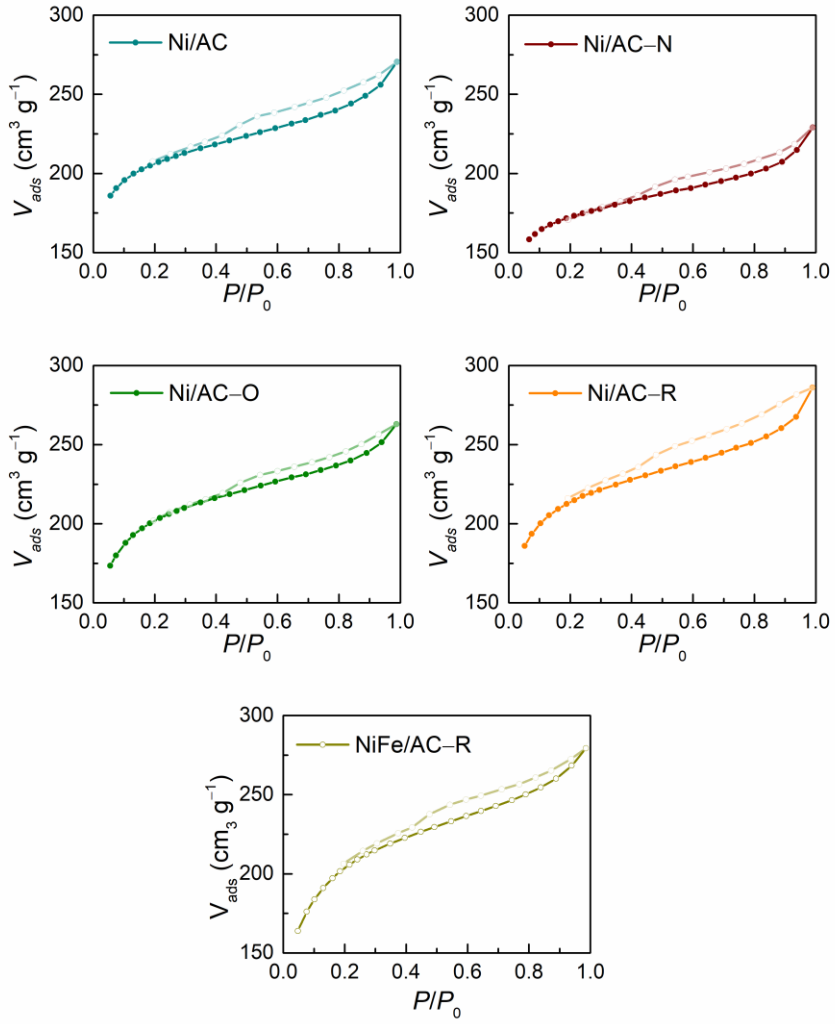

Figure 3S.4. Comparison of N_2 adsorption–desorption isotherms measured at −196 °C for the as-synthesized CO_2 methanation catalysts Ni/AC, Ni/AC−N, Ni/AC−O, Ni/AC−R, and NiFe/AC−R.

6.2.2 Transmission electron microscopy

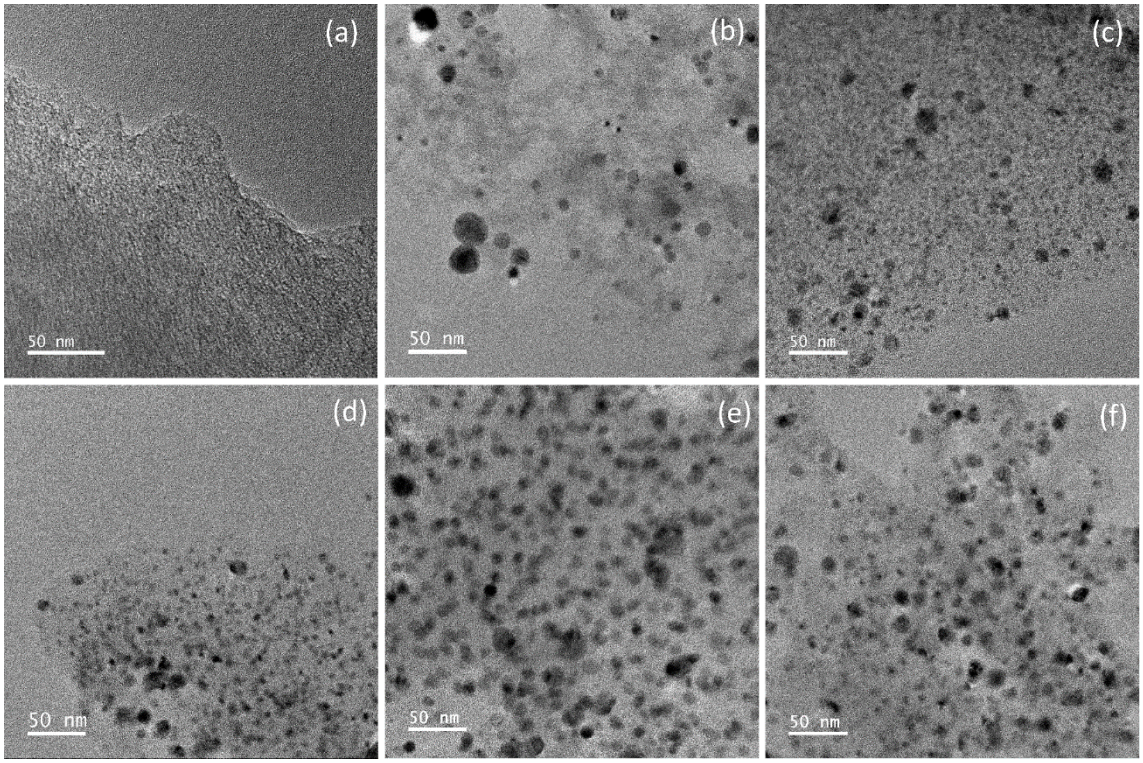

Figure 3S.5. Low-magnification TEM images of AC (a) Ni/AC (b), Ni/AC−N (c), Ni/AC−O (d), Ni/AC−R (e), and bimetallic NiFe/AC−R catalysts for CO_2 methanation.

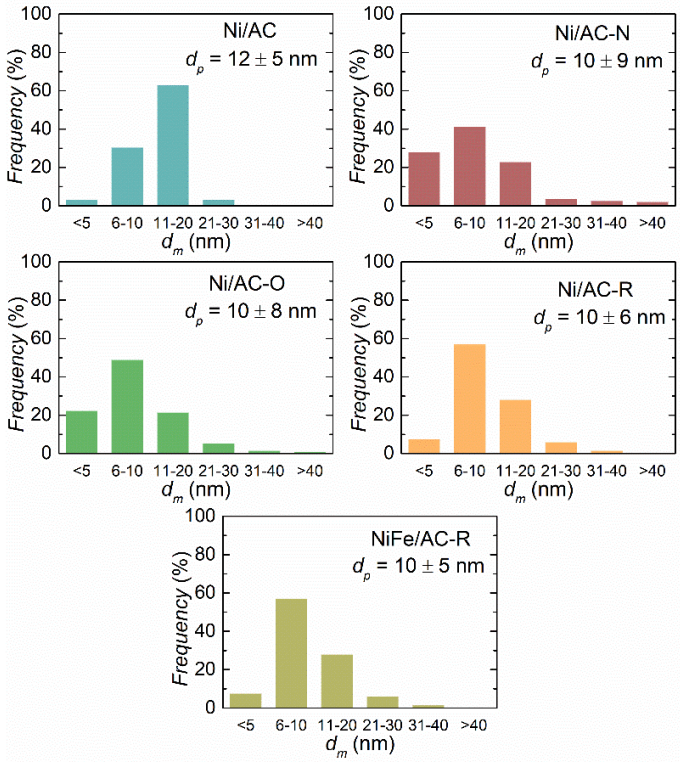

Figure 3S.6. Comparison of the size distribution of Ni NPs in Ni/AC, Ni/AC−N, Ni/AC−O, Ni/AC−R, and bimetallic NiFe/AC−R, estimated from TEM images.

6.2.3 Temperature Programmed Desorption

Three peaks were identified in the deconvolution of the CO evolution in the TPD analysis of the samples (Figure 3S.7) and they correspond to (1) carboxylic anhydrides, (2) phenols, and (3) carbonyl/quinones. It is important to note that N_2 presents the same m/z than CO, thus, in the case of sample Ni/AC−N, the amount of CO is higher due to contribution of N_2. Regarding CO_2 evolution profile, all samples present a first sharp peak below 400 °C, even though the sample was pre-treated at this temperature, which is characteristic of a catalytic decomposition of the material promoted by Ni,[43] followed by a peak above 400 °C, corresponding to the oxygen functional groups present in the material.

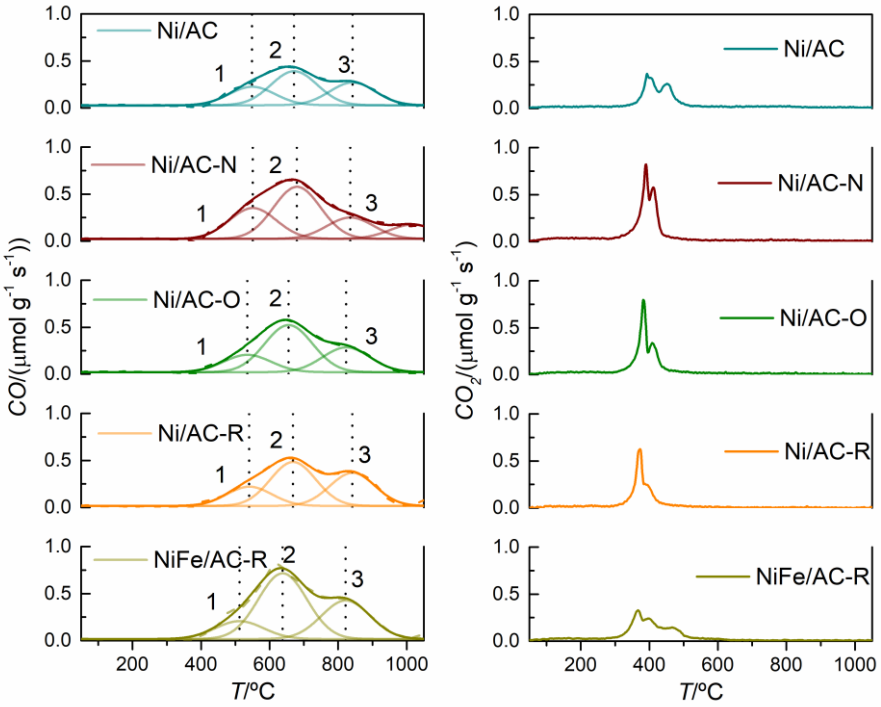

Figure 3S.7. TPD profiles of Ni/AC, Ni/AC–N, Ni/AC–O, Ni/AC–R, and bimetallic NiFe/AC–R, showing the CO (left) and CO_2 (right) evolution. The CO evolution peak was deconvoluted in three peaks: (1) carboxylic anhydrides; (2) phenols; (3) carbonyl/quinones.

Table 3S.3. Relative percentage of each peak, corresponding to the different groups ((1) carboxylic anhydrides, (2) phenols, and (3) carbonyl/quinones) in the CO evolution graphic.

Sample	CO Peak 1 (%)	CO Peak 2 (%)	CO Peak 3 (%)
Ni/AC	25	45	30
Ni/AC−N	30	50	20
Ni/AC−O	19	53	28
Ni/AC−R	20	46	34
NiFe/AC−R	15	54	32

6.3 Simulation of Thermodynamic Equilibrium of CO_2 Methanation

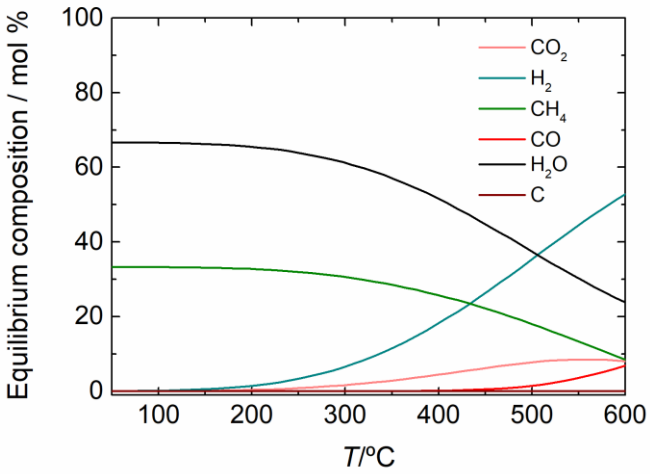

Figure 3S.8. Thermodynamic equilibrium composition as a function of the temperature.

6.4 Catalysts Characterization after prolonged catalytic testing

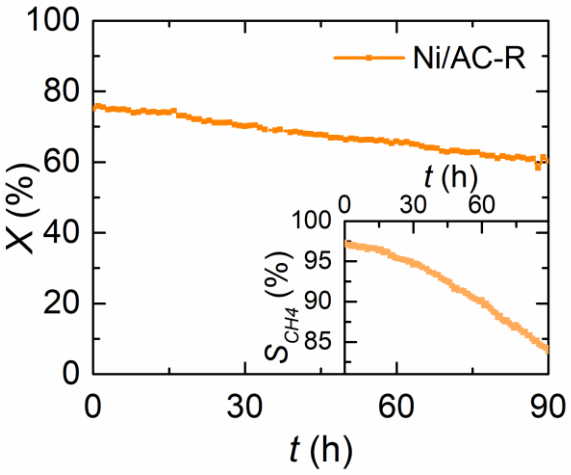

Figure 3S.9. X_{CO2} and S_{CH4} as a function of a prolonged time on stream (90 h) at 450 °C for Ni/AC−R. Reaction conditions: P = 1 bar; $WHSV$ = 60 000 mL g^{-1} h^{-1}; CO_2 : H_2 = 1 : 4.

6.5 Characterization of the Ni/AC−R before and after TOS

6.5.1. Electron microscopy

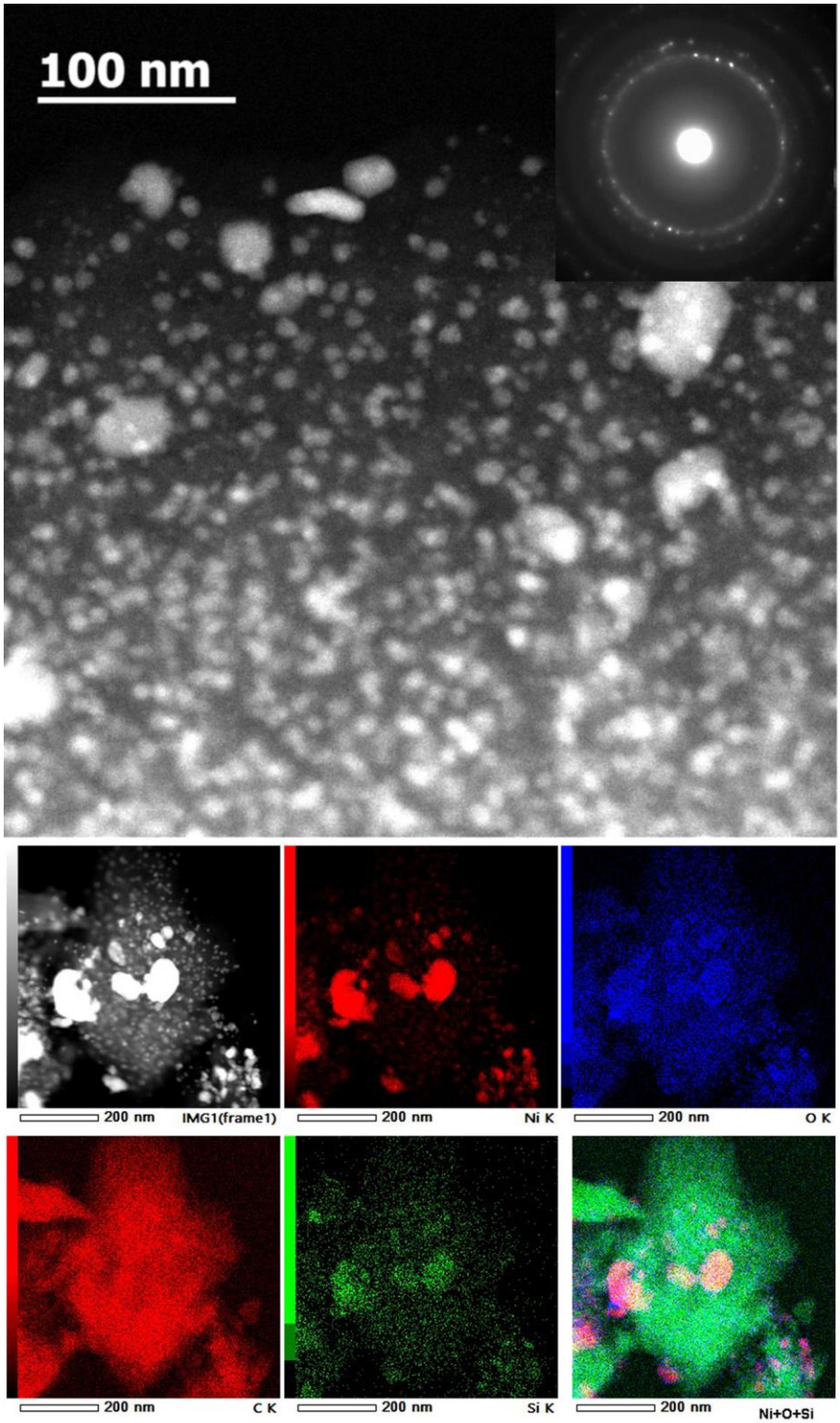

Figure 3S.10. HAADF−STEM images of Ni NPs in as-synthesized Ni/AC−R catalyst, together with elemental maps for Ni, O, C and their mixture. Inset in top panel is the corresponding ED pattern.

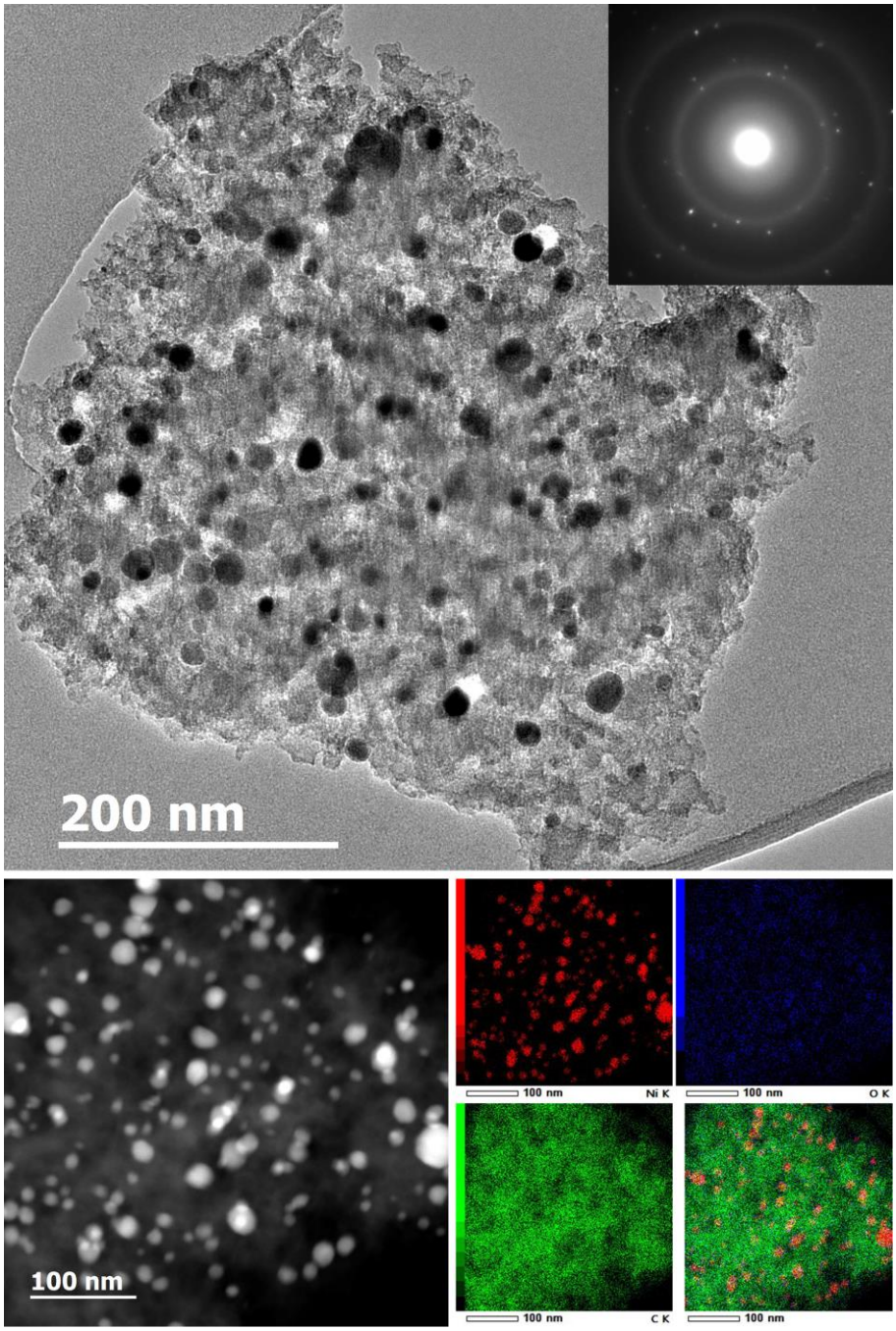

Figure 3S.11. TEM and HAADF−STEM images of Ni NPs in spent Ni/AC−R catalyst after 90 h on stream experiment, together with elemental maps for Ni, O, C and their mixture. Inset in top panel is the corresponding ED pattern.

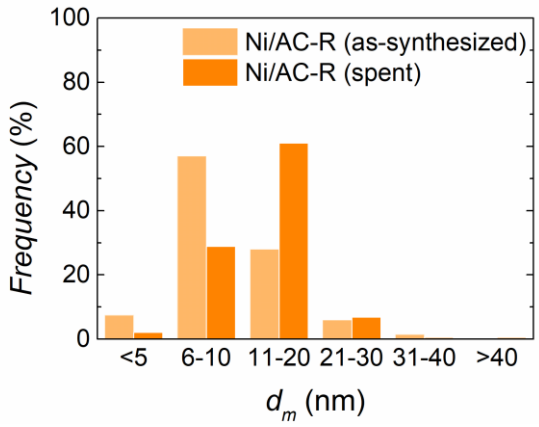

Figure 3S.12. Particle size distribution of the Ni NPs in as-synthesized Ni/AC−R and the same catalyst after the long time on stream experiment (90 h), calculated using the TEM images (spent Ni/AC−R).

6.5.2 X-ray photoelectron spectroscopy

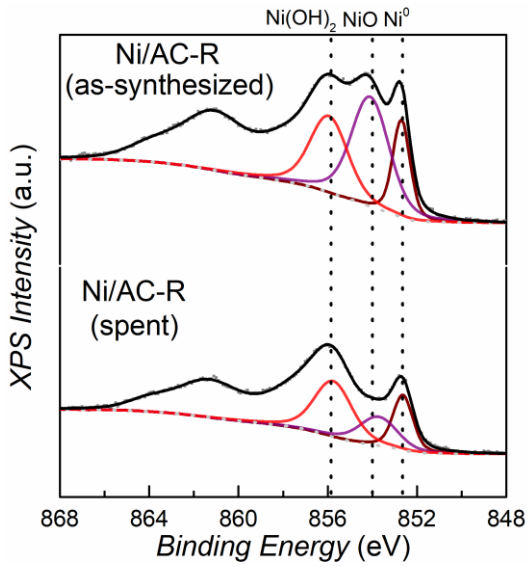

Figure 3S.13. High-resolution XPS data for Ni $2p_{3/2}$ region of as-synthesized Ni/AC−R and the same catalyst after the long time on stream reaction experiment (90 h) (Ni/AC−R spent).

Table 3S.4. Relative atomic percentage (at%) of Ni^0, NiO and $Ni(OH)_2$ phases in as-synthesized Ni/ AC−R and the same catalyst after the long time on stream experiment (90 h) (spent Ni/AC−R), as estimated by XPS analysis.

Sample	Ni^0 (relative at%)	NiO (relative at%)	$Ni(OH)_2$ (relative at%)
Ni/AC−R (as-synthesized)	12	48	33
Ni/AC−R (spent)	26	26	49

References

(1) Sabatier, P., & Senderens, J. B. Nouvelles Synthèses Du Mèthane. *Comptes Rendus Hebd. des Séances l'Académie des Sci.* **1902**, *134*, 514–516.

(2) Rönsch, S.; Schneider, J.; Matthischke, S.; Schlüter, M.; Götz, M.; Lefebvre, J.; Prabhakaran, P.; Bajohr, S. Review on Methanation - From Fundamentals to Current Projects. *Fuel* **2016**, *166*, 276–296. https://doi.org/10.1016/j.fuel.2015.10.111.

(3) Miao, B.; Ma, S. S. K.; Wang, X.; Su, H.; Chan, S. H. Catalysis Mechanisms of CO_2 and CO Methanation. *Catal. Sci. Technol.* **2016**, *6* (12), 4048–4058. https://doi.org/10.1039/C6CY00478D.

(4) Shashidhara, G. M.; Ravindram, M. A Kinetic Study of the Methanation of CO_2 over Ni-Al_2O_3 Catalyst. *React. Kinet. Catal. Lett.* **1988**, *37* (2), 451–456.

(5) Marconi, E.; Tuti, S.; Luisetto, I. Structure-Sensitivity of CO_2 Methanation over Nanostructured Ni Supported on CeO_2 Nanorods. *Catalysts* **2019**, *9* (4), 1–13. https://doi.org/10.3390/catal9040375.

(6) Zhang, Z.; Tian, Y.; Zhang, L.; Hu, S.; Xiang, J. Impacts of Nickel Loading on Properties, Catalytic Behaviors of Ni/γAl_2O_3 Catalysts and the Reaction Intermediates Formed in Methanation of CO_2. *Int. J. Hydrogen Energy* **2019**, *44* (18), 9291–9306. https://doi.org/10.1016/j.ijhydene.2019.02.129.

(7) Vogt, C.; Groeneveld, E.; Kamsma, G.; Nachtegaal, M.; Lu, L.; Kiely, C. J.; Berben, P. H.; Meirer, F.; Weckhuysen, B. M. Unraveling Structure Sensitivity in CO_2 Hydrogenation over Nickel. *Nat. Catal.* **2017**, *1*, 127–134. https://doi.org/10.1038/s41929-017-0016-y.

(8) Li, J.; Lin, Y.; Pan, X.; Miao, D.; Ding, D.; Cui, Y.; Dong, J.; Bao, X. Enhanced CO_2 Methanation Activity of Ni/Anatase Catalyst by Tuning Strong Metal–Support Interactions. *ACS Catal.* **2019**, *9* (7), 6342–6348. https://doi.org/10.1021/acscatal.9b00401.

(9) Li, X.; Wang, Y.; Zhang, G.; Sun, W.; Bai, Y.; Zheng, L.; Han, X. Influence of Mg-Promoted Ni-Based Catalyst Supported on Coconut Shell Carbon for CO_2 Methanation. *ChemistrySelect* **2019**, 838–845. https://doi.org/10.1002/slct.201803369.

(10) Westermann, A.; Azambre, B.; Bacariza, M. C.; Graça, I.; Ribeiro, M. F.; Lopes, J. M.; Henriques, C. Insight into CO_2 Methanation Mechanism over NiUSY Zeolites: An Operando IR Study. *Appl. Catal. B Environ.* **2015**, *174–175*, 120–125. https://doi.org/10.1016/j.apcatb.2015.02.026.

(11) Zhen, W.; Li, B.; Lu, G.; Ma, J. Enhancing Catalytic Activity and Stability for CO_2 Methanation on Ni@MOF-5 via Control of Active Species Dispersion. *Chem. Commun.* **2015**, *51*, 1728–1731. https://doi.org/10.1039/C4CC08733J.

(12) Younas, M.; Sethupathi, S.; Mohamed, A. R. CO_2 Methanation over Ni and Rh Based Catalysts : Process Optimization at Moderate Temperature. *Int J Energy Res.* **2018**, *42*, 3289–3302. https://doi.org/10.1002/er.4082.

(13) Kesavan, J. K.; Luisetto, I.; Tuti, S.; Meneghini, C.; Battocchio, C.; Iucci, G. Ni Supported on YSZ: XAS and XPS Characterization and Catalytic Activity for CO_2 Methanation. *J. Mater. Sci.* **2017**, *52* (17), 10331–10340. https://doi.org/10.1007/s10853-017-1179-2.

(14) Zhou, G.; Wu, T.; Xie, H.; Zheng, X. Effects of Structure on the Carbon Dioxide Methanation Performance of Co-Based Catalysts. *Int. J. Hydrogen Energy* **2013**, *38* (24), 10012–10018. https://doi.org/10.1016/j.ijhydene.2013.05.130.

(15) Le, T. A.; Kim, M. S.; Lee, S. H.; Park, E. D. CO and CO_2 Methanation Over Supported Cobalt Catalysts. *Top. Catal.* **2017**, *60* (9–11), 714–720. https://doi.org/10.1007/s11244-017-0788-y.

(16) Kuśmierz, M. Kinetic Study on Carbon Dioxide Hydrogenation over Ru/γ-Al_2O_3 Catalysts. *Catal. Today* **2008**, *137* (2–4), 429–432. https://doi.org/10.1016/j.cattod.2008.03.003.

(17) Toemen, S.; Abu Bakar, W. A. W.; Ali, R. Effect of Ceria and Strontia over Ru/Mn/Al_2O_3 Catalyst: Catalytic Methanation, Physicochemical and Mechanistic Studies. *J. CO_2 Util.* **2016**, *13*, 38–49.

https://doi.org/10.1016/j.jcou.2015.11.005.

(18) Karelovic, A.; Ruiz, P. CO_2 Hydrogenation at Low Temperature over Rh/γ-Al_2O_3 Catalysts : Effect of the Metal Particle Size on Catalytic Performances and Reaction Mechanism. *Appl. Catal. B, Environ.* **2012**, *113–114*, 237–249. https://doi.org/10.1016/j.apcatb.2011.11.043.

(19) Park, J. N.; McFarland, E. W. A Highly Dispersed Pd-Mg/SiO_2 Catalyst Active for Methanation of CO_2. *J. Catal.* **2009**, *266* (1), 92–97. https://doi.org/10.1016/j.jcat.2009.05.018.

(20) Kwak, J. H.; Kovarik, L.; Szanyi, J. Heterogeneous Catalysis on Atomically Dispersed Supported Metals: CO_2 Reduction on Multifunctional Pd Catalysts. *ACS Catal.* **2013**, *3* (9), 2094–2100. https://doi.org/10.1021/cs4001392.

(21) Swalus, C.; Jacquemin, M.; Poleunis, C.; Bertrand, P.; Ruiz, P. CO_2 Methanation on Rh/γ-Al_2O_3 Catalyst at Low Temperature: "In Situ" Supply of Hydrogen by Ni/Activated Carbon Catalyst. *Appl. Catal. B Environ.* **2012**, *125*, 41–50. https://doi.org/10.1016/j.apcatb.2012.05.019.

(22) Le, M. C.; Van, K. Le; Nguyen, T. H. T.; Nguyen, N. H. The Impact of Ce-Zr Addition on Nickel Dispersion and Catalytic Behavior for CO_2 Methanation of Ni/AC Catalyst at Low Temperature. *J. Chem.* **2017**, *2017*.

(23) Cam, L. M.; Ha, N. T. T.; Khu, L. Van; Ha, N. N.; Brown, T. C. Carbon Dioxide Methanation Over Nickel Catalysts Supported on Activated Carbon at Low Temperature. *Aust. J. Chem.* **2019**, *72*, 969–977. https://doi.org/10.1071/CH19355.

(24) Figueiredo, J. L.; Pereira, M. F. R. R.; Freitas, M. M. A. A.; Órfão, J. J. M. Modification of the Surface Chemistry of Activated Carbons. *Carbon N. Y.* **1999**, *37* (9), 1379–1389. https://doi.org/10.1016/S0008-6223(98)00333-9.

(25) Soares, O. S. G. P.; Órfão, J. J. M.; Pereira, M. F. R. Nitrate Reduction Catalyzed by Pd-Cu and Pt-Cu Supported on Different Carbon Materials. *Catal. Letters* **2010**, *139* (3–4), 97–104. https://doi.org/10.1007/s10562-010-0424-y.

(26) Soares, O. S. G. P.; Rodrigues, C. S. D.; Madeira, L. M.; Pereira, M. F. R. Heterogeneous Fenton-like Degradation of p-Nitrophenol over Tailored Carbon-Based Materials. *Catalysts* **2019**, *9* (3), 258. https://doi.org/10.3390/catal9030258.

(27) Serp, P.; Figueiredo, J. L. *Carbon Materials for Catalysis*; Serp, P., Figueiredo, J. L., Eds.; Wiley: New Jersey, 2009.

(28) Ha, N. N.; Thi, N.; Ha, T.; Khu, L. Van; Cam, L. M. Theoretical Study of Carbon Dioxide Activation by Metals (Co, Cu, Ni) Supported on Activated Carbon. *J Mol Model* **2015**, No. 21, 322. https://doi.org/10.1007/s00894-015-2864-1.

(29) Li, Z.; Zhao, T.; Zhang, L. Promotion Effect of Additive Fe on Al_2O_3 Supported Ni Catalyst for CO_2 Methanation. *Appl. Organomet. Chem.* **2018**, *32* (5), 1–7. https://doi.org/10.1002/aoc.4328.

(30) Mebrahtu, C.; Krebs, F.; Perathoner, S.; Abate, S.; Centi, G.; Palkovits, R. Hydrotalcite Based Ni-Fe/(Mg, Al)O:X Catalysts for CO_2 Methanation-Tailoring Fe Content for Improved CO Dissociation, Basicity, and Particle Size. *Catal. Sci. Technol.* **2018**, *8* (4), 1016–1027. https://doi.org/10.1039/c7cy02099f.

(31) Hwang, S.; Hong, U. G.; Lee, J.; Baik, J. H.; Koh, D. J.; Lim, H.; Song, I. K. Methanation of Carbon Dioxide over Mesoporous Nickel-m-Alumina (M = Fe, Zr, Ni, Y, and Mg) Xerogel Catalysts: Effect of Second Metal. *Catal. Letters* **2012**, *142* (7), 860–868. https://doi.org/10.1007/s10562-012-0842-0.

(32) Mutz, B.; Belimov, M.; Wang, W.; Sprenger, P.; Serrer, M.-A.; Wang, D.; Pfeifer, P.; Kleist, W.; Grunwaldt, J.-D. Potential of an Alumina Supported Ni_3Fe Catalyst in the Methanation of CO_2: Impact of Alloy Formation on Activity and Stability. *ACS Catal.* **2017**, *7*, 6802–6814. https://doi.org/10.1021/acscatal.7b01896.

(33) Kustov, A. L.; Frey, A. M.; Larsen, K. E.; Johannessen, T.; Nørskov, J. K.; Christensen, C. H. CO Methanation over Supported Bimetallic Ni-Fe Catalysts: From Computational Studies towards Catalyst Optimization. *Appl. Catal. A Gen.* **2007**, *320*, 98–104. https://doi.org/10.1016/j.apcata.2006.12.017.

(34) Andersson, M. P.; Bligaard, T.; Kustov, A.; Larsen, K. E.; Greeley, J.; Johannessen, T.; Christensen, C. H.; Nørskov, J. K. Toward Computational Screening in Heterogeneous Catalysis: Pareto-Optimal Methanation Catalysts. *J. Catal.* **2006**, *239* (2), 501–506. https://doi.org/10.1016/j.jcat.2006.02.016.

(35) Bligaard, T.; Nørskov, J. K.; Dahl, S.; Matthiesen, J.; Christensen, C. H.; Sehested, J. The Brønsted-Evans-Polanyi Relation and the Volcano Curve in Heterogeneous Catalysis. *J. Catal.* **2004**, *224* (1), 206–217. https://doi.org/10.1016/j.jcat.2004.02.034.

(36) Burger, T.; Koschany, F.; Thomys, O.; Köhler, K.; Hinrichsen, O. CO_2 Methanation over Fe- and Mn-Promoted Co-Precipitated Ni-Al Catalysts: Synthesis, Characterization and Catalysis Study. *Appl. Catal. A Gen.* **2018**, *558* (December 2017), 44–54. https://doi.org/10.1016/j.apcata.2018.03.021.

(37) Hwang, S.; Hong, U. G.; Lee, J.; Seo, J. G.; Baik, J. H.; Koh, D. J.; Lim, H.; Song, I. K. Methanation of Carbon Dioxide over Mesoporous Ni-Fe-Al_2O_3 Catalysts Prepared by a Coprecipitation Method: Effect of Precipitation Agent. *J. Ind. Eng. Chem.* **2013**, *19* (6), 2016–2021. https://doi.org/10.1016/j.jiec.2013.03.015.

(38) Pandey, D.; Deo, G. Promotional Effects in Alumina and Silica Supported Bimetallic Ni-Fe Catalysts during CO_2 Hydrogenation. *J. Mol. Catal. A Chem.* **2014**, *382*, 23–30. https://doi.org/10.1016/j.molcata.2013.10.022.

(39) Pandey, D.; Deo, G. Effect of Support on the Catalytic Activity of Supported Ni-Fe Catalysts for the CO_2 Methanation Reaction. *J. Ind. Eng. Chem.* **2016**, *33*, 99−107. https://doi.org/10.1016/j.jiec.2015.09.019.

(40) Soares, O. S. G. P.; Rocha, R. P.; Gonçalves, A. G.; Figueiredo, J. L.; Órfão, J. J. M.; Pereira, M. F. R. Easy Method to Prepare N-Doped Carbon Nanotubes by Ball Milling. *Carbon N. Y.* **2015**, *91*, 114−121. https://doi.org/10.1016/j.carbon.2015.04.050.

(41) Menéndez, J. A.; Xia, B.; Phillips, J.; Radovic, L. R. On the Modification and Characterization of Chemical Surface Properties of Activated Carbon: Microcalorimetric, Electrochemical, and Thermal Desorption Probes. *Langmuir* **1997**, *13* (13), 3414–3421. https://doi.org/10.1021/la9602022.

(42) Gao, J.; Wang, Y.; Ping, Y.; Hu, D.; Xu, G.; Gu, F.; Su, F. A Thermodynamic Analysis of Methanation Reactions of Carbon Oxides for the Production of Synthetic Natural Gas. *RSC Adv.* **2012**, *2* (6), 2358–2368. https://doi.org/10.1039/C2RA00632D.

(43) Adsuar-García, M. D.; Flores-Lasluisa, J. X.; Azar, F. Z.; Román-Martínez, M. C. Carbon-Black-Supported Ru Catalysts for the Valorization of Cellulose through Hydrolytic Hydrogenation. *Catalysts* **2018**, *8* (12). https://doi.org/10.3390/catal8120572.

(44) Romero-sáez, M.; Dongil, A. B.; Benito, N.; Espinoza-gonzález, R.; Escalona, N.; Gracia, F. CO_2 Methanation over Nickel-ZrO_2 Catalyst Supported on Carbon Nanotubes : A Comparison between Two Impregnation Strategies. *Appl. Catal. B Environ.* **2018**, *237* (March), 817–825. https://doi.org/10.1016/j.apcatb.2018.06.045.

(45) Gao, J.; Jiang, Q.; Liu, Y.; Liu, W.; Chu, W.; Su, D. S. Probing the Enhanced Catalytic Activity of Carbon Nanotube Supported Ni-LaOx Hybrids for the CO_2 Reduction Reaction. *Nanoscale* **2018**, *10*, 14207−14219. https://doi.org/10.1039/c8nr03882a.

(46) Payne, B. P.; Biesinger, M. C.; McIntyre, N. S. Use of Oxygen/Nickel Ratios in the XPS Characterisation of Oxide Phases on Nickel Metal and Nickel Alloy Surfaces. *J. Electron Spectros. Relat. Phenomena* **2012**, *185* (5–7), 159−166. https://doi.org/10.1016/j.elspec.2012.06.008.

(47) Biesinger, M. C.; Payne, B. P.; Grosvenor, A. P.; Lau, L. W. M.; Gerson, A. R.; Smart, R. S. C. Resolving Surface Chemical States in XPS Analysis of First Row Transition Metals, Oxides and Hydroxides: Cr, Mn, Fe, Co and Ni. *Appl. Surf. Sci.* **2011**, *257* (7), 2717–2730. https://doi.org/10.1016/j.apsusc.2010.10.051.

(48) Chicinaş, I.; Pop, V.; Isnard, O.; Le Breton, J. M.; Juraszek, J. Synthesis and Magnetic Properties of Ni_3Fe Intermetallic Compound Obtained by Mechanical Alloying. *J. Alloys Compd.* **2003**, *352* (1–2), 34–40. https://doi.org/10.1016/S0925-8388(02)01135-0.

(49) Figueiredo, J. L.; Pereira, M. F. R. The Role of Surface Chemistry in Catalysis with Carbons. *Catal. Today* **2010**, *150*, 2–7. https://doi.org/10.1016/j.cattod.2009.04.010.

(50) Shafeeyan, M. S.; Daud, W. M. A. W.; Houshmand, A.; Shamiri, A. A Review on Surface Modification of Activated Carbon for Carbon Dioxide Adsorption. *J. Anal. Appl. Pyrolysis* **2010**, *89* (2), 143−151. https://doi.org/10.1016/j.jaap.2010.07.006.

(51) Wang, W.; Duong-Viet, C.; Ba, H.; Baaziz, W.; Tuci, G.; Caporali, S.; Nguyen-Dinh, L.; Ersen, O.; Giambastiani,

G.; Pham-Huu, C. Nickel Nanoparticles Decorated Nitrogen-Doped Carbon Nanotubes (Ni/N-CNT); A Robust Catalyst for the Efficient and Selective CO_2 Methanation. *ACS Appl. Energy Mater.* **2019**, *2* (2), 1111−1120. https://doi.org/10.1021/acsaem.8b01681.

(52) Hu, F.; Tong, S.; Lu, K.; Chen, C.; Su, F.; Zhou, J.; Lu, Z.; Wang, X.; Feng, G.; Zhang, R. Reduced Graphene Oxide Supported Ni-Ce Catalysts for CO_2 Methanation: The Support and Ceria Promotion Effects. *J. CO_2 Util.* **2019**, *34* (June), 676–687. https://doi.org/10.1016/j.jcou.2019.08.020.

(53) Valinejad Moghaddam, S.; Rezaei, M.; Meshkani, F.; Daroughegi, R. Carbon Dioxide Methanation over Ni-M/Al_2O_3 (M: Fe, CO, Zr, La and Cu) Catalysts Synthesized Using the One-Pot Sol-Gel Synthesis Method. *Int. J. Hydrogen Energy* **2018**, *43* (34), 16522−16533. https://doi.org/10.1016/j.ijhydene.2018.07.013.

(54) Pandey, D.; Deo, G. Effect of Support on the Catalytic Activity of Supported Ni-Fe Catalysts for the CO_2 Methanation Reaction. *J. Ind. Eng. Chem.* **2016**, *33*, 99−107. https://doi.org/10.1016/j.jiec.2015.09.019.

Chapter 4

Understanding the importance of N-doping for CNT-supported Ni catalysts for CO_2 methanation

Gonçalves, L. P. L.; Meledina, M.; Meledin, A.; Petrovykh, D. Y.; Sousa, J. P. S.; Kolen'ko, Y. V.; Soares, O. S. G. P.; Pereira, M. F. R. *Understanding the importance of N-doping for CNT-supported Ni catalysts for CO_2 methanation*. Carbon, **2021**, 195, 35-43.

Abstract

The N−doping of carbon nanotubes (CNTs) is widely accepted as an effective way to enhance the catalytic performance of CNT-supported Ni catalysts for CO_2 methanation. To demonstrate, in a direct systematic comparison, the importance of N−doping for producing high-performance CO_2 methanation catalysts, we developed two catalysts composed of 15 wt% Ni on pristine (Ni/CNT) and N−doped CNT (Ni/CNT−N) and correlated their catalytic performance with their properties. Compared to Ni/CNT, Ni/CNT−N achieved a higher X_{CO2} of 81.2% with S_{CH4} = 99.2% at a lower temperature of 400 °C, exhibiting excellent stability over 48 h time-on-stream testing. Our comprehensive comparative study demonstrated that the N−doped CNT support featured a better distribution of the Ni sites that were strongly interacting with the support, even with atomically dispersed Ni being observed by HAADF-STEM. This higher dispersion, enabled by the anchoring sites provided by the N−doping, is one of the main reasons for the enhanced performance of Ni/CNT−N, because it increases the H_2 uptake capacity.

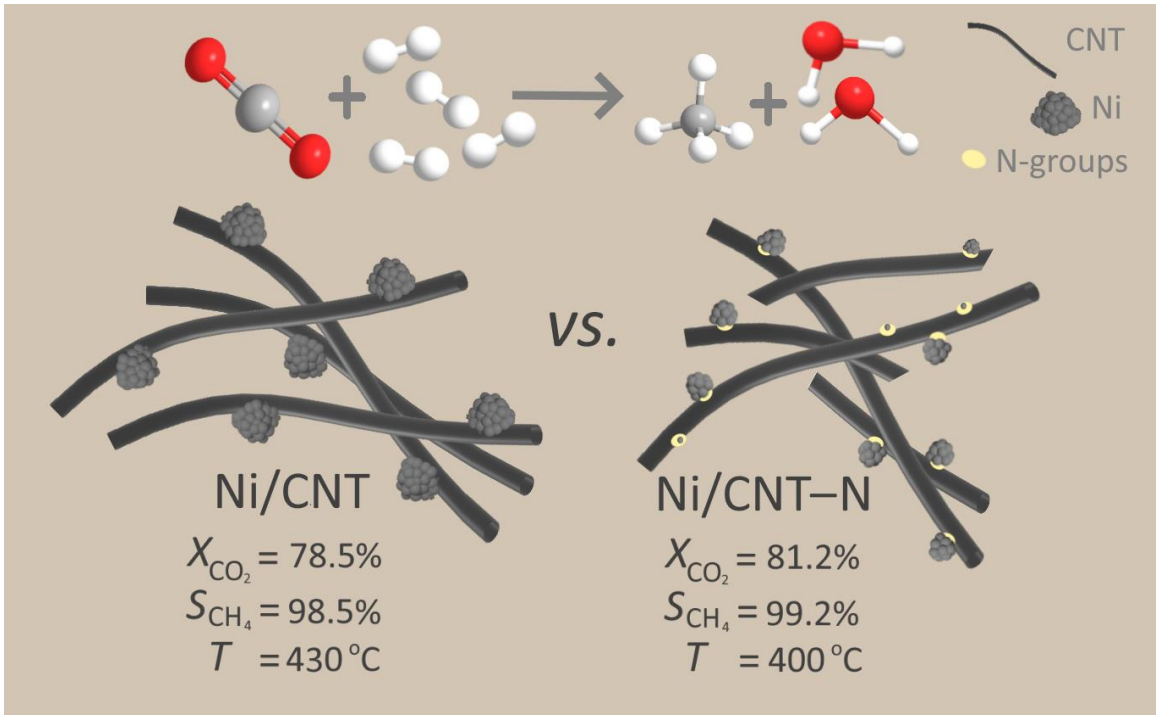

1. Introduction

In the field of gas-phase heterogeneous catalysis, carbon nanotubes (CNTs) have been intensively explored as catalysts themselves and, mainly, as supporting materials for the preparation of metallic catalysts [1]. Several different aspects have been taken into account while employing CNTs for catalysis. For instance, the formation of hot spots within the catalytic bed during thermal catalysis is often responsible for the sintering of catalytically active metallic nanoparticles, leading to the subsequent loss in the catalyst performance [2–4]. CNTs exhibit high thermal conductivity and excellent thermal stability [4,5]; therefore, these materials are of particular interest for exothermic reactions, wherein their use can prevent the undesired formation of hot spots, thus increasing the durability of the supported metallic catalysts [4–7]. Another interesting aspect of the CNTs is their versatile surface chemistry that has been extensively investigated for the design and preparation of high-performing and durable catalysts. Specifically, CNTs possess a graphitic structure, containing unsaturated C atoms at the edges of the constituent graphene layers. These C atoms afford the incorporation of different O-, N- or S-containing functionalities into the CNT structure [8]. This capability to dope CNT materials with heteroatoms has led to the application of metal-free heteroatom-doped CNTs as catalysts themselves [9–11]. Furthermore, the doping of CNTs with the aforementioned heteroatoms has been shown to improve the performance of supported metal catalysts. For example, N−doped CNTs have been reported to support well dispersed catalytically active metal nanoparticles, and sometimes to contribute to the adsorption of the reactant gases, such as CO_2 [6,12].

In our research [13,14], we are focusing on the so-called Sabatier reaction of CO_2 methanation ($CO_2 + 4H_2 \rightarrow CH_4 + H_2O$; $\Delta H_{298K} = -165$ kJ mol^{-1}). This reaction provides an interesting pathway to produce a carbon-neutral e-CH_4 fuel in power-to-gas plants [15], thus significantly reducing CO_2 emissions to the atmosphere. More specifically, the power-to-gas technology combines the

generation of green H_2 by water electrolysis using renewable electricity and its further use for hydrogenation of captured anthropogenic CO_2 in an electrified catalytic reactor powered by renewable electricity to finally deliver the e-CH_4 fuel. While H_2 is a sustainable fuel itself, unfortunately, it requires special infrastructure for storage and transportation [16]. Hence, the aforementioned production of e-CH_4 would allow to overcome the challenges of handling hydrogen, since the resultant e-CH_4 can be directly distributed within the current gas pipeline, storage, and distribution networks.

Although CO_2 methanation is a thermodynamically favorable reaction, it has significant kinetic barriers that can be reduced by means of active and selective catalysts [17,18]. The typical catalysts for the reaction are group-VIII metals, such as Ni, Co, Ru, Rh, and Pd. Currently, a particular focus is placed on Ni, which has an optimal combination of high activity, excellent selectivity, high abundance, and low price [17]. The most commonly used supporting materials for the aforementioned metal catalysts are metal oxides, such as Al_2O_3, TiO_2, ZrO_2 and CeO_2 [19–21]. Besides, the successful applications of other supporting materials, such as zeolites [22] and metal organic frameworks [23], have also been reported. Moreover, the use of carbon-based supports for CO_2 methanation catalysts has been recently explored. For instance, activated carbon [13,14,24], CNTs [4,6,7,12,25–27], carbon nanofibers [28,29], and graphene [30,31] have been successfully applied for the preparation of efficient CO_2 methanation catalysts.

In our laboratories, we are pursuing the development of carbon-supported Ni-based catalysts for CO_2 methanation. Our previous studies have shown that the carbon-supported-Ni (Ni/C) catalysts for CO_2 methanation exhibit several unique features: (*i*) good dispersion of the Ni nanoparticles over the supporting material, (*ii*) stability of a Ni/C catalyst at high temperatures, (*iii*) hydrogenation reaction at low temperature, and (*iv*) high CO_2 coverage over Ni/C catalyst facilitating the hydrogenation [13,14,32]. Importantly, these unique features were largely achieved through judicious tailoring of activated-carbon supporting materials; hence we became interested in a direct

systematic comparison of pristine CNTs and N−doped CNTs as supporting materials for Ni catalysts.

Accordingly, two Ni catalysts supported on commercially available CNT (Ni/CNT) and on synthesized N−doped CNT (Ni/CNT–N), both with 15 wt% Ni loading, were successfully prepared. They were extensively characterized before and after reaction, and their catalytic performance in CO_2 methanation reaction was investigated, allowing a detailed comparative study between the Ni/CNT and Ni/CNT–N catalysts. In particular, we were able to demonstrate the importance of N−doping in high-performing carbon-supported catalysts for CO_2 methanation, understanding the basis for the better catalytic performance of Ni/CNT–N.

2. Experimental

To obtain N-doped CNTs (referred to as CNT−N), melamine was co-ball-milled with CNTs (NC3100™ − Nanocyl) as N source and annealed at 600 °C (10 °C min^{-1}) for 1 h under a flow of N_2 [33]. Preliminary to the selection of N-doping as a way to enhance the performance of CNT support, different treatments were performed on CNT in an attempt to determine which surface modification would be more beneficial in the case of CNT. The N-doping and surface reduction treatments performed in AC in Chapter 3 were repeated in CNT. Interestingly in the case of CNT, the trend was contrary to the one observed for AC. The Ni catalysts supported on N-doped CNT (Ni/CNT−N) presented improved catalytic performance when compared to those supported on reduced CNT (Ni/CNT−R) (Appendix 3).

The Ni/CNT and Ni/CNT−N catalysts were prepared by the incipient wetness impregnation method using $Ni(NO_3)_2{\cdot}6H_2O$ as Ni precursor for a loading of 15 wt% - established to be an optimal one on the course of our initial catalytic screening. The samples were annealed under N_2 atmosphere and further reduced under H_2 atmosphere. The temperature of the heat treatments was determined by H_2 temperature programmed reduction.

The resultant supports and catalysts were characterized by physisorption, elemental analysis, H_2 temperature programmed reduction (H_2–TPR), H_2 pulse chemisorption, powder X-ray diffraction (XRD), X-ray photoelectron spectroscopy (XPS), transmission electron microscopy (TEM), high-angle annular dark-field scanning TEM (HAADF–STEM) and energy dispersive X-ray spectroscopy in STEM mode (STEM–EDX).

Their activity, selectivity, and stability in CO_2 methanation were evaluated in a Microactivity XS15 system (PID Eng & Tech), using a fixed bed quartz reactor (d_{int} = 1 cm). The products in the outflow were analyzed online by a GC 1000 gas chromatograph (DANI), equipped with a thermal conductivity detector (TCD) and a GS-CarbonPLOT capillary column, using He as carrier gas and a continuous flow of N_2 as internal standard. Each catalyst (100 mg) was pre-treated *in situ* under H_2 flow (40 $cm^3\ min^{-1}$) at the reduction temperature for 30 min, at 1 bar. After that, the reactor temperature was decreased to 200 °C under He (50 $cm^3\ min^{-1}$), and then, the reactor was fed with 10% CO_2, 40% H_2 (the stoichiometric composition) and 50% He, with a total flow rate of 100 $cm^3\ min^{-1}$. A temperature ramping from 200 °C to 500 °C was performed under reaction conditions to evaluate the performance of each sample at various temperatures. Additionally, the isothermal time on stream (TOS) experiments were conducted under the same reaction conditions to evaluate the stability of the best performing samples.

More experimental details for the synthesis of the catalysts and their detailed characterization are summarized in Chapter 2.

3. Results

3.1 Characterization of the synthesized catalysts

We started by confirming the success of the N−doping procedure by determining the chemical composition of the supporting materials via elemental analysis, which established that the N−doped CNT contained 5 wt%

of N (Table S1), which agrees with the XPS result that also presented 5 wt% of N.

Furthermore, we analyzed the textural properties of pristine CNTs, synthesized N−doped CNTs and the resultant Ni/CNT and Ni/CNT−N catalysts for CO_2 methanation. All the samples show a Type II isotherm, characteristic of non-porous or macroporous materials, and a H3 hysteresis characteristic of carbon materials exhibiting some mesoporosity (Figure 4S.2) [23,24]. This meso/macro porosity results from the free spaces among the CNT bundles. Upon the introduction of Ni, the types of isotherms did not change (Figure 4S.2). Interestingly the pore-size distribution of the N−doped CNTs was found to be quite different compared to that in pristine CNTs. Specifically, the CNTs show an important contribution of pores with width > 20 nm, while N−doped CNTs have almost no pores with such a large width (Figure 4S.3). The specific surface area (S_{BET}) of pristine and N−doped CNTs was estimated to be quite similar (Table 4.1, 197 $m^2\ g^{-1}$ cf. 202 $m^2\ g^{-1}$), suggesting that our N−doping protocol does not change the specific surface area. This might be a result of a compensatory action between the ball milling procedure and the introduction of the N−groups: it would be expected for the ball milling procedure to increase the S_{BET} by opening the ends of the CNTs and decreasing their entanglement, the effects which can be observed by TEM (Figure 4S.4); on the other hand, the N−doping procedure can lead to some blocking of the pores. Slightly higher S_{BET} values were estimated for the derivative Ni/CNT (213 $m^2\ g^{-1}$) and Ni/CNT−N (225 $m^2\ g^{-1}$) catalysts, which suggests that the impregnation and reduction procedure to deposit the Ni nanoparticles could have led to some opening of the nanotubes; small Ni nanoparticles also present a relevant geometrical surface area that contributes to the specific surface area of the samples (Figure 4S.5). The total pore volume (V_P) slightly decreases after Ni deposition (Table 4.1), most likely because of some aggregation of the CNT bundles [34,35].

After establishing the textural characteristics of the synthesized catalysts, we further analyzed their phase composition by means of XRD. Figure 4.1 shows

that both Ni/CNT and Ni/CNT–N catalysts exhibit similar phase composition. In particular, the peak at 26° corresponds to the graphitic carbon of the CNTs. Besides carbon, the catalysts consist of metallic Ni (ICDD #04-016-4761) and NiO (ICDD #04-004-8992). Notably, the observed Bragg reflections are broad, which is typical for nanocrystalline materials.

Table 4.1. Selected textural, morphological and catalytic properties (T_{50} – temperature at which the sample reaches 50% X_{CO2} and $Y_{CH4,MAX}$ – maximum methane yield) for pristine CNT, synthesized N-doped CNT as well as Ni/CNT and Ni/CNT–N catalysts for CO_2 methanation.

Sample	S_{BET} ($m^2\ g^{-1}$)	$V_{P,P/P0=0.95}$ ($cm^3\ g^{-1}$)	S_M ($m^2\ g_{cat}^{-1}$)[b]	d_{Ni} (nm)[c]	d_{Ni} after TOS (nm)[c]
CNT	202	0.42	--	--	--
N-doped CNT	197	0.49	--	--	--
Ni/CNT	213	0.38	0.3	16 ± 7	17 ± 7
Ni/CNT–N	225	0.44	1.1	6 ± 3	8 ± 4

[a]Estimated by N_2 physisorption. [b]Estimated by H_2 pulse chemisorption. [c]Estimated by the analysis of TEM images.

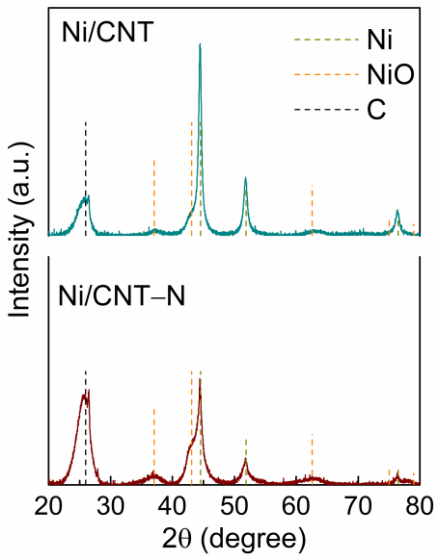

Figure 4.1. XRD patterns of the Ni/CNT, and Ni/CNT–N catalysts, indicating the presence of graphitic carbon, metallic Ni and NiO.

Next, we performed H_2–TPR to study the reducibility of the catalysts, and the obtained H_2–TPR profiles are presented in Figure 4.2. While Ni/CNT

demonstrates two peaks of H_2 consumption at low temperature (< 400 °C), Ni/CNT−N shows three peaks in this temperature region that can be assigned to H_2 consumption by NiO weakly bound on the walls of CNT−N. Specifically, the first peak at 297 °C in Ni/CNT−N profile can be associated with the reduction of NiO species confined within the CNT−N nanotubes [4,27,36]. Notably, this peak is absent in the case of Ni/CNT catalyst.

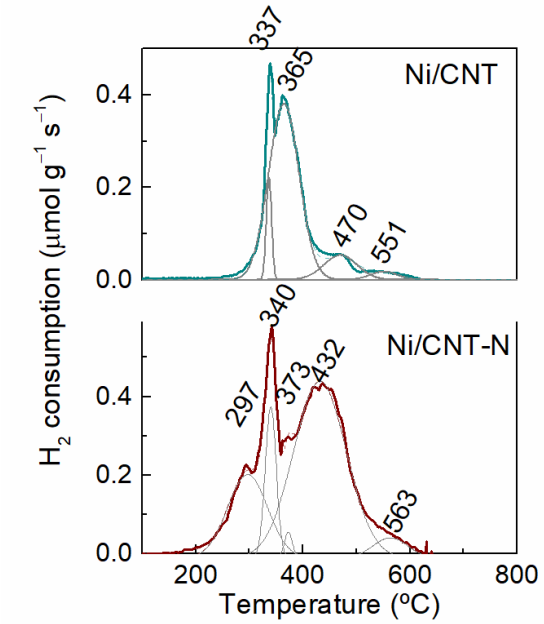

Figure 4.2. Comparison of the H_2−TPR profiles for Ni/CNT and Ni/CNT−N catalysts. The grey lines are the deconvolution of the peaks.

In the 300–400 °C range, both catalysts exhibit two peaks at similar temperatures that can be attributed to highly dispersed NiO species, strongly interacting with the exterior walls of the CNTs [4,27]. Above 400 °C, the catalysts exhibit two more peaks of NiO reduction, wherein Ni/CNT−N shows more pronounced features, suggesting that this catalyst incorporates a larger number of highly dispersed NiO species compared to Ni/CNT. Evidence for such metal dispersion in the catalysts was further provided by H_2 pulse chemisorption, which revealed the Ni/CNT−N catalyst having almost 3.5 times higher metallic surface area (S_M) than that in the Ni/CNT catalyst (Table 4.1). Consistently with H_2−TPR studies, this result indicates that Ni/CNT−N exhibits a large quantity of NiO species well dispersed on the support.

Having established textural and compositional properties of our catalysts, we then investigated their morphology, microstructure and fine chemical composition by means of electron microscopy and also the chemical composition by means of XPS. It is important to note, however, that the interpretation of these results should be made taking in mind the limitations of the experimental protocols and sample handling. In particular, even though the fresh catalysts are subjected to a reduction treatment, they are characterized after exposure to ambient air, which can oxidize the surfaces of transition-metal nanoparticles to some extent. However, before the catalytic testing, the fresh catalysts undergo an *in situ* reduction pre-treatment in the reactor, meaning that metallic nanoparticles are considered when interpreting their catalytic activity.

Figure 4S.4 shows low-magnification TEM images of the Ni/CNT and Ni/CNT–N catalysts. Ni/CNT–N consists of small catalyst nanoparticles with an average size of ≈ 6 nm (Figure 4S.5, Table 4.1) that are well-dispersed over the N−doped CNTs (Figure 4S.4d,e,f). In contrast, the average size of catalyst nanoparticles supported on pristine CNTs is found to be significantly larger, namely, ≈ 16 nm (Figure 4S.5, Table 4.1). Moreover, the nanoparticles in the Ni/CNT catalyst sometimes exhibit agglomerated appearance (Figure 4S.4a,b,c). The observed difference in the size and dispersion of the catalytic nanoparticles over pristine and N−doped CNTs is also clearly seen during the comparison of the respective low-magnification HAADF−STEM images (Figure 4.3a cf. Figure 4.3e).

Furthermore, the fine microstructure of the catalyst nanoparticles in the Ni/CNT and Ni/CNT–N catalysts was also found to be quite different. Specifically, the nanoparticles dispersed on the pristine CNTs in Ni/CNT exhibit Ni@NiO core-shell appearance (Figure 4.3b,c,d). In contrast, small nanoparticles in Ni/CNT−N are mainly NiO (Figure 4.3f,h). More interestingly, the latter catalyst exhibits some bright-contrast dot-like features in the representative HAADF−STEM image (marked by white arrows in Figure 4.3g). Most likely, these bright dots are atomically dispersed Ni sites and/or clusters

of a few Ni atoms that are well-anchored on the N−doped CNTs, which have been previously reported on similar materials [37,38].

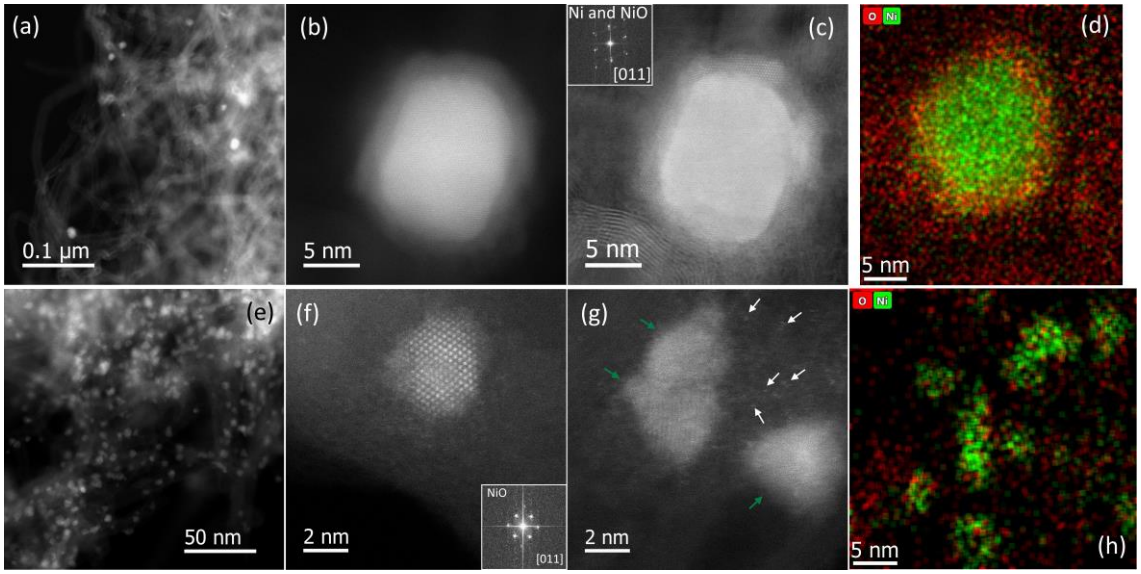

Figure 4.3. Representative low-magnification (a,e) and high-resolution (b,f,g) HAADF−STEM images and Fourier transform (FT) pattern [inset in panel (f)], together with high-resolution (c) ADF−STEM image and the corresponding STEM–EDX O and Ni mixture maps of the Ni/CNT (a–d) and Ni/CNT−N (e–h).

Our complementary XPS analysis confirmed that the surface of the catalysts is composed of a mixture of Ni and NiO, in agreement with the other characterization results. From the deconvolution of the Ni $2p_{3/2}$ spectra of both Ni/CNT and Ni/CNT−N (Figure 4.4, top), one can observe the presence of a lower binding energy component at 852.9 ± 0.1 eV that can be assigned to metallic Ni^0 species. Other components at 854.0 ± 0.1 eV and 855.9 ± 0.1 eV are consistent with Ni^{2+} in NiO, along with satellite peaks from Ni^{2+} at 861.1 ± 0.2 eV and 864.5± 0.5 eV [14,39]. Notably, such combination of components has been previously assigned to Ni^{2+} in a thin nickel oxide layer over metallic Ni^0 [14,39–41]. The relative at% of Ni^0 is, however, different between the two catalysts (Table 4S.2): Ni/CNT has 9.4 at% Ni^0, while Ni/CNT−N has only 6.4 at%. The C 1s, O 1s and N 1s spectra of the materials are shown in Figure 4S.8Figure 4S.9Figure 4S.10, respectively [13,42,43]. Importantly, the N 1s spectra (Figure 4S.10) indicate that the N−doped CNT supporting material mainly comprises pyridinic (N-6) and pyrrolic (N-5) groups with some quaternary groups (N-Q), thus evidencing successful N−doping

[42]. The analysis of N 1s spectra also demonstrated that the N content, at least at the surface of the samples, decreased after the introduction of Ni (Table 4S.3). However, there are no qualitative changes in the N 1s spectra after Ni addition.

Thermogravimetric analysis (TGA) (Figure 4S.11) demonstrated that, under inert atmosphere, the Ni/CNT and Ni/CNT−N catalysts are stable (i.e., did not lose mass) up to around 500 °C. Above this temperature, there is a decrease in the mass of the samples, related to the decomposition of the carbon support. When the atmosphere is changed to air, the burn of the CNT is observed with an abrupt decrease in the mass of the samples, followed by a small increase in mass at the end of the experiment, possibly related to the oxidation of the Ni nanoparticles.

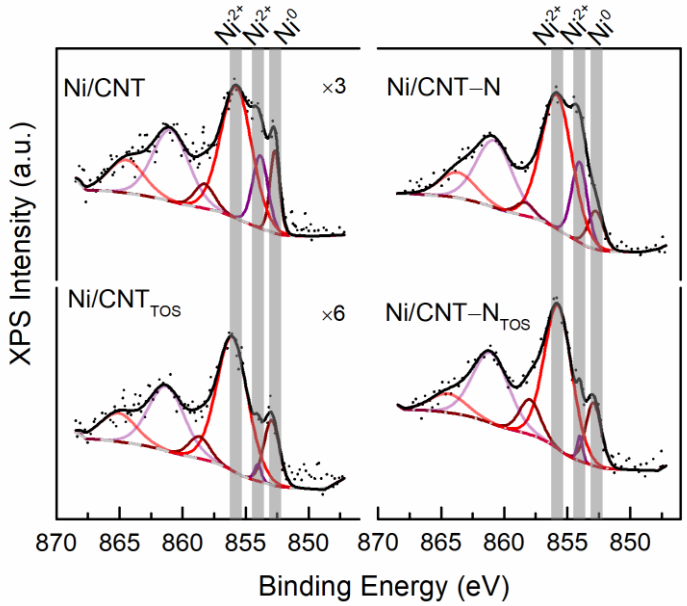

Figure 4.4. High-resolution XPS data for the Ni $2p_{3/2}$ region collected from the as-synthesized Ni/CNT and Ni/CNT−N catalysts (top) and after their time-on-stream (TOS) testing for 2 days (bottom). Dots: raw data; black lines: overall fits; colored lines: fits of individual components; dashed lines: background.

3.2 Catalytic performance in CO_2 methanation

With well-characterized Ni/CNT and Ni/CNT−N catalysts in hand, we further measured their catalytic properties in the CO_2 methanation reaction: CO_2

conversion (X_{CO2}) and selectivity to CH_4 (S_{CH4}) were investigated as a function of the reaction temperature. As expected, the X_{CO2} increases with the temperature for both catalysts until it reaches the thermodynamic equilibrium value and then starts to decrease (Figure 4.5a). Interestingly, Ni/CNT−N achieves a higher X_{CO2} of 81.2% with S_{CH4} = 99.2% at a lower temperature of 400 °C, with an activity (r) of 207 mol dm^{-3} kg^{-1}, when compared to Ni/CNT that achieves a maximum X_{CO2} of 78.5% with S_{CH4} = 98.5% and r = 192 mol dm^{-3} kg^{-1} at a higher temperature of 430 °C (Table 4.2). Accordingly, the maximum CH_4 yield (Y_{CH4}) over the Ni/CNT was calculated to be 77.3%, while Ni/CNT−N is able to reach a higher Y_{CH4} of 80.6% (Table 4.2). Comparing the temperature at which each catalyst achieves 50% of X_{CO2}, (T_{50}), the Ni/CNT−N again performs better, with a T_{50} = 350 °C compared to a T_{50} = 370 °C established for Ni/CNT (Table 4.2). Overall, the Ni/CNT−N catalyst achieves higher X_{CO2} and S_{CH4} at temperatures below 430 °C, while above this temperature the performance of the catalysts is similar. We note that reducing the samples at 400 °C for 3 h prior to the catalytic experiments prevented the influence of the contributions exhibited in TPR at this temperature range on these measurements.

Table 4.2. Comparison of the catalytic performance in terms X_{CO2}, S_{CH4}, and activity (r) for Ni/CNT and Ni/CNT−N catalysts at 400 °C and 430 °C, together with the temperature at which the sample reaches 50% X_{CO2} (T_{50}) and the maximum methane yield ($Y_{CH4,MAX}$), that occurs at 430 °C and 400 °C for Ni/CNT and Ni/CNT−N, respectively.

Sample	400 °C			430 °C			T_{50} (°C)	$Y_{CH4,MAX}$
	X_{CO2} (%)	S_{CH4} (%)	r (mol dm^{-3} kg^{-1})	X_{CO2} (%)	S_{CH4} (%)	r (mol dm^{-3} kg^{-1})		
Ni/CNT	69.9	97.9	171	78.5	98.5	192	370	77.3
Ni/CNT−N	81.2	99.2	207	81.1	99.0	207	350	80.6

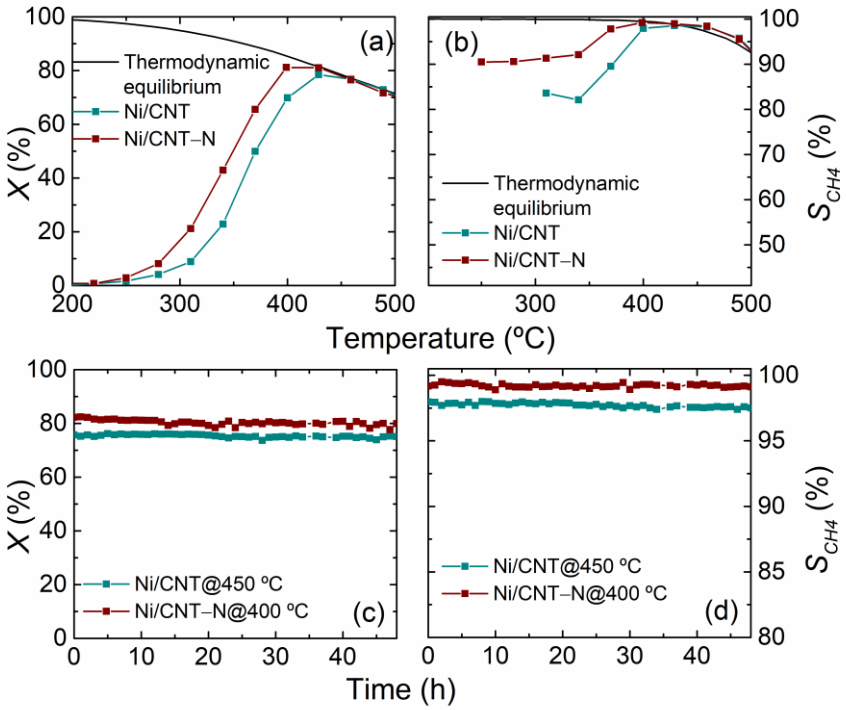

Figure 4.5. Comparison of the CO_2 conversion X_{CO2} (a) and CH_4 selectivity S_{CH4} (b) as a function of temperature for the Ni/CNT and Ni/CNT−N catalysts. Results of the isothermal TOS testing for 48 h in terms of X_{CO2} (c) and S_{CH4} (d). The thermodynamic equilibrium lines are shown in the graphics and were calculated using a model based on the minimization of Gibbs free-energy of the existing species. Reaction conditions: P = 1 bar; $WHSV$ = 60 000 $cm^3\ g^{-1}\ h^{-1}$; $CO_2 : H_2$ = 1 : 4.

We also evaluated the stability of Ni/CNT and Ni/CNT−N catalysts in terms of X_{CO2} and S_{CH4} (Figure 4.5c,d). Both materials exhibited excellent stability over 48 h of isothermal TOS testing, with negligible loss in X_{CO2} and S_{CH4} over this period of time. An additional experiment, with prolonged TOS of 90 h demonstrated that the best performing Ni/CNT−N catalysts maintained excellent stability over this period of time (Figure 4S.12).

3.3 Characterization of the catalysts after TOS

To understand the impact of the CO_2 methanation reaction conditions on the composition and microstructure of the catalysts, we further characterized the TOS-tested Ni/CNT and Ni/CNT−N by XPS and electron microscopy.

XPS (Figure 4.4, bottom) revealed that the TOS-tested catalysts are still a mixture of Ni and NiO. At the same time, the relative at% of metallic Ni

increases in both materials (Table 4S.2). In the case of Ni/CNT, the Ni^0 at% increases from 9.4% to 11.1%, while in Ni/CNT−N it increases from 6.4% to 12.2%, evidencing that the catalyst nanoparticles underwent reduction under the reductive methanation reaction conditions. Importantly, after reaction, both samples exhibit similar Ni^0 at%, which indicates that the highly dispersed NiO species on Ni/CNT−N (Figure 4.3e–h) are reduced under the reaction conditions to a similar extent as the nanoparticles in Ni/CNT. Furthermore, it is interesting that the Ni^{2+} component that presents the major decrease in intensity in the TOS-tested samples is the one at 854 eV, indicating that it is a specific oxidized Ni species that is likely being reduced.

Under the CO_2 methanation reaction conditions, the primary pathways to possible gasification of the C-based support would be via hydrogenation. We do not observe any evidence of significant hydrogenation among the oxidized C components in the C 1s spectra after TOS (Figure 4S.8), which would be the most affected by hydrogenation. In an additional consideration largely independent of the gasification mechanism, the resulting physical damage to the CNT material would have reduced the C 1s shake-up component [44], which is also not observed in the C 1s spectra after TOS (Figure 4S.8). Likewise, the N content in the Ni/CNT−N sample after the long TOS experiment would have been expected to change significantly under some pathways of C gasification or, more generally, of support hydrogenation, but no such change is evident in Table 4S.3.

Analysis of the TEM images (Figure 4S.6) and the resultant particle-size distributions (Figure 4S.7) indicates that the catalytic nanoparticles in both TOS tested Ni/CNT and Ni/CNT−N materials underwent only a negligible increase in average size due to sintering, reaching the average sizes of ≈17 nm and ≈8 nm (Table 4.1), respectively.

HAADF−STEM images and STEM−EDX maps of the catalysts after TOS testing reveal that the catalyst nanoparticles in TOS tested Ni/CNT (Figure 4S.6a–c) and Ni/CNT−N (Figure 4S.6d–f) have a Ni@NiO core-shell nanostructure. Notably, the presence of atomically dispersed Ni species is no longer

observed in TOS-tested Ni/CNT−N, highlighting the sintering of such fine species during CO_2 methanation at 400 °C for 48 h.

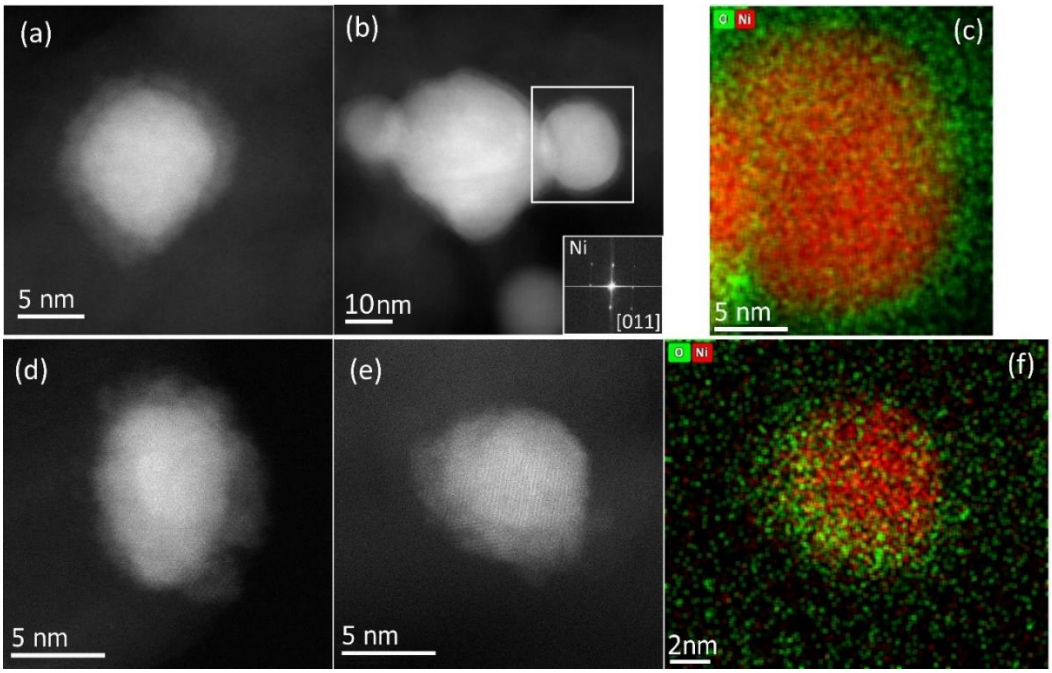

Figure 4.6. Representative high-resolution HAADF−STEM images (a,b,d,e,) and Fourier transform (FT) pattern [inset in panel (b)] of the resultant catalyst particles in TOS-tested Ni/CNT (a,b) and Ni/CNT−N (d,e) catalysts, together with the respective STEM−EDX Ni and O mixture maps, confirming the Ni@NiO core-shell nanostructure of the catalyst particles in spent Ni/CNT (c) and Ni/CNT−N (f).

4. Discussion

Our study demonstrates that N−doping of the CNTs leads to the development of a Ni-based Ni/CNT−N catalyst with significantly improved performance towards CO_2 methanation as compared to its non-doped Ni/CNT counterpart. Specifically, Ni/CNT−N catalyst has a T_{50} = 350 °C and achieves a X_{CO2} of 81.2% with S_{CH4} = 99.2% at 400 °C, while the Ni/CNT catalyst has a T_{50} = 370 °C and achieves a maximum X_{CO2} of 78.5% with S_{CH4} = 98.5% at higher temperature of 430 °C. While achieving high catalytic performance for the as-synthesized Ni/CNT−N material was not the main objective of this work, its catalytic properties compare favorably with the results reported in the literature, making Ni/CNT−N a useful model N−doped CNT material for the direct comparison with the Ni/CNT counterpart aimed at elucidating the salient

properties provided by N−doping of CNTs for catalytic performance in CO_2 methanation.

For example, Gödde *et al*. [12] reported a 30% Ni/NCNT catalyst, which reached X_{CO2} = 86.1% at 350 °C, although using a lower weight hourly space velocity (*WHSV*) than that in the present study (10 000 g cm^3 min^{-1} vs. 60 000 g cm^3 min^{-1}). At higher *WHSV* = 50 000 g cm^3 min^{-1}, they were able to obtain X_{CO2} = 50.9% with S_{CH4} = 95.8% at 340 °C (Table 4S.4). In another work, Wang *et al*. [6] reported a X_{CO2} = 80% with S_{CH4} = 99% at 360 °C with *WHSV* = 60 000 g cm^3 min^{-1} for their Ni catalyst supported on N−doped CNTs (Table 4S.4). Interestingly, the as-synthesized Ni/CNT−N achieved better catalytic properties than did our previously reported Ni catalyst supported on N−doped activated carbon, which reached X_{CO2} = 70% with $S_{CH4} \approx$ 95% at 450 °C [13] (Table 4S.4). This improvement in the catalytic properties provides direct evidence that N−doped carbon nanotubes are a better supporting material for Ni-based CO_2 methanation catalysts than is N−doped activated carbon.

Other types of systems, also based on CNTs but not on N−doped ones, have been evaluated using different types of promotion. Gao *et al*. [26] reported a catalyst comprising 10% Ni and 2%La supported on oxidized CNT that achieved 82.8% of X_{CO2} with 100% S_{CH4} at 320 °C (Table 4S.4). Furthermore, Wang *et al*. [4] reported a catalyst comprising 12% Ni and 4.5% Ce supported on CNT that achieved 83.8% of X_{CO2} with 99.8% S_{CH4} at 350 °C (Table 4S.4).

It has been reported that the N−sites could provide binding sites for the Ni species enabling a good dispersion of the Ni precursor during impregnation, and also preventing agglomeration of the nanoparticles during the thermal treatments [6,12–14,45,46]. Accordingly, we propose that the experimentally observed higher CO_2 methanation performance of Ni/CNT−N than that of Ni/CNT is a result of the higher dispersion of the catalytically active Ni phase over N−doped CNTs. This conclusion is supported by our multiple characterization methods that evidenced the existence of fine catalytic

particles (even atomically dispersed Ni species) well-dispersed over N−doped CNTs.

On the other hand, the presence of highly dispersed Ni species leads to the difficulty in their reduction due to strong interaction with the support, as confirmed by H_2−TPR. This resulted in the presence of NiO catalyst nanoparticles in Ni/CNT−N, while Ni/CNT was found to consist of metallic Ni nanoparticles covered with a NiO shell.

Even though the catalysts demonstrated excellent stability over 48 h of TOS, their characterization after the TOS-testing allowed for the identification of the changes that they underwent during prolonged CO_2 methanation. Interestingly, the Ni^0 at% is similar in both TOS-tested Ni/CNT and Ni/CNT−N, suggesting that, even though the Ni species in Ni/CNT−N are more difficult to reduce, under CO_2 methanation conditions, they undergo reduction to a similar extent as in the case of Ni/CNT. This reduction of the Ni phase occurs as a consequence of subjecting the catalysts to the reductive methanation conditions for the prolonged TOS. Interestingly, it seems that it is a specific oxidized Ni species that is being reduced since the Ni^{2+} component that presents the major decrease in intensity in the TOS-tested samples is the one at 854 eV. Furthermore, the resultant catalyst nanoparticles in TOS-tested Ni/CNT−N are morphologically similar to those in TOS-tested Ni/CNT, forming a core-shell nanostructure of Ni@NiO but preserving their small particle size.

5. Conclusions

We successfully prepared Ni-based catalysts supported on CNTs and N−doped CNTs, compared their catalytic properties in CO_2 methanation, evaluated their stability, and performed comprehensive characterization to understand the property-performance relationship.

Our Ni/CNT−N catalyst achieves a X_{CO2} of 81.2% with S_{CH4} = 99.2% at 400 °C, while the pristine CNT counterpart, Ni/CNT, achieves a maximum X_{CO2} of 78.5% with S_{CH4} = 98.5% at a higher temperature of 430 °C. Furthermore, both

catalysts exhibit outstanding stability over 48 h of TOS testing, with no sign of deactivation. The enhanced performance of Ni/CNT−N is a result of the good dispersion of the Ni phase over N−doped CNTs, as confirmed by TEM, HAADF–STEM, H_2 TPR, and H_2 pulse chemisorption. These encouraging results compare well to those reported previously, thus offering new opportunities for designing high-performing CO_2 methanation catalysts throughout judicious modification of the supporting material.

6. Supplementary Information

6.1 Loading Study

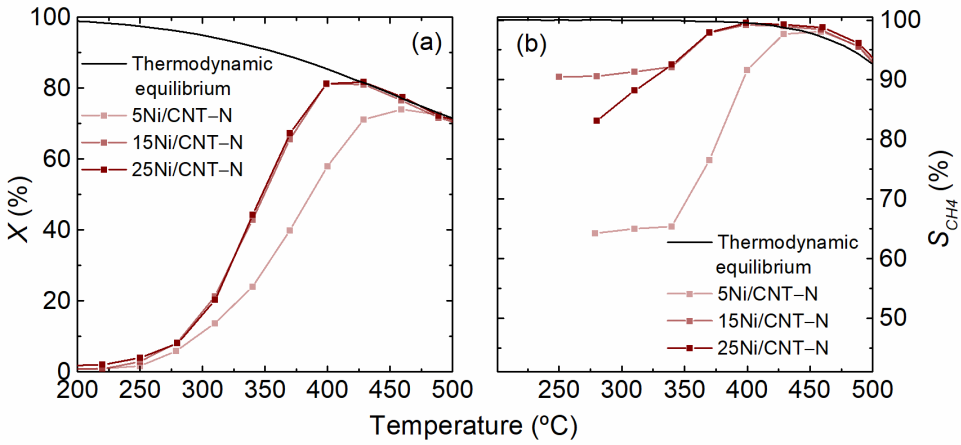

Figure 4S.1. Comparison of the CO_2 conversion X_{CO2} (a) and CH_4 selectivity S_{CH4} (b) as a function of temperature for the 5Ni/CNT−N, 15Ni/CNT−N, and 25Ni/CNT−N catalysts with different Ni loadings of 5%, 15% and 25%, respectively. The catalytic data indicate that the optimal loading of Ni onto N-doped CNTs is 15%. The thermodynamic equilibrium curves are shown in the graphics and were calculated using a model based on the minimization of Gibbs free-energy of the existing species. Methanation conditions: P = 1 bar; $WHSV$ = 60 000 $cm^3\ g^{-1}\ h^{-1}$; CO_2 : H_2 = 1 : 4

6.2 N_2 Physisorption

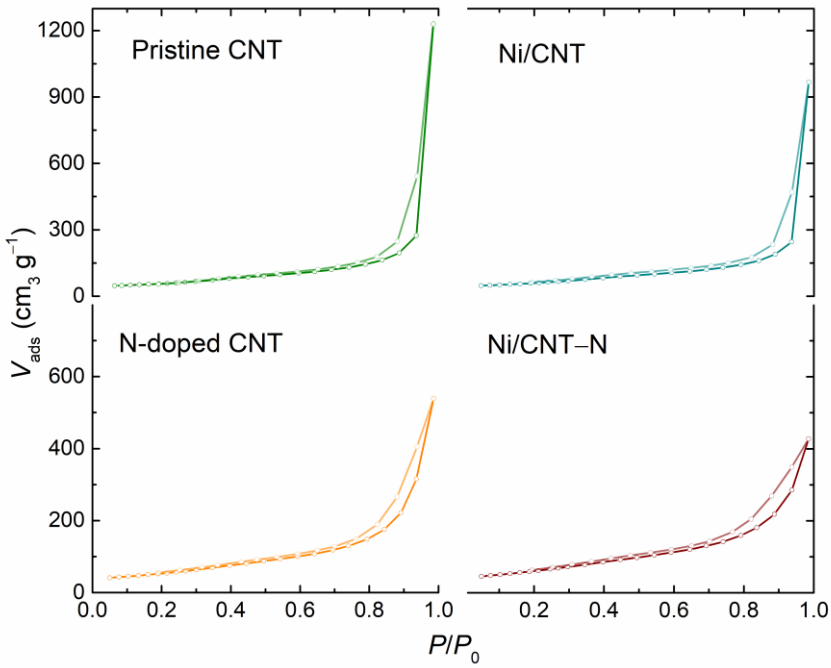

Figure 4S.2. Comparison of N_2 adsorption–desorption isotherms measured for the pristine CNTs and N-doped CNTs supporting materials, as well as for the derivative Ni/CNT and Ni/CNT–N methanation catalysts with 15% Ni loading.

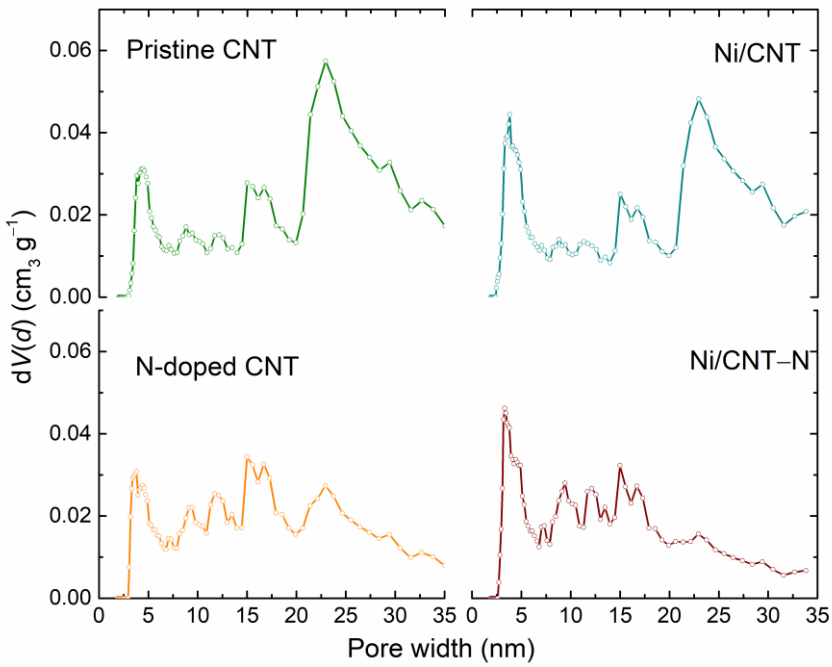

Figure 4S.3. Pore size distribution obtained using the non-local density functional theory (NLDFT), where a cylindrical-pore model is assumed, for the pristine CNTs and N-doped CNTs supporting materials, as well as for the derivative Ni/CNT and Ni/ CNT–N methanation catalysts with 15% Ni loading.

6.3 Transmission Electron Microscopy

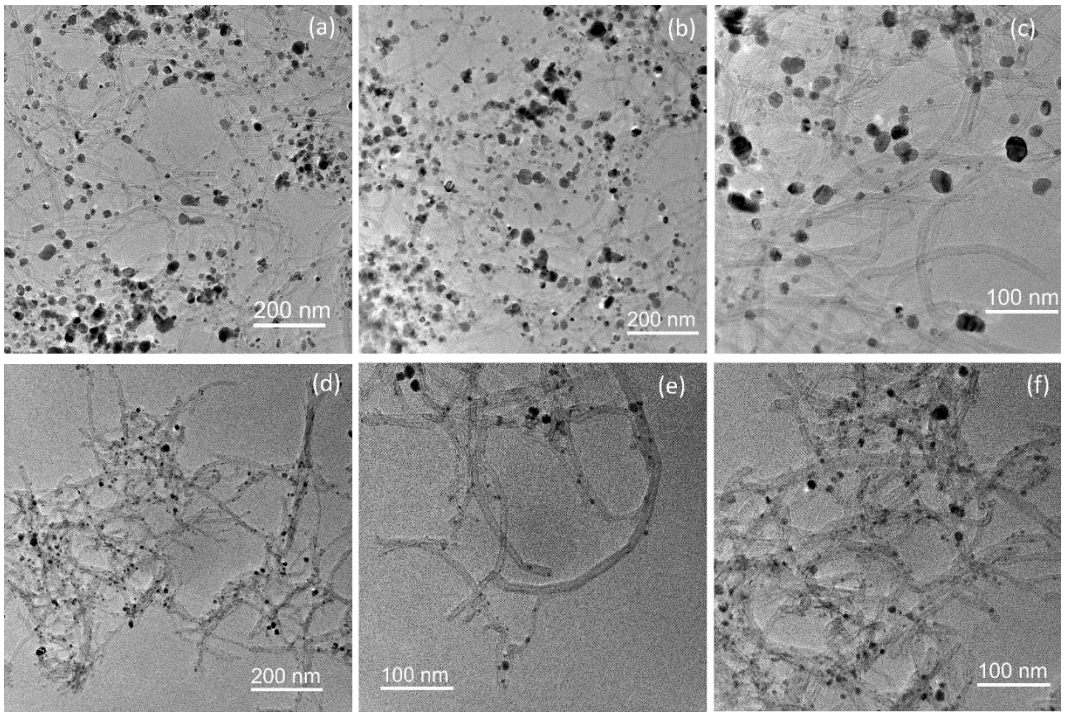

Figure 4S.4. Representative low-magnification TEM images of the as-synthesized Ni/CNT (a–c) and Ni/CNT–N (d–f) methanation catalysts.

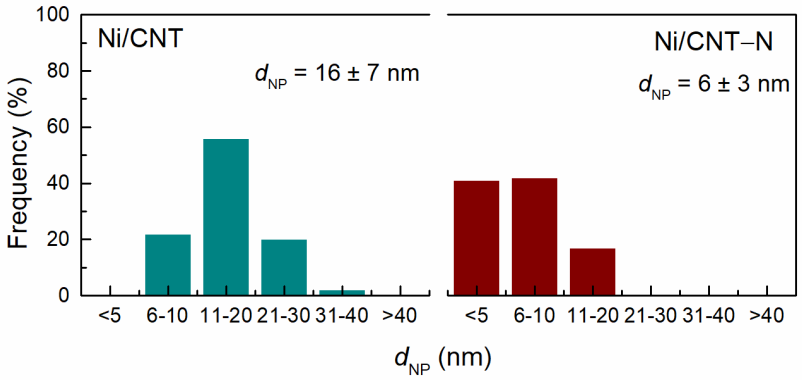

Figure 4S.5. Comparison of the catalyst particle size distribution in the as-synthesized Ni/CNT and Ni/CNT–N, estimated by the analysis of the TEM images.

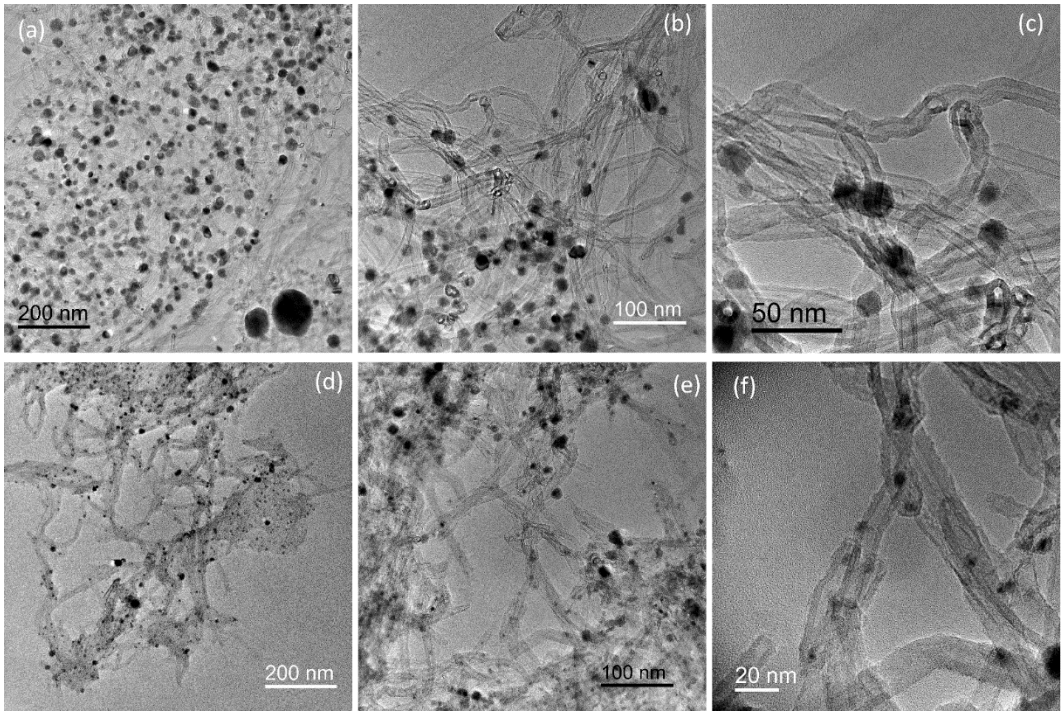

Figure 4S.6. Representative low-magnification TEM images of the spent Ni/CNT (a–c) and Ni/CNT−N (d–f) methanation catalysts after their TOS testing for 48 h.

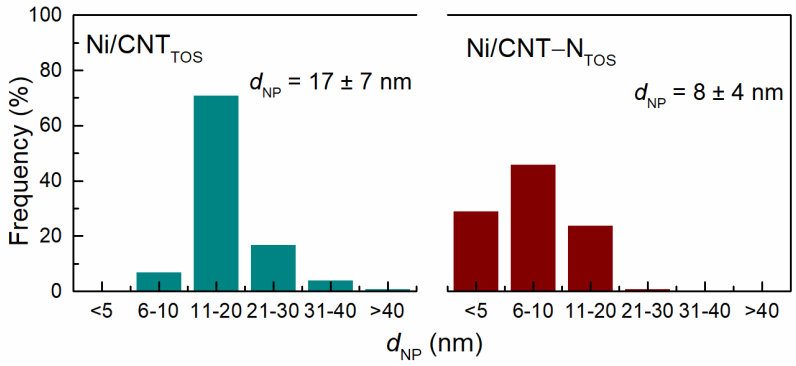

Figure 4S.7. Comparison of the catalyst particle size distribution in the spent Ni/CNT and Ni/CNT−N after TOS testing for 48 h, estimated by the analysis of the TEM images.

6.4 X-ray photoelectron spectroscopy

Five peaks were identified in the C 1s region (Figure 4S.8), which correspond to the aromatic and aliphatic carbon, (C1) at 284.6 eV, the phenols, and CN groups (in N-doped CNT) (C2) at 285.9 ± 0.2 eV, keto-groups (C3) at 287.7 ± 0.2 eV, carboxylic groups (C4) at 289.3 ± 0.1 eV, and the plasmon loss ($C_{shake-up}$) at 291.4 ± 0.1 eV [38,39].

Regarding O 1s region (Figure 4S.9), in the case of the supporting materials, pristine CNTs and N-doped CNTs, five peaks were identified, which correspond to oxygen in C=O groups (O1) at 530.8 ± 0.1 eV; hydroxyls, ethers and C=O in esters, amides, anhydrides (O2) at 532.1 eV; C–O groups in esters and anhydrides (O3) at 533.5 eV; carboxylic groups (O4) at 534.5 eV; and water at 536.2 ± 0.1 eV. In the case of the CNT−N and Ni/CNT−N catalysts, six peaks were identified, which correspond to oxygen in metal oxides (MO) at 529.9 ± 0.1 eV; oxygen in C=O groups (O1) at 531.3 ± 0.1 eV; hydroxyls, ethers and C=O in esters, amides, anhydrides (O2) at 532.1± 0.1 eV; C–O groups in esters and anhydrides (O3) at 533.2± 0.1 eV; carboxylic groups (O4) at 534.1± 0.2 eV; and water at 536.1 ± 0.3 eV [13,38].

Furthermore, the N 1s spectra (Figure 4S.10) for N-doped CNTs, the as-synthesized Ni/CNT−N and TOS-tested Ni/CNT−N demonstrate that the samples present mainly pyridinic groups (N-6) and pyrrolic (N-5) groups at 398.4 ± 0.4 eV and 400.1 ± 0.1 eV, respectively, as well as some quaternary groups (N-Q) at 401.9 ± 0.4 eV. It is also possible to observe π excitation at 496.5± 1.3 eV [13,38].

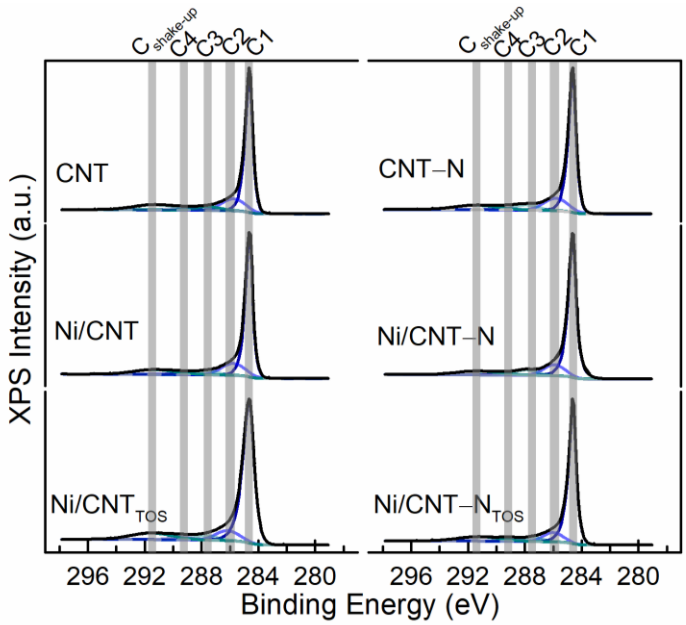

Figure 4S.8. High-resolution XPS data for C 1s region for pristine CNTs and N-doped CNTs, as well as for the as-synthesized and TOS-tested Ni/CNT and Ni/CNT−N catalysts. Symbols: raw data; black lines: overall fits; colored lines: fits of individual components; dashed lines: background. C1: aromatic and aliphatic carbon; C2: phenols, and CN groups; C3: keto-groups; C4: carboxylic groups; $C_{shake\text{-}up}$: plasmon loss.

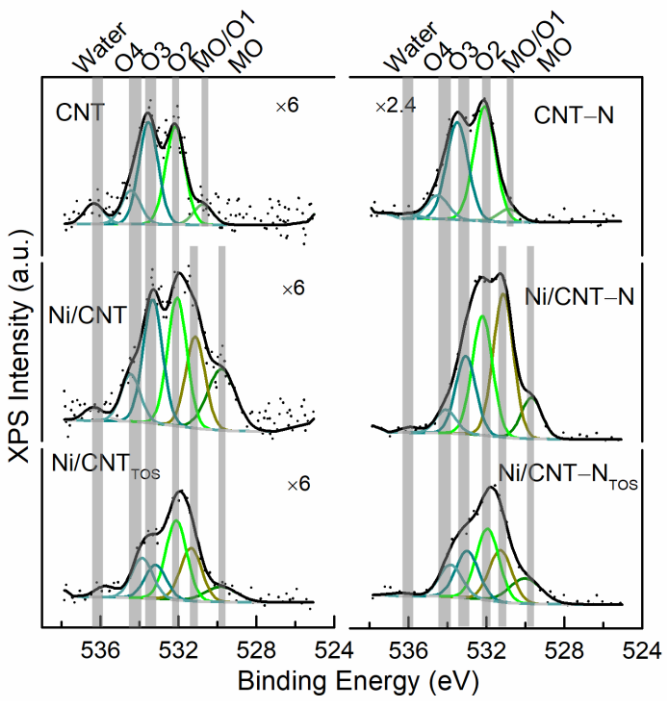

Figure 4S.9. High-resolution XPS data O 1s region for pristine CNTs and N-doped CNTs, as well as for the as-synthesized and TOS-tested Ni/CNT and Ni/CNT–N catalysts. Symbols: raw data; black lines: overall fits; colored lines: fits of individual components; dashed lines: background. MO: O in metal oxides; O1: C=O; O2: hydroxyls, ethers and C=O in esters, amides, anhydrides; O3: C–O in esters and anhydrides; O4: carboxylic groups.

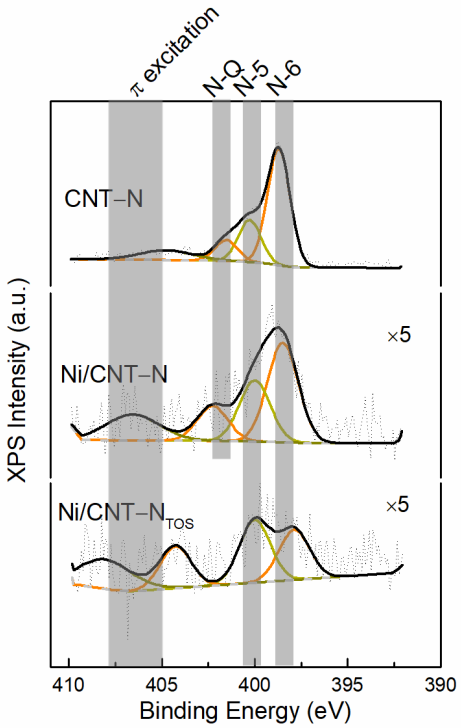

Figure 4S.10. High-resolution XPS data N 1s region for N-doped CNTs, as well as for the as-synthesized and TOS-tested Ni/CNT–N catalysts. Symbols: raw data; black lines: overall fits; colored lines: fits of individual components; dashed lines: background. N-6: pyridinic groups; N-5: pyridonic or pyrrolic groups; N-Q: quaternary groups.

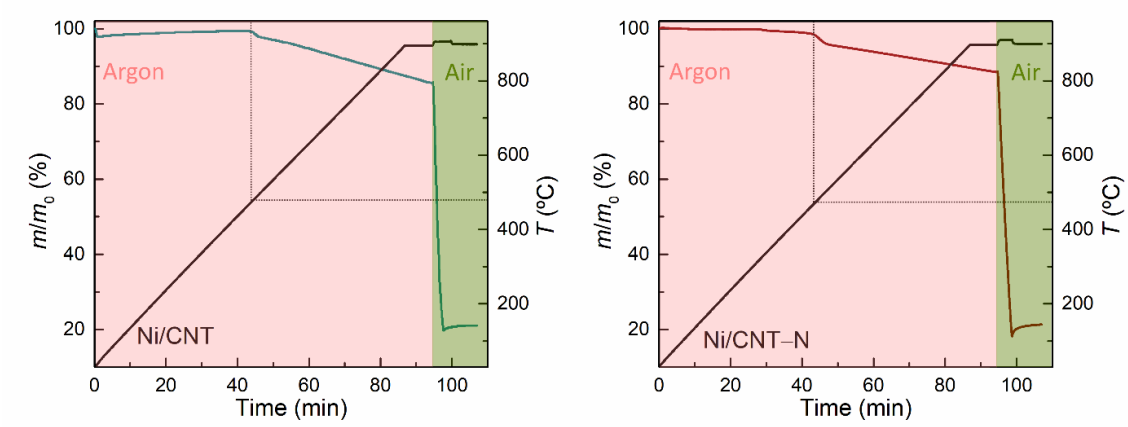

Figure 4S.11. Thermogravimetric analysis (TGA) of the Ni/CNT and Ni/CNT–N catalysts until 900 °C with a heating rate of 10 °C min^{-1} under Argon, with an isothermal step of 7 min and a final isothermal step at 900 °C under air for 13 min.

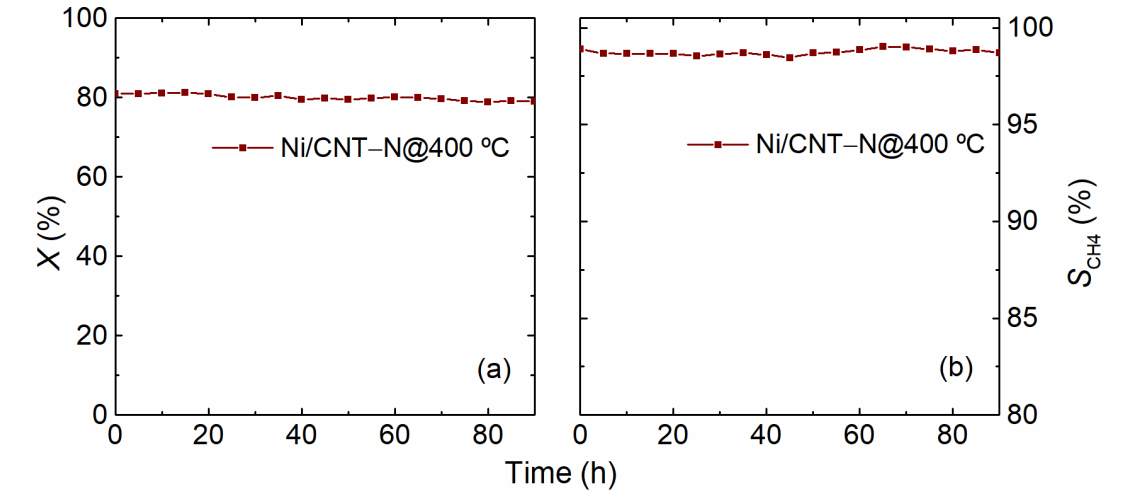

Figure 4S.12. Results of the isothermal TOS testing for 90 h in terms of X_{CO2} (a) and S_{CH4} (b) for the Ni/CNT–N catalyst. Methanation conditions: T = 400 °C; P = 1 bar; $WHSV$ = 60 000 $cm^3\ g^{-1}\ h^{-1}$; $CO_2 : H_2 = 1 : 4$.

6.5 Tables

Table 4S.1. Elemental composition of pristine CNT and the synthesized CNT–N.

	C (%)	H (%)	N (%)	S (%)	O (%)
CNT	99.0	0.1	0.0	0.0	0.1
CNT–N	92.9	0.2	5.0	0.0	1.2

Table 4S.2. Relative atomic percentage (at%) of Ni^0 and Ni^{2+} in the as-synthesized and TOS-tested Ni/CNT and Ni/CNT−N catalysts, as quantified by XPS analysis.

	Ni^0 (relative at%)	**Ni^{2+} (relative at%)**
Ni/CNT	9.4	90.6
Ni/CNT−N	6.4	93.6
Ni/CNT_{TOS}	11.1	88.9
$Ni/CNT-N_{TOS}$	12.2	87.8

Table 4S.3. Relative atomic percentage (at%) of C, N, and O in the CNT and CNT−N supports, as well as the as-synthesized and TOS-tested Ni/CNT and Ni/CNT−N catalysts, as quantified by XPS analysis.

	C (relative at%)	**O (relative at%)**	**N (relative at%)**
CNT	99	1	--
CNT−N	94	2	4
Ni/CNT	99	1	--
Ni/CNT−N	93	6	1
Ni/CNT_{TOS}	99	1	--
$Ni/CNT-N_{TOS}$	95	4	1

Table 4S.4. Comparison of the catalytic properties of the catalysts of the present work (Ni/CNT and Ni/CNT−N) with similar catalysts already reported in the literature, including the conditions used in the catalytic system and the reaction experiment in each case.

	Ni (wt%)	***P* (bar)**	**CO_2 : H_2**	***WHSV* (g cm^3 min^{-1})**	**$X_{CO2,MAX}$ (%)**	**$S_{CH4,MAX}$ (%)**	**$T_{optimal}$ (°C)**	**T_{50} (°C)**	**Ref.**
Ni/CNT	15	1	1 : 4	60 000	78.5	98.5	430	370	This work
Ni/CNT−N	15	1	1 : 4	60 000	81.2	99.2	400	350	This work
Ni/NCNT	30	1	1 : 4	50 000	50.9	95.8	340	340	[12]
Ni/N-CNT	10	1	1 : 4	60 000	80	99	360	≈290	[6]
Ni/AC−N	15	1	1 : 4	60 000	70	95	450	≈400	[13]
10Ni-2La/oCNT	10	1	1 : 4	24 000	82.8	100	≈320	≈250	[26]
12Ni4.5Ce/CNT	12	1	1 : 4	30 000	83.8	99.8	350	≈270	[4]

References

(1) Serp, P.; Castillejos, E. Catalysis in Carbon Nanotubes. *ChemCatChem* **2010**, 2 (1), 41–47. https://doi.org/10.1002/cctc.200900283.

(2) Agnelli, M.; Swaan, H. M.; Marquez-Alvarez, C.; Martin, G. A.; Mirodatos, C. CO Hydrogenation on a Nickel Catalyst: II. A Mechanistic Study by Transient Kinetics and Infrared Spectroscopy. *J. Catal*. **1998**, 175 (1), 117–128. https://doi.org/10.1006/jcat.1998.1978.

(3) Li, L.; Zheng, J.; Liu, Y.; Wang, W.; Huang, Q.; Chu, W. Impacts of SiC Carrier and Nickel Precursor of NiLa/Support Catalysts for CO_2 Selective Hydrogenation to Synthetic Natural Gas (SNG). *ChemistrySelect* **2017**, 2 (13), 3750–3757. https://doi.org/https://doi.org/10.1002/slct.201601745.

(4) Wang, W.; Chu, W.; Wang, N.; Yang, W.; Jiang, C. Mesoporous Nickel Catalyst Supported on Multi-Walled Carbon Nanotubes for Carbon Dioxide. *Int. J. Hydrogen Energy* **2015**, 41 (2), 967–975. https://doi.org/10.1016/j.ijhydene.2015.11.133.

(5) Serp, P.; Figueiredo, J. L. Carbon Materials for Catalysis; Serp, P., Figueiredo, J. L., Eds.; Wiley: New Jersey, **2009**.

(6) Wang, W.; Duong-Viet, C.; Ba, H.; Baaziz, W.; Tuci, G.; Caporali, S.; Nguyen-Dinh, L.; Ersen, O.; Giambastiani, G.; Pham-Huu, C. Nickel Nanoparticles Decorated Nitrogen-Doped Carbon Nanotubes (Ni/N-CNT); A Robust Catalyst for the Efficient and Selective CO_2 Methanation. *ACS Appl. Energy Mater.* **2019**, 2 (2), 1111–1120. https://doi.org/10.1021/acsaem.8b01681.

(7) Li, J.; Zhou, Y.; Xiao, X.; Wang, W.; Wang, N.; Qian, W.; Chu, W. Regulation of Ni−CNT Interaction on Mn-Promoted Nickel Nanocatalysts Supported on Oxygenated CNTs for CO_2 Selective Hydrogenation. *ACS Appl. Mater. Interfaces* **2018**, 10, 41224–41236. https://doi.org/10.1021/acsami.8b04220.

(8) Rocha, R. P.; Pereira, M. F. R. Tuning CNT Properties for Metal-Free Environmental Catalytic Applications. *C* **2016**, 2, 17. https://doi.org/10.3390/c2030017.

(9) Soares, O. S. G. P.; Rocha, R. P.; Gonçalves, A. G.; Figueiredo, J. L.; Órfão, J. J. M.; Pereira, M. F. R. Highly Active N-Doped Carbon Nanotubes Prepared by an Easy Ball Milling Method for Advanced Oxidation Processes. *Appl. Catal. B Environ.* **2016**, 192, 296–303. https://doi.org/10.1016/j.apcatb.2016.03.069.

(10) Rocha, R. P.; G.P. Soares, O. S.; Gonçalves, A. G.; Órfão, J. J. M.; Pereira, M. F. R.; Figueiredo, J. L. Different Methodologies for Synthesis of Nitrogen Doped Carbon Nanotubes and Their Use in Catalytic Wet Air Oxidation. *Appl. Catal. A Gen.* **2017**, 548 (April), 62–70. https://doi.org/10.1016/j.apcata.2017.08.033.

(11) Soares, O. S. G. P.; Rocha, R. P.; Órfão, J. J. M.; Pereira, M. F. R.; Figueiredo, J. L. Mechanothermal Approach for N-, S-, P-, and B-Doping of Carbon Nanotubes: Methodology and Catalytic Performance in Wet Air Oxidation. *C* **2019**, 5 (2), 30. https://doi.org/10.3390/c5020030.

(12) Gödde, J.; Merko, M.; Xia, W.; Muhler, M. Nickel Nanoparticles Supported on Nitrogen–Doped Carbon Nanotubes Are a Highly Active, Selective and Stable CO_2 Methanation Catalyst. *J. Energy Chem.* **2021**, 54, 323–331. https://doi.org/10.1016/j.jechem.2020.06.007.

(13) Gonçalves, L. P. L.; Sousa, J. P. S.; Soares, O. S. G. P.; Bondarchuk, O.; Lebedev, O. I.; Kolen'ko, Y. V.; Pereira, M. F. R. The Role of Surface Properties in CO_2 Methanation over Carbon-Supported Ni Catalysts and Their Promotion by Fe. *Catal. Sci. Technol.* **2020**, 10 (21), 7217. https://doi.org/10.1039/D0CY01254H.

(14) Gonçalves, L. P. L.; Serov, A.; McCool, G.; Dicome, M.; Sousa, J. P. S.; Soares, O. S. G. P.; Bondarchuk, O.; Petrovykh, D. Y.; Lebedev, O. I.; Pereira, M. F. R.; Kolen'ko, Y. New Opportunity for Carbon-Supported Ni-based Electrocatalysts: Gas-phase CO_2 Methanation. *ChemCatChem* **2021**, 13, 1–11. https://doi.org/10.1002/cctc.202101284.

(15) Bailera, M.; Lisbona, P.; Romeo, L. M.; Espatolero, S. Power to Gas Projects Review: Lab, Pilot and Demo Plants for Storing Renewable Energy and CO_2. *Renew. Sustain. Energy Rev.* **2017**, 69 (November 2016), 292–312. https://doi.org/10.1016/j.rser.2016.11.130.

(16) Niaz, S.; Manzoor, T.; Pandith, A. H. Hydrogen Storage: Materials, Methods and Perspectives. *Renew. Sustain. Energy Rev.* **2015**, 50, 457–469. https://doi.org/10.1016/j.rser.2015.05.011.

(17) Ashok, J.; Pati, S.; Hongmanorom, P.; Tianxi, Z.; Junmei, C.; Kawi, S. A Review of Recent Catalyst Advances in CO_2 Methanation Processes. *Catal. Today* **2020**, 356 (May), 471–489. https://doi.org/10.1016/j.cattod.2020.07.023.

(18) Miao, B.; Ma, S. S. K.; Wang, X.; Su, H.; Chan, S. H. Catalysis Mechanisms of CO_2 and CO Methanation. *Catal. Sci. Technol.* **2016**, 6 (12), 4048–4058. https://doi.org/10.1039/C6CY00478D.

(19) Zhang, Z.; Tian, Y.; Zhang, L.; Hu, S.; Xiang, J. Impacts of Nickel Loading on Properties, Catalytic Behaviors of $Ni/\gamma Al_2O_3$ Catalysts and the Reaction Intermediates Formed in Methanation of CO_2. *Int. J. Hydrogen Energy* **2019**, 44 (18), 9291–9306. https://doi.org/10.1016/j.ijhydene.2019.02.129.

(20) Ma, Y.; Liu, J.; Chu, M.; Yue, J.; Cui, Y.; Xu, G. Cooperation Between Active Metal and Basic Support in Ni-Based Catalyst for Low-Temperature CO_2 Methanation. *Catal. Letters* **2020**, 150 (5), 1418–1426. https://doi.org/10.1007/s10562-019-03033-w.

(21) Wen, X.; Xu, L.; Chen, M.; Shi, Y.; Lv, C.; Cui, Y.; Wu, X.; Cheng, G.; Wu, C. e.; Miao, Z.; Wang, F.; Hu, X. Exploring the Influence of Nickel Precursors on Constructing Efficient Ni-Based CO_2 Methanation Catalysts Assisted with *in-Situ* Technologies. *Appl. Catal. B Environ.* **2021**, 297 (April), 120486. https://doi.org/10.1016/j.apcatb.2021.120486.

(22) Westermann, A.; Azambre, B.; Bacariza, M. C.; Graça, I.; Ribeiro, M. F.; Lopes, J. M.; Henriques, C. Insight into CO2 Methanation Mechanism over NiUSY Zeolites: An Operando IR Study. *Appl. Catal. B Environ.* **2015**, 174–175, 120–125. https://doi.org/10.1016/j.apcatb.2015.02.026.

(23) Zhen, W.; Li, B.; Lu, G.; Ma, J. Enhancing Catalytic Activity and Stability for CO_2 Methanation on Ni@MOF-5 via Control of Active Species Dispersion. *Chem. Commun.* **2015**, 51, 1728–1731. https://doi.org/10.1039/C4CC08733J.

(24) Ha, N. N.; Thi, N.; Ha, T.; Khu, L. Van; Cam, L. M. Theoretical Study of Carbon Dioxide Activation by Metals (Co, Cu, Ni) Supported on Activated Carbon. *J Mol Model* **2015**, No. 21, 322. https://doi.org/10.1007/s00894-015-2864-1.

(25) Kangvansura, P.; Chew, L. M.; Saengsui, W.; Santawaja, P.; Poo-arporn, Y.; Muhler, M.; Schulz, H.; Worayingyong, A. Product Distribution of CO_2 Hydrogenation by K- and Mn-Promoted Fe Catalysts Supported on N-Functionalized Carbon Nanotubes. *Catal. Today* **2016**, 275, 59–65. https://doi.org/10.1016/j.cattod.2016.02.045.

(26) Gao, J.; Jiang, Q.; Liu, Y.; Liu, W.; Chu, W.; Su, D. S. Probing the Enhanced Catalytic Activity of Carbon Nanotube Supported Ni-LaOx Hybrids for the CO_2 Reduction Reaction. *Nanoscale* **2018**, 10, 14207–14219. https://doi.org/10.1039/c8nr03882a.

(27) Romero-sáez, M.; Dongil, A. B.; Benito, N.; Espinoza-González, R.; Escalona, N.; Gracia, F. CO_2 Methanation over Nickel-ZrO_2 Catalyst Supported on Carbon Nanotubes : A Comparison between Two Impregnation Strategies. *Appl. Catal. B Environ.* **2018**, 237 (March), 817–825. https://doi.org/10.1016/j.apcatb.2018.06.045.

(28) Roldán, L.; Marco, Y.; García-Bordejé, E. Function of the Support and Metal Loading on Catalytic Carbon Dioxide Reduction Using Ruthenium Nanoparticles Supported on Carbon Nanofibers. *ChemCatChem* **2015**, 7, 1347–1356. https://doi.org/10.1002/cctc.201500016.

(29) Roldán, L.; Marco, Y.; García-Bordejé, E. Origin of the Excellent Performance of Ru on Nitrogen- Doped Carbon Nanofibers for CO_2 Hydrogenation to CH_4. *ChemSusChem* **2017**, 10 (6), 1139–1144. https://doi.org/10.1002/cssc.201601217.

(30) Jurca, B.; Bucur, C.; Primo, A.; Concepción, P.; Parvulescu, V. I.; García, H. N-Doped Defective Graphene from Biomass as Catalyst for CO_2 Hydrogenation to Methane. *ChemCatChem* **2019**, 11 (3), 985–990. https://doi.org/10.1002/cctc.201801984.

(31) Hu, F.; Tong, S.; Lu, K.; Chen, C.; Su, F.; Zhou, J.; Lu, Z.; Wang, X.; Feng, G.; Zhang, R. Reduced Graphene Oxide Supported Ni-Ce Catalysts for CO_2 Methanation: The Support and Ceria Promotion Effects. *J. CO_2 Util.* **2019**, 34 (June), 676–687. https://doi.org/10.1016/j.jcou.2019.08.020.

(32) Gonçalves, L. P. L.; Mielby, J.; Soares, O. S. G. P.; Sousa, J. P. S.; Petrovykh, D. Y.; Lebedev, O. I.; Pereira, M. F. R.; Kegnæs, S.; Kolen'ko, Y. V. Elucidating the CO_2 Methanation Mechanisms on High-Performing Carbon/Ceria-Supported Ni Catalysts Using Modulation Excitation *in situ* DRIFTS. *Appl. Catal. B Environ* **2022** https://doi.org/10.1016/j.apcatb.2022.121376.

(33) Soares, O. S. G. P.; Rocha, R. P.; Gonçalves, A. G.; Figueiredo, J. L.; Órfão, J. J. M.; Pereira, M. F. R. Easy Method to Prepare N-Doped Carbon Nanotubes by Ball Milling. *Carbon* **2015**, 91, 114–121. https://doi.org/10.1016/j.carbon.2015.04.050.

(34) Kim, D. Y.; Kim, J. H.; Li, M.; Noda, S.; Kim, J.; Kim, K. S.; Kim, K. S.; Yang, C. M. Controllable Pore Structures of Pure and Sub-Millimeter-Long Carbon Nanotubes. *Appl. Surf. Sci.* **2021**, 566, 150751. https://doi.org/10.1016/j.apsusc.2021.150751.

(35) Likodimos, V.; Steriotis, T. A.; Papageorgiou, S. K.; Romanos, G. E.; Marques, R. R. N.; Rocha, R. P.; Faria, J. L.; Pereira, M. F. R.; Figueiredo, J. L.; Silva, A. M. T.; Falaras, P. Controlled Surface Functionalization of Multiwall Carbon Nanotubes by HNO_3 Hydrothermal Oxidation. *Carbon* **2014**, 69, 311–326. https://doi.org/10.1016/j.carbon.2013.12.030.

(36) Chen, W.; Fan, Z.; Pan, X.; Bao, X. Effect of Confinement in Carbon Nanotubes on the Activity of Fischer−Tropsch Iron Catalyst. *J. Am. Chem. Soc.* **2008**, 130 (29), 9414–9419. https://doi.org/10.1021/ja8008192.

(37) Lu, P.; Yang, Y.; Yao, J.; Wang, M.; Dipazir, S.; Yuan, M.; Zhang, J.; Wang, X.; Xie, Z.; Zhang, G. Facile Synthesis of Single-Nickel-Atomic Dispersed N-Doped Carbon Framework for Efficient Electrochemical CO_2 Reduction. *Appl. Catal. B Environ.* **2019**, 241, 113–119. https://doi.org/https://doi.org/10.1016/j.apcatb.2018.09.025.

(38) Zhang, T.; Han, X.; Yang, H.; Han, A.; Hu, E.; Li, Y.; Yang, X.; Wang, L.; Liu, J.; Liu, B. Atomically Dispersed Nickel(I) on an Alloy-Encapsulated Nitrogen-Doped Carbon Nanotube Array for High-Performance Electrochemical CO_2 Reduction Reaction. *Angew. Chemie Int. Ed.* **2020**, 59 (29), 12055–12061. https://doi.org/https://doi.org/10.1002/anie.202002984.

(39) Biesinger, M. C.; Payne, B. P.; Lau, L. W. M.; Gerson, A.; Smart, R. S. C. X-Ray Photoelectron Spectroscopic Chemical State Quantification of Mixed Nickel Metal, Oxide and Hydroxide Systems. *Surf. Interface Anal.* **2009**, 41 (4), 324–332. https://doi.org/10.1002/sia.3026.

(40) Owens-Baird, B.; Xu, J.; Petrovykh, D. Y.; Bondarchuk, O.; Ziouani, Y.; González-Ballesteros, N.; Yox, P.; Sapountzi, F. M.; Niemantsverdriet, H.; Kolen'ko, Y. V; Kovnir, K. NiP_2: A Story of Two Divergent Polymorphic Multifunctional Materials. *Chem. Mater.* **2019**, 31 (9), 3407–3418. https://doi.org/10.1021/acs.chemmater.9b00565.

(41) Owens-Baird, B.; Sousa, J. P. S.; Ziouani, Y.; Petrovykh, D. Y.; Zarkevich, N. A.; Johnson, D. D.; Kolen'ko, Y. V; Kovnir, K. Crystallographic Facet Selective HER Catalysis: Exemplified in FeP and NiP_2 Single Crystals. *Chem. Sci.* **2020**, 11 (19), 5007–5016. https://doi.org/10.1039/D0SC00676A.

(42) Figueiredo, J. L.; Pereira, M. F. R. The Role of Surface Chemistry in Catalysis with Carbons. *Catal. Today* **2010**, 150, 2–7. https://doi.org/10.1016/j.cattod.2009.04.010.

(43) Gonçalves, L. P. L.; Christensen, D. B.; Meledina, M.; Salonen, L. M.; Petrovykh, D. Y.; Carbó-Argibay, E.; Sousa, J. P. S.; Soares, O. S. G. P.; Pereira, M. F. R.; Kegnæs, S.; Kolen'Ko, Y. V. Selective Formic Acid Dehydrogenation at Low Temperature over a RuO_2/COF Pre-Catalyst Synthesized on the Gram Scale. *Catal. Sci. Technol.* **2020**, 10 (7), 1991–1995. https://doi.org/10.1039/d0cy00145g.

(44) Lachman, N.; Sui, X.; Bendikov, T.; Cohen, H.; Wagner, H. D. Electronic and Mechanical Degradation of Oxidized CNTs. *Carbon* **2012**, 50 (5), 1734–1739. https://doi.org/10.1016/j.carbon.2011.12.009.

(45) Fu, T.; Li, Z. Highly Dispersed Cobalt on N-Doped Carbon Nanotubes with Improved Fischer–Tropsch Synthesis Activity. *Catal. Commun.* **2014**, 47, 54–57. https://doi.org/https://doi.org/10.1016/j.catcom.2014.01.008.

(46) Chernyak, S. A.; Stolbov, D. N.; Ivanov, A. S.; Klokov, S. V; Egorova, T. B.; Maslakov, K. I.; Eliseev, O. L.; Maximov, V. V; Savilov, S. V; Lunin, V. V. Effect of Type and Localization of Nitrogen in Graphene Nanoflake Support on Structure and Catalytic Performance of Co-Based Fischer-Tropsch Catalysts. *Catal. Today* **2020**, 357, 193–202. https://doi.org/https://doi.org/10.1016/j.cattod.2019.02.044.

Chapter 5

New Opportunity for Carbon-Supported Ni-based Electrocatalysts: Gas-Phase CO_2 Methanation

Gonçalves, L. P. L.; Serov, A.; McCool, G.; Dicome, M.; J. P. S.; Soares, O. S. G. P.; Bondarchuk, Petrovykh, D. Y.; O.; Lebedev, O. I.; Pereira, M. F. R.; Kolen'ko, Y. V. *New Opportunity for Carbon-Supported Ni-based Electrocatalysts: Gas-phase CO_2 Methanation*. ChemCatChem. **2021**, 13, 4770.

Abstract

The cost-effectiveness and excellent performance of conductive-carbon-supported Ni-based electrocatalysts make them attractive materials for hydrogen oxidation and evolution reactions. However, they were previously unused in gas-phase hydrogenation reactions. In this work, we have expanded the applicability of commercially available advanced Ni/C, NiMo/C and NiRe/C materials from electrocatalysis to heterogeneous catalysis of CO_2 methanation. Our catalytic testing efforts indicate that the monometallic Ni/C material demonstrates the best CO_2 methanation properties, achieving an excellent CO_2 conversion of 83% at 400 °C with nearly complete selectivity to CH_4 of 99.7%, plus exhibiting intact performance during 90 h of time-on-stream testing. Such catalytic properties are among the highest reported to date among carbon-supported Ni-based methanation catalysts. Excellent performance of Ni/C stems from the good dispersion of the Ni nanoparticles over N-containing carbon support material.

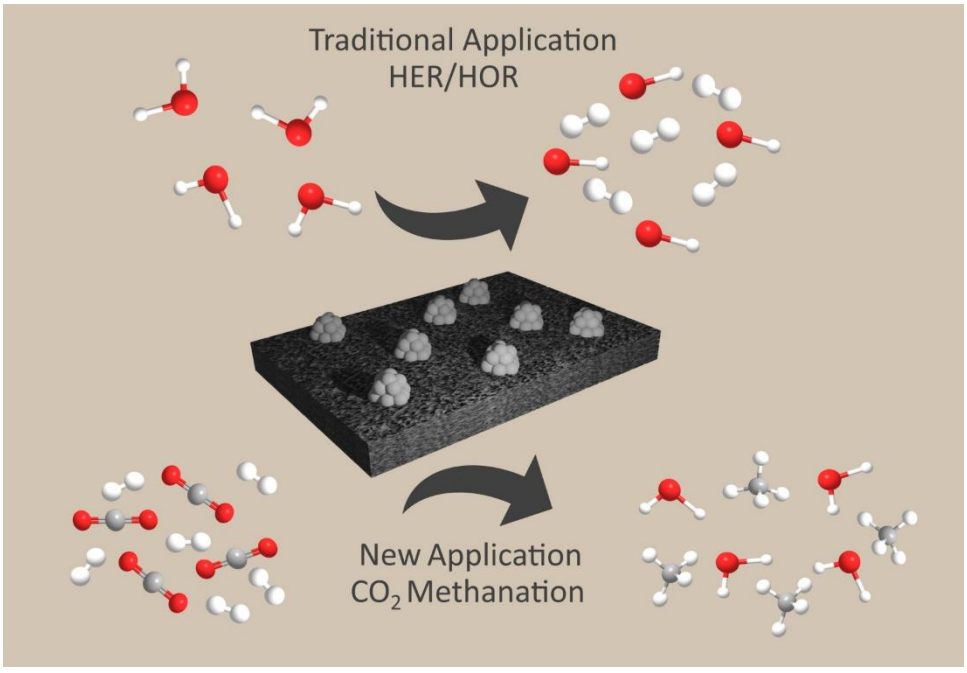

1. Introduction

Both heterogeneous catalysis and electrocatalysis can effectively hydrogenate anthropogenic CO_2 to renewable CH_4 fuel, providing promising pathways to reducing CO_2 emissions [1–5]. The similarity between heterogeneous catalysis and electrocatalysis is notable in that both processes involve sequences of bond breaking and formation [6]. Moreover, both processes often employ generally similar catalytic materials, which are comprised of catalytically active metallic phase on a supporting material, wherein the latter provides the base for a good spatial dispersion and stability of the active metallic nanoparticles (NPs), as well as accelerates the diffusion of reactants. Conversely, from the materials point of view, one of the fundamental differences between the supporting materials for heterogeneous catalysis vs electrocatalysts is that the latter ones should be anchored on conductive supporting materials to ensure good electrical connectivity/conductivity between the catalytically active phase and the respective electrode. Therefore, conductive carbon materials with high surface area are usually used as supports in the various fields of electrocatalysis. Accordingly, extensive research efforts have been undertaken to improve the electrocatalytic performance of the carbon-supported electrocatalysts through optimization of structural, textural, and electronic properties of the carbons, such as their degree of graphitization, surface area, porosity, defects, and surface functional groups. For example, our recent work demonstrated that Ni-based materials supported on different types of commercially available carbons, such as carbon paper, carbon cloth, and VULCAN XCmax 22 conductive carbon, offer access to a diverse range of active and stable water reduction/oxidation electrocatalysts [7–10].

We also recently embarked on the synthesis and investigation of catalysts for non-electrocatalytic gas-phase CO_2 methanation ($CO_2 + 4H_2 \leftrightarrow CH_4 + 2H_2O$, $\Delta H_{298K} = -165$ kJ mol^{-1}). This is a thermodynamically favorable hydrogenation reaction, but it has significant kinetic barriers, hence requiring a catalyst to achieve good CO_2 conversion and high selectivity to the desired CH_4 product.

Ni-based catalysts supported on metal oxides (e.g., Al_2O_3) have been widely studied for this gas-phase reaction and today are adopted by the industry. This adoption is mainly due to the important fact that Ni exhibits the optimal combination of activity, selectivity, and especially, cost, in comparison, for example, to those of the platinum-group metal catalysts (e.g., Ru-based) [11–15].

Notably, besides the industrially important metal oxides, other types of supporting materials, such as zeolites [16], metal-organic frameworks [17] and carbons [2,18–20] have been investigated for CO_2 methanation, albeit to a far lesser extent. The limited historical interest in carbon-based supporting materials for catalysts for CO_2 methanation is primarily due to the high probability of their gasification ($C_{(s)} + H_{2(g)} \rightarrow CH_{x(g)}$) during this high temperature ($T \geq 400$ °C) hydrogenation reaction. As demonstrated in our recent work [2], however, some carbon materials can be appropriately modified and exhibit excellent stability over long time on stream (TOS).

Specifically, we studied the performance of Ni-based catalysts supported on activated carbon with different surface chemistries and achieved the best performance with a catalyst comprised of Ni NPs supported on reduced activated carbon with O-free Lewis basic sites [2]. That study suggested that the methanation reaction is highly dependent on the basicity of the carbon support. The stability of that material over long time on stream (TOS) demonstrated a small loss in conversion of 8% and selectivity of 6% after 48 h. The stability was further improved by promotion with Fe, leading to a smaller loss in conversion of 3% and selectivity of 2%.

Previous studies suggest a few additional factors that improve performance of Ni catalysts on carbon-based supports. Wang et al. [3] evaluated the performance of Ni supported on nitrogen-doped carbon nanotubes (N–CNT) and the catalyst was demonstrated to be active and selective to CH_4. The authors attributed the good performance of the catalyst to the high thermal conductivity of N–CNT supporting material, which guarantees the dispersion of the reaction heat throughout the catalyst bed, while the nitrogen doping favors the CO_2 adsorption and consequent methanation. Additionally, for Ni-

based catalysts supported on reduced graphene oxide (RGO), Hu et al. reported [4] that the RGO-supported Ni catalysts exhibited higher activity than did Ni supported on activated carbon or Al_2O_3, mainly due to larger specific surface area of RGO that favored the formation of small Ni NPs, as well as due to the surface O groups that allowed a stable anchoring of the NPs. The performance of the catalyst was further improved by introduction of Ce into the catalytic system.

Overall, the carbon-based supports thus possess fundamental properties that can be extremely valuable for heterogeneous catalysis: their high surface area and high pore volume, relative to, e.g., metal oxides, their good mechanical stability and thermal conductivity, and their surface chemistry that is more amendable to modification than that of other types of supports [21].

Their promising catalytic properties notwithstanding, designing, producing, and testing carbon-supported Ni-based materials dedicated for applications in gas-phase catalysis of CO_2 methanation is both time- and resource-intensive undertaking. As indicated earlier, a possible "shortcut" in developing such materials is suggested by many similar properties found among the vast family of electrocatalysts that have been investigated and applied in the fields of fuel cells, water electrolysis, and CO_2 electroreduction [22–24]. For industrial applications, these materials already offer strategies for optimization and scale-up of their synthesis, making them attractive candidates for expanding to applications in the gas-phase CO_2 methanation reaction. Accordingly, we tested the hypothesis that commercial carbon-supported Ni electrocatalysts could selectively hydrogenate CO_2 to CH_4 in gas-phase, thus expanding the scope of these advanced materials beyond the electrocatalysis area.

We also investigated exploiting another similarity between the gas-phase catalysis and electrocatalysis, whereby the same transition metals are used for promoting the performance of Ni-based catalysts. Specifically, Ni–Mo and Ni–Re alloys have been widely studied as electrocatalysts, for example, for hydrogen oxidation and evolution reactions [25,26]. The beneficial electronic interaction between the *d*-orbitals of an iron-group metal, Ni, and refractory

metals, Re and Mo, decreases the binding energy of the hydrogen atoms to the electrocatalyst surface in comparison to that for pure Ni, thus boosting the activity of the bimetallic electrocatalysts. In gas-phase methanation, Mo is known to be highly selective to methane, even though it presents poor activity [27] and Re promotion of Ni-based catalysts has been shown to be beneficial for CO_2 methanation [28,29]. Therefore, we selected Mo and Re for testing in bimetallic catalysts, in an attempt to improve the performance of monometallic Ni/C in CO_2 methanation.

To test the suitability and performance of electrocatalysts in gas-phase catalysis, we investigated gas-phase CO_2 methanation over a set of commercially available Ni-based electrocatalysts supported on Engineered Catalyst Support™ conductive carbon material that were obtained from Pajarito Powder. The stability of the materials was also studied by means of long-term time-on-stream testing, including an assessment of the structural and compositional changes in the materials via their detailed characterization before and after long-term CO_2 methanation.

2. Experimental

Commercially available monometallic Ni/C and bimetallic NiMo/C and NiRe/C electrocatalysts supported on ECS-4601 carbon material (Engineered Catalyst Support™, Pajarito Powder, LLC) were synthesized by thermal reduction of metal precursors: nickel nitrate, ammonium molybdate and ammonium perrhenate. Calculated amount of ECS-4601 carbon support was added to the respective metal solution, in the amount to obtain 50% of Ni loading in the final Ni/C catalyst, 50% of NiMo with 85:15 at% ratio in the NiMo/C catalyst, as well as 50% of NiRe with 87:13 at% ratio in the NiRe/C catalyst. After 1 h of stirring, pH of solution was adjusted to 13 using 5 M NaOH, followed by the precipitation of metal compounds. The precipitate was washed with DI water until pH ≈ 6.5. Washed precipitate was then dried at 85 °C for 12 h. The dry mixture was ground with mortar and pestle, and the resultant fine powder was reduced at 450 °C for 1 h under 100 cm^3 min^{-1} flow of 7%H_2/N_2 gas mixture.

Finally, the catalyst was passivated in a flow of 0.1%O_2/He at room temperature for 8 h.

The catalysts were characterized by N_2 physisorption at −196 °C, H_2 pulse chemisorption, powder X-ray diffraction (XRD), X-ray photoelectron spectroscopy (XPS), transmission electron microscopy (TEM), high-angle annular dark-field scanning TEM (HAADF–STEM), and energy-dispersive X-ray spectroscopy in STEM mode (STEM−EDX). Their catalytic properties in gas-phase CO_2 methanation were evaluated in a Microactivity XS15 system (PID Eng & Tech), using a fixed bed quartz reactor. After an *in situ* reduction pre-treatment on the catalyst, the reactor was fed with the stoichiometric gas mixture of 10% CO_2 and 40% H_2, balanced by 50% He, with a total flowrate of 100 $cm^3\ min^{-1}$ (*WHSV* = 60 000 $cm^3\ g^{-1}\ h^{-1}$) at the pressure of 1 bar. A temperature ramping from 200 °C to 500 °C was performed under reaction conditions to evaluate the performance of each sample as a function of the temperature and long-term time-on-stream (TOS) testing was performed under the same conditions referred before; however, under isothermal conditions at the established temperature of optimal catalytic performance of the respective catalyst. The reaction products were analysed online by gas chromatography. More details about materials and methods are given in Chapter 2.

3. Results

3.1 CO_2 methanation

As mentioned in the introduction, Ni-based catalysts (e.g., Ni/Al_2O_3) have attracted research interest because of their good performance in CO_2 methanation while being a cost-effective option compared to the expensive platinum group metal catalysts (e.g., Ru). Therefore, to provide new opportunities for the commercially available Ni/C, NiMo/C and NiRe/C hydrogen evolution/oxidation electrocatalysts, we investigated their catalytic

properties in gas-phase CO_2 methanation by evaluating their activity, selectivity, and stability.

A typical parameter used for the performance evaluation of CO_2 methanation catalysts is T_{50}, the temperature at which the conversion, X_{CO2}, over the catalyst reaches X_{CO2} = 50%. Generally, the catalyst is more competitive if it shows high activity at lower temperatures, thus reducing energy demand for CO_2 hydrogenation to CH_4. Figure 5.1a,b show the CO_2 conversion, X_{CO2}, and selectivity to methane, S_{CH4}, respectively, of the Ni/C, NiMo/C and NiRe/C catalysts in the studied temperature range (200–500 °C). We observed that all three catalysts are active and selective to CH_4 at temperatures above 250 °C. Compared to Ni/C and NiRe/C catalysts, the NiMo/C achieves higher conversion at temperatures below 325 °C, which is its T_{50} (Table 5.1). As temperature increases above 325 °C, the activity of the bimetallic NiMo/C catalyst drops below that of the monometallic Ni/C counterpart. Remarkably, Ni/C reaches a X_{CO2} = 83% with S_{CH4} = 99.7% at 400 °C, i.e., values close to the thermodynamic equilibrium of the reaction, particularly for X_{CO2}, for which it outperforms both bimetallic catalysts (Figure 5.1a,b). This monometallic Ni/C catalyst has a T_{50} of 330 °C, which is slightly higher than that of bimetallic NiMo/C (325 °C) (Table 5.1).

Table 5.1. Textural properties, H_2 uptake, mean nanoparticle diameter, temperature at which X_{CO2} = 50% (T_{50}), and maximum X_{CO2} for Ni/C, NiMo/C and NiRe/C catalysts.

	S_{BET} ($m^2\ g^{-1}$) [a]	d_{pores} (nm) [a]	V_p ($cm^3\ g^{-1}$) [a]	H_2 uptake (mol g^{-1}) [b]	d_{NP} (nm) [c]	d_{NP} after TOS (nm) [c]	T_{50} (°C)	X_{CO2} (Max) (%)
Ni/C	334	5.5	0.544	37.7	10 ± 4	14 ± 12	330	83
NiMo/C	369	5.5	0.648	12.7	14 ± 5	15 ± 10	325	70
NiRe/C	371	6.5	0.634	29.7	14 ± 10	16 ± 10	360	74

[a] Estimated by N_2 physisorption. [b] Estimated by H_2 pulse chemisorption, [c] Estimated by the analysis of TEM images

Comparing the bimetallic NiMo/C and NiRe/C catalysts, NiMo/C exhibits higher X_{CO2} and S_{CH4} at lower temperatures, reaching X_{CO2} = 70% with S_{CH4} = 98.4% at 400 °C (Figure 5.1a,b). As temperature increases above 400 °C, NiRe/C exhibits higher X_{CO2} reaching X_{CO2} = 74% with S_{CH4} = 97.7% at

460 °C, values that are close to the thermodynamic equilibrium of the reaction (Figure 5.1a,b). Furthermore, the bimetallic NiRe/C catalyst is characterized by the highest T_{50} of 360 °C among the three catalysts (Table 5.1).

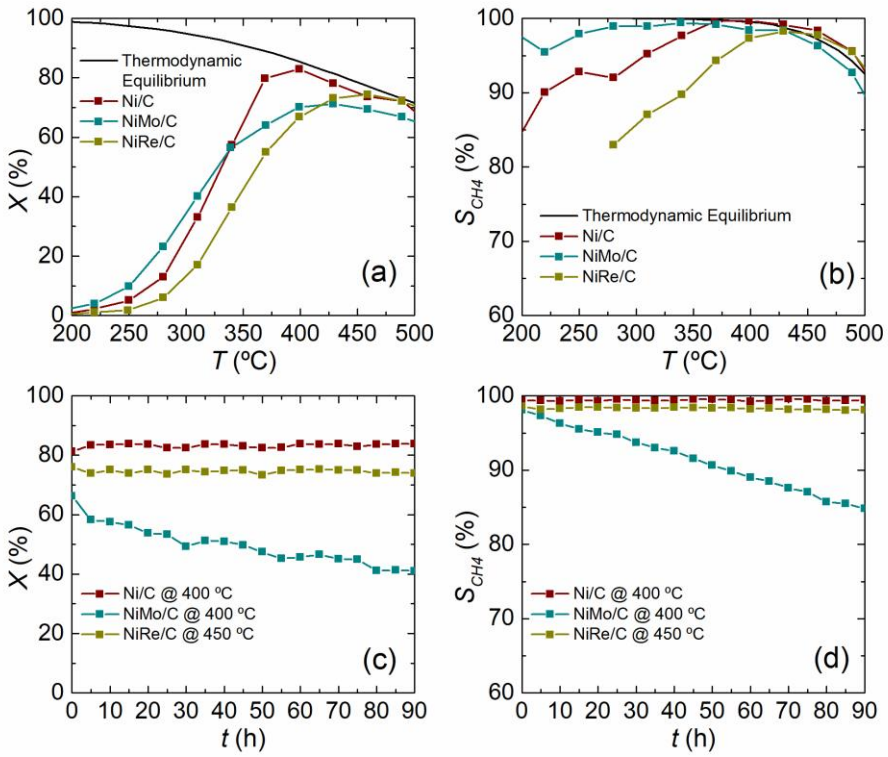

Figure 5.1. CO_2 conversion X_{CO2} (a) and CH_4 selectivity S_{CH4} (b) in 200–500 °C temperature range for Ni/C, NiMo/C and NiRe/C catalysts, together with the evolution of X_{CO2} (c) and S_{CH4} (d) during long-term time-on-stream (TOS) testing. Reaction conditions: P = 1 bar; $WHSV$ = 60 000 $cm^3\ g^{-1}\ h^{-1}$; CO_2:H_2 = 1:4.

The observed good performance of commercial Ni/C, NiMo/C and NiRe/C electrocatalysts in gas-phase CO_2 methanation is encouraging. To assess whether methanation reaction can be a new application for these materials, we further investigated their stability in this gas-phase hydrogenation reaction. In particular, we performed long-term time-on-stream (TOS) studies at the temperatures where the catalysts exhibit the highest X_{CO2}, namely, T = 400 °C for Ni/C and NiMo/C and T = 450 °C for NiRe/C. Figure 5.1c,d show the time-dependent X_{CO2} and S_{CH4} data, respectively, collected for all three catalysts. The Ni/C and NiRe/C demonstrate good stability over 90 h of CO_2 methanation, maintaining well both X_{CO2} and S_{CH4} during TOS. The notable exception was

NiMo/C, which exhibits a gradual degradation of the catalytic properties, with a decrease in X_{CO2} of 25% and in S_{CH4} of 13% over 90 h of TOS testing.

3.2 Characterization of the catalysts before methanation

The catalytic properties discussed above provide strong support for our hypothesis that advanced carbon-supported Ni-based electrocatalysts can be successfully employed as catalysts for gas-phase CO_2 methanation. To correlate the observed catalytic trends with the properties of the materials, we performed a comprehensive characterization of the as-received Ni/C, NiMo/C and NiRe/C catalysts.

Figure 5S.1 depicts N_2 physisorption isotherms for the catalysts, while Figure 5S.2 shows their resultant pore size distributions. All the samples exhibit similar textural properties, presenting Type II isotherms with comparable pore size distributions. The specific surface area, S_{BET}, of the mesoporous catalysts was estimated to be 350 ± 20 $m^2\ g^{-1}$, while the average mesopore size, d_{pore}, was found to be 5.5 nm in the case of Ni/C and NiMo/C and 6.5 nm in the case of NiRe/C (Table 5.1). For further investigation, we performed H_2 pulse chemisorption measurements over the catalysts. The H_2 uptake of the materials, and consequently, their catalytically active surface area, correlates well with their catalytic performance in CO_2 methanation. Specifically, H_2 uptake data are consistent with the CO_2 methanation performance of the catalysts (Table 5.1, Figure 5.1), where they also show the same trend: Ni/C > NiRe/C > NiMo/C. Importantly, monometallic Ni/C catalyst shows markedly higher H_2 uptake per gram of material than the bimetallic counterparts, consistent with its best performance in CO_2 hydrogenation (Figure 5.1).

The powder X-ray diffraction (XRD) patterns for all the catalysts are shown in Figure 5.2. The graphitic carbon peak from the carbon supporting material is present at 28° in all the samples. The other Bragg peaks are broadened, which is typical for nanocrystalline samples. The pattern of monometallic Ni/C

catalyst is indexed to metallic Ni (ICDD #04-016-4761) with an admixture of NiO (ICDD #04-004-8992) secondary phase.

In the case of NiMo/C and NiRe/C, there are peaks corresponding to Ni and NiO, however, the presence of Mo- and Re-containing phases is not conclusive from the XRD data, most likely due to overlapping of some characteristic Bragg peaks.

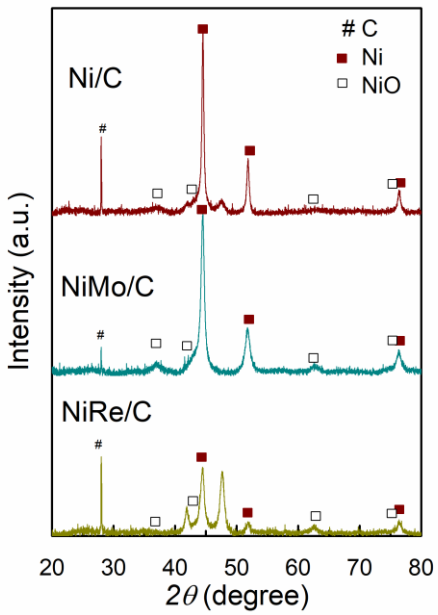

Figure 5.2. XRD patterns of the Ni/C, NiMo/C and NiRe/C catalysts, showing the presence of the peaks corresponding to Carbon, Ni and NiO in all catalysts.

XPS analysis demonstrated that for all the as-received catalysts, two different phases are observed from the deconvolution of the XPS data of Ni $2p_{3/2}$ (Figure 5.3,Table 5.2). The lower energy component (852.7 eV) is assigned to Ni^0 in metallic Ni species, while the components at 853.9 ± 0.2 eV and 855.8 ± 0.2 eV are consistent with Ni^{2+} in nickel oxide phase, and the ones at 861.1 ± 0.3 eV and 863.6 ± 0.4 eV are satellite peaks from Ni^{2+} [30]. The presence of multiple components in the 851–858 eV BE range is typical for nanoscale oxidation layers on Ni and Ni compounds [9,30,31] with the combination of three main components at ca. 852.7, 853.9, and 855.8 eV in Figure 5.3a-c, being most consistent with a thin, predominantly Ni^{2+}, nickel oxide layer on metallic Ni. Furthermore, analyzing the O 1s spectra of the samples (Figure 5S.3), one can observe that there are two peaks at 529.9 ± 0.3 eV and 531.2 ± 0.2 eV that

correspond to oxygen in metal oxides, presumably in nickel oxide. From Table 5S.1, it is possible to observe that the atomic % of Ni^{2+} is similar to that of the O from metal oxide components of O 1s (the slightly higher value of O at% is due to the non-uniform morphology and a contribution of O in the organic phase to the peak at 531.2 ± 0.2 eV) [32].

For NiMo/C, the Mo 3d spectra (Figure 5.3d) show two distinct components: Mo(IV) oxide (Mo^{4+}) composed by a doublet at 229.3 ± 0.4 eV and 232.4 ± 0.4 eV and Mo(VI) oxide (Mo^{6+}) at 232.4 ± 0.0 eV and 235.5 ± 0.0 eV [33].

For NiRe/C, the Re 4f spectra (Figure 5.3e) show Re^{4+} with a doublet at 42.3 eV and 44.7 eV and Re^{7+} at 45.5 eV and 47.9 eV [34,35].

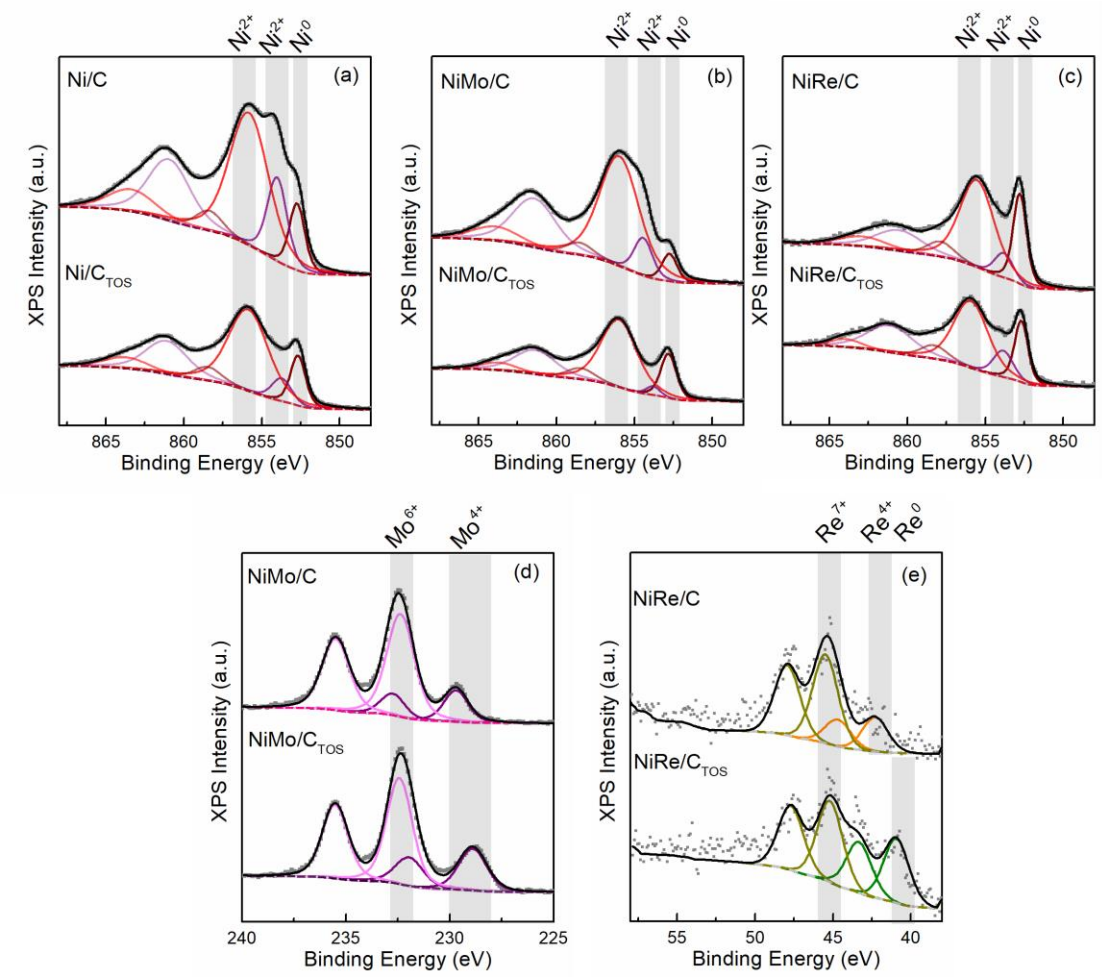

Figure 5.3. High-resolution XPS data for the Ni $2p_{3/2}$ region collected from as-received and TOS-tested Ni/C (a), NiMo/C (b), and NiRe/C (c) catalysts, together with Mo 3d region collected from NiMo/C (d) and Re 4f region collected from NiRe/C (d). Symbols: raw data; black lines: overall fits; coloured lines: fits of individual components; dashed lines: background.

Table 5.2. XPS relative atomic percentage (at%) of Ni^0 and Ni^{2+} from Ni $2p_{3/2}$ spectra, Mo^0, Mo^{4+} and Mo^{6+} from Mo 3d spectra and Re^0, Re^{4+} and Re^{7+} from Re 4f spectra in Ni/C, NiMo/C and NiRe/C catalysts and after their TOS testing.

	Ni^0 (relative at%)	Ni^{2+} (relative at%)	Mo^{4+} (relative at%)	Mo^{6+} (relative at%)	Re^0 (relative at%)	Re^{4+} (relative at%)	Re^{7+} (relative at%)
Ni/C	8.67	87.00	--	--	--	--	--
Ni/C_{TOS}	11.49	83.22	--	--	--	--	--
NiMo/C	4.86	91.35	21.43	78.57	--	--	--
$NiMo/C_{TOS}$	14.57	79.35	29.90	69.07	--	--	--
NiRe/C	18.78	75.13	--	--	0	25.00	75.00
$NiRe/C_{TOS}$	15.41	78.08	--	--	50.00	0	50.00

We further conducted microstructural investigation of the as-received catalysts by means of transmission electron microscopy (TEM). The average nanoparticle diameter (d_{NP}) was determined by the analysis of several TEM images (Figure 5S.6, Figure 5S.7) and the estimated values are presented in Table 5.1, while the corresponding particle size distributions are shown in Figure 5S.8. The metallic NPs appear to be well dispersed on largely amorphous carbon supporting materials. The monometallic Ni/C catalyst exhibits the smallest $d_{NP} \approx 10$ nm, with a narrow size distribution; both bimetallic NiMo/C and NiRe/C catalysts have larger $d_{NP} \approx 14$ nm. Figure 5.4 shows high-resolution TEM (HRTEM) images of representative nanoparticles in each catalyst. In the bimetallic NiMo/C and NiRe/C, one can clearly observe a layer around the nanoparticles (Figure 5.4c–f, Figure 5S.7b,c). In NiRe/C, this shell resembles graphitic carbon [36,37], while in NiMo/C the shell is composed of epitaxially grown MoO_2 (Figure 5.4d) and ultrasmall Mo NPs at the surface of Ni NPs (Figure 5.4c). In contrast, no shell was observed in the monometallic Ni/C catalyst (Figure 5.4a,b, Figure 5S.7a).

To elucidate the chemical composition, we carried out high-angle annular dark-field imaging in scanning TEM mode (HAADF–STEM) showing *Z*-contrast of the catalysts, together with the corresponding energy-dispersive X-ray spectroscopy maps in STEM mode (STEM–EDX), which highlight the distribution of the key constituent elements.

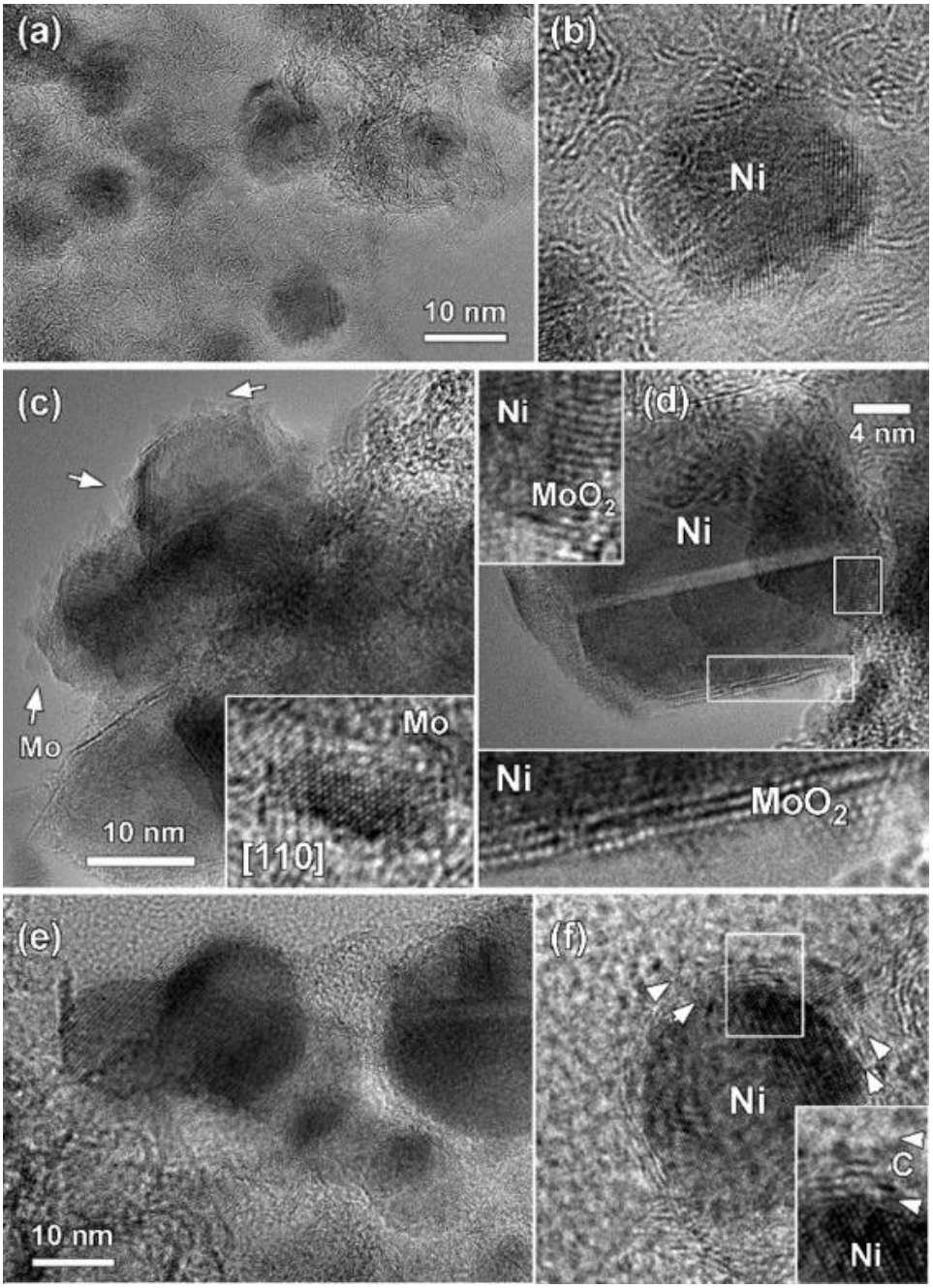

Figure 5.4. HRTEM images of the NPs in Ni/C (a, b), NiMo/C (c, d) and NiRe/C (e, f), evidencing no shell being present over Ni NPs (b) in Ni/C, an epitaxially grown MoO_2 shell with few atomic layers (d), as well as ultrasmall Mo NPs (c) over Ni NPs in NiMo/C; and a carbon shell around Ni NPs (f) in NiRe/C.

The representative Figure 5.5, Figure 5S.9a, Figure 5S.10a, and Figure 5S.11a show HAADF–STEM and STEM–EDX data collected from Ni/C, NiMo/C and NiRe/C. In the case of monometallic Ni/C, it is clear that the NPs are composed of Ni well-supported on carbon (Figure 5.5a, Figure 5S.9a). The EDX maps of the bimetallic NiMo/C catalysts demonstrate a high concentration of both metals in the areas where NPs are present, and that the metals are

homogeneously distributed across the catalysts (Figure 5.5b, Figure 5S.10a), while in the case of NiRe/C, the EDX signal of Re is quite weak (Figure 5.5c, Figure 5S.11a), indicating that a low amount of this element is present.

3.3 Characterization of the catalysts after TOS testing

To further understand the impact of the methanation reaction on the evolution of the structural properties of the catalysts, as well as to find out the reasons for different stability of the catalysts, we characterized all three materials after prolonged TOS testing (Figure 5.1c,d) by means of XRD, XPS, and TEM.

In the XRD patterns of the TOS-tested catalysts (Figure 5S.5), the Bragg peaks corresponding to the NiO admixture are absent, indicating that much of the NiO was reduced to metallic Ni under reductive reaction conditions of the methanation (H_2 atmosphere at high temperature).

In the Ni $2p_{3/2}$ spectral region of the TOS-tested catalysts (Figure 5.3), the binding energy of each component remains similar for all the materials; however, there was a change in the relative atomic percentage of each component (Table 5.2), consistent with reduction, which is further supported by the respective O 1s spectra (Figure 5S.3), wherein the nickel oxide O 1s components contribution is smaller than that of the organic components. In the case of NiRe/C, however, there is no increase in relative intensity of Ni^0, with concomitant qualitative and quantitative indications in the Re 4f region that Re oxides were reduced, suggesting an interplay of reduction chemistry between Ni and Re. In contrast, in NiMo/C, the presence of Mo does not dramatically affect the reduction of Ni, while Mo oxidation states undergo only minimal changes. The latter observation, in particular, indicates minimal (if any) formation of intermediate oxidation states of Mo, which can be readily observed by XPS in nanostructured Mo-based catalysts [38]. In C 1s region, presented in Figure 5S.4, we do not observe any significant modification after TOS testing [39,40].

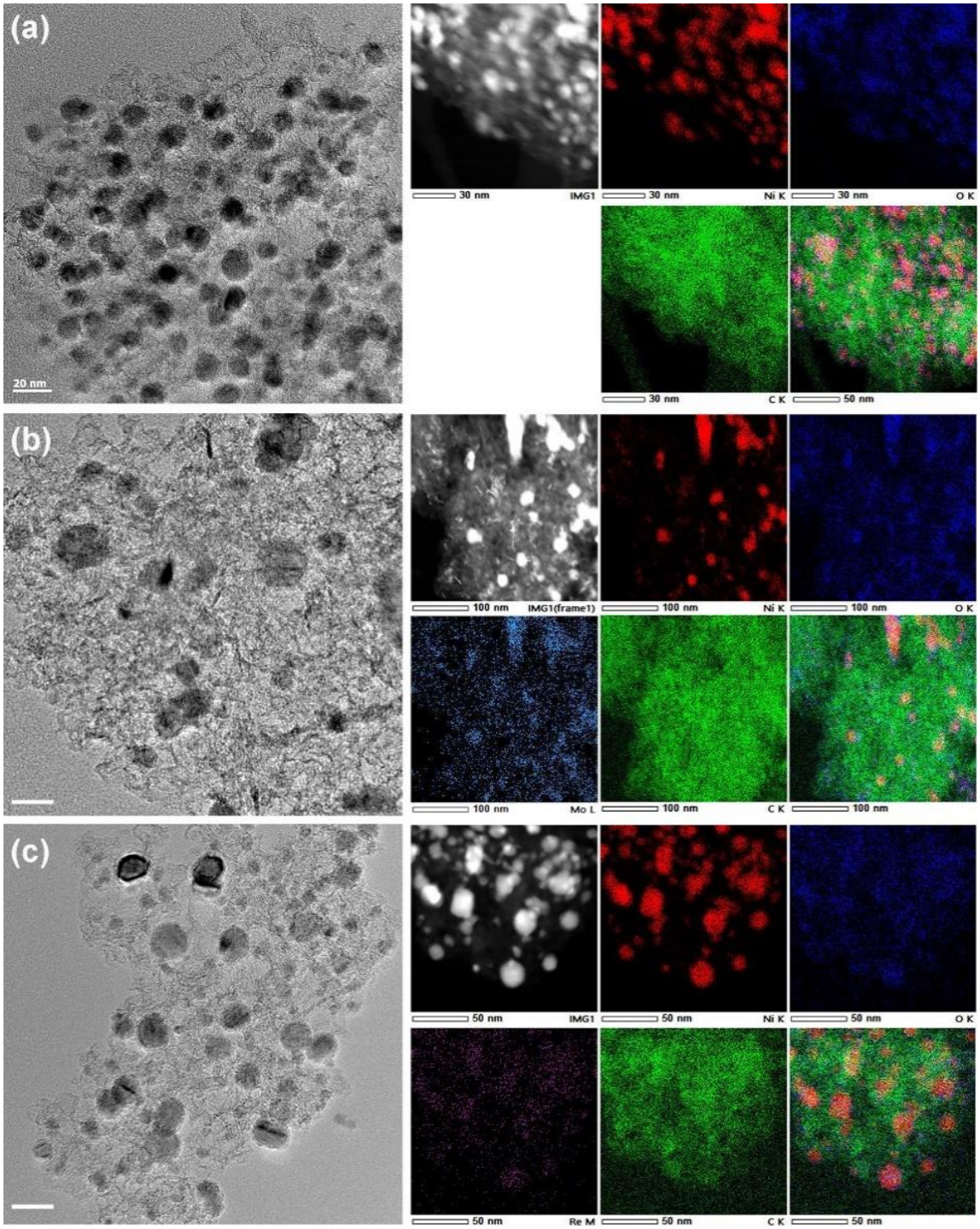

Figure 5.5. Low magnification bright field TEM images, low magnification HAADF–STEM images and simultaneously acquired STEM–EDX elemental mappings for Ni/C (a), NiMo/C (b), and NiRe/C (c) catalysts.

With the aim of exploring the microstructural changes in the catalysts after TOS-testing, we analyzed the spent catalysts by electron microscopy. Because of the sintering at high temperatures (400–450 °C) during methanation reaction, we observe a slight increase in the average particle size of the

catalysts (Figure 5S.6a–c, Figure 5S.7a–c compared to Figure 5S.6d–f, Figure 5S.7d–f), which were estimated to be 14 ± 12 nm, 15 ± 10 nm and 16 ± 10 nm for Ni/C_{TOS}, NiMo/C_{TOS}, and NiRe/C_{TOS}, respectively. Notably, the particle size distributions become significantly broader compared to those for the as-received catalysts (Figure 5S.8). Furthermore, EDX mapping demonstrates that there was some segregation of Mo in NiMo/C_{TOS} (Figure 5S.10c) and Re in NiRe/C_{TOS} (Figure 5S.11c) during TOS testing.

4. Discussion

We show through experiments and detailed characterization that commercially available advanced hydrogen oxidation/evolution electrocatalysts can have another practical application as catalysts for gas-phase CO_2 methanation. Monometallic Ni/C catalyst as well as two bimetallic NiRe/C and NiMo/C catalysts have been investigated, the latter testing for synergistic promotion of CO_2 methanation [2].

When interpreting the results of our structural and chemical characterization of the catalysts, it is important to keep in mind the implications of the experimental protocols and sample handling. Specifically, both as-received and TOS-tested catalysts help to elucidate the properties of the same during the catalytic testing, but both show some effects of oxidation that is not present during the catalytic testing. As-received catalysts have been passivated under O_2/He atmosphere, the treatment that stabilizes them for storage and transport, but is likely to oxidize the surfaces of transition-metal nanoparticles. Immediately before the catalytic testing, the as-received catalysts undergo an *in situ* reduction pre-treatment in the reactor. The resulting primarily metallic nanoparticles are presumptively considered when interpreting their catalytic activity. Finally, the TOS-tested catalysts are characterized after exposure to ambient air, which is likely to oxidize the surfaces of transition-metal nanoparticles. Accordingly, the structural and chemical *transformations* (particularly those away from metal oxides) between the as-received and TOS-tested catalysts are considered when elucidating the effects of the catalytic

testing. In contrast, the quantification of the surface oxide phases is primarily performed to check for consistency with the presumptive effects of, respectively, the passivation treatment and exposure to air.

Our structural characterization results show that the as-received catalysts consist mainly of metallic NPs with oxidized surfaces, which is expected due to the synthetic surface passivation by oxygen during the final step of the materials preparation. These surface oxide phases were found to be effectively reduced to the respective metals during CO_2 methanation, as highlighted by our XPS and HAADF–STEM characterization results for the TOS-tested catalysts. A rigorous quantification of the thickness of an overlayer from XPS data requires a sufficiently flat surface with a well-defined layer structure [41]; overlayers of a more complex composition also can be quantified, albeit with increased uncertainty, based on systematic measurements [31,42–44]. For metal nanoparticles in the size range summarized in Table 5.1, the thickness of an oxide layer can be estimated from XPS data only semi-quantitatively, due to the variability of the particle shapes and sizes as well as unknown uniformity of the oxide layer. Based on an interpolation from the data for crystal surfaces with a similar surface composition [31], the peak intensity ratios in Figure 5.3a suggest an oxide layer thickness of ca. 3–4 nm for Ni particles in Ni/C. The Ni/C spectrum in Figure 5.3a is also in qualitative agreement with the reference Ni 2p spectra for a ca. 3.3 nm NiO layer on a polished Ni surface [30]. The limited extent of oxidation of Ni nanoparticles in Ni/C is consistent, for example, with a similar presence of Ni metal signal in nanoparticles measured by XPS after multiple days of storage and transport in ambient air [45]; in that case, the presence of oxygen co-located with Ni was also clear in HAADF–STEM images, but no strong NiO features were present in XRD data.

The formation of an alloy between Ni and Mo in NiMo/C and between Ni and Re in NiRe/C was ruled out since no peaks for these alloys were found in XRD patterns of the samples, nor was alloy formation detected by TEM analysis. In fact, in NiMo/C, TEM revealed the presence of Ni NPs covered by ultrasmall Mo NPs and, in some cases, an epitaxially grown MoO_2 shell. Our TEM results

also show that the metallic NPs in all three catalysts exhibit small particle sizes with similar size distributions, while being uniformly dispersed on amorphous carbon supporting material.

The three catalysts demonstrated a clear performance trend: Ni/C > NiRe/C > NiMo/C, wherein best-performing monometallic Ni/C achieved a high maximum X_{CO2} = 83% with S_{CH4} = 99.7% at 400 °C, having T_{50} = 330 °C. This performance compares favorably with our recent work [2], where a catalyst composed of 15% Ni supported on reduced activated carbon achieved X_{CO2} = 76% with S_{CH4} = 97% at 450 °C, having T_{50} ≈ 385 °C. The observed catalytic properties of Ni/C are also comparable to reported for Ni supported on N-doped CNT catalyst, which exhibited high activity and selectivity, namely X_{CO2} = 80% with S_{CH4} = 99% at 360 °C [3].

The high performance of Ni/C compares favorably to that reported for the catalyst most used in the industry (Ni/Al_2O_3), taking into account both the Ni loading and reaction temperature. For example, in a study of the effect of Ni loading in Ni/γ-Al_2O_3 catalysts, Zhang et al.[12] obtained a maximum X_{CO2} ≈ 65% with S_{CH4} ≈ 100% at 350 °C with 50% Ni/γ-Al_2O_3 (i.e., Ni loading similar to that of Ni/C); they used conditions similar to those used in our study but at lower *WHSV*. When Liu et al. [46] tested a 20% Ni/Al_2O_3 catalyst, at conditions similar to those used in our study (except higher *WHSV* = 90 000 $cm^3\ g^{-1}\ h^{-1}$), they achieved a maximum X_{CO2} = 73% with S_{CH4} = 97% at 420 °C, i.e., a lower conversion, when compared to the results for our Ni/C; addition of vanadium oxide enhanced the performance of the catalyst. At the same 400 °C temperature that Ni/C performed best in our study (although at slightly higher *WHSV* = 120 000 $cm^3\ g^{-1}\ h^{-1}$), Ma et al. [47] tested a 20% Ni/Al_2O_3 catalyst and obtained a maximum X_{CO2} ≈ 70% with S_{CH4} ≈ 95%; the performance was slightly improved when CeO_2 was used as support. Zhao et al. [48] tested a 15% Ni/Al_2O_3 catalyst (at lower *WHSV* = 48 000 $cm^3\ g^{-1}\ h^{-1}$) and to reach a maximum X_{CO2} ≈ 80% with S_{CH4} > 95%, i.e., to reach performance similar to that of our Ni/C catalyst, they had to use a temperature of 450 °C; addition of Mn enhanced the performance of the catalyst.

On other Ni-based catalysts supported on commonly used metal oxides, for e.g., a Ni/CeO_2 catalyst [49] tested under conditions similar to those in our study reached X_{CO2} = 81% with S_{CH4} = 100% at 350 °C, i.e., a similar conversion but at a lower temperature than our Ni/C catalyst. Furthermore, 5% Ni/ZrO_2 catalyst [50] reached X_{CO2} = 79.1% with S_{CH4} = 96.7% at 350 °C, a slightly lower conversion but also at a lower temperature.

We note that the Engineered Catalyst Support™ conductive carbon employed in the current study has 2.2% of nitrogen from the surface functional groups (Table 5S.1), which is essential for achieving the good performance of the catalyst, since N groups improve the dispersion of Ni NPs over the support by providing binding sites that facilitate the Ni stabilization, as well as improve the CO_2 adsorption capacity of the sample [2–4,39].

Importantly, the monometallic Ni/C material demonstrated excellent stability over 90 h of TOS testing at 400 °C with no noticeable losses in X_{CO2} or S_{CH4}, a promising result because this temperature is in the range applied in existing Power-to-gas technologies [51]. In terms of stability, the main effect of TOS testing for 90 h at 400 °C was a slight increase in average NP diameter (Figure 5S.8), indicating moderate sintering of Ni NPs under reaction conditions.

Unfortunately, regarding the bimetallic catalysts, we found that the addition of Mo and Re into Ni catalyst is not beneficial for CO_2 methanation, despite promising indications from previous literature reports that motivated our selection of these two metals [27–29].

Although our NiMo/C catalyst demonstrates higher X_{CO2} values at low temperatures, the maximum X_{CO2} of bimetallic NiMo/C was lower than that of the monometallic Ni/C counterpart. For Mo, a major difference between our NiMo/C material and those described in the literature was the local chemical environment, with apparent segregation of Mo and no evidence of alloying in NiMo/C, as discussed earlier. In a contrasting literature example, Huo et al. [52] prepared β-Mo_2C and Ni/β-Mo_2C catalysts and investigated them in methanation of carbon monoxide. The β-Mo_2C catalyst exhibited high CO

conversion but low CH_4 selectivity while Ni/β-Mo_2C presented excellent CO conversion, CH_4 selectivity and stability, which was attributed to the formation of Ni_3Mo_3N in Ni–Mo carbide. In another Mo carbide example, Wang et al. [53] studied Mo_2C/ZrO_2 for sulfur-resistant CO methanation, presenting good conversion, selectivity and stability, with good sulfur-resistance. No evidence of similar Mo chemistry was detected in NiMo/C by XPS, which is very sensitive to the chemical environment of Mo [38]. Furthermore, NiMo/C showed poor stability, losing 25% of X_{CO2} and 13% of S_{CH4} over 90 h. One could attribute this poor stability trend to the segregation of Mo phase in some areas of the catalyst under reaction conditions (Figure 5S.10c).

NiRe/C exhibited lower X_{CO2} than did Ni/C over the full range of tested temperatures. A theoretical study of the effect of Re on the C–O bond scission and on the selectivity of CO_2 methanation on a Ni-based catalyst by Yuan et al. [28] concluded that the strong oxygen affinity of Re was the main reason for the enhanced CH_4 selectivity. Accordingly, the lack of enhancement in NiRe/C is difficult to rationalize, as XPS clearly indicates that not only Re chemistry was transformed during the reaction, but its presence also affected the transformation of Ni (Table 5.2, Figure 5.3c,e). In contrast to NiMo/C, the NiRe/C catalyst was stable over 90 h of TOS; albeit sintering of Re into large particles was also observed in some parts of the catalyst (Figure 5S.11c). The stability of NiRe/C is aligned with findings of Dong et al. [29] on using Re as promoter for a Ni-based catalyst supported on coal combustion fly ash, which concluded that Re promotion leads to the enhancement of the anti-sintering and anti-coking properties of the catalyst.

To summarize, while we have yet to rationalize the observed lower maximum conversion of the bimetallic catalysts, we consider the following two factors as likely to be important: (*i*) there is lack of the formation of the respective alloys in bimetallic catalysts that hinders synergetic effects; and (*ii*) both bimetallic catalysts exhibit a shell around the Ni NPs (Figure 5.4), which covers the active Ni phase of the catalyst and thus prevents the effective H_2 chemisorption during CO_2 methanation reaction, as evidenced by the H_2 uptake results (Table

5.1). The decreasing of the optimal operation temperature of the CO_2 methanation over cost-effective carbon-supported Ni catalysts to values below 400 °C is a challenge of interest to our work that we will address in the future via synergetic bimetallic catalyst approach while using metals other than Mo and Re.

5. Conclusions

In recent years, the growing availability of renewable energy at competitive prices has boosted the field of electrocatalysis, aiming at the effective use of this energy to combat CO_2 emission via establishing new effective electrochemical routes to the production of chemicals. Accordingly, the library of well designed, engineered, and produced electrocatalysts keeps constantly expanding. Our work clarifies that some of these advanced materials could be strategically valuable for other areas of the catalysis, as demonstrated herein by the example of classical Sabatier CO_2 methanation reaction. More specifically, we reveal that commercially available carbon-supported Ni-based hydrogen oxidation/evolution electrocatalysts can be successfully employed in gas-phase CO_2 hydrogenation to CH_4. Monometallic Ni/C catalyst achieves excellent performance in this reaction at 400 °C, showing X_{CO2} = 83% with S_{CH4} = 99.7%. Furthermore, the catalyst exhibits outstanding stability over 90 h TOS testing, with no sign of deactivation. This remarkable performance of Ni/C is essentially governed by good dispersion of Ni NPs over advanced carbon supporting material, high H_2 uptake of Ni NPs, as well as the presence of N-containing groups in the supporting carbon that stabilizes Ni NPs and improves the CO_2 adsorption capacity. The introduction of Mo and Re into Ni/C does not improve the catalytic properties of the respective bimetallic NiMo/C and NiRe/C materials, leading to a decrease in overall activity and selectivity. Moreover, NiMo/C exhibits poor stability over 90 h of TOS testing, while the addition of Re has little impact on the stability behavior. Nevertheless, this work offers a new opportunity to amplify the scope of applications of these novel electrocatalytic materials through heterogeneous gas-phase catalysis.

6. Supplementary Information

6.1 Characterization Results

6.1.1 N_2 Physisorption at −196 °C

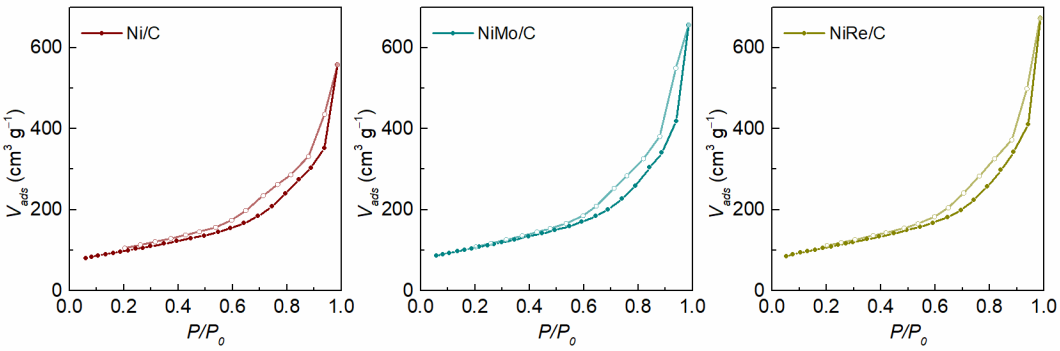

Figure 5S.1. Comparison of N_2 adsorption–desorption isotherms measured at −196 °C for the as-received Ni/C, NiMo/C and NiRe/C catalysts.

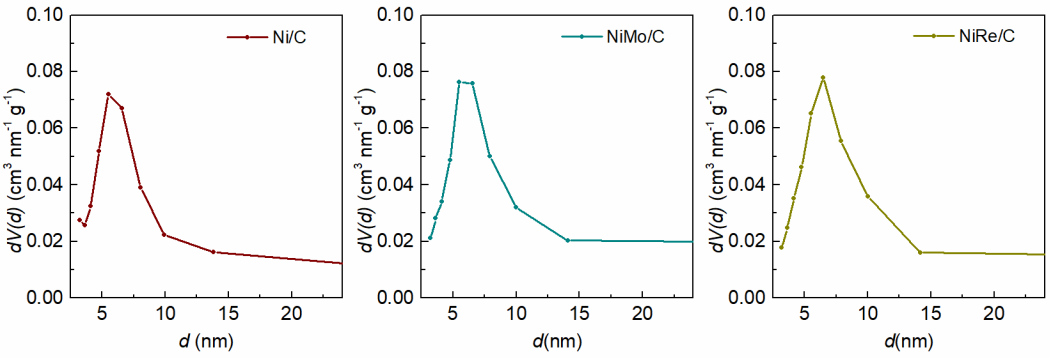

Figure 5S.2. Comparison of the pore size distribution for the as-received Ni/C, NiMo/C and NiRe/C catalysts, determined by BJH method, showing a similar pore size distribution for all catalysts.

Table 5S.1. Elemental composition of ECS (Engineered Catalyst Support™) carbon supporting material from Pajarito Powder.

	N %	C %	O %
ECS−4601	2.2	88.9	9.8

6.1.2 X-ray Photoelectron Spectroscopy

Five peaks were identified in the C 1s region of the as-received catalysts (Figure 5S.3, left panel), as well as in the catalysts after TOS testing (Figure 5S.3, right panel), which correspond to the aromatic and aliphatic carbon ($C_{ar,al}$) at 284.6 eV, the hydroxyl groups and (COH) at 285.9 ± 0.1 eV, carbonyl groups

(C=O) at 287.4 ± 0.1 eV, carboxylic groups (COOH) at 289.3 ± 0.1 eV, and the plasmon loss ($C_{shake-up}$) at 291.6 eV [39,40].

The N content was found to be very low in the samples, hindering the correct fitting of the respective spectra.

Table 5S.2. XPS atomic percentage (at%) of Ni^0, Ni^{2+} and O from metal oxide in Ni/C, NiMo/C and NiRe/C catalysts and the same catalyst after TOS testing.

	Ni^0 at%	Ni^{2+} at%	O from metal oxide
Ni/C	0.9	8.6	10.6
Ni/C_{TOS}	0.5	3.6	5.6
NiMo/C	0.3	6.0	9.1
$NiMo/C_{TOS}$	0.7	3.7	7.1
NiRe/C	0.7	2.8	3.3
$NiRe/C_{TOS}$	0.5	2.3	3.5

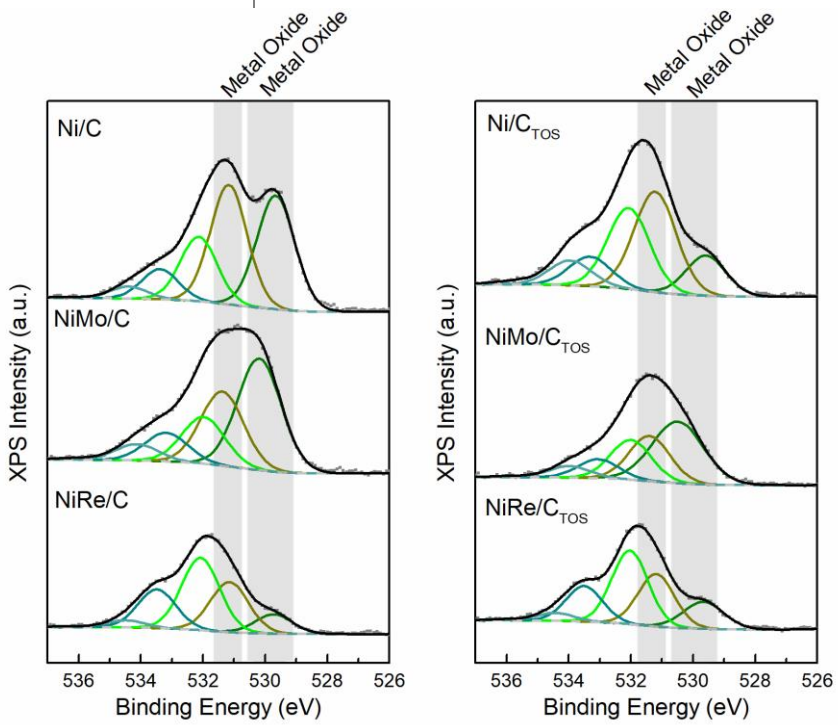

Figure 5S.3. High-resolution XPS data for O 1s region for Ni/C, NiMo/C and NiRe/C (left panel) and the same catalysts after TOS testing (right panel). Symbols: raw data; black lines: overall fits; colored lines: fits of individual components; dashed lines: background.

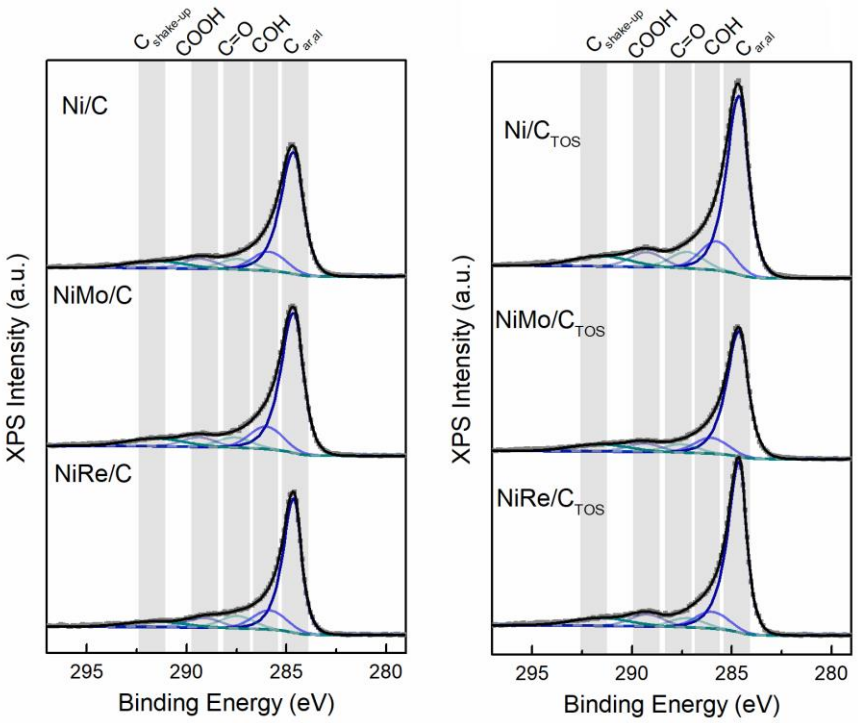

Figure 5S.4. High-resolution XPS data of C 1s region for Ni/C, NiMo/C and NiRe/C (left panel) and the same catalysts after TOS testing (right panel). Symbols: raw data; black lines: overall fits; colored lines: fits of individual components; dashed lines: background. $C_{ar,al}$,: aromatic and aliphatic carbon; COH: hydroxyl groups; C=O: carbonyl groups; COOH: carboxylic groups; $C_{shake-up}$: plasmon loss.

6.1.3 Powder X-ray Diffraction

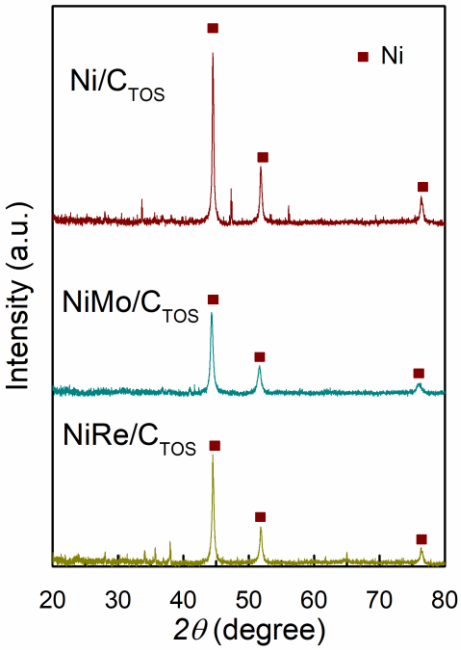

Figure 5S.5. XRD patterns of the Ni/C_{TOS}, NiMo/C_{TOS} and NiRe/C_{TOS} after 90 h of TOS testing showing the presence of the peaks corresponding to metallic Ni in all catalysts.

6.1.4 Transmission Electron Microscopy

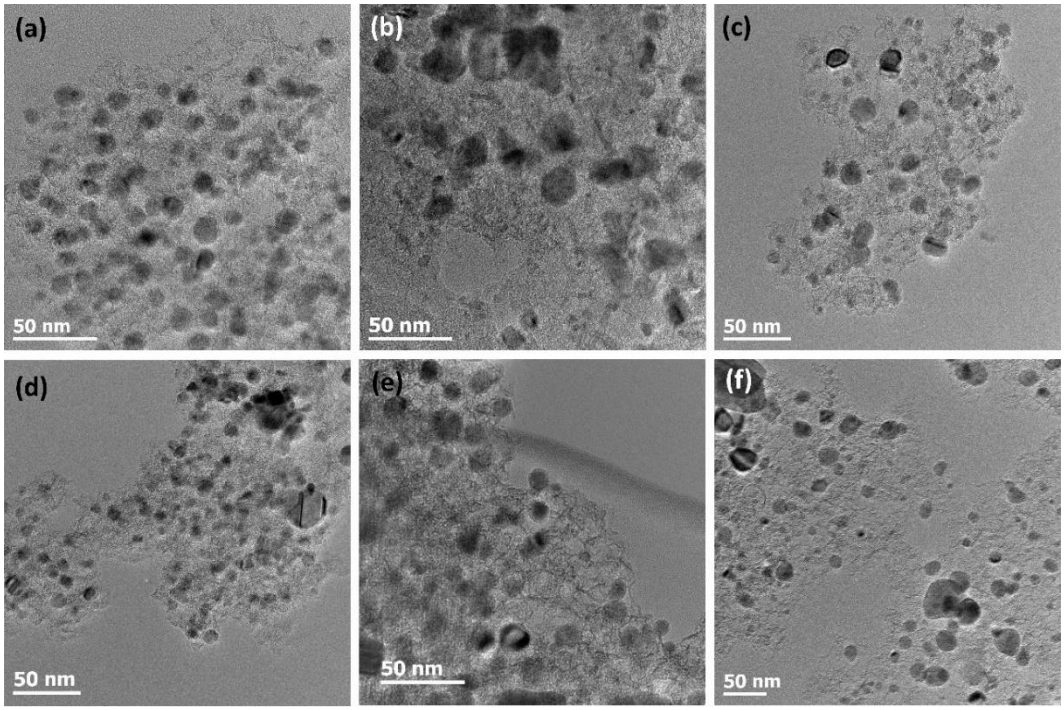

Figure 5S.6. Representative low-magnification TEM images of as-received Ni/C (a), NiMo/C (b) and NiRe/C (c) catalysts and after their TOS testing: Ni/C_{TOS} (d), NiMo/C_{TOS} (e) and NiRe/C_{TOS} (f).

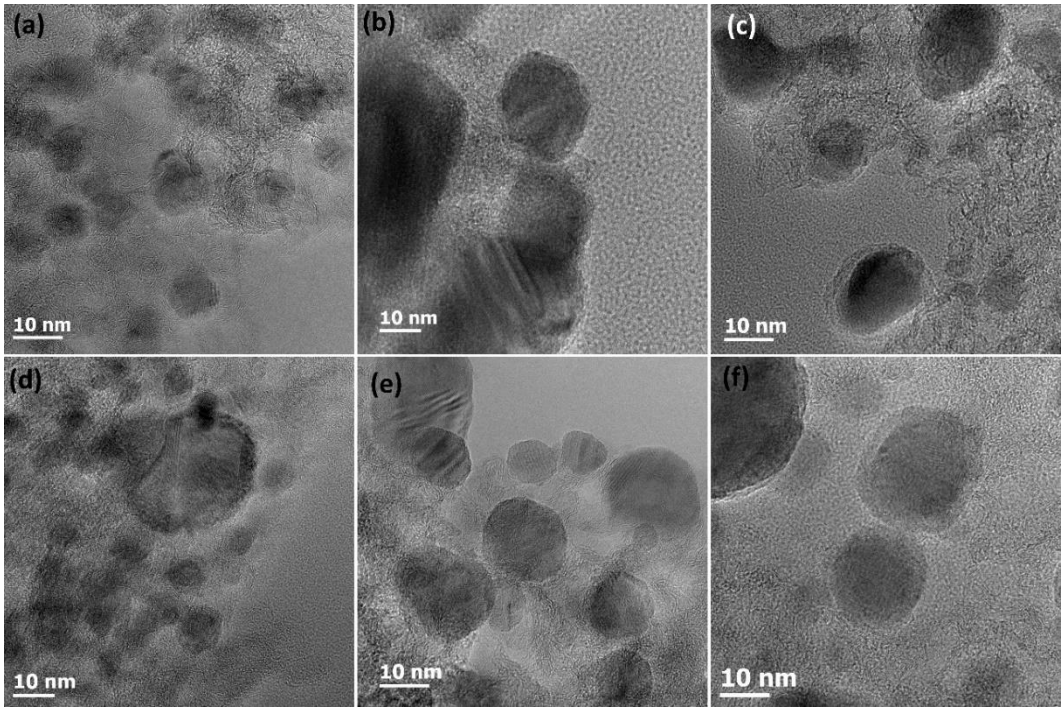

Figure 5S.7. Representative high-magnification TEM images of as-received Ni/C (a), NiMo/C (b) and NiRe/C (c) catalysts and after their TOS testing: Ni/C_{TOS} (d), NiMo/C_{TOS} (e) and NiRe/C_{TOS} (f).

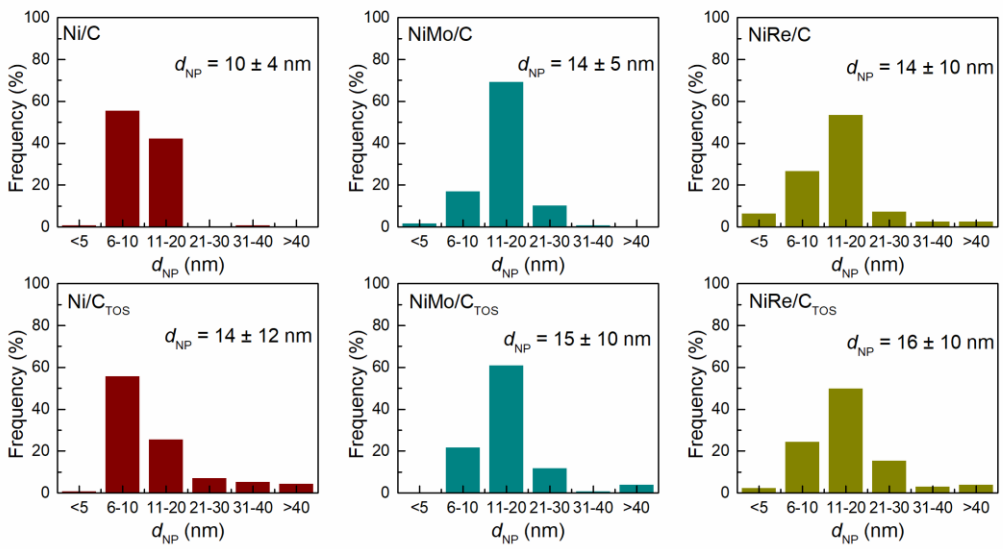

Figure 5S.8. Comparison of the size distributions of the NPs in as-received Ni/C, Ni/C, Ni/C and TOS-tested Ni/C$_{TOS}$, NiMo/C$_{TOS}$, NiRe/C$_{TOS}$ materials, as estimated by the statistical analysis of TEM images.

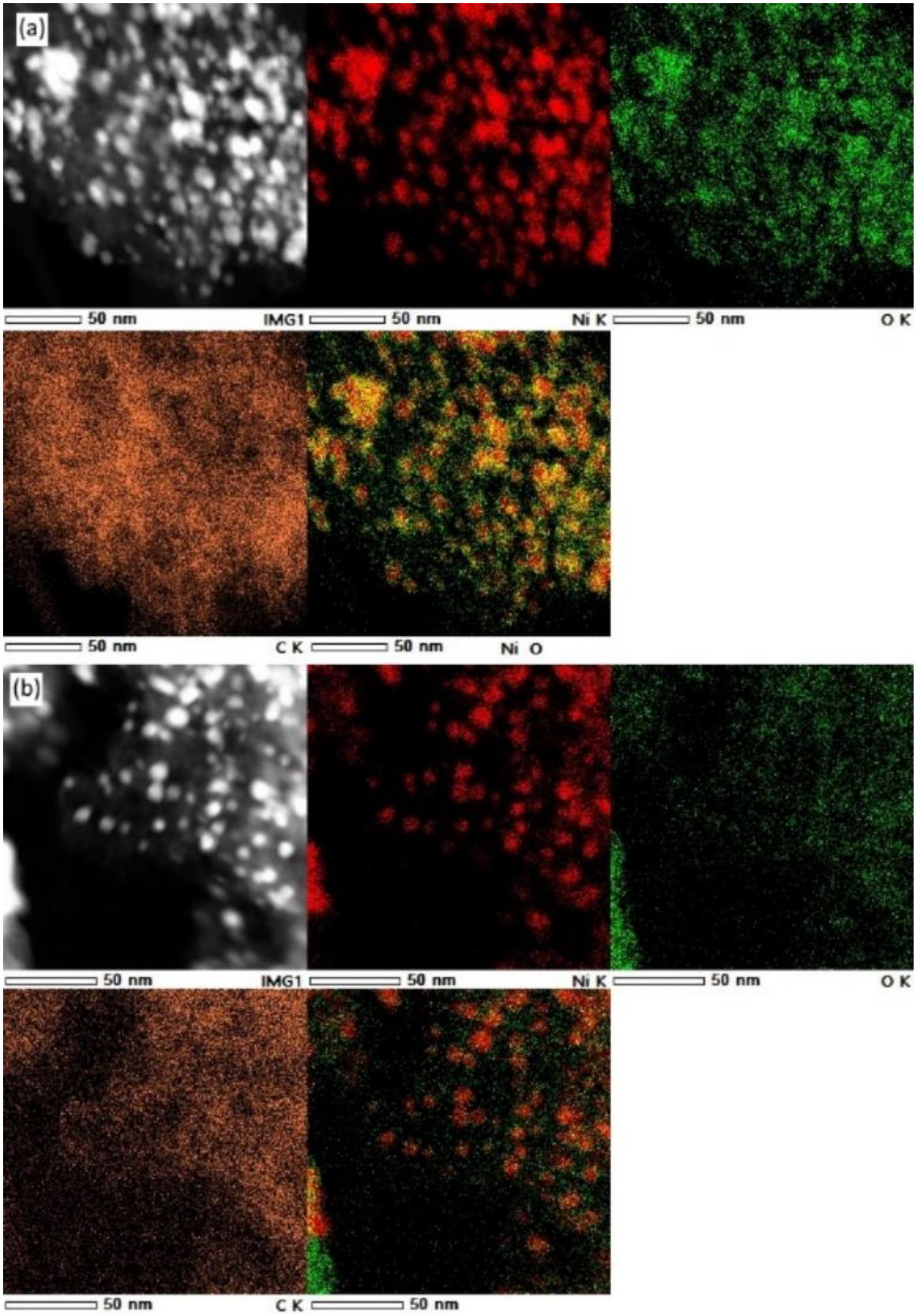

Figure 5S.9. HAADF–STEM images of the NPs in as-received Ni/C (a) and TOS-tested Ni/C_{TOS} (b) materials, together with the simultaneously collected EDX elemental maps for Ni, O, C and Ni + O mixture

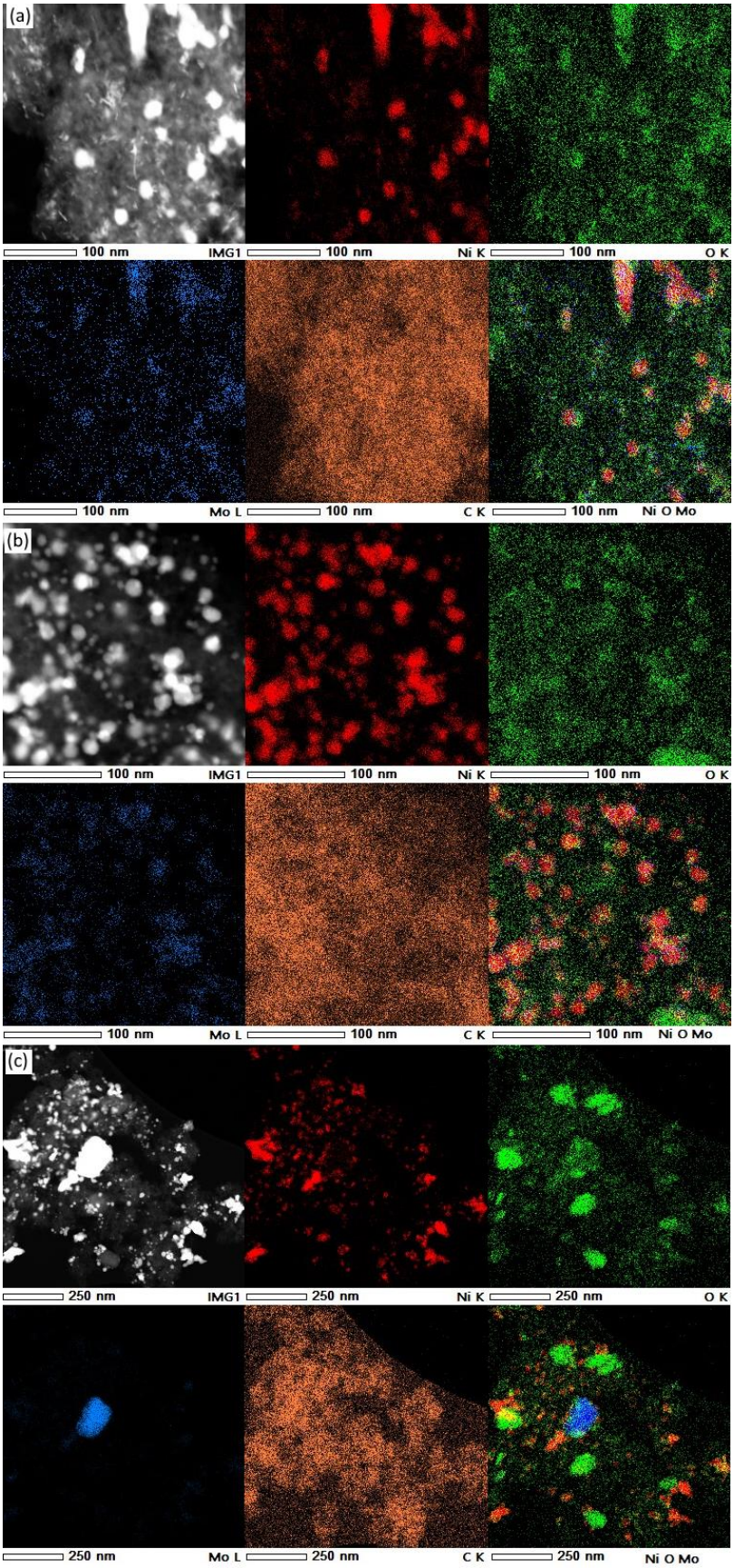

Figure 5S.10. HAADF−STEM images of the NPs in as-received NiMo/C (a) and TOS-tested NiMo/C_{TOS} (b, c) materials, together with the simultaneously collected EDX elemental maps for Ni, O, Mo, C and Ni + O +Mo mixture

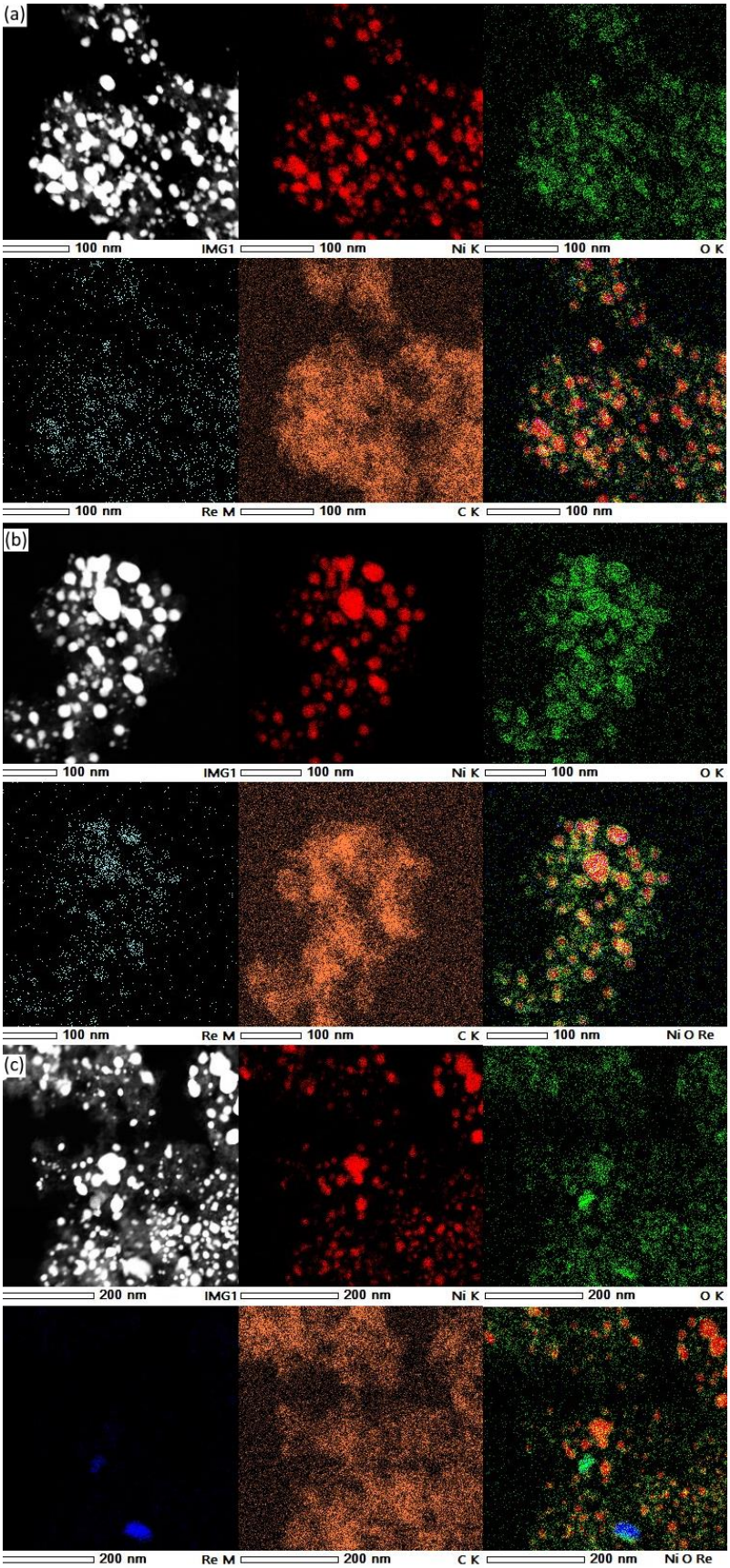

Figure 5S.11. HAADF−STEM images of the NPs in as-received NiRe/C (a) and TOS-tested NiRe/C_{TOS} (b, c) materials, together with the simultaneously collected EDX elemental maps for Ni, O, Re, C and Ni + O +Re mixture.

References

(1) Zhao, Z.; Peng, X.; Liu, X.; Sun, X.; Shi, J.; Han, L.; Li, G.; Luo, J. Efficient and Stable Electroreduction of CO_2 to CH_4 on CuS Nanosheet Arrays. *J. Mater. Chem. A* **2017**, *5* (38), 20239–20243. https://doi.org/10.1039/c7ta05507b.

(2) Gonçalves, L. P. L.; Sousa, J. P. S.; Soares, O. S. G. P.; Bondarchuk, O.; Lebedev, O. I.; Kolen'ko, Y. V.; Pereira, M. F. R. The Role of Surface Properties in CO_2 Methanation over Carbon-Supported Ni Catalysts and Their Promotion by Fe. *Catal. Sci. Technol.* **2020**, *10* (21), 7217. https://doi.org/10.1039/d0cy01254h.

(3) Wang, W.; Duong-Viet, C.; Ba, H.; Baaziz, W.; Tuci, G.; Caporali, S.; Nguyen-Dinh, L.; Ersen, O.; Giambastiani, G.; Pham-Huu, C. Nickel Nanoparticles Decorated Nitrogen-Doped Carbon Nanotubes (Ni/N-CNT); A Robust Catalyst for the Efficient and Selective CO_2 Methanation. *ACS Appl. Energy Mater.* **2019**, *2* (2), 1111−1120. https://doi.org/10.1021/acsaem.8b01681.

(4) Hu, F.; Tong, S.; Lu, K.; Chen, C.; Su, F.; Zhou, J.; Lu, Z.; Wang, X.; Feng, G.; Zhang, R. Reduced Graphene Oxide Supported Ni-Ce Catalysts for CO_2 Methanation: The Support and Ceria Promotion Effects. *J. CO_2 Util.* **2019**, *34* (June), 676–687. https://doi.org/10.1016/j.jcou.2019.08.020.

(5) Zheng, Y.; Wang, Y.; Yuan, Y.; Huang, H. Metal-Based Heterogeneous Electrocatalysts for Electrochemical Reduction of Carbon Dioxide to Methane: Progress and Challenges. *ChemNanoMat* **2021**, *7* (5), 502–514. https://doi.org/https://doi.org/10.1002/cnma.202100063.

(6) Wieckowski, A.; Neurock, M. Contrast and Synergy between Electrocatalysis and Heterogeneous Catalysis. *Adv. Phys. Chem.* **2011**, *2011*, 1−18. https://doi.org/10.1155/2011/907129.

(7) Costa, J. D.; Lado, J. L.; Carbó-Argibay, E.; Paz, E.; Gallo, J.; Cerqueira, M. F.; Rodríguez-Abreu, C.; Kovnir, K.; Kolen'Ko, Y. V. Electrocatalytic Performance and Stability of Nanostructured Fe-Ni Pyrite-Type Diphosphide Catalyst Supported on Carbon Paper. *J. Phys. Chem. C* **2016**, *120* (30), 16537−16544. https://doi.org/10.1021/acs.jpcc.6b05783.

(8) Xu, J.; Wei, X.; Costa, J. D.; Lado, J. L.; Owens-Baird, B.; Gonçalves, L. P. L.; Fernandes, S. P. S.; Heggen, M.; Petrovykh, D. Y.; Dunin-Borkowski, R. E.; Kovnir, K.; Kolen'ko, Y. V. Interface Engineering in Nanostructured Nickel Phosphide Catalyst for Efficient and Stable Water Oxidation. *ACS Catal.* **2017**, acscatal.7b01954. https://doi.org/10.1021/acscatal.7b01954.

(9) Owens-Baird, B.; Xu, J.; Petrovykh, D. Y.; Bondarchuk, O.; Ziouani, Y.; González-Ballesteros, N.; Yox, P.; Sapountzi, F. M.; Niemantsverdriet, H.; Kolen'ko, Y. V; Kovnir, K. NiP_2: A Story of Two Divergent Polymorphic Multifunctional Materials. *Chem. Mater.* **2019**, *31* (9), 3407–3418. https://doi.org/10.1021/acs.chemmater.9b00565.

(10) Sapountzi, F. M.; Orlova, E. D.; Sousa, J. P. S.; Salonen, L. M.; Lebedev, O. I.; Zafeiropoulos, G.; Tsampas, M. N.; Niemantsverdriet, H. J. W.; Kolen'ko, Y. V. FeP Nanocatalyst with Preferential [010] Orientation Boosts the Hydrogen Evolution Reaction in Polymer-Electrolyte Membrane Electrolyzer. *Energy & Fuels* **2020**, *34* (5), 6423–6429. https://doi.org/10.1021/acs.energyfuels.0c00793.

(11) Shashidhara, G. M.; Ravindram, M. A Kinetic Study of the Methanation of CO_2 over Ni-Al_2O_3 Catalyst. *React. Kinet. Catal. Lett.* **1988**, *37* (2), 451–456.

(12) Zhang, Z.; Tian, Y.; Zhang, L.; Hu, S.; Xiang, J. Impacts of Nickel Loading on Properties, Catalytic Behaviors of Ni/ГAl$_2$O$_3$ Catalysts and the Reaction Intermediates Formed in Methanation of CO_2. *Int. J. Hydrogen Energy* **2019**, *44* (18), 9291–9306. https://doi.org/10.1016/j.ijhydene.2019.02.129.

(13) Vogt, C.; Groeneveld, E.; Kamsma, G.; Nachtegaal, M.; Lu, L.; Kiely, C. J.; Berben, P. H.; Meirer, F.; Weckhuysen, B. M. Unraveling Structure Sensitivity in CO_2 Hydrogenation over Nickel. *Nat. Catal.* **2017**, *1*, 127−134. https://doi.org/10.1038/s41929-017-0016-y.

(14) Marconi, E.; Tuti, S.; Luisetto, I. Structure-Sensitivity of CO_2 Methanation over Nanostructured Ni Supported on CeO_2 Nanorods. *Catalysts* **2019**, *9* (4), 1−13. https://doi.org/10.3390/catal9040375.

(15) Li, J.; Lin, Y.; Pan, X.; Miao, D.; Ding, D.; Cui, Y.; Dong, J.; Bao, X. Enhanced CO_2 Methanation Activity of Ni/Anatase Catalyst by Tuning Strong Metal–Support Interactions. *ACS Catal.* **2019**, *9* (7), 6342–6348. https://doi.org/10.1021/acscatal.9b00401.

(16) Westermann, A.; Azambre, B.; Bacariza, M. C.; Graça, I.; Ribeiro, M. F.; Lopes, J. M.; Henriques, C. Insight into CO_2 Methanation Mechanism over NiUSY Zeolites: An Operando IR Study. *Appl. Catal. B Environ.* **2015**, *174*–*175*, 120–125. https://doi.org/10.1016/j.apcatb.2015.02.026.

(17) Zhen, W.; Li, B.; Lu, G.; Ma, J. Enhancing Catalytic Activity and Stability for CO_2 Methanation on Ni@MOF-5 via Control of Active Species Dispersion. *Chem. Commun.* **2015**, *51*, 1728–1731. https://doi.org/10.1039/C4CC08733J.

(18) Swalus, C.; Jacquemin, M.; Poleunis, C.; Bertrand, P.; Ruiz, P. CO_2 Methanation on Rh/γ-Al_2O_3 Catalyst at Low Temperature: "In Situ" Supply of Hydrogen by Ni/Activated Carbon Catalyst. *Appl. Catal. B Environ.* **2012**, *125*, 41–50. https://doi.org/10.1016/j.apcatb.2012.05.019.

(19) Le, M. C.; Van, K. Le; Nguyen, T. H. T.; Nguyen, N. H. The Impact of Ce-Zr Addition on Nickel Dispersion and Catalytic Behavior for CO_2 Methanation of Ni/AC Catalyst at Low Temperature. *J. Chem.* **2017**, *2017*.

(20) Cam, L. M.; Ha, N. T. T.; Khu, L. Van; Ha, N. N.; Brown, T. C. Carbon Dioxide Methanation Over Nickel Catalysts Supported on Activated Carbon at Low Temperature. *Aust. J. Chem.* **2019**, *72*, 969–977. https://doi.org/10.1071/CH19355.

(21) Serp, P.; Figueiredo, J. L. *Carbon Materials for Catalysis*; Serp, P., Figueiredo, J. L., Eds.; Wiley: New Jersey, 2009.

(22) Zheng, W.; Wang, Y.; Shuai, L.; Wang, X.; He, F.; Lei, C.; Li, Z.; Yang, B.; Lei, L.; Yuan, C.; Qiu, M.; Hou, Y.; Feng, X. Highly Boosted Reaction Kinetics in Carbon Dioxide Electroreduction by Surface-Introduced Electronegative Dopants. *Adv. Funct. Mater.* **2021**, *31* (15), 2008146. https://doi.org/https://doi.org/10.1002/adfm.202008146.

(23) Li, F.; Hong, S.; Wu, T.-S.; Li, X.; Masa, J.; Soo, Y.-L.; Sun, Z. Atomically Dispersed Nickel Sites for Selective Electroreduction of CO_2. *ACS Appl. Energy Mater.* **2019**, *2* (12), 8836–8842. https://doi.org/10.1021/acsaem.9b01828.

(24) Gong, M.; Zhou, W.; Tsai, M.-C.; Zhou, J.; Guan, M.; Lin, M.-C.; Zhang, B.; Hu, Y.; Wang, D.-Y.; Yang, J.; Pennycook, S. J.; Hwang, B.-J.; Dai, H. Nanoscale Nickel Oxide/Nickel Heterostructures for Active Hydrogen Evolution Electrocatalysis. *Nat. Commun.* **2014**, *5* (1), 4695. https://doi.org/10.1038/ncomms5695.

(25) Kuznetsov, V. V.; Gamburg, Y. D.; Batalov, R. S.; Zhulikov, V. V.; Zaitsev, V. A. Hydrogen Evolution on Catalytically Active Electrodeposited Ni-Re Alloy: Electrochemical Impedance Study. *Russ. J. Electrochem.* **2018**, *54* (7), 598–603. https://doi.org/10.1134/S1023193518070054.

(26) Kabir, S.; Lemire, K.; Artyushkova, K.; Roy, A.; Odgaard, M.; Schlueter, D.; Oshchepkov, A.; Bonnefont, A.; Savinova, E.; Sabarirajan, D. C.; Mandal, P.; Crumlin, E. J.; Zenyuk, I. V.; Atanassov, P.; Serov, A. Platinum Group Metal-Free NiMo Hydrogen Oxidation Catalysts: High Performance and Durability in Alkaline Exchange Membrane Fuel Cells. *J. Mater. Chem. A* **2017**, *5* (46), 24433–24443. https://doi.org/10.1039/c7ta08718g.

(27) Kuznecova, I.; Gusca, J. Property Based Ranking of CO and CO_2 Methanation Catalysts. *Energy Procedia* **2017**, *128*, 255–260. https://doi.org/10.1016/j.egypro.2017.09.068.

(28) Yuan, H.; Zhu, X.; Han, J.; Wang, H.; Ge, Q. Rhenium-Promoted Selective CO_2 Methanation on Ni-Based Catalyst. *J. CO_2 Util.* **2018**, *26* (February), 8–18. https://doi.org/10.1016/j.jcou.2018.04.010.

(29) Dong, X.; Jin, B.; Cao, S.; Meng, F.; Chen, T.; Ding, Q.; Tong, C. Facile Use of Coal Combustion Fly Ash (CCFA) as Ni-Re Bimetallic Catalyst Support for High-Performance CO_2 Methanation. *Waste Manag.* **2020**, *107*, 244–251. https://doi.org/10.1016/j.wasman.2020.04.014.

(30) Biesinger, M. C.; Payne, B. P.; Lau, L. W. M.; Gerson, A.; Smart, R. S. C. X-Ray Photoelectron Spectroscopic Chemical State Quantification of Mixed Nickel Metal, Oxide and Hydroxide Systems. *Surf. Interface Anal.* **2009**, *41* (4), 324–332. https://doi.org/10.1002/sia.3026.

(31) Owens-Baird, B.; Sousa, J. P. S.; Ziouani, Y.; Petrovykh, D. Y.; Zarkevich, N. A.; Johnson, D. D.; Kolen'ko, Y. V;

Kovnir, K. Crystallographic Facet Selective HER Catalysis: Exemplified in FeP and NiP_2 Single Crystals. *Chem. Sci.* **2020**, *11* (19), 5007–5016. https://doi.org/10.1039/D0SC00676A.

(32) Payne, B. P.; Biesinger, M. C.; McIntyre, N. S. Use of Oxygen/Nickel Ratios in the XPS Characterisation of Oxide Phases on Nickel Metal and Nickel Alloy Surfaces. *J. Electron Spectros. Relat. Phenomena* **2012**, *185* (5–7), 159–166. https://doi.org/10.1016/j.elspec.2012.06.008.

(33) Li, X.; Henderson, J. D.; Filice, F. P.; Zagidulin, D.; Biesinger, M. C.; Sun, F.; Qian, B.; Shoesmith, D. W.; Noël, J. J.; Ogle, K. The Contribution of Cr and Mo to the Passivation of Ni22Cr and Ni22Cr10Mo Alloys in Sulfuric Acid. *Corros. Sci.* **2020**, *176* (July), 109015. https://doi.org/10.1016/j.corsci.2020.109015.

(34) Ma, L.; Yan, L.; Lu, A. H.; Ding, Y. Effect of Re Promoter on the Structure and Catalytic Performance of Ni-Re/Al_2O_3 Catalysts for the Reductive Amination of Monoethanolamine. *RSC Adv.* **2018**, *8* (15), 8152–8163. https://doi.org/10.1039/c7ra12891f.

(35) Nikolova, D.; Edreva-Kardjieva, R.; Kolev, H.; Gabrovska, M. Promoted Re/Al_2O_3 Systems as Sour Water-Gas Shift Catalysts. *Catal. Today* **2020**, *357* (May 2019), 590–601. https://doi.org/10.1016/j.cattod.2019.05.038.

(36) Haslam, G. E.; Chin, X. Y.; Burstein, G. T. Passivity and Electrocatalysis of Nanostructured Nickel Encapsulated in Carbon. *Phys. Chem. Chem. Phys.* **2011**, *13* (28), 12968–12974. https://doi.org/10.1039/c1cp20701f.

(37) Fan, L.; Liu, P. F.; Yan, X.; Gu, L.; Yang, Z. Z.; Yang, H. G.; Qiu, S.; Yao, X. Atomically Isolated Nickel Species Anchored on Graphitized Carbon for Efficient Hydrogen Evolution Electrocatalysis. *Nat. Commun.* **2016**, *7* (March), 1–7. https://doi.org/10.1038/ncomms10667.

(38) Bao, X. Q.; Petrovykh, D. Y.; Alpuim, P.; Stroppa, D. G.; Guldris, N.; Fonseca, H.; Costa, M.; Gaspar, J.; Jin, C.; Liu, L. Amorphous Oxygen-Rich Molybdenum Oxysulfide Decorated p-Type Silicon Microwire Arrays for Efficient Photoelectrochemical Water Reduction. *Nano Energy* **2015**, *16*, 130–142. https://doi.org/10.1016/j.nanoen.2015.06.014.

(39) Figueiredo, J. L.; Pereira, M. F. R. The Role of Surface Chemistry in Catalysis with Carbons. *Catal. Today* **2010**, *150*, 2–7. https://doi.org/10.1016/j.cattod.2009.04.010.

(40) Gonçalves, L. P. L.; Christensen, D. B.; Meledina, M.; Salonen, L. M.; Petrovykh, D. Y.; Carbó-Argibay, E.; Sousa, J. P. S.; Soares, O. S. G. P.; Pereira, M. F. R.; Kegnæs, S.; Kolen'Ko, Y. V. Selective Formic Acid Dehydrogenation at Low Temperature over a RuO_2/COF Pre-Catalyst Synthesized on the Gram Scale. *Catal. Sci. Technol.* **2020**, *10* (7), 1991–1995. https://doi.org/10.1039/d0cy00145g.

(41) Petrovykh, D. Y.; Sullivan, J. M.; Whitman, L. J. Quantification of Discrete Oxide and Sulfur Layers on Sulfur-Passivated InAs by XPS. *Surf. Interface Anal.* **2005**, *37* (11), 989–997. https://doi.org/https://doi.org/10.1002/sia.2095.

(42) Stine, R.; Aifer, E. H.; Whitman, L. J.; Petrovykh, D. Y. Passivation of GaSb and InAs by PH-Activated Thioacetamide. *Appl. Surf. Sci.* **2009**, *255* (16), 7121–7125. https://doi.org/https://doi.org/10.1016/j.apsusc.2009.03.010.

(43) Fears, K. P.; Petrovykh, D. Y.; Clark, T. D. Evaluating Protocols and Analytical Methods for Peptide Adsorption Experiments. **2013**, 1–15.

(44) Fears, K. P.; Clark, T. D.; Petrovykh, D. Y. Residue-Dependent Adsorption of Model Oligopeptides on Gold. *J. Am. Chem. Soc.* **2013**, *135* (40), 15040–15052. https://doi.org/10.1021/ja404346p.

(45) Salimian, M.; Ivanov, M.; Deepak, F. L.; Petrovykh, D. Y.; Bdikin, I.; Ferro, M.; Kholkin, A.; Titus, E.; Goncalves, G. Synthesis and Characterization of Reduced Graphene Oxide/Spiky Nickel Nanocomposite for Nanoelectronic Applications. *J. Mater. Chem. C* **2015**, *3* (43), 11516–11523. https://doi.org/10.1039/C5TC02619A.

(46) Liu, Q.; Gu, F.; Lu, X.; Liu, Y.; Li, H.; Zhong, Z.; Xu, G.; Su, F. Enhanced Catalytic Performances of Ni/Al_2O_3 Catalyst via Addition of V_2O_3 for CO Methanation. *Appl. Catal. A Gen.* **2014**, *488*, 37–47. https://doi.org/10.1016/j.apcata.2014.09.028.

(47) Ma, Y.; Liu, J.; Chu, M.; Yue, J.; Cui, Y.; Xu, G. Cooperation Between Active Metal and Basic Support in Ni-Based Catalyst for Low-Temperature CO_2 Methanation. *Catal. Letters* **2020**, *150* (5), 1418–1426. https://doi.org/10.1007/s10562-019-03033-w.

(48) Zhao, K.; Li, Z.; Bian, L. CO_2 Methanation and Co-Methanation of CO and CO_2 over Mn-Promoted Ni/Al_2O_3 Catalysts. *Front. Chem. Sci. Eng.* **2016**, *10* (2), 273–280. https://doi.org/10.1007/s11705-016-1563-5.

(49) Hongmanorom, P.; Ashok, J.; Chirawatkul, P.; Kawi, S. Interfacial Synergistic Catalysis over Ni Nanoparticles Encapsulated in Mesoporous Ceria for CO_2 Methanation. *Appl. Catal. B Environ.* **2021**, *297* (June), 120454. https://doi.org/10.1016/j.apcatb.2021.120454.

(50) Jia, X.; Zhang, X.; Rui, N.; Hu, X.; Liu, C. Structural Effect of Ni ZrO_2 Catalyst on CO_2 Methanation with Enhanced Activity. *Appl. Catal. B Environ.* **2019**, *244* (June 2018), 159–169. https://doi.org/10.1016/j.apcatb.2018.11.024.

(51) Götz, M.; Lefebvre, J.; Mörs, F.; McDaniel Koch, A.; Graf, F.; Bajohr, S.; Reimert, R.; Kolb, T. Renewable Power-to-Gas: A Technological and Economic Review. *Renew. Energy* **2016**, *85*, 1371–1390. https://doi.org/10.1016/j.renene.2015.07.066.

(52) Huo, X.; Wang, Z.; Huang, J.; Zhang, R.; Fang, Y. One-Step Synthesis of Bulk Mo and Ni-Mo Carbides for Methanation. *RSC Adv.* **2016**, *6* (29), 24353–24360. https://doi.org/10.1039/c5ra23870f.

(53) Wang, B.; Wang, C.; Yu, W.; Li, Z.; Xu, Y.; Ma, X. Effects of Preparation Method and Mo_2C Loading on the Mo_2C/ZrO_2 Catalyst for Sulfur-Resistant Methanation. *Mol. Catal.* **2020**, *482* (92), 110668. https://doi.org/10.1016/j.mcat.2019.110668.

Chapter 6

In situ study of CO_2 methanation over carbon-supported Ni nanoparticles: formation and role of a NiO shell

MacArthur, K. E.; Basak, S.; Gonçalves, L. P. L.; Sousa, J. P. S.; Soares, O. S. G. P.; Pereira, M. F. R.; Eichel, R. A.; Kolen'ko, Yu. V. *In situ* study of CO_2 methanation over carbon-supported Ni nanoparticles: formation and role of a NiO shell. Submitted. **2022**.

Abstract

In situ transmission electron microscopy (TEM) provided direct insights into the dynamics of high-performing nickel nanoparticle catalyst supported on reduced activated carbon during CO_2 methanation. The formation of a NiO shell around the metallic Ni core was imaged during catalytic reaction. Such Ni@NiO core–shell nanoparticles played a key role in the CO_2 methanation, as evidenced by their dynamic behavior under the reaction conditions. The formation mechanism of the Ni@NiO nanostructures during CO_2 methanation is proposed and discussed. Building up of carbon coke over the catalyst nanoparticles was not revealed by *in situ* TEM, ruling out this route of the catalyst deactivation. On the other hand, a slight increase in particle size of the catalyst was observed, which could be the reason for its deactivation.

1. Introduction

The CO_2 methanation reaction has been the subject of intense studies, since it offers an interesting pathway to produce a carbon-neutral methane fuel (e-CH_4), thus reducing the CO_2 emissions to the atmosphere.[1–5] Mostly Ni-based catalysts supported on a variety of supporting materials, such as metal oxides,[6–8] zeolites,[9] metal organic frameworks,[10] and carbons,[3,11–18] are used for CO_2 methanation. Interestingly, the supporting material plays a major role in the catalysts performance, and it has been demonstrated that the same active phase, such as Ni nanoparticles, can present different activity, selectivity and stability, depending on the supporting material being used.[3,5,11,19] Besides the fact that CO_2 methanation involves reactant diffusion, adsorption, surface reaction, products desorption, and diffusion, the metal-support interactions can also play a role in the catalytic mode of action, which is consequently reflected in the performance of the catalyst.[3,20]

Notably, the mechanism of the CO_2 methanation is still under debate. The proposed mechanisms are largely governed by the catalytic system and the reaction conditions, and the methanation could proceed through (*i*) the associative pathway, in which CO_2 is adsorbed associatively with a former adsorbed H atom, forming formate as an intermediate, and (*ii*) the dissociative pathway, where CO_2 is dissociated in CO, which is the main intermediate of the reaction.[4] Usually, the proposed mechanisms for CO_2 methanation over Ni-based catalysts hypothesized the dissociation of H_2 on the Ni nanoparticles, while CO_2 adsorption usually occurs on the supporting material or nickel-support interface with dissociation and further carbonyl adsorption on Ni nanoparticles.[21]

Understanding the behavior of the supported Ni catalyst under the reaction conditions and elucidating the associated methanation mechanism is crucial for the rational design of high-performing catalyst materials. Hence, i*n situ* techniques have been extensively used to elucidate the mechanism of CO_2 methanation over various supported catalytic systems. For instance, *in situ*

infrared (IR) spectroscopy has been used for underpinning the reaction intermediates, [20,22–25] while X-ray photoelectron spectroscopy (XPS) and near edge X-ray absorption fine structure (NEXAFS) have been employed to elucidate the chemical nature of the real catalysts under methanation conditions.[26,27] At the same time, the fine microstructural modifications, that the supported Ni catalysts undergo during CO_2 methanation, have been studied to a lesser extent. For example, deactivation of the Ni catalysts is often attributed to the sintering of the Ni nanoparticles and/or coke building up on the active phase, which has been investigated by *ex situ* transmission electron microscopy (TEM).[4,28] Importantly, *in situ* observation of fine microstructural modifications should assist in understanding and further developing active, selective and stable methanation catalysts. Hence, in this study, *in situ* TEM is applied to elucidate the behavior of the Ni catalyst supported on the reduced activated carbon during CO_2 methanation, affording insight into the catalyst real microstructure and its dynamics.

The understanding and atomic level information provided by aberration-corrected TEM is unparalleled, particularly for the study of catalyst nanoparticles. Unfortunately, the vacuum requirements for the electron beam affords only the investigation of static materials before and after subjecting them to the catalytic environment. This post-mortem analysis can make it difficult to underpin the specifics of a catalytic reaction mechanism, without being able to observe the structures under a realistic environment. The development of specialized holders based on microelectromechanical systems (MEMs) now allows us to contain gas near the sample up to 0.1 MPa in pressure with precise heat and pressure control. Two silicon nitride chips are placed together creating a small nanoreactor chamber. Thin (30 nm) electron transparent windows are present in these chips to allow penetration by the electron beam, thus affording structural characterization of the samples under realistic reactive conditions.

2. Experimental

Reduced AC with an increased number of Lewis basic sites (AC−R) was prepared by heat treatment in H_2 at 900 °C.[41] Next, Ni NPs were anchored on the resultant support, using the convenient incipient wetness impregnation (IWI) method, with $Ni(NO_3)_2{\cdot}6H_2O$ as Ni precursor.

The as-synthesized Ni/AC−R catalyst was analyzed in an image-corrected Titan-300 electron microscope (FEI), operating at 300 kV. Three separated *in situ* experiments were performed: the study of the nanoparticles behavior under (*i*) CO_2 methanation reaction conditions with a pre-treatment under H_2 in Ar (ratio 4:96), (*ii*) CO_2 methanation reaction conditions without the reduction treatment beforehand, and (*iii*) a flow of only CO_2. Heating was carried out at 400, 450 and 500 °C.

More experimental details are summarized in Chapter 2.

3. Results and Discussion

Our earlier study[3] demonstrated excellent CO_2 methanation performance of a Ni catalyst supported on reduced activated carbon (Ni/AC−R). Interestingly, after 90 h of CO_2 methanation at 450 °C and 0.1 MPa, with 10% H_2, 40% CO_2 and 50% He, a distinct crystalline shell of Ni oxide was formed on the surface of the Ni nanoparticles supported on AC−R. Figure 6.1 shows TEM images of the Ni nanoparticles pre- and post-reaction, with the oxide shell of thickness 2–3 nm denoted by the green dashed line in Figure 6.1b. It was intriguing to observe a Ni oxide shell on the Ni nanoparticles after prolonged CO_2 methanation, since it was expected that metallic Ni was the active phase of the reaction. However, after cooling to room temperature, the samples were transferred in air for the post-reaction analysis; therefore, it was unclear whether the oxide shell was formed during the air transfer or as a consequence of the reaction conditions. Herein, we carried out a series of systematic *in situ* gas studies using a specialized DENSsolutions Climate holder in order to elucidate the origin and effect of the observed Ni-oxide shell.

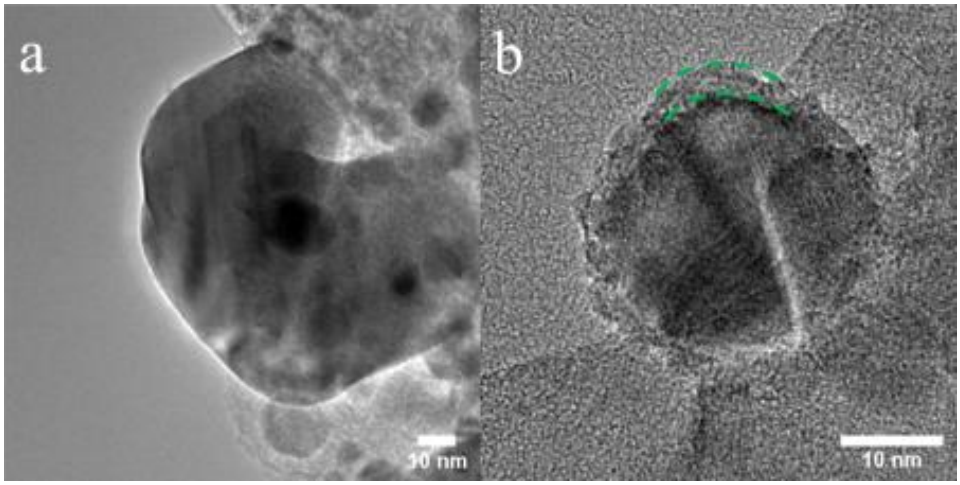

Figure 6.1. Summary of the *ex situ* analysis results, before (a) and after (b) CO_2 methanation for 90 h. The formed Ni@NiO core-shell nanostructure is highlighted by the green dashed line in panel (b).

The Ni/AC−R catalyst was loaded into the Climate holder, reduced under a H_2 environment, and then imaged under the reactive H_2 and CO_2 gases providing methanation conditions. It was found that once a temperature of 450 °C was reached under the reactive gases the Ni nanoparticles began to dynamically change shape whilst still maintaining crystallinity. The first example of this shape change with time can be seen in Figure 6.2 as a growth/reduction in some of the particle facets. No oxide shell is visible in this example, most likely due to the large amount of scattering from the thick AC−R supporting material.

Towards the edge of the AC−R supporting material, the oxide shell on the structure of the Ni nanoparticles is clearly visible (Figure 6.3), along with a rough polycrystalline layer outside the nanoparticles (Figure 6S.1 for high-resolution image). The particles towards the edge of the AC−R support changed more dynamically, and in some cases, appeared almost molten, rolling around within an oxide shell. This behavior was seen regardless of whether or not the reducing H_2 pre-treatment was applied; Figure 6.3a shows the sample without H_2 reduction and Figure 6.3b shows it with H_2 reduction pre-treatment. Primarily we noticed that the formation of the oxide-shell was not a mechanism of deactivation of the particles. In fact, the most dynamic behavior was seen for particles with an oxide-shell, thereby suggesting a permeable structure in which the reactive gases can penetrate in order to reach the Ni active sites.

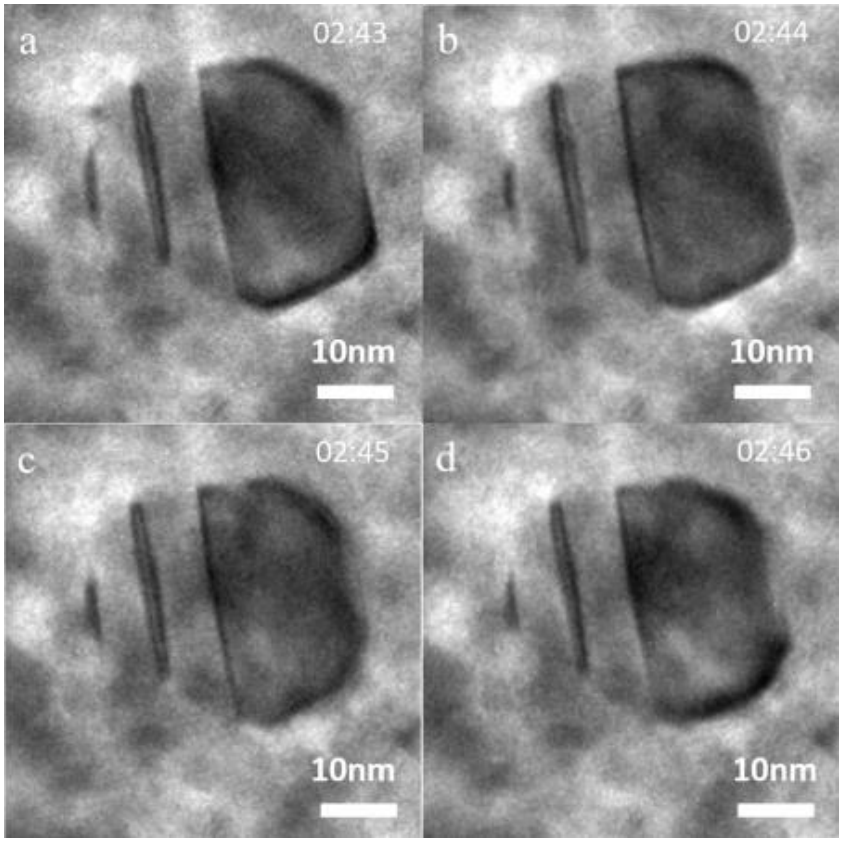

Figure 6.2. *In situ* time-series of TEM images showing an active particle away from the edge of the carbon support. Conditions: T = 450 °C, CO_2:H_2 = 1:3.

Using *in situ* X-ray photoelectron spectroscopy (XPS), Heine and co-workers[29] reported the formation of NiO even at room temperature in CO_2 gas alone, which requires the transfer of two electrons from metallic Ni to the CO_2 molecule, forming Ni^{2+} due to oxidation of Ni and CO due to reduction of CO_2. However, after the introduction of H_2 into the system mimicking methanation conditions, NiO species were found to be reduced again to metallic Ni. In another interesting study that uses *in situ* XPS and *in situ* near edge X-ray absorption fine structure (NEXAFS) spectroscopies, Giorgianni and co-workers[30] reported a similar behavior, wherein metallic Ni surface was found to oxidize rapidly upon exposure to CO_2. Under methanation conditions (i.e., CO_2 + H_2), while *in situ* XPS revealed that Ni is predominantly in a reduced state, *in situ* NEXAFS indicated that the shell of Ni nanoparticles is prevalently in a Ni^{2+} state due to incomplete reduction. Interestingly, Mutz and co-workers[31] showed that, in the presence of CO_2, Ni starts to oxidize after the removal of H_2 from the gas flow. When H_2 is again introduced into the stream,

the reduced fraction of metallic Ni was found to increase to 94% yet having 6% fraction of oxidized Ni.

In our study, it would not be expectable for the Ni nanoparticles to oxidize, since they are under an atmosphere rich in H_2; however, CO_2 should be responsible for the oxidation of the surface of the Ni nanoparticles, thus forming NiO shell. The Ni^0 species can be oxidized by CO_2 to form Ni^{2+} species, activating the CO_2 as well, to form CO.[32] Importantly, an experiment where only CO_2 gas was used (Figure 6S.2) shows that the presence of both H_2 and CO_2 is required for the oxide-shell formation, since in the presence of only CO_2, the whole particle can be seen to oxidize rather than only 2−3 nm of the surface. Therefore, the synergetic relationship between CO_2 and H_2 should be responsible for the formation of the Ni@NiO core-shell structure during CO_2 methanation, as observed herein.

The formation of this Ni@NiO core-shell structure under reaction conditions might be one of the reasons for the good performance of this catalyst. On the one hand, the NiO formation in close contact with the support, where CO_2 is adsorbed, leads to the activation of this molecule,[25,32] while Ni in the core is responsible for H_2 dissociation, since the dynamic nature of the oxide shell allows for the diffusion of the H_2 to the metallic Ni core of the nanoparticles. This way, both reactants can be in close contact, which facilitates the reaction. On the other hand, the NiO might present oxygen vacancies, which are known to induce the dissociation and activation of CO_2 on the surface of the catalyst.[33] It has been reported before that the rate-determining step for CO_2 methanation reaction should be related to the availability of adjacent adsorbed H to hydrogenate adsorbed CO;[34] thus, this proximity of CO_2 activation and CO formation on NiO shell and H_2 dissociation in Ni core, might explain the good performance of the catalyst.[3]

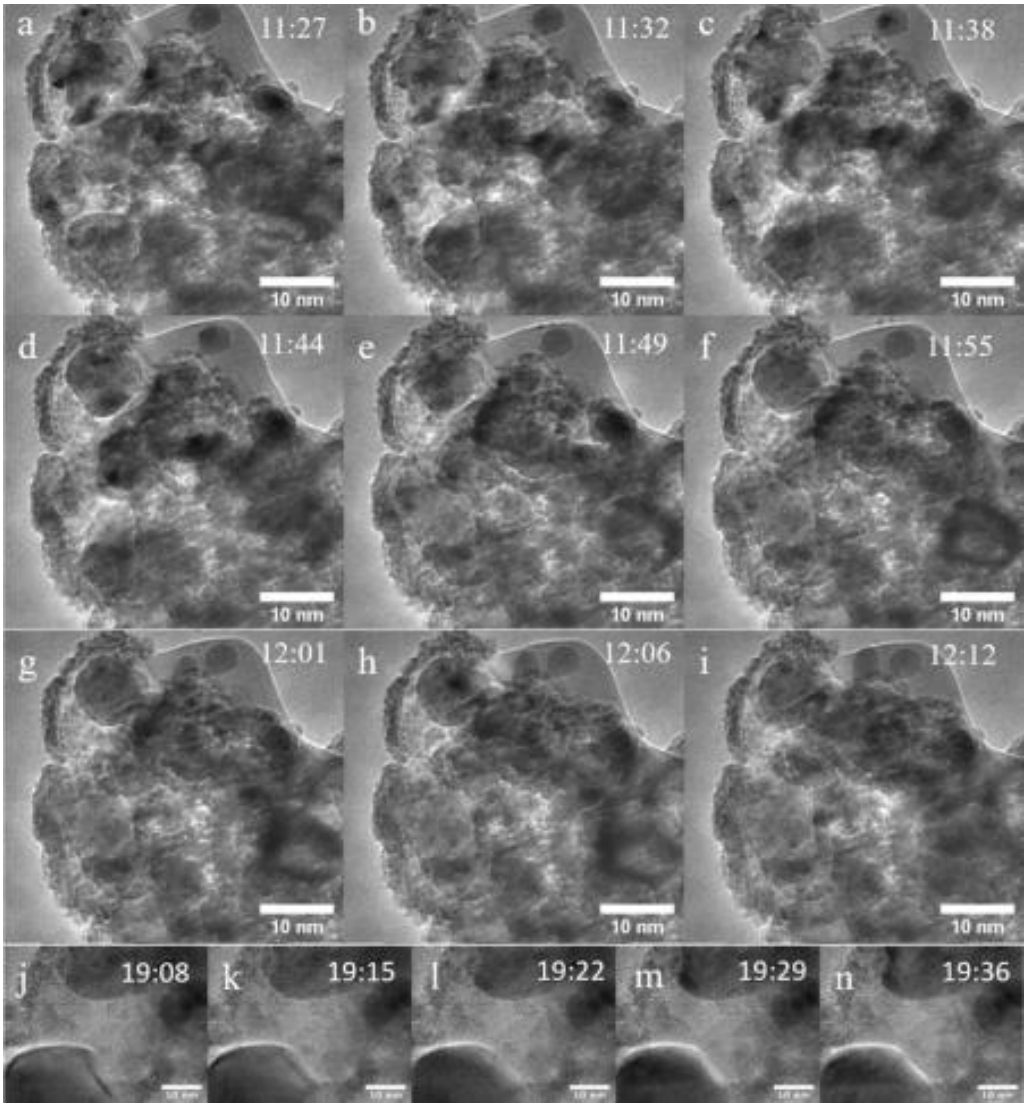

Figure 6.3. Low magnification time-series for active nanoparticles changing dynamically under reaction conditions without H_2 pre-treatment (a). *In situ* time-series of TEM images showing a non-activate particle (no H_2 pre-treatment) in the top right and an active particle (H_2 pre-treatment) in the bottom left (b). The oxide shell is visible in both cases. The time stamp in the top left-hand corner of each image shows the time in minutes and seconds since reaching the methanation reaction conditions.

After examining the dynamic behavior of the particles under a reactive methanation environment, we then explored the mechanisms of deactivation of the catalyst. The main deactivation mechanism was observed to be related to a particle size increase. The larger particle on the top right of Figure 6.3b demonstrated no dynamic changes, while the smaller particle within the same field of view demonstrated to be very active. Upon cooling, the particle structures stabilized to fill the oxide shell again (this can be seen in Figure 6S.3), yielding a structure that matches the original *ex situ* characterization (Figure 6.1b). Finally, a post *in situ* experiment energy dispersive X-ray spectroscopy

in scanning TEM mode (STEM–EDX) was performed to confirm the shell composition as a 2−3 nm thick NiO shell (Figure 6.4).

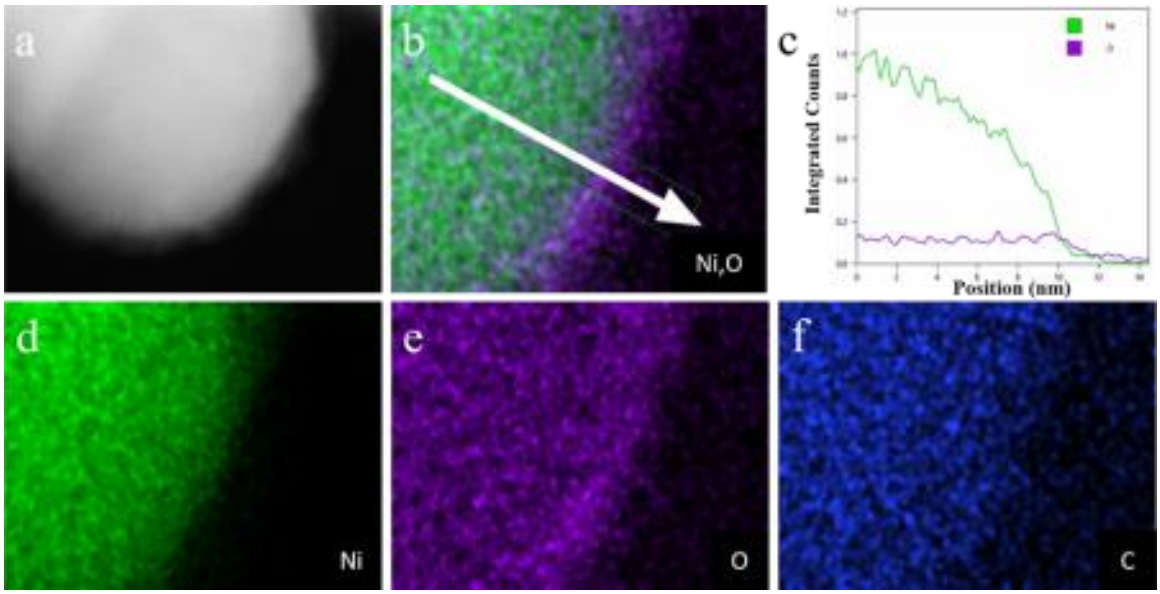

Figure 6.4. Post *in situ* STEM–EDX analysis of the catalyst nanoparticle showing the annular dark-field STEM overlay, EDX maps for Ni, O, C and Ni/O mixture, as well as STEM−EDX line scan at the edge of a catalyst particle (indicated by the arrow in Ni/O EDX mixture map) revealing the presence of Ni and O.

Our experimental *in situ* TEM findings have demonstrated that the nickel oxide shell observed on the catalytic Ni nanoparticles supported on reduced activated carbon in our previous study[3] is in fact formed under reaction conditions of CO_2 methanation, and it is expected to be an integral part of the reaction process (Figure 6.5). We believe that this oxide structure presents a permeable nature, allowing for the penetration of the reaction gases to the active metallic Ni core, otherwise dynamic changes would not continue to be observed in the nanoparticles demonstrating a shell. We hypothesize that the oxide acts as an enhancer of the CO_2 adsorption/activation while Ni in the core is responsible for H_2 dissociation, which leads to both reactants being in close proximity, accomplishing CO_2 methanation. Furthermore, we observed *in situ* that the main deactivation mechanism observed was related to a particle size increase.

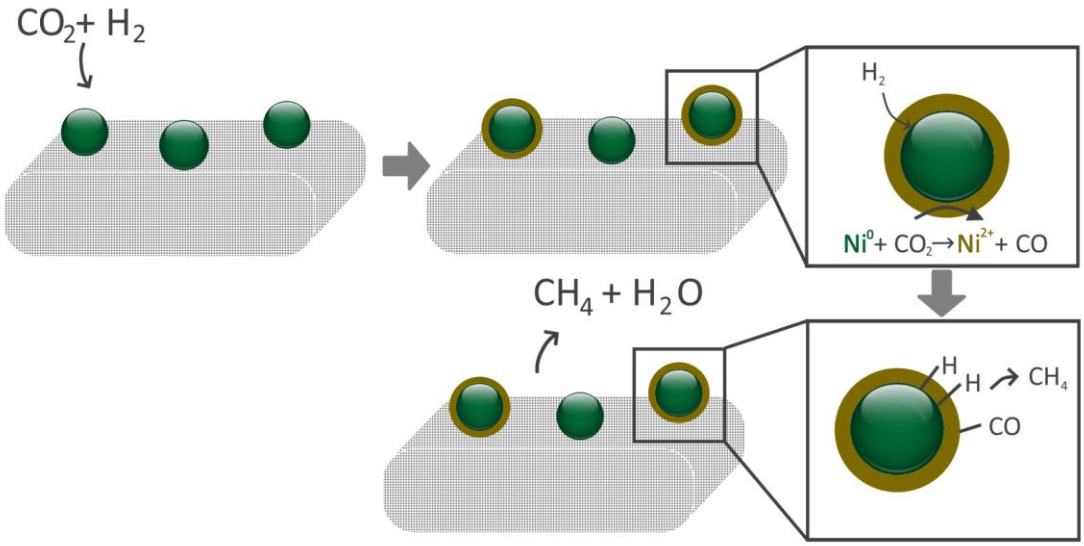

Figure 6.5. Schematic representation of the hypothesized mechanism of the Ni@NiO nanostructure formation during CO_2 methanation over Ni/AC−R catalyst.

4. Conclusions

In summary, we have reported *in situ* TEM investigation of our previously reported high-performing nickel nanoparticle catalyst supported on reduced activated carbon.[3] The unprecedented *in situ* formation of a NiO shell around the metallic Ni core was directly imaged and followed under CO_2 methanation conditions. An important proposed feature of real Ni@NiO core–shell catalyst nanoparticles is a coupling of the enhanced CO_2 adsorption/activation over the NiO shell with H_2 dissociation over Ni core, bringing reactants and intermediates together to facilitate CO_2 hydrogenation into CH_4. Hence, this work presents new opportunities for the judicious design and realization of high-performing and stable core–shell catalysts for CO_2 methanation reaction, in particular, and other interesting CO_2 hydrogenation reactions, in general.

5. Supplementary material

5.1 Additional TEM images

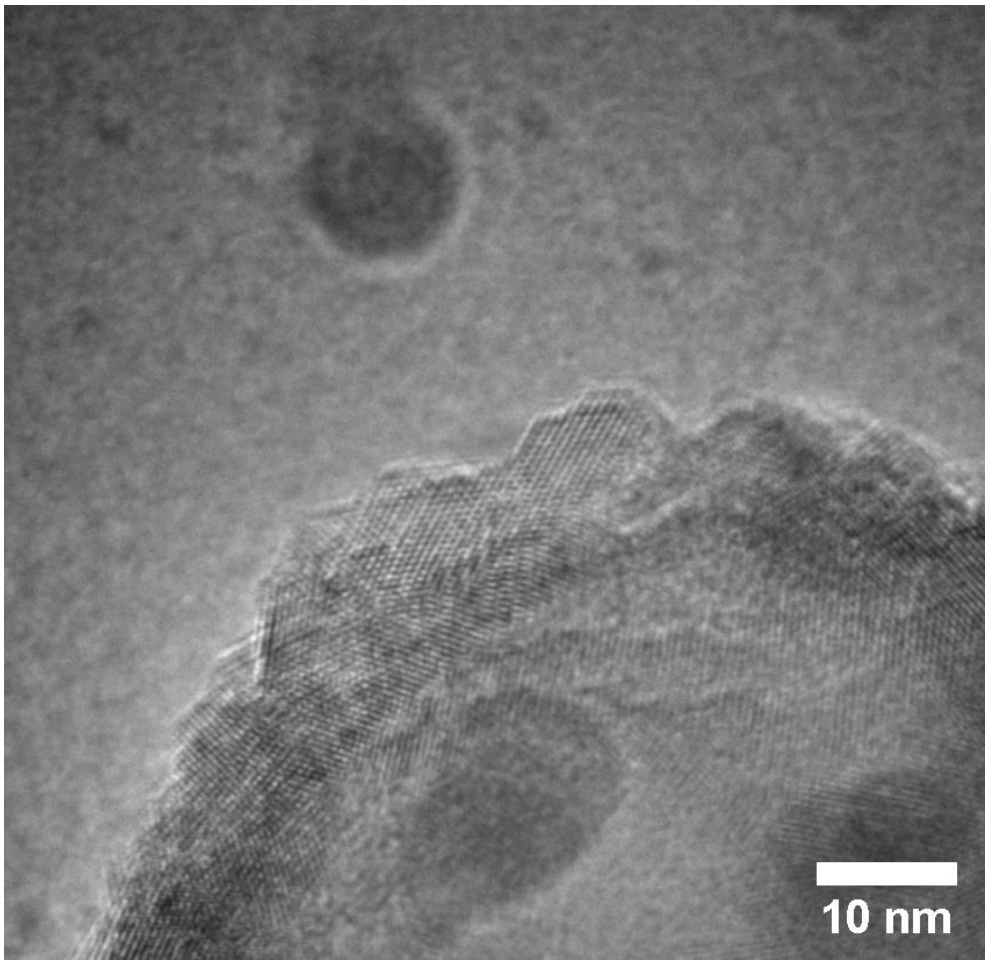

Figure 6S.1. High resolution *in situ* TEM image evidencing the polycrystalline NiO shell formation abound Ni nanoparticle catalyst during CO_2 methanation.

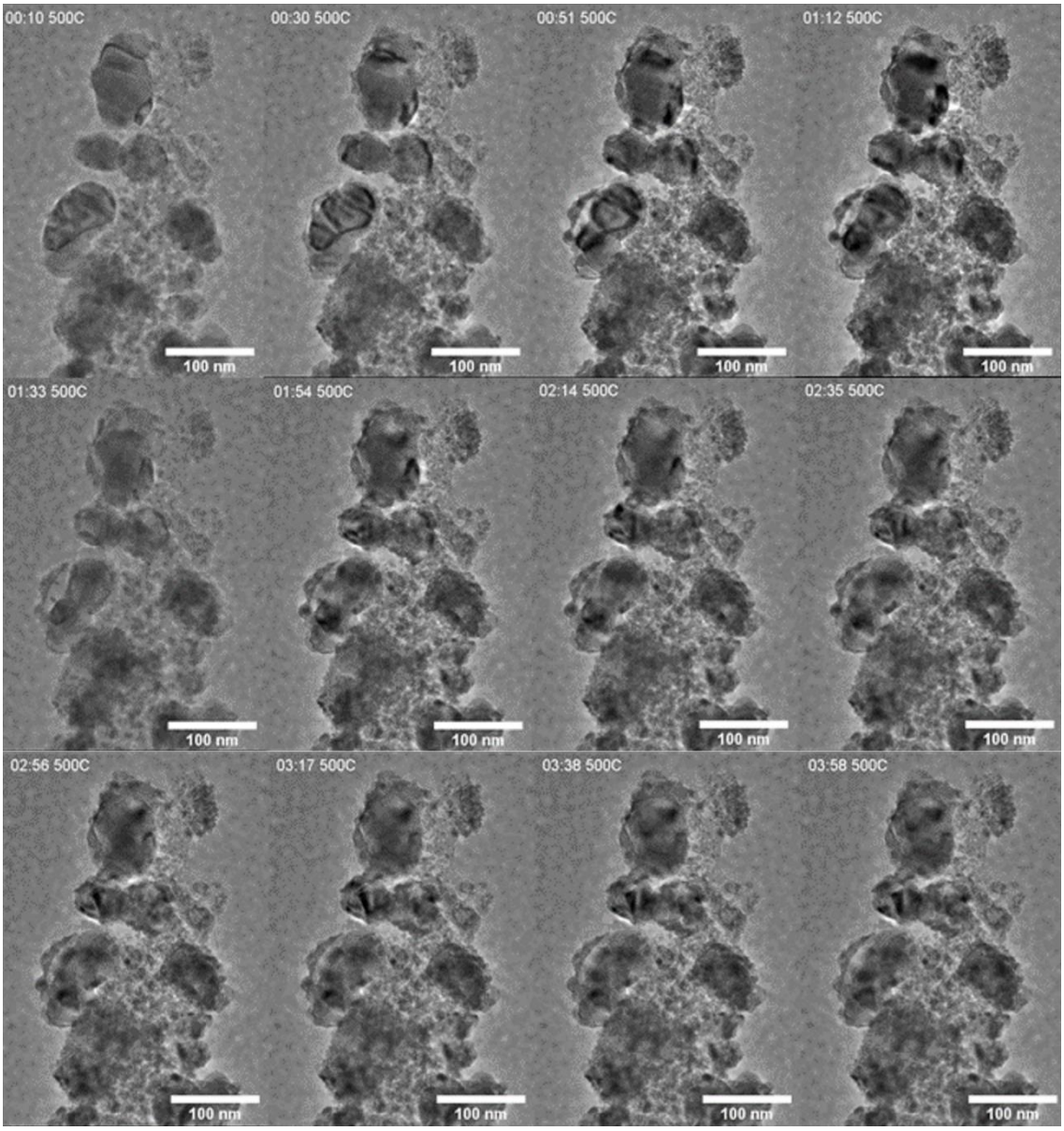

Figure 6S.2. Sequence of *in situ* TEM images of Ni nanoparticles oxidizing under a CO_2 environment at 500 °C. In sharp contrast to the formation of Ni@NiO core–shell catalyst nanoparticles under methanation reaction conditions (i.e., CO_2 + H_2), the entire oxidation of Ni catalyst nanoparticle into NiO is evidenced in the presence of CO_2 alone, i.e., without H_2.

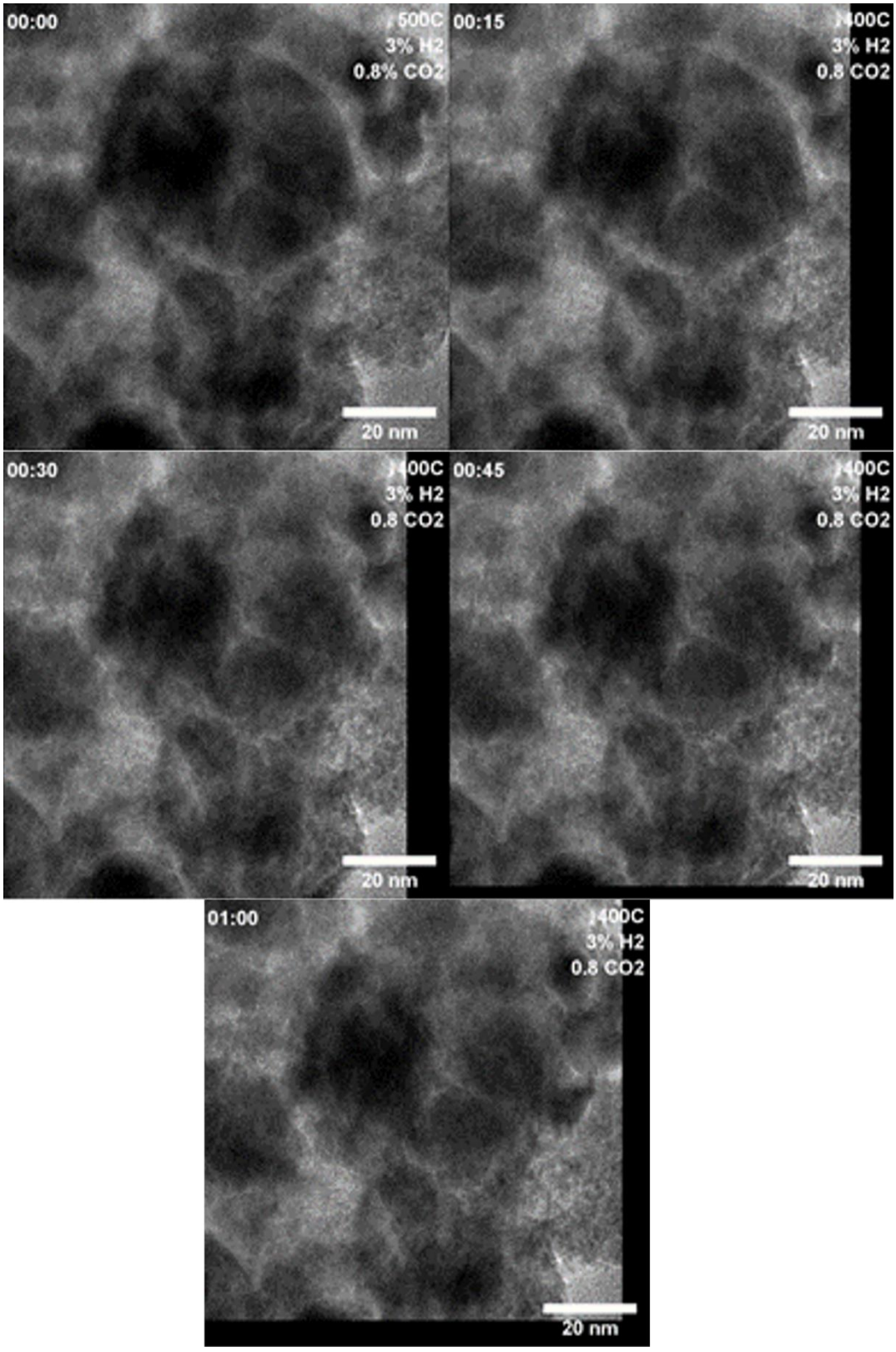

Figure 6S.3. Sequence of *in situ* TEM images of the catalyst deactivation during the temperature decrease.

5.2 Experiments Conditions

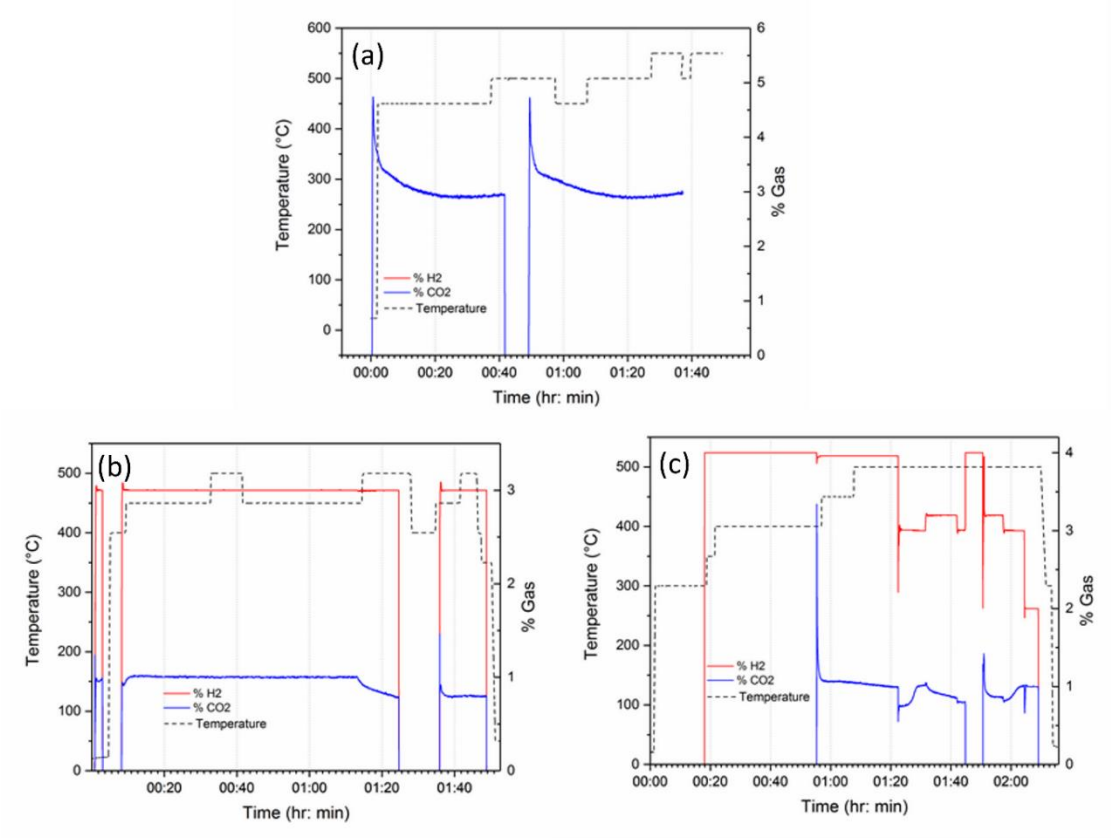

Figure 6S.4. Experimental conditions (temperature, CO_2 and CH_4 concentration) in the different experiments: (a) in the experiment with a flow of only CO_2; (b) in the experiment under reaction conditions without H_2 pre-treatment; and (c) in the experiment under reaction conditions with H_2 pre-treatment.

References

(1) Bailera, M.; Lisbona, P.; Romeo, L. M.; Espatolero, S. Power to Gas Projects Review: Lab, Pilot and Demo Plants for Storing Renewable Energy and CO_2. *Renew. Sustain. Energy Rev.* **2017**, *69* (November 2016), 292–312. https://doi.org/10.1016/j.rser.2016.11.130.

(2) Ashok, J.; Pati, S.; Hongmanorom, P.; Tianxi, Z.; Junmei, C.; Kawi, S. A Review of Recent Catalyst Advances in CO_2 Methanation Processes. *Catal. Today* **2020**, *356* (May), 471–489. https://doi.org/10.1016/j.cattod.2020.07.023.

(3) Gonçalves, L. P. L.; Sousa, J. P. S.; Soares, O. S. G. P.; Bondarchuk, O.; Lebedev, O. I.; Kolen'ko, Y. V.; Pereira, M. F. R. The Role of Surface Properties in CO_2 Methanation over Carbon-Supported Ni Catalysts and Their Promotion by Fe. *Catal. Sci. Technol.* **2020**, *10* (21), 7217. https://doi.org/10.1039/D0CY01254H.

(4) Miao, B.; Ma, S. S. K.; Wang, X.; Su, H.; Chan, S. H. Catalysis Mechanisms of CO_2 and CO Methanation. *Catal. Sci. Technol.* **2016**, *6* (12), 4048–4058. https://doi.org/10.1039/C6CY00478D.

(5) Goodarzi, F.; Kang, L.; Wang, F. R.; Joensen, F.; Kegnæs, S.; Mielby, J. Methanation of Carbon Dioxide over Zeolite-Encapsulated Nickel Nanoparticles. *ChemCatChem* **2018**, *10* (7), 1566–1570. https://doi.org/10.1002/cctc.201701946.

(6) Zhang, Z.; Tian, Y.; Zhang, L.; Hu, S.; Xiang, J. Impacts of Nickel Loading on Properties, Catalytic Behaviors of Ni/γ-Al_2O_3 Catalysts and the Reaction Intermediates Formed in Methanation of CO_2. *Int. J. Hydrogen Energy* **2019**, *44* (18), 9291–9306. https://doi.org/10.1016/j.ijhydene.2019.02.129.

(7) Ma, Y.; Liu, J.; Chu, M.; Yue, J.; Cui, Y.; Xu, G. Cooperation Between Active Metal and Basic Support in Ni-Based Catalyst for Low-Temperature CO_2 Methanation. *Catal. Letters* **2020**, *150* (5), 1418–1426. https://doi.org/10.1007/s10562-019-03033-w.

(8) Wen, X.; Xu, L.; Chen, M.; Shi, Y.; Lv, C.; Cui, Y.; Wu, X.; Cheng, G.; Wu, C. e.; Miao, Z.; Wang, F.; Hu, X. Exploring the Influence of Nickel Precursors on Constructing Efficient Ni-Based CO_2 Methanation Catalysts Assisted with in-Situ Technologies. *Appl. Catal. B Environ.* **2021**, *297* (April), 120486. https://doi.org/10.1016/j.apcatb.2021.120486.

(9) Westermann, A.; Azambre, B.; Bacariza, M. C.; Graça, I.; Ribeiro, M. F.; Lopes, J. M.; Henriques, C. Insight into CO_2 Methanation Mechanism over NiUSY Zeolites: An Operando IR Study. *Appl. Catal. B Environ.* **2015**, *174–175*, 120–125. https://doi.org/10.1016/j.apcatb.2015.02.026.

(10) Zhen, W.; Li, B.; Lu, G.; Ma, J. Enhancing Catalytic Activity and Stability for CO_2 Methanation on Ni@MOF-5 via Control of Active Species Dispersion. *Chem. Commun.* **2015**, *51*, 1728–1731. https://doi.org/10.1039/C4CC08733J.

(11) Gonçalves, L. P. L.; Serov, A.; McCool, G.; Dicome, M.; Sousa, J. P. S.; Soares, O. S. G. P.; Bondarchuk, O.; Petrovykh, D. Y.; Lebedev, O. I.; Pereira, M. F. R.; Kolen'ko, Y. New Opportunity for Carbon-Supported Ni-based Electrocatalysts: Gas-phase CO_2 Methanation. *ChemCatChem* **2021**, *13*, 1–11. https://doi.org/10.1002/cctc.202101284.

(12) Ha, N. N.; Thi, N.; Ha, T.; Khu, L. Van; Cam, L. M. Theoretical Study of Carbon Dioxide Activation by Metals (Co, Cu, Ni) Supported on Activated Carbon. *J Mol Model* **2015**, No. 21, 322. https://doi.org/10.1007/s00894-015-2864-1.

(13) Wang, W.; Duong-Viet, C.; Ba, H.; Baaziz, W.; Tuci, G.; Caporali, S.; Nguyen-Dinh, L.; Ersen, O.; Giambastiani, G.; Pham-Huu, C. Nickel Nanoparticles Decorated Nitrogen-Doped Carbon Nanotubes (Ni/N-CNT); A Robust Catalyst for the Efficient and Selective CO_2 Methanation. *ACS Appl. Energy Mater.* **2019**, *2* (2), 1111–1120. https://doi.org/10.1021/acsaem.8b01681.

(14) Gödde, J.; Merko, M.; Xia, W.; Muhler, M. Nickel Nanoparticles Supported on Nitrogen–Doped Carbon Nanotubes Are a Highly Active, Selective and Stable CO_2 Methanation Catalyst. *J. Energy Chem.* **2021**, *54*, 323–331. https://doi.org/10.1016/j.jechem.2020.06.007.

(15) Kangvansura, P.; Chew, L. M.; Saengsui, W.; Santawaja, P.; Poo-arporn, Y.; Muhler, M.; Schulz, H.; Worayingyong, A. Product Distribution of CO_2 Hydrogenation by K- and Mn-Promoted Fe Catalysts Supported on N-Functionalized Carbon Nanotubes. *Catal. Today* **2016**, *275*, 59–65. https://doi.org/10.1016/j.cattod.2016.02.045.

(16) Wang, W.; Chu, W.; Wang, N.; Yang, W.; Jiang, C. Mesoporous Nickel Catalyst Supported on Multi-Walled Carbon Nanotubes for Carbon Dioxide. *Int. J. Hydrogen Energy* **2015**, *41* (2), 967–975. https://doi.org/10.1016/j.ijhydene.2015.11.133.

(17) Gao, J.; Jiang, Q.; Liu, Y.; Liu, W.; Chu, W.; Su, D. S. Probing the Enhanced Catalytic Activity of Carbon Nanotube Supported Ni-LaOx Hybrids for the CO_2 Reduction Reaction. *Nanoscale* **2018**, *10*, 14207−14219. https://doi.org/10.1039/c8nr03882a.

(18) Romero-sáez, M.; Dongil, A. B.; Benito, N.; Espinoza-gonzález, R.; Escalona, N.; Gracia, F. CO_2 Methanation over Nickel-ZrO_2 Catalyst Supported on Carbon Nanotubes : A Comparison between Two Impregnation Strategies. *Appl. Catal. B Environ.* **2018**, *237* (March), 817–825. https://doi.org/10.1016/j.apcatb.2018.06.045.

(19) Tsiotsias, A. I.; Charisiou, N. D.; Yentekakis, I. V.; Goula, M. A. Bimetallic Ni-Based Catalysts for CO_2 Methanation: A Review. *Nanomaterials* **2021**, *11* (1), 1–34. https://doi.org/10.3390/nano11010028.

(20) Lee, Y. H.; Ahn, J. Y.; Nguyen, D. D.; Chang, S. W.; Kim, S. S.; Lee, S. M. Role of Oxide Support in Ni Based Catalysts for CO_2 Methanation. *RSC Adv.* **2021**, *11* (29), 17648−17657. https://doi.org/10.1039/d1ra02327f.

(21) Aldana, P. A. U.; Ocampo, F.; Kobl, K.; Louis, B.; Thibault-Starzyk, F.; Daturi, M.; Bazin, P.; Thomas, S.; Roger, A. C. Catalytic CO2 Valorization into CH4 on Ni-Based Ceria-Zirconia. Reaction Mechanism by Operando IR Spectroscopy. *Catal. Today* **2013**, *215*, 201–207. https://doi.org/10.1016/j.cattod.2013.02.019.

(22) Gonçalves, L. P. L.; Mielby, J.; Soares, O. S. G. P.; Sousa, J. P. S.; Petrovykh, D. Y.; Lebedev, O. I.; Pereira, M. F. R.; Kegnæs, S.; Kolen'ko, Y. V. Elucidating the CO_2 Methanation Mechanisms on High-Performing Carbon/Ceria-Supported Ni Catalysts Using Modulation Excitation *in situ* DRIFTS. *Prep.*

(23) Hao, Z.; Shen, J.; Lin, S.; Han, X.; Chang, X.; Liu, J.; Li, M.; Ma, X. Decoupling the Effect of Ni Particle Size and Surface Oxygen Deficiencies in CO_2 Methanation over Ceria Supported Ni. *Appl. Catal. B Environ.* **2021**, *286* (November 2020), 119922. https://doi.org/10.1016/j.apcatb.2021.119922.

(24) Huynh, H. L.; Zhu, J.; Zhang, G.; Shen, Y.; Tucho, W. M.; Ding, Y.; Yu, Z. Promoting Effect of Fe on Supported Ni Catalysts in CO_2 Methanation by in Situ DRIFTS and DFT Study. *J. Catal.* **2020**, *392*, 266–277. https://doi.org/10.1016/j.jcat.2020.10.018.

(25) Cárdenas-Arenas, A.; Quindimil, A.; Davó-Quiñonero, A.; Bailón-García, E.; Lozano-Castelló, D.; De-La-Torre, U.; Pereda-Ayo, B.; González-Marcos, J. A.; González-Velasco, J. R.; Bueno-López, A. Isotopic and in Situ DRIFTS Study of the CO_2 Methanation Mechanism Using Ni/CeO_2 and Ni/Al_2O_3 Catalysts. *Appl. Catal. B Environ.* **2020**, *265* (November 2019), 118538. https://doi.org/10.1016/j.apcatb.2019.118538.

(26) Giorgianni, G.; Mebrahtu, C.; Schuster, M. E.; Large, A. I.; Held, G.; Ferrer, P.; Venturini, F.; Grinter, D.; Palkovits, R.; Perathoner, S.; Centi, G.; Abate, S.; Arrigo, R. Elucidating the Mechanism of the CO_2 Methanation Reaction over Ni-Fe Hydrotalcite-Derived Catalysts via Surface-Sensitive *in situ* XPS and NEXAFS. *Phys. Chem. Chem. Phys.* **2020**, *22* (34), 18788−18797. https://doi.org/10.1039/d0cp00622j.

(27) Beaumont, S. K.; Alayoglu, S.; Specht, C.; Michalak, W. D.; Pushkarev, V. V.; Guo, J.; Kruse, N.; Somorjai, G. A. Combining in situ NEXAFS Spectroscopy and CO_2 Methanation Kinetics to Study Pt and Co Nanoparticle Catalysts Reveals Key Insights into the Role of Platinum in Promoted Cobalt Catalysis. *J. Am. Chem. Soc.* **2014**, *136* (28), 9898–9901. https://doi.org/10.1021/ja505286j.

(28) Strucks, P.; Failing, L.; Kaluza, S. A Short Review on Ni-Catalyzed Methanation of CO_2: Reaction Mechanism, Catalyst Deactivation, Dynamic Operation . *Chemie Ing. Tech.* **2021**, No. 10, 1−12. https://doi.org/10.1002/cite.202100049.

(29) Heine, C.; Lechner, B. A. J.; Bluhm, H.; Salmeron, M. Recycling of CO_2: Probing the Chemical State of the Ni(111) Surface during the Methanation Reaction with Ambient-Pressure X-Ray Photoelectron Spectroscopy. *J. Am. Chem. Soc.* **2016**, *138* (40), 13246−13252. https://doi.org/10.1021/jacs.6b06939.

(30) Giorgianni, G.; Mebrahtu, C.; Schuster, M. E.; Large, A. I.; Held, G.; Ferrer, P.; Venturini, F.; Grinter, D.; Palkovits, R.; Perathoner, S.; Centi, G.; Abate, S.; Arrigo, R. Elucidating the Mechanism of the CO_2 Methanation Reaction over Ni-Fe Hydrotalcite-Derived Catalysts: Via Surface-Sensitive in Situ XPS and NEXAFS. *Phys. Chem. Chem. Phys.* **2020**, *22* (34), 18788−18797. https://doi.org/10.1039/d0cp00622j.

(31) Mutz, B.; Carvalho, H. W. P.; Mangold, S.; Kleist, W.; Grunwaldt, J. D. Methanation of CO_2: Structural Response of a Ni-Based Catalyst under Fluctuating Reaction Conditions Unraveled by Operando Spectroscopy. *J. Catal.* **2015**, *327*, 48–53. https://doi.org/10.1016/j.jcat.2015.04.006.

(32) Zhou, G.; Liu, H.; Cui, K.; Jia, A.; Hu, G.; Jiao, Z.; Liu, Y.; Zhang, X. Role of Surface Ni and Ce Species of Ni/CeO_2 Catalyst in CO_2 Methanation. *Appl. Surf. Sci.* **2016**, *383*, 248–252. https://doi.org/10.1016/j.apsusc.2016.04.180.

(33) Du, Y.; Qin, C.; Xu, Y.; Xu, D.; Bai, J.; Ding, M.; Qin, C.; Xu, Y.; Xu, D.; Bai, J.; Ding, M. Ni Nanoparticles Dispersed on Oxygen Vacancies-Rich CeO_2 Nanoplates for Enhanced Low-Temperature CO_2 Methanation Performance. **2021**. https://doi.org/10.1016/j.cej.2021.129402.

(34) Vogt, C.; Groeneveld, E.; Kamsma, G.; Nachtegaal, M.; Lu, L.; Kiely, C. J.; Berben, P. H.; Meirer, F.; Weckhuysen, B. M. Unravelling Structure Sensitivity in CO_2 Hydrogenation over Nickel. *Nat. Catal.* **2018**, *1* (2), 127−134. https://doi.org/10.1038/s41929-017-0016-y.

Chapter 7

In situ investigation of the CO_2 methanation on carbon/ceria-supported Ni catalysts using modulation-excitation DRIFTS

Gonçalves, L. P. L.; Mielby, J.; Soares, O. S. G. P.; Sousa, J. P. S.; Petrovykh, D. Y.; Lebedev, O. I.; Pereira, M. F. R.; Kegnæs, S.; Kolen'ko, Yu. V. *In situ investigation of the CO_2 methanation on carbon/ceria-supported Ni catalysts using modulation-excitation DRIFTS*. Appl. Catal. B Environ. **2022**, 312, 121376.

Abstract

The development of novel cost-efficient, high-performing catalysts for CO_2 methanation that are active at low temperatures can be optimized through the understanding of the reaction mechanism on different materials. A series of Ni-based catalysts supported on CeO_2 and carbon/CeO_2 composites was investigated, showing that Ni nanoparticles supported on a carbon/CeO_2 composite with a 50:50 weight ratio and on pure CeO_2 have excellent low-temperature activity and achieve up to 87% CO_2 conversion with full selectivity towards CH_4 at 370 °C. Importantly, meaningful insights on the reaction mechanism were gathered for the different types of materials by using the emerging ME–PSD–DRIFTS technique. The study of the rate of formation/consumption of the various intermediates showed that the CO_2 methanation reaction follows a combination of the CO and formate pathways in the case of Ni on pure CeO_2; however, in the case of Ni on the carbon/CeO_2 composite, it follows only the formate pathway.

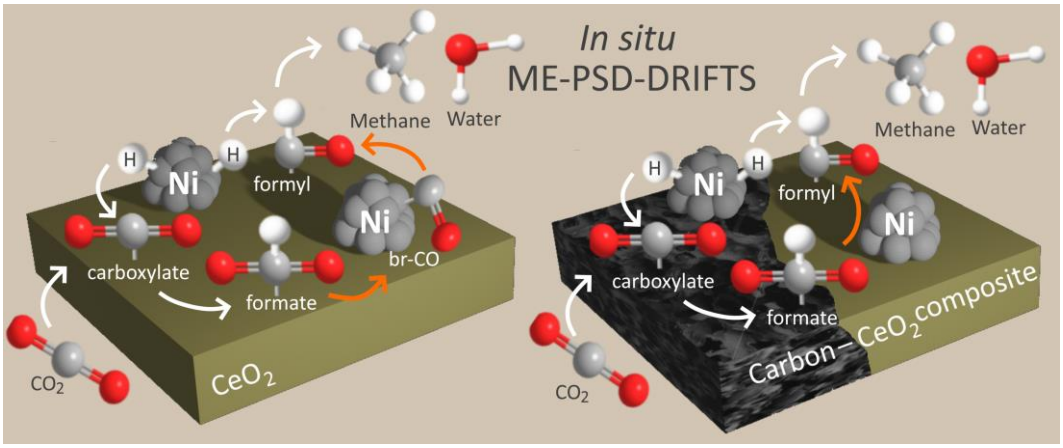

1. Introduction

The CO_2 methanation reaction ($CO_2 + 4H_2 \rightarrow CH_4 + 2H_2O$, $\Delta H_{298K} = -165$ kJ mol^{-1}) is the most thermodynamically favorable reaction of CO_2 hydrogenation, and is a promising way to convert anthropogenic CO_2 back to CH_4 fuel [1-4]. The hydrogenation proceeds through an eight-electron reduction process with consequent significant kinetic barriers, thus requiring the action of a catalyst. From the mechanistic perspective, extensive research has been conducted on CO_2 methanation. Nevertheless, the reaction mechanism is still vigorously debated, since it depends on the catalytic material and the hydrogenation conditions [1,3]. The most predominant mechanisms proposed in the literature can be grouped in two different categories: (i) the dissociative pathway, where CO_2 is dissociated into CO, which acts as the main intermediate, and (ii) the associative pathway, where CO_2 is molecularly adsorbed associatively with a H atom previously adsorbed on the surface, forming formate as an intermediate, i.e., without CO formation [3].

CO_2 methanation has played a significant role in understanding CO_2 hydrogenation and the associated development of catalysts. Importantly, researchers continue to exploit different catalysts to achieve high CO_2 conversion and complete selectivity towards CH_4. For example, a number of catalysts based on transition metals (Ni, Co, Fe) or platinum-group metals (Ru, Rh) dispersed on porous supporting materials have been developed [2,5-12]. Notably, Ni-based catalysts, compared to platinum-group metals, exhibit an optimal combination of activity, selectivity, and low price [2,5,6]. Despite the advances of using Ni catalysts for CO_2 methanation, a way to reduce the reaction temperature from the current ≥ 400 °C while preserving high catalytic performance remains a challenge.

One interesting approach to address this challenge is to develop Ni catalysts supported on novel materials. Traditionally, alumina (Al_2O_3) is used as supporting material for Ni methanation catalysts [13-15]. In contrast, we and other

researchers have focused on carbon supporting materials [2,5,16,17]. An exciting feature of these high-surface-area porous supports are their versatile surface properties [18]. Specifically, via modification of their surface chemistry, carbon materials can exhibit increased basicity, which improves the CO_2 coverage of the catalyst, since it is an acidic molecule, thus enhancing the CO_2 methanation performance at lower reaction temperatures [2]. Compared to the more common Ni supported on metal oxides, the research on Ni supported on carbon materials is less advanced, motivating a fundamental investigation of such alternative catalytic systems [2,5].

Among the metal-oxide supporting materials, despite being based on a rare-earth metal, ceria (CeO_2) has emerged as a promising alternative to Al_2O_3 because it enhances the metal–support interactions, leading to high dispersion of the resultant Ni nanoparticles over the support. Moreover, owing to the enhanced surface coverage by CO_2 species, enabled by the CeO_2 surface basicity, it improves the low-temperature catalytic performance of the catalysts in CO_2 methanation [19–26]. These positive effects of CeO_2 stimulated us to develop high-performing carbon/ceria-supported Ni catalysts for CO_2 methanation, as well as to conduct a comparative mechanistic study of CO_2 hydrogenation over these catalysts.

In this work, we report the successful precipitation synthesis of a composite supporting material consisting of reduced activated carbon (ACR) and CeO_2 (ACR–CeO_2) as well as pure CeO_2, followed by deposition of Ni nanoparticles via the incipient wetness impregnation route. An important feature of our findings is the remarkable reduction by 80 °C of the optimal temperature of the CO_2 methanation reaction, compared to that for a CeO_2-free Ni/ACR catalyst developed in our previous study [2], thus significantly improving the sustainability of the methanation approach without jeopardizing the catalytic performance. Furthermore, we conducted a detailed *in situ* modulation-excitation phase-sensitive-detection diffuse-reflectance infrared Fourier-transform spectroscopy (ME–PSD–DRIFTS) investigation of the methanation

over the newly synthesized high-performing Ni/ACR–CeO_2 and Ni/CeO_2 catalysts, to obtain key mechanistic insights.

2. Experimental

In the present work, we synthesized reduced activated carbon (AC−R) with Lewis base sites by heat-treatment of a commercial NORIT GAC 1240 PLUS activated carbon (CABOT) at 900 °C for 1 h under H_2 flow.[2] Pure CeO_2 and composite ACR–CeO_2 supporting materials were prepared by a precipitation method adapted from elsewhere.[26] Briefly, $Ce(NO_3)_3{\cdot}6H_2O$ is precipitated by NaOH under vigorous stirring, along with the addition of calculated amounts of AC−R for the composite ACR–CeO_2 synthesis. The 15% Ni nanoparticles were deposited onto as-synthesized supporting materials via incipient wetness impregnation using $Ni(NO_3)_3{\cdot}6H_2O$, followed by heat treatment to decompose nitrate, thus generating metallic Ni (Ni/CeO_2 and Ni/ACR−CeO_2). Additionally, a ACR−MgO composite was preliminarily tested and compared to ACR–CeO_2 (Appendix 6), but due to its lower performance, it was discarded from the study.

The synthesized materials were characterized by N_2 physisorption at −196 °C, powder X-ray diffraction (XRD), H_2 temperature programmed reduction (H_2–TPR), H_2–chemisorption, X-ray photoelectron spectroscopy (XPS), transmission electron microscopy (TEM), energy-dispersive X-ray spectroscopy in scanning TEM mode (STEM–EDX).

The activity, selectivity, and stability of the synthesized catalysts in CO_2 methanation were evaluated in a Microactivity XS15 system (PID Eng & Tech), using a fixed bed quartz reactor ($Ø_{int}$ = 1 cm). Outflow products were analyzed online using a GC 1000 gas chromatograph (DANI), equipped with a thermal conductivity detector (TCD) and a GSCarbonPLOT capillary column, while using He as the carrier gas and a continuous flow of N_2 as the internal standard. Each catalyst (100 mg) was diluted by inert SiC material, and then was pre-treated *in situ* under H_2 flow (40 $cm^3\ min^{-1}$) at its reduction temperature for

30 min, at 1 bar. After that, the reactor temperature was decreased to 100 °C under He (50 cm^3 min^{-1}), and then, the reactor was fed with 10% CO_2, 40% H_2 (the stoichiometric composition) and 50% He, with a total flowrate of 100 cm^3 min^{-1}. A temperature ramping from 100 to 500 °C was performed under reaction conditions to evaluate the catalytic properties of the catalysts at various temperatures. Additionally, isothermal time-on-stream (TOS) experiments were conducted under the same reaction conditions to evaluate the stability of the catalysts.

CO_2 adsorption and CO_2 methanation over the synthesized materials were probed using steady-state *in situ* diffuse reflectance infrared Fourier transform spectroscopy (DRIFTS) using a Nicolet iS50 FTIR spectrometer (Thermo Scientific), equipped with a Mercury-Cadmium-Telluride (MCT) detector and a high temperature reaction chamber (Harrick Scientific). Additionally, the CO_2 methanation over the prepared materials was investigated by *in situ* modulation excitation phase-sensitive detection DRIFTS (ME–PSD–DRIFTS) using the same spectrometer. The ME-PSD analysis highlight the species that change with the modulation frequency *f*. The collected spectra were converted into the so-called frequency domain by Fast Fourier Transform (FFT). The data was then filtered at the modulation frequency and converted into the phase-domain by Inverse Fast Fourier Transform (IFFT).

Detailed experimental information is presented in Chapter 2.

3. Results

3.1 CO_2 methanation over Ni/CeO_2 and Ni/ACR–CeO_2

In our previous study [2], a novel methanation catalyst with 15 wt% Ni loading over ACR having O-free Lewis basic sites (denoted as Ni/ACR) has been developed, exhibiting CO_2 conversion (X_{CO2}) of 76% and selectivity towards CH_4 (S_{CH4}) of 97%, but at a fairly high reaction temperature of 450 °C. To increase the conversion while lowering the reaction temperature, we sought to

introduce CeO_2, thus forming a composite supporting material with ACR. We began by optimizing the CeO_2 loading in the ACR–CeO_2 composite support. It was established that 15 wt% Ni catalyst supported on ACR–CeO_2 with ACR : CeO_2 weight ratio of 50 : 50 exhibits the optimal catalytic properties in CO_2 methanation (Figure 7S.1). Hence, we further conducted our studies with this catalyst, hereafter referred to as Ni/ACR–CeO_2.

With the optimized composite catalyst in hand, we investigated its methanation performance and compared it to a control 15 wt% Ni catalyst supported on pure CeO_2 (denoted as Ni/CeO_2).

Figure 7.1a,b show the obtained X_{CO2} and S_{CH4} results in the temperature range of 200–500 °C. Both catalysts start to convert CO_2 from ca. 200 °C reaching X_{CO2} = 50% at 280 °C, the so-called T_{50}.

Upon the temperature increase, the catalysts further achieve CO_2 conversions that are very close to the thermodynamic equilibrium, exhibiting maximum X_{CO2} of 85.7% (Ni/CeO_2) and 87.4% (Ni/ACR–CeO_2) at a notably low temperature of only 370 °C (Figure 7.1a). In terms of S_{CH4}, the catalysts also demonstrate values comparable to the thermodynamic equilibrium over the range of the studied temperatures, with $S_{CH4} \approx 100\%$ at maximum X_{CO2} (Figure 7.1a,b), with the only byproduct being CO. We finally investigated the stability of the catalysts through a long time-on-stream (TOS) testing at the best performing temperature of 370 °C. It was established that both the control Ni/CeO_2 and composite Ni/ACR−CeO_2 demonstrate excellent stability over 90 h on stream with no loss in either X_{CO2} or S_{CH4} (Figure 7.1c,d). Importantly, a comparison of the catalytic properties between the new carbon/ceria-containing Ni/ACR–CeO_2 and our previously reported carbon-containing Ni/ACR [2] (Figure 7.1) evidently highlights that the compositing of ACR with CeO_2 not only leads to a significant improvement in the methanation performance but also simultaneously lowers the optimal reaction temperature by 80 °C (from 450 °C for Ni/ACR to 370 °C for Ni/ACR–CeO_2). Moreover, the compositing of ACR with CeO_2 leads to an improvement in stability at the

respective optimal temperature of the resultant Ni/ACR–CeO_2 catalyst, relative to that of Ni/ACR [2] (Figure 7.1).

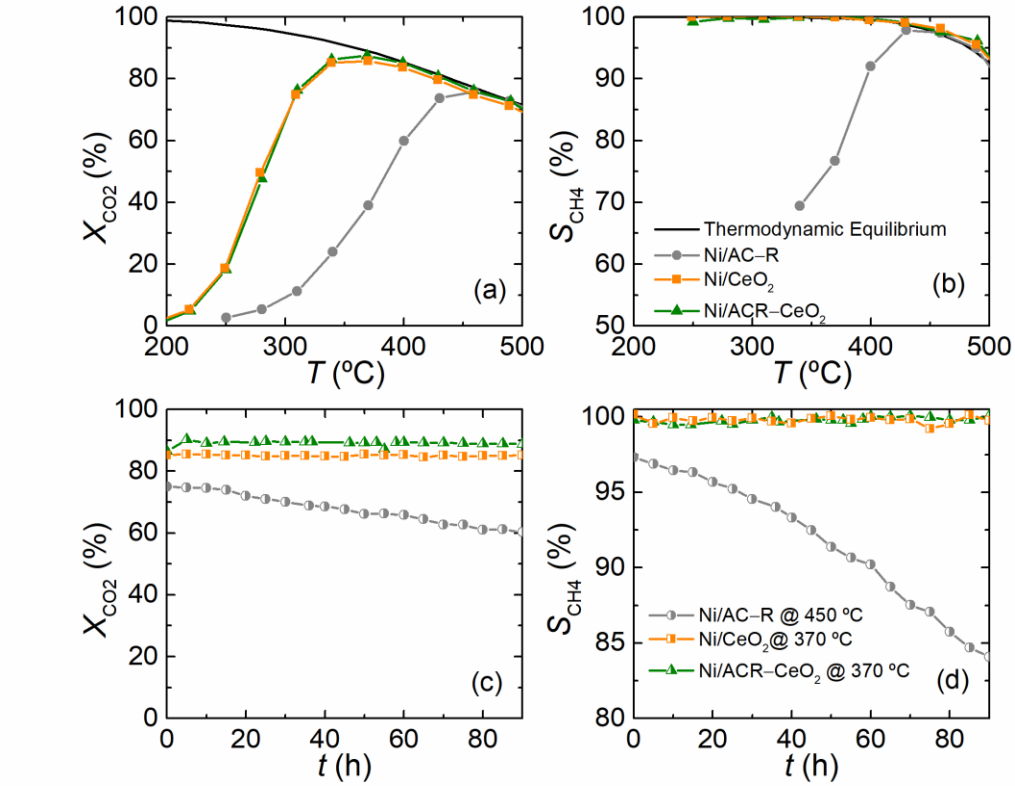

Figure 7.1. Comparison of X_{CO2} (a) and S_{CH4} (b) as a function of reaction temperature, together with the stability testing results in terms of X_{CO2} (c) and S_{CH4} (d) over 90 h TOS of the new Ni/CeO_2 and Ni/ACR-CeO_2 catalysts in comparison with previously reported ceria-free Ni/AC−R[2]. The thermodynamic equilibrium curves were calculated using a model based on the minimization of Gibbs free-energy of the existing species. Methanation conditions: P = 1 bar; $WHSV$ = 60 000 $cm^3\ g^{-1}\ h^{-1}$; CO_2 : H_2 (V:V) = 1 : 4.

3.2 Characterization of the catalysts

Our catalytic testing reveals that both Ni/CeO_2 and Ni/ACR–CeO_2 exhibit similarly excellent catalytic properties at reasonably low reaction temperatures, despite being based on different supporting materials. Therefore, we characterized the catalysts to determine the parameters that govern the methanation performance.

Even though Ni/CeO_2 and Ni/ACR–CeO_2 have similar catalytic properties (Figure 7.1), the data presented in Table 7.1 demonstrate that the catalysts exhibit quite different textural properties. The textural properties of the

synthesized materials were estimated using Brunauer–Emmett–Teller (BET) and Barrett–Joyner–Halenda (BJH) methods. Pure CeO_2 support has a relatively low specific surface area (S_{BET}) of 104 $m^2\ g^{-1}$, while the pure ACR support has about 7-fold higher S_{BET} = 784 $m^2\ g^{-1}$. As expected, the composite ACR–CeO_2 exhibits a S_{BET} = 373 $m^2\ g^{-1}$ that is higher than that of pure CeO_2, but lower than that of pure ACR. This trend is sustained for the respective Ni catalysts supported on the two materials, exhibiting a decreasing order in S_{BET} Ni/ACR–CeO_2 > Ni/CeO_2 (Table 7.1). The addition of Ni leads to a slight decrease in S_{BET} compared to the respective supporting materials (Table 7.1). Both CeO_2 and ACR–CeO_2 supports, and the derivative catalysts present Type IV isotherms (Figure 7S.2); the pore-size-distribution data (Figure 7S.3) reveal that Ni/CeO_2 exhibits a higher number of pores having larger width, while Ni/ACR−CeO_2 has a peak in the smaller width range, also containing pores with diameters higher than 5 nm.

Next, we probed the metal–support interactions and metallic surface areas of Ni/CeO_2 and Ni/ACR–CeO_2. The comparison of hydrogen temperature-programmed reduction (H_2–TPR) profiles of Ni/CeO_2 and Ni/ACR–CeO_2 demonstrate different metal–support interactions between Ni nanoparticles and the supporting materials (Figure 7S.4a). Specifically, Ni/CeO_2 exhibits a large peak at 360 °C with a shoulder at 404 °C, as well as two small shoulders at 334 °C and 464 °C. In contrast, Ni/ACR–CeO_2 exhibits a large peak at a lower temperature of 320 °C with two high-temperature shoulders at 392 °C and 502 °C. Apparently, Ni/CeO_2 is largely composed of Ni species that exhibit a stronger interaction with pure CeO_2 support, compared to that in composite Ni/ACR–CeO_2. Regarding the Ni surface area (S_M), measured using H_2 pulse chemisorption, it was estimated that Ni/ACR–CeO_2 exhibits more than 1.5 times higher metallic Ni surface than does Ni/CeO_2 (Table 7.1). The H_2–TPR of the supporting materials was also assessed (Figure 7S.4b) and it was observed that the H_2 consumed for CeO_2 reduction is minimal when comparing to the H_2 consumed for the reduction of the Ni-based catalysts. Additionally, the analysis of the H_2−TPR profiles indicate that the ACR−CeO_2 support is a homogeneous mixture that interacts in a way that the reduction profile of the Ni/ACR−CeO_2

sample is different than that of the other two supports (CeO_2 and ACR), and not a combination of both Ni/CeO_2 and Ni/ACR [2] H_2-TPR profiles.

To gain structural insight into the synthesized materials, we further investigated their phase composition using powder X-ray diffraction (XRD). According to the XRD patterns (Figure 7S.5), the as-synthesized pure and composite supports contain cubic CeO_2 phase (ICDD #04-006-1932). In contrast, the respective Ni catalysts additionally contain cubic metallic Ni (ICDD #04-016-4761), with no secondary phases being present. There is possibly a graphitic carbon peak, but since it should be present at 28 °, overlapping with a peak from CeO_2, it is impossible to access its presence. The average size of Ni and CeO_2 crystallites was assessed from XRD data using the Scherrer equation (Table 7.1), and the size of Ni crystallites in Ni/CeO_2 (ca. 9 nm) was estimated to be nearly 2 times larger than in Ni/ACR–CeO_2 (ca. 5 nm), which is consistent with the smaller S_M of Ni/CeO_2.

Table 7.1. Textural properties [specific surface area (S_{BET}), and total pore volume (V_p)], average size of CeO_2 crystallites ($d_{c,CeO2}$), and Ni crystallites ($d_{c,Ni}$), metallic Ni surface area (S_M), temperature at which X_{CO2} = 50% (T_{50}), and maximum X_{CO2}, attained at 450 °C for Ni/AC−R[2] and 370 °C for Ni/CeO_2 and Ni/ACR−CeO_2.

	S_{BET} ($m^2\ g^{-1}$)	$V_{P,P/P0=0.95}$ ($cm^3\ g^{-1}$)	$d_{c,Ni}$ (nm)[b]	$d_{c,CeO2}$ (nm)[b]	S_M ($m^2\ g_{cat}^{-1}$)[c]	T_{50} (°C)	Max X_{CO2} (%)
AC−R[2]	784	0.48	–	–	–	–	0
CeO_2	104	0.17	–	7	–	–	12
ACR–CeO_2	373	0.33	–	6	–	–	11
Ni/AC−R[2]	656	0.41	8	--	2.73	385	76
Ni/CeO_2	82	0.14	9	7	1.66	280	86
Ni/ACR–CeO_2	386	0.30	5	5	2.57	280	87

[a]Estimated by N_2 physisorption. [b]Estimated from XRD data using Scherrer equation. [c]Estimated by H_2 pulse chemisorption.

X-ray photoelectron spectroscopy (XPS) analysis revealed that both catalysts, Ni/CeO_2 and Ni/ACR–CeO_2, exhibited two different Ni phases, observed from the deconvolution of the XPS data for Ni $2p_{3/2}$ (Figure 7.2). The lower energy component (853.0 ± 0.1 eV) is assigned to Ni^0 in metallic Ni species, while the components at 854.4 ± 0.2 eV and 856.4 ± 0.1 eV are consistent with Ni^{2+} in nickel-oxide phase, and the ones at 861.3 ± 0.3 eV and 864.3 ± 0.1 eV are

satellite peaks from Ni^{2+}. The Ni $2p_{3/2}$ spectral envelopes of the catalysts resemble the typical spectra for nanoscale oxidation layers on Ni and Ni compounds, being consistent with a thin, predominantly Ni^{2+}, nickel oxide layer on metallic Ni [5,28–30]. The binding energies (BEs) of fitting components are presented in Table 7S.1 and the relative atomic percentages (at%) of Ni^0 and Ni^{2+} are presented in Table 7S.2. The relative atomic percentage of Ni^0 is similar in Ni/ACR–CeO_2 and Ni/CeO_2 catalysts, at 4.2 at% and 4.4 at%, respectively (Table 7S.2).

The Ce 3d spectra also revealed the presence of mixed Ce phases (Figure 7.2) in both samples. The spectra can be represented as five pairs of doublets, identified in Figure 7.2 as u and v for the Ce $3d_{3/2}$ and Ce $3d_{5/2}$ spin–orbit components, with spin–orbit splitting of 18.4 ± 0.5 eV for all the samples, consistent with those found in the literature [31,32]. These spectra were fitted using a method similar to that reported by Zhang *et al.* [32] where the u''' peak is fixed and the remaining peaks are fitted according to the u''' position.

The v^0, u^0, v′, and u′ are attributed to Ce^{3+}, while the highest biding energy peaks, v‴ and u‴, are attributed to the primary components of Ce^{4+}, and the remaining v, u, v″, and u″, are identified as "shake-down" states, as reported by Mullins *et al*. [31,33] Table 7S.2 presents the BEs of each of these components. Importantly, we note that there is a small overlap of the Ni $2p_{1/2}$ components (orange lines and symbols below 881 eV in Figure 7.2) and the low-BE components in the Ce 3d spectra. This overlap was accounted for by including in the Ce 3d fitting procedure Ni $2p_{1/2}$ components (orange lines in Figure 7.2), with fixed parameters based on the more reliable fits in the Ni $2p_{3/2}$ region.

The Ce 3d peaks in Ni/ACR–CeO_2 are noticeably narrower than those in Ni/CeO_2, which likely indicates that ceria nanoparticles are in a more uniform electrostatic environment in Ni/ACR–CeO_2, where they are in a good electrical contact with the carbon substrate.

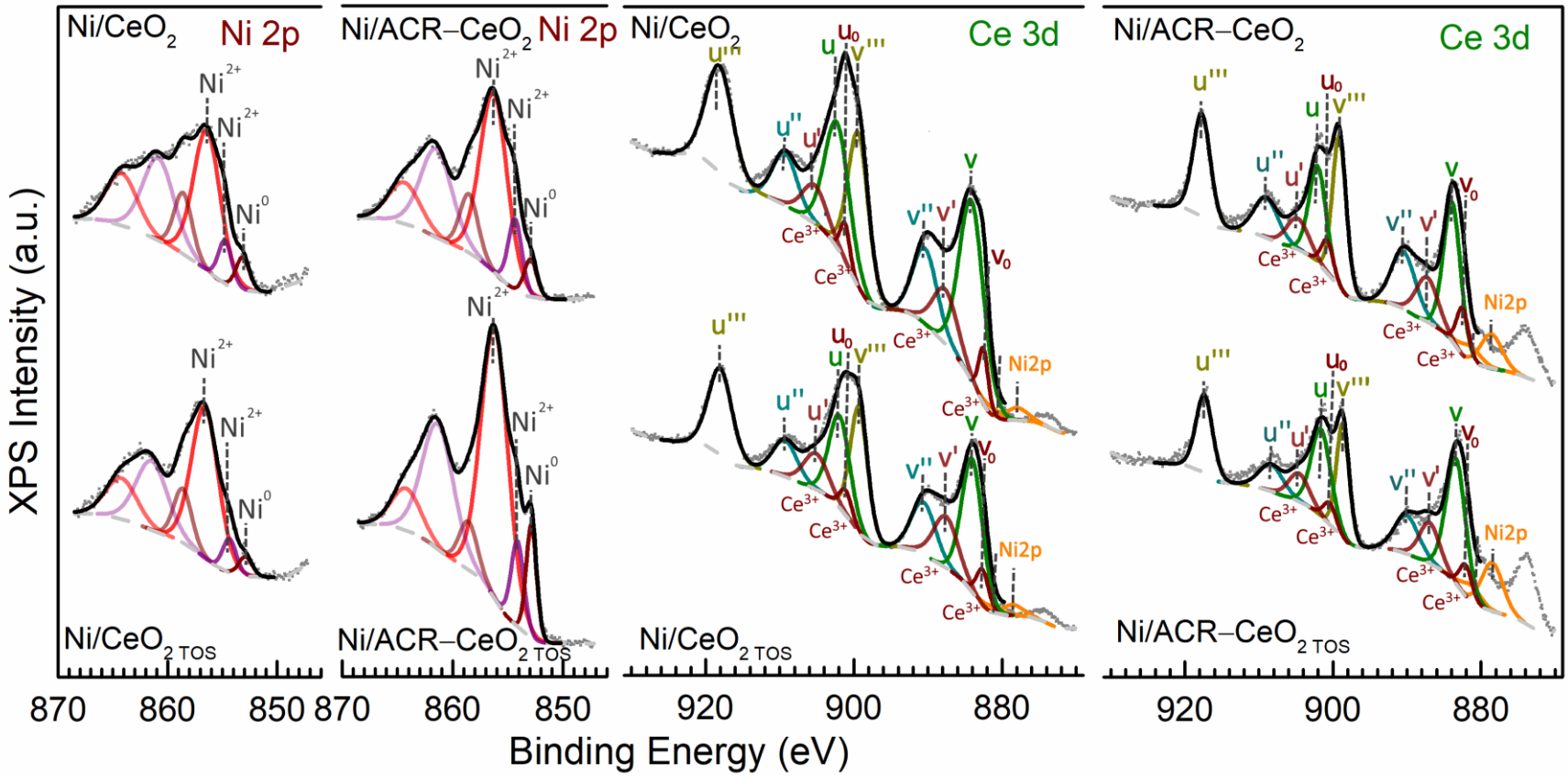

Figure 7.2. High-resolution XPS data for the Ni $2p_{3/2}$ and Ce 3d region collected from as-synthesized and TOS-tested Ni/CeO_2 and $Ni/ACR–CeO_2$. Symbols: raw data; black lines: overall fits; colored lines: fits of individual components; dashed lines: background.

The amount of Ce^{4+} and reduced Ce^{3+} is quantified in Table 7S.2. Interestingly, the Ni/ACR–CeO_2 catalyst exhibits a higher relative at% of Ce^{3+} (20.5 at%) compared to Ni/ACR–CeO_2 that contains 16.4 at% Ce^{3+}.

The C 1s spectra of Ni/ACR–CeO_2 were also analyzed, and the results are presented in Figure 7S.6 [34,35].

Interested in understanding the microstructural properties of the catalysts, we then conducted transmission electron microscopy (TEM) and energy-dispersive X-ray spectroscopy in scanning STEM mode (STEM–EDX) analyses. These studies reveal metallic Ni nanoparticles well-dispersed over nanocrystalline CeO_2 and amorphous-like ACR. Figure 7.3a shows TEM image of Ni nanoparticles in Ni/CeO_2, where it is possible to distinguish only some large Ni particles (ca. 30–50 nm) dispersed over CeO_2 support. Figure 7.3e shows Ni nanoparticles dispersed on composite ACR–CeO_2 support in Ni/ACR–CeO_2, wherein the Ni particles (ca. 5–10 nm) dispersed on ACR and some larger Ni particles (ca. 30–50 nm) on CeO_2 are observed. It is important to note that the imaging contrast between the Ni and CeO_2 nanoparticles is very low, thus it is difficult to differentiate the two types of nanoparticles in the electron microscopy images. Therefore, the size ranges indicated are merely representative of the observed identifiable nanoparticles, leading to a gap between the Ni nanoparticles sizes from TEM and those estimated by XRD, which is more representative.

Although it is difficult to distinguish the smaller Ni particles on the CeO_2 support due to the low contrast on the TEM images, the respective STEM–EDX maps evidence that there are also small Ni particles dispersed on CeO_2 material in both Ni/CeO_2 and Ni/ACR–CeO_2 catalysts (Figure 7.3d,h). A closer look at CeO_2 supporting material in Ni/CeO_2 (Figure 7.3c) and Ni/ACR–CeO_2 (Figure 7.3g) catalysts reveals that the ceria consists of agglomerated CeO_2 nanoparticles (ca. 5–10 nm), preferentially faceted by the {110} plane.

Interestingly, high-resolution TEM (HRTEM) imaging of Ni nanoparticles in Ni/CeO_2 and Ni/ACR–CeO_2 reveals that the particles in both catalysts exhibit

Ni@NiO core-shell appearance. As an example, Figure 7.4a,b show HRTEM images of a Ni nanoparticle in Ni/ACR–CeO_2 catalyst, together with the corresponding Fourier transform (FT) patterns for the Ni core and NiO shell.

Furthermore, multiple twinning of the Ni nanoparticle can be observed in the HRTEM images, marked by white arrow heads.

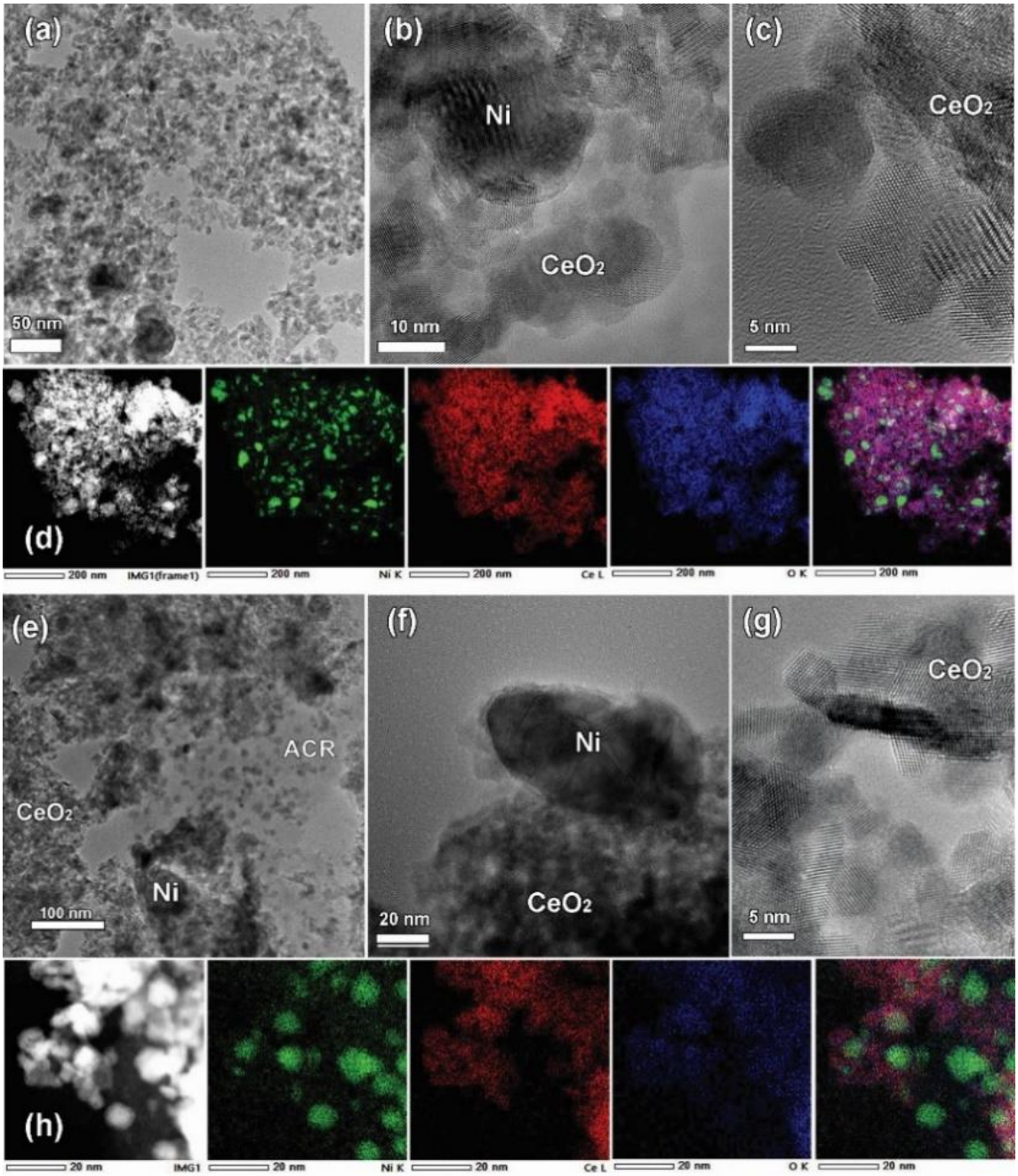

Figure 7.3. TEM images of Ni nanoparticles dispersed on CeO_2 (a) and ACR–CeO_2 (e) supporting materials, together with the representative HRTEM images of Ni and CeO_2 nanoparticles in the Ni/CeO_2 (b,c) and Ni/ACR–CeO_2 (f,g) catalysts. Low-magnification STEM images of the Ni/CeO_2 (d) and Ni/ACR–CeO_2 (h) catalysts, together with the respective STEM–EDX maps for Ni, Ce, O and their mixture.

Even though there was no loss in X_{CO2} and S_{CH4} over 90 h of TOS testing (Figure 7.1c,d), we decided to investigate the impact of the reaction conditions on the microstructure and chemical composition of the catalysts by means of electron microscopy and XPS.

The Ni $2p_{3/2}$ spectra (Figure 7.2) of the samples after TOS testing (Ni/$CeO_{2\,TOS}$ and Ni/ACR–$CeO_{2\,TOS}$) include fitting components at BEs similar to those of the components in the spectra of fresh Ni/CeO_2 and Ni/ACR–CeO_2 catalysts. Considering the relative Ni^0 atomic content (Table 7S.2), however, we observed that it decreases to 2.8 at% (cf. 4.4 %) in the case of Ni/$CeO_{2\,TOS}$ and, on the contrary, increases to 7.4 at% (cf. 4.2 at%) in the case of Ni/ACR–$CeO_{2\,TOS}$. In the Ce 3d spectra (Figure 7.2), again the positions of the peaks remain similar for both catalysts after 90 h of TOS, but there are differences in the Ce^{3+}/Ce^{4+} ratio before and after TOS in both Ni/CeO_2 and Ni/ACR–CeO_2. The Ce^{3+} atomic content in Ni/CeO_2 increases to 21.3 at% (cf. 16.4 at%), while in Ni/ACR–CeO_2, it remains approximately constant with 19.9 at% (cf. 20.5 at%).

From Figure 7S.8a-d, one can see that the TOS-tested Ni/CeO_2 maintains the microstructure of the Ni nanoparticles dispersed over the ceria support composed by small CeO_2 nanoparticles (ca. 5–10 nm), similar to that in pristine Ni/CeO_2 (Figure 7.3a). In contrast, TOS-tested Ni/ACR–CeO_2 undergoes significant microstructural changes within CeO_2 support. Specifically, Figure 7S.8e evidences the appearance of CeO_2 particles with a needle-like shape after 90 h of methanation. Such nanoneedles were not observed in pristine Ni/ACR–CeO_2 (Figure 7.3e) or pristine and TOS-tested Ni/CeO_2 (Figure 7.3a, Figure 7S.8a).

Notably, a closer look at Ni particles in TOS-tested Ni/CeO_2 (Figure 7S.8c) and Ni/ACR–CeO_2 (Figure 7.4c,d) indicates a preservation of Ni@NiO core-shell nanostructure of the catalyst after prolonged methanation.

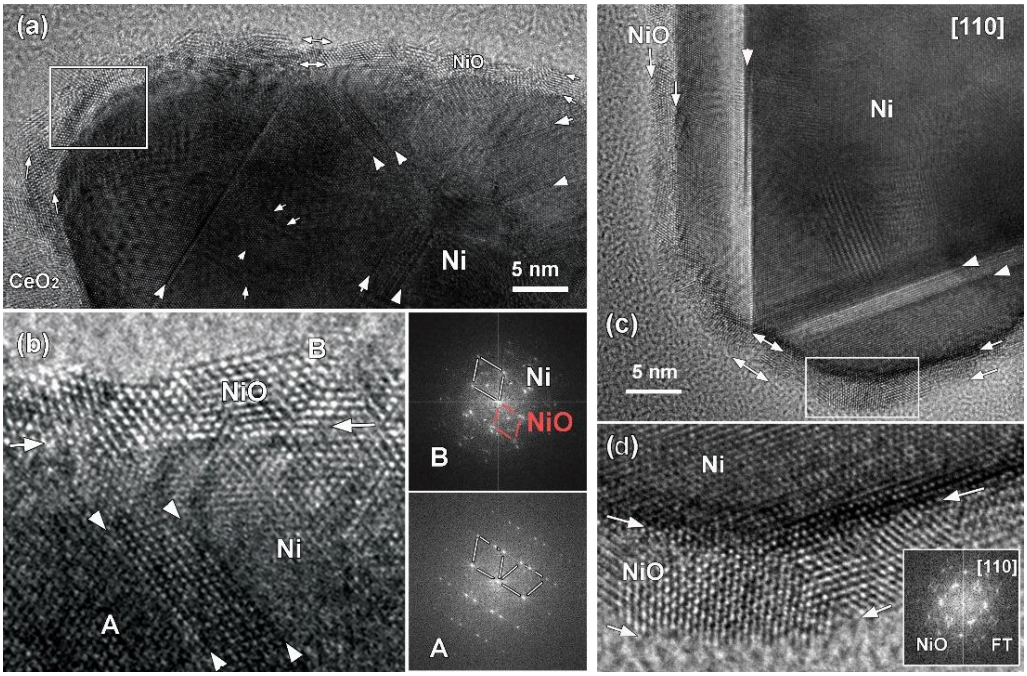

Figure 7.4. HRTEM imaging of the surface of a single Ni nanoparticle in the as-synthesized Ni/ACR-CeO_2 catalyst (a) and zoom-in (white rectangle) image (b) and in the same catalyst after its TOS testing for 90 h (c,d), revealing the core-shell appearance of the nanoparticles. The insets in (b,d) show the FT patterns from the corresponding regions. The white arrows mark the NiO shell and the white arrow heads depict the twinning within the Ni nanoparticles.

3.3 Probing the mechanism of CO_2 methanation by *in situ* DRIFTS

Having in hand two well-characterized high-performing methanation catalysts, we further conducted *in situ* DRIFTS studies to elucidate the reaction mechanism over Ni/CeO_2 and Ni/ACR-CeO_2. This technique is used to understand the reaction mechanism in heterogeneous catalysis, probing the adsorbed species on the catalysts under reaction conditions. There are some drawbacks of this technique. Specifically, it detects not only the intermediate species but also the sample background, noise, and spectator species, making it difficult to distinguish what are the real intermediates of the reaction [36,37].

Furthermore, the intermediate species have a short lifetime, making it even more difficult to differentiate them from the remaining species, which are present under steady-state conditions. Fortunately, the modulation-excitation (ME) technique offers an interesting solution for overcoming the aforementioned drawbacks. It is based on the introduction of a rapid periodic perturbation on the testing system, to which only the intermediate species of

the reaction respond. The resultant spectroscopic signal is then analyzed by phase-sensitive detection (PSD) technique to enhance the signal-to-noise ratio and to extract the information about intermediate species that responded to the modulation signal, thus avoiding the signal from the spectator species [10,36–40].

We started by performing steady-state *in situ* DRIFTS for CO_2 adsorption and then for CO_2 methanation at 250, 300, and 350 °C. In this temperature range, the X_{CO2} goes from low to almost complete. Figure 7S.9 shows the full range spectra for each experiment, along with a discussion of the observed trends for hydroxyl groups, gaseous CO_2, and gaseous CH_4 [41]. Figure 7.5 displays a zoom-in of the region below 2000 cm^{-1}, which carries important information about the CO_2 adsorption and methanation mechanisms, while Table 7.2 summarizes the respective band assignment. During CO_2 adsorption (Figure 7.5a,c), two bands detected at 1500 and 1370 cm^{-1} (ν_{as} / ν_s) can be attributed to formate (HCOO) species, which are probably close to a reduced Ce site in CeO_2, because they have a low $\Delta_{as\text{-}s}$ = 130 / 150 cm^{-1} [10,26]. Two other bands are observed at 1600 and 1280 cm^{-1} (ν_{as} / ν_s), that can be assigned to bi-dentate carbonates (b–CO_3), along with the band at 1030 cm^{-1} [10,26]. Moreover, a small band at 1415 cm^{-1} is also observed in the spectrum of Ni/CeO_2 at 250 °C, which can be attributed to poly-dentate (p–CO_3) carbonates Interestingly, a small amount of methoxy species (OCH_3) are present in the CO_2 adsorption spectra without H_2 being present, corresponding to the bands at 1080–1060 cm^{-1} [24,25]; therefore, residual H_2 should be present on the Ni nanoparticles from the reduction pre-treatment which might lead to the methoxy formation during CO_2 adsorption step.

When H_2 is introduced into the gas flow to mimic the methanation conditions (Figure 7.5b,d), the bands corresponding to b–CO_3 and HCOO remain at similar wavenumbers as during the CO_2 adsorption probing; however, the difference in intensity between them decreases. Furthermore, the methoxy bands increase and a new band appears at 1710 cm^{-1} for both catalysts that can be attributed to the formation of formyl (CHO) groups [24].

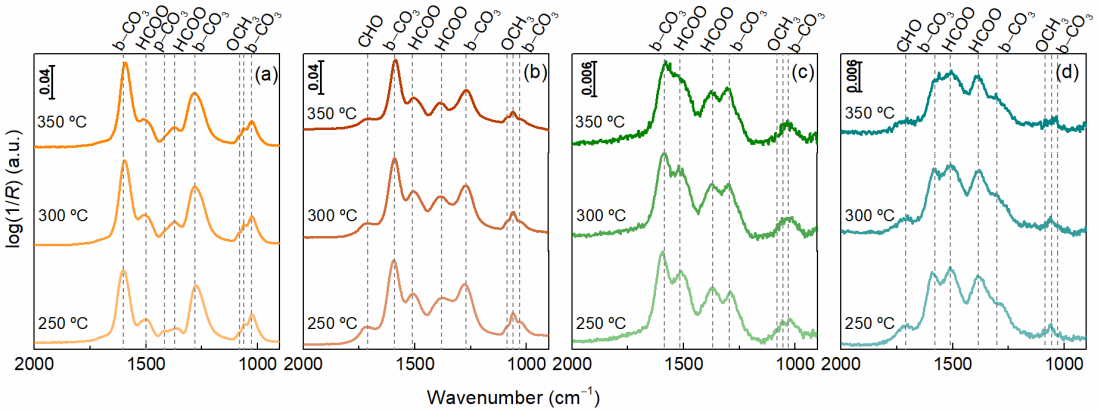

Figure 7.5. Steady-state *in situ* DRIFTS studies of CO_2 adsorption and methanation over Ni/CeO_2 (a,b) and Ni/ACR–CeO_2 (c,d) catalysts. Experimental conditions for CO_2 adsorption: P = 1 bar; CO_2 flowrate of 2.5 $cm^3\ min^{-1}$; N_2 flowrate of 100 $cm^3\ min^{-1}$; m_{cat} = 15 mg. Experimental conditions of CO_2 methanation: P = 1 bar; CO_2 flowrate of 2.5 $cm^3\ min^{-1}$; 10%H_2/N_2 gas mixture flowrate of 100 $cm^3\ min^{-1}$; m_{cat} = 15 mg. The dashed lines indicate the positions of the observed peaks.

To gain a deeper understanding of the reaction mechanism, we next conducted modulation-excitation phase-sensitive detection DRIFTS (ME–PSD–DRIFTS), allowing for a better signal-to-noise ratio plus distinguishing spectator and intermediate species. The modulated conditions applied in the experiments were a change in flowrate from A (CO_2 = 2.5 $cm^3\ min^{-1}$ and 10%H_2/N_2 = 100 $cm^3\ min^{-1}$) to B (CO_2 = 2.5 $cm^3\ min^{-1}$ and N_2 = 100 $cm^3\ min^{-1}$). Figure 7.6 shows the phase-resolved spectra of the modulation excitation *in situ* DRIFTS studies conducted for Ni/CeO_2 at 250, 300, and 350 °C. A comparison of Figure 7.5 and Figure 7.6 show that the data from the ME–PSD–DRIFTS experiments look quite different from those of the steady state experiments. In particular, three main differences can be identified: (*i*) the peak detected in the steady-state spectra at 1700 cm^{-1} (Figure 7.5b) is actually caused by a convolution of 2 peaks that are out-of-phase during modulation (Figure 7.6); (*ii*) instead of 4 peaks observed in the steady-state spectra between 1700 and 1200 cm^{-1} (Figure 7.5b), the phase-resolved spectra show 7 peaks (Figure 7.6), indicating the appearance of new groups not identified in the steady-state spectra, namely, p−CO_3 and carboxylate ($CO_2^{\delta-}$) groups (Table 7.2); and (*iii*) two from those 7 peaks are out-of-phase with the others (Figure 7.6).

Table 7.2. Assignment of the bands observed during steady-state DRIFTS and ME–PSD–DRIFTS experiments: hydroxyl groups (OH^-), gaseous methane (CH_4), gaseous carbon dioxide (CO_2), bridged carbon monoxide (br−CO), formyl groups (CHO), bi-dentate carbonates (b−CO_3), poly-dentate carbonates (p−CO_3), formates (HCOO), carboxylate ($CO_2^{-\delta}$), and methoxy groups (OCH_3).

	Steady-state *in situ* DRIFTS				***In situ* ME−PSD−DRIFTS**	
	CO_2 adsorption		CO_2 methanation		CO_2 adsorption	
	Ni/CeO_2	Ni/ACR−CeO_2	Ni/CeO_2	Ni/ACR−CeO_2	Ni/CeO_2	Ni/ACR−CeO_2
	Wavenumber (cm^{-1})					
CO_2/ OH^-	3750–3550	3750–3550	3750–3550	3750–3550	3750–3550	3750–3550
CH_4	–	–	–	3017	3017	3017
CO_2	2400–2250	2400–2250	2400–2250	2400–2250	2400–2250	2400–2250
CO gas	–	–	–	2200–2100	2200–2100	2200–2100
br−CO	–	–	–	–	1760	1770
CHO	–	–	1710	1710	1700	1700
b−CO_3	1600 1280 1030	1585 1295 1030	1590 1270 1030	1580 1300 1030	1610 1290 1020	1600 1290 1020
p−CO_3	1415 –	– –	– –	– –	1450 1405	1450 1405
HCOO	1500 1370	1520 1370	1510 1380	1510 1385	1520 1360	1530 1360
$CO_2^{-\delta}$	–	–	–	–	1240	1240
OCH_3	1080 1060	1080 1060	1080 1060	1080 1060	1080 1060	1080 1060

With regards to the aforementioned first difference, the band at 1700 cm^{-1} is indicative of the formyl (CHO) group, while the band at 1760 cm^{-1} is most likely related to bridged CO (br–CO) on Ni^0 sites [20,24]. The appearance of br–CO on

Ni^0 should be related to two reactions occurring simultaneously: it can be formed by direct dissociation of CO_2 over Ni, and it can be a product of HCOO dissociation, since the presence of $CO2^{\delta-}$, b-CO_3, p-CO_3 and HCOO bands indicate that CO_2 should also be adsorbed and hydrogenated on CeO_2.

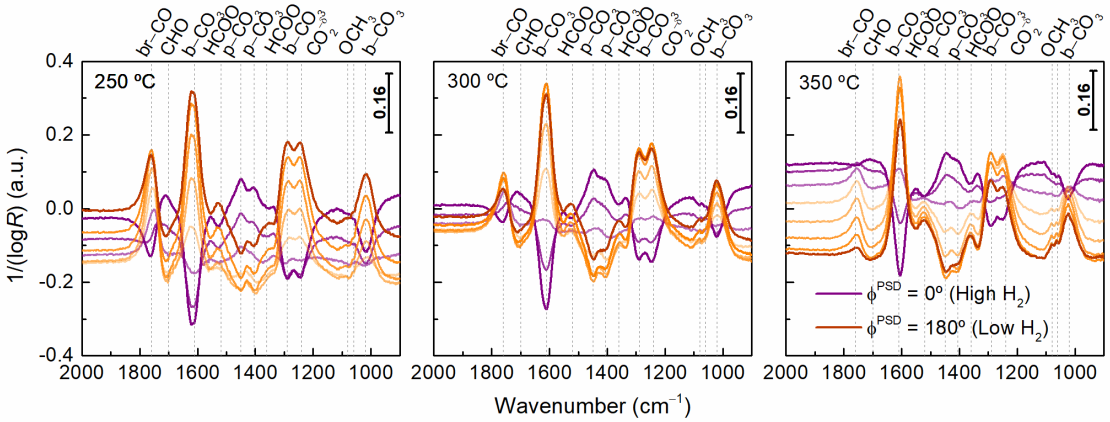

Figure 7.6. Phase-resolved spectra of the modulation excitation *in situ* DRIFTS studies conducted for the Ni/CeO_2 catalyst at 250, 300 and 350 °C. Experimental conditions: P = 1 bar; flowrate A: CO_2 = 2.5 cm^3 min^{-1} and 10% H_2/N_2 = 100 cm^3 min^{-1}; flowrate B: CO_2 = 2.5 cm^3 min^{-1} and N_2 = 100 cm^3 min^{-1}; m_{cat} = 15 mg. The dashed lines indicate the positions of the peaks.

Furthermore, there is a possibility that br–CO can be hydrogenated to CHO in the presence of H_2, as previously reported [24]. This is a likely scenario since the respective bands are out of phase with each other, indicating that br–CO is hydrogenated to CHO on the surface of CeO_2 in the presence of H_2. A more detailed analysis of the phase delay φ (the time to reach maximum accumulation) for both br–CO and CHO species over Ni/CeO_2 at 300 °C, show that they differ by 180 ° [φ(br–CO) = 108 ° and φ(CHO) = 288 °]. This phase delay means that the CHO is formed at the same time as br–CO is consumed. Another possible scenario would be that this phase delay is dependent on that of the H_2, which would mean that H_2 favors the net formation of b–CO and disfavors the formation of CHO, leading to the maximum coverage of b–CO being observed mostly in phase with H_2, whereas CHO is mostly out of phase to H_2. However, since the phase delays are not close to 0° or 180°, which would be close to the value where H_2 is maximum and minimum, respectively, due to low residence time, the first option is more probable: br–CO should be hydrogenated to CHO in the presence of H_2. Notably, it is not possible to

present the phase delay values for the remaining intermediates due to the accumulation of multiple maxima.

More detailed analysis of the differences between the steady-state and ME–PSD data reveal that while the bands from b–CO_3 appear at the same positions (Table 7.2) [10,26], the set of bands associated with HCOO in the steady-state spectra (Figure 7.5b) are, in fact, a convolution of different species, namely, HCOO and p–CO_3 (Figure 7.6, Table 7.2) [10]. Notably, the later p–CO_3 assignment could also be ascribed to mono-dentate carbonates (m–CO_3), but the low $\Delta_{as\text{-}s}$ suggests the presence of p–CO_3 rather than m–CO_3 [10]. In that case, p–CO_3 appearance is out-of-phase with b–CO_3 appearance, which indicate that the coordination of the carbonates may be changing from b–CO_3 to p–CO_3. Previously, this effect was explained as a change in carbonate adsorption configuration over CeO_2 as a consequence of its reduction state. Specifically, in the absence of H_2 (φ^{PSD} = 180 °), CeO_2 is partially oxidized, and when it is reduced in the presence of H_2 (φ^{PSD} = 0 °), the b–CO_3 reconfigures to either m–CO_3 or p–CO_3 [10].

Finally, only one peak was observed at 1270 cm^{-1} in the steady-state spectrum (Figure 7.5b). After phase-sensitive detection analysis (PSD), two peaks are distinguished (Figure 7.6): one from b–CO_3 and another one that we assign to $CO_2^{\delta-}$ (Table 7.2), typically forming when CO_2 is adsorbed on the surface of CeO_2 [10,24–26,42]. Finally, we assign the bands at 1080−1060 cm^{-1} (Figure 7.6) to methoxy (OCH_3) species [24,25], and the one at 1060 cm^{-1} corresponds to b–CO_3 (Table 7.2) [26].

When we compare the spectra at different temperatures (Figure 7.6), we observe that the bands remain at the same positions in all spectra, although their relative intensities varied. The change in intensity is particularly clear from the relative difference between the two peaks assigned to br–CO on Ni^0 and CHO, respectively. In contrast, the peaks from b–CO_3 and p–CO_3 remain intense, as they are known to be relatively stable [10].

Motivated by this detailed insight, we then proceeded to investigate the composite Ni/ACR–CeO_2 catalyst by ME–PSD–DRIFTS. Due to the absorption of most of the IR radiation by the activated carbon, we observe a lower signal-to-noise ratio for Ni/ACR–CeO_2 (Figure 7.7) compared to Ni/CeO_2 (Figure 7.6). Nevertheless, we were still able to draw some conclusions from the phase-resolved spectra. First, the same species are detected in the ME–PSD–DRIFTS spectra of Ni/ACR–CeO_2, as in the case of Ni/CeO_2, moreover at nearly the same band positions (Figure 7.6,Figure 7.7). However, three main differences were identified between methanation behaviors of these two catalysts: (*i*) in Ni/ACR–CeO_2, the relative intensity of br–CO band in comparison with CHO band (Figure 7.7) is lower than in the case of Ni/CeO_2 (Figure 7.6); (*ii*) as the reaction temperature increases the presence of CO is not observed for Ni/ACR–CeO_2 (Figure 7.7); and (*iii*) the bands corresponding to p–CO_3 are significantly less pronounced for Ni/ACR–CeO_2 (Figure 7.7) than for Ni/CeO_2 (Figure 7.6). These differences show that, in sharp contrast to Ni/CeO_2, there is no direct transformation between br–CO and CHO over the Ni/ACR–CeO_2 catalyst, which is further confirmed by the absence of CO at high temperatures (Figure 7.7).

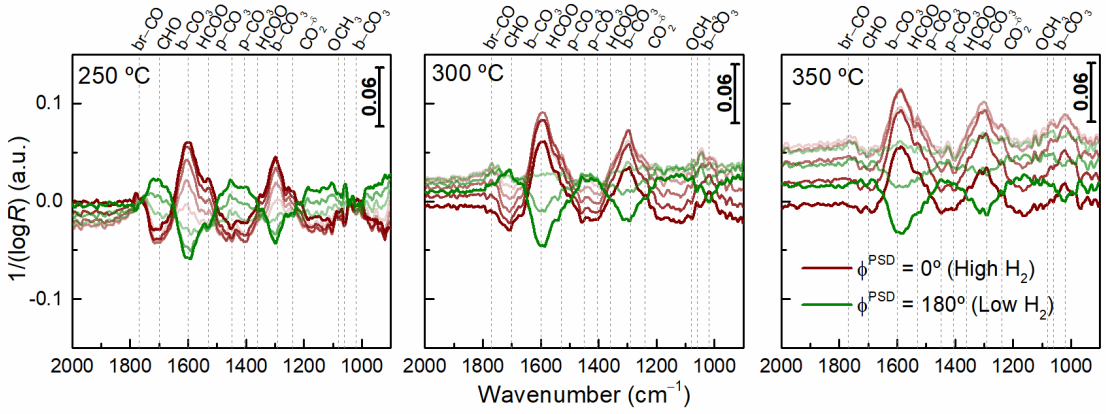

Figure 7.7. Phase-resolved spectra of the modulation excitation *in situ* DRIFTS studies conducted for the Ni/ACR–CeO_2 catalyst at 250, 300 and 350 °C. Experimental conditions: P = 1 bar; flowrate A: CO_2 = 2.5 cm^3 min^{-1} and 10% H_2/N_2 = 100 cm^3 min^{-1}; flowrate B: CO_2 = 2.5 cm^3 min^{-1} and N_2 = 100 cm^3 min^{-1}; m_{cat} = 15 mg. The dashed lines indicate the positions of the peaks.

The full-range *in situ* ME–PSD–DRIFTS spectra may help to explain the general trends of the methanation over the synthesized catalysts and deviations between them. Figure 7S.10 shows that, with the Ni/CeO_2 catalyst, the band corresponding to gaseous CH_4 at 3017 cm^{-1} is not present at 250 °C but it appears at 300 °C. Figure 7S.11 shows the same observations with the Ni/ACR−CeO_2 catalyst. For both samples, the band corresponding to gaseous CO at 2200–2100 cm^{-1} starts to be apparent at 300 °C and is even more pronounced at 350 °C (Figure 7S.10, Figure 7S.11) [25]. For comparison, we also investigated the pure CeO_2 and composite ACR–CeO_2 supports without Ni being present and the obtained results are displayed in Figure 7S.12 and Figure 7S.13, respectively.

4. Discussion

It is well known that CeO_2-supported Ni catalysts have high activity and selectivity for CO_2 methanation at low temperatures, typically ≤ 400°C. Most likely, these properties are related to the improved metal–support interactions between Ni and CeO_2 and a high surface coverage of CO_2, alternatively, they can be explained by the reducibility of CeO_2 [43].

Based on our previous work [2], we hypothesized that an interesting approach to obtain high-performing methanation catalyst would be the preparation of Ni catalyst supported on composite supporting material consisting of reduced activated carbon and CeO_2.

Furthermore, we wanted to study whether such compositing would generate an active, selective, and stable methanation catalyst that operates at a temperature below 400 °C. Thus, we synthesized a set of 15 wt% Ni catalysts supported on ACR–CeO_2 with different ratios of ACR : CeO_2, as well as a 15 wt% Ni catalyst supported on pure CeO_2 (Ni/CeO_2) for reference. Figure 7S.1 shows that Ni/ACR–CeO_2 with ACR : CeO_2 weight ratio of 50 : 50 afforded the best methanation performance. Besides improving the activity and selectivity compared to those for our previously reported Ni/ACR, the Ni/ACR–

CeO_2 catalyst achieved improved stability over long TOS at the respective optimal temperature. This improvement can be explained by the different interactions between the Ni and the pure ACR and ACR–CeO_2 composite but also by the fact that lowering the reaction temperature to 370 °C (cf. 450 °C) decreases the possibility of Ni deactivation over long TOS.

Significantly, although half of the supporting material in Ni/ACR–CeO_2 is in fact reduced activated carbon, we observed that the catalytic properties of the composite catalyst are comparable or even slightly better than that of Ni/CeO_2 (Figure 7.1). This result highlights that our compositing strategy is a useful tool for reducing the usage of the expensive rare-earth CeO_2 oxide by replacing this oxide with a cost-effective carbon material. As explained in our previous work [2], the Lewis basic sites present on the ACR supporting material improve the Ni dispersion, and furthermore, its basicity is responsible for an improved CO_2 adsorption capacity over the catalyst, enabling CO_2 to be close to the Ni active sites.

The characterization of the samples allowed some property-performance relationships to be established. Even though the samples presented comparable catalytic performance, they are composed of materials with different textural properties. Furthermore, the Ni species on Ni/CeO_2 exhibit a stronger interaction with pure CeO_2 support, compared to that in composite Ni/ACR–CeO_2, which can be a hypothesis for the fact that Ni/ACR–CeO_2 presented slightly better activity at lower temperature. The reducibility of CeO_2 could also be a possible reason for slight differences in catalytic performance [43]; however, it is difficult to compare the reducibility of CeO_2 in CeO_2 and ACR−CeO_2 supports by H_2−TPR analysis because ACR can undergo decomposition above 500 °C, which influences with the TPR profile of the sample above this temperature. The microscopy analysis demonstrated that in both samples, the particles exhibit Ni@NiO core-shell appearance.

XPS analysis revealed that both catalysts, Ni/CeO_2 and Ni/ACR–CeO_2, exhibited two different Ni phases, corresponding to metallic Ni and NiO, with Ce 3d spectra also revealing the presence of mixed Ce phases in both

samples. Interestingly, relative at% of Ce^{3+} is different in both samples, with the Ni/ACR–CeO_2 catalyst exhibiting a higher value. It is known that the oxygen vacancies can be formed in the transformation process of Ce^{4+} into Ce^{3+}; thus, the amount of oxygen vacancies is usually proportional to the Ce^{3+} amount [44]. Therefore, we can hypothesize that Ni/ACR–CeO_2 catalyst may contain a higher amount of oxygen vacancies, which are known to be important in the methanation reaction, than does Ni/CeO_2. This hypothesis cannot be supported by the analysis of the O 1s spectra because the O 1s spectra of Ni/ACR–CeO_2 contain components from the organic phase of ACR, in addition to the components related to CeO_2 (Figure 7S.7) [31,33,34,45].

After the stability experiment over a long TOS, the major modification was observed in Ni/ACR–CeO_2, in which the CeO_2 particles presented a needle-like shape. Most likely, the presence of steam, a sub-product of the reaction, leads to hydrothermal recrystallization of the initial CeO_2 nanoparticles into CeO_2 nanoneedles. This recrystallization is apparently templated by the presence of ACR, since carbon-free Ni/CeO_2 did not exhibit the appearance of the CeO_2 needles after TOS testing (Figure 7S.8a). The carbon balance, that was close to zero, and the fact that our catalysts do not suffer deactivation over 90 h, indicate that carbon deposition should be minimal, if present at all, in these systems.

Our studies of CO_2 methanation over Ni/CeO_2 and Ni/ACR–CeO_2 have established that both catalysts demonstrated outstanding catalytic activity, selectivity, and stability in CO_2 methanation (Figure 7.1). Notably, Ni catalysts supported on CeO_2 are among the materials exhibiting the highest methanation performance reported in the literature. To our gratification, the observed catalytic properties for our Ni/CeO_2 and Ni/ACR–CeO_2 catalysts compare favorably to the reported ones. Specifically, our catalysts achieved a maximum X_{CO2} of 86 and 87%, with $S_{CH4} \approx 100\%$ at 370 °C, while having a T_{50} of 280 °C; this T_{50} is similar or even lower from most of the reported in the literature for similar catalytic systems (Table 7S.3). For example, *Rui et al.* [20] prepared two different CeO_2 supports that were used for the preparation of

two Ni-based catalysts, which could achieve $X_{CO2} \approx 85\%$ with $S_{CH4} \approx 100\%$ at 275 °C ($T_{50} \approx 260$ °C) and 350 °C ($T_{50} \approx 280$ °C). In another interesting report, which compares two differently synthesized Ni on CeO_2 catalysts, *Ye et al.* [24] observed $X_{CO2} = 82.5\%$ and $S_{CH4} = 94.8\%$ at 250 °C with Ni/CeO_2–SGM catalyst (synthesized via sol-gel method), as well as $X_{CO2} = 69.8\%$ and $S_{CH4} = 84.8\%$, at 450 °C with Ni/CeO_2-IM (prepared by a simple impregnation method). They used conditions similar to those in the present study, albeit at a lower (10 000 cf. 60 000 $cm^3\ g^{-1}\ h^{-1}$) weight hourly space velocity (*WHSV*); the catalysts exhibited a T_{50} of ≈ 240 °C and ≈ 380 °C, respectively. In another study with two differently synthesized CeO_2 supports, with and without a g–C_3N_4 template, *Yu et al.* [25] obtained two Ni-based catalysts exhibiting T_{50} of 305 °C and 330 °C, with maximum $X_{CO2} \approx 75\%$ and $S_{CH4} \approx 100\%$, at 350 °C and 400 °C, for the catalyst prepared with g–C_3N_4 template and without, respectively, also at a lower *WHSV* (10 000 cf. 60 000 $cm^3\ g^{-1}\ h^{-1}$). *Cárdenas-Arenas et al.* [26] prepared a Ni/CeO_2 catalyst that reached ≈ 85% X_{CO2} with ≈ 100% S_{CH4} at 375 °C, with T_{50} of ≈ 280 °C.

The mechanism of the CO_2 methanation over Ni/CeO_2 catalysts has been a subject of intensive research. *Zhang et al.* [19] investigated the reaction mechanism on Ni/CeO_2 by first-principles calculations and concluded that the reaction on this catalyst follows the CO pathway through reverse water gas shift, rather than the formate (HCOO) formation or direct C–O bond cleavage pathways. Based on *in situ* DRIFTS study, *Lee et al.* [23] compared the mechanism of CO_2 methanation for Ni-based catalysts supported on different materials. They concluded that the Ni/CeO_2 catalyst, dissociates CO_2 into CO, which then participates in the CO_2 methanation reaction at high temperature. In another study with a Ni/CeO_2 catalyst synthesized by the sol-gel method, *Ye et al.* [24] suggested that the reaction occurred through a formate (HCOO) pathway with formyl (CHO) intermediate. Furthermore, the authors suggested that the good performance of the catalysts was related to the effective dissociation of H_2 by Ni and the strong adsorption/activation of CO_2 by CeO_2 support. Based on a DRIFTS study, *Rui et al.* [20] determined that the reaction proceeded through the

CO pathway over Ni/CeO_2 catalyst, namely, by direct C−O bond cleavage via reverse water gas shift reaction followed by the methanation of the resultant CO.

Although some studies have indicated that CO_2 methanation over Ni/CeO_2 proceeds through the CO pathway [19,20,23], our results show that the methanation over our Ni/CeO_2 follows a combination of CO pathway and the formate (HCOO) pathway, where CO forms through HCOO dissociation.

For Ni/CeO_2, we observed from steady-state *in situ* DRIFTs experiments (Figure 7.5) that the CO_2 adsorption on the catalyst resulted in the formation of b–CO_3 and HCOO. When H_2 was added to the gas flow generating methanation conditions, another band attributed to CHO appeared, indicating that CHO is an important intermediate for the methanation over Ni/CeO_2 catalyst.

The ME−PSD−DRIFT methodology improved the signal-to-noise ratio and allowed us to distinguish between the spectator and intermediate species. Now for Ni/CeO_2, it was possible to observe that the peak attributed to CHO in the steady-state *in situ* DRIFTS was in fact composed of two peaks out-of-phase with each other, namely, br–CO on Ni^0 and CHO [20,24].

Based on the collected experimental *in situ* ME–PSD–DRIFTS evidence (Figure 7.6, Figure 7S.10, Figure 7S.12 and Table 7.2), Scheme 7.1 outlines the envisioned mechanism of the CO_2 methanation over synthesized Ni/CeO_2. There are two possibilities for the formation of br–CO on Ni^0: by direct dissociation of CO_2 over Ni, or dissociation of HCOO. In the second case, specifically, CO_2 is adsorbed on the CeO_2 surface as $CO_2^{\delta-}$, which then forms b–CO_3/p–CO_3 species [42]. These species are then hydrogenated by the hydrogen dissociated over Ni^0 to form HCOO, which is further dissociated forming br–CO on Ni^0. Next, the br–CO is firstly hydrogenated to CHO over the CeO_2 [24] and then to OCH_3, as observed in the respective *in situ* ME–PSD–DRIFTS spectra (Figure 7.6, Table 7.2). It is difficult to access the phase delay of the methoxy species, due to a small signal being observed, but according

to the literature, the presence of OCH_3 indicate that CHO should be hydrogenated to this species. Eventually, the as-formed OCH_3 is sequentially hydrogenated to CH_4 and released as the end-product.

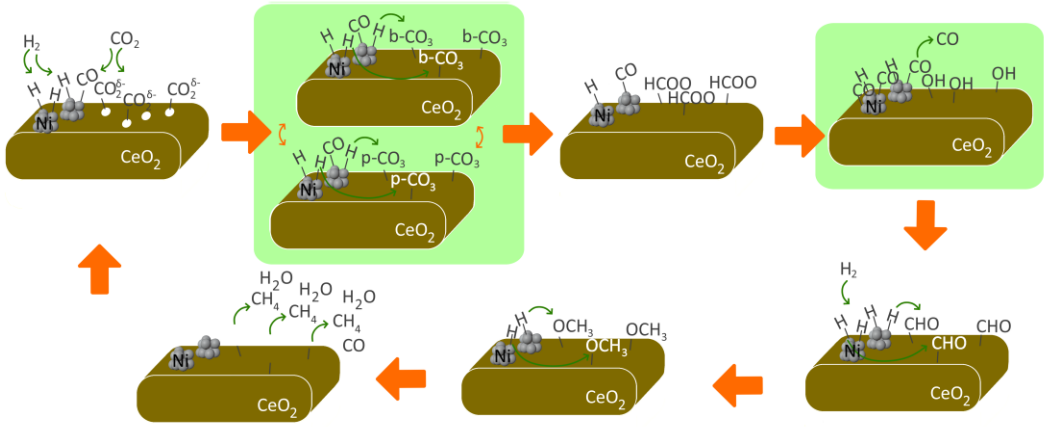

Scheme 7.1. Proposed mechanism for the CO_2 methanation over Ni/CeO_2 catalyst, displaying the formation/transformation of the reaction intermediates as elucidated by in situ ME–PSD–DRIFTS. The green boxes mark the differences in the mechanism between the two samples (Scheme 7.1 vs. Scheme 7.2).

There is an alternative pathway in which br–CO could be only involved in CO formation and not in the formation of the desired CH_4, and, accordingly, CHO would be formed through direct dissociation of HCOO. However, the fact that b–CO and CHO bands are 180 ° out-of-phase with each other (Figure 7.6) strongly suggests that their transformation is directly correlated, which rules out this pathway.

When comparing the carbon-containing Ni/ACR–CeO_2 to the carbon-free Ni/CeO_2, our characterization data indicate that the catalysts are quite different. Ni/ACR–CeO_2 has a significantly higher surface area, porosity, and metallic Ni surface area, with smaller Ni nanoparticles size in comparison with Ni/CeO_2. At the same time, Ni/CeO_2 is expected to have stronger metal–support interactions. The observation of similar methanation properties for

such different catalysts leads to the hypothesis that the CO_2 methanation over Ni/ACR–CeO_2 and Ni/CeO_2 might proceed through different mechanisms.

The presence of CHO and especially the br–CO intermediates are less pronounced in Ni/ACR–CeO_2 (Figure 7.7), while the relative intensity of the HCOO, compared to the other species, appears to be higher (Figure 7.7) than in the case of Ni/CeO_2 (Figure 7.6). Additionally, at higher temperature of 350 °C, the presence of the band from br–CO is not observed (Figure 7.7). This could be explained by the fact that the consumption rate of CO on this catalyst is more favored by high temperatures than the formation rate, leading to less accumulation of this intermediate. However, if we consider that CO is hydrogenated to CHO, the instantaneous reaction (with lack of CO accumulation) would lead to a higher accumulation of CHO, if CHO is not hydrogenated at the same rate as CO, which is not observed. Therefore, the disappearance of the band from br–CO at high temperatures is related to desorption, instead of hydrogenation to CHO.

Thus, the data indicate that the br–CO does not play a significant role in the reaction pathway but may be related to the formation of the CO byproduct (Scheme 7.2(b)).

Regarding Ni catalysts supported on carbon materials, *Hu et al.* [17] concluded that the methanation over Ni catalyst supported on graphene aerogel followed the formate pathway, with carbonate intermediates being present, i.e., without the formation of CO. Consistently with this report, the CO_2 methanation over our carbon-containing Ni/ACR–CeO_2 catalyst proceeds through the formate pathway, which is depicted on Scheme 7.2 (a). The methanation starts with the adsorption of CO_2 as $CO_2^{\delta-}$, followed by the formation of b–CO_3/p–CO_3 species [42]. Those are then hydrogenated to HCOO, similarly to what we observed for the carbon-free Ni/CeO_2. At the same time, in sharp contrast to Ni/CeO_2, br–CO was not detected for Ni/ACR–CeO_2 at higher temperatures (350 °C). This fact indicates the significant difference between methanation over Ni/CeO_2 and Ni/ACR–CeO_2, wherein over the composite catalyst, the formate (HCOO) is directly dissociated to formyl (CHO) [46], then following the same pathway as

over the Ni/CeO_2. In particular, CHO is further hydrogenated to methoxy and finally to methane end product.

With regards to the proposed mechanisms (Scheme 7.1, Scheme 7.2), it is important to emphasize that some of the H_2 can be partially dissociated on the CeO_2 surface (i.e., not only on the Ni^0). This is suggested by *in situ* ME–PSD–DRIFTS of pure CeO_2 and composite ACR–CeO_2 supporting materials, revealing the presence of partially hydrogenated HCOO and OCH_3 species (Figure 7S.12, Figure 7S.13).

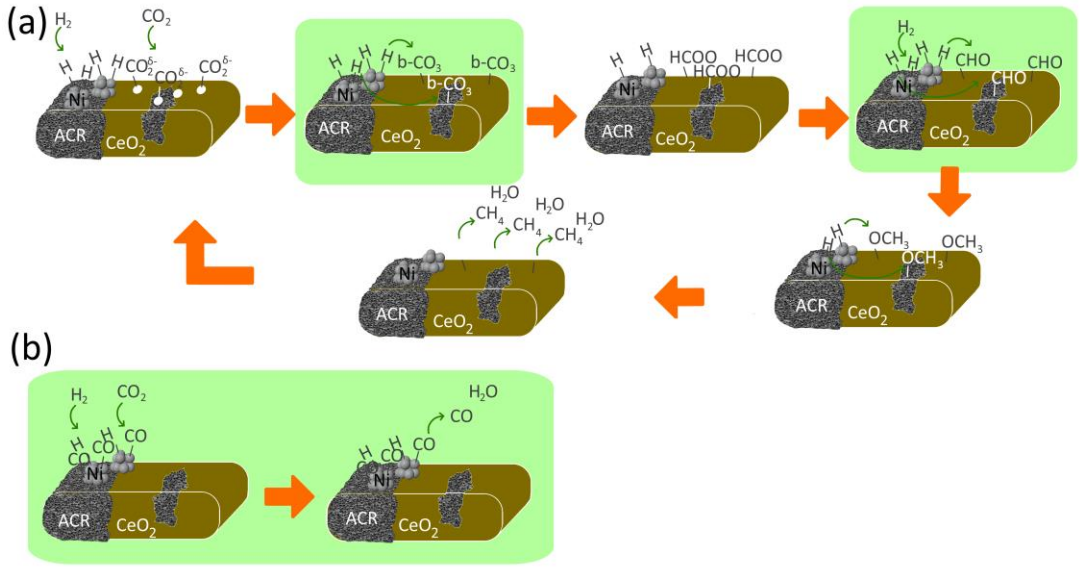

Scheme 7.2. Proposed mechanism for the CO_2 methanation over Ni/ARC–CeO_2 catalyst, displaying the formation/transformation of the reaction intermediates as elucidated by in situ ME–PSD–DRIFTS. (a) illustrates the mechanism of CH_4 formation while (b) depicts the mechanism of CO formation. The green boxes mark the differences in the mechanism between the two samples (Scheme 7.1 vs. Scheme 7.2).

Interestingly, our detailed electron microscopy investigation of the microstructural changes, together with the XPS analysis, within the catalysts after 90 h of time-on-stream testing evidences that even though the catalysts did not lose their catalytic performance over 90 h (Figure 7.1c,d), their fine microstructure and chemical composition were indeed affected.

The analysis of the Ni $2p_{3/2}$ and Ce 3d spectra of the fresh and TOS tested Ni/CeO_2 and Ni/ACR–CeO_2 revealed alterations in the Ni^0 content and the Ce^{3+}/Ce^{4+} ratios. The Ni^0 relative at% increase in Ni/ACR–$CeO_{2\,TOS}$ indicating that the Ni nanoparticles likely undergo a further reduction under the reductive

conditions of the CO_2 methanation reaction, probably due to the higher reducibility and weaker metal-support interactions in this sample (Figure 7S.4). On the contrary, an increase in the Ni^0 relative at% is observed in Ni/CeO_2. Regarding the CeO_2 support, Ce 3d spectra indicate that the relative at% of Ce^{3+}, and consequently the amount of oxygen vacancies remain similar in the Ni/ACR–$CeO_{2\,TOS}$, while, in contrast, increasing under reaction conditions in Ni/CeO_2.

The microstructural changes are mostly reflected by the preservation of the shell around Ni particles in both TOS-tested Ni/CeO_2 and Ni/ACR-CeO_2 materials (Figure 7.4, Figure 7S.8). The catalytic functions of the observed NiO shells are not well understood and our future work underpinning the role of the shell in the CO_2 methanation over high-performing Ni catalysts is ongoing.

5. Conclusions

A set of Ni catalysts deposited either on pure CeO_2 or composite carbon–CeO_2 supporting materials have been synthesized and characterized. CO_2 methanation with excellent conversion, selectivity and stability at favorably low reaction temperature was achieved using the as-synthesized Ni/CeO_2 and Ni/ACR–CeO_2 catalysts.

Our work demonstrated that compositing carbon with CeO_2 within the supporting material afforded an effective reduction in the usage of the expensive rare-earth CeO_2 while providing access to not only a cost-effective but also a high-performing methanation catalyst operating at low temperature. The mechanism of the CO_2 methanation over the newly synthesized catalysts was investigated by means of *in situ* spectroscopy, using the emerging ME−PSD−DRIFTS technique. The collected insights uncovered that the methanation over Ni/CeO_2 proceeded via a combination of the CO and formate pathways, while in Ni/ACR–CeO_2 it proceeded exclusively via the formate pathway. The main underlying mechanistic difference between the catalysts is that, during methanation over carbon-free Ni/CeO_2, the reaction is

mediated by CO from both CO_2 and formate dissociation, while carbon-containing Ni/ACR–CeO_2 catalyst is producing CH_4 without intermediate CO formation. Overall, these results illustrated that even partial modification of the supporting material for Ni methanation catalysts can influence the reaction mechanism.

6. Supplementary Information

6.1 Composite loading study

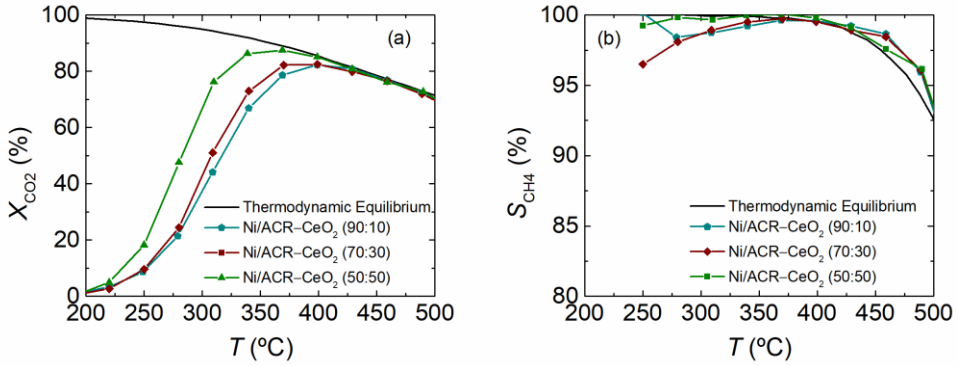

Figure 7S.1. Comparison of the CO_2 conversion X_{CO2} (a) and CH_4 selectivity S_{CH4} (b), as a function of temperature for the Ni/ACR–CeO_2 catalysts having different weight percentage ratios of AC−R to CeO_2: 90 : 10, 70 : 30 and 50 : 50. The thermodynamic equilibrium lines are shown in the graphics and were calculated using a model based on the minimization of Gibbs free-energy of the existing species. Methanation conditions: P = 1 bar; $WHSV$ = 60 000 cm^3 g^{-1} h^{-1}; CO_2 : H_2 = 1 : 4.

6.2 Characterization

6.2.1 N_2 Physisorption

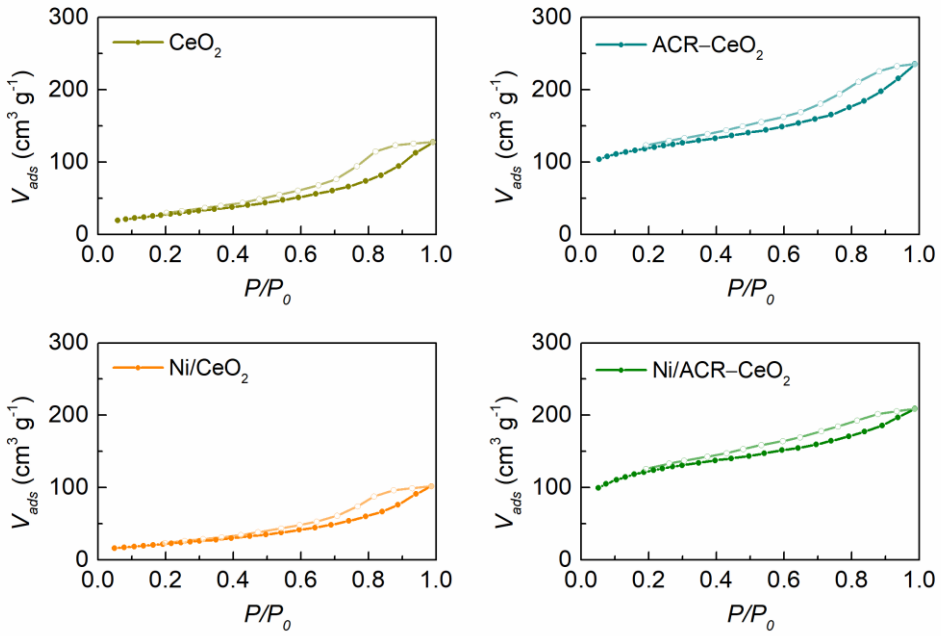

Figure 7S.2. Comparison of N_2 adsorption–desorption isotherms measured at −196 °C for the synthesized CeO_2 and ACR–CeO_2 supporting materials, as well as for the respective Ni/CeO_2 and Ni/ACR–CeO_2 catalysts with 15 wt% Ni loading.

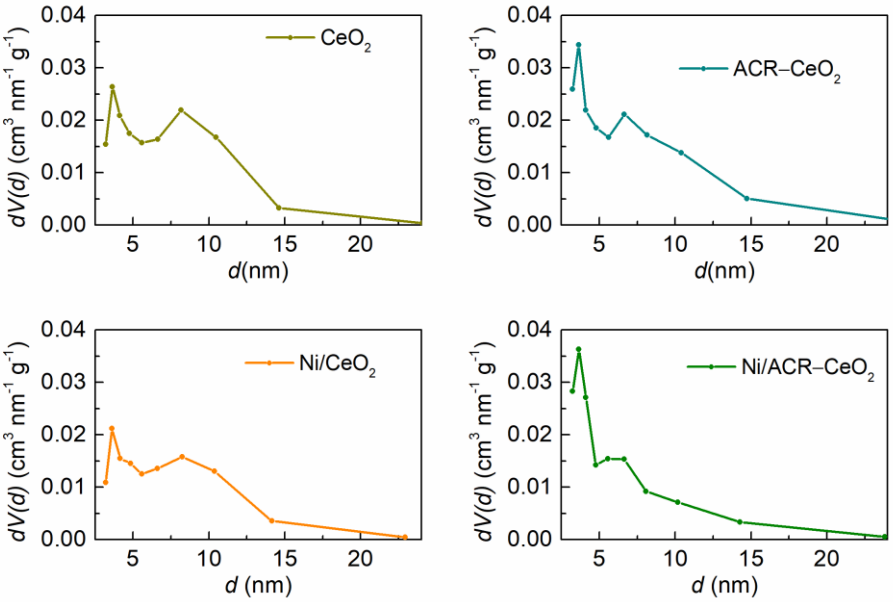

Figure 7S.3. Comparison of pore size distributions for the synthesized CeO_2 and ACR-CeO_2 supporting materials, as well as for the respective Ni/CeO_2 and Ni/ACR-CeO_2 catalysts with 15 wt% Ni loading.

6.2.2 H_2 Temperature Programmed Reduction

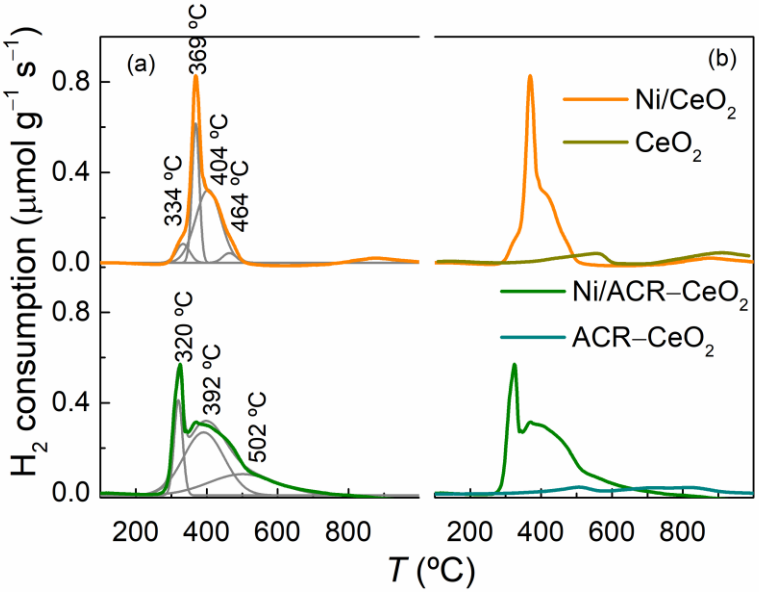

Figure 7S.4. Comparison of the (a) H_2–TPR profiles for Ni/CeO_2 and Ni/ACR-CeO_2 catalysts, as well as comparison with the (b) H_2–TPR profiles of the catalysts and the respective CeO_2 and ACR-CeO_2 supports.

6.2.3 Powder X-ray Diffraction

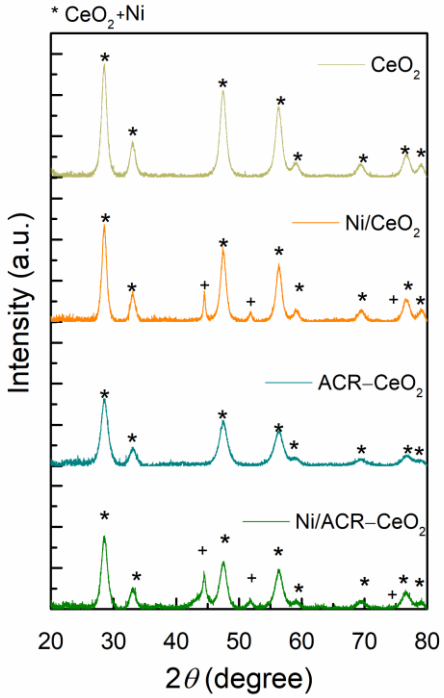

Figure 7S.5 XRD patterns of the CeO_2 and ACR–CeO_2 supporting materials and the respective Ni/CeO_2 and Ni/ACR–CeO_2 catalysts with 15 wt% Ni loading. Bragg reflections corresponding to cubic CeO_2 (ICDD #04-006-1932) and metallic Ni (ICDD #04-016-4761) are marked by * and +, respectively.

6.2.4 X-ray Photoelectron Spectroscopy

Four peaks were identified in the C 1s region of fresh Ni/ACR−CeO_2, and after TOS Ni/ACR−$CeO_{2\,TOS}$ (Figure 7S.6), which correspond to the aromatic and aliphatic carbon ($C_{ar,al}$) at 284.8 ± 0.1 eV, the hydroxyl groups (COH) at 286.2 ± 0.1 eV, carboxylic groups (COOH) at 289.2 ± 0.2 eV, and the plasmon loss ($C_{shake\text{-}up}$) at 291.1 ± 0.1 eV.[34,36]

Regarding O 1s region (Figure 7S.7), in the case of the Ni/CeO_2 and Ni/$CeO_{2\,TOS}$, three main peaks were identified, which correspond to lattice O species (O^{2-}) binding to Ce^{3+} and Ce^{4+}, at 529.7 ± 0.2 eV (O1); surface OH groups and O vacancies in CeO_2, at 531.2 ± 0.0 eV (O2), and O vacancies in CeO_2 at 532.5 ± 0.4 eV (O3). In the case of Ni/ACR−CeO_2 and Ni/ACR−$CeO_{2\,TOS}$ the O3 peak can also be attributed to hydroxyls, ethers and C=O in esters, amides, and anhydrides in AC−R, and, additionally, two more peaks are observed, attributed to C–O in esters and anhydrides in AC−R at

533.2 ± 0.1 eV (O4), and carboxylic groups in AC−R at 534.5 ± 0.5 eV (O5).[30,32,34,35]

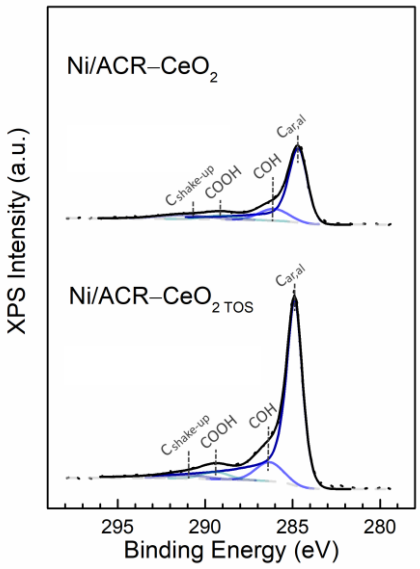

Figure 7S.6. High-resolution XPS data for C 1s region for fresh Ni/ACR−CeO_2, and after TOS Ni/ACR−$CeO_{2\ TOS}$. Symbols: raw data; black lines: overall fits; colored lines: fits of individual components; dashed lines: background. $C_{ar,al}$: aromatic and aliphatic carbon; COH: hydroxyl groups; COOH: carboxylic groups; $C_{shake\text{-}up}$: plasmon loss.

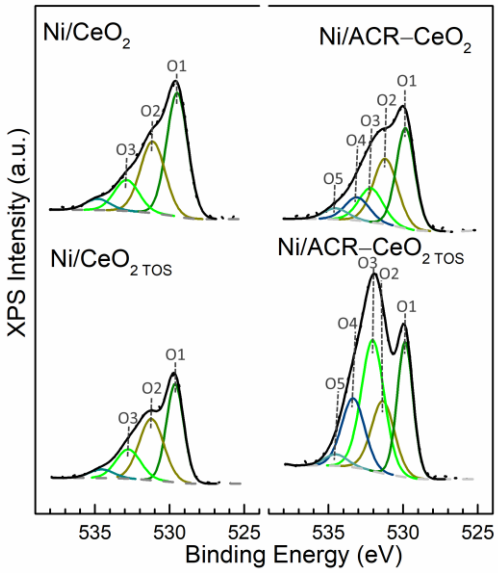

Figure 7S.7. High-resolution XPS data O 1s region for fresh Ni/CeO_2 and Ni/ACR−CeO_2, and after TOS Ni/$CeO_{2\ TOS}$ and Ni/ACR−$CeO_{2\ TOS}$. Symbols: raw data; black lines: overall fits; colored lines: fits of individual components; dashed lines: background. O1: lattice O species (O^{2-}) binding to Ce^{3+} and Ce^{4+}, O2: surface OH groups, O vacancies in CeO_2; O3: O vacancies in CeO_2, and hydroxyls, ethers and C=O in esters, amides, anhydrides in AC−R; O4: C–O in esters and anhydrides in AC−R; O5: carboxylic groups in AC−R.

Table 7S.1. Binding energies (BE) and assignment of the peaks positions identified in C 1s, O 1s, Ni 2p and Ce 3d spectra of fresh Ni/CeO_2 and Ni/ACR−CeO_2, and after TOS Ni/$CeO_{2\ TOS}$ and Ni/ACR−$CeO_{2\ TOS}$.

		Ni/CeO_2	**Ni/$CeO_{2\ TOS}$**	**Ni/ACR-CeO_2**	**Ni/ACR-$CeO_{2\ TOS}$**
				BE (eV)	
C 1s[a]	$C_{ar,al}$	--	--	284.7	284.9
	COH	--	--	286.1	286.3
	COOH	--	--	289.1	289.4
	$C_{shakeup}$	--	--	291.2	291.0
O 1s[b]	O1	529.5	529.6	529.8	529.9
	O2	531.1	531.2	531.2	531.4
	O3	532.9	532.8	532.2	532.0
	O4	534.8	534.6	533.1	533.3
	O5	--	--	534.5	534.5
Ni 2p[c]	Ni^0	853.2	852.9	852.9	852.9
	Ni^{2+}	854.8	854.4	854.4	854.1
	Ni^{2+}	856.4	856.6	856.3	856.2
	satellite	858.6	858.6	858.5	858.6
	Ni^{2+} (sat)	860.9	861.5	861.5	861.4
	Ni^{2+} (sat)	864.2	864.2	864.4	864.2
Ce 3d[d]	v^0	882.5	882.6	882.5	882.1
	u^0	901.2	901.1	900.8	900.8
	v	884.1	884.0	883.9	883.4
	u	902.3	902.0	902.1	902.1
	v'	887.7	887.6	887.3	887.0
	u'	905.4	905.1	904.8	904.8
	v''	890.4	890.6	890.5	890.0
	u''	909.3	909.3	909.0	909.0
	v'''	899.4	899.3	899.1	898.7
	u'''	918.1	918.0	917.7	917.7

[a] $C_{ar,al}$: aromatic and aliphatic carbon; COH: hydroxyl groups; COOH: carboxylic groups; $C_{shake\text{-}up}$: plasmon loss. [b] O1: lattice O species (O^{2-}) binding to Ce^{3+} and Ce^{4+}, O2: surface OH groups, O vacancies in CeO_2; O3: O vacancies in CeO_2, and hydroxyls, ethers and C=O in esters, amides, anhydrides in AC−R; O4: C–O in esters and anhydrides in AC−R; O5: carboxylic groups in AC−R. [C] Ni^0: metallic Ni; Ni^{2+}: Ni oxide; Ni^{2+} (sat): Ni^{2+} satellite. [d] v^0, u^0, v', and u' correspond to Ce^{3+}; v, u, v'', u'', v''', and u''' correspond to Ce^{4+}.

Table 7S.2. Relative atomic percentage (at%) of Ni^0, Ni^{2+}, Ce^{3+}, and Ce^{4+} phases, determined by XPS, in fresh Ni/CeO_2 and $Ni/ACR-CeO_2$, and after TOS $Ni/CeO_{2\,TOS}$ and $Ni/ACR-CeO_{2\,TOS}$.

		Ni/CeO_2	**$Ni/CeO_{2\,TOS}$**	**$Ni/ACR\text{-}CeO_2$**	**$Ni/ACR\text{-}CeO_{2\,TOS}$**
		at%			
Ni 2p	Ni^0	4.4	2.8	4.2	7.4
	Ni^{2+}	66.7	86.7	66.8	87.1
Ce 3d	Ce^{3+}	16.4	21.3	20.5	19.9
	Ce^{4+}	83.6	78.7	79.5	80.1

6.2.5 Transmission Electron Microscopy

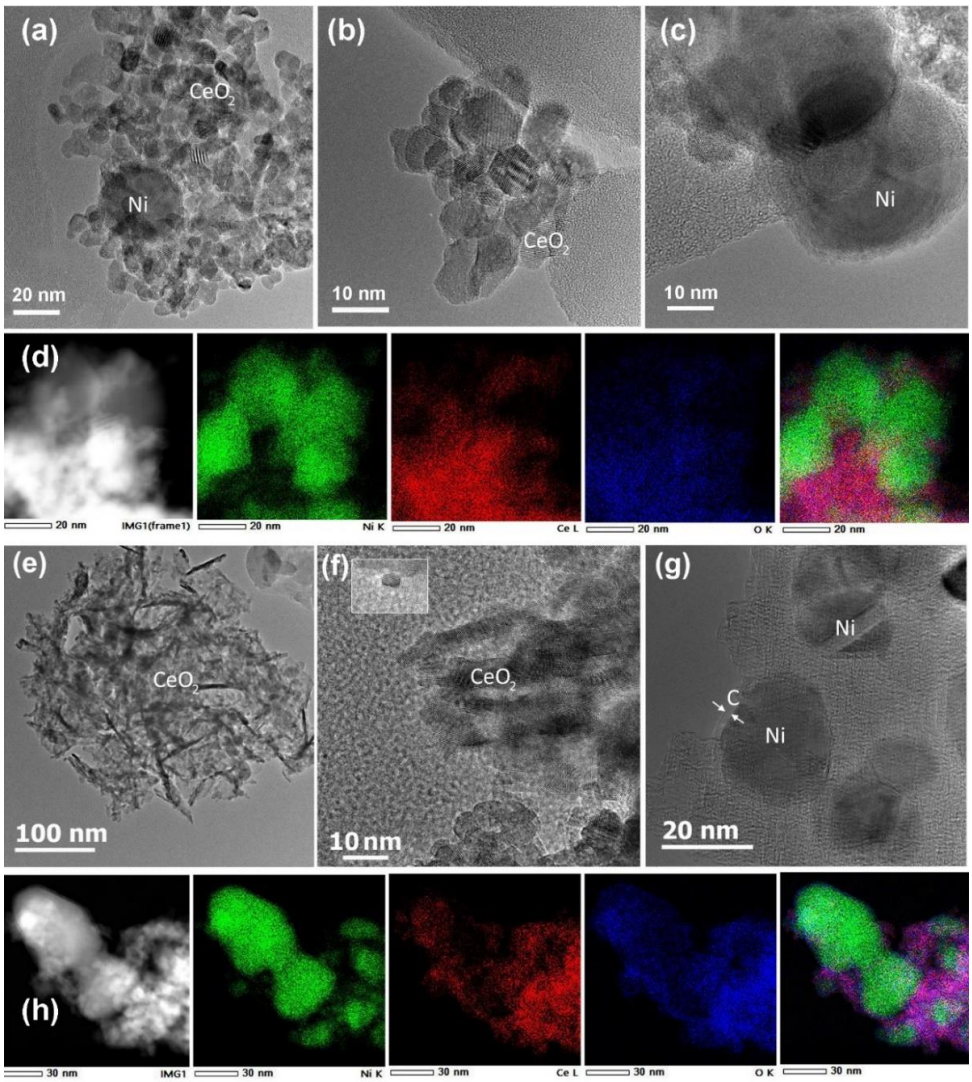

Figure 7S.8. Comparison of the microstructure and elemental distribution for the TOS tested $Ni/CeO_{2\,TOS}$ and $Ni/ACR\text{-}CeO_{2\,TOS}$ catalysts. Showing TEM images of Ni nanoparticles dispersed on CeO_2 support in $Ni/CeO_{2\,TOS}$ (a), together with the representative HRTEM images of particles (b), and Ni nanoparticles (c) on this sample and STEM-EDX mapping (d); and TEM images TOS tested $Ni/ACR\text{-}CeO_{2\,TOS}$ catalyst (e), together with the representative HRTEM images of CeO_2 particles (f), and Ni nanoparticles (g), presenting a carbon shell, on this sample and STEM-EDX mapping (h).

6.3 Steady-state *in situ* DRIFTS

From Figure 7S.9, it is possible to note that first, upon CO_2 adsorption (i.e., in the absence of H_2), a group of bands around 3750−3550 cm^{-1} is observed for both Ni/CeO_2 and $Ni/ACR\text{–}CeO_2$ catalysts. These bands correspond to hydroxyl groups on the surface of CeO_2. [18,19] Another detected group of bands at 2400−2250 cm^{-1} is associated with gaseous CO_2. [19] When H_2 is then introduced into the gas flow mimicking methanation conditions, the bands from hydroxyl groups and gaseous CO_2 diminish drastically. Interestingly, there seems to be no modification in these bands with increasing temperature. At the same time, the band at 3017 cm^{-1} corresponding to gaseous CH_4 [18,19,22] is clearly observed at 300 and 350 °C for $Ni/ACR\text{–}CeO_2$ (Figure 7S.6d), marking the formation of the reaction product.

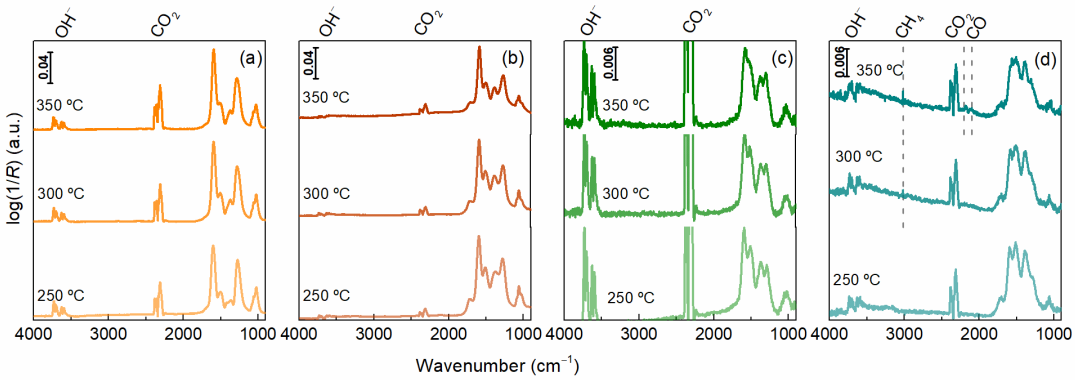

Figure 7S.9. Steady-state *in situ* DRIFTS studies of CO_2 adsorption and CO_2 methanation over Ni/CeO_2 (a,b) and $Ni/ACR\text{–}CeO_2$ (c,d) catalysts. Experimental conditions for CO_2 adsorption: P = 1 bar; CO_2 flowrate of 2.5 cm^3 min^{-1}; N_2 flowrate of 100 cm^3 min^{-1}; m_{cat} = 15 mg. Experimental conditions for CO_2 methanation: P = 1 bar; CO_2 flowrate of 2.5 cm^3 min^{-1}; 10%H_2/N_2 gas mixture flowrate of 100 cm^3 min^{-1}; m_{cat} = 15 mg.

6.4 ME-PSD-DRIFTS

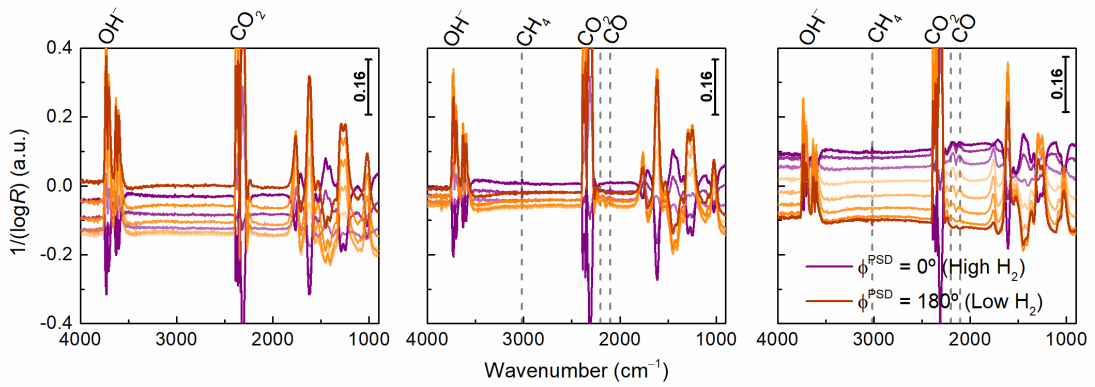

Figure 7S.10. Phase-resolved spectra of the modulation excitation *in situ* DRIFTS studies for Ni/CeO_2 conducted at 250, 300 and 350 °C. Experiment conditions: P = 1 bar; flowrate A: CO_2 = 2.5 cm^3 min^{-1} and N_2 = 100 cm^3 min^{-1}; flowrate B: CO_2 = 2.5 cm^3 min^{-1} and 10% H_2/N_2 = 100 cm^3 min^{-1}; m_{cat} = 15 mg. The dashed lines indicate the peak positions.

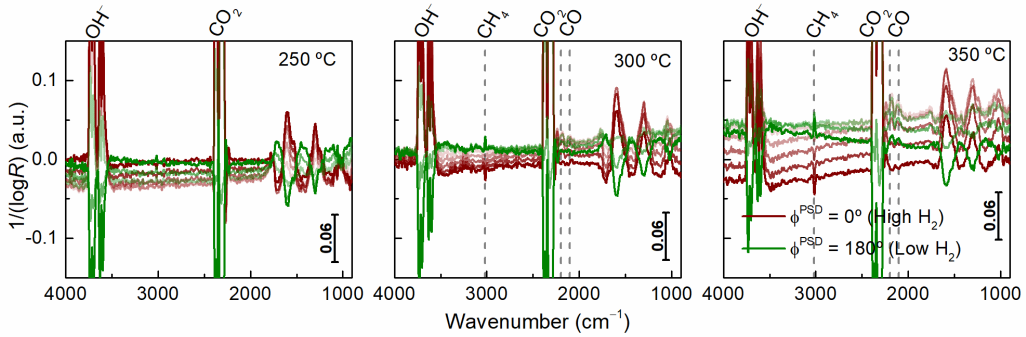

Figure 7S.11. Phase-resolved spectra of the modulation excitation *in situ* DRIFTS studies for Ni/ACR−CeO_2 conducted at 250, 300 and 350 °C. Experiment conditions: P = 1 bar; flowrate A: CO_2 = 2.5 cm^3 min^{-1} and N_2 = 100 cm^3 min^{-1}; flowrate B: CO_2 = 2.5 cm^3 min^{-1} and 10% H_2/N_2 = 100 cm^3 min^{-1}; m_{cat} = 15 mg. The dashed lines indicate the peak positions.

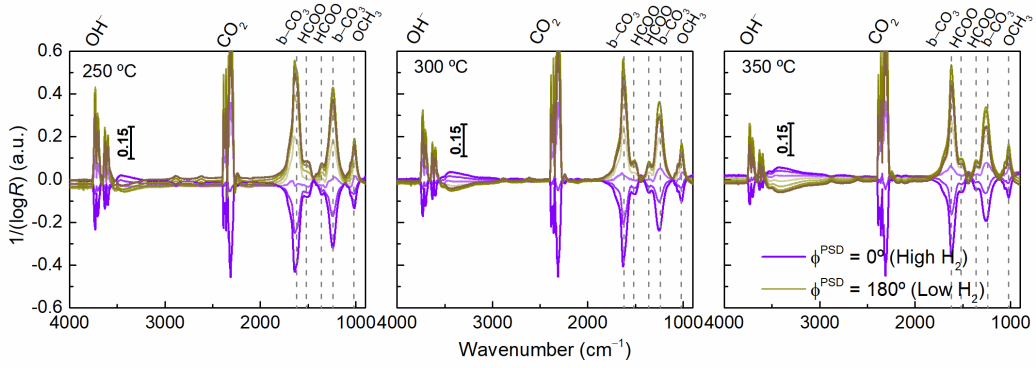

Figure 7S.12. Phase-resolved spectra of the modulation excitation *in situ* DRIFTS studies for pure CeO_2 supporting material conducted at 250, 300 and 350 °C. Experiment conditions: P = 1 bar; flowrate A: CO_2 = 2.5 cm^3 min^{-1} and N_2 = 100 cm^3 min^{-1}; flowrate B: CO_2 = 2.5 cm^3 min^{-1} and 10% H_2/N_2 = 100 cm^3 min^{-1}; m_{cat} = 15 mg. The dashed lines indicate the peak positions.

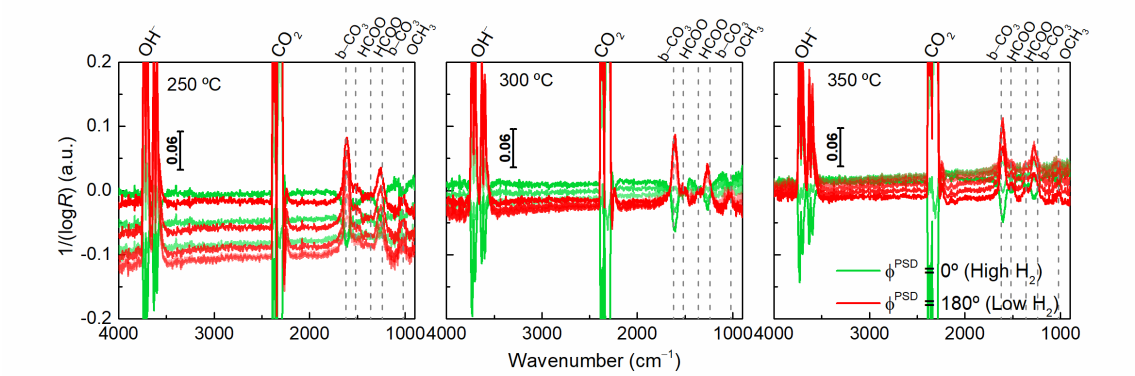

Figure 7S.13. Phase-resolved spectra of the modulation excitation *in situ* DRIFTS studies for the composite ACR–CeO_2 supporting material conducted at 250, 300 and 350 °C. Experiment conditions: P = 1 bar; flowrate A: CO_2 = 2.5 cm^3 min^{-1} and N_2 = 100 cm^3 min^{-1}; flowrate B: CO_2 = 2.5 cm^3 min^{-1} and 10% H_2/N_2 = 100 cm^3 min^{-1}; m_{cat} = 15 mg. The dashed lines indicate the peak positions.

Table 7S.3. Comparison of the catalytic properties of the catalysts of the present work (Ni/CeO_2 and Ni/ACR−CeO_2) with similar catalysts already reported in the literature, including the conditions used in the catalytic system and the reaction experiment in each case.

	Ni (wt%)	P (bar)	CO_2:H_2	*WHSV* (g cm^3 min^{-1})	$X_{CO2,\ MAX}$ (%)	$S_{CH4,\ MAX}$ (%)	$T_{optimal}$ (°C)	T_{50} (°C)	Ref.
Ni/CeO_2	15	1	1:4	60 000	86	100	370	280	This Work
Ni/ACR−CeO_2	15	1	1:4	60 000	87	100	370	180	This Work
Ni/CeO_2–P	10	1	1:4	--	≈85	≈100	275	≈260	[20]
Ni/CeO_2–C	10	1	1:4	--	≈85	≈100	350	≈280	[20]
Ni/CeO_2–SGM	20	1	1:4	10 000	82.5	94.8	250	≈240	[24]
Ni/CeO_2–IM	20	1	1:4	10 000	69.8	84.8	450	≈380	[24]
Ce–Ni–CN	--	1	1:4	10 000	75	100	350	305	[25]
Ce–Ni	--	1	1:4	10 000	75	100	400	330	[25]
Ni/CeO_2	8.5	1	1:4	30 000	≈85	≈100	375	≈280	[26]

References

(1) Ashok, J.; Pati, S.; Hongmanorom, P.; Tianxi, Z.; Junmei, C.; Kawi, S. A Review of Recent Catalyst Advances in CO_2 Methanation Processes. *Catal. Today* **2020**, *356* (May), 471–489. https://doi.org/10.1016/j.cattod.2020.07.023.

(2) Gonçalves, L. P. L.; Sousa, J. P. S.; Soares, O. S. G. P.; Bondarchuk, O.; Lebedev, O. I.; Kolen'ko, Y. V.; Pereira, M. F. R. The Role of Surface Properties in CO_2 Methanation over Carbon-Supported Ni Catalysts and Their Promotion by Fe. *Catal. Sci. Technol.* **2020**, *10* (21), 7217. https://doi.org/10.1039/D0CY01254H.

(3) Miao, B.; Ma, S. S. K.; Wang, X.; Su, H.; Chan, S. H. Catalysis Mechanisms of CO_2 and CO Methanation. *Catal. Sci. Technol.* **2016**, *6* (12), 4048–4058. https://doi.org/10.1039/C6CY00478D.

(4) Goodarzi, F.; Kang, L.; Wang, F. R.; Joensen, F.; Kegnæs, S.; Mielby, J. Methanation of Carbon Dioxide over Zeolite-Encapsulated Nickel Nanoparticles. *ChemCatChem* **2018**, *10* (7), 1566–1570. https://doi.org/10.1002/cctc.201701946.

(5) Gonçalves, L. P. L.; Serov, A.; McCool, G.; Dicome, M.; Sousa, J. P. S.; Soares, O. S. G. P.; Bondarchuk, O.; Petrovykh, D. Y.; Lebedev, O. I.; Pereira, M. F. R.; Kolen'ko, Y. New Opportunity for Carbon-Supported Ni-based Electrocatalysts: Gas-phase CO_2 Methanation. *ChemCatChem* **2021**, *13*, 1–11. https://doi.org/10.1002/cctc.202101284.

(6) Zhang, Z.; Tian, Y.; Zhang, L.; Hu, S.; Xiang, J. Impacts of Nickel Loading on Properties, Catalytic Behaviors of $Ni/\Gamma Al_2O_3$ Catalysts and the Reaction Intermediates Formed in Methanation of CO_2. *Int. J. Hydrogen Energy* **2019**, *44* (18), 9291–9306. https://doi.org/10.1016/j.ijhydene.2019.02.129.

(7) Le, T. A.; Kim, M. S.; Lee, S. H.; Park, E. D. CO and CO_2 Methanation Over Supported Cobalt Catalysts. *Top. Catal.* **2017**, *60* (9–11), 714–720. https://doi.org/10.1007/s11244-017-0788-y.

(8) Zhou, G.; Wu, T.; Xie, H.; Zheng, X. Effects of Structure on the Carbon Dioxide Methanation Performance of Co-Based Catalysts. *Int. J. Hydrogen Energy* **2013**, *38* (24), 10012–10018. https://doi.org/10.1016/j.ijhydene.2013.05.130.

(9) Williamson, D. L.; Jones, M. D.; Mattia, D. Highly Selective, Iron-Driven CO_2 Methanation. *Energy Technol.* **2019**, *7* (2), 294–306. https://doi.org/10.1002/ente.201800923.

(10) Hemmingsson, F.; Schaefer, A.; Skoglundh, M.; Carlsson, P. A. CO_2 Methanation over Rh/CeO_2 Studied with Infrared Modulation Excitation Spectroscopy and Phase Sensitive Detection. *Catalysts* **2020**, *10* (6), 601. https://doi.org/10.3390/catal10060601.

(11) Chen, H.; Goodarzi, F.; Mu, Y.; Chansai, S.; Mielby, J. J.; Mao, B.; Sooknoi, T.; Hardacre, C.; Kegnæs, S.; Fan, X. Effect of Metal Dispersion and Support Structure of Ni/Silicalite-1 Catalysts on Non-Thermal Plasma (NTP) Activated CO_2 Hydrogenation. *Appl. Catal. B Environ.* **2020**, *272* (April), 119013. https://doi.org/10.1016/j.apcatb.2020.119013.

(12) Rasmussen, K. H.; Goodarzi, F.; Christensen, D. B.; Mielby, J.; Kegnæs, S. Stabilization of Metal Nanoparticle Catalysts via Encapsulation in Mesoporous Zeolites by Steam-Assisted Recrystallization. *ACS Appl. Nano Mater.* **2019**, *2* (12), 8083–8091. https://doi.org/10.1021/acsanm.9b02205.

(13) Champon, I.; Bengaouer, A.; Chaise, A.; Thomas, S.; Roger, A. C. Carbon Dioxide Methanation Kinetic Model on a Commercial Ni/Al_2O_3 Catalyst. *J. CO_2 Util.* **2019**, *34* (June), 256–265. https://doi.org/10.1016/j.jcou.2019.05.030.

(14) Garbarino, G.; Riani, P.; Magistri, L.; Busca, G. A Study of the Methanation of Carbon Dioxide on Ni/Al_2O_3 Catalysts at Atmospheric Pressure. *Int. J. Hydrogen Energy* **2014**, *39* (22), 11557–11565. https://doi.org/10.1016/j.ijhydene.2014.05.111.

(15) Wang, W.; Duong-Viet, C.; Ba, H.; Baaziz, W.; Tuci, G.; Caporali, S.; Nguyen-Dinh, L.; Ersen, O.; Giambastiani, G.; Pham-Huu, C. Nickel Nanoparticles Decorated Nitrogen-Doped Carbon Nanotubes (Ni/N-CNT); A Robust Catalyst for the Efficient and Selective CO_2 Methanation. *ACS Appl. Energy Mater.* **2019**, *2* (2), 1111–1120.

https://doi.org/10.1021/acsaem.8b01681.

(16) Hu, F.; Chen, X.; Tu, Z.; Lu, Z.-H.; Feng, G.; Zhang, R. Graphene Aerogel Supported Ni for CO_2 Hydrogenation to Methane. *Ind. Eng. Chem. Res.* **2021**, *60* (33), 12235−12243. https://doi.org/10.1021/acs.iecr.1c01953.

(17) Figueiredo, J. L.; Pereira, M. F. R.; Freitas, M. M. A.; Órfão, J. J. M. Characterization of Active Sites on Carbon Catalysts. *Ind. Eng. Chem. Res.* **2007**, *46* (12), 4110–4115. https://doi.org/10.1021/ie061071v.

(18) Zhang, J.; Yang, Y.; Liu, J.; Xiong, B. Mechanistic Understanding of CO_2 Hydrogenation to Methane over Ni/CeO_2 Catalyst. *Appl. Surf. Sci.* **2021**, *558* (December 2020), 149866. https://doi.org/10.1016/j.apsusc.2021.149866.

(19) Rui, N.; Zhang, X.; Zhang, F.; Liu, Z.; Cao, X.; Xie, Z.; Zou, R.; Senanayake, S. D.; Yang, Y.; Rodriguez, J. A.; Liu, C. J. Highly Active Ni/CeO_2 Catalyst for CO_2 Methanation: Preparation and Characterization. *Appl. Catal. B Environ.* **2021**, *282* (September 2020), 119581. https://doi.org/10.1016/j.apcatb.2020.119581.

(20) Hongmanorom, P.; Ashok, J.; Chirawatkul, P.; Kawi, S. Interfacial Synergistic Catalysis over Ni Nanoparticles Encapsulated in Mesoporous Ceria for CO_2 Methanation. *Appl. Catal. B Environ.* **2021**, *297* (June), 120454. https://doi.org/10.1016/j.apcatb.2021.120454.

(21) Tada, S.; Shimizu, T.; Kameyama, H.; Haneda, T.; Kikuchi, R. Ni/CeO_2 Catalysts with High CO_2 Methanation Activity and High CH_4 Selectivity at Low Temperatures. *Int. J. Hydrogen Energy* **2012**, *37* (7), 5527–5531. https://doi.org/10.1016/j.ijhydene.2011.12.122.

(22) Lee, Y. H.; Ahn, J. Y.; Nguyen, D. D.; Chang, S. W.; Kim, S. S.; Lee, S. M. Role of Oxide Support in Ni Based Catalysts for CO_2 Methanation. *RSC Adv.* **2021**, *11* (29), 17648−17657. https://doi.org/10.1039/d1ra02327f.

(23) Ye, R. P.; Li, Q.; Gong, W.; Wang, T.; Razink, J. J.; Lin, L.; Qin, Y. Y.; Zhou, Z.; Adidharma, H.; Tang, J.; Russell, A. G.; Fan, M.; Yao, Y. G. High-Performance of Nanostructured Ni/CeO_2 Catalyst on CO_2 Methanation. *Appl. Catal. B Environ.* **2020**, *268* (March 2019), 118474. https://doi.org/10.1016/j.apcatb.2019.118474.

(24) Yu, Y.; Chan, Y. M.; Bian, Z.; Song, F.; Wang, J.; Zhong, Q.; Kawi, S. Enhanced Performance and Selectivity of CO_2 Methanation over g-C_3N_4 Assisted Synthesis of Ni–CeO_2 Catalyst: Kinetics and DRIFTS Studies. *Int. J. Hydrogen Energy* **2018**, *43* (32), 15191−15204. https://doi.org/10.1016/j.ijhydene.2018.06.090.

(25) Cárdenas-Arenas, A.; Quindimil, A.; Davó-Quiñonero, A.; Bailón-García, E.; Lozano-Castelló, D.; De-La-Torre, U.; Pereda-Ayo, B.; González-Marcos, J. A.; González-Velasco, J. R.; Bueno-López, A. Isotopic and in Situ DRIFTS Study of the CO_2 Methanation Mechanism Using Ni/CeO_2 and Ni/Al_2O_3 Catalysts. *Appl. Catal. B Environ.* **2020**, *265* (November 2019), 118538. https://doi.org/10.1016/j.apcatb.2019.118538.

(26) Faria, P. C. C.; Órfão, J. J. M.; Pereira, M. F. R. A Novel Ceria – Activated Carbon Composite for the Catalytic Ozonation of Carboxylic Acids. *Catal. Commun.* **2008**, *9*, 2121–2126. https://doi.org/10.1016/j.catcom.2008.04.009.

(27) Owens-Baird, B.; Xu, J.; Petrovykh, D. Y.; Bondarchuk, O.; Ziouani, Y.; González-Ballesteros, N.; Yox, P.; Sapountzi, F. M.; Niemantsverdriet, H.; Kolen'ko, Y. V; Kovnir, K. NiP_2: A Story of Two Divergent Polymorphic Multifunctional Materials. *Chem. Mater.* **2019**, *31* (9), 3407–3418. https://doi.org/10.1021/acs.chemmater.9b00565.

(28) Biesinger, M. C.; Payne, B. P.; Lau, L. W. M.; Gerson, A.; Smart, R. S. C. X-Ray Photoelectron Spectroscopic Chemical State Quantification of Mixed Nickel Metal, Oxide and Hydroxide Systems. *Surf. Interface Anal.* **2009**, *41* (4), 324–332. https://doi.org/10.1002/sia.3026.

(29) Owens-Baird, B.; Sousa, J. P. S.; Ziouani, Y.; Petrovykh, D. Y.; Zarkevich, N. A.; Johnson, D. D.; Kolen'ko, Y. V; Kovnir, K. Crystallographic Facet Selective HER Catalysis: Exemplified in FeP and NiP_2 Single Crystals. *Chem. Sci.* **2020**, *11* (19), 5007–5016. https://doi.org/10.1039/D0SC00676A.

(30) Bêche, E.; Charvin, P.; Perarnau, D.; Abanades, S.; Flamant, G. Ce 3d XPS Investigation of Cerium Oxides and Mixed Cerium Oxide ($Ce_xTi_yO_z$). *Surf. Interface Anal.* **2008**, *40* (November 2007), 264–267. https://doi.org/10.1002/sia.2686.

(31) Zhang, F.; Wang, P.; Koberstein, J.; Khalid, S.; Chan, S. W. Cerium Oxidation State in Ceria Nanoparticles Studied with X-Ray Photoelectron Spectroscopy and Absorption near Edge Spectroscopy. *Surf. Sci.* **2004**, *563* (1–3), 74–82. https://doi.org/10.1016/j.susc.2004.05.138.

(32) Mullins, D. R.; Overbury, S. H.; Huntley, D. R. Electron Spectroscopy of Single Crystal and Polycrystalline Cerium Oxide Surfaces. *Surf. Sci.* **1998**, *409* (2), 307–319. https://doi.org/10.1016/S0039-6028(98)00257-X.

(33) Nolan, M.; Fearon, J. E.; Watson, G. W. Oxygen Vacancy Formation and Migration in Ceria. *Solid State Ionics* **2006**, *177* (35–36), 3069–3074. https://doi.org/10.1016/j.ssi.2006.07.045.

(34) Figueiredo, J. L.; Pereira, M. F. R. The Role of Surface Chemistry in Catalysis with Carbons. *Catal. Today* **2010**, *150*, 2–7. https://doi.org/10.1016/j.cattod.2009.04.010.

(35) Liao, X.; Zhang, Y.; Hill, M.; Xia, X.; Zhao, Y.; Jiang, Z. Highly Efficient Ni/CeO2 Catalyst for the Liquid Phase Hydrogenation of Maleic Anhydride. *Appl. Catal. A Gen.* **2014**, *488*, 256–264. https://doi.org/10.1016/j.apcata.2014.09.042.

(36) Gonçalves, L. P. L.; Christensen, D. B.; Meledina, M.; Salonen, L. M.; Petrovykh, D. Y.; Carbó-Argibay, E.; Sousa, J. P. S.; Soares, O. S. G. P.; Pereira, M. F. R.; Kegnæs, S.; Kolen'Ko, Y. V. Selective Formic Acid Dehydrogenation at Low Temperature over a RuO_2/COF Pre-Catalyst Synthesized on the Gram Scale. *Catal. Sci. Technol.* **2020**, *10* (7), 1991−1995. https://doi.org/10.1039/d0cy00145g.

(37) Srinivasan, P. D.; Patil, B. S.; Zhu, H.; Bravo-Suárez, J. J. Application of Modulation Excitation-Phase Sensitive Detection-DRIFTS for: *In Situ*/Operando Characterization of Heterogeneous Catalysts. *React. Chem. Eng.* **2019**, *4* (5), 862–883. https://doi.org/10.1039/c9re00011a.

(38) Urakawa, A.; Bürgi, T.; Baiker, A. Sensitivity Enhancement and Dynamic Behavior Analysis by Modulation Excitation Spectroscopy : Principle and Application in Heterogeneous Catalysis. *Chem. Eng. Sci.* **2009**, *63* (2008), 4902–4909. https://doi.org/10.1016/j.ces.2007.06.009.

(39) Aguirre, A.; Collins, S. E. Selective Detection of Reaction Intermediates Using Concentration- Modulation Excitation DRIFT Spectroscopy. *Catal. Today* **2013**, *205*, 34–40. https://doi.org/10.1016/j.cattod.2012.08.020.

(40) Baurecht, D.; Fringeli, U. P. Quantitative Modulated Excitation Fourier Transform Infrared Spectroscopy. *Rev. Sci. Instrum.* **2001**, *72* (10), 3782–3792. https://doi.org/10.1063/1.1400152.

(41) Srinivasan, P. D.; Khivantsev, K.; Tengco, J. M. M.; Zhu, H.; Bravo-Suárez, J. J. Enhanced Ethanol Dehydration on γ-Al_2O_3 Supported Cobalt Catalyst. *J. Catal.* **2019**, *373*, 276–296. https://doi.org/10.1016/j.jcat.2019.03.024.

(42) Yu, Y.; Bian, Z.; Wang, Z.; Wang, J.; Tan, W.; Zhong, Q.; Kawi, S. CO_2 Methanation on Ni-$Ce_{0.8}$ $M_{0.2}$ O_2 (M=Zr, Sn or Ti) Catalyst: Suppression of CO via Formation of Bridging Carbonyls on Nickel. *Catal. Today* **2020**, *2* (July), DOI:10.1016/j.cattod.2020.07.049. https://doi.org/10.1016/j.cattod.2020.07.049.

(43) Huynh, H. L.; Zhu, J.; Zhang, G.; Shen, Y.; Tucho, W. M.; Ding, Y.; Yu, Z. Promoting Effect of Fe on Supported Ni Catalysts in CO_2 Methanation by *in situ* DRIFTS and DFT Study. *J. Catal.* **2020**, *392*, 266–277. https://doi.org/10.1016/j.jcat.2020.10.018.

Chapter 8

Conclusions and Future Work

1. Main Conclusions

The main goal of this thesis was the development and understanding of the behavior of high-performing catalysts capable of achieving high CO_2 conversion (X_{CO2}) and complete methane selectivity (S_{CH4}) in the CO_2 methanation reaction, at lower temperatures than those currently used in the industry (≥ 400 °C). For that, judiciously tailored carbon materials were investigated as a way to obtain high-performing Ni-based catalysts. Due to the advantageous properties of carbon materials, specifically the high surface area and the possibility to easily tailor their surface properties, they are good candidates for being employed as the supporting materials for CO_2 methanation catalysts, even though they were not extensively studied for this specific application. Furthermore, the addition of a second metal to the typical monometallic Ni catalysts has been proved to be an interesting strategy for enhancing the performance of the resultant catalysts, since the interaction between the two metals can lead to beneficial modifications in the electronic and geometrical properties of the catalysts. In this work, it was decided to evaluate the possibility of using carbon materials for this application, as well as to study the possibility of preparing bimetallic catalysts with enhanced catalytic properties.

1.1 Carbon materials as catalyst supports

Starting with the study of activated carbon (AC) as support for Ni-based catalysts for CO_2 methanation, the tailoring of the surface properties of these materials was investigated. It was observed that the basicity of the support plays a major role in the performance of the catalyst since the Ni catalyst supported on the most basic carbon material afforded the best performance. It was established that the performance of the catalysts was solely correlated with the surface properties of the AC supports, which was evidenced by the fact that the catalysts exhibited similar textural properties, mean size of Ni nanoparticles, phase and surface compositions of the active Ni nanoparticles,

and their reducibility profiles. Therefore, the better performance of the functionalized supports compared to the pristine one was established to be related to the good Ni dispersion and better CO_2 adsorption. With Ni on reduced AC, a slight but gradual deactivation of the catalyst over time-on-stream CO_2 methanation for 90 h was observed and was found to be associated with the sintering of catalytic Ni nanoparticles. Furthermore, the formation of nanoparticles with distinct Ni@NiO core-shell nanostructure was observed for this catalyst after 90 h of time-on-stream.

With these results in hands, a different type of carbon material – carbon nanotubes (CNT) – was further studied. Different surface treatments were performed on CNT to determine which surface modification would be more beneficial, in the case of CNT, for CO_2 methanation. Interestingly, in the case of CNT, the trend was contrary to the one observed for AC. The Ni catalyst supported on N-doped CNT demonstrated the best catalytic performance when compared to that supported on reduced CNT or pristine CNT. Therefore, Ni on N-doped CNT was then investigated in detail to understand the reasoning for its topmost performance. The Ni catalyst supported on N-doped CNT achieved a higher X_{CO2} and S_{CH4} at a lower temperature than the one supported on the pristine CNT counterpart, and furthermore, both catalysts exhibit outstanding stability over 48 h of TOS testing, with no sign of deactivation. The enhanced performance of Ni on N-doped CNT was established to be a result of the good dispersion of the Ni phase over N-doped CNTs, as evidenced by TEM, HAADF–STEM, H_2 TPR, and H_2 pulse chemisorption.

Carbon xerogel containing nitrogen was the third type of carbon material evaluated as supporting material for CO_2 methanation Ni catalysts; unfortunately, the performance of the resultant catalyst was found to be significantly lower when compared to the catalysts supported on AC and CNT materials (Appendix 4).

The referred results indicate that both AC and CNT present an excellent opportunity to be explored as catalyst supports in the rational design of

improved catalysts; however, the development of new catalysts is a time- and resource-consuming process. Therefore, it was decided to explore a shortcut for discovering efficient catalysts by taking advantage of existing Ni on carbon electrocatalysts used for other applications, such as hydrogen evolution and oxidation reactions. A commercially available carbon-supported Ni-based hydrogen oxidation/evolution electrocatalyst was successfully employed in gas-phase CO_2 hydrogenation to CH_4, achieving excellent performance in this reaction with outstanding stability over 90 h. The work demonstrated that some of the well designed, engineered, and produced electrocatalysts could be strategically valuable for the CO_2 methanation reaction.

Finally, to design an optimal supporting material guided by accumulated knowledge, a composite material of reduced activated carbon and CeO_2 was investigated. A set of Ni catalysts deposited either on pure CeO_2 or composite carbon–CeO_2 supporting materials were successfully synthesized, and the resultant materials achieved excellent conversion, selectivity and stability at favorably low reaction temperature when compared to the CeO_2-free Ni on reduced AC catalyst. Importantly, compositing carbon with CeO_2 in the supporting material allowed for an efficient reduction in the usage of the expensive rare-earth cerium oxide while affording not only a cost-effective but also a high-performing methanation catalyst.

1.2 Bimetallic catalysts

Bimetallic catalysts were evaluated in reduced activated carbon, CeO_2 and carbon-CeO_2 supports.

NiFe bimetallic catalysts were the first to be studied on the reduced activated carbon support. It was concluded that the catalytic performance of the Ni catalyst was enhanced in terms of activity and selectivity, while simultaneously, the reduction of the temperature of methanation reaction was achieved through a judicious Fe promotion. Furthermore, the deactivation of the monometallic catalyst during prolonged time-on-stream CO_2 methanation could be prevented by the addition of Fe. Overall, the optimal combination of

15 wt% Ni and 5 wt% Fe in the reduced activated carbon support led to an increase in the performance at a lower temperature as well as an improvement in the stability, when compared to the monometallic 15 wt% Ni on reduced activated carbon counterpart. Interestingly, the same improvement was not achieved when adding Fe to the Ni on N-doped CNT catalyst presented in Chapter 4 (Appendix 5).

These promising results lead to the investigation of other second metals in bimetallic Ni catalysts (Appendix 7). NiMg, NiY, NiCr, NiAl, Ni, and NiSn catalysts supported on reduced AC, all prepared with 15 wt% Ni and 5 wt% of the other metal were evaluated for CO_2 methanation reaction and from these catalysts, NiMg on reduced AC demonstrated the most promising results. However, this catalyst showed unsatisfactory stability and did not exhibit comparable performance to the best performing Ni on CeO_2 and Ni on carbon−CeO_2 composite, suggesting the need for a further understanding and optimization study of this bimetallic catalyst.

Finally, commercially available NiMo and NiRe bimetallic electrocatalysts supported on carbon were also investigated. Unfortunately, the introduction of Mo and Re led to a decrease in the overall activity and selectivity of the monometallic Ni on carbon electrocatalyst. Moreover, NiMo on carbon exhibited poor stability over 90 h of time-on-stream testing, while the addition of Re did not affect the stability behavior.

1.3 *In situ* studies

The mechanism of the CO_2 methanation over different catalysts has been a topic of intensive research; however, it is still a subject of debate since it depends on several aspects, such as the catalyst used and the reaction conditions. Importantly, for the rational development of new and improved catalyst materials, understanding the reaction mechanism and the changes that the catalysts undergo under reaction conditions is crucial.

The thesis presented herein comprised both the study of the CO_2 reaction mechanism on the developed catalysts and the microstructural changes that the catalysts undergo at the methanation conditions.

An *in situ* TEM study on the Ni on reduced AC catalyst was performed to understand the microstructural changes observed in the catalyst after 90 h of time-on-stream, namely, the formation of the Ni@NiO core-shell nanostructure. The study demonstrated that the NiO shell around the metallic Ni core was found to be formed *in situ* under CO_2 methanation conditions. It was hypothesized that the formation of the Ni@NiO core–shell structure in the catalyst nanoparticles is beneficial due to a coupling of the enhanced CO_2 adsorption/activation over the NiO shell with H_2 dissociation over the Ni core, bringing reactants and intermediates together to facilitate CO_2 methanation.

Furthermore, an *in situ* ME-PSD-DRIFTS study allowed for the elucidation of the reaction mechanism. In this case, Ni on carbon−CeO_2 composite and Ni on CeO_2 were investigated. Ni on reduced AC was not included in the study because the reduced AC support, unfortunately, absorbs most of the IR radiation. Thus, it is not possible to analyze this material using DRIFTS. The mechanism of the CO_2 methanation over Ni on CeO_2 catalysts was found to proceed throughout both CO and formate pathways, while in the case of Ni on carbon−CeO_2 composite, it only follows the formate pathway. Importantly, some differences in the intermediate steps of the reaction were found between these catalysts. The main established difference is that, during methanation over Ni on CeO_2, the reaction is mediated by CO from formate dissociation, while over Ni on carbon–CeO_2 catalyst, CH_4 is formed without intermediate CO formation. Thus, it was established that even a partial modification of the supporting material for Ni methanation catalysts can influence the reaction mechanism.

1.4 Developed catalysts

From the different sets of catalysts synthesized and evaluated, the topmost performing catalysts could be selected. Figure 8.1 presents a comparison of the CO_2 conversion (X_{CO2}) as a function of the optimal temperature ($T_{optimal}$) for the topmost performing catalysts of each set. Selectivity to methane was higher than 99% for all the catalysts at these conditions (except for Ni/AC−R for which it was 98%). It is possible to conclude that the Ni catalyst supported on the reduced activated carbon-CeO_2 composite (Ni/ACR−CeO_2) exhibits the highest X_{CO2} = 87% at the lowest optimal temperature of 370 °C, followed by its counterpart supported on pure CeO_2 (Ni/CeO_2), which obtained slightly lower conversion at the same temperature. Taking into account the CO_2 conversion and optimal temperature, the following order of performance can be established: Ni/ACR−CeO_2 > Ni/CeO_2 > Ni/C > Ni/CNT−N ≈ NiMg/AC−R > NiFe/AC−R > Ni/AC−R. Where Ni/C is the Ni on carbon electrocatalyst, Ni/CNT−N is the Ni on N-doped carbon nanotubes, and Ni/AC−R, NiFe/AC−R and NiMg/AC−R are Ni, NiMg and NiFe supported on reduced activated carbon, respectively.

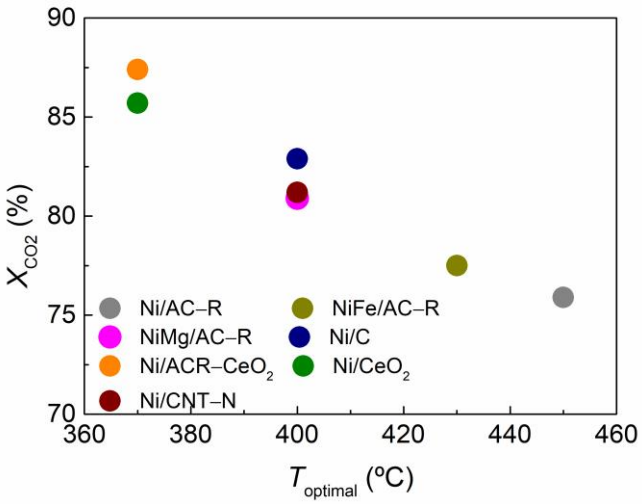

Figure 8.1. Comparison of the CO_2 conversion (X_{CO2}) as a function of the optimal temperature ($T_{optimal}$) for the topmost performing catalysts.

2. Future Work

The work described in this thesis demonstrated that carbon materials are a valuable option to be used as catalyst supports in CO_2 methanation catalysts. However, there is still plenty of room for design and improvement of this type of materials. Thus, the following suggestions for future work are proposed:

- an additional investigation to understand the reasoning behind the instability of the NiMg on reduced AC catalyst, ultimately to derive high-performing and durable NiMg-based catalysts. This would be important since the addition of Mg led to promising results in terms of activity and selectivity at lower temperatures; however, the stability of this catalyst was found to be unsatisfactory, which leaves space for further research efforts;
- the preparation of composite materials with CeO_2 and other types of carbon materials. An interesting approach could be the compositing with N-doped CNT since this material demonstrated to be a good support for Ni-based catalysts, achieving high conversion and selectivity in CO_2 methanation reaction;
- a kinetic study using the topmost performing catalysts developed in this thesis;
- the evaluation of the performance of the topmost performing catalysts developed in this thesis under real industrial conditions. The CO_2 methanation reaction can be used for different applications, such as biomethane upgrading or renewable energy storage, therefore:
    - for the first application, since biomethane usually presents 40% of CO_2 in its composition, the catalysts should be tested under a gas feed composed of CH_4 and CO_2, and the trace compounds usually found in raw biomethane (H_2S, N_2, O_2). A parametric study should be performed to evaluate the influence of the different variables and operation conditions, in order to find the optimal reaction conditions and to establish the feasibility of the use of these materials for such application;

- for the renewable energy storage, the performance should be evaluated under dynamic conditions, where the H_2 percentage in the flow should fluctuate, mimicking the real conditions of a Power-to-Gas plant, where the H_2 supply is intermittent as it is produced by electrolysis using intermittent renewable energy sources. This fluctuation of H_2 supply might hinder the stability of the catalysts; therefore, their stability should be evaluated at such conditions.

- the study of the developed catalysts in different applications, such as electrocatalysis. Since it was demonstrated that electrocatalysts can be efficiently used for gas phase CO_2 methanation, the reverse (use of CO_2 methanation catalysts for electrocatalysis applications) should be investigated.

Appendices

Appendix 1 – Calibration Curves and Calculation Example

Calibration Curves

Figure A1.1 to Figure A1.4 present the linear fitting of the curves of concentration of N_2, CO_2, CH_4 and CO, respectively, as a function of the chromatogram peak area. The equation of the fitting is shown in each graphic, as well as the R squared value.

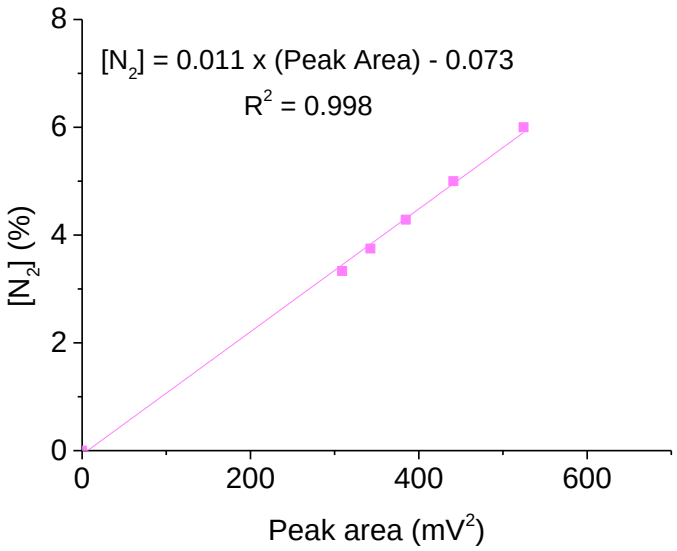

Figure A1.1. Linear fitting of N_2 concentration vs peak area.

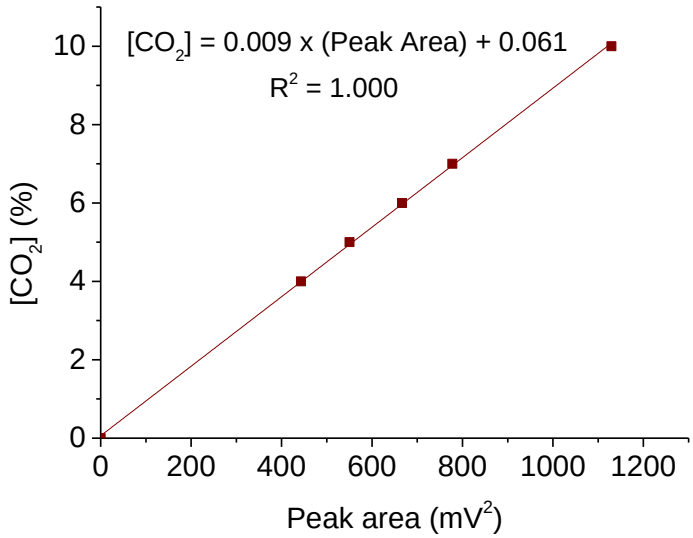

Figure A1.2. Linear fitting of CO_2 concentration vs peak area.

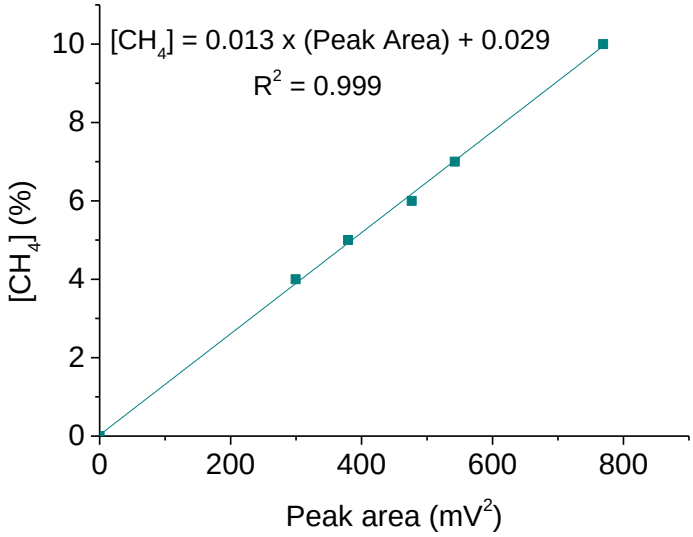

Figure A1.3. Linear fitting of CH_4 concentration vs peak area.

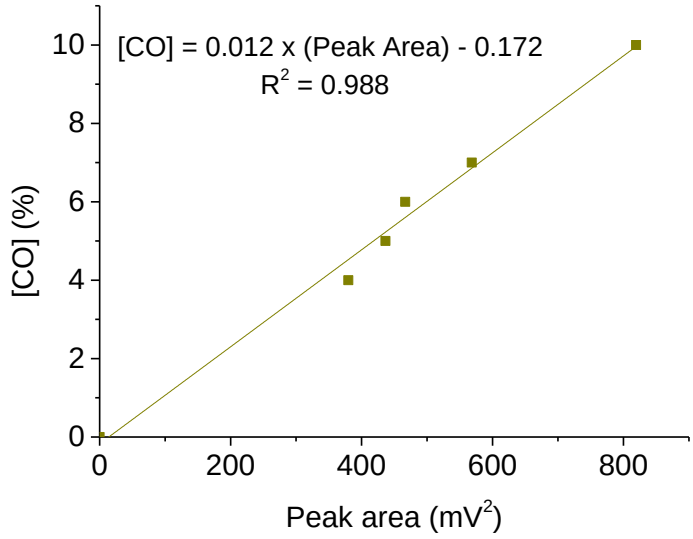

Figure A1.4. Linear fitting of CO concentration vs peak area.

Table A1.1 lists the Response Factor (RF) and Relative Response Factor (RRF) values for N_2, CO_2, CH_4 and CO. The RRF value is used to determine the concentration of each gas in the flow, analyzed by the GC.

Table A1.1. Response Factor (RF) and Relative Response Factor (RRF) values for N_2, CO_2, CH_4

Gas	RF	RRF
N_2	89.9	--
CO_2	111.2	1.2
CH_4	76.9	0.9
CO	84.6	0.9

Calculation Example

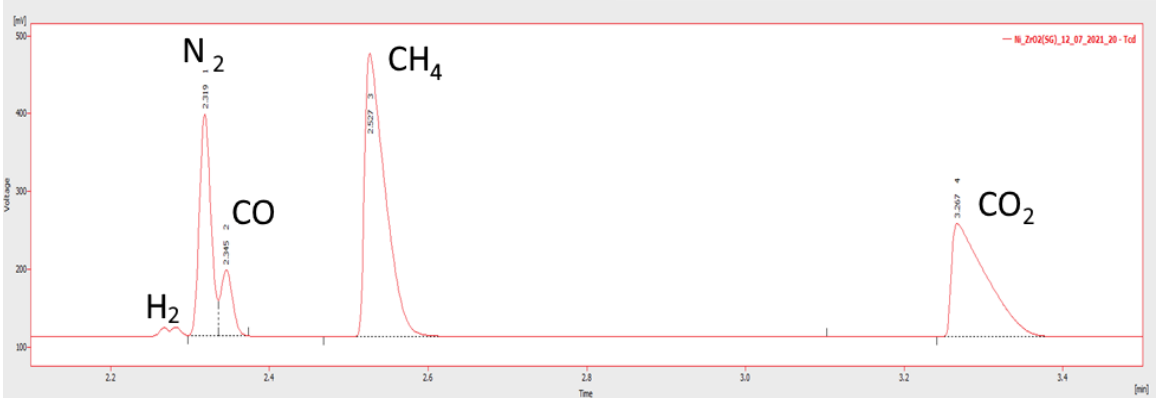

Figure A1.5. Example of a chromatogram of the products of the reaction.

	Reten. Time [min]	Area [mV.s]	Height [mV]	Area [%]	Height [%]	W05 [min]	Compound Name
1	2.319	285.843	284.023	19.5	32.3	0.02	
2	2.345	87.587	84.658	6.0	9.6	0.02	
3	2.527	651.455	364.253	44.4	41.5	0.03	
4	3.267	442.586	145.067	30.2	16.5	0.05	
	Total	1467.471	878.002	100.0	100.0		

Figure A1.6. Example of the results table of the chromatograms from which the peak areas are collected.

The calculations of each gas concentration were done, considering that the gas flowrate changes with the conversion of CO_2 since the stoichiometry of the reaction determines that for each 5 mol of reactants (CO_2 + H_2) reacted, only 3 mol of products (CH_4 + H_2O) are formed. Therefore, the flowrate of products depends on the conversion of CO_2.

$$CO_2(g) + 4H_2(g) \leftrightarrow CH_4(g) + 2H_2O(g) \quad (1)$$

As such, N_2 (3 $cm^3\ min^{-1}$) was used as internal standard, in order to determine the total flow rate (Q_T/$cm^3\ min^{-1}$) of products as follows:

$$[N_2]_{\%} = a \times Area\ N_2 + b \quad (2)$$

$$[CO_2]_{\%} = \frac{Area\ CO_2}{Area\ N_2} \times \frac{1}{RRF_{CO_2}} \times [N_2] \quad (3)$$

$$F_{CO_2} = \frac{[CO_2]_{\%}}{100} \times \frac{Q_T}{V_M} \quad (4)$$

$$[CH_4] = \frac{Area\ CH_4}{Area\ N_2} \times \frac{1}{RRF_{CH_4}} \times [N_2] \quad (5)$$

$$F_{CH_4} = \frac{[CH_4]_{\%}}{100} \times \frac{Q_T}{V_M} \quad (6)$$

$$[CO] = \frac{Area\ CO}{Area\ N_2} \times \frac{1}{RRF_{CO}} \times [N_2] \quad (7)$$

$$F_{CO} = \frac{[CO]_{\%}}{100} \times \frac{Q_T}{V_M} \quad (8)$$

Where $[N_2]_{\%}$, $[CO_2]_{\%}$, $[CH_4]_{\%}$, $[CO]_{\%}$ is the concentration in percentage of each gas in the flow, *a* and *b* are the constants of the equation of the linear fitting of N_2 concentration vs peak area (Figure A1.1), Q_T is the total flowrate in $cm^3\ min^{-1}$, Q_{N2} is the N_2 flowrate in $cm^3\ min^{-1}$, *RRF* is the relative response factor, F_{CO2}, F_{CH4}, and F_{CO} are the molar flowrates of each gas in $mol\ min^{-1}$, and V_M is the molar volume of a gas in PTN conditions.

Therefore, CO_2 conversion (X_{CO2}), CH_4 and CO selectivities (S_{CH4}, S_{CO}), and CH_4 and CO yields (Y_{CH4}, Y_{CO}) are determined as follows:

$$\mathrm{X}\ (\%) = \frac{\mathrm{F}_{CO_2,in} - \mathrm{F}_{CO_2,out}}{\mathrm{F}_{CO_2,in}} \times 100 \quad (6)$$

$$S_{\mathrm{CH_4}} = \frac{\mathrm{F}_{CH_4,out}}{\mathrm{F}_{CH_4,out} + \mathrm{F}_{CO,out}} \times 100 \quad (7)$$

$$S_{CO} = \frac{\mathrm{F}_{CO,out}}{\mathrm{F}_{CH_4,out} + \mathrm{F}_{CO,out}} \times 100 \quad (8)$$

$$Y_{\mathrm{CH_4}} = \frac{X \times S_{\mathrm{CH_4}}}{100} \quad (9)$$

$$Y_{CO} = \frac{X \times S_{\mathrm{CO}}}{100} \quad (10)$$

Appendix 2 – Influence of the Ni and Fe loading

Previous to all the studies conducted, we performed an optimization of the Ni loading on pristine AC. We evaluated the performance of three catalysts containing 5, 15, and 25 wt% Ni loading, supported on pristine AC.

Figure A2.1 presents the conversion of CO_2 (X_{CO2}) and selectivity to methane (S_{CH4}) for each catalyst. It is possible to observe that with 5% Ni loading, the catalyst exhibited null conversion, whereas with 15% it presents a X_{CO2} similar to the catalyst with 25%. However, in terms of S_{CH4}, the 15Ni/AC catalyst have higher S_{CH4} than 25Ni/AC. Therefore, 15% was the loading selected for most of the studies.

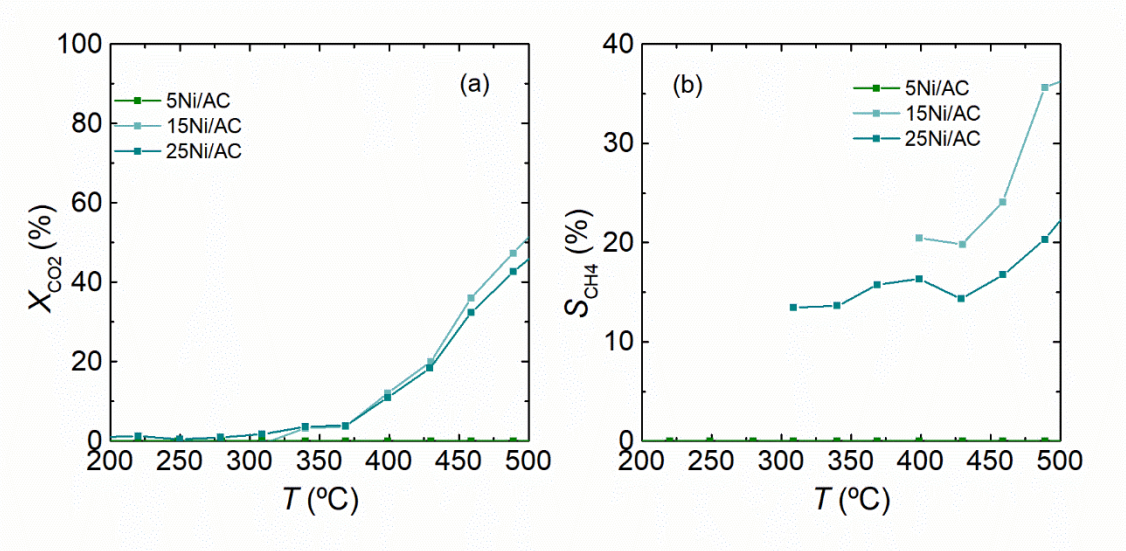

Figure A2.1. Comparison of the catalytic properties of the synthesized Ni catalysts supported on pristine AC, with different Ni loadings (5, 15, and 25 wt% Ni): X_{CO2} (a), and S_{CH4} (b) as a function of temperature. Reaction conditions: P = 1 bar; $WHSV$ = 60 000 mL g^{-1} h^{-1}; CO_2 : H_2 = 1 : 4.

The influence of Ni and Fe loading and weight ratios was also investigated in pristine activated carbon, previous to the preparation of the NiFe/AC−R catalyst reported in Chapter 3 [1]. Figure A2.2 presents the conversion of CO_2 (X_{CO2}) and selectivity to methane (S_{CH4}) for catalysts with different Ni:Fe weight ratios: 18:2, 15:5, and 10:10, at different temperatures. Interestingly, the addition of Fe at the different ratios tested led to a significant improvement in the obtained X_{CO2} comparing to the monometallic Ni/AC catalysts. The

catalysts obtained similar X_{CO2} in the range of temperatures tested, reaching a X_{CO2} close to 60% at 500 °C. However, the S_{CH4} was different depending on the Ni:Fe ratio used. From the tested ratios, Ni:Fe = 15:5 obtained the highest S_{CH4}, reaching S_{CH4} ≈ 80%.

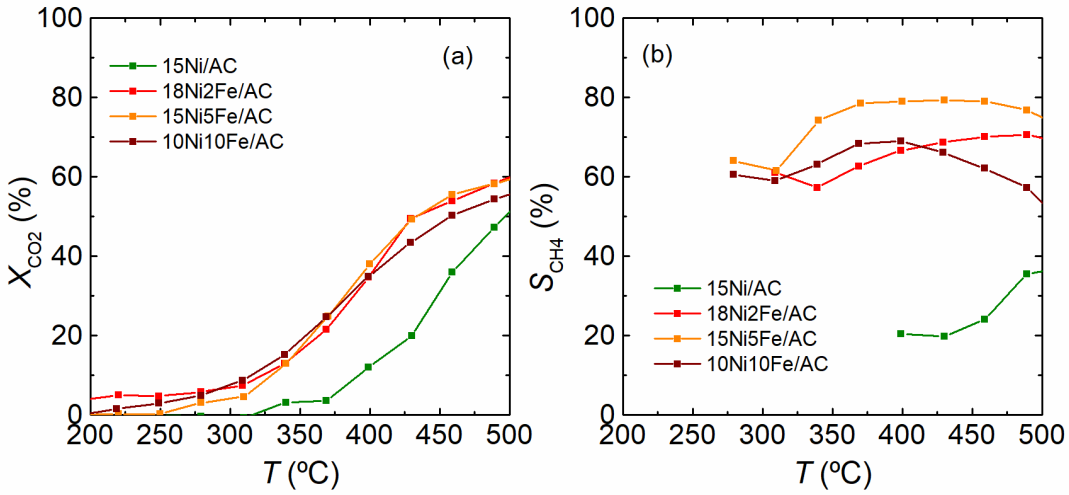

Figure A2.2. Comparison of the catalytic properties of the synthesized NiFe catalysts supported on pristine AC, with different Ni:Fe ratios: X_{CO2} (a), and S_{CH4} (b) as a function of temperature. Reaction conditions: P = 1 bar; $WHSV$ = 60 000 mL g^{-1} h^{-1}; CO_2 : H_2 = 1 : 4.

Therefore, with a 15:5 (3:1) weight ratio, we evaluated the influence of the total metal loading with 16 wt%, 20 wt%, and 24 wt%. Figure A2.3 shows the X_{CO2} and S_{CH4} for catalysts with different metal weight ratios. The three metal loadings evaluated achieved similar X_{CO2} over the range of temperatures tested, achieving maximum X_{CO2} ≈ 60% at 500 °C. However, the S_{CH4} was different depending on the total metal loading used, and the 20 wt% sample (15Ni5Fe/AC) exhibited the highest S_{CH4}. Therefore, this was the selected loading to the experiments that followed and are presented in Chapter 3.

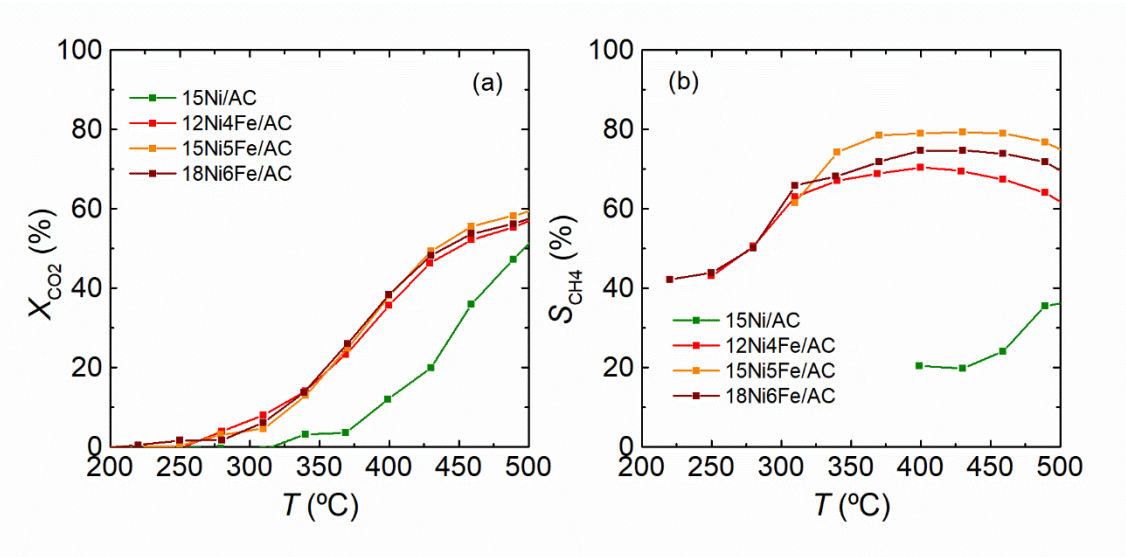

Figure A2.3. Comparison of the catalytic properties of the synthesized NiFe catalysts supported on pristine AC, with different NiFe loadings: X_{CO2} (a), and S_{CH4} (b) as a function of temperature. Reaction conditions: P = 1 bar; $WHSV$ = 60 000 mL g^{-1} h^{-1}; CO_2 : H_2 = 1 : 4.

Appendix 3 – CNT with different surface chemistries

Taking into account the results from Chapter 3 preliminary to the results presented in Chapter 4, different treatments were performed on CNT in an attempt to determine which surface modification would be more beneficial in the case of CNT. The N-doping and surface reduction treatments performed in AC in Chapter 3 were repeated in CNT. Interestingly in the case of CNT, the trend was contrary to the one observed for AC. The Ni catalysts supported on N-doped CNT (Ni/CNT−N) demonstrated improved catalytic performance when compared to those supported on reduced CNT (Ni/CNT−R), as can be observed in Figure A3.1. Therefore, Chapter 4 describes the detailed study of Ni supported on CNT−N as catalyst for CO_2 methanation and its comparison with a similar catalyst supported on pristine CNT.

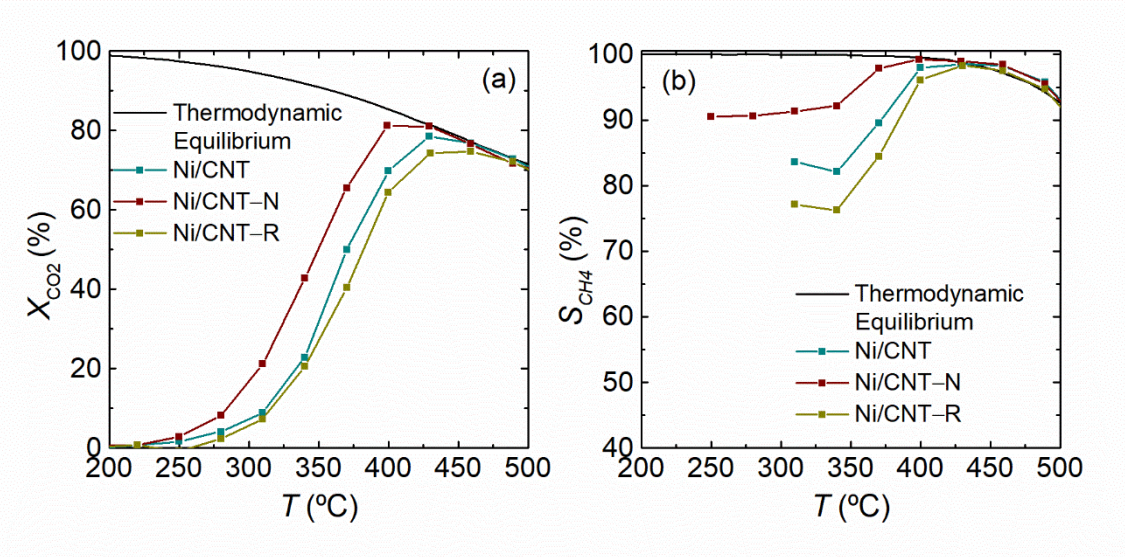

Figure A3.1. Comparison of the catalytic properties of Ni catalysts supported on CNT with different surface chemistries (Ni/CNT, Ni/CNT−N, and Ni/CNT−R): X_{CO2} (a), and S_{CH4} (b) as a function of temperature, together with the respective thermodynamic equilibrium curves. Reaction conditions: P = 1 bar; $WHSV$ = 60 000 mL g^{-1} h^{-1}; CO_2 : H_2 = 1 : 4.

Appendix 4 – N-doped Carbon Materials

As it was demonstrated in Chapters 3 and 4, N-containing carbon materials can present enhanced activity and selectivity in the CO_2 methanation reaction. Herein, we compared the performance of three different types of carbon materials (Carbon nanotubes – CNT; Activated Carbon – AC; Carbon Xerogel – XG) containing N-functionalities and compared their performance as support for Ni-based catalysts on CO_2 methanation.

Figure A4.1 presents a comparison of the catalytic properties in terms of CO_2 conversion (X_{CO2}) and methane selectivity (S_{CH4}) of the synthesized Ni catalysts supported on N-containing CNT (Ni/CNT−N), AC (Ni/AC−N), and XG (Ni/XG−N), as a function of temperature. It is possible to determine a performance order (Ni/CNT−N > Ni/AC−N > Ni/XG−N), with Ni/CNT−N exhibiting X_{CO2} = 81.2% and S_{CH4} = 99.2% at 400 °C, while Ni/AC−N presents lower X_{CO2} = 70.4% and S_{CH4} = 93.5% at higher T = 450 °C, and Ni/XG−N exhibits even lower X_{CO2} = 56.8% and S_{CH4} = 73.0% at even higher T = 500 °C. Since the XG did not present very promising results, further studies were not conducted with this material.

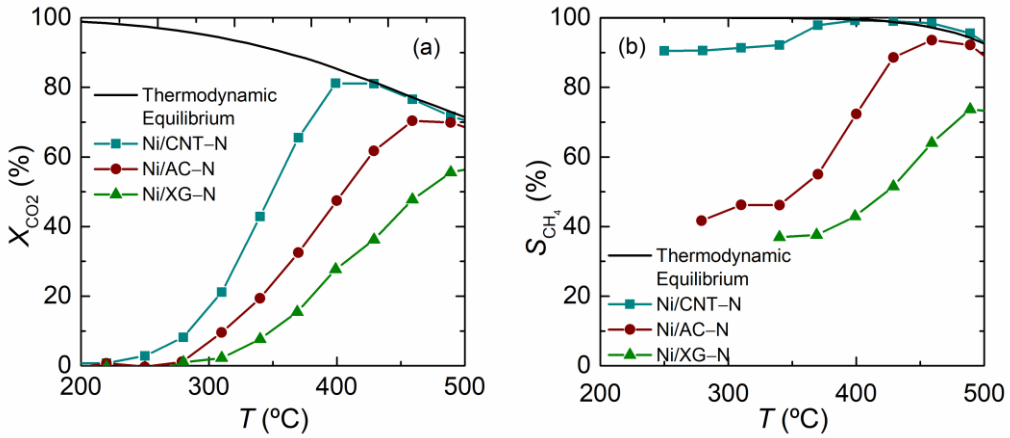

Figure A4.1. Comparison of the catalytic properties of the synthesized Ni catalysts supported on N-containing CNT (Ni/CNT−N), AC (Ni/AC−N), and XG (Ni/XG−N): X_{CO2} (a), and S_{CH4} (b) as a function of temperature, together with the respective thermodynamic equilibrium curves. Reaction conditions: P = 1 bar; $WHSV$ = 60 000 mL g^{-1} h^{-1}; CO_2 : H_2 = 1 : 4.

Appendix 5 – NiFe bimetallic catalysts on different supports

Taking into account the results presented in Chapter 3, in which a NiFe bimetallic catalyst obtained enhanced performance for CO_2 methanation, when compared to its monometallic Ni counterpart, we evaluated the influence of the addition of Fe to the catalyst presented in Chapter 4 (Ni/CNT−N). A catalyst with 15 wt% Ni and 5 wt% Fe was prepared on CNT−N support, and the results of its performance for CO_2 methanation reaction are presented in Figure A6.1. In the case of NiFe/CNT−N the X_{CO2} was higher than Ni/CNT−N at lower temperatures; however, the maximum X_{CO2} is similar to that of monometallic Ni/CNT−N catalyst (X_{CO2} = 81%), and it was achieved at the same temperature of ≈ 400 °C, with similar S_{CH4}, close to 100%. Therefore, the addition of Fe to the Ni on CNT−N catalyst does not lead to a beneficial effect in the same extent as in the AC−R support.

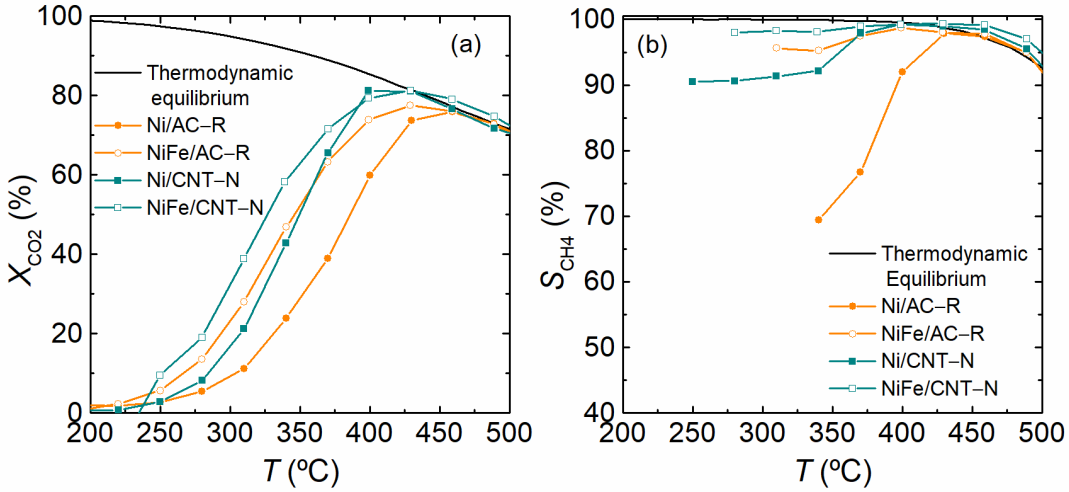

Figure A5.1. Comparison of the catalytic properties of the synthesized Ni and NiFe catalysts supported on reduce activated carbon (Ni/AC−R and NiFe/AC−R) and N-containing CNT (Ni/CNT−N and NiFe/CNT−N): X_{CO2} (a), and S_{CH4} (b) as a function of temperature, together with the respective thermodynamic equilibrium curves. Reaction conditions: P = 1 bar; $WHSV$ = 60 000 mL g^{-1} h^{-1}; CO_2 : H_2 = 1 : 4.

Appendix 6 – CeO_2 vs MgO as composite material with AC−R

In Chapter 6, a carbon/ceria supporting material is evaluated for Ni-based catalysts for CO_2 methanation. A preliminary work to this Chapter was performed in order to evaluate which oxide would suit better for this application. CeO_2 and MgO were composited with AC−R and used as supporting material for Ni catalysts. The results of each catalytic material, Ni/ACR−CeO_2 and Ni/ACR−MgO, in CO_2 methanation are presented in Figure A6.1 and compared with Ni/AC−R. Ni supported ACR−MgO composite achieved a higher X_{CO2} and S_{CH4} than Ni/AC−R in the range of temperatures tested, reaching a X_{CO2} = 83% with S_{CH4} = 99.5% at 400 °C. Ni/ACR−CeO_2 reached a higher X_{CO2} of 87% at lower temperature of 370 °C and thus was selected for the further studies presented in Chapter 6.

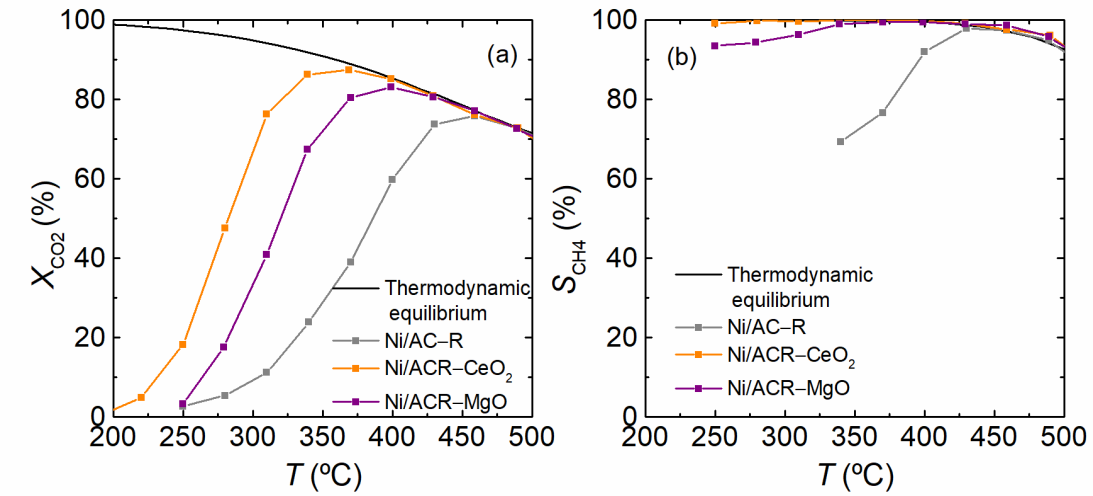

Figure A6.1. Comparison of the catalytic properties of the synthesized Ni catalysts supported on AC−R (Ni/AC−R), ACR−CeO_2 composite (Ni/ACR−CeO_2), and ACR−MgO composite (Ni/ACR−MgO): X_{CO2} (a), and S_{CH4} (b) as a function of temperature, together with the respective thermodynamic equilibrium curves. Reaction conditions: P = 1 bar; $WHSV$ = 60 000 mL g^{-1} h^{-1}; CO_2 : H_2 = 1 : 4.

Appendix 7 – Bimetallic Catalysts for CO_2 methanation – Performance evaluation of the use of different second metals on Ni catalysts supported on AC−R

Bimetallic catalysts are known to be capable of enhancing the performance of the monometallic counterparts since the interaction between the two metals can change their electronic and geometric properties. In Chapter 3, we presented the enhanced performance of NiFe/AC−R, when compared to Ni/AC−R. Herein, we decided to evaluate the performance of different bimetallic catalysts for CO_2 methanation.

Figure A7.1 presents a comparison of the catalytic properties of the monometallic Ni/AC−R and bimetallic NiFe/AC−R, NiMg/AC−R, NiY/AC−R, NiCr/AC−R, NiAl/AC−R, NiAg/AC−R, and NiSn/AC−R catalysts, all prepared with 15 wt% Ni and 5 wt% of the other metal. These second metals were selected due to presenting interesting properties for this application: Al was used since Al_2O_3 is the most used support for this application,[2] Mg can increase the basicity of the catalyst, enhancing the CO_2 coverage,[3] Ag and Sn can prevent coke deposition on Ni catalysts,[4,5] Y also increases the catalysts basicity, and is capable of increasing the metal-support interactions and preventing coke formation,[6,7] and Cr is known to act as stabilizer, retarding the sintering of the nanoparticles.[8]

From the tested catalysts, NiMg/AC−R, NiY/AC−R, NiFe/AC−R, and NiCr/AC−R exhibited enhanced activity, when compared to Ni/AC−R, while NiAl/AC−R and NiAg/AC−R presented lower activity than Ni/AC−R. NiSn/AC−R demonstrated null activity. Interestingly, NiMg/AC−R exhibited the topmost X_{CO2} from the tested catalysts, exhibiting X_{CO2} = 80.9% with S_{CH4} = 99.4% at 400 °C.

The NiMg loading on the catalyst was optimized by testing the catalytic performance of catalysts with different loadings, namely with Ni:Mg weight ratios of 15:5, 15:2.5, 18:6, 15:15, and 12:4. The catalytic results are presented

in Figure A7.3. The optimal loading found was the one initially used, 15 wt% Ni and 5 wt% Mg. Increasing the loading of either Ni or Mg did not lead to an increase in the activity of the catalysts but decreasing the loading of either Ni or Mg led to a decrease in activity; therefore, 15:5 was found to be the optimal loading.

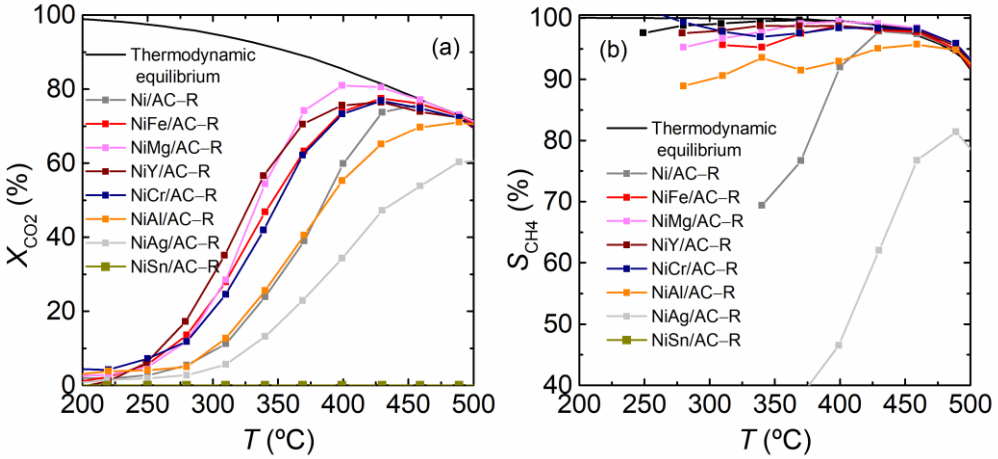

Figure A7.1. Comparison of the catalytic properties of the synthesized monometallic (Ni/AC−R) and bimetallic (NiMg/AC−R, NiY/AC−R, NiCr/AC−R, NiAl/AC−R, NiAg/AC−R, and NiSn/AC−R) catalysts supported on AC−R: X_{CO2} (a), and S_{CH4} (b) as a function of temperature, together with the respective thermodynamic equilibrium curves. Reaction conditions: P = 1 bar; $WHSV$ = 60 000 mL g^{-1} h^{-1}; CO_2 : H_2 = 1 : 4.

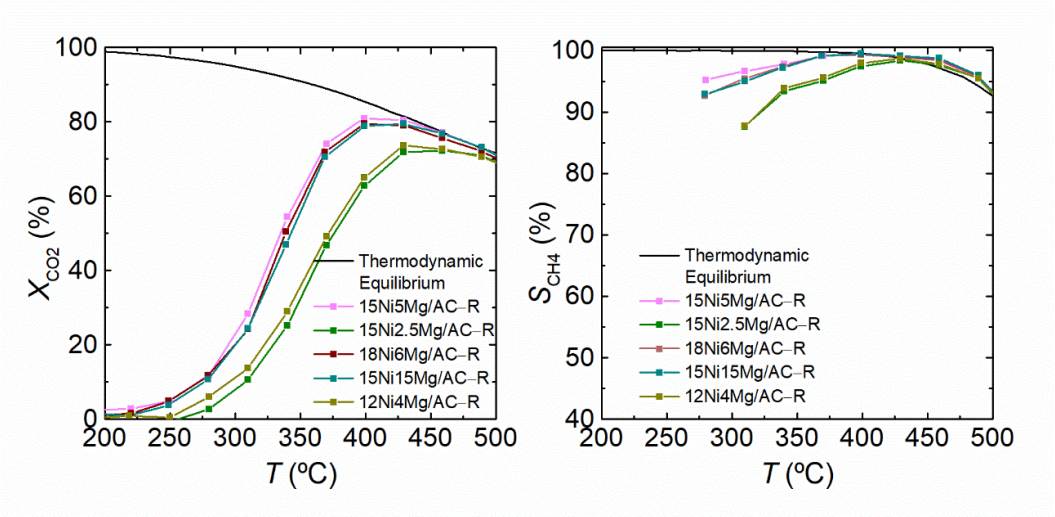

Figure A7.2. Comparison of the catalytic properties of the best performing bimetallic catalyst (NiMg/AC−R) with different Ni and Mg loadings: X_{CO2} (a), and S_{CH4} (b) as a function of temperature, together with the respective thermodynamic equilibrium curves. Reaction conditions: P = 1 bar; $WHSV$ = 60 000 mL g^{-1} h^{-1}; CO_2 : H_2 = 1 : 4.

We proceeded to evaluate the stability of the best performing catalyst, NiMg/AC−R, through a long time on stream (TOS) experiment, and the results are presented in Figure A7.3. The results were not as promising as expected. The stability of this catalyst in terms of X_{CO2} was not satisfactory since it lost 34% of X_{CO2} over 90 h of TOS.

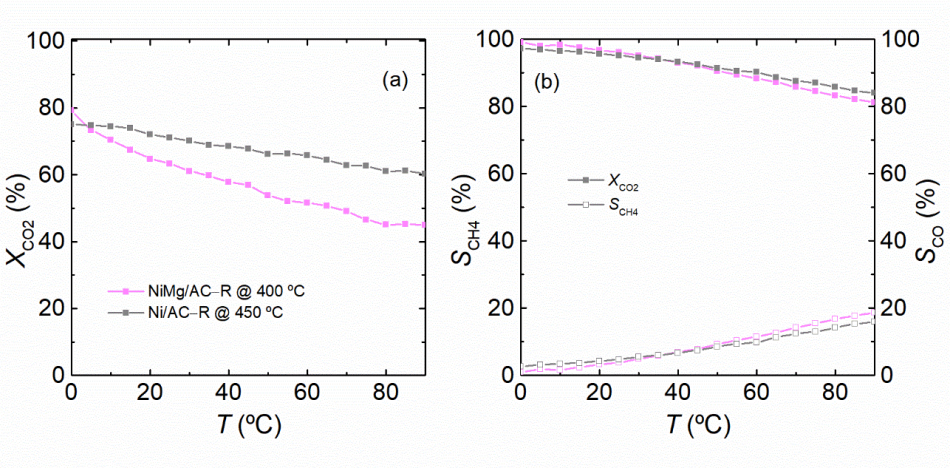

Figure A7.3. Evolution of X_{CO2} (c), and S_{CH4} and S_{CO} (d) during long-term time-on-stream (TOS) testing for 90 h for the best performing bimetallic catalysts (NiMg/AC−R and NiY/AC−R), compared to the monometallic Ni/AC−R. Reaction conditions: P = 1 bar; $WHSV$ = 60 000 cm^3 g^{-1} h^{-1}; CO_2:H_2 = 1:4.

Taking these results into consideration, and the fact that NiMg/AC−R was the best performing catalyst from this set of samples, although it was not stable, we decided to prepare a NiMg catalyst on the CeO_2 and ACR−CeO_2 supports developed in Chapter 6. Figure A7.4 presents the catalytic results for NiMg/CeO_2 and NiMg/ACR−CeO_2 and compares them with bimetallic NiMg/AC−R and monometallic Ni/CeO_2 and Ni/ACR−CeO_2. Interestingly, the performance of NiMg catalyst is higher in ACR−CeO_2 support when compared to the same catalyst on AC−R support; however, it is lower when supported on CeO_2. Independently of the support used, the bimetallic NiMg catalysts exhibited lower X_{CO2} than the monometallic Ni/CeO_2 and Ni/ACR−CeO_2.

Therefore, even though the activity and selectivity results of NiMg/AC−R were encouraging, the fact that this catalyst demonstrated unsatisfactory stability and did not present comparable performance to our best performing Ni/CeO_2 and Ni/ACR−CeO_2 led to the need for an additional study of optimization of the preparation of this bimetallic catalyst.

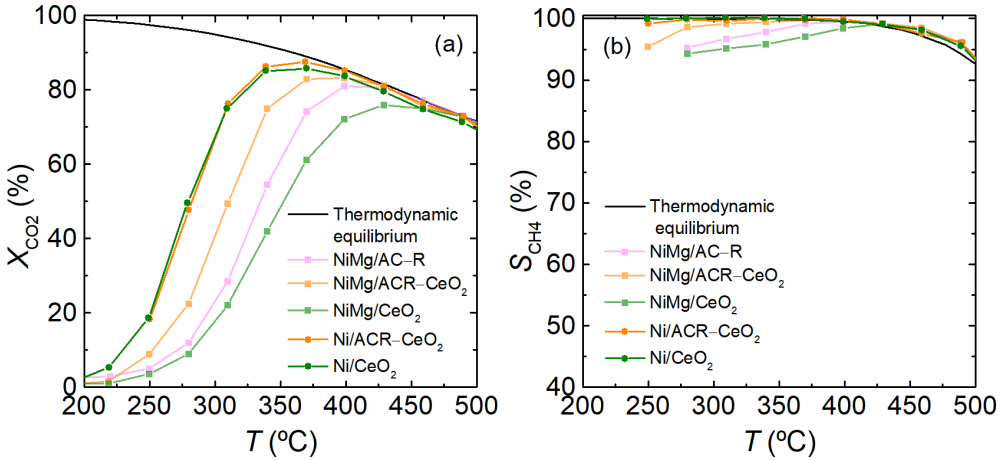

Figure A7.4. Comparison of the catalytic properties of the best performing bimetallic catalyst (NiMg) supported on AC−R, ACR−CeO_2, and CeO_2, and the monometallic Ni catalyst on the same supports: X_{CO2} (a), and S_{CH4} (b) as a function of temperature, together with the respective thermodynamic equilibrium curves. Reaction conditions: P = 1 bar; $WHSV$ = 60 000 mL g^{-1} h^{-1}; CO_2 : H_2 = 1 : 4.

References

(1) Gonçalves, L. P. L.; Sousa, J. P. S.; Soares, O. S. G. P.; Bondarchuk, O.; Lebedev, O. I.; Kolen'ko, Y. V.; Pereira, M. F. R. The Role of Surface Properties in CO_2 Methanation over Carbon-Supported Ni Catalysts and Their Promotion by Fe. *Catal. Sci. Technol.* **2020**, *10* (21), 7217. https://doi.org/10.1039/d0cy01254h.

(2) Garbarino, G.; Riani, P.; Magistri, L.; Busca, G. A Study of the Methanation of Carbon Dioxide on Ni/Al_2O_3 Catalysts at Atmospheric Pressure. *Int. J. Hydrogen Energy* **2014**, *39* (22), 11557–11565. https://doi.org/10.1016/j.ijhydene.2014.05.111.

(3) Siakavelas, G. I.; Charisiou, N. D.; AlKhoori, A.; AlKhoori, S.; Sebastian, V.; Hinder, S. J.; Baker, M. A.; Yentekakis, I. V.; Polychronopoulou, K.; Goula, M. A. Highly Selective and Stable Ni/La-M (M=Sm, Pr, and Mg)-CeO_2 Catalysts for CO_2 Methanation. *J. CO_2 Util.* **2021**, *51* (June), 101618. https://doi.org/10.1016/j.jcou.2021.101618.

(4) Parizotto, N. V; Rocha, K. O.; Damyanova, S.; Passos, F. B. Alumina-Supported Ni Catalysts Modified with Silver for the Steam Reforming of Methane : Effect of Ag on the Control of Coke Formation. **2007**, *330*, 12–22. https://doi.org/10.1016/j.apcata.2007.06.022.

(5) Hou, Z.; Yokota, O.; Tanaka, T.; Yashima, T. Surface Properties of a Coke-Free Sn Doped Nickel Catalyst for the CO_2 Reforming of Methane. *Appl. Surf. Sci.* **2004**, *233*, 58–68. https://doi.org/10.1016/j.apsusc.2004.03.223.

(6) Sun, C.; Świrk, K.; Wierzbicki, D.; Motak, M.; Grzybek, T.; Da Costa, P. On the Effect of Yttrium Promotion on Ni-Layered Double Hydroxides-Derived Catalysts for Hydrogenation of CO_2 to Methane. *Int. J. Hydrogen Energy* **2021**, *46* (22), 12169–12179. https://doi.org/10.1016/j.ijhydene.2020.03.202.

(7) Świrk, K.; Gálvez, M. E.; Motak, M.; Grzybek, T.; Rønning, M.; Da Costa, P. Yttrium Promoted Ni-Based Double-Layered Hydroxides for Dry Methane Reforming. *J. CO_2 Util.* **2018**, *27* (April), 247–258. https://doi.org/10.1016/j.jcou.2018.08.004.

(8) Liu, Q.; Zhong, Z.; Gu, F.; Wang, X.; Lu, X.; Li, H.; Xu, G.; Su, F. CO Methanation on Ordered Mesoporous Ni – Cr – Al Catalysts: Effects of the Catalyst Structure and Cr Promoter on the Catalytic Properties. *J. Catal.* **2016**, *337*, 221–232. https://doi.org/10.1016/j.jcat.2016.01.023.

Appendix 8 – Published Articles

Catalysis Science & Technology

ROYAL SOCIETY OF CHEMISTRY

PAPER

Cite this: *Catal. Sci. Technol.*, 2020, **10**, 7217

The role of surface properties in CO_2 methanation over carbon-supported Ni catalysts and their promotion by Fe†

Liliana P. L. Gonçalves, [ab] Juliana P. S. Sousa,[a] O. Salomé G. P. Soares,[b] Oleksandr Bondarchuk,[a] Oleg I. Lebedev,[c] Yury V. Kolen'ko *[a] and M. Fernando R. Pereira *[b]

Received 22nd June 2020,
Accepted 21st August 2020

DOI: 10.1039/d0cy01254h

rsc.li/catalysis

The surface chemistry of the activated carbon supporting material was tailored to investigate the influence of O and N groups as well as O-free Lewis basic sites on the performance of Ni-based catalysts for CO_2 methanation. Catalytic experiments demonstrated that 15% Ni on carbon with O-free Lewis basic sites showed the best performance (X_{CO_2} = 76%, S_{CH_4} = 97%, T = 450 °C, P = 1 bar), suggesting that the methanation reaction is highly dependent on the basicity of the support. Promotion with 5% Fe enabled the decrease of the optimal reaction temperature while improving the stability of the catalyst. Microstructural and compositional studies of the catalyst after a prolonged time on stream experiment suggested that the slight but gradual catalyst deactivation during methanation is associated with the sintering of Ni nanoparticles and the development of a distinct Ni@NiO core–shell nanostructure.

Introduction

The Sabatier reaction for CO_2 methanation is the hydrogenation of CO_2 to produce CH_4 ($CO_2 + 4H_2 \leftrightarrow CH_4 + 2H_2O$, $\Delta H_{298K} = -165$ kJ mol^{-1}).[1] This widely-studied reaction presents great potential since it can be used as a solution to combat CO_2 emissions by converting it into CH_4 gas fuel with the help of H_2 produced using renewable energy. Although CO_2 methanation is a thermodynamically favourable reaction, it has significant kinetic barriers, requiring a catalyst to achieve good CO_2 conversion and selectivity to CH_4. The reaction can occur through two pathways in different catalysts: (i) CO_2 is adsorbed associatively with a formerly adsorbed H atom, forming formate as an intermediate, without CO formation (associative scheme), or (ii) CO_2 adsorbs dissociatively on the catalyst and CO acts as an intermediate of the reaction (dissociative scheme).[2,3]

Several studies have been conducted on metal-based catalysts for CO_2 methanation, and mainly group VIII transition metals, such as Ni,[4–13] Co,[14,15] Ru,[16,17] Rh,[12,18] and Pd,[19,20] have been found to be active. From this set, Ni-based catalysts are the most commonly used, owing to the optimal combination of activity, selectivity and cost.[4–12] For instance, a typical industrial Ni/Al_2O_3 catalyst can achieve a CO_2 conversion $X_{CO_2} \approx$ 80–90% at 400 °C with selectivity towards CH_4 $S_{CH_4} \approx$ 100%.

Notably, it is still challenging to achieve high X_{CO_2} at low temperatures with Ni catalysts due to the high activation energy involved in this process. Ni catalysts also feature low stability at higher temperatures due to sintering of the catalyst nanoparticles, degradation *via* formation of volatile $Ni(CO)_4$, and coke build-up on active Ni sites under severe reaction conditions.[9]

An interesting way to improve the performance of Ni catalysts is to use an appropriate supporting material. The properties of the supporting material, such as the surface area, pore size, hierarchical structure, surface chemistry, and metal–support interaction (MSI), have been reported to be an excellent tool-box for tailoring the performance of the catalyst and its stability.[5,8,9,11] Specifically, mainly metal oxide supporting materials have been investigated, such as Al_2O_3, SiO_2, TiO_2, and CeO_2,[4–8] but recently, new types of supports have emerged, such as zeolites[10] and metal–organic frameworks.[11] By contrast, the investigation of activated carbon (AC) supporting materials for CO_2 methanation catalysts remains remarkably scarce.[9,12,21–23] Drawing on our extended experience in catalytically-relevant carbon materials, we decided to investigate AC as a support for Ni-based catalysts for CO_2 methanation.[24–26]

[a] *International Iberian Nanotechnology Laboratory (INL), Avenida Mestre José Veiga, 4715-330 Braga, Portugal. E-mail: yury.kolenko@inl.int*
[b] *Laboratory of Separation and Reaction Engineering – Laboratory of Catalysis and Materials (LSRE-LCM), Faculdade de Engenharia, Universidade do Porto, Rua Dr. Roberto Frias, 4200-465 Porto, Portugal. E-mail: fpereira@fe.up.pt*
[c] *Laboratoire CRISMAT, UMR 6508, CNRS-ENSICAEN, Caen 14050, France*

† Electronic supplementary information (ESI) available: Materials and methods, additional characterization data, and catalytic experiments (PDF). See DOI: 10.1039/d0cy01254h

This journal is © The Royal Society of Chemistry 2020

AC is a cost-effective carbon material exhibiting a high surface area, controlled pore size distribution and high degree of graphitization. Moreover, AC can be doped with non-metal N, O and other elements, providing access to interesting supporting materials with tailored surface properties.[27]

Furthermore, AC has been extensively studied as a CO_2 adsorbent, demonstrating a high efficiency at low pressure,[28] which has been implicated in CO_2 methanation.[22]

Cam *et al.*[23] investigated the CO_2 methanation reaction on AC-supported Ni with different metal loadings. They attributed the good performance of the catalyst to the high reducibility of Ni species on the AC support. Furthermore, Li *et al.*[9] studied Ni-based catalysts supported on coconut shell carbon and concluded that the high surface area of this type of support induced a better dispersion of the Ni nanoparticles (NPs), exhibiting a better performance when compared to those supported on Al_2O_3 and ZrO_2. Despite these insights, a systematic study of the role of surface properties in CO_2 methanation over AC-supported Ni catalysts has not been conducted.

Another interesting approach to improve the performance of a catalyst, in this case working on the active metal side, is the addition of a second active metal. The resultant bimetallic catalyst can present higher catalytic activity than the monometallic counterpart, since the interaction between the surfaces of the two metals can change the electronic and geometric structure of the catalyst, increasing its activity and selectivity.

Fe has been often studied as a co-metal for Ni methanation catalysts, and it has been shown to improve both the activity and stability of the catalyst, due to several factors. Specifically, the formation of the Ni–Fe alloy potentially increases the reducibility of Ni, due to the distinct redox properties of Fe, reducing the MSI.[29–32] Fe can also improve the stabilization of the Ni phase, allowing a better distribution of the metal phase and preventing sintering under reaction conditions. Furthermore, the formation of the alloy can facilitate CO dissociation on the catalyst due to an optimal CO dissociation energy at the surface of the alloy, which is considered the rate-determining step of the reaction in the dissociative mechanism.[30–39]

Notably, there is no study of NiFe catalysts on AC support materials, and therefore we decided to address this in the current study.

We modified the surface of AC in order to study the influence of different surface properties on the performance of **Ni/AC** catalysts for CO_2 methanation. AC with oxygen functional groups, N-doped AC, and reduced AC with increased Lewis basic sites were prepared, Ni nanoparticles were supported on each material and compared with Ni supported on pristine AC. Furthermore, a bimetallic NiFe catalyst was prepared with the best-performing support in order to evaluate the influence of Fe addition on the performance of the catalyst. The materials were fully characterized and their activity and selectivity for the CO_2 methanation reaction were evaluated. The results of this study provide new insights into the influence of the surface chemistry of the support, as well as the addition of Fe on the catalyst performance for CO_2 methanation. Our results demonstrate that an increase in the basicity of the support leads to higher CO_2 methanation activity, while the addition of Fe leads to higher catalyst activity at lower temperatures as well as better stability.

Experimental

In the present work, we modified the surface of commercial AC to investigate the influence of different surface chemistries on the catalyst performance. AC was oxidized with 5 M HNO_3 in a Soxhlet apparatus to obtain a sample with a higher amount of oxygen functional groups (**AC–O**).[24] N-Doped AC (**AC–N**) was synthesized by mixing AC with melamine as a N source using a ball mill, followed by heat treatment at 600 °C under N_2.[40] Finally, reduced AC with an increased number of Lewis basic sites (**AC–R**) was prepared by heat treatment in H_2 at 900 °C.[41]

Next, Ni NPs were anchored on the resultant supports, as well as on pristine AC, while NiFe NPs were anchored on the best-performing support. For this, we employed the convenient incipient wetness impregnation (IWI) method, using $Ni(NO_3)_2{\cdot}6H_2O$ and $Fe(NO_3)_3{\cdot}9H_2O$ as Ni and Fe precursors, respectively, followed by reduction in H_2 at temperatures established by H_2 temperature-programmed reduction (H_2-TPR), which were 400 °C in the case of **Ni/AC**, **Ni/AC–O**, **Ni/AC–R**, and **NiFe/AC–R** and 300 °C in the case of **Ni/AC–N**. Based on preliminary catalytic testing, the optimal Ni loading was found to be 15% and Fe loading 5%.

The resultant supports and catalysts, namely **AC**, **AC–N**, **AC–O**, and **AC–R**, and **Ni/AC**, **Ni/AC–N**, **Ni/AC–O**, **Ni/AC–R**, and **NiFe/AC–R**, were characterized by N_2 physisorption, elemental analysis, point of zero charge (pH_{PZC}) measurement, X-ray photoelectron spectroscopy (XPS), transmission electron microscopy (TEM), high-angle annular dark-field scanning transmission electron microscopy (HAADF–STEM), electron diffraction (ED), energy-dispersive X-ray spectroscopy in STEM mode (STEM–EDX), X-ray diffraction (XRD), H_2-TPR, H_2-chemisorption, and temperature-programmed desorption (TPD).

The activity, selectivity, and stability of the catalysts in CO_2 methanation were evaluated in a Microactivity XS15 system (PID Eng & Tech), using a fixed bed quartz reactor (d_{int} = 1 cm). The products in the outflow were analyzed online using a GC 1000 gas chromatograph (DANI), equipped with a thermal conductivity detector (TCD) and a GS-CarbonPLOT capillary column, using He as the carrier gas and a continuous flow of N_2 as the internal standard. Each catalyst (100 mg) was pre-treated *in situ* under H_2 flow (40 cm^3 min^{-1}) at the reduction temperature for 30 min, at 1 bar. After that, the reactor temperature was decreased to 200 °C under He (50 cm^3 min^{-1}), and then, the reactor was fed with 10% CO_2, 40% H_2 (the stoichiometric composition) and

This journal is © The Royal Society of Chemistry 2020

50% He, with a total flow rate of 100 cm^3 min^{-1}. A temperature ramping from 200 to 500 °C was performed under reaction conditions to evaluate the performance of each sample at various temperatures. Additionally, isothermal time on stream (TOS) experiments were conducted under the same reaction conditions to evaluate the stability of the best performing samples.

More experimental details for the synthesis of the catalysts and their detailed characterization are summarized in the ESI.†

Results

Topmost performance of the Ni catalyst supported on reduced AC

We began by performing a light-off experiment for the CO_2 methanation reaction over the 200–500 °C temperature range using the synthesized Ni catalysts (Fig. 1). All the carbon materials without Ni (**AC**, **AC–N**, **AC–O**, **AC–R**) were initially tested and their activities were found to be null (data not shown). For the Ni-containing catalysts, the conversion of CO_2 increases with the temperature until it reaches the maximum at 450 °C for **Ni/AC–N** (X_{CO_2} = 70%) and **Ni/AC–R** (X_{CO_2} = 76%) catalysts (Fig. 1). The other two catalysts, **Ni/AC** (X_{CO_2} = 54%) and **Ni/AC–O** (X_{CO_2} = 62%), achieve their maximum conversion only at 500 °C (Fig. 1). A similar behaviour was observed in terms of the selectivity (S_{CH_4}) and yield (Y_{CH_4}) of CH_4 and it is important to note that the only other product formed was CO. A further increase above the optimal temperature resulted in a decrease of activity due to thermodynamic reasons, wherein higher temperature favours methane steam reforming and the reverse water gas shift (RWGS) reaction.[42]

Compared to the calculated thermodynamic equilibrium curves (Fig. 1), X_{CO_2} remains below the thermodynamic limits, especially at low temperatures. This is most likely due to the kinetic barrier for the full reduction of C^{4+} in CO_2 to C^{4-} in CH_4, an 8 e^- process that requires a high activation energy. When looking at Y_{CH_4}, one can assume that at low temperatures (200–450 °C) the methanation reaction over our catalysts was probably a kinetically controlled reaction. Thermodynamically, Y_{CH_4} should decrease with temperature; in contrast, our experiments show an increasing trend.

The catalysts with modified surface properties (**Ni/AC–N**, **Ni/AC–O**, **Ni/AC–R**) demonstrate significantly improved performance in comparison to the Ni catalyst supported on pristine AC (**Ni/AC**). For the highest X_{CO_2}, S_{CH_4} and Y_{CH_4}, the catalytic performance order was established to be **Ni/AC–R** > **Ni/AC–N** > **Ni/AC–O** ≫ **Ni/AC**. Notably, from all the prepared catalysts with different surface functionalities, **Ni/AC–R** exhibits the topmost performance, achieving X_{CO_2} = 76% and S_{CH_4} = 97% at 450 °C, approaching the thermodynamic limit at this temperature.

Similar material characteristics but distinct surface properties of the synthesized Ni catalysts

To understand the activity trend, the catalysts were extensively characterized. N_2 adsorption–desorption isotherms indicate that both the supports (Fig. S1, Table S1†) and the catalysts (Fig. S4,† Table 1) exhibit similar textural properties, with the catalysts showing a high S_{BET} of *ca.* 650 m^2 g^{-1} (except **Ni/AC–N**, which has a slightly lower S_{BET} of 480 m^2 g^{-1}).

The elemental composition results (Table S1†) confirm the higher amount of O in the **AC–O** support (9.6% *cf.* 7.0% in **AC**) as a result of the oxidation treatment, the lower amount of O in **AC–R** (3.8%), caused by the reduction treatment, and the higher amount of N in **AC–N** (5.8% *cf.* 0.0% in **AC**) compared to the results obtained in pristine **AC**. These results are in good agreement with the XPS data obtained for the supporting materials (Fig. S2 and S3 and Table S2†).

Furthermore, temperature-programmed desorption (Fig. S7,† Table 1) allowed quantification of the amount of oxygen containing groups in the samples, which is directly correlated

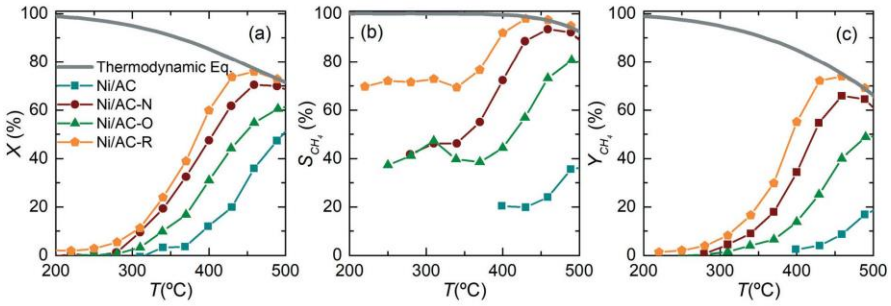

Fig. 1 Comparison of the catalytic properties of the synthesized Ni catalysts supported on ACs with different surface functionalities: X_{CO_2} (a), S_{CH_4} (b) and Y_{CH_4} (c) as a function of temperature, together with the respective thermodynamic equilibrium curves. Reaction conditions: P = 1 bar; WHSV = 60 000 mL g^{-1} h^{-1}; CO_2 : H_2 = 1 : 4.

Table 1 Textural properties, mean Ni NP diameter (d_p), TPD, and H_2-chemisorption results of the as-synthesized Ni-based CO_2 methanation catalysts **Ni/AC**, **Ni/AC–N**, **Ni/AC–O**, **Ni/AC–R**, and **NiFe/AC–R**, together with the pH_{PZC} of the respective supports (**AC**, **AC–N**, **AC–O** and **AC–R**)

Sample	S_{BET} ($m^2\ g^{-1}$)	$V_{P/P0=0.95}$ ($cm^3\ g^{-1}$)	V_{micro} ($cm^3\ g^{-1}$)	d_p[a] (nm)	pH_{PZC} (support)	CO peak 3[b,c] (relative %)	CO_2[c] ($\mu mol\ g^{-1}$)	H_2 chemisorbed[d] ($\mu mol\ g^{-1}$)	Metallic Ni surface area[d] ($m^2\ g_{cat}^{-1}$)
Ni/AC	653	0.40	0.27	12 ± 5	7.9	30	519	19.1	1.49
Ni/AC–N	480	0.30	0.20	10 ± 9	7.1	20	673	15.2	1.18
Ni/AC–O	634	0.39	0.26	10 ± 8	2.1	28	555	19.5	1.53
Ni/AC–R	656	0.41	0.27	10 ± 6	9.4	34	417	34.9	2.73
NiFe/AC–R	659	0.42	0.25	10 ± 5	9.4	30	551	23.6	—

[a] Determined by TEM. [b] Peak 3 of the CO evolution graph, relative to carbonyl–quinone groups. [c] Determined by TPD. [d] Determined by H_2-chemisorption.

with the acidity/basicity of the **Ni/AC**, **Ni/AC–O**, and **Ni/AC–R** samples.[43] Generally, the acidity of a sample increases with the increase of surface oxygen groups that decompose as CO_2 (*i.e.* carboxylic acids and anhydrides). It can be observed in Table 1 that the amount of CO_2 evolved from the samples' decomposition follows the order **Ni/AC–O** > **Ni/AC** ≫ **Ni/AC–R**. Additionally, from the oxygen containing groups present in a carbon material, those that contribute more to the basicity of a sample are carbonyl–quinone groups, which decompose as CO at high temperatures during TPD. It can be observed in Table 1 that the relative percentage of these groups (peak 3), analysed by CO evolution from TPD (Fig. S7†), compared to the others that decompose as CO, is higher in the case of **Ni/AC–R**. Thus, we can conclude that the basicity of these samples follows the order **Ni/AC–R** ≫ **Ni/AC** > **Ni/AC–O**, which is confirmed by pH_{PZC} (Table 1). Regarding **Ni/AC–N**, the basicity of this sample is related to the amount of N-groups, and both elemental composition analysis and XPS confirmed the increased amount of N-groups in this sample.

TEM results (Table 1, Fig. S5 and S6†) indicate that the mean size of Ni NPs and their spatial dispersion over functionalized ACs are quite similar, with $d_p \approx 10$ nm; although NPs supported on pristine AC present a slightly higher $d_p \approx 12$ nm. However, observing H_2-chemisorption results (Table 1), the best-performing sample, **Ni/AC–R**, presents a higher metallic Ni surface area compared to the other samples, which have similar values.

The phase composition of the NPs was studied by XRD analysis, which demonstrated that all the Ni catalysts were composed of metallic Ni NPs (Fig. 2a), as reflected by the presence of the Ni(111) peak at $2\theta = 44.4°$, the Ni(200) peak at $2\theta = 51.8°$, and the Ni(220) peak at $2\theta = 76.4°$.[5,6] Interestingly, peaks corresponding to the NiO phase were not detected in any catalysts.[13]

Ni/AC, **Ni/AC–O** and **Ni/AC–R** show similar reducibility profiles (Fig. 2b) with two main peaks: (i) at *ca.* 330 °C due to the reduction of the Ni species that are weakly interacting with the carbon support, and (ii) at *ca.* 380 °C, related to the reduction of Ni species that interact more strongly with the carbon support. The Ni catalyst on N-doped AC (**Ni/AC–N**) demonstrates a slightly distinct profile from the other catalysts, with three main peaks at lower temperatures (*ca.* 280, 315, and 340 °C).

For all the catalysts, three different components are observed from the deconvolution of the XPS data of Ni $2p_{3/2}$ (Fig. 3). The lower energy component (852.8 eV) is assigned to Ni^0 species, while the component at 854.2 ± 0.2 eV is assigned to the NiO phase, and the one at 856.0 ± 0.1 eV to the $Ni(OH)_2$ phase.[13,44–47] Even though all the samples were reduced under H_2 at the temperatures established by H_2-TPR experiments, it is reasonable to expect the presence of NiO and $Ni(OH)_2$ phases due to the inevitable oxidation of the metallic Ni surface upon exposure to ambient conditions.

Lowering the temperature of methanation and increasing the stability of Ni catalysts by Fe promotion

We examined whether the catalytic performance of the best **Ni/AC–R** material could be improved by adding Fe as a second active metal. For this purpose, several Ni–Fe

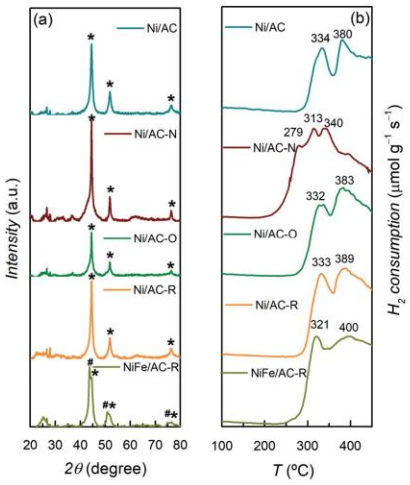

Fig. 2 Comparison of XRD patterns (a) and H_2-TPR profiles (b) of **Ni/AC**, **Ni/AC–N**, **Ni/AC–O**, **Ni/AC–R**, and bimetallic **NiFe/AC–R** catalysts for CO_2 methanation.

This journal is © The Royal Society of Chemistry 2020

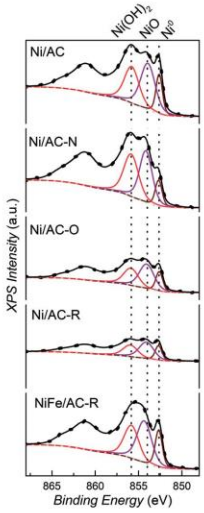

Fig. 3 High-resolution XPS data for the Ni $2p_{3/2}$ region collected from **Ni/AC**, **Ni/AC–N**, **Ni/AC–O**, **Ni/AC–R**, and bimetallic **NiFe/AC–R** catalysts. Symbols: raw data; black lines: overall fits; coloured lines: fits of individual components; dashed lines: background.

bimetallic catalysts were prepared. After the catalytic screening of the synthesized materials with different loadings (data not shown), the optimal Ni and Fe co-loading was established to be 15% of Ni and 5% of Fe. The XRD analysis of this bimetallic **NiFe/AC–R** catalyst indicates the formation of a NiFe alloy. Specifically, the broadening of the diffraction peaks and their shift towards lower 2θ, namely, 43.7°, 50.8° and 74.8°, suggest the presence of a phase mixture of metallic Ni and Ni–Fe alloy (Fig. 2a).[31,32,48] According to the TEM results, the bimetallic **NiFe/AC–R** exhibits a mean particle size of $d_p \approx 10$ nm, which is similar to that of monometallic **Ni/AC–R** (Fig. S5 and S6†). The H_2-TPR profile of **NiFe/AC–R** shows two main peaks at 321 and 400 °C. Comparing these temperatures with those of monometallic **Ni/AC–R**, the reduction of the Ni species in **NiFe/AC–R** occurs at lower temperature: thus, the addition of Fe leads to a weaker MSI.

Regarding catalytic properties, the resultant **NiFe/AC–R** exhibits higher conversion and selectivity at lower temperatures (250–450 °C) in comparison to the monometallic **Ni/AC–R** counterpart (Fig. 4a and b). In particular, the bimetallic catalyst demonstrates excellent X_{CO_2} = 77% and S_{CH_4} = 98%, which are similar to those of the best monometallic **Ni/AC–R**, however, obtained at a lower temperature (430 °C *cf.* 450 °C). We compared further the stability of monometallic **Ni/AC–R** and bimetallic **NiFe/AC–R** catalysts by testing them at 450 °C for 48 h. Remarkably, while **Ni/AC–R** demonstrates a loss in X_{CO_2} of 8% and in S_{CH_4} of 6%, the promoted **NiFe/AC–R** shows only a marginal loss in X_{CO_2} of 3% and in S_{CH_4} of 2% (Fig. 4c).

Formation of Ni@NiO core–shell nanostructure after time-on-stream testing

Since we observed a slight deactivation of the **Ni/AC–R** catalyst with time (Fig. 4c), we suspected that the deactivation might be related to microstructural changes in the catalyst. Therefore, we subjected **Ni/AC–R** to prolonged time-on-stream (TOS) methanation at 450 °C for 90 h (Fig. S9†), and then compared the catalyst appearance and chemical composition before and after this testing through electron microscopy.

TEM (Fig. 5a) and HAADF–STEM (Fig. S10†) observations of the as-synthesized **Ni/AC–R** catalyst indicate that the Ni NPs are well-anchored and quite uniformly distributed over the **AC–R** support. This is also highlighted by the corresponding STEM–EDX elemental maps for Ni and C (Fig. S10†).

On the other hand, TEM and HAADF–STEM imaging of the spent **Ni/AC–R** catalyst after 90 h of TOS experiment

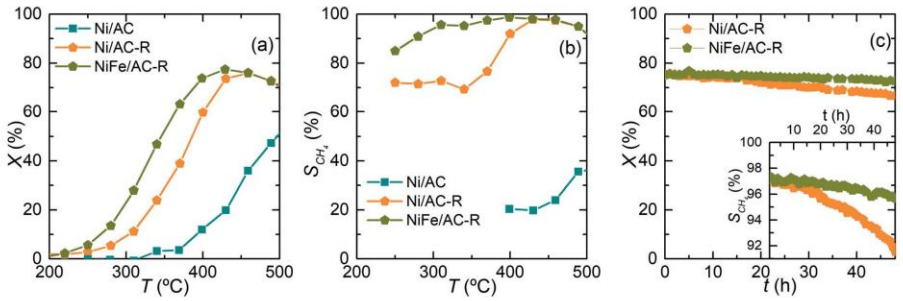

Fig. 4 Comparison of the catalytic properties of the best Ni catalyst **Ni/AC–R** and **NiFe/AC–R** promoted by Fe: X_{CO_2} and S_{CH_4} as a function of temperature (a and b) as well as time-on-stream (TOS) at 450 °C (c). Reaction conditions: P = 1 bar; WHSV = 60 000 mL g^{-1} h^{-1}; CO_2 : H_2 = 1 : 4.

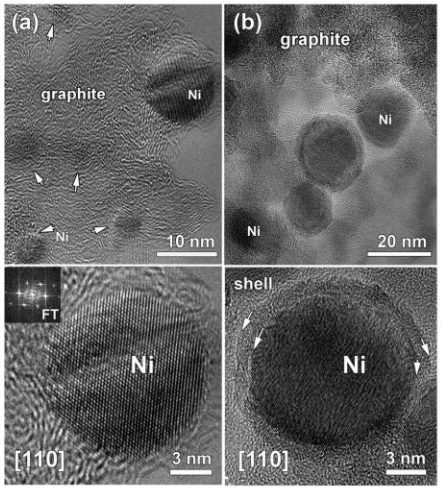

Fig. 5 Low magnification bright field TEM images and selected [110] HRTEM images of single NPs of as-synthesized (a) and spent (b) **Ni/AC–R** catalysts after long time-on-stream CO_2 methanation at 450 °C for 90 h, which evidence the development of core–shell Ni NPs.

reveals the growth of Ni NPs from the original 10 ± 6 nm to 13 ± 6 nm (Fig. S11 and S12†), while the NPs remain well-dispersed over **AC–R** (Fig. S11†). Interestingly, our high-resolution TEM and HAADF–STEM investigations of the spent **Ni/AC–R** after 90 h of methanation at 450 °C evidence the formation of NPs with a distinct Ni@NiO core–shell nanostructure (Fig. 5b and 6). Also, XPS analysis of the as-synthesized and spent **Ni/AC–R** catalysts indicates that the methanation induces a change in the chemical composition of the surface of the Ni catalyst. Specifically, the relative amounts of Ni^0 and $Ni(OH)_2$ increase while the amount of NiO decreases after TOS testing (Fig. S13, Table S4†).

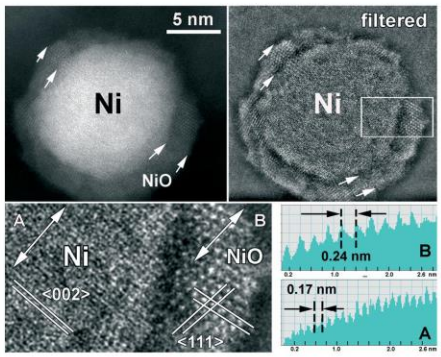

Fig. 6 HAADF–STEM image of a core–shell NP (left upper panel) and its noise filtered image (right upper panel). The core of the NP is depicted with white arrows. The magnified HAADF–STEM filtered image marked with a white box and the corresponding intensity scan line profile perpendicular to lattice plane direction (double head arrows) confirm different *d*-spacings and evidence that the core is Ni (A) while the shell is NiO (B).

Discussion

Here we present the investigation of the influence of the surface chemistry of activated carbon supporting materials of Ni-based catalysts for CO_2 methanation. We prepared, characterized, and tested Ni nanocatalysts supported on oxidized AC, N-doped AC, and reduced AC possessing Lewis basic sites. Furthermore, we studied the influence of the addition of Fe to the best-performing monometallic Ni catalyst and compared the catalytic properties of the monometallic and bimetallic catalysts.

Role of the surface chemistry

From the combination of catalytic and characterization results, we assume that the performance trend of the catalysts (**Ni/AC–R** > **Ni/AC–N** > **Ni/AC–O** ≫ **Ni/AC**) can be correlated with the surface properties of AC supports. This claim is supported by the fact that the catalysts exhibit similar (i) textural properties, (ii) mean size of Ni NPs, (iii) phase and surface compositions of the active Ni NPs, and (iv) reducibility profiles. We thus inferred that the observed catalytic performance trend most likely corresponds to the surface chemistry of the carbon materials.

The better performance of the functionalized supports compared to the pristine one is related to two factors: (i) good Ni dispersion and (ii) better CO_2 adsorption. Due to the lack of any specifically designed surface functionality, pristine **AC** demonstrates worse dispersion of the Ni NPs (bigger NPs observed by TEM) and, consequently, low performance of the respective **Ni/AC** catalyst.

The **AC–O** support has a higher amount of O-groups when compared to the other supports, as well as a higher degree of oxidation (determined by the ratio of total oxygen to total carbon, O_t/C_t, Table S2†),[24] which leads to a good dispersion of the Ni NPs (smaller NPs observed by TEM), responsible for the better performance of **Ni/AC–O** than **Ni/AC** (Fig. 1).

Regarding **AC–N**, the presence of N-groups has two benefits: (i) they improve the Ni dispersion (smaller NPs observed by TEM) by providing binding sites that facilitate the Ni stabilization on the support, and also (ii) improve the CO_2 adsorption capacity of the sample.[49–51] These two factors lead to the better performance of **Ni/AC–N** as compared to **Ni/AC** and **Ni/AC–O** (Fig. 1), regardless of the fact that **Ni/AC–N** has a slightly lower S_{BET} than the other samples.

Ni/AC–R showed the best performance among all the tested catalysts (Fig. 1), which can be attributed to (i) the good Ni dispersion and higher metallic Ni surface area than in all the other samples, and to (ii) the basicity of this

This journal is © The Royal Society of Chemistry 2020

support. The higher metallic Ni surface area can be related to the fact that the **AC–R** support presents a higher amount of oxygen-free Lewis basic sites on the graphene layers, with resonating π-electrons of carbon aromatic rings. These resonating π-electrons attract protons, which might be the reason for the higher dispersion of the Ni nanoparticles on this support, since the metal proton dispersion is enhanced during impregnation.[50] Furthermore, as shown in Table 1, **AC–R** exhibits the highest basicity (the highest pH_{PZC} = 9.4, the lowest total amount of oxygen surface groups (amount of CO_2 released during TPD), and a higher relative amount of carbonyl–quinone groups compared to the other oxygen containing groups) due to the presence of a large number of O-free Lewis basic sites and carbonyl–quinone groups, since most of the acidic O groups were removed during the thermal treatment at 900 °C in H_2. The basicity improves the CO_2 adsorption capacity over **Ni/AC–R** and, as shown by recent investigations,[50,51] high basicity enables gradients of CO_2 concentration to be close to the Ni active sites, thus boosting performance.

Other carbon materials have been studied for CO_2 methanation. Hu *et al.*[52] studied Ni catalysts supported on reduced graphene oxide (RGO), which was more active and selective than **Ni/AC** and Ni/γ-Al_2O_3. Interestingly, the Ni/RGO catalyst achieved a similar CO_2 conversion (X_{CO_2} = 78.4% at 350 °C) to our best-performing **Ni/AC–R** catalyst, although at lower weight hourly space velocity (WHSV). They attributed the better performance of the catalyst to the RGO high surface area that favours the formation of fine Ni NPs, as well as to the O-containing functional groups on RGO that promote the stable anchoring of the NPs.

Li *et al.*[9] studied Ni catalysts supported on coconut shell carbon (CSC), which also displayed a conversion (X_{CO_2} = 77.1% at 450 °C) similar to our best catalyst **Ni/AC–R**, but again at lower WHSV. They also attributed the better performance of the catalyst, compared to other supports (Al_2O_3 and ZrO_2), to the large specific surface area of the CSC, promoting a better Ni dispersion. Additionally, they showed that adding Mg to the catalyst improved its performance due to the increase in the catalyst's basicity, which is consistent with our results.

Romero-Sáez *et al.*[44] investigated Ni catalysts supported on carbon nanotubes (CNTs), and the Ni/CNT catalyst showed $X_{CO_2} \approx 50\%$ with $S_{CH_4} \approx 30\%$ at 450 °C. They could drastically improve the S_{CH_4} by adding ZrO_2 to the Ni/CNT catalyst, achieving $S_{CH_4} \approx 97\%$. In another study, Wang *et al.*[51] demonstrated that a Ni catalyst supported on N-doped CNTs exhibited high basicity, and accordingly showed good performance with X_{CO_2} = 80% and S_{CH_4} = 99% at 360 °C.

For several decades, ACs were known to be interesting supporting materials for catalysis, but here we demonstrated that the surface modification of these readily available materials is a convenient strategy to boost the catalytic properties: by increasing the surface basicity of the supporting material (**Ni/AC–R**), we increased the X by 22% and the S_{CH_4} by 60% *cf.* **Ni/AC**. Our results allow us to conclude that the basicity of the support plays a major role in the performance of the catalyst since the most basic catalyst (**Ni/AC–R**) presented the best performance.

Role of the promotion by Fe

The bimetallic **NiFe/AC–R** exhibits higher conversion and selectivity than the monometallic **Ni/AC–R** at lower temperatures. These results are consistent with the reported literature, where it has been shown that the formation of a Ni–Fe alloy is of great importance since it can facilitate CO dissociation on the catalyst due to an optimal CO dissociation energy at the surface of the alloy, as revealed by DFT calculations, and also confirmed experimentally.[31,33–35] Furthermore, the weaker MSI in **NiFe/AC–R** *cf.* **Ni/AC–R** (Fig. 2b) is an additional reason for the better performance of the bimetallic catalyst, since it is closely related to the CO dissociation energy.[31–33]

Valinejad Moghaddam *et al.*[53] studied the addition of different metal promoters to Ni/Al_2O_3 catalysts. They concluded that among the tested metals, Fe was the most promising promoter, allowing X_{CO_2} of 78% and S_{CH_4} of 99% to be achieved at 350 °C. Notably, the WHSV was lower than that we used in the current study (9000 *cf.* 60 000 mL g^{-1} h^{-1}), and when it was increased to 30 000 mL g^{-1} h^{-1}, the obtained X_{CO_2} was significantly lower. However, regarding other supports, the same effect was not so apparent. Pandey *et al.*[54] studied the influence of Fe addition to Ni catalysts supported on various supporting materials, such as Al_2O_3, ZrO_2, TiO_2, SiO_2 and Nb_2O_5. They concluded that Al_2O_3 exhibited a higher enhancement in activity as a consequence of Fe addition compared to the other supporting materials, and these results were attributed to the enhanced ability of Al_2O_3 to adsorb CO_2.

The results obtained from the long TOS experiment evidence that the addition of Fe leads to an increase in the stability of the **Ni/AC–R** methanation catalyst, which is most likely due to the stabilization of Ni by Fe, preventing the sintering of Ni NPs.

Based on the characterization results of **Ni/AC–R** after prolonged TOS, we observed microstructural and compositional changes; however, we are uncertain whether these occur owing to the oxidation of the spent catalyst under exposure to ambient conditions, or they are due to sintering-induced *in situ* restructuring of the Ni surface under the methanation reaction. Therefore, our ongoing research is directed towards *in situ* TEM investigation of the **Ni/AC–R** and **NiFe/AC–R** catalysts under reaction conditions to piece together the fine microstructure and chemical composition for understanding the exact reasons behind their weak but gradual deactivation.

Conclusions

A convenient strategy taking advantage of fine-tuning the surface functionality of activated carbon supporting materials can be used to prepare highly active and selective Ni catalysts

for CO_2 methanation. We observed that the basicity of the support plays a major role in the performance of the catalyst since the most basic catalyst (**Ni/AC–R**) presented the best performance. Importantly, enhancing the catalytic performance of the Ni catalyst while simultaneously reducing the temperature of the methanation reaction is possible through judicious Fe promotion. Slight but gradual deactivation of the monometallic catalyst during prolonged time-on-stream CO_2 methanation is primarily associated with Ni NP sintering, which can be prevented by the addition of Fe. Interestingly, post-reaction *ex situ* analysis of the spent Ni catalyst evidenced distinct changes in its chemical composition and microstructure.

Conflicts of interest

There are no conflicts to declare.

Acknowledgements

L. P. L. G. is thankful for the support of FCT PhD grant SFRH/BD/128986/2017. This work was financially supported by: Associate Laboratory LSRE-LCM – UIDB/50020/2020 – funded by national funds through FCT/MCTES (PIDDAC). OSGPS acknowledges FCT funding under the Scientific Employment Stimulus - Institutional Call CEECINST/00049/2018.

Notes and references

1 J. B. Sabatier and P. Senderens, *C. R. Hebd. Seances Acad. Sci.*, 1902, **134**, 514–516.
2 S. Rönsch, J. Schneider, S. Matthischke, M. Schlüter, M. Götz, J. Lefebvre, P. Prabhakaran and S. Bajohr, *Fuel*, 2016, **166**, 276–296.
3 B. Miao, S. S. K. Ma, X. Wang, H. Su and S. H. Chan, *Catal. Sci. Technol.*, 2016, **6**, 4048–4058.
4 G. M. Shashidhara and M. Ravindram, *React. Kinet. Catal. Lett.*, 1988, **37**, 451–456.
5 E. Marconi, S. Tuti and I. Luisetto, *Catalysts*, 2019, **9**, 1–13.
6 Z. Zhang, Y. Tian, L. Zhang, S. Hu and J. Xiang, *Int. J. Hydrogen Energy*, 2019, **44**, 9291–9306.
7 C. Vogt, E. Groeneveld, G. Kamsma, M. Nachtegaal, L. Lu, C. J. Kiely, P. H. Berben, F. Meirer and B. M. Weckhuysen, *Nat. Catal.*, 2017, **1**, 127–134.
8 J. Li, Y. Lin, X. Pan, D. Miao, D. Ding, Y. Cui, J. Dong and X. Bao, *ACS Catal.*, 2019, **9**, 6342–6348.
9 X. Li, Y. Wang, G. Zhang, W. Sun, Y. Bai, L. Zheng and X. Han, *ChemistrySelect*, 2019, 838–845.
10 A. Westermann, B. Azambre, M. C. Bacariza, I. Graça, M. F. Ribeiro, J. M. Lopes and C. Henriques, *Appl. Catal., B*, 2015, **174–175**, 120–125.
11 W. Zhen, B. Li, G. Lu and J. Ma, *Chem. Commun.*, 2015, **51**, 1728–1731.
12 M. Younas, S. Sethupathi and A. R. Mohamed, *Int. J. Energy Res.*, 2018, **42**, 3289–3302.
13 J. K. Kesavan, I. Luisetto, S. Tuti, C. Meneghini, C. Battocchio and G. Iucci, *J. Mater. Sci.*, 2017, **52**, 10331–10340.
14 G. Zhou, T. Wu, H. Xie and X. Zheng, *Int. J. Hydrogen Energy*, 2013, **38**, 10012–10018.
15 T. A. Le, M. S. Kim, S. H. Lee and E. D. Park, *Top. Catal.*, 2017, **60**, 714–720.
16 M. Kuśmierz, *Catal. Today*, 2008, **137**, 429–432.
17 S. Toemen, W. A. W. Abu Bakar and R. Ali, *J. CO2 Util.*, 2016, **13**, 38–49.
18 A. Karelovic and P. Ruiz, *Appl. Catal., B*, 2012, **113–114**, 237–249.
19 J. N. Park and E. W. McFarland, *J. Catal.*, 2009, **266**, 92–97.
20 J. H. Kwak, L. Kovarik and J. Szanyi, *ACS Catal.*, 2013, **3**, 2094–2100.
21 C. Swalus, M. Jacquemin, C. Poleunis, P. Bertrand and P. Ruiz, *Appl. Catal., B*, 2012, **125**, 41–50.
22 M. C. Le, K. Le Van, T. H. T. Nguyen and N. H. Nguyen, *J. Chem.*, 2017, **2017**, 4361056.
23 L. M. Cam, N. T. T. Ha, L. Van Khu, N. N. Ha and T. C. Brown, *Aust. J. Chem.*, 2019, **72**, 969–977.
24 J. L. Figueiredo, M. F. R. R. Pereira, M. M. A. A. Freitas, J. J. M. Orfao and J. J. M. Órfão, *Carbon*, 1999, **37**, 1379–1389.
25 O. S. G. P. Soares, J. J. M. Órfão and M. F. R. Pereira, *Catal. Lett.*, 2010, **139**, 97–104.
26 O. S. G. P. Soares, C. S. D. Rodrigues, L. M. Madeira and M. F. R. Pereira, *Catalysts*, 2019, **9**, 258.
27 P. Serp and J. L. Figueiredo, *Carbon Materials for Catalysis*, 2009.
28 N. N. Ha, N. Thi, T. Ha, L. Van Khu and L. M. Cam, *J. Mol. Model.*, 2015, 1–9.
29 Z. Li, T. Zhao and L. Zhang, *Appl. Organomet. Chem.*, 2018, **32**, 1–7.
30 C. Mebrahtu, F. Krebs, S. Perathoner, S. Abate, G. Centi and R. Palkovits, *Catal. Sci. Technol.*, 2018, **8**, 1016–1027.
31 S. Hwang, U. G. Hong, J. Lee, J. H. Baik, D. J. Koh, H. Lim and I. K. Song, *Catal. Lett.*, 2012, **142**, 860–868.
32 B. Mutz, M. Belimov, W. Wang, P. Sprenger, M.-A. Serrer, D. Wang, P. Pfeifer, W. Kleist and J.-D. Grunwaldt, *ACS Catal.*, 2017, **7**, 6802–6814.
33 A. L. Kustov, A. M. Frey, K. E. Larsen, T. Johannessen, J. K. Nørskov and C. H. Christensen, *Appl. Catal., A*, 2007, **320**, 98–104.
34 M. P. Andersson, T. Bligaard, A. Kustov, K. E. Larsen, J. Greeley, T. Johannessen, C. H. Christensen and J. K. Nørskov, *J. Catal.*, 2006, **239**, 501–506.
35 T. Bligaard, J. K. Nørskov, S. Dahl, J. Matthiesen, C. H. Christensen and J. Sehested, *J. Catal.*, 2004, **224**, 206–217.
36 T. Burger, F. Koschany, O. Thomys, K. Köhler and O. Hinrichsen, *Appl. Catal., A*, 2018, **558**, 44–54.
37 S. Hwang, U. G. Hong, J. Lee, J. G. Seo, J. H. Baik, D. J. Koh, H. Lim and I. K. Song, *J. Ind. Eng. Chem.*, 2013, **19**, 2016–2021.
38 D. Pandey and G. Deo, *J. Mol. Catal. A: Chem.*, 2014, **382**, 23–30.
39 D. Pandey and G. Deo, *J. Ind. Eng. Chem.*, 2016, **33**, 99–107.
40 O. S. G. P. Soares, R. P. Rocha, A. G. Gonçalves, J. L. Figueiredo, J. J. M. Órfão and M. F. R. Pereira, *Carbon*, 2015, **91**, 114–121.
41 J. A. Menéndez, B. Xia, J. Phillips and L. R. Radovic, *Langmuir*, 1997, **13**, 3414–3421.

This journal is © The Royal Society of Chemistry 2020

42 J. Gao, Y. Wang, Y. Ping, D. Hu, G. Xu, F. Gu and F. Su, *RSC Adv.*, 2012, **2**, 2358–2368.
43 M. D. Adsuar-García, J. X. Flores-Lasluisa, F. Z. Azar and M. C. Román-Martínez, *Catalysts*, 2018, **8**(12), 572.
44 M. Romero-Sáez, A. B. Dongil, N. Benito, R. Espinoza-González, N. Escalona and F. Gracia, *Appl. Catal., B*, 2018, **237**, 817–825.
45 J. Gao, Q. Jiang, Y. Liu, W. Liu, W. Chu and D. S. Su, *Nanoscale*, 2018, **10**, 14207–14219.
46 B. P. Payne, M. C. Biesinger and N. S. McIntyre, *J. Electron Spectrosc. Relat. Phenom.*, 2012, **185**, 159–166.
47 M. C. Biesinger, B. P. Payne, A. P. Grosvenor, L. W. M. Lau, A. R. Gerson and R. S. C. Smart, *Appl. Surf. Sci.*, 2011, **257**, 2717–2730.
48 I. Chicinaș, V. Pop, O. Isnard, J. M. Le Breton and J. Juraszek, *J. Alloys Compd.*, 2003, **352**, 34–40.
49 J. L. Figueiredo and M. F. R. Pereira, *Catal. Today*, 2010, **150**, 2–7.
50 M. S. Shafeeyan, W. M. A. W. Daud, A. Houshmand and A. Shamiri, *J. Anal. Appl. Pyrolysis*, 2010, **89**, 143–151.
51 W. E. I. Wang, C. Duong-Viet, H. Ba, W. Baaziz and G. Tuci, *ACS Appl. Energy Mater.*, 2019, **2**, 1111–1120.
52 F. Hu, S. Tong, K. Lu, C. Chen, F. Su, J. Zhou, Z. Lu, X. Wang, G. Feng and R. Zhang, *J. CO2 Util.*, 2019, **34**, 676–687.
53 S. Valinejad Moghaddam, M. Rezaei, F. Meshkani and R. Daroughegi, *Int. J. Hydrogen Energy*, 2018, **43**, 16522–16533.
54 D. Pandey and G. Deo, *J. Ind. Eng. Chem.*, 2016, **33**, 99–107.

This journal is © The Royal Society of Chemistry 2020

Carbon 195 (2022) 35–43

Contents lists available at ScienceDirect

Carbon

journal homepage: www.elsevier.com/locate/carbon

Understanding the importance of N–doping for CNT-supported Ni catalysts for CO_2 methanation

Liliana P.L. Gonçalves [a, b, c], Maria Meledina [d, e], Alexander Meledin [d, e], Dmitri Y. Petrovykh [a], Juliana P.S. Sousa [a], O. Salomé G.P. Soares [b, c], Yury V. Kolen'ko [a, **], M. Fernando R. Pereira [b, c, *]

[a] International Iberian Nanotechnology Laboratory (INL), Avenida Mestre José Veiga s/n, 4715-330, Braga, Portugal
[b] LSRE-LCM - Laboratory of Separation and Reaction Engineering, Laboratory of Catalysis and Materials, Faculty of Engineering, University of Porto, Rua Dr. Roberto Frias, 4200-465, Porto, Portugal
[c] ALiCE - Associate Laboratory in Chemical Engineering, Faculty of Engineering, University of Porto, Rua Dr. Roberto Frias, 4200-465, Porto, Portugal
[d] RWTH Aachen University, Central Facility for Electron Microscopy, Aachen, Germany
[e] Ernst Ruska Centre for Microscopy and Spectroscopy with Electrons, Jülich, Germany

ARTICLE INFO

Article history:
Received 7 December 2021
Received in revised form
23 March 2022
Accepted 25 March 2022

Keywords:
Carbon nanotubes
CO_2 methanation
N-doping
HAADF-STEM

ABSTRACT

The N–doping of carbon nanotubes (CNTs) is widely accepted as an effective way to enhance the catalytic performance of CNT-supported Ni catalysts for CO_2 methanation. To demonstrate, in a direct systematic comparison, the importance of N–doping for producing high-performance CO_2 methanation catalysts, we developed two catalysts composed of 15 wt% Ni on pristine (Ni/CNT) and N–doped CNT (Ni/CNT–N) and correlated their catalytic performance with their properties. Compared to Ni/CNT, Ni/CNT–N achieved a higher X_{CO2} of 81.2% with S_{CH4} ~ 99.2% at a lower temperature of 400 °C, exhibiting excellent stability over 48 h time-on-stream testing. Our comprehensive comparative study demonstrated that the N–doped CNT support featured a better distribution of the Ni sites that were strongly interacting with the support, even with atomically dispersed Ni being observed by HAADF-STEM. This higher dispersion, enabled by the anchoring sites provided by the N–doping, is one of the main reasons for the enhanced performance of Ni/CNT–N, because it increases the H_2 uptake capacity.

© 2022 Elsevier Ltd. All rights reserved.

1. Introduction

In the field of gas-phase heterogeneous catalysis, carbon nanotubes (CNTs) have been intensively explored as catalysts themselves and, mainly, as supporting materials for the preparation of metallic catalysts [1]. Several different aspects have been taken into account while employing CNTs for catalysis. For instance, the formation of hot spots within the catalytic bed during thermal catalysis is often responsible for the sintering of catalytically active metallic nanoparticles, leading to the subsequent loss in the catalyst performance [2–4]. CNTs exhibit high thermal conductivity and excellent thermal stability [4,5]; therefore, these materials are of particular interest for exothermic reactions, wherein their use can prevent the undesired formation of hot spots, thus increasing the durability of the supported metallic catalysts [4–7]. Another interesting aspect of the CNTs is their versatile surface chemistry that has been extensively investigated for the design and preparation of high-performing and durable catalysts. Specifically, CNTs possess a graphitic structure, containing unsaturated C atoms at the edges of the constituent graphene layers. These C atoms afford the incorporation of different O-, N- or S-containing functionalities into the CNT structure [8]. This capability to dope CNT materials with heteroatoms has led to the application of metal-free heteroatom-doped CNTs as catalysts themselves [9–11]. Furthermore, the doping of CNTs with the aforementioned heteroatoms has been shown to improve the performance of supported metal catalysts. For example, N–doped CNTs have been reported to support well dispersed catalytically active metal nanoparticles, and sometimes to contribute to the adsorption of the reactant gases, such as CO_2 [6,12].

* Corresponding author. LSRE-LCM – Laboratory of Separation and Reaction Engineering – Laboratory of Catalysis and Materials, Faculty of Engineering, University of Porto, Rua Dr. Roberto Frias, 4200-465, Porto, Portugal.
** Corresponding author. International Iberian Nanotechnology Laboratory (INL), Avenida Mestre José Veiga s/n, 4715-330, Braga, Portugal
E-mail addresses: yury.kolenko@inl.int (Y.V. Kolen'ko), fpereira@fe.up.pt (M.F.R. Pereira).

https://doi.org/10.1016/j.carbon.2022.03.059
0008-6223/© 2022 Elsevier Ltd. All rights reserved.

In our research [13,14], we are focusing on the so-called Sabatier reaction of CO_2 methanation ($CO_2 + 4H_2 \rightarrow CH_4 + H_2O$; $\Delta H_{298K} = -165$ kJ mol^{-1}). This reaction provides an interesting pathway to produce a carbon-neutral e-CH_4 fuel in power-to-gas plants [15], thus significantly reducing CO_2 emissions to the atmosphere. More specifically, the power-to-gas technology combines the generation of green H_2 by water electrolysis using renewable electricity and its further use for hydrogenation of captured anthropogenic CO_2 in an electrified catalytic reactor powered by renewable electricity to finally deliver the e-CH_4 fuel. While H_2 is a sustainable fuel itself, unfortunately, it requires special infrastructure for storage and transportation [16]. Hence, the aforementioned production of e-CH_4 would allow to overcome the challenges of handling hydrogen, since the resultant e-CH_4 can be directly distributed within the current gas pipeline, storage, and distribution networks.

Although CO_2 methanation is a thermodynamically favorable reaction, it has significant kinetic barriers that can be reduced by means of active and selective catalysts [17,18]. The typical catalysts for the reaction are group-VIII metals, such as Ni, Co, Ru, Rh, and Pd. Currently, a particular focus is placed on Ni, which has an optimal combination of high activity, excellent selectivity, high abundance, and low price [17]. The most commonly used supporting materials for the aforementioned metal catalysts are metal oxides, such as Al_2O_3, TiO_2, ZrO_2 and CeO_2 [19–21]. Besides, the successful applications of other supporting materials, such as zeolites [22] and metal organic frameworks [23], have also been reported. Moreover, the use of carbon-based supports for CO_2 methanation catalysts has been recently explored. For instance, activated carbon [13,14,24], CNTs [4,6,7,12,25–27], carbon nanofibers [28,29], and graphene [30,31] have been successfully applied for the preparation of efficient CO_2 methanation catalysts.

In our laboratories, we are pursuing the development of carbon-supported Ni-based catalysts for CO_2 methanation. Our previous studies have shown that the carbon-supported-Ni (Ni/C) catalysts for CO_2 methanation exhibit several unique features: (i) good dispersion of the Ni nanoparticles over the supporting material, (ii) stability of a Ni/C catalyst at high temperatures, (iii) hydrogenation reaction at low temperature, and (iv) high CO_2 coverage over Ni/C catalyst facilitating the hydrogenation [13,14,32]. Importantly, these unique features were largely achieved through judicious tailoring of activated-carbon supporting materials; hence we became interested in a direct systematic comparison of pristine CNTs and N–doped CNTs as supporting materials for Ni catalysts.

Accordingly, two Ni catalysts supported on commercially available CNT (Ni/CNT) and on synthesized N–doped CNT (Ni/CNT–N), both with 15 wt% Ni loading, were successfully prepared. They were extensively characterized before and after reaction, and their catalytic performance in CO_2 methanation reaction was investigated, allowing a detailed comparative study between the Ni/CNT and Ni/CNT–N catalysts. In particular, we were able to demonstrate the importance of N–doping in high-performing carbon-supported catalysts for CO_2 methanation, understanding the basis for the better catalytic performance of Ni/CNT–N.

2. Materials and methods

2.1. Materials

NC3100™ CNTs were obtained from Nanocyl, melamine (≥99%) was purchased from Fluka, $Ni(NO_3)_2{\cdot}6H_2O$ (≥97.0%) was purchased from Sigma Aldrich while SiC was purchased from VWR. Ultrapure water (18.2 MΩ cm^{-2}) was generated using a Milli-Q Advantage A10 system (Millipore).

2.2. Preparation of N–doped CNTs

To obtain N–doped CNTs (referred to as CNT–N), 0.6 g of CNTs and 0.26 g of N, using melamine as N source, were co-ball-milled in a closed pot at a vibration frequency of 15 vibrations s^{-1} for 4 h using a MM200 ball-milling (Retsch). After that, the resultant fine powdered mixture was heated at 10 °C min^{-1} and annealed at 600 °C for 1 h under a flow of N_2 at 100 cm^3 min^{-1} [33].

2.3. Preparation of Ni catalysts

Supported Ni catalysts were prepared by the incipient wetness impregnation method. Briefly, 0.5 g of the supporting material was placed in an ultrasonic bath, and an aqueous solution of $Ni(NO_3)_2{\cdot}6H_2O$ was slowly added to obtain a nominal Ni loading of 15%. This loading was selected in our preliminary catalytic screening, as a further increase did not significantly change the conversion and selectivity (Fig. S1). The sample was further left under ultrasonic vibration for 90 min, and then dried at 120 °C overnight. Finally, the samples were annealed under N_2 atmosphere and further reduced under H_2 atmosphere. The samples were placed in a quartz tube reactor and heated to 400 °C at 10 °C min^{-1}, followed by annealing at this temperature for 1 h under a N_2 flow rate of 100 cm^3 min^{-1}. After that, the N_2 flow was switched to 50 cm^3 min^{-1} of H_2 and the samples were then reduced under these conditions for 3 h, thus affording 15%Ni/CNT and 15%Ni/CNT–N catalysts for CO_2 methanation (further referred to as **Ni/CNT** and **Ni/CNT–N**, respectively). This reduction temperature was selected because, according to the H_2 Temperature Programmed Reduction profiles of the samples, approximately at this temperature both samples exhibit overlapping high intensity peaks in H_2 consumption. A long reduction time (3 h) was used, instead of a higher temperature, to avoid the sintering of Ni and the formation of larger Ni nanoparticles.

2.4. Characterization

The N_2 adsorption-desorption isotherms were collected using NOVA 4200e multi-station setup (Quantachrome). Prior to the physisorption, the samples (ca. 100 mg) were degassed at 170 °C for 3 h. The specific surface area (S_{BET}) was calculated by the Brunauer–Emmett–Teller (BET) method, and the total pore volume (V_p) was determined from the amount of N_2 adsorbed at relative pressure $P/P_0 = 0.95$. The pore size distribution was estimated using the non-local density functional theory (NLDFT) assuming a cylindrical-pore model.

H_2 temperature programmed reduction (H_2–TPR) was performed using the AMI–200 catalyst characterization apparatus (Altamira Instruments), equipped with a thermal conductivity detector (TCD), high precision mass flow controllers (MFCs) and a furnace with air cooling. About 100 mg of sample was loaded into a U-shaped quartz tube, which was then placed into the furnace. Before the heating, the system was flushed by an Ar flow rate of 25 cm^3 min^{-1}, and then H_2 diluted with Ar (5%H_2/Ar) was used as reducing atmosphere. While the reducing gas was flowing through the system at 25 cm^3 min^{-1}, the temperature was raised to 1000 °C with a heating rate of 10 °C min^{-1}.

H_2 pulse chemisorption was performed in the same setup as H_2–TPR. Approximately 100 mg of sample was pre-treated *in situ* under H_2 for 30 min at 450 °C, then cooled down to 35 °C and flushed with Ar. After that, 58 μL pulses of H_2 were injected into Ar carrier gas flow until the area of the hydrogen peak on the chromatograph was identical. The metallic Ni surface area (S_M) was

calculated assuming that two Ni atoms are required for the adsorption of one H_2 molecule according to the following equation:

$$S_M = \frac{n_m^a N_n}{n_s}$$

Where S_M is the specific surface area of the metal ($m^2\ g_{cat}^{-1}$), n_m^a is the quantity of adsorbed hydrogen (mol g_{cat}^{-1}), N is the Avogadro's number, n is the number of metal atoms needed to adsorb a H_2 molecule, and n_s is the number of atoms in the surface per unit of area. Elemental analysis was carried out on a vario MICRO cube and a rapid OXY cube analyser from Elemental. Each element (CHNS/O) was determined by combustion of the sample at 1050 °C and calculated by the mean of three independent measurements, using a per-day calibration with a standard compound.

Powder X-ray diffraction (XRD) was performed on a X'Pert PRO diffractometer (PANanalytical), equipped with Ni-filtered Cu K_α radiation and a PIXcel detector. A Bragg-Brentano geometry was used in a 2θ range from 20° to 80° with step size of 0.01° and a time per step of 300 s. Recorded XRD patterns were matched to International Centre for Diffraction Data (ICDD) PDF-4 database using HighScore software package (PANalytical).

X-ray photoelectron spectroscopy (XPS) was performed in a ESCALAB 250Xi (Thermo Scientific) using a monochromated microfocused Al K_α X-ray source. Powdered samples were pressed into carbon tape, which was directly attached to the sample holder. Charge neutralization was accomplished by a flood gun producing low-energy (≤1 eV) beams of Ar^+ ions and electrons. Fitting of the XPS spectra was performed using the Avantage software (Thermo Fisher Scientific), in which the peaks were fitted with a Gaussian–Lorentzian function. Binding energies were calibrated relative to the C 1s peak for aliphatic and aromatic carbon at 284.6 eV.

Transmission electron microscopy (TEM) observations were conducted using a JEOL 2100 electron microscope operated at 200 kV. The samples were prepared by dispersing powder samples in ethanol and dropping the dispersion onto a carbon coated copper grid. The particle size distribution was estimated using ImageJ software by measuring at least 100 particles on the collected TEM images. Additionally, the microstructure and chemical composition of the initial and spent catalysts were investigated by high-angle annular dark-field scanning TEM (HAADF–STEM) and energy dispersive X-ray spectroscopy in STEM mode (STEM–EDX) using a Titan electron microscope (FEI), equipped with a Super-X EDX system and operated at 200 kV.

Thermogravimetric analysis (TGA) was performed using a Mettler-Toledo TGA/DSC 1 STAR equipment, by heating the samples under Ar flow from 30 to 900 °C, at a heating rate of 10 °C min^{-1}, while performing two isothermal steps: 7 min under Ar and 13 min under air.

2.5. CO_2 methanation

The catalytic CO_2 methanation experiments were carried out in a Microactivity XS15 system (PID Eng & Tech), using a fixed-bed quartz reactor ($Ø_{int}$ = 1 cm). The reaction products in the outflow were analyzed by online GC 1000 gas chromatograph (DANI), equipped with a TCD and a GS-CarbonPLOT capillary column, while using He as carrier gas and a continuous flow of N_2 as an internal standard. A condenser in the Microactivity XS15 system removes the water byproduct before the gas is injected into the GC. 100 mg of the catalyst were diluted by inert SiC for the following reasons: (*i*) to assure a sufficient bed height thus allowing the insertion of the thermocouple into the catalytic bed, (*ii*) to enable the required space velocity, and (*iii*) to omit the formation of hot spots in the catalytic bed. Next, the catalyst/SiC mixture was led into a fixed-bed quartz reactor. Each catalyst was pre-treated *in situ* under a H_2 flow rate of 40 $cm^3\ min^{-1}$ at 400 °C for 30 min, at 1 bar. After that, the reactor temperature was decreased to 200 °C under a He flow rate of 50 $cm^3\ min^{-1}$, and then, the reactor was fed with the stoichiometric gas mixture of 10% CO_2 and 40% H_2, balanced by 50% He, having a total flow rate of 100 $cm^3\ min^{-1}$, and thus providing weight hourly space velocity (*WHSV*) of 60 000 $cm^3\ g^{-1}\ h^{-1}$. The CO_2 methanation was conducted at the pressure of 1 bar. A temperature ramping from 200 °C to 500 °C was performed under reaction conditions to evaluate the catalytic properties of the synthesized materials as a function of the reaction temperature.

To evaluate the stability of the catalysts, long-term time-on-stream (TOS) testing was performed under the same reaction conditions referred before; however, under isothermal conditions at the established temperature of optimal catalytic performance of the respective catalyst.

Conversion of CO_2 (X_{CO2}) and selectivity to methane (S_{CH4}) were calculated as follows, anticipating CO as the only by-product:

$$X(\%) = \frac{[CO_2]_{in} - [CO_2]_{out}}{[CO_2]_{in}} \times 100$$

$$S_{CH_4} = \frac{[CH_4]_{out}}{[CH_4]_{out} + [CO]_{out}} \times 100$$

Where $[CO_2]_{in}$ and $[CO_2]_{out}$ are the concentration of CO_2 in moles min^{-1} in the inlet and outlet gas flow, respectively. $[CH_4]_{out}$ and $[CO]_{out}$ are the concentration of CH_4 and CO in moles min^{-1} in the outlet gas flow, respectively.

Thermodynamic equilibrium analysis was performed using the simulation software HSC Chemistry®. The equilibrium compositions of the system were determined at specified operating conditions (temperature, pressure and feed composition) using a model based on the minimization of Gibbs free-energy of the existing CH_4, H_2O, CO_2, CO, H_2 and solid carbon species.

3. Results

3.1. Characterization of the synthesized catalysts

We started by confirming the success of the N–doping procedure by determining the chemical composition of the supporting materials via elemental analysis, which established that the N–doped CNT contained 5 wt% of N (Table S1), which agrees with the XPS measurement that revealed 5 wt% of N.

Furthermore, we analyzed the textural properties of pristine CNTs, synthesized N–doped CNTs and the resultant **Ni/CNT** and **Ni/CNT–N** catalysts for CO_2 methanation. All the samples show a Type II isotherm, characteristic of non-porous or macroporous materials, and a H3 hysteresis characteristic of carbon materials exhibiting some mesoporosity (Fig. S2) [23,24]. This meso/macro porosity results from the free spaces among the CNT bundles. Upon the introduction of Ni, the types of isotherms did not change (Fig. S2). Interestingly, the pore-size distribution of the N–doped CNTs was found to be quite different compared to that in pristine CNTs. Specifically, the CNTs show an important contribution of pores with width >20 nm, while N–doped CNTs have almost no pores with such a large width (Fig. S3). The specific surface area (S_{BET}) of pristine and N–doped CNTs was estimated to be quite similar (Table 1, 197 $m^2\ g^{-1}$ cf. 202 $m^2\ g^{-1}$), suggesting that our N–doping protocol does not change the specific surface area. This might be a result of a compensatory action between the ball milling procedure and the introduction of the N–groups: it would be expected for the

Table 1
Selected textural, and morphological properties for pristine **CNT**, synthesized **CNT**–**N** as well as **Ni/CNT** and **Ni/CNT**–**N** catalysts for CO_2 methanation.

	S_{BET} ($m^2\ g^{-1}$)[a]	V_p ($cm^3\ g^{-1}$)[a]	S_M ($m^2\ g_{cat}^{-1}$)[b]	d_{Ni} (nm)[c]	d_{Ni} after TOS (nm)[c]
CNT	202	0.42	–	–	–
CNT–N	197	0.49	–	–	–
Ni/CNT	213	0.38	0.3	16 ± 7	17 ± 7
Ni/CNT–N	225	0.44	1.1	6 ± 3	8 ± 4

[a]Estimated by N_2 physisorption.
[b]Estimated by H_2 pulse chemisorption.
[c]Estimated by the analysis of TEM images.

ball milling procedure to increase the S_{BET} by opening the ends of the CNTs and decreasing their entanglement, the effects which can be observed by TEM (Fig. S4); on the other hand, the N–doping procedure can lead to some blocking of the pores. Slightly higher S_{BET} values were estimated for the derivative Ni/CNT (213 $m^2\ g^{-1}$) and Ni/CNT–N (225 $m^2\ g^{-1}$) catalysts, which suggests that the impregnation and reduction procedure to deposit the Ni nanoparticles could have led to some opening of the nanotubes; small Ni nanoparticles also present a relevant geometrical surface area that contributes to the specific surface area of the samples (Fig. S5). The total pore volume (V_p) slightly decreases after Ni deposition (Table 1), most likely because of some aggregation of the CNT bundles [34,35].

After establishing the textural characteristics of the synthesized catalysts, we further analyzed their phase composition by means of XRD. Fig. 1 shows that both **Ni/CNT** and **Ni/CNT**–**N** catalysts exhibit similar phase composition. In particular, the peak at 26° corresponds to the graphitic carbon of the CNTs. Besides carbon, the catalysts consist of metallic Ni (ICDD #04-016-4761) and NiO (ICDD #04-004-8992). Notably, the observed Bragg reflections are broad, which is typical for nanocrystalline materials.

Next, we performed H_2–TPR to study the reducibility of the catalysts, and the obtained H_2–TPR profiles are presented in Fig. 2. While **Ni/CNT** exhibits two peaks of H_2 consumption at low temperature (<400 °C), **Ni/CNT**–**N** shows three peaks in this temperature region that can be assigned to H_2 consumption by NiO weakly bound on the walls of CNT–N. Specifically, the first peak at 297 °C in **Ni/CNT**–**N** profile can be associated with the reduction of NiO species confined within the CNT–N nanotubes [4,27,36]. Notably, this peak is absent in the case of **Ni/CNT** catalyst.

In the 300–400 °C range, both catalysts exhibit two peaks at similar temperatures that can be attributed to highly dispersed NiO species, strongly interacting with the exterior walls of the CNTs [4,27]. Above 400 °C, the catalysts exhibit two more peaks of NiO reduction, wherein **Ni/CNT**–**N** shows more pronounced features, suggesting that this catalyst incorporates a larger number of highly

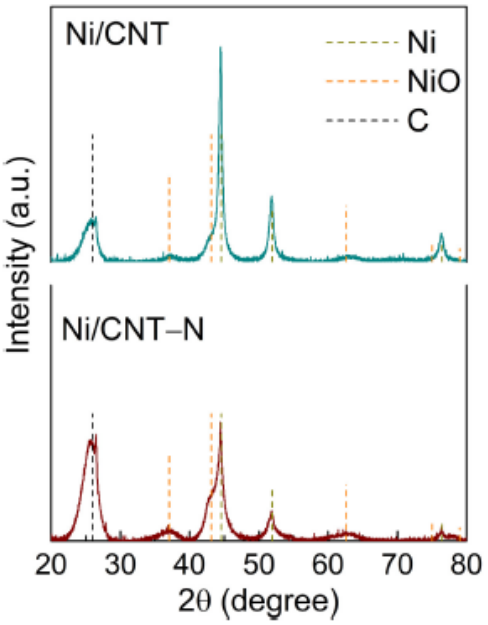

Fig. 1. XRD patterns of the **Ni/CNT** and **Ni/CNT**–**N** catalysts, indicating the presence of graphitic carbon, metallic Ni and NiO. (A colour version of this figure can be viewed online.)

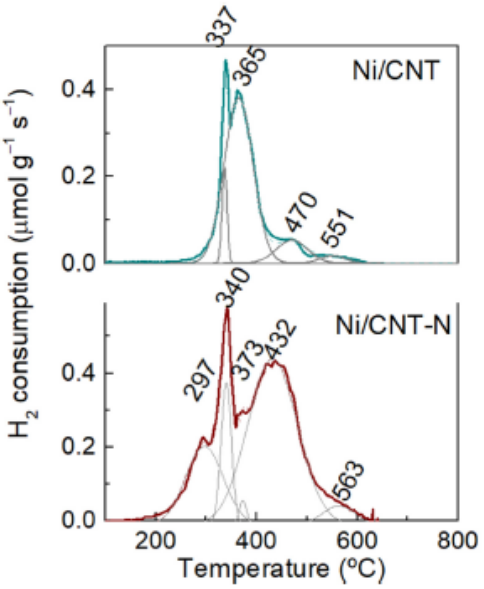

Fig. 2. Comparison of the H_2–TPR profiles for **Ni/CNT** and **Ni/CNT**–**N** catalysts. The grey lines are the deconvolution of the peaks. (A colour version of this figure can be viewed online.)

dispersed NiO species compared to **Ni/CNT**. Evidence for such metal dispersion in the catalysts was further provided by H_2 pulse chemisorption, which revealed the **Ni/CNT–N** catalyst having almost 3.5 times higher metallic surface area (S_M) than that in the **Ni/CNT** catalyst (Table 1). Consistently with H_2–TPR studies, this result indicates that **Ni/CNT–N** exhibits a large quantity of NiO species well dispersed on the support.

Having established textural and compositional properties of our catalysts, we then investigated their morphology, microstructure and fine chemical composition by means of electron microscopy and also the chemical composition by means of XPS. It is important to note, however, that the interpretation of these results should be made taking into account the limitations of the experimental protocols and sample handling. In particular, even though the fresh catalysts are subjected to a reduction treatment, they are characterized after exposure to ambient air, which can oxidize the surfaces of transition-metal nanoparticles to some extent. However, before the catalytic testing, the fresh catalysts undergo an *in situ* reduction pre-treatment in the reactor, meaning that metallic nanoparticles are considered when interpreting their catalytic activity.

Fig. S4 shows low-magnification TEM images of the **Ni/CNT** and **Ni/CNT–N** catalysts. **Ni/CNT–N** consists of small catalyst nanoparticles with an average size of ≈ 6 nm (Fig. S5, Table 1) that are well-dispersed over the N–doped CNTs (Figs. S4d,e,f). In contrast, the average size of catalyst nanoparticles supported on pristine CNTs is found to be significantly larger, namely, ≈ 16 nm (Fig. S5, Table 1). Moreover, the nanoparticles in the **Ni/CNT** catalyst sometimes exhibit agglomerated appearance (Figs. S4a,b,c). The observed difference in the size and dispersion of the catalytic nanoparticles over pristine and N–doped CNTs is also clearly seen during the comparison of the respective low-magnification HAADF–STEM images (Fig. 3a cf. Fig. 3e).

Furthermore, the fine microstructure of the catalyst nanoparticles in the **Ni/CNT** and **Ni/CNT–N** catalysts was also found to be quite different. Specifically, the nanoparticles dispersed on the pristine CNTs in **Ni/CNT** exhibit Ni@NiO core-shell appearance (Fig. 3b,c,d). In contrast, small nanoparticles in **Ni/CNT–N** are mainly NiO (Fig. 3f,h). More interestingly, the latter catalyst exhibits some bright-contrast dot-like features in the representative HAADF–STEM image (marked by white arrows in Fig. 3g). Most likely, these bright dots are atomically dispersed Ni sites and/or clusters of a few Ni atoms that are well-anchored on the N–doped CNTs, which have been previously reported on similar materials [37,38].

Our complementary XPS analysis confirmed that the surface of the catalysts is composed of a mixture of Ni and NiO, in agreement with the other characterization results. From the deconvolution of the Ni $2p_{3/2}$ spectra of both **Ni/CNT** and **Ni/CNT–N** (Fig. 4, top), one

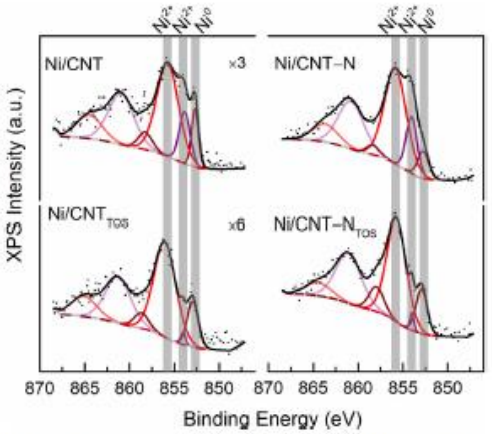

Fig. 4. High-resolution XPS data for the Ni $2p_{3/2}$ region collected from the as-synthesized **Ni/CNT** and **Ni/CNT–N** catalysts (top) and after their time-on-stream (TOS) testing for 2 days (bottom). Dots: raw data; black lines: overall fits; colored lines: fits of individual components; dashed lines: background. (A colour version of this figure can be viewed online.)

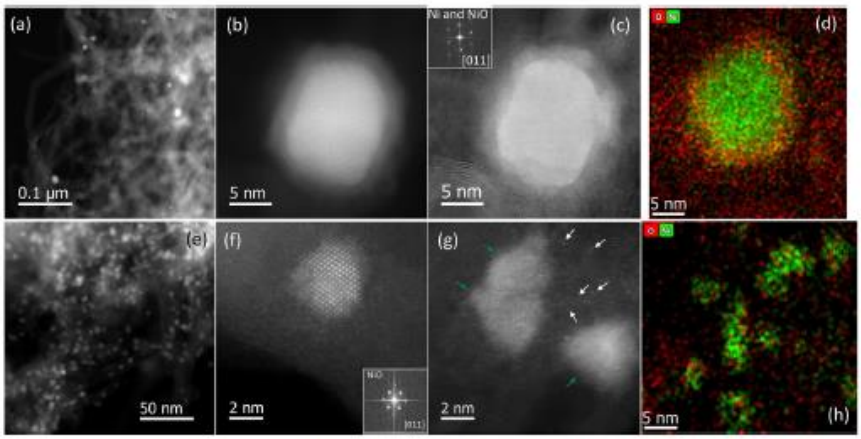

Fig. 3. Representative low-magnification (a,e) and high-resolution (b,f,g) HAADF–STEM images and Fourier transform (FT) pattern [inset in panel (f)], together with high-resolution (c) ADF–STEM image and the corresponding STEM–EDX O and Ni mixture maps of the **Ni/CNT** (a–d) and **Ni/CNT–N** (e–h). The white arrows in (g) indicate the Ni single atoms and atom clusters, while the green arrows indicate the Ni nanoparticles. (A colour version of this figure can be viewed online.)

can observe the presence of a lower binding energy component at 852.9 ± 0.1 eV that can be assigned to metallic Ni^0 species. Other components at 854.0 ± 0.1 eV and 855.9 ± 0.1 eV are consistent with Ni^{2+} in NiO, along with satellite peaks from Ni^{2+} at 861.1 ± 0.2 eV and 864.5 ± 0.5 eV [14,39]. Notably, such combination of components has been previously assigned to Ni^{2+} in a thin nickel oxide layer over metallic Ni^0 [14,39–41]. The relative at% of Ni^0 is, however, different between the two catalysts (Table S2): **Ni/CNT** has 9.4 at% Ni^0, while **Ni/CNT–N** has only 6.4 at%. The C 1s, O 1s and N 1s spectra of the materials are shown in Fig. S8, S9 and S10, respectively [13,42,43]. Importantly, the N 1s spectra (Fig. S10) indicate that the N–doped CNT supporting material mainly comprises pyridinic (N-6) and pyrrolic (N-5) groups with some quaternary groups (N-Q), thus evidencing successful N–doping [42]. The analysis of N 1s spectra also demonstrated that the N content, at least at the surface of the samples, decreased after the introduction of Ni (Table S3). However, there are no qualitative changes in the N 1s spectra after Ni addition.

Thermogravimetric analysis (TGA) (Fig. S11) demonstrated that, under inert atmosphere, the **Ni/CNT** and **Ni/CNT–N** catalysts are stable (i.e., did not lose mass) up to around 500 °C. Above this temperature, there is a decrease in the mass of the samples, related to the decomposition of the carbon support. When the atmosphere is changed to air, the burn of the CNT is observed with an abrupt decrease in the mass of the samples, followed by a small increase in mass at the end of the experiment, possibly related to the oxidation of the Ni nanoparticles.

3.2. Catalytic performance in CO_2 methanation

With well-characterized **Ni/CNT** and **Ni/CNT–N** catalysts in hand, we further measured their catalytic properties in the CO_2 methanation reaction: CO_2 conversion (X_{CO2}) and selectivity to CH_4 (S_{CH4}) were investigated as a function of the reaction temperature. As expected, the X_{CO2} increases with the temperature for both catalysts until it reaches the thermodynamic equilibrium value and then starts to decrease (Fig. 5a). Interestingly, **Ni/CNT–N** achieves a higher X_{CO2} of 81.2% with S_{CH4} = 99.2% at a lower temperature of 400 °C, with an activity (r) of 207 mol dm^{-3} kg^{-1}, when compared to **Ni/CNT** that achieves a maximum X_{CO2} of 78.5% with S_{CH4} = 98.5% and r = 192 mol dm^{-3} kg^{-1} at a higher temperature of 430 °C (Table 2). Accordingly, the maximum CH_4 yield (Y_{CH4}) over the **Ni/CNT** was calculated to be 77.3%, while **Ni/CNT–N** is able to reach a higher Y_{CH4} of 80.6% (Table 2). Comparing the temperature at which each catalyst achieves 50% of X_{CO2}, (T_{50}), the **Ni/CNT–N** again performs better, with a T_{50} = 350 °C compared to a T_{50} = 370 °C established for **Ni/CNT** (Table 2). Overall, the **Ni/CNT–N** catalyst achieves higher X_{CO2} and S_{CH4} at temperatures below 430 °C, while above this temperature the performance of the catalysts is similar. We note that reducing the samples at 400 °C for 3 h prior to the catalytic experiments prevented the influence of the contributions exhibited in TPR at this temperature range on these measurements.

We also evaluated the stability of **Ni/CNT** and **Ni/CNT–N** catalysts in terms of X_{CO2} and S_{CH4} (Fig. 5c and d). Both materials exhibited excellent stability over 48 h of isothermal TOS testing, with negligible loss in X_{CO2} and S_{CH4} over this period of time. An additional experiment, with prolonged TOS of 90 h demonstrated that the best performing **Ni/CNT–N** catalysts maintained excellent stability over this period of time (Fig. S12).

3.3. Characterization of the catalysts after TOS by XPS and TEM

To understand the impact of the CO_2 methanation reaction conditions on the composition and microstructure of the catalysts, we further characterized the TOS-tested **Ni/CNT** and **Ni/CNT–N** by XPS and electron microscopy.

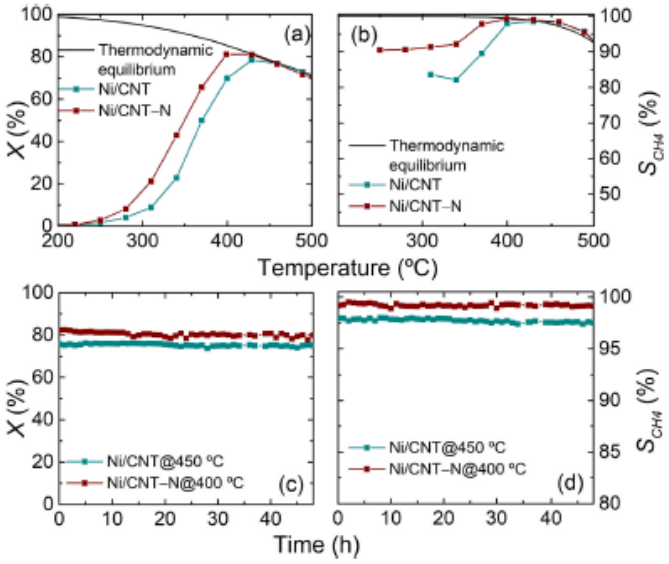

Fig. 5. Comparison of the CO_2 conversion X_{CO2} (a) and CH_4 selectivity S_{CH4} (b) as a function of temperature for the **Ni/CNT** and **Ni/CNT–N** catalysts. Results of the isothermal TOS testing for 48 h in terms of X_{CO2} (c) and S_{CH4} (d). The thermodynamic equilibrium lines are shown in the graphics and were calculated using a model based on the minimization of Gibbs free-energy of the existing species. Reaction conditions: P = 1 bar; $WHSV$ = 60 000 cm^3 g^{-1} h^{-1}; CO_2: H_2 = 1 : 4. (A colour version of this figure can be viewed online.)

Table 2
Comparison of the catalytic performance in terms X_{CO2}, S_{CH4}, and activity (r) for Ni/CNT and Ni/CNT–N catalysts at 400 °C and 430 °C, together with the temperature at which the sample reaches 50% X_{CO2} (T_{50}) and the maximum methane yield ($Y_{CH4,MAX}$), that occurs at 430 °C and 400 °C for Ni/CNT and Ni/CNT–N, respectively.

	400 °C			430 °C			T_{50} (°C)	$Y_{CH4,MAX}$
	X_{CO2} (%)	S_{CH4} (%)	r (mol dm^{-3} kg^{-1})	X_{CO2} (%)	S_{CH4} (%)	r (mol dm^{-3} kg^{-1})		
Ni/CNT	69.9	97.9	171	78.5	98.5	192	370	77.3
Ni/CNT–N	81.2	99.2	207	81.1	99.0	207	350	80.6

XPS (Fig. 4, bottom) revealed that the TOS-tested catalysts are still a mixture of Ni and NiO. At the same time, the relative at% of metallic Ni increases in both materials (Table S2). In the case of **Ni/CNT**, the Ni^0 at% increases from 9.4% to 11.1%, while in **Ni/CNT–N** it increases from 6.4% to 12.2%, evidencing that the catalyst nanoparticles underwent reduction under the reductive methanation reaction conditions. Importantly, after reaction, both samples exhibit similar Ni^0 at%, which indicates that the highly dispersed NiO species on **Ni/CNT–N** (Fig. 3e–h) are reduced under the reaction conditions to a similar extent as the nanoparticles in **Ni/CNT**. Furthermore, it is interesting that the Ni^{2+} component that exhibits the major decrease in intensity in the TOS-tested samples is the one at 854 eV, indicating that it is a specific oxidized Ni species that is likely being reduced.

Under the CO_2 methanation reaction conditions, the primary pathways to possible gasification of the C-based support would be via hydrogenation. We do not observe any evidence of significant hydrogenation among the oxidized C components in the C 1s spectra after TOS (Fig. S8), which would be the most affected by hydrogenation. In an additional consideration largely independent of the gasification mechanism, the resulting physical damage to the CNT material would have reduced the C 1s shake-up component [44], which is also not observed in the C 1s spectra after TOS (Fig. S8). Likewise, the N content in the **Ni/CNT–N** sample after the long TOS experiment would have been expected to change significantly under some pathways of C gasification or, more generally, of support hydrogenation, but no such change is evident in Table S3.

Analysis of the TEM images (Fig. S6) and the resultant particle-size distributions (Fig. S7) indicates that the catalytic nanoparticles in both TOS-tested **Ni/CNT** and **Ni/CNT–N** materials underwent only a negligible increase in average size due to sintering, reaching the average sizes of ≈ 17 nm and ≈8 nm (Table 1), respectively.

HAADF–STEM images and STEM–EDX maps of the catalysts after TOS testing reveal that the catalyst nanoparticles in TOS-tested **Ni/CNT** (Fig. 6a–c) and **Ni/CNT–N** (Fig. 6d–f) have a Ni@NiO core-shell nanostructure. Notably, the presence of atomically dispersed Ni species is no longer observed in TOS-tested **Ni/CNT–N**, highlighting the sintering of such fine species during CO_2 methanation at 400 °C for 48 h.

4. Discussion

Our study demonstrates that N–doping of the CNTs leads to the development of a Ni-based **Ni/CNT–N** catalyst with significantly improved performance towards CO_2 methanation as compared to its non-doped **Ni/CNT** counterpart. Specifically, **Ni/CNT–N** catalyst has a T_{50} = 350 °C and achieves a X_{CO2} of 81.2% with S_{CH4} = 99.2% at 400 °C, while the **Ni/CNT** catalyst has a T_{50} = 370 °C and achieves a maximum X_{CO2} of 78.5% with S_{CH4} = 98.5% at higher temperature of 430 °C. While achieving high catalytic performance for the as-synthesized **Ni/CNT–N** material was not the main objective of this work, its catalytic properties compare favorably with the results reported in the literature, making **Ni/CNT–N** a useful model N–doped CNT material for the direct comparison with the **Ni/CNT** counterpart, aimed at elucidating the salient properties provided by N–doping of CNTs for catalytic performance in CO_2 methanation.

For example, Gödde et al. [12] reported a 30% Ni/NCNT catalyst, which reached X_{CO2} = 86.1% at 350 °C, although using a lower weight hourly space velocity (*WHSV*) than that in the present study (10 000 cm^3 g^{-1} h^{-1} vs. 60 000 cm^3 g^{-1} h^{-1}). At higher *WHSV* = 50 000 cm^3 g^{-1} h^{-1}, they were able to obtain X_{CO2} = 50.9% with S_{CH4} = 95.8% at 340 °C (Table S4). In another work, Wang et al. [6] reported a X_{CO2} = 80% with S_{CH4} = 99% at 360 °C with *WHSV* = 60 000 cm^3 g^{-1} h^{-1} for their Ni catalyst supported on N–doped CNTs (Table S4). Interestingly, the as-synthesized **Ni/CNT–N** achieved better catalytic properties than did our previously reported Ni catalyst supported on N–doped activated carbon, which reached X_{CO2} = 70% with S_{CH4} ≈ 95% at 450 °C [13] (Table S4). This improvement in the catalytic properties provides direct evidence that N–doped carbon nanotubes are a better supporting material for Ni-based CO_2 methanation catalysts than is N–doped activated carbon.

Other types of systems, also based on CNTs but not on N–doped ones, have been evaluated using different types of promotion. Gao et al. [26] reported a catalyst comprising 10% Ni and 2% La supported on oxidized CNT that achieved 82.8% of X_{CO2} with 100% S_{CH4} at 320 °C (Table S4). Furthermore, Wang et al. [4] reported a catalyst comprising 12% Ni and 4.5% Ce supported on CNT that achieved 83.8% of X_{CO2} with 99.8% S_{CH4} at 350 °C (Table S4).

It has been reported that the N–sites could provide binding sites for the Ni species enabling a good dispersion of the Ni precursor during impregnation, and also preventing agglomeration of the nanoparticles during the thermal treatments [6,12–14,45,46]. Accordingly, we propose that the experimentally observed higher CO_2 methanation performance of **Ni/CNT–N** than that of **Ni/CNT** is a result of the higher dispersion of the catalytically active Ni phase over N–doped CNTs. This conclusion is supported by our multiple characterization methods that evidenced the existence of fine catalytic particles (even atomically dispersed Ni species) well-dispersed over N–doped CNTs.

On the other hand, the presence of highly dispersed Ni species leads to the difficulty in their reduction due to strong interaction with the support, as confirmed by H_2–TPR. This resulted in the presence of NiO catalyst nanoparticles in **Ni/CNT–N**, while **Ni/CNT** was found to consist of metallic Ni nanoparticles covered with a NiO shell.

Even though the catalysts demonstrated excellent stability over 48 h of TOS, their characterization after the TOS testing allowed for the identification of the changes that they underwent during prolonged CO_2 methanation. Interestingly, the Ni^0 at% is similar in both TOS-tested **Ni/CNT** and **Ni/CNT–N**, suggesting that, even though the Ni species in **Ni/CNT–N** are more difficult to reduce, under CO_2 methanation conditions, they undergo reduction to a similar extent as in the case of **Ni/CNT**. This reduction of the Ni phase occurs as a consequence of subjecting the catalysts to the reductive methanation conditions for the prolonged TOS. Interestingly, it seems that it is a specific oxidized Ni species that is being reduced since the Ni^{2+} component that presents the major decrease in intensity in the TOS-tested samples is the one at 854 eV. Furthermore, the

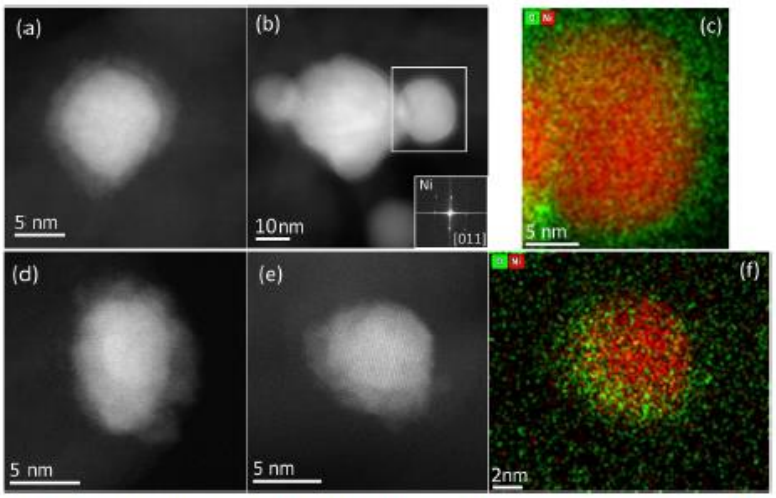

Fig. 6. Representative high-resolution HAADF–STEM images (a,b,d,e) and Fourier transform (FT) pattern [inset in panel (b)] of the resultant catalyst particles in TOS-tested **Ni/CNT** (a,b) and **Ni/CNT–N** (d,e) catalysts, together with the respective STEM–EDX Ni and O mixture maps, confirming the Ni@NiO core-shell nanostructure of the catalyst particles in spent **Ni/CNT** (c) and **Ni/CNT–N** (f). (A colour version of this figure can be viewed online.)

resultant catalyst nanoparticles in TOS-tested **Ni/CNT–N** are morphologically similar to those in TOS-tested **Ni/CNT**, forming a core-shell nanostructure of Ni@NiO but preserving their small particle size.

5. Conclusions

We successfully prepared Ni-based catalysts supported on CNTs and N–doped CNTs, compared their catalytic properties in CO_2 methanation, evaluated their stability, and performed comprehensive characterization to understand the property-performance relationship.

Our **Ni/CNT–N** catalyst achieves a X_{CO2} of 81.2% with S_{CH4} = 99.2% at 400 °C, while the pristine CNT counterpart, **Ni/CNT**, achieves a maximum X_{CO2} of 78.5% with S_{CH4} = 98.5% at a higher temperature of 430 °C. Furthermore, both catalysts exhibit outstanding stability over 48 h of TOS testing, with no sign of deactivation. The enhanced performance of **Ni/CNT–N** is a result of the good dispersion of the Ni phase over N–doped CNTs, as confirmed by TEM, HAADF–STEM, H_2 TPR, and H_2 pulse chemisorption. These encouraging results compare well to those reported previously, thus offering new opportunities for designing high-performing CO_2 methanation catalysts throughout judicious modification of the supporting material.

CRediT authorship contribution statement

Liliana P.L. Gonçalves: Conceptualization, Data curation, Formal analysis, Investigation, Methodology, Writing – original draft. **Maria Meledinad:** Data curation, Formal analysis, Investigation, Methodology, Writing – review & editing. **Alexander Meledin:** Data curation, Formal analysis, Investigation, Methodology, Writing – review & editing. **Dmitri Y. Petrovykh:** Data curation, Formal analysis, Writing – review & editing. **Juliana P.S. Sousa:** Supervision, Writing – review & editing. **O. Salomé G.P. Soares:** Conceptualization, Funding acquisition, Methodology, Project administration, Resources, Supervision, Visualization, Writing – review & editing. **Yury V. Kolen'ko:** Conceptualization, Funding acquisition, Project administration, Resources, Supervision, Writing – review & editing. **M. Fernando R. Pereira:** Conceptualization, Funding acquisition, Project administration, Resources, Supervision, Writing – review & editing.

Declaration of competing interest

The authors declare that they have no known competing financial interests or personal relationships that could have appeared to influence the work reported in this paper.

Acknowledgements

L.P.L.G. thanks the Portuguese Foundation for Science and Technology (FCT) for the PhD grant (SFRH/BD/128986/2017). This work was financially supported by LA/P/0045/2020 (ALiCE), UIDB/50020/2020 and UIDP/50020/2020 (LSRE-LCM), funded by national funds through FCT/MCTES (PIDDAC). O.S.G.P.S. acknowledges FCT funding under the Scientific Employment Stimulus - Institutional Call (CEECINST/00049/2018). Yu.V.K. thanks the FCT for support under the CritMag Project (PTDC/NAN-MAT/28745/2017).

Appendix A. Supplementary data

Supplementary data to this article can be found online at https://doi.org/10.1016/j.carbon.2022.03.059.

References

[1] P. Serp, E. Castillejos, Catalysis in carbon nanotubes, ChemCatChem 2 (1) (2010) 41–47.
[2] M. Agnelli, H.M. Swaan, C. Marquez-Alvarez, G.A. Martin, C. Mirodatos, CO hydrogenation on a nickel catalyst: II. A mechanistic study by transient

kinetics and infrared spectroscopy, J. Catal. 175 (1) (1998) 117–128.
[3] L. Li, J. Zheng, Y. Liu, W. Wang, Q. Huang, W. Chu, Impacts of SiC carrier and nickel precursor of Ni/La/support catalysts for CO_2 selective hydrogenation to synthetic natural gas (SNG), ChemistrySelect 2 (13) (2017) 3750–3757.
[4] W. Wang, W. Chu, N. Wang, W. Yang, C. Jiang, Mesoporous nickel catalyst supported on multi-walled carbon nanotubes for carbon dioxide, Int. J. Hydrogen Energy 41 (2) (2015) 967–975.
[5] P. Serp, J.L. Figueiredo, Carbon Materials for Catalysis, Wiley, New Jersey, 2009.
[6] W. Wang, C. Duong-Viet, H. Ba, W. Baaziz, G. Tuci, S. Caporali, L. Nguyen-Dinh, O. Ersen, G. Giambastiani, C. Pham-Huu, Nickel nanoparticles decorated nitrogen-doped carbon nanotubes (Ni/N-CNT); A robust catalyst for the efficient and selective CO_2 methanation, ACS Appl. Energy Mater. 2 (2) (2019) 1111–1120.
[7] J. Li, Y. Zhou, X. Xiao, W. Wang, N. Wang, W. Qian, W. Chu, Regulation of Ni–CNT interaction on Mn-promoted nickel nanocatalysts supported on oxygenated CNTs for CO_2 selective hydrogenation, ACS Appl. Mater. Interfaces 10 (2018) 41224–41236.
[8] R.P. Rocha, M.F.R. Pereira, Tuning CNT properties for metal-free environmental catalytic applications, Chimia 2 (2016) 17.
[9] O.S.G.P. Soares, R.P. Rocha, A.G. Gonçalves, J.L. Figueiredo, J.J.M. Órfão, M.F.R. Pereira, Highly active N-doped carbon nanotubes prepared by an easy ball milling method for advanced oxidation processes, Appl. Catal. B Environ. 192 (2016) 296–303.
[10] R.P. Rocha, G.P. Soares, A.G.O.S. Gonçalves, J.J.M. Órfão, M.F.R. Pereira, J.L. Figueiredo, Different methodologies for synthesis of nitrogen doped carbon nanotubes and their use in catalytic wet air oxidation, Appl. Catal. Gen. 548 (April) (2017) 62–70.
[11] O.S.G.P. Soares, R.P. Rocha, J.J.M. Órfão, M.F.R. Pereira, J.L. Figueiredo, Mechanothermal approach for N-, S-, P-, and B-doping of carbon nanotubes: methodology and catalytic performance in wet air oxidation, Chimia 5 (2) (2019) 30.
[12] J. Gödde, M. Merko, W. Xia, M. Muhler, Nickel nanoparticles supported on nitrogen–doped carbon nanotubes are a highly active, selective and stable CO_2 methanation catalyst, J. Energy Chem. 54 (2021) 323–331.
[13] L.P.L. Gonçalves, J.P.S. Sousa, O.S.G.P. Soares, O. Bondarchuk, O.I. Lebedev, Y.V. Kolen'ko, M.F.R. Pereira, The role of surface properties in CO_2 methanation over carbon-supported Ni catalysts and their promotion by Fe, Catal. Sci. Technol. 10 (21) (2020) 7217.
[14] L.P.L. Gonçalves, A. Serov, G. McCool, M. Dicome, J.P.S. Sousa, O.S.G.P. Soares, O. Bondarchuk, D.Y. Petrovykh, O.I. Lebedev, M.F.R. Pereira, Y. Kolen'ko, New opportunity for carbon-supported Ni-based electrocatalysts: gas-phase CO_2 methanation, ChemCatChem 13 (2021) 1–11.
[15] M. Bailera, P. Lisbona, L.M. Romeo, S. Espatolero, Power to Gas projects review: lab, pilot and demo plants for storing renewable energy and CO_2, Renew. Sustain. Energy Rev. 69 (November 2016) (2017) 292–312.
[16] S. Niaz, T. Manzoor, A.H. Pandith, Hydrogen storage: materials, methods and perspectives, Renew. Sustain. Energy Rev. 50 (2015) 457–469.
[17] J. Ashok, S. Pati, P. Hongmanorom, Z. Tianxi, C. Junmei, S. Kawi, A review of recent catalyst advances in CO_2 methanation processes, Catal. Today 356 (May) (2020) 471–489.
[18] B. Miao, S.S.K. Ma, X. Wang, H. Su, S.H. Chan, Catalysis mechanisms of CO_2 and CO methanation, Catal. Sci. Technol. 6 (12) (2016) 4048–4058.
[19] Z. Zhang, Y. Tian, L. Zhang, S. Hu, J. Xiang, Impacts of nickel loading on properties, catalytic behaviors of $Ni/\gamma Al_2O_3$ catalysts and the reaction intermediates formed in methanation of CO_2, Int. J. Hydrogen Energy 44 (18) (2019) 9291–9306.
[20] Y. Ma, J. Liu, M. Chu, J. Yue, Y. Cui, G. Xu, Cooperation between active metal and basic support in Ni-based catalyst for low-temperature CO_2 methanation, Catal. Lett. 150 (5) (2020) 1418–1426.
[21] X. Wen, L. Xu, M. Chen, Y. Shi, C. Lv, Y. Cui, X. Wu, G. Cheng, C.e. Wu, Z. Miao, F. Wang, X. Hu, Exploring the influence of nickel precursors on constructing efficient Ni-based CO_2 methanation catalysts assisted with in-situ technologies, Appl. Catal. B Environ. 297 (April) (2021) 120486.
[22] A. Westermann, B. Azambre, M.C. Bacariza, I. Graça, M.F. Ribeiro, J.M. Lopes, C. Henriques, Insight into CO_2 methanation mechanism over NiUSY zeolites: an operando IR study, Appl. Catal. B Environ. 174–175 (2015) 120–125.
[23] W. Zhen, B. Li, G. Lu, J. Ma, Enhancing catalytic activity and stability for CO_2 methanation on Ni@MOF-5 via control of active species dispersion, Chem. Commun. 51 (2015) 1728–1731.
[24] N.N. Ha, N. Thi, T. Ha, L. Van Khu, L.M. Cam, Theoretical study of carbon dioxide activation by metals (Co, Cu, Ni) supported on activated carbon, J. Mol. Model. (21) (2015) 322.
[25] P. Kangvansura, L.M. Chew, W. Saengsui, P. Santawaja, Y. Poo-arporn, M. Muhler, H. Schulz, A. Worayingyong, Product distribution of CO_2 hydrogenation by K- and Mn-promoted Fe catalysts supported on N-functionalized carbon nanotubes, Catal. Today 275 (2016) 59–65.
[26] J. Gao, Q. Jiang, Y. Liu, W. Liu, W. Chu, D.S. Su, Probing the enhanced catalytic activity of carbon nanotube supported Ni-LaOx hybrids for the CO_2 reduction reaction, Nanoscale 10 (2018) 14207–14219.
[27] M. Romero-sáez, A.B. Dongil, N. Benito, R. Espinoza-gonzález, N. Escalona, F. Gracia, CO_2 methanation over nickel-ZrO_2 catalyst supported on carbon nanotubes : a comparison between two impregnation strategies, Appl. Catal. B Environ. 237 (March) (2018) 817–825.
[28] L. Roldán, Y. Marco, E. García-Bordejé, Function of the support and metal loading on catalytic carbon dioxide reduction using ruthenium nanoparticles supported on carbon nanofibers, ChemCatChem 7 (2015) 1347–1356.
[29] L. Roldán, Y. Marco, E. García-Bordejé, Origin of the excellent performance of Ru on nitrogen- doped carbon nanofibers for CO_2 hydrogenation to CH_4, ChemSusChem 10 (6) (2017) 1139–1144.
[30] B. Jurca, C. Bucur, A. Primo, P. Concepción, V.I. Parvulescu, H. García, N-doped defective graphene from biomass as catalyst for CO_2 hydrogenation to methane, ChemCatChem 11 (3) (2019) 985–990.
[31] F. Hu, S. Tong, K. Lu, C. Chen, F. Su, J. Zhou, Z. Lu, X. Wang, G. Feng, R. Zhang, Reduced graphene oxide supported Ni-Ce catalysts for CO_2 methanation: the support and ceria promotion effects, J. CO_2 Util. 34 (June) (2019) 676–687.
[32] L.P.L. Gonçalves, J. Mielby, O.S.G.P. Soares, J.P.S. Sousa, D.Y. Petrovykh, O.I. Lebedev, M.F.R. Pereira, S. Kegnæs, Y.V. Kolen'ko, *In situ* investigation of the CO_2 methanation on carbon/ceria-supported Ni catalysts using modulation-excitation DRIFTS, Appl. Catal. B Environ. (2022), https://doi.org/10.1016/j.apcatb.2022.121376.
[33] O.S.G.P. Soares, R.P. Rocha, A.G. Gonçalves, J.L. Figueiredo, J.J.M. Órfão, M.F.R. Pereira, Easy method to prepare N-doped carbon nanotubes by ball milling, Carbon N. Y. 91 (2015) 114–121.
[34] D.Y. Kim, J.H. Kim, M. Li, S. Noda, J. Kim, K.S. Kim, K.S. Kim, C.M. Yang, Controllable pore structures of pure and sub-millimeter-long carbon nanotubes, Appl. Surf. Sci. 566 (2021) 150751.
[35] V. Likodimos, T.A. Steriotis, S.K. Papageorgiou, G.E. Romanos, R.R.N. Marques, R.P. Rocha, J.L. Faria, M.F.R. Pereira, J.L. Figueiredo, A.M.T. Silva, P. Falaras, Controlled surface functionalization of multiwall carbon nanotubes by HNO_3 hydrothermal oxidation, Carbon 69 (2014) 311–326.
[36] W. Chen, Z. Fan, X. Pan, X. Bao, Effect of confinement in carbon nanotubes on the activity of Fischer–Tropsch iron catalyst, J. Am. Chem. Soc. 130 (29) (2008) 9414–9419.
[37] P. Lu, Y. Yang, J. Yao, M. Wang, S. Dipazir, M. Yuan, J. Zhang, X. Wang, Z. Xie, G. Zhang, Facile synthesis of single-nickel-atomic dispersed N-doped carbon framework for efficient electrochemical CO_2 reduction, Appl. Catal. B Environ. 241 (2019) 113–119.
[38] T. Zhang, X. Han, H. Yang, A. Han, E. Hu, Y. Li, X. Yang, L. Wang, J. Liu, B. Liu, Atomically dispersed nickel(I) on an alloy-encapsulated nitrogen-doped carbon nanotube Array for high-performance electrochemical CO_2 reduction reaction, Angew. Chem. Int. Ed. 59 (29) (2020) 12055–12061.
[39] M.C. Biesinger, B.P. Payne, L.W.M. Lau, A. Gerson, R.S.C. Smart, X-ray photoelectron spectroscopic chemical state Quantification of mixed nickel metal, oxide and hydroxide systems, Surf. Interface Anal. 41 (4) (2009) 324–332.
[40] B. Owens-Baird, J. Xu, D.Y. Petrovykh, O. Bondarchuk, Y. Ziouani, N. González-Ballesteros, P. Yox, F.M. Sapountzi, H. Niemantsverdriet, Y.V. Kolen'ko, K. Kovnir, NiP_2: a story of two divergent polymorphic multifunctional materials, Chem. Mater. 31 (9) (2019) 3407–3418.
[41] B. Owens-Baird, J.P.S. Sousa, Y. Ziouani, D.Y. Petrovykh, N.A. Zarkevich, D.D. Johnson, Y.V. Kolen'ko, K. Kovnir, Crystallographic facet selective HER catalysis: exemplified in FeP and NiP_2 single crystals, Chem. Sci. 11 (19) (2020) 5007–5016.
[42] J.L. Figueiredo, M.F.R. Pereira, The role of surface chemistry in catalysis with carbons, Catal. Today 150 (2010) 2–7.
[43] L.P.L. Gonçalves, D.B. Christensen, M. Meledina, L.M. Salonen, D.Y. Petrovykh, E. Carbó-Argibay, J.P.S. Sousa, O.S.G.P. Soares, M.F.R. Pereira, S. Kegnæs, Y.V. Kolen'Ko, Selective formic acid dehydrogenation at low temperature over a RuO_2/CDF pre-catalyst synthesized on the gram scale, Catal. Sci. Technol. 10 (7) (2020) 1991–1995.
[44] N. Lachman, X. Sui, T. Bendikov, H. Cohen, H.D. Wagner, Electronic and mechanical degradation of oxidized CNTs, Carbon N. Y. 50 (5) (2012) 1734–1739.
[45] T. Fu, Z. Li, Highly dispersed cobalt on N-doped carbon nanotubes with improved Fischer–Tropsch synthesis activity, Catal. Commun. 47 (2014) 54–57.
[46] S.A. Chernyak, D.N. Stolbov, A.S. Ivanov, S.V. Klokov, T.B. Egorova, K.I. Maslakov, O.I. Eliseev, V.V. Maximov, S.V. Savilov, V.V. Lunin, Effect of type and localization of nitrogen in graphene nanoflake support on structure and catalytic performance of Co-based Fischer-Tropsch catalysts, Catal. Today 357 (2020) 193–202.

New Opportunity for Carbon-Supported Ni-based Electrocatalysts: Gas-Phase CO_2 Methanation

Liliana P. L. Gonçalves,[a, b] Alexey Serov,[c] Geoffrey McCool,[d] Mikaela Dicome,[d] Juliana P. S. Sousa,[a] O. Salomé G. P. Soares,[b] Oleksandr Bondarchuk,[a] Dmitri Y. Petrovykh,[a] Oleg I. Lebedev,[e] M. Fernando R. Pereira,[b] and Yury V. Kolen'ko*[a]

The cost-effectiveness and excellent performance of conductive-carbon-supported Ni-based electrocatalysts make them attractive materials for hydrogen oxidation and evolution reactions. However, they were previously unused in gas-phase hydrogenation reactions. In this work, we have expanded the applicability of commercially available advanced Ni/C, NiMo/C and NiRe/C materials from electrocatalysis to heterogeneous catalysis of CO_2 methanation. Our catalytic testing efforts indicate that the monometallic Ni/C material demonstrates the best CO_2 methanation properties, achieving an excellent CO_2 conversion of 83% at 400 °C with nearly complete selectivity to CH_4 of 99.7%, plus exhibiting intact performance during 90 h of time-on-stream testing. Such catalytic properties are among the highest reported to date among carbon-supported Ni-based methanation catalysts. Excellent performance of Ni/C stems from the good dispersion of the Ni nanoparticles over N-containing carbon support material.

Introduction

Both heterogeneous catalysis and electrocatalysis can effectively hydrogenate anthropogenic CO_2 to renewable CH_4 fuel, providing promising pathways to reducing CO_2 emissions.[1–5] The similarity between heterogeneous catalysis and electrocatalysis is notable in that both processes involve sequences of bond breaking and formation.[6] Moreover, both processes often employ generally similar catalytic materials, which are comprised of catalytically active metallic phase on a supporting material, wherein the latter provides the base for a good spatial dispersion and stability of the active metallic nanoparticles (NPs), as well as accelerates the diffusion of reactants. Conversely, from the materials point of view, one of the fundamental differences between the supporting materials for heterogeneous catalysis vs electrocatalysts is that the latter ones should be anchored on conductive supporting materials to ensure good electrical connectivity/conductivity between the catalytically active phase and the respective electrode. Therefore, conductive carbon materials with high surface area are usually used as supports in the various fields of electrocatalysis. Accordingly, extensive research efforts have been undertaken to improve the electrocatalytic performance of the carbon-supported electrocatalysts through optimization of structural, textural, and electronic properties of the carbons, such as their degree of graphitization, surface area, porosity, defects, and surface functional groups. For example, our recent work demonstrated that Ni-based materials supported on different types of commercially available carbons, such as carbon paper, carbon cloth, and VULCAN® XCmax™ 22 conductive carbon, offer access to a diverse range of active and stable water reduction/oxidation electrocatalysts.[7–10]

We also recently embarked on the synthesis and investigation of catalysts for non-electrocatalytic gas-phase CO_2 methanation [Eq. (1)].

$$CO_2 + 4H_2 \leftrightarrow CH_4 + 2H_2O,\ \Delta H_{298K} = -165\ kJ\ mol^{-1} \quad (1)$$

This is a thermodynamically favorable hydrogenation reaction, but it has significant kinetic barriers, hence requiring a catalyst to achieve good CO_2 conversion and high selectivity to the desired CH_4 product. Ni-based catalysts supported on metal oxides (e.g., Al_2O_3) have been widely studied for this gas-phase reaction and today are adopted by the industry. This adoption is mainly due to the important fact that Ni exhibits the optimal

[a] L. P. L. Gonçalves, Dr. J. P. S. Sousa, Dr. O. Bondarchuk, Dr. D. Y. Petrovykh, Dr. Y. V. Kolen'ko
International Iberian Nanotechnology Laboratory (INL)
4715-330 Braga (Portugal)
E-mail: yury.kolenko@inl.int
[b] L. P. L. Gonçalves, Dr. O. S. G. P. Soares, Prof. M. F. R. Pereira
Laboratory of Separation and Reaction Engineering
Laboratory of Catalysis and Materials (LSRE-LCM)
Faculdade de Engenharia
Universidade do Porto
4200-465 Porto (Portugal)
[c] Dr. A. Serov
Electrification and Energy Infrastructures Division
Oak Ridge National Laboratory
(previously affiliated with
Pajarito Powder, LLC)
37932 Oak Ridge, TN (USA)
[d] G. McCool, M. Dicome
Pajarito Powder, LLC
Albuquerque, NM (USA)
[e] Dr. O. I. Lebedev
Laboratoire CRISMAT
UMR 6508, CNRS-ENSICAEN
Caen 14050 (France)

Supporting information for this article is available on the WWW under https://doi.org/10.1002/cctc.202101284

This publication is part of a Special Collection on "Supported Nanoparticles and Single-Atoms for Catalysis: Energy and Environmental Applications". Please check the ChemCatChem homepage for more articles in the collection.

© 2021 Wiley-VCH GmbH

combination of activity, selectivity, and, especially, cost, in comparison, for example, to those of the platinum-group metal catalysts (e.g., Ru-based).[11–15]

Notably, besides the industrially important metal oxides, other types of supporting materials, such as zeolites,[16] metal-organic frameworks[17] and carbons[2,18–20] have been investigated for CO_2 methanation, albeit to a far lesser extent. The limited historical interest in carbon-based supporting materials for catalysts for CO_2 methanation is primarily due to the high probability of their gasification [Eq. (2)] during this high-temperature ($T \geq 400\,^{\circ}C$) hydrogenation reaction. As demonstrated in our recent work,[2] however, some carbon materials can be appropriately modified and exhibit excellent stability over long time-on- stream (TOS).

$$C_{(s)} + H_{2(g)} \rightarrow CH_{x(g)} \quad (2)$$

Specifically, we studied the performance of Ni-based catalysts supported on activated carbon with different surface chemistries and achieved the best performance with a catalyst comprised of Ni NPs supported on reduced activated carbon with O-free Lewis-basic sites.[2] That study suggested that the methanation reaction is highly dependent on the basicity of the carbon support. The stability of that material over long TOS demonstrated a small loss in conversion of 8% and selectivity of 6% after 48 h. The stability was further improved by promotion with Fe, leading to a smaller loss in conversion of 3% and selectivity of 2%.

Previous studies suggest a few additional factors that improve performance of Ni catalysts on carbon-based supports. Wang et al.[3] evaluated the performance of Ni supported on nitrogen-doped carbon nanotubes (N–CNT) and the catalyst was demonstrated to be active and selective to CH_4. The authors attributed the good performance of the catalyst to the high thermal conductivity of N–CNT supporting material, which ensures the dispersion of the reaction heat throughout the catalyst bed, while the nitrogen doping favors the CO_2 adsorption and consequent methanation. Additionally, for Ni-based catalysts supported on reduced graphene oxide (RGO), Hu et al. reported[4] that the RGO-supported Ni catalysts exhibited higher activity than did Ni supported on activated carbon or Al_2O_3, mainly due to larger specific surface area of RGO that favored the formation of small Ni NPs, as well as due to the surface O groups that allowed a stable anchoring of the NPs. The performance of the catalyst was further improved by introduction of Ce into the catalytic system.

Overall, the carbon-based supports thus possess fundamental properties that can be extremely valuable for heterogeneous catalysis: their high surface area and high pore volume, relative to, e.g., metal oxides, their good mechanical stability and thermal conductivity, and their surface chemistry that is more amendable to modification than that of other types of supports.[21]

Their promising catalytic properties notwithstanding, designing, producing, and testing carbon-supported Ni-based materials dedicated for applications in gas-phase catalysis of CO_2 methanation is both a time- and resource-intensive undertaking. As indicated earlier, a possible "shortcut" in developing such materials is suggested by many similar properties found among the vast family of electrocatalysts that have been investigated and applied in the fields of fuel cells, water electrolysis, and CO_2 electroreduction.[22–24] For industrial applications, these materials already offer strategies for optimization and scale-up of their synthesis, making them attractive candidates for expanding to applications in the gas-phase CO_2 methanation reaction. Accordingly, we tested the hypothesis that commercial carbon-supported Ni electrocatalysts could selectively hydrogenate CO_2 to CH_4 in gas-phase, thus expanding the scope of these advanced materials beyond the electrocatalysis area.

We also investigated exploiting another similarity between the gas-phase catalysis and electrocatalysis, whereby the same transition metals are used for promoting the performance of Ni-based catalysts. Specifically, Ni–Mo and Ni–Re alloys have been widely studied as electrocatalysts, for example, for hydrogen oxidation and evolution reactions.[25,26] The beneficial electronic interaction between the *d*-orbitals of an iron-group metal, Ni, and refractory metals, Re and Mo, decreases the binding energy of the hydrogen atoms to the electrocatalyst surface in comparison to that for pure Ni, thus boosting the activity of the bimetallic electrocatalysts. In gas-phase methanation, Mo is known to be highly selective to methane, even though it exhibits poor activity,[27] and Re promotion of Ni-based catalysts has been shown to be beneficial for CO_2 methanation.[28,29] Therefore, we selected Mo and Re for testing in bimetallic catalysts, in an attempt to improve the performance of monometallic Ni/C in CO_2 methanation.

To test the suitability and performance of electrocatalysts in gas-phase catalysis, we investigated gas-phase CO_2 methanation over a set of commercially available Ni-based electrocatalysts supported on Engineered Catalyst Support™ conductive carbon material that were obtained from Pajarito Powder. The stability of the materials was also studied by means of long-term time-on-stream testing, including an assessment of the structural and compositional changes in the materials via their detailed characterization before and after long-term CO_2 methanation.

Results and Discussion

CO_2 methanation

As mentioned in the introduction, Ni-based catalysts (e.g., Ni/Al_2O_3) have attracted research interest because of their good performance in CO_2 methanation while being a cost-effective option compared to the expensive platinum-group metal catalysts (e.g., Ru). Therefore, to provide new opportunities for the commercially available **Ni/C**, **NiMo/C** and **NiRe/C** hydrogen evolution/oxidation electrocatalysts, we investigated their catalytic properties in gas-phase CO_2 methanation by evaluating their activity, selectivity, and stability.

A typical parameter used for the performance evaluation of CO_2 methanation catalysts is T_{50}, the temperature at which the

© 2021 Wiley-VCH GmbH

conversion, X_{CO2}, over the catalyst reaches $X_{CO2}=50\%$. Generally, the catalyst is more competitive if it shows high activity at lower temperatures, thus reducing the energy demand for CO_2 hydrogenation to CH_4. Figures 1a,b show the CO_2 conversion, X_{CO2}, and selectivity to methane, S_{CH4}, respectively, of the **Ni/C**, **NiMo/C** and **NiRe/C** catalysts in the studied temperature range (200–500 °C). We observed that all three catalysts are active and selective to CH_4 at temperatures above 250 °C. Compared to **Ni/C** and **NiRe/C** catalysts, the **NiMo/C** achieves higher conversion at temperatures below 325 °C, which is its T_{50} (Table 1). As temperature increases above 325 °C, the activity of the bimetallic **NiMo/C** catalyst drops below that of the monometallic **Ni/C** counterpart. Remarkably, **Ni/C** reaches a $X_{CO2}=83\%$ with $S_{CH4}=99.7\%$ at 400 °C, i.e., values close to the thermodynamic equilibrium of the reaction, particularly for X_{CO2}, for which it outperforms both bimetallic catalysts (Figures 1a,b). This monometallic **Ni/C** catalyst has a T_{50} of 330 °C, which is slightly higher than that of bimetallic **NiMo/C** (325 °C) (Table 1).

Comparing the bimetallic **NiMo/C** and **NiRe/C** catalysts, **NiMo/C** exhibits higher X_{CO2} and S_{CH4} at lower temperatures, reaching $X_{CO2}=70\%$ with $S_{CH4}=98.4\%$ at 400 °C (Figures 1a,b). As temperature increases above 400 °C, **NiRe/C** exhibits higher X_{CO2}, reaching $X_{CO2}=74\%$ with $S_{CH4}=97.7\%$ at 460 °C, values that are close to the thermodynamic equilibrium of the reaction (Figures 1a,b).

Furthermore, the bimetallic **NiRe/C** catalyst is characterized by the highest T_{50} of 360 °C among the three catalysts (Table 1).

The observed good performance of commercial **Ni/C**, **NiMo/C** and **NiRe/C** electrocatalysts in gas-phase CO_2 methanation is encouraging. To assess whether methanation reaction can be a new application for these materials, we further investigated their stability in this gas-phase hydrogenation reaction. In particular, we performed long-term TOS studies at the temperatures where the catalysts exhibit the highest X_{CO2}, namely, $T=400$ °C for **Ni/C** and **NiMo/C**, and $T=450$ °C for **NiRe/C**.

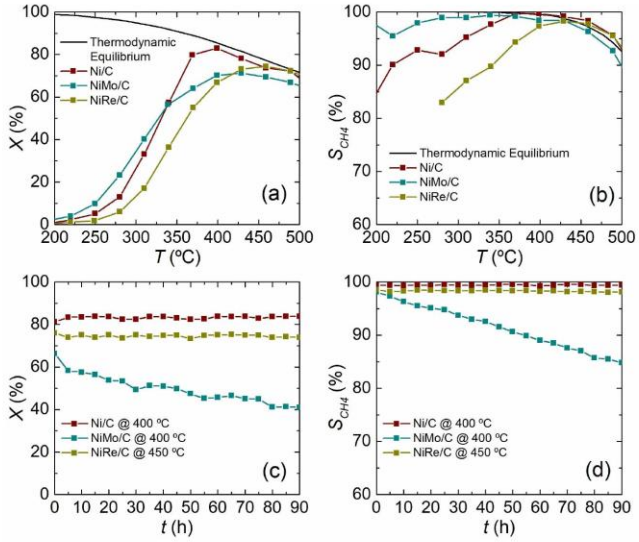

Figure 1. CO_2 conversion X_{CO2} (a) and CH_4 selectivity S_{CH4} (b) in 200–500 °C temperature range for **Ni/C**, **NiMo/C**, and **NiRe/C** catalysts, together with the evolution of X_{CO2} (c) and S_{CH4} (d) during long-term time-on-stream (TOS) testing. Reaction conditions: $P=1$ bar; $WHSV=60\,000\ cm^3 g^{-1} h^{-1}$; $CO_2:H_2=1:4$.

Table 1. Textural properties, H_2 uptake, mean nanoparticle diameter, temperature at which $X_{CO2}=50\%$ (T_{50}), and maximum X_{CO2} for **Ni/C**, **NiMo/C** and **NiRe/C** catalysts.

	S_{BET}[a] [$m^2 g^{-1}$]	d_{pores}[a] [nm]	V_p[a] [$cm^3 g^{-1}$]	H_2 uptake[b] [$mol\,g^{-1}$]	d_{NP}[c] [nm]	d_{NP} after TOS[c] [nm]	T_{50} [°C]	X_{CO2} (Max) [%]
Ni/C	334	5.5	0.544	37.7	10 ± 4	14 ± 12	330	83
NiMo/C	369	5.5	0.648	12.7	14 ± 5	15 ± 10	325	70
NiRe/C	371	6.5	0.634	29.7	14 ± 10	16 ± 10	360	74

[a] Estimated by N_2 physisorption. [b] Estimated by H_2 pulse chemisorption, [c] Estimated by the analysis of TEM images.

© 2021 Wiley-VCH GmbH

Figures 1c,d show the time-dependent X_{CO2} and S_{CH4} data, respectively, collected for all three catalysts. The **Ni/C** and **NiRe/C** demonstrate good stability over 90 h of CO_2 methanation, maintaining well both X_{CO2} and S_{CH4} during TOS. The notable exception was **NiMo/C**, which exhibits a gradual degradation of the catalytic properties, with a decrease in X_{CO2} of 25% and in S_{CH4} of 13% over 90 h of TOS testing.

Characterization of the catalysts before methanation

The catalytic properties discussed above provide strong support for our hypothesis that advanced carbon-supported Ni-based electrocatalysts can be successfully employed as catalysts for gas-phase CO_2 methanation. To correlate the observed catalytic trends with the properties of the materials, we performed a comprehensive characterization of the as-received **Ni/C**, **NiMo/C**, and **NiRe/C** catalysts.

Figure S1 depicts N_2 physisorption isotherms for the catalysts, while Figure S2 shows their resultant pore-size distributions. All the samples exhibit similar textural properties, presenting Type II isotherms with comparable pore-size distributions. The specific surface area, S_{BET}, of the mesoporous catalysts was estimated to be $350 \pm 20\ m^2 g^{-1}$, while the average mesopore size, d_{pore}, was found to be 5.5 nm in the case of **Ni/C** and **NiMo/C**, and 6.5 nm in the case of **NiRe/C** (Table 1). For further investigation, we performed H_2 pulse chemisorption measurements over the catalysts. The H_2 uptake of the materials, and, consequently, their catalytically active surface area, correlates well with their catalytic performance in CO_2 methanation. Specifically, H_2 uptake data are consistent with the CO_2 methanation performance of the catalysts (Table 1, Figure 1), where they also show the same trend: **Ni/C** > **NiRe/C** > **NiMo/C**. Importantly, monometallic **Ni/C** catalyst shows markedly higher H_2 uptake per gram of material than do the bimetallic counterparts, consistent with its best performance in CO_2 hydrogenation (Figure 1).

The powder X-ray diffraction (XRD) patterns for all the catalysts are shown in Figure 2. The graphitic carbon peak from the carbon supporting material is present at 28° in all the samples. The other Bragg peaks are broadened, which is typical for nanocrystalline samples. The pattern of monometallic **Ni/C** catalyst is indexed to metallic Ni (ICDD #04-016-4761) with an admixture of NiO (ICDD #04-004-8992) secondary phase.

In the case of **NiMo/C** and **NiRe/C**, there are peaks corresponding to Ni and NiO, however, the presence of Mo- and Re-containing phases is not conclusive from the XRD data, most likely due to overlapping of some characteristic Bragg peaks.

X-ray photoelectron spectroscopy (XPS) analysis demonstrated that for all the as-received catalysts, two different phases are observed from the deconvolution of the XPS data of Ni $2p_{3/2}$ (Figure 3). The lower energy component (852.7 eV) is assigned to Ni^0 in metallic Ni species, while the components at 853.9 ± 0.2 eV and 855.8 ± 0.2 eV are consistent with Ni^{2+} in nickel oxide phase, and the ones at 861.1 ± 0.3 eV and 863.6 ± 0.4 eV are satellite peaks from Ni^{2+}.[30] The presence of multiple components in the 851–858 eV BE range is typical for nanoscale oxidation layers on Ni and Ni compounds[9,30,31] with the combination of three main components at ca. 852.7, 853.9, and 855.8 eV in Figure 3a–c, being most consistent with a thin, predominantly Ni^{2+}, nickel oxide layer on metallic Ni. Furthermore, analyzing the O 1s spectra of the samples (Figure S3), one can observe that there are two peaks at 529.9 ± 0.3 eV and 531.2 ± 0.2 eV that correspond to oxygen in metal oxides, presumably in nickel oxide. From Table S1, it is possible to observe that the atomic % of Ni^{2+} is similar to that of the O from metal oxide components of O 1s (the slightly higher value of O at% is due to the non-uniform morphology and a contribution of O in the organic phase to the peak at 531.2 ± 0.2 eV).[32]

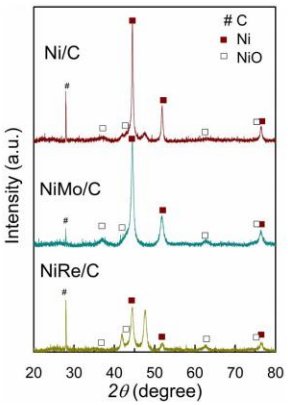

Figure 2. XRD patterns of the **Ni/C**, **NiMo/C**, and **NiRe/C** catalysts, showing the presence of the peaks corresponding to Carbon, Ni and NiO in all catalysts.

For **NiMo/C**, the Mo 3d spectra (Figure 3d) show two distinct components: Mo(IV) oxide (Mo^{4+}) composed by a doublet at 229.3 ± 0.4 eV and 232.4 ± 0.4 eV and Mo(VI) oxide (Mo^{6+}) at 232.4 ± 0.0 eV and 235.5 ± 0.0 eV.[33]

For **NiRe/C**, the Re 4f spectra (Figure 3e) show Re^{4+} with a doublet at 42.3 eV and 44.7 eV and Re^{7+} at 45.5 eV and 47.9 eV.[34,35]

We further conducted microstructural investigation of the as-received catalysts by means of transmission electron microscopy (TEM). The average nanoparticle diameter (d_{NP}) was determined by the analysis of several TEM images (Figures S6, S7) and the estimated values are presented in Table 1, while the corresponding particle-size distributions are shown in Figure S8. The metallic NPs appear to be well dispersed on largely amorphous carbon supporting materials. The monometallic **Ni/C** catalyst exhibits the smallest $d_{NP} \approx 10$ nm, with a narrow size distribution; both bimetallic **NiMo/C** and **NiRe/C** catalysts have larger $d_{NP} \approx 14$ nm. Figure 4 shows high-resolution TEM (HRTEM) images of representative nanoparticles in each catalyst.

© 2021 Wiley-VCH GmbH

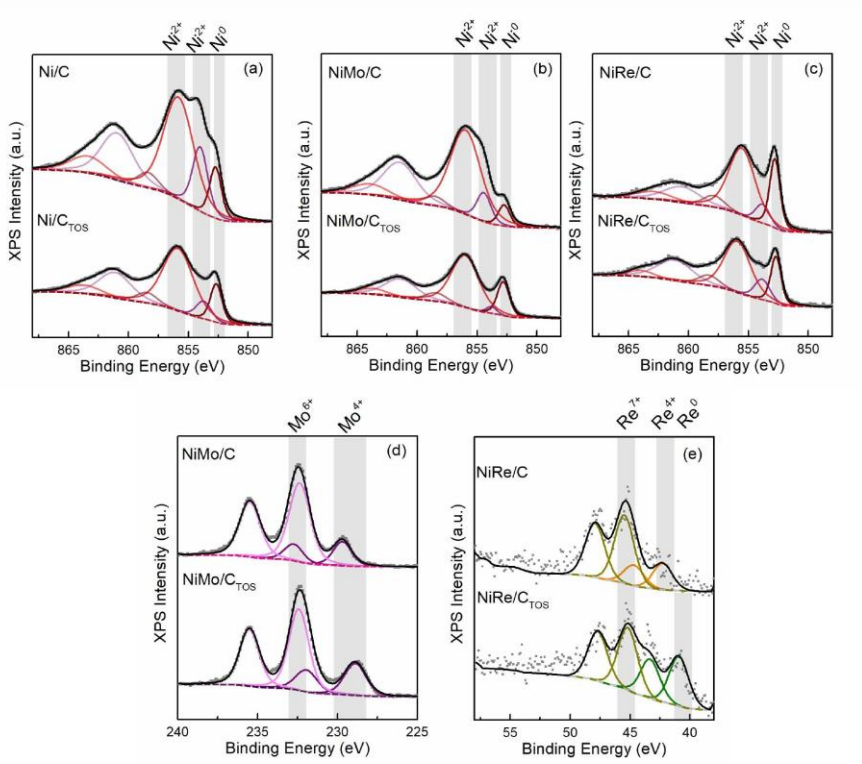

Figure 3. High-resolution XPS data for the Ni $2p_{3/2}$ region collected from as-received and TOS-tested **Ni/C** (a), **NiMo/C** (b), and **NiRe/C** (c) catalysts, together with Mo 3d region collected from **NiMo/C** (d) and Re 4f region collected from **NiRe/C** (e). Symbols: raw data; black lines: overall fits; colored lines: fits of individual components; dashed lines: background.

In the bimetallic **NiMo/C** and **NiRe/C**, one can clearly observe a layer around the nanoparticles (Figures 4c–f, S7b,c). In **NiRe/C**, this shell resembles graphitic carbon,[36,37] while in **NiMo/C** the shell is composed of epitaxially grown MoO_2 (Figure 4d) and ultrasmall Mo NPs at the surface of Ni NPs (Figure 4c). In contrast, no shell was observed in the monometallic **Ni/C** catalyst (Figures 4a, b, S7a).

To elucidate the chemical composition, we carried out high-angle annular dark-field imaging in scanning TEM mode (HAADF-STEM) showing *Z*-contrast of the catalysts, together with the corresponding energy-dispersive X-ray spectroscopy maps in STEM mode (STEM-EDX), which highlight the distribution of the key constituent elements. The representative Figures 5, S9a, S10a, and S11a show HAADF-STEM and STEM-EDX data collected from **Ni/C**, **NiMo/C**, and **NiRe/C**. In the case of monometallic **Ni/C**, it is clear that the NPs are composed of Ni well-supported on carbon (Figure 5a, S9a). The EDX maps of the bimetallic **NiMo/C** catalysts demonstrate a high concentration of both metals in the areas where NPs are present, and that the metals are homogeneously distributed across the catalysts (Figures 5b, S10a), while in the case of **NiRe/C**, the EDX signal of Re is quite weak (Figures 5c, S11a), indicating that a low amount of this element is present.

Characterization of the catalysts after TOS testing

To further understand the impact of the methanation reaction on the evolution of the structural properties of the catalysts, as well as to find out the reasons for different stability of the catalysts, we characterized all three materials after prolonged TOS testing (Figures 1c, d) by means of XRD, XPS, and TEM.

In the XRD patterns of the TOS-tested catalysts (Figure S5), the Bragg peaks corresponding to the NiO admixture are

© 2021 Wiley-VCH GmbH

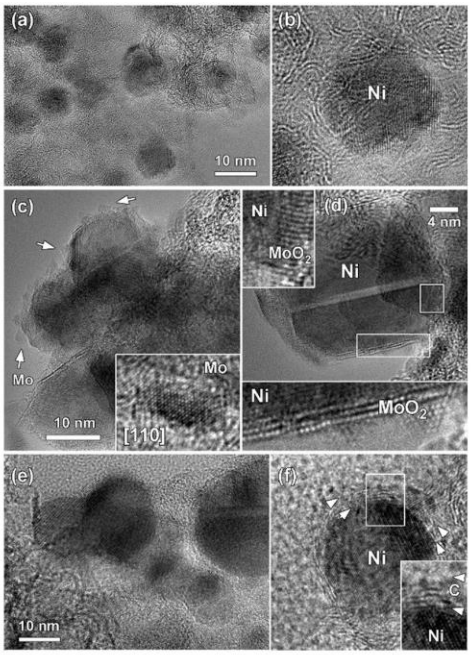

Figure 4. HRTEM images of the NPs in **Ni/C** (a, b), **NiMo/C** (c, d), and **NiRe/C** (e, f), evidencing no shell being present over Ni NPs (b) in **Ni/C**, an epitaxially grown MoO_2 shell with few atomic layers (d), as well as ultrasmall Mo NPs (c) over Ni NPs in **NiMo/C**; and a carbon shell around Ni NPs (f) in **NiRe/C**.

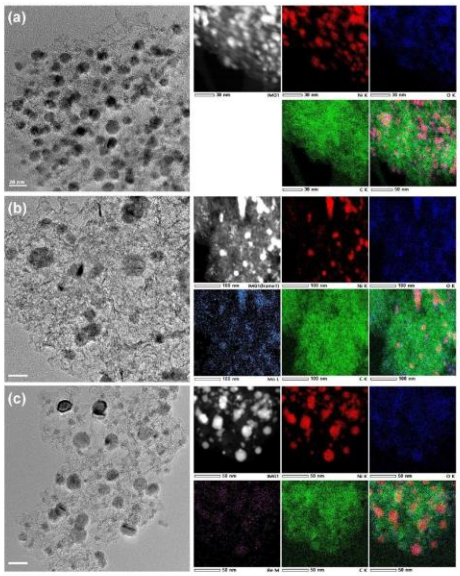

Figure 5. Low-magnification bright-field TEM images, low-magnification HAADF-STEM images and simultaneously acquired STEM-EDX elemental mappings for **Ni/C** (a), **NiMo/C** (b), and **NiRe/C** (c) catalysts.

absent, indicating that much of the NiO was reduced to metallic Ni under reductive reaction conditions of the methanation (H_2 atmosphere at high temperature).

In the Ni $2p_{3/2}$ spectral region of the TOS-tested catalysts (Figure 3), the binding energy of each component remains similar for all the materials; however, there was a change in the relative atomic percentage of each component (Table 2), consistent with reduction, which is further supported by the respective O 1s spectra (Figure S3), wherein the nickel-oxide O 1s components contribution is smaller than that of the organic components. In the case of **NiRe/C**, however, there is no increase in relative intensity of Ni^0, with concomitant qualitative and quantitative indications in the Re 4f region that Re oxides were reduced, suggesting an interplay of reduction chemistry between Ni and Re. In contrast, in **NiMo/C**, the presence of Mo does not dramatically affect the reduction of Ni, while Mo oxidation states undergo only minimal changes. The latter observation, in particular, indicates minimal (if any) formation of intermediate oxidation states of Mo, which can be readily observed by XPS in nanostructured Mo-based catalysts.[38] In C 1s region, presented in Figure S4, we do not observe any significant modification after TOS testing.[39,40]

With the aim of exploring the microstructural changes in the catalysts after TOS testing, we analyzed the spent catalysts by electron microscopy. Because of the sintering at high

Table 2. XPS relative atomic percentage (at%) of Ni^0 and Ni^{2+} from Ni $2p_{3/2}$ spectra, Mo^0, Mo^{4+} and Mo^{6+} from Mo 3d spectra and Re^0, Re^{4+} and Re^{7+} from Re 4f spectra in **Ni/C**, **NiMo/C** and **NiRe/C** catalysts and after their TOS testing.

	Ni^0 [relative at %]	Ni^{2+} [relative at %]	Mo^{4+} [relative at %]	Mo^{6+} [relative at %]	Re^0 [relative at %]	Re^{4+} [relative at %]	Re^{7+} [relative at %]
Ni/C	8.67	87.00	–	–	–	–	–
Ni/C$_{TOS}$	11.49	83.22	–	–	–	–	–
NiMo/C	4.86	91.35	21.43	78.57	–	–	–
NiMo/C$_{TOS}$	14.57	79.35	29.90	69.07	–	–	–
NiRe/C	18.78	75.13	–	–	0	25.00	75.00
NiRe/C$_{TOS}$	15.41	78.08	–	–	50.00	0	50.00

© 2021 Wiley-VCH GmbH

temperatures (400–450 °C) during methanation reaction, we observe a slight increase in the average particle size of the catalysts (Figures S6a–c, S7a–c compared to Figures S6d–f, S7d–f), which were estimated to be 14 ± 12 nm, 15 ± 10 nm and 16 ± 10 nm for **Ni/C$_{TOS}$**, **NiMo/C$_{TOS}$**, and **NiRe/C$_{TOS}$**, respectively. Notably, the particle-size distributions become significantly broader compared to those for the as-received catalysts (Figure S8). Furthermore, EDX mapping demonstrates that there was some segregation of Mo in **NiMo/C$_{TOS}$** (Figure S10c) and Re in **NiRe/C$_{TOS}$** (Figure S11c) during TOS testing.

Discussion

We show through experiments and detailed characterization that commercially available advanced hydrogen oxidation/evolution electrocatalysts can have another practical application as catalysts for gas-phase CO_2 methanation. Monometallic **Ni/C** catalyst as well as two bimetallic **NiRe/C** and **NiMo/C** catalysts have been investigated, the latter testing for synergistic promotion of CO_2 methanation.[2]

When interpreting the results of our structural and chemical characterization of the catalysts, it is important to keep in mind the implications of the experimental protocols and sample handling. Specifically, both as-received and TOS-tested catalysts help to elucidate the properties of the same during the catalytic testing, but both show some effects of oxidation that is not present during the catalytic testing. As-received catalysts have been passivated under O_2/He atmosphere, the treatment that stabilizes them for storage and transport, but is likely to oxidize the surfaces of transition-metal nanoparticles. Immediately before the catalytic testing, the as-received catalysts undergo an *in situ* reduction pre-treatment in the reactor. The resulting primarily metallic nanoparticles are presumptively considered when interpreting their catalytic activity. Finally, the TOS-tested catalysts are characterized after exposure to ambient air, which is likely to oxidize the surfaces of transition-metal nanoparticles. Accordingly, the structural and chemical *transformations* (particularly those away from metal oxides) between the as-received and TOS-tested catalysts are considered when elucidating the effects of the catalytic testing. In contrast, the quantification of the surface oxide phases is primarily performed to check for consistency with the presumptive effects of, respectively, the passivation treatment and exposure to air.

Our structural characterization results show that the as-received catalysts consist mainly of metallic NPs with oxidized surfaces, which is expected due to the synthetic surface passivation by oxygen during the final step of the materials preparation. These surface oxide phases were found to be effectively reduced to the respective metals during CO_2 methanation, as highlighted by our XPS and HAADF-STEM characterization results for the TOS-tested catalysts. A rigorous quantification of the thickness of an overlayer from XPS data requires a sufficiently flat surface with a well-defined layer structure;[41] overlayers of a more complex composition also can be quantified, albeit with increased uncertainty, based on systematic measurements.[31,42–44] For metal nanoparticles in the size range summarized in Table 1, the thickness of an oxide layer can be estimated from XPS data only semi-quantitatively, due to the variability of the particle shapes and sizes as well as unknown uniformity of the oxide layer. Based on an interpolation from the data for crystal surfaces with a similar surface composition,[31] the peak intensity ratios in Figure 3a suggest an oxide layer thickness of ca. 3–4 nm for Ni particles in Ni/C. The Ni/C spectrum in Figure 3a is also in qualitative agreement with the reference Ni 2p spectra for a ca. 3.3 nm NiO layer on a polished Ni surface.[30] The limited extent of oxidation of Ni nanoparticles in Ni/C is consistent, for example, with a similar presence of Ni metal signal in nanoparticles measured by XPS after multiple days of storage and transport in ambient air;[45] in that case, the presence of oxygen co-located with Ni was also clear in HAADF-STEM images, but no strong NiO features were present in XRD data.

The formation of an alloy between Ni and Mo in **NiMo/C** and between Ni and Re in **NiRe/C** was ruled out since no peaks for these alloys were found in XRD patterns of the samples, nor was alloy formation detected by TEM analysis. In fact, in **NiMo/C**, TEM revealed the presence of Ni NPs covered by ultrasmall Mo NPs and, in some cases, an epitaxially grown MoO_2 shell. Our TEM results also show that the metallic NPs in all three catalysts exhibit small particle sizes with similar size distributions, while being uniformly dispersed on amorphous carbon supporting material.

The three catalysts demonstrated a clear performance trend: **Ni/C** > **NiRe/C** > **NiMo/C**, wherein best-performing monometallic **Ni/C** achieved a high maximum X_{CO2} = 83 % with S_{CH4} = 99.7 % at 400 °C, having T_{50} = 330 °C. This performance compares favorably with our recent work,[2] where a catalyst composed of 15 % Ni supported on reduced activated carbon achieved X_{CO2} = 76 % with S_{CH4} = 97 % at 450 °C, having T_{50} ≈ 385 °C. The observed catalytic properties of **Ni/C** are also comparable to those reported for Ni supported on N-doped CNT catalyst, which exhibited high activity and selectivity, namely X_{CO2} = 80 % with S_{CH4} = 99 % at 360 °C.[3]

The high performance of **Ni/C** compares favorably to that reported for the catalyst most used in the industry (Ni/Al_2O_3), taking into account both the Ni loading and reaction temperature. For example, in a study of the effect of Ni loading in Ni/γ-Al_2O_3 catalysts, Zhang et al.[12] obtained a maximum X_{CO2} ≈ 65 % with S_{CH4} ≈ 100 % at 350 °C with 50 % Ni/γ-Al_2O_3 (i.e., Ni loading similar to that of **Ni/C**); they used conditions similar to those used in our study but at lower weight hourly space velocity (*WHSV*). When Liu et al.[46] tested a 20 % Ni/Al_2O_3 catalyst, at conditions similar to those used in our study (except higher *WHSV* = 90 000 cm^3 g^{-1} h^{-1}), they achieved a maximum X_{CO2} = 73 % with S_{CH4} = 97 % at 420 °C, i.e., a lower conversion, when compared to the results for our **Ni/C**; addition of vanadium oxide enhanced the performance of the catalyst. At the same 400 °C temperature that **Ni/C** performed best in our study (although at slightly higher *WHSV* = 120 000 cm^3 g^{-1} h^{-1}), Ma et al.[47] tested a 20 % Ni/Al_2O_3 catalyst and obtained a maximum X_{CO2} ≈ 70 % with S_{CH4} ≈ 95 %; the performance was slightly improved when CeO_2 was used as support. Zhao et al.[48] tested a 15 % Ni/Al_2O_3 catalyst (at lower *WHSV* = 48 000 cm^3 g^{-1} h^{-1})

© 2021 Wiley-VCH GmbH

and to reach a maximum $X_{CO2} \approx 80\%$ with $S_{CH4} > 95\%$, i.e., to reach performance similar to that of our **Ni/C** catalyst, they had to use a temperature of 450 °C; addition of Mn enhanced the performance of the catalyst.

On other Ni-based catalysts supported on commonly used metal oxides, e.g., a Ni/CeO_2 catalyst[49] tested under conditions similar to those in our study reached $X_{CO2} = 81\%$ with $S_{CH4} = 100\%$ at 350 °C, i.e., a similar conversion but at a lower temperature than did our **Ni/C** catalyst. Furthermore, 5% Ni/ZrO_2 catalyst[50] reached $X_{CO2} = 79.1\%$ with $S_{CH4} = 96.7\%$ at 350 °C, a slightly lower conversion but also at a lower temperature.

We note that the Engineered Catalyst Support™ conductive carbon employed in the current study has 2.2% of nitrogen from the surface functional groups (Table S1), which is essential for achieving the good performance of the catalyst, since N groups improve the dispersion of Ni NPs over the support by providing binding sites that facilitate the Ni stabilization, as well as improve the CO_2 adsorption capacity of the sample.[2–4,39]

Importantly, the monometallic **Ni/C** material demonstrated excellent stability over 90 h of TOS testing at 400 °C with no noticeable losses in X_{CO2} or S_{CH4}, a promising result because this temperature is in the range applied in existing Power-to-Gas technologies.[51] In terms of stability, the main effect of TOS testing for 90 h at 400 °C was a slight increase in average NP diameter (Figure S8), indicating moderate sintering of Ni NPs under reaction conditions.

Unfortunately, regarding the bimetallic catalysts, we found that the addition of Mo and Re into Ni catalyst is not beneficial for CO_2 methanation, despite promising indications from previous literature reports that motivated our selection of these two metals.[27–29]

Although our **NiMo/C** catalyst demonstrates higher X_{CO2} values at low temperatures, the maximum X_{CO2} of bimetallic **NiMo/C** was lower than that of the monometallic **Ni/C** counterpart. For Mo, a major difference between our **NiMo/C** material and those described in the literature was the local chemical environment, with apparent segregation of Mo and no evidence of alloying in **NiMo/C**, as discussed earlier. In a contrasting literature example, Huo et al.[52] prepared β-Mo_2C and Ni/β-Mo_2C catalysts and investigated them in methanation of carbon monoxide. The β-Mo_2C catalyst exhibited high CO conversion but low CH_4 selectivity while Ni/β-Mo_2C presented excellent CO conversion, CH_4 selectivity and stability, which was attributed to the formation of Ni_3Mo_3N in Ni–Mo carbide. In another Mo carbide example, Wang et al.[53] studied Mo_2C/ZrO_2 for sulfur-resistant CO methanation, presenting good conversion, selectivity and stability, with good sulfur-resistance. No evidence of similar Mo chemistry was detected in **NiMo/C** by XPS, which is very sensitive to the chemical environment of Mo.[38] Furthermore, **NiMo/C** showed poor stability, losing 25% of X_{CO2} and 13% of S_{CH4} over 90 h. One could attribute this poor stability trend to the segregation of Mo phase in some areas of the catalyst under reaction conditions (Figure S10c).

NiRe/C exhibited lower X_{CO2} than did **Ni/C** over the full range of tested temperatures. A theoretical study of the effect of Re on the C–O bond scission and on the selectivity of CO_2 methanation on a Ni-based catalyst by Yuan et al.[28] concluded that the strong oxygen affinity of Re was the main reason for the enhanced CH_4 selectivity. Accordingly, the lack of enhancement in **NiRe/C** is difficult to rationalize, as XPS clearly indicates that not only Re chemistry was transformed during the reaction, but its presence also affected the transformation of Ni (Table 2, Figure 3c,e). In contrast to **NiMo/C**, the **NiRe/C** catalyst was stable over 90 h of TOS; albeit sintering of Re into large particles was also observed in some parts of the catalyst (Figure S11c). The stability of **NiRe/C** is aligned with findings of Dong et al.[29] on using Re as promoter for a Ni-based catalyst supported on coal-combustion fly ash, which concluded that Re promotion leads to the enhancement of the anti-sintering and anti-coking properties of the catalyst.

To summarize, while we have yet to rationalize the observed lower maximum conversion of the bimetallic catalysts, we consider the following two factors as likely to be important: (*i*) there is lack of the formation of the respective alloys in bimetallic catalysts that hinders synergetic effects; and (*ii*) both bimetallic catalysts exhibit a shell around the Ni NPs (Figure 4), which covers the active Ni phase of the catalyst and thus prevents the effective H_2 chemisorption during CO_2 methanation reaction, as evidenced by the H_2 uptake results (Table 1). The decreasing of the optimal operation temperature of the CO_2 methanation over cost-effective carbon-supported Ni catalysts to values below 400 °C is a challenge of interest to our work that we will address in the future via synergetic bimetallic catalyst approach, while using metals other than Mo and Re.

Conclusion

In recent years, the growing availability of renewable energy at competitive prices has boosted the field of electrocatalysis, aiming at the effective use of this energy to combat CO_2 emission via establishing new effective electrochemical routes to the production of chemicals. Accordingly, the library of well designed, engineered, and produced electrocatalysts keeps constantly expanding. Our work clarifies that some of these advanced materials could be strategically valuable for other areas of the catalysis, as demonstrated herein by the example of the classical Sabatier CO_2 methanation reaction. More specifically, we reveal that commercially available carbon-supported Ni-based hydrogen oxidation/evolution electrocatalysts can be successfully employed in gas-phase CO_2 hydrogenation to CH_4. Monometallic **Ni/C** catalyst achieves excellent performance in this reaction at 400 °C, showing $X_{CO2} = 83\%$ with $S_{CH4} = 99.7\%$. Furthermore, the catalyst exhibits outstanding stability over 90 h TOS testing, with no sign of deactivation. This remarkable performance of **Ni/C** is essentially governed by good dispersion of Ni NPs over advanced carbon supporting material, high H_2 uptake of Ni NPs, as well as the presence of N-containing groups in the supporting carbon that stabilizes Ni NPs and improves the CO_2 adsorption capacity. The introduction of Mo and Re into **Ni/C** does not improve the catalytic properties of the respective bimetallic **NiMo/C** and **NiRe/C** materials, leading to a decrease in overall activity and

© 2021 Wiley-VCH GmbH

selectivity. Moreover, **NiMo/C** exhibits poor stability over 90 h of TOS testing, while the addition of Re has little impact on the stability behavior. Nevertheless, this work offers a new opportunity to amplify the scope of applications of these novel electrocatalytic materials through heterogeneous gas-phase catalysis.

Experimental Section

Commercially available monometallic **Ni/C** and bimetallic **NiMo/C** and **NiRe/C** electrocatalysts supported on ECS-4601 carbon material (Engineered Catalyst Support™, Pajarito Powder, LLC) were synthesized by thermal reduction of metal precursors: nickel nitrate, ammonium molybdate and ammonium perrhenate. Calculated amount of ECS-4601 carbon support was added to the respective metal solution, in the amount to obtain 50% of Ni loading in the final **Ni/C** catalyst, 50% of NiMo with 85:15 at% ratio in the **NiMo/C** catalyst, as well as 50% of NiRe with 87:13 at% ratio in the **NiRe/C** catalyst. After 1 h of stirring, pH of solution was adjusted to 13 using 5 M NaOH, followed by the precipitation of metal compounds. The precipitate was washed with DI water until pH ≈6.5. Washed precipitate was then dried at 85 °C for 12 h. The dry mixture was ground with mortar and pestle, and the resultant fine powder was reduced at 450 °C for 1 h under 100 $cm^3 min^{-1}$ flow of 7 %H_2/N_2 gas mixture. Finally, the catalyst was passivated in a flow of 0.1 % O_2/He at room temperature for 8 h.

The catalysts were characterized by N_2 physisorption at −196 °C, H_2 pulse chemisorption, powder X-ray diffraction (XRD), X-ray photoelectron spectroscopy (XPS), transmission electron microscopy (TEM), high-angle annular dark-field scanning TEM (HAADF-STEM), and energy-dispersive X-ray spectroscopy in STEM mode (STEM-EDX). Their catalytic properties in gas-phase CO_2 methanation were evaluated in a Microactivity XS15 system (PID Eng & Tech), using a fixed bed quartz reactor. After an *in situ* reduction pre-treatment on the catalyst, the reactor was fed with the stoichiometric gas mixture of 10 % CO_2 and 40 % H_2, balanced by 50 % He, with a total flowrate of 100 $cm^3 min^{-1}$ ($WHSV$ = 60 000 $cm^3 g^{-1} h^{-1}$) at the pressure of 1 bar. A temperature ramping from 200 °C to 500 °C was performed under reaction conditions to evaluate the performance of each sample as a function of the temperature and long-term time-on-stream (TOS) testing was performed under the same conditions referred before, however, under isothermal conditions at the established temperature of optimal catalytic performance of the respective catalyst. The reaction products were analyzed online by gas chromatography. More details about materials and methods are given in Supporting Information.

Acknowledgements

L.P.L.G. thanks the Portuguese Foundation for Science and Technology (FCT) for the PhD grant support (SFRH/BD/128986/2017). This work was partially supported by the Associate Laboratory LSRE-LCM (UIDB/50020/2020) funded by national funds through FCT/MCTES (PIDDAC). O.S.G.P.S. acknowledges FCT funding under the Scientific Employment Stimulus – Institutional Call CEECINST/00049/2018. Yu.V.K. thanks the FCT for support under the CritMag Project (PTDC/NAN-MAT/28745/2017). Pajarito gratefully acknowledges financial support from US DOE DE-FE0031878. A.S. gratefully acknowledges financial support from Oak Ridge National Laboratory SEED 10609 project "Single-Atom Catalysts for CO_2 Conversion". AS gratefully acknowledgment catalysts samples provided by Pajarito Powder, LLC.

Conflict of Interest

The authors declare no conflict of interest.

Keywords: catalyst stability · heterogeneous catalysis · microstructure · nanocatalysts · nickel

[1] Z. Zhao, X. Peng, X. Liu, X. Sun, J. Shi, L. Han, G. Li, J. Luo, *J. Mater. Chem. A* **2017**, *5*, 20239–20243.
[2] L. P. L. Gonçalves, J. P. S. Sousa, O. S. G. P. Soares, O. Bondarchuk, O. I. Lebedev, Y. V. Kolen'ko, M. F. R. Pereira, *Catal. Sci. Technol.* **2020**, *10*, 7217.
[3] W. Wang, C. Duong-Viet, H. Ba, W. Baaziz, G. Tuci, S. Caporali, L. Nguyen-Dinh, O. Ersen, G. Giambastiani, C. Pham-Huu, *ACS Appl. Energ. Mater.* **2019**, *2*, 1111–1120.
[4] F. Hu, S. Tong, K. Lu, C. Chen, F. Su, J. Zhou, Z. Lu, X. Wang, G. Feng, R. Zhang, *J. CO2 Util.* **2019**, *34*, 676–687.
[5] Y. Zheng, Y. Wang, Y. Yuan, H. Huang, *ChemNanoMat* **2021**, *7*, 502–514.
[6] A. Wieckowski, M. Neurock, *Adv. Phys. Chem.* **2011**, *2011*, 1–18.
[7] J. D. Costa, J. L. Lado, E. Carbó-Argibay, E. Paz, J. Gallo, M. F. Cerqueira, C. Rodríguez-Abreu, K. Kovnir, Y. V. Kolen'Ko, *J. Phys. Chem. C* **2016**, *120*, 16537–16544.
[8] J. Xu, X. Wei, J. D. Costa, J. L. Lado, B. Owens-Baird, L. P. L. Gonçalves, S. P. S. Fernandes, M. Heggen, D. Y. Petrovykh, R. E. Dunin-Borkowski, K. Kovnir, Y. V. Kolen'ko, *ACS Catal.* **2017**, *7*, 5450–5455.
[9] B. Owens-Baird, J. Xu, D. Y. Petrovykh, O. Bondarchuk, Y. Ziouani, N. González-Ballesteros, P. Yox, F. M. Sapountzi, H. Niemantsverdriet, Y. V. Kolen'ko, K. Kovnir, *Chem. Mater.* **2019**, *31*, 3407–3418.
[10] F. M. Sapountzi, E. D. Orlova, J. P. S. Sousa, L. M. Salonen, O. I. Lebedev, G. Zafeiropoulos, M. N. Tsampas, H. J. W. Niemantsverdriet, Y. V. Kolen'-ko, *Energy Fuels* **2020**, *34*, 6423–6429.
[11] G. M. Shashidhara, M. Ravindram, *React. Kinet. Catal. Lett.* **1988**, *37*, 451–456.
[12] Z. Zhang, Y. Tian, L. Zhang, S. Hu, J. Xiang, *Int. J. Hydrogen Energy* **2019**, *44*, 9291–9306.
[13] C. Vogt, E. Groeneveld, G. Kamsma, M. Nachtegaal, L. Lu, C. J. Kiely, P. H. Berben, F. Meirer, B. M. Weckhuysen, *Nat. Catal.* **2017**, *1*, 127–134.
[14] E. Marconi, S. Tuti, I. Luisetto, *Catalysts* **2019**, *9*, 1–13.
[15] J. Li, Y. Lin, X. Pan, D. Miao, D. Ding, Y. Cui, J. Dong, X. Bao, *ACS Catal.* **2019**, *9*, 6342–6348.
[16] A. Westermann, B. Azambre, M. C. Bacariza, I. Graça, M. F. Ribeiro, J. M. Lopes, C. Henriques, *Appl. Catal. B* **2015**, *174–175*, 120–125.
[17] W. Zhen, B. Li, G. Lu, J. Ma, *Chem. Commun.* **2015**, *51*, 1728–1731.
[18] C. Swalus, M. Jacquemin, C. Poleunis, P. Bertrand, P. Ruiz, *Appl. Catal. B* **2012**, *125*, 41–50.
[19] M. C. Le, K. Le Van, T. H. T. Nguyen, N. H. Nguyen, *J. Chem,* **2017**, *2017*, 4361056.
[20] L. M. Cam, N. T. T. Ha, L. Van Khu, N. N. Ha, T. C. Brown, *Aust. J. Chem.* **2019**, *72*, 969–977.
[21] T. J. Bandosz, in *Carbon Materials for Catalysis* (eds. P. Serp, J. L. Figueiredo), Wiley, **2009**, pp. 45-82..
[22] W. Zheng, Y. Wang, L. Shuai, X. Wang, F. He, C. Lei, Z. Li, B. Yang, L. Lei, C. Yuan, M. Qiu, Y. Hou, X. Feng, *Adv. Funct. Mater.* **2021**, *31*, 2008146.
[23] F. Li, S. Hong, T.-S. Wu, X. Li, J. Masa, Y.-L. Soo, Z. Sun, *ACS Appl. Energ. Mater.* **2019**, *2*, 8836–8842.
[24] M. Gong, W. Zhou, M.-C. Tsai, J. Zhou, M. Guan, M.-C. Lin, B. Zhang, Y. Hu, D.-Y. Wang, J. Yang, S. J. Pennycook, B.-J. Hwang, H. Dai, *Nat. Commun.* **2014**, *5*, 4695.
[25] V. V. Kuznetsov, Y. D. Gamburg, R. S. Batalov, V. V. Zhulikov, V. A. Zaitsev, *Russ. J. Electrochem.* **2018**, *54*, 598–603.
[26] S. Kabir, K. Lemire, K. Artyushkova, A. Roy, M. Odgaard, D. Schlueter, A. Oshchepkov, A. Bonnefont, E. Savinova, D. C. Sabarirajan, P. Mandal, E. J. Crumlin, I. V. Zenyuk, P. Atanassov, A. Serov, *J. Mater. Chem. A* **2017**, *5*, 24433–24443.
[27] I. Kuznecova, J. Gusca, *Energy Procedia* **2017**, *128*, 255–260.
[28] H. Yuan, X. Zhu, J. Han, H. Wang, Q. Ge, *J. CO_2 Util.* **2018**, *26*, 8–18.

© 2021 Wiley-VCH GmbH

[29] X. Dong, B. Jin, S. Cao, F. Meng, T. Chen, Q. Ding, C. Tong, *Waste Manage.* **2020**, *107*, 244–251.
[30] M. C. Biesinger, B. P. Payne, L. W. M. Lau, A. Gerson, R. S. C. Smart, *Surf. Interface Anal.* **2009**, *41*, 324–332.
[31] B. Owens-Baird, J. P. S. Sousa, Y. Ziouani, D. Y. Petrovykh, N. A. Zarkevich, D. D. Johnson, Y. V. Kolen'ko, K. Kovnir, *Chem. Sci.* **2020**, *11*, 5007–5016.
[32] B. P. Payne, M. C. Biesinger, N. S. McIntyre, *J. Electron Spectrosc. Relat. Phenom.* **2012**, *185*, 159–166.
[33] X. Li, J. D. Henderson, F. P. Filice, D. Zagidulin, M. C. Biesinger, F. Sun, B. Qian, D. W. Shoesmith, J. J. Noël, K. Ogle, *Corros. Sci.* **2020**, *176*, 109015.
[34] L. Ma, L. Yan, A. H. Lu, Y. Ding, *RSC Adv.* **2018**, *8*, 8152–8163.
[35] D. Nikolova, R. Edreva-Kardjieva, H. Kolev, M. Gabrovska, *Catal. Today* **2020**, *357*, 590–601.
[36] G. E. Haslam, X. Y. Chin, G. T. Burstein, *Phys. Chem. Chem. Phys.* **2011**, *13*, 12968–12974.
[37] L. Fan, P. F. Liu, X. Yan, L. Gu, Z. Z. Yang, H. G. Yang, S. Qiu, X. Yao, *Nat. Commun.* **2016**, *7*, 1–7.
[38] X. Q. Bao, D. Y. Petrovykh, P. Alpuim, D. G. Stroppa, N. Guldris, H. Fonseca, M. Costa, J. Gaspar, C. Jin, L. Liu, *Nano Energy* **2015**, *16*, 130–142.
[39] J. L. Figueiredo, M. F. R. Pereira, *Catal. Today* **2010**, *150*, 2–7.
[40] L. P. L. Gonçalves, D. B. Christensen, M. Meledina, L. M. Salonen, D. Y. Petrovykh, E. Carbó-Argibay, J. P. S. Sousa, O. S. G. P. Soares, M. F. R. Pereira, S. Kegnæs, Y. V. Kolen'Ko, *Catal. Sci. Technol.* **2020**, *10*, 1991–1995.
[41] D. Y. Petrovykh, J. M. Sullivan, L. J. Whitman, *Surf. Interface Anal.* **2005**, *37*, 989–997.
[42] R. Stine, E. H. Aifer, L. J. Whitman, D. Y. Petrovykh, *Appl. Surf. Sci.* **2009**, *255*, 7121–7125.
[43] K. P. Fears, D. Y. Petrovykh, T. D. Clark, *Biointerphases*, **2013**, *8*, 20. .
[44] K. P. Fears, T. D. Clark, D. Y. Petrovykh, *J. Am. Chem. Soc.* **2013**, *135*, 15040–15052.
[45] M. Salimian, M. Ivanov, F. L. Deepak, D. Y. Petrovykh, I. Bdikin, M. Ferro, A. Kholkin, E. Titus, G. Goncalves, *J. Mater. Chem. C* **2015**, *3*, 11516–11523.
[46] Q. Liu, F. Gu, X. Lu, Y. Liu, H. Li, Z. Zhong, G. Xu, F. Su, *Appl. Catal. A* **2014**, *488*, 37–47.
[47] Y. Ma, J. Liu, M. Chu, J. Yue, Y. Cui, G. Xu, *Catal. Lett.* **2020**, *150*, 1418–1426.
[48] K. Zhao, Z. Li, L. Bian, *Front. Chem.* **2016**, *10*, 273–280.
[49] P. Hongmanorom, J. Ashok, P. Chirawatkul, S. Kawi, *Appl. Catal. B* **2021**, *297*, 120454.
[50] X. Jia, X. Zhang, N. Rui, X. Hu, C. Liu, *Appl. Catal. B* **2019**, *244*, 159–169.
[51] M. Götz, J. Lefebvre, F. Mörs, A. McDaniel Koch, F. Graf, S. Bajohr, R. Reimert, T. Kolb, *Renewable Energy* **2016**, *85*, 1371–1390.
[52] X. Huo, Z. Wang, J. Huang, R. Zhang, Y. Fang, *RSC Adv.* **2016**, *6*, 24353–24360.
[53] B. Wang, C. Wang, W. Yu, Z. Li, Y. Xu, X. Ma, *J. Mol. Catal.* **2020**, *482*, 110668.

Manuscript received: August 30, 2021
Revised manuscript received: September 13, 2021
Accepted manuscript online: September 16, 2021
Version of record online: October 8, 2021

© 2021 Wiley-VCH GmbH

Applied Catalysis B: Environmental 312 (2022) 121376

Contents lists available at ScienceDirect

Applied Catalysis B: Environmental

journal homepage: www.elsevier.com/locate/apcatb

In situ investigation of the CO_2 methanation on carbon/ceria-supported Ni catalysts using modulation-excitation DRIFTS

Liliana P.L. Gonçalves [a,b,c], Jerrik Mielby [d], O. Salomé G.P. Soares [b,c], Juliana P.S. Sousa [a], Dmitri Y. Petrovykh [a], Oleg I. Lebedev [e], M. Fernando R. Pereira [b,c,*], Søren Kegnæs [d,**], Yury V. Kolen'ko [a,**]

[a] International Iberian Nanotechnology Laboratory, 4715-330 Braga, Portugal
[b] Laboratory of Separation and Reaction Engineering – Laboratory of Catalysis and Materials (LSRE-LCM), Faculty of Engineering, University of Porto, 4200-465 Porto, Portugal
[c] ALICE - Associate Laboratory in Chemical Engineering, Faculty of Engineering, University of Porto, Rua Dr. Roberto Frias, 4200-465 Porto, Portugal
[d] DTU Chemistry, Technical University of Denmark, Kemitorvet 207, 2800 Kongens Lyngby, Denmark
[e] Laboratoire CRISMAT, UMR 6508, CNRS-ENSICAEN, Caen 14050, France

ARTICLE INFO

Keywords:
Heterogeneous catalysis
Carbon dioxide
Methane
Reaction mechanism
In situ DRIFTS

ABSTRACT

The development of novel cost-efficient, high-performing catalysts for CO_2 methanation that are active at low temperatures can be optimized through the understanding of the reaction mechanism on different materials. A series of Ni-based catalysts supported on CeO_2 and carbon/CeO_2 composites was investigated, showing that Ni nanoparticles supported on a carbon/CeO_2 composite with a 50:50 wt ratio and on pure CeO_2 have excellent low-temperature activity and achieve up to 87% CO_2 conversion with full selectivity towards CH_4 at 370 °C. Importantly, meaningful insights on the reaction mechanism were gathered for the different types of materials by using the emerging ME–PSD–DRIFTS technique. The study of the rate of formation/consumption of the various intermediates showed that the CO_2 methanation reaction follows a combination of the CO and formate pathways in the case of Ni on pure CeO_2; however, in the case of Ni on the carbon/CeO_2 composite, it follows only the formate pathway.

1. Introduction

The CO_2 methanation reaction ($CO_2 + 4\,H_2 \rightarrow CH_4 + 2\,H_2O$, $\Delta H_{298\,K} = -165\ kJ\ mol^{-1}$) is the most thermodynamically favorable reaction of CO_2 hydrogenation, and is a promising way to convert anthropogenic CO_2 back to CH_4 fuel [1–4]. The hydrogenation proceeds through an eight-electron reduction process with consequent significant kinetic barriers, thus requiring the action of a catalyst. From the mechanistic perspective, extensive research has been conducted on CO_2 methanation. Nevertheless, the reaction mechanism is still vigorously debated, since it depends on the catalytic material and the hydrogenation conditions [1,3]. The most predominant mechanisms proposed in the literature can be grouped in two different categories: (i) the dissociative pathway, where CO_2 is dissociated into CO, which acts as the main intermediate, and (ii) the associative pathway, where CO_2 is molecularly adsorbed associatively with a H atom previously adsorbed on the surface, forming formate as an intermediate, i.e., without CO formation [3].

CO_2 methanation has played a significant role in understanding CO_2 hydrogenation and the associated development of catalysts. Importantly, researchers continue to exploit different catalysts to achieve high CO_2 conversion and complete selectivity towards CH_4. For example, a number of catalysts based on transition metals (Ni, Co, Fe) or platinum-group metals (Ru, Rh) dispersed on porous supporting materials have been developed [2,5–12]. Notably, Ni-based catalysts, compared to platinum-group metals, exhibit an optimal combination of activity, selectivity, and low price [2,5,6]. Despite the advances in using Ni catalysts for CO_2 methanation, a way to reduce the reaction temperature from the current $\geq$ 400 °C while preserving high catalytic performance remains a challenge.

One interesting approach to address this challenge is to develop Ni

* Corresponding author at: Laboratory of Separation and Reaction Engineering – Laboratory of Catalysis and Materials (LSRE-LCM), Faculty of Engineering, University of Porto, 4200-465 Porto, Portugal.
** Corresponding authors.
E-mail addresses: fpereira@fe.up.pt (M.F.R. Pereira), skk@kemi.dtu.dk (S. Kegnæs), yury.kolenko@inl.int (Y.V. Kolen'ko).

https://doi.org/10.1016/j.apcatb.2022.121376
Received 15 December 2021; Received in revised form 22 February 2022; Accepted 3 April 2022
Available online 5 April 2022
0926-3373/© 2022 The Authors. Published by Elsevier B.V. This is an open access article under the CC BY license (http://creativecommons.org/licenses/by/4.0/).

catalysts supported on novel materials. Traditionally, alumina (Al_2O_3) is used as supporting material for Ni methanation catalysts [13–15]. In contrast, we and other researchers have focused on carbon supporting materials [2,5,16,17]. An exciting feature of these high-surface-area porous supports are their versatile surface properties [18]. Specifically, via modification of their surface chemistry, carbon materials can exhibit increased basicity, which improves the CO_2 coverage of the catalyst, since it is an acidic molecule, thus enhancing the CO_2 methanation performance at lower reaction temperatures [2]. Compared to the more common Ni supported on metal oxides, the research on Ni supported on carbon materials is less advanced, motivating a fundamental investigation of such alternative catalytic systems [2,5].

Among the metal-oxide supporting materials, despite being based on a rare-earth metal, ceria (CeO_2) has emerged as a promising alternative to Al_2O_3 because it enhances the metal–support interactions, leading to high dispersion of the resultant Ni nanoparticles over the support. Moreover, owing to the enhanced surface coverage by CO_2 species, enabled by the CeO_2 surface basicity, it improves the low-temperature catalytic performance of the catalysts in CO_2 methanation [19–26]. These positive effects of CeO_2 motivated us to develop high-performing carbon/ceria-supported Ni catalysts for CO_2 methanation, as well as to conduct a comparative mechanistic study of CO_2 hydrogenation over these catalysts.

In this work, we report the successful precipitation synthesis of a composite supporting material consisting of reduced activated carbon (ACR) and CeO_2 (ACR–CeO_2) as well as pure CeO_2, followed by deposition of Ni nanoparticles via the incipient wetness impregnation route. An important feature of our findings is the remarkable reduction by 80 °C of the optimal temperature of the CO_2 methanation reaction, compared to that for a CeO_2-free Ni/ACR catalyst developed in our previous study [2], thus significantly improving the sustainability of the methanation approach without jeopardising the catalytic performance. Furthermore, we conducted a detailed *in situ* modulation-excitation phase-sensitive-detection diffuse-reflectance infrared Fourier-transform spectroscopy (ME–PSD–DRIFTS) investigation of the methanation over the newly synthesized high-performing Ni/ACR–CeO_2 and Ni/CeO_2 catalysts, to obtain key mechanistic insights.

2. Experimental methods

2.1. Synthesis

In the present work, we synthesized reduced activated carbon (ACR) with Lewis base sites by heat-treatment of a commercial NORIT GAC 1240 PLUS activated carbon (CABOT) at 900 °C for 1 h under H_2 flow [2]. Pure CeO_2 and composite ACR–CeO_2 supporting materials were prepared by a precipitation method adapted from elsewhere [27]. Briefly, $Ce(NO_3)_3{\cdot}6H_2O$ is precipitated by NaOH under vigorous stirring, along with the addition of calculated amounts of ACR for the composite ACR–CeO_2 synthesis. The 15% Ni nanoparticles were deposited onto as-synthesized supporting materials via incipient wetness impregnation using $Ni(NO_3)_3{\cdot}6H_2O$, followed by heat treatment to decompose nitrate, thus generating metallic Ni (**Ni/CeO_2** and **Ni/ACR−CeO_2**).

2.2. Characterisation

The synthesized materials were characterized by N_2 physisorption, powder X-ray diffraction (XRD), H_2 temperature programmed reduction (H_2–TPR), H_2–chemisorption, X-ray photoelectron spectroscopy (XPS), transmission electron microscopy (TEM), energy-dispersive X-ray spectroscopy in scanning TEM mode (STEM–EDX).

2.3. Catalytic testing

The activity, selectivity, and stability of the synthesized catalysts in CO_2 methanation were evaluated in a Microactivity XS15 system (PID Eng & Tech), using a fixed bed quartz reactor ($Ø_{int}$ = 1 cm). Outflow products were analyzed online using a GC 1000 gas chromatograph (DANI), equipped with a thermal conductivity detector (TCD) and a GS-CarbonPLOT capillary column, while using He as the carrier gas and a continuous flow of N_2 as the internal standard. Each catalyst (100 mg) was diluted by inert SiC material, and then was pre-treated in situ under H_2 flow (40 $cm^3\ min^{-1}$) at its reduction temperature for 30 min, at 1 bar. After that, the reactor temperature was decreased to 100 °C under He (50 $cm^3\ min^{-1}$), and then, the reactor was fed with 10% CO_2, 40% H_2 (the stoichiometric composition) and 50% He, with a total flowrate of 100 $cm^3\ min^{-1}$. A temperature ramping from 100 to 500 °C at a rate of 5 °C min^{-1} was performed under reaction conditions to evaluate the catalytic properties of the catalysts at various temperatures. Additionally, isothermal time-on-stream (TOS) experiments were conducted under the same reaction conditions to evaluate the stability of the catalysts.

2.4. In situ spectroscopy

CO_2 adsorption and CO_2 methanation over the synthesized materials were probed using steady-state *in situ* diffuse reflectance infrared Fourier transform spectroscopy (DRIFTS) using a Nicolet iS50 FTIR spectrometer (Thermo Scientific), equipped with a Mercury-Cadmium-Telluride (MCT) detector and a high temperature reaction chamber (Harrick Scientific). Additionally, the CO_2 methanation over the prepared materials was investigated by *in situ* modulation excitation phase-sensitive detection DRIFTS (ME–PSD–DRIFTS) using the same spectrometer. The ME-PSD analysis highlight the species that change with the modulation frequency (f). The collected spectra were converted into the so-called frequency domain by Fast Fourier Transform (FFT). The data was then filtered at the modulation frequency and converted into the phase-domain by Inverse Fast Fourier Transform (IFFT). Activated carbon absorbs most of the IR radiation, so it was not possible to perform DRIFTS analyses in the Ni/ACR sample.

Readers interested in the detailed experimental information are referred to the Supplementary material (SM).

3. Results

3.1. CO_2 methanation over Ni/CeO_2 and Ni/ACR–CeO_2

In our previous study [2], a novel methanation catalyst with 15 wt% Ni loading over ACR having O-free Lewis basic sites (denoted as **Ni/ACR**) has been developed, exhibiting CO_2 conversion (X_{CO2}) of 76% and selectivity towards CH_4 (S_{CH4}) of 97%, but at a fairly high reaction temperature of 450 °C. To increase the conversion while lowering the reaction temperature, we sought to introduce CeO_2, thus forming a composite supporting material with ACR. We began by optimizing the CeO_2 loading in the ACR–CeO_2 composite support. It was established that 15 wt% Ni catalyst supported on ACR–CeO_2 with ACR:CeO_2 weight ratio of 50:50 exhibits the optimal catalytic properties in CO_2 methanation (Fig. S1). Hence, we further conducted our studies with this catalyst, hereafter referred to as **Ni/ACR–CeO_2**.

With the optimized composite catalyst in hand, we investigated its methanation performance and compared it to a control 15 wt% Ni catalyst supported on pure CeO_2 (denoted as **Ni/CeO_2**).

Fig. 1a,b show the obtained X_{CO2} and S_{CH4} results in the temperature range of 200–500 °C. Both catalysts start to convert CO_2 from ca. 200 °C reaching X_{CO2} = 50% at 280 °C, the so-called T_{50}.

Upon the temperature increase, the catalysts further achieve CO_2 conversions that are very close to the thermodynamic equilibrium, exhibiting maximum X_{CO2} of 85.7% (**Ni/CeO_2**) and 87.4% (**Ni/ACR–CeO_2**) at a notably low temperature of only 370 °C (Fig. 1a). In terms of S_{CH4}, the catalysts also demonstrate values comparable to the thermodynamic equilibrium over the range of the studied temperatures, with $S_{CH4} \approx$ 100% at maximum X_{CO2} (Fig. 1a,b), with the only

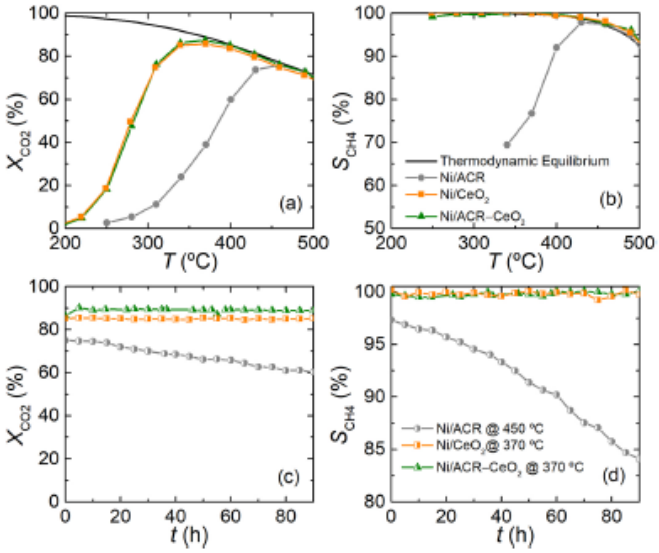

Fig. 1. Comparison of X_{CO2} (a) and S_{CH4} (b) as a function of reaction temperature, together with the stability testing results in terms of X_{CO2} (c) and S_{CH4} (d) over 90 h TOS of the new Ni/CeO_2 and Ni/ACR–CeO_2 catalysts in comparison with previously reported ceria-free Ni/ACR [2]. The thermodynamic equilibrium curves were calculated using a model based on the minimization of Gibbs free-energy of the existing species. Methanation conditions: $P = 1$ bar; $WHSV = 60\,000$ cm^3 g^{-1} h^{-1}; CO_2: H_2 (V:V) = 1: 4.

byproduct being CO. We finally investigated the stability of the catalysts through a long time-on-stream (TOS) testing at the best performing temperature of 370 °C. It was established that both the control **Ni/CeO_2** and composite **Ni/ACR–CeO_2** demonstrate excellent stability over 90 h on stream with no loss in either X_{CO2} or S_{CH4} (Fig. 1c,d). Importantly, a comparison of the catalytic properties between the new carbon/ceria-containing **Ni/ACR–CeO_2** and our previously reported carbon-containing **Ni/ACR** [2] (Fig. 1) evidently highlights that the compositing of ACR with CeO_2 not only leads to a significant improvement in the methanation performance but also simultaneously lowers the optimal reaction temperature by 80 °C (from 450 °C for **Ni/ACR** to 370 °C for **Ni/ACR–CeO_2**). Moreover, the compositing of ACR with CeO_2 leads to an improvement in stability at the respective optimal temperature of the resultant **Ni/ACR–CeO_2** catalyst, relative to that of **Ni/ACR** [2] (Fig. 1).

3.2. Characterisation of the catalysts

Our catalytic testing reveals that both **Ni/CeO_2** and **Ni/ACR–CeO_2** exhibit similarly excellent catalytic properties at reasonably low reaction temperatures, despite being based on different supporting materials. Therefore, we characterized the catalysts to determine the parameters that govern the methanation performance.

Even though **Ni/CeO_2** and **Ni/ACR–CeO_2** have similar catalytic properties (Fig. 1), the data presented in Table 1 demonstrate that the catalysts exhibit quite different textural properties. The textural properties of the synthesized materials were estimated using Brunauer–Emmett–Teller (BET) and Barrett–Joyner–Halenda (BJH) methods. Pure CeO_2 support has a relatively low specific surface area (S_{BET}) of 104 m^2 g^{-1}, while the pure ACR support has about 7-fold higher S_{BET} = 784 m^2 g^{-1}. As expected, the composite ACR–CeO_2 exhibits a S_{BET} = 373 m^2 g^{-1} that is higher than that of pure CeO_2, but lower than that of pure ACR. This trend is sustained for the respective Ni catalysts supported on the two materials, exhibiting a decreasing order in S_{BET} **Ni/ACR–CeO_2** > **Ni/CeO_2** (Table 1). The addition of Ni leads to a slight decrease in S_{BET} compared to the respective supporting materials (Table 1). Both CeO_2 and ACR–CeO_2 supports, and the derivative catalysts present Type IV isotherms (Fig. S2); the pore-size-distribution data (Fig. S3) reveal that **Ni/CeO_2** exhibits a higher number of pores having larger width, while **Ni/ACR–CeO_2** has a peak in the smaller width range, also containing pores with diameters higher than 5 nm.

Next, we probed the metal–support interactions and metallic surface areas of **Ni/CeO_2** and **Ni/ACR–CeO_2**. The comparison of hydrogen temperature-programmed reduction (H_2–TPR) profiles of **Ni/CeO_2** and

Table 1
Textural properties [specific surface area (S_{BET}), and total pore volume (V_p)], average size of CeO_2 crystallites ($d_{c,CeO2}$), and Ni crystallites ($d_{c,Ni}$), metallic Ni surface area (S_M), temperature at which X_{CO2} = 50% (T_{50}), and maximum X_{CO2}, attained at 450 °C for Ni/ACR [2] and 370 °C for Ni/CeO_2 and Ni/ACR–CeO_2.

	S_{BET} (m^2 g^{-1})[a]	V_p (cm^3 g^{-1})[a]	$d_{c,Ni}$ (nm)[b]	$d_{c,CeO2}$ (nm)[b]	S_M (m^2 g$_{cat}^{-1}$)[c]	T_{50} (° C)	Max X_{CO2} (%)
ACR [2]	784	0.48	–	–	–	–	0
CeO_2	104	0.17	–	7	–	–	12
ACR–CeO_2	373	0.33	–	6	–	–	11
Ni/ACR [2]	656	0.41	8	–	2.73	385	76
Ni/CeO_2	82	0.14	9	7	1.66	280	86
Ni/ACR–CeO_2	386	0.30	5	5	2.57	280	87

[a] Estimated by N_2 physisorption.
[b] Estimated from XRD data using Scherrer equation.
[c] Estimated by H_2 pulse chemisorption.

Ni/ACR–CeO_2 demonstrate different metal–support interactions between Ni nanoparticles and the supporting materials (Fig. S4a). Specifically, **Ni/CeO_2** exhibits a large peak at 360 °C with a shoulder at 404 °C, as well as two small shoulders at 334 °C and 464 °C. In contrast, **Ni/ACR–CeO_2** exhibits a large peak at a lower temperature of 320 °C with two high-temperature shoulders at 392 °C and 502 °C. Apparently, **Ni/CeO_2** is largely composed of Ni species that exhibit a stronger interaction with pure CeO_2 support, compared to that in composite **Ni/ACR–CeO_2**. Regarding the Ni surface area (S_M), measured using H_2 pulse chemisorption, it was estimated that **Ni/ACR–CeO_2** exhibits more than 1.5 times higher metallic Ni surface than does **Ni/CeO_2** (Table 1). The H_2–TPR of the supporting materials was also assessed (Fig. S4b) and it was observed that the H_2 consumed for CeO_2 reduction is minimal when comparing to the H_2 consumed for the reduction of the Ni-based catalysts. Additionally, the analysis of the H_2 –TPR profiles indicate that the ACR–CeO_2 support is a homogeneous mixture that interacts in a way that the reduction profile of the **Ni/ACR–CeO_2** sample is different than that of the other two supports (CeO_2 and ACR), and not a combination of both **Ni/CeO_2** and **Ni/ACR** [2] H_2-TPR profiles.

To gain structural insight into the synthesized materials, we further investigated their phase composition using powder X-ray diffraction (XRD). According to the XRD patterns (Fig. S5), the as-synthesized pure and composite supports contain cubic CeO_2 phase (ICDD #04–006–1932). In contrast, the respective Ni catalysts additionally contain cubic metallic Ni (ICDD #04–016–4761), with no secondary phases being present. There is possibly a graphitic carbon peak, but since it should be present at 28°, overlapping with a peak from CeO_2, it is impossible to access its presence. The average size of Ni and CeO_2 crystallites was assessed from XRD data using the Scherrer equation (Table 1), and the size of Ni crystallites in **Ni/CeO_2** (ca. 9 nm) was estimated to be nearly 2 times larger than in **Ni/ACR–CeO_2** (ca. 5 nm), which is consistent with the smaller S_M of **Ni/CeO_2**.

X-ray photoelectron spectroscopy (XPS) analysis revealed that both catalysts, **Ni/CeO_2** and **Ni/ACR–CeO_2**, exhibited two different Ni phases, observed from the deconvolution of the XPS data for Ni $2p_{3/2}$ (Fig. 2). The lower energy component (853.0 ± 0.1 eV) is assigned to Ni^0 in metallic Ni species, while the components at 854.4 ± 0.2 eV and 856.4 ± 0.1 eV are consistent with Ni^{2+} in nickel-oxide phase, and the ones at 861.3 ± 0.3 eV and 864.3 ± 0.1 eV are satellite peaks from Ni^{2+}. The Ni $2p_{3/2}$ spectral envelopes of the catalysts resemble the typical spectra for nanoscale oxidation layers on Ni and Ni compounds, being consistent with a thin, predominantly Ni^{2+}, nickel oxide layer on metallic Ni [5,28–30]. The binding energies (BEs) of fitting components are presented in Table S1 and the relative atomic percentages (at%) of Ni^0 and Ni^{2+} are presented in Table S2. The relative atomic percentage of Ni^0 is similar in **Ni/ACR–CeO_2** and **Ni/CeO_2** catalysts, at 4.2 at% and 4.4 at%, respectively (Table S2).

The Ce 3d spectra also revealed the presence of mixed Ce phases (Fig. 2) in both samples. The spectra can be represented as five pairs of doublets, identified in Fig. 2 as u and v for the Ce $3d_{3/2}$ and Ce $3d_{5/2}$ spin–orbit components, with spin–orbit splitting of 18.4 ± 0.5 eV for all the samples, consistent with those found in the literature [31,32]. These spectra were fitted using a method similar to that reported by Zhang et al. [32] where the u''' peak is fixed and the remaining peaks are constrained according to the u''' position.

The v^0, u^0, v', and u' are attributed to Ce^{3+}, while the highest biding energy peaks, v''' and u''', are attributed to the primary components of Ce^{4+}, and the remaining v, u, v'', and u'', are identified as "shake-down" states, as reported by Mullins et al. [31,33] Table S2 presents the BEs of each of these components. Importantly, we note that there is a small overlap of the Ni $2p_{1/2}$ components (orange lines and symbols below 881 eV in Fig. 2) and the low-BE components in the Ce 3d spectra. This overlap was accounted for by including in the Ce 3d fitting procedure Ni $2p_{1/2}$ components (orange lines in Fig. 2), with fixed parameters based on the more reliable fits in the Ni $2p_{3/2}$ region.

The Ce 3d peaks in **Ni/ACR–CeO_2** are noticeably narrower than those in **Ni/CeO_2**, which likely indicates that ceria nanoparticles are in a more uniform electrostatic environment in **Ni/ACR–CeO_2**, where they are in a good electrical contact with the carbon substrate.

The amount of Ce^{4+} and reduced Ce^{3+} is quantified in Table S2. Interestingly, the **Ni/ACR–CeO_2** catalyst exhibits a higher relative at% of Ce^{3+} (20.5 at%) compared to **Ni/ACR–CeO_2** that contains 16.4 at% Ce^{3+}.

The C 1s spectra of **Ni/ACR–CeO_2** were also analyzed, and the results are presented in Fig. S6 [35,36].

Interested in understanding the microstructural properties of the catalysts, we then conducted transmission electron microscopy (TEM) and energy-dispersive X-ray spectroscopy in scanning STEM mode (STEM–EDX) analyses. These studies reveal metallic Ni nanoparticles well-dispersed over nanocrystalline CeO_2 and amorphous-like ACR. Fig. 3a shows TEM image of Ni nanoparticles in **Ni/CeO_2**, where it is possible to distinguish only some large Ni particles (ca. 30–50 nm) dispersed over CeO_2 support. Fig. 3e shows Ni nanoparticles dispersed on composite ACR–CeO_2 support in **Ni/ACR–CeO_2**, wherein the Ni particles (ca. 5–10 nm) dispersed on ACR and some larger Ni particles (ca. 30–50 nm) on CeO_2 are observed. It is important to note that the imaging contrast between the Ni and CeO_2 nanoparticles is very low, thus it is difficult to differentiate the two types of nanoparticles in the electron microscopy images. Therefore, the size ranges indicated are merely representative of the observed identifiable nanoparticles, leading

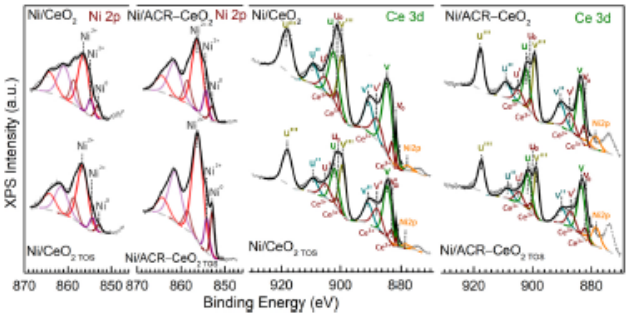

Fig. 2. High-resolution XPS data for the Ni $2p_{3/2}$ and Ce 3d region collected from as-synthesized and TOS-tested Ni/CeO_2 and Ni/ACR–CeO_2. Symbols: raw data; black lines: overall fits; colored lines: fits of individual components; dashed lines: background. The observed binding energies (BE) and assignment of the peak positions are summarized in Table S1.

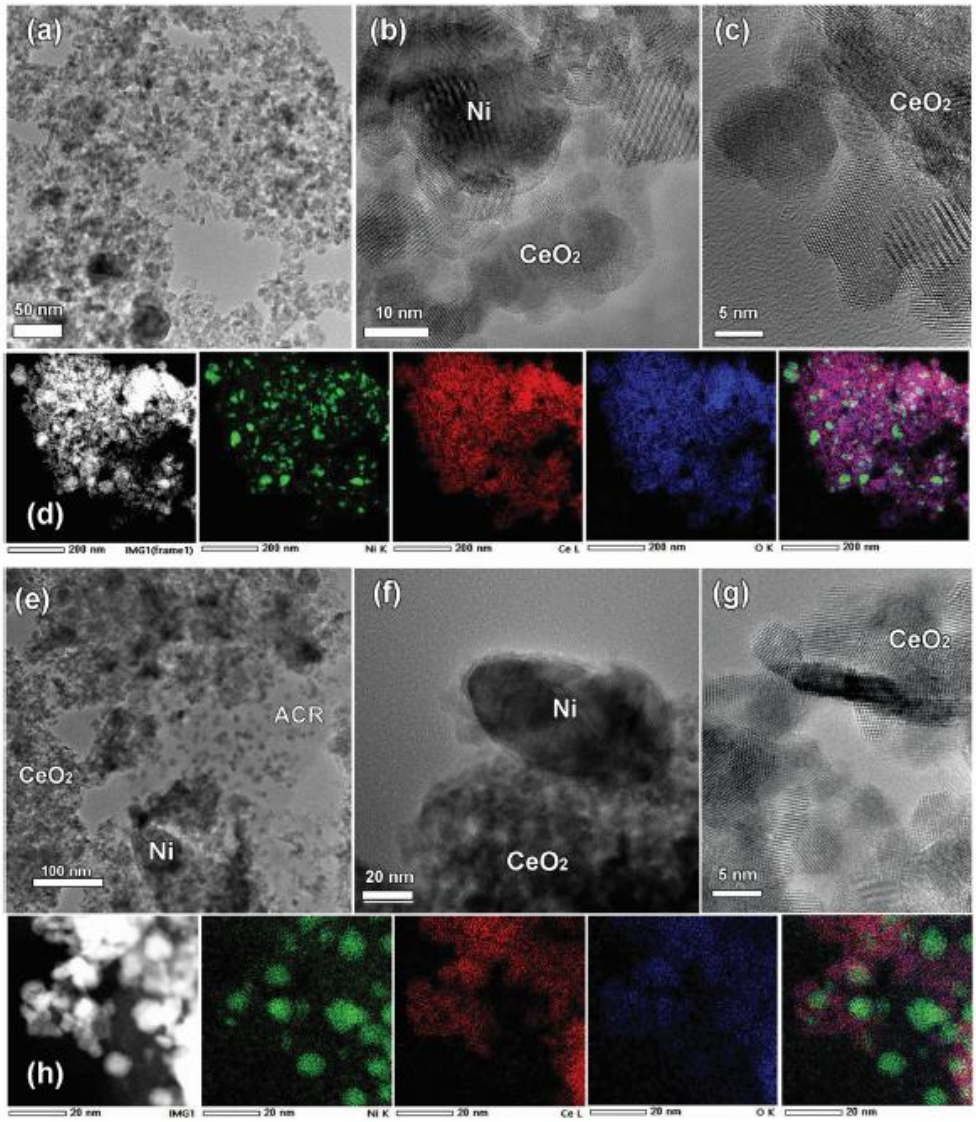

Fig. 3. TEM images of Ni nanoparticles dispersed on CeO_2 (a) and ACR–CeO_2 (e) supporting materials, together with the representative HRTEM images of Ni and CeO_2 nanoparticles in the Ni/CeO_2 (b,c) and Ni/ACR–CeO_2 (f,g) catalysts. Low-magnification STEM images of the Ni/CeO_2 (d) and Ni/ACR–CeO_2 (h) catalysts, together with the respective STEM–EDX maps for Ni, Ce, O and their mixture.

to a gap between the Ni nanoparticles sizes from TEM and those estimated by XRD, which is more representative.

Although it is difficult to distinguish the smaller Ni particles on the CeO_2 support due to the low contrast on the TEM images, the respective STEM–EDX maps evidence that there are also small Ni particles dispersed on CeO_2 material in both **Ni/CeO_2** and **Ni/ACR–CeO_2** catalysts (Fig. 3d,h). A closer look at CeO_2 supporting material in **Ni/CeO_2** (Fig. 3c) and **Ni/ACR–CeO_2** (Fig. 3g) catalysts reveals that the ceria consists of agglomerated CeO_2 nanoparticles (ca. 5–10 nm), preferentially faceted by the {110} plane.

Interestingly, high-resolution TEM (HRTEM) imaging of Ni nanoparticles in **Ni/CeO$_2$** and **Ni/ACR–CeO$_2$** reveals that the particles in both catalysts exhibit Ni@NiO core-shell appearance. As an example, Fig. 4a,b show HRTEM images of a Ni nanoparticle in **Ni/ACR–CeO$_2$** catalyst, together with the corresponding Fourier transform (FT) patterns for the Ni core and NiO shell. Furthermore, multiple twinning of the Ni nanoparticle can be observed in the HRTEM images, marked by white arrow heads.

Even though there was no loss in X_{CO2} and S_{CH4} over 90 h of TOS testing (Fig. 1c,d), we decided to investigate the impact of the reaction conditions on the microstructure and chemical composition of the catalysts by means of electron microscopy and XPS.

The Ni 2p$_{3/2}$ spectra (Fig. 2) of the samples after TOS testing (**Ni/CeO$_2$ $_{TOS}$** and **Ni/ACR–CeO$_2$ $_{TOS}$**) include fitting components at BEs similar to those of the components in the spectra of fresh **Ni/CeO$_2$** and **Ni/ACR–CeO$_2$** catalysts. Considering the relative Ni^0 atomic content (Table S2), however, we observed that it decreases to 2.8 at% (cf. 4.4%) in the case of **Ni/CeO$_2$ $_{TOS}$** and, on the contrary, increases to 7.4 at% (cf. 4.2 at%) in the case of **Ni/ACR–CeO$_2$ $_{TOS}$**. In the Ce 3d spectra (Fig. 2), again the positions of the peaks remain similar for both catalysts after 90 h of TOS, but there are differences in the Ce^{3+}/Ce^{4+} ratio before and after TOS in both **Ni/CeO$_2$** and **Ni/ACR–CeO$_2$**. The Ce^{3+} atomic content in **Ni/CeO$_2$** increases to 21.3 at% (cf. 16.4 at%), while in **Ni/ACR–CeO$_2$**, it remains approximately constant with 19.9 at% (cf. 20.5 at%).

From Figs. S8a-d, one can see that the TOS-tested **Ni/CeO$_2$** maintains the microstructure of the Ni nanoparticles dispersed over the ceria support composed by small CeO_2 nanoparticles (ca. 5–10 nm), similar to that in pristine **Ni/CeO$_2$** (Fig. 3a). In contrast, TOS-tested **Ni/ACR–CeO$_2$** undergoes significant microstructural changes within CeO_2 support. Specifically, Fig. S8e evidences the appearance of CeO_2 particles with a needle-like shape after 90 h of methanation. Such nanoneedles were not observed in pristine **Ni/ACR–CeO$_2$** (Fig. 3e) or pristine and TOS-tested **Ni/CeO$_2$** (Fig. 3a, S8a).

Notably, a closer look at Ni particles in TOS-tested **Ni/CeO$_2$** (Fig. S8c) and **Ni/ACR–CeO$_2$** (Fig. 4c,d) indicates a preservation of Ni@NiO core-shell nanostructure of the catalyst after prolonged methanation.

3.3. Probing the mechanism of CO_2 methanation by *in situ* DRIFTS

Having in hand two well-characterized high-performing methanation catalysts, we further conducted *in situ* DRIFTS studies to elucidate the reaction mechanism over **Ni/CeO$_2$** and **Ni/ACR–CeO$_2$**. This technique is used to understand the reaction mechanism in heterogeneous catalysis, probing the adsorbed species on the catalysts under reaction conditions. There are some drawbacks of this technique. Specifically, it detects not only the intermediate species but also the sample background, noise, and spectator species, making it difficult to distinguish what are the real intermediates of the reaction [37,38].

Furthermore, the intermediate species have a short lifetime, making it even more difficult to differentiate them from the remaining species, which are present under steady-state conditions. Fortunately, the modulation-excitation (ME) technique offers an interesting solution for overcoming the aforementioned drawbacks. It is based on the introduction of a rapid periodic perturbation on the testing system, to which only the intermediate species of the reaction respond. The resultant spectroscopic signal is then analyzed by phase-sensitive detection (PSD) technique to enhance the signal-to-noise ratio and to extract the information about intermediate species that responded to the modulation signal, thus avoiding the signal from the spectator species [10,37–41].

We started by performing steady-state *in situ* DRIFTS for CO_2 adsorption and then for CO_2 methanation at 250, 300, and 350 °C. In this temperature range, the X_{CO2} goes from low to almost complete. Fig. S9 shows the full range spectra for each experiment, along with a discussion of the observed trends for hydroxyl groups, gaseous CO_2, and gaseous CH_4 [42]. Fig. 5 displays a zoom-in of the region below 2000 cm^{-1}, which carries important information about the CO_2 adsorption and methanation mechanisms, while Table 2 summarizes the respective band assignment. During CO_2 adsorption (Fig. 5a,c), two bands detected at 1500 and 1370 cm^{-1} (υ_{as} / υ_s) can be attributed to formate (HCOO) species, which are probably close to a reduced Ce site in CeO_2, because they have a low Δ_{as-s} = 130 / 150 cm^{-1} [10,26]. Two other bands are observed at 1600 and 1280 cm^{-1} (υ_{as} / υ_s), that can be assigned to bi-dentate carbonates (b–CO_3), along with the band at 1030 cm^{-1} [10,26]. Moreover, a small band at 1415 cm^{-1} is also observed in the spectrum of **Ni/CeO$_2$** at 250 °C, which can be attributed

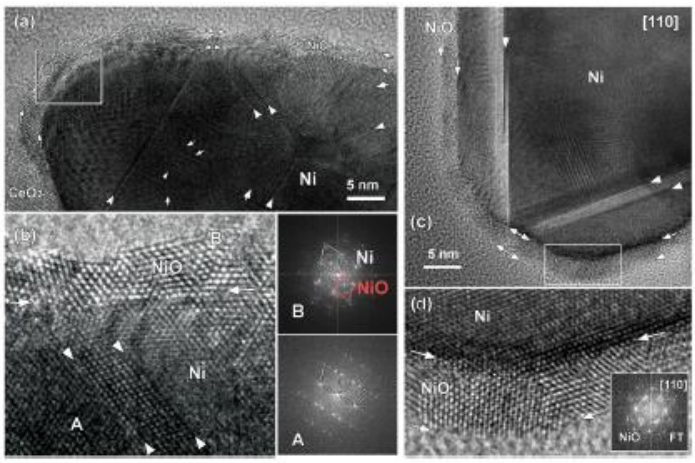

Fig. 4. HRTEM imaging of the surface of a single Ni nanoparticle in the as-synthesized Ni/ACR–CeO_2 catalyst (a) and zoom-in (white rectangle) image (b) and in the same catalyst after its TOS testing for 90 h (c,d), revealing the core-shell appearance of the nanoparticles. The insets in (b,d) show the FT patterns from the corresponding regions. The white arrows mark the NiO shell and the white arrow heads depict the twinning within the Ni nanoparticles.

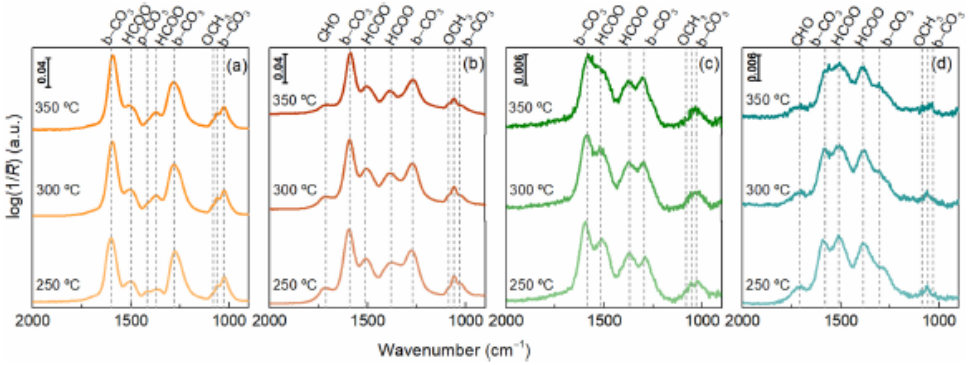

Fig. 5. Steady-state *in situ* DRIFTS studies of CO_2 adsorption and methanation over Ni/CeO_2 (a,b) and $Ni/ACR–CeO_2$ (c,d) catalysts. Experimental conditions for CO_2 adsorption: $P = 1$ bar; CO_2 flowrate of 2.5 $cm^3\ min^{-1}$; N_2 flowrate of 100 $cm^3\ min^{-1}$; $m_{cat} = 15$ mg. Experimental conditions of CO_2 methanation: $P = 1$ bar; CO_2 flowrate of 2.5 $cm^3\ min^{-1}$; 10%H_2/N_2 gas mixture flowrate of 100 $cm^3\ min^{-1}$; $m_{cat} = 15$ mg. The dashed lines indicate the positions of the observed peaks.

Table 2
Assignment of the bands observed during steady-state DRIFTS and ME–PSD–DRIFTS experiments: hydroxyl groups (OH^-), gaseous methane (CH_4), gaseous carbon dioxide (CO_2), bridged carbon monoxide (br–CO), formyl groups (CHO), bi-dentate carbonates (b–CO_3), poly-dentate carbonates (p – CO_3), formates (HCOO), carboxylate ($CO_2^{-\delta}$), and methoxy groups (OCH_3).

	Steady-state *in situ* DRIFTS				*In situ* ME–PSD–DRIFTS	
	CO_2 adsorption		CO_2 methanation		CO_2 adsorption	
	Ni/CeO_2	$Ni/ACR–CeO_2$	Ni/CeO_2	$Ni/ACR–CeO_2$	Ni/CeO_2	$Ni/ACR–CeO_2$
	Wavenumber (cm^{-1})					
CO_2/ OH^-	3750 – 3550	3750 – 3550	3750 – 3550	3750 – 3550	3750 – 3550	3750 – 3550
CH_4	–	–	–	3017	3017	3017
CO_2	2400 – 2250	2400 – 2250	2400 – 2250	2400 – 2250	2400 – 2250	2400 – 2250
CO gas	–	–	–	2200 – 2100	2200 – 2100	2200 – 2100
br–CO	–	–	–	–	1760	1770
CHO	–	–	1710	1710	1700	1700
b–CO_3	1600	1585	1590	1580	1610	1600
	1280	1295	1270	1300	1290	1290
	1030	1030	1030	1030	1020	1020
p – CO_3	1415	–	–	–	1450	1450
	–	–	–	–	1405	1405
HCOO	1500	1520	1510	1510	1520	1530
	1370	1370	1380	1385	1360	1360
$CO_2^{-\delta}$	–	–	–	–	1240	1240
OCH_3	1080	1080	1080	1080	1080	1080
	1060	1060	1060	1060	1060	1060

to poly-dentate (p–CO_3) carbonates Interestingly, a small amount of methoxy species (OCH_3) are present in the CO_2 adsorption spectra without H_2 being present, corresponding to the bands at 1080–1060 cm^{-1} [24,25]; therefore, residual H_2 should be present on the Ni nanoparticles from the reduction pre-treatment which might lead to the methoxy formation during CO_2 adsorption step.

When H_2 is introduced into the gas flow to mimic the methanation conditions (Fig. 5b,d), the bands corresponding to b–CO_3 and HCOO remain at similar wavenumbers as during the CO_2 adsorption probing; however, the difference in intensity between them decreases. Furthermore, the methoxy bands increase and a new band appears at 1710 cm^{-1} for both catalysts that can be attributed to the formation of formyl (CHO) groups [24].

To gain a deeper understanding of the reaction mechanism, we next conducted modulation-excitation phase-sensitive detection DRIFTS (ME–PSD–DRIFTS), allowing for a better signal-to-noise ratio plus distinguishing spectator and intermediate species. The modulated conditions applied in the experiments were a change in flowrate from A (CO_2 = 2.5 $cm^3\ min^{-1}$ and 10%H_2/N_2 = 100 $cm^3\ min^{-1}$) to B (CO_2 = 2.5 $cm^3\ min^{-1}$ and N_2 = 100 $cm^3\ min^{-1}$). Fig. 6 shows the phase-resolved spectra of the modulation excitation *in situ* DRIFTS studies conducted for Ni/CeO_2 at 250, 300, and 350 °C. A comparison of Fig. 5 and Fig. 6 show that the data from the ME–PSD–DRIFTS experiments look quite different from those of the steady state experiments. In particular, three main differences can be identified: (i) the peak detected in the steady-state spectra at 1700 cm^{-1} (Fig. 5b) is actually caused by a convolution of 2 peaks that are out-of-phase during modulation (Fig. 6); (ii) instead of 4 peaks observed in the steady-state spectra between 1700 and 1200 cm^{-1} (Fig. 5b), the phase-resolved spectra show 7 peaks (Fig. 6), indicating the appearance of new groups not identified in the steady-state spectra, namely, p – CO_3 and carboxylate ($CO_2^{-\delta}$) groups (Table 2); and (iii) two from those 7 peaks are out-of-phase with the others (Fig. 6).

With regards to the aforementioned first difference, the band at 1700 cm^{-1} is indicative of the formyl (CHO) group, while the band at 1760 cm^{-1} is most likely related to bridged CO (br–CO) on Ni^0 sites [20, 24]. The appearance of br–CO on Ni^0 should be related to two reactions occurring simultaneously: it can be formed by direct dissociation of CO_2

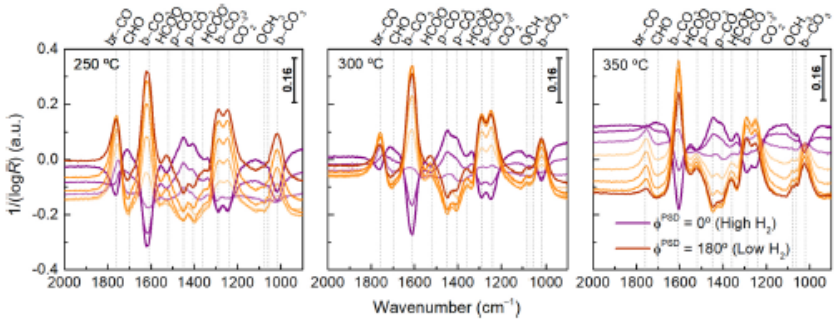

Fig. 6. Phase-resolved spectra of the modulation excitation *in situ* DRIFTS studies conducted for the Ni/CeO_2 catalyst at 250, 300 and 350 °C. Experimental conditions: $P = 1$ bar; flowrate A: $CO_2 = 2.5$ cm^3 min^{-1} and $10\%H_2/N_2 = 100$ cm^3 min^{-1}; flowrate B: $CO_2 = 2.5$ cm^3 min^{-1} and $N_2 = 100$ cm^3 min^{-1}; $m_{cat} = 15$ mg. The dashed lines indicate the positions of the peaks.

over Ni, and it can be a product of HCOO dissociation, since the presence of $CO_2^{\delta-}$, b–CO_3, p–CO_3 and HCOO bands indicate that CO_2 should also be adsorbed and hydrogenated on CeO_2.

Furthermore, there is a possibility that br–CO can be hydrogenated to CHO in the presence of H_2, as previously reported [24]. This is a likely scenario since the respective bands are out of phase with each other, indicating that br–CO is hydrogenated to CHO on the surface of CeO_2 in the presence of H_2. A more detailed analysis of the phase delay φ (the time to reach maximum accumulation) for both br–CO and CHO species over **Ni/CeO$_2$** at 300 °C, show that they differ by 180° [φ(br–CO) = 108° and φ(CHO) = 288°]. This phase delay means that the CHO is formed at the same time as br–CO is consumed. Another possible scenario would be that this phase delay is dependent on that of the H_2, which would mean that H_2 favors the net formation of b–CO and disfavors the formation of CHO, leading to the maximum coverage of b–CO being observed mostly in phase with H_2, whereas CHO is mostly out of phase to H_2. However, since the phase delays are not close to 0° or 180°, which would be close to the value where H_2 is maximum and minimum, respectively, due to low residence time, the first option is more probable: br–CO should be hydrogenated to CHO in the presence of H_2. Notably, it is not possible to present the phase delay values for the remaining intermediates due to the accumulation of multiple maxima.

More detailed analysis of the differences between the steady-state and ME–PSD data reveal that while the bands from b–CO_3 appear at the same positions (Table 2) [10,26], the set of bands associated with HCOO in the steady-state spectra (Fig. 5b) are, in fact, a convolution of different species, namely, HCOO and p–CO_3 (Fig. 6, Table 2) [10]. Notably, the later p–CO_3 assignment could also be ascribed to mono-dentate carbonates (m–CO_3), but the low Δ_{as-s} suggests the presence of p–CO_3 rather than m–CO_3 [10]. In that case, p–CO_3 appearance is out-of-phase with b–CO_3 appearance, which indicate that the coordination of the carbonates may be changing from b–CO_3 to p–CO_3. Previously, this effect was explained as a change in carbonate adsorption configuration over CeO_2 as a consequence of its reduction state. Specifically, in the absence of H_2 ($\phi^{PSD} = 180°$), CeO_2 is partially oxidized, and when it is reduced in the presence of H_2 ($\phi^{PSD} = 0°$), the b–CO_3 reconfigures to either m–CO_3 or p–CO_3 [10].

Finally, only one peak was observed at 1270 cm^{-1} in the steady-state spectrum (Fig. 5b). After phase-sensitive detection analysis (PSD), two peaks are distinguished (Fig. 6): one from b–CO_3 and another one that we assign to $CO_2^{\delta-}$ (Table 2), typically forming when CO_2 is adsorbed on the surface of CeO_2 [10,24–26,43]. Finally, we assign the bands at 1030 – 1060 cm^{-1} (Fig. 6) to methoxy (OCH_3) species [24,25], and the one at 1060 cm^{-1} corresponds to b–CO_3 (Table 2) [26].

When we compare the spectra at different temperatures (Fig. 6), we observe that the bands remain at the same positions in all spectra, although their relative intensities varied. The change in intensity is particularly clear from the relative difference between the two peaks assigned to br–CO on Ni^0 and CHO, respectively. In contrast, the peaks from b–CO_3 and p–CO_3 remain intense, as they are known to be relatively stable [10].

Motivated by this detailed insight, we then proceeded to investigate the composite **Ni/ACR–CeO$_2$** catalyst by ME–PSD–DRIFTS. Due to the absorption of most of the IR radiation by the activated carbon, we observe a lower signal-to-noise ratio for **Ni/ACR–CeO$_2$** (Fig. 7) compared to **Ni/CeO$_2$** (Fig. 6). Nevertheless, we were still able to draw some conclusions from the phase-resolved spectra. First, the same species are detected in the ME–PSD–DRIFTS spectra of **Ni/ACR–CeO$_2$**, as in the case of **Ni/CeO$_2$**, moreover at nearly the same band positions (Figs. 6,7). However, three main differences were identified between methanation behaviors of these two catalysts: (i) in **Ni/ACR–CeO$_2$**, the relative intensity of br–CO band in comparison with CHO band (Fig. 7) is lower than in the case of **Ni/CeO$_2$** (Fig. 6); (ii) as the reaction temperature increases the presence of CO is not observed for **Ni/ACR–CeO$_2$** (Fig. 7); and (iii) the bands corresponding to p–CO_3 are significantly less pronounced for **Ni/ACR–CeO$_2$** (Fig. 7) than for **Ni/CeO$_2$** (Fig. 6). These differences show that, in sharp contrast to **Ni/CeO$_2$**, there is no direct transformation between br–CO and CHO over the **Ni/ACR–CeO$_2$** catalyst, which is further confirmed by the absence of CO at high temperatures (Fig. 7).

The full-range *in situ* ME–PSD–DRIFTS spectra may help to explain the general trends of the methanation over the synthesized catalysts and deviations between them. Fig. S10 shows that, with the **Ni/CeO$_2$** catalyst, the band corresponding to gaseous CH_4 at 3017 cm^{-1} is not present at 250 °C but it appears at 300 °C. Fig. S11 shows the same observations with the **Ni/ACR—CeO$_2$** catalyst. For both samples, the band corresponding to gaseous CO at 2200–2100 cm^{-1} starts to be apparent at 300 °C and is even more pronounced at 350 °C (Figs. S10, S11) [25]. For comparison, we also investigated the pure CeO_2 and composite ACR–CeO_2 supports without Ni being present and the obtained results are displayed in Figs. S12 and S13, respectively.

4. Discussion

It is well known that CeO_2-supported Ni catalysts have high activity and selectivity for CO_2 methanation at low temperatures, typically $\leq$ 400 °C. Most likely, these properties are related to the improved metal–support interactions between Ni and CeO_2 and a high surface coverage of CO_2, alternatively, they can be explained by the reducibility of CeO_2 [44].

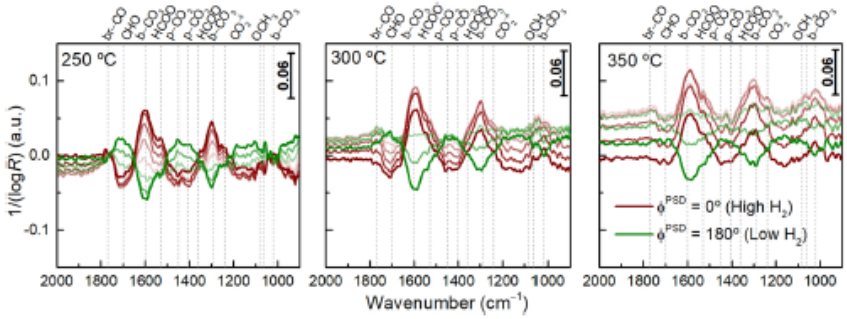

Fig. 7. Phase-resolved spectra of the modulation excitation *in situ* DRIFTS studies conducted for the Ni/ACR–CeO_2 catalyst at 250, 300 and 350 °C. Experimental conditions: P = 1 bar; flowrate A: CO_2 = 2.5 cm^3 min^{-1} and 10%H_2/N_2 = 100 cm^3 min^{-1}; flowrate B: CO_2 = 2.5 cm^3 min^{-1} and N_2 = 100 cm^3 min^{-1}; m_{cat} = 15 mg. The dashed lines indicate the positions of the peaks.

Based on our previous work [2], we hypothesized that an interesting approach to obtain high-performing methanation catalyst would be the preparation of Ni catalyst supported on composite supporting material consisting of reduced activated carbon and CeO_2.

Furthermore, we wanted to study whether such compositing would generate an active, selective, and stable methanation catalyst that operates at a temperature below 400 °C. Thus, we synthesized a set of 15 wt% Ni catalysts supported on ACR–CeO_2 with different ratios of ACR:CeO_2, as well as a 15 wt% Ni catalyst supported on pure CeO_2 (**Ni/CeO_2**) for reference. Fig. S1 shows that **Ni/ACR–CeO_2** with ACR:CeO_2 weight ratio of 50:50 afforded the best methanation performance. Besides improving the activity and selectivity compared to those for our previously reported **Ni/ACR**, the **Ni/ACR–CeO_2** catalyst achieved improved stability over long TOS at the respective optimal temperature. This improvement can be explained by the different interactions between the Ni and the pure ACR and ACR–CeO_2 composite and also by the fact that lowering the reaction temperature to 370 °C (cf. 450 °C) decreases the possibility of Ni deactivation over long TOS.

Significantly, although half of the supporting material in **Ni/ACR–CeO_2** is reduced activated carbon, we observed that the catalytic properties of the composite catalyst are comparable or even slightly better than those of **Ni/CeO_2** (Fig. 1). This result highlights that our compositing strategy is a useful tool for reducing the usage of the expensive rare-earth CeO_2 by replacing this oxide with a cost-effective carbon material. As explained in our previous work [2], the Lewis basic sites present on the ACR supporting material improve the Ni dispersion, and furthermore, its basicity is responsible for an improved CO_2 adsorption capacity over the catalyst, enabling CO_2 to be close to the Ni active sites.

The characterization of the samples allowed some property-performance relationships to be established. Even though the samples presented comparable catalytic performance, they are composed of materials with different textural properties. Furthermore, the Ni species on **Ni/CeO_2** exhibit a stronger interaction with pure CeO_2 support, compared to that in composite **Ni/ACR–CeO_2**, which can be a hypothesis for the fact that **Ni/ACR–CeO_2** presented slightly better activity at lower temperature. The reducibility of CeO_2 could also be a possible reason for slight differences in catalytic performance [44]; however, it is difficult to compare the reducibility of CeO_2 in **Ni/CeO_2** and ACR–CeO_2 supports by H_2 –TPR analysis because ACR can undergo decomposition above 500 °C, which influences with the TPR profile of the sample above this temperature. The microscopy analysis demonstrated that in both samples, the particles exhibit Ni@NiO core-shell appearance.

XPS analysis revealed that both catalysts, **Ni/CeO_2** and **Ni/ACR–CeO_2**, exhibited two different Ni phases, corresponding to metallic Ni and NiO, with Ce 3d spectra also revealing the presence of mixed Ce phases in both samples. Interestingly, relative at% of Ce^{3+} is different in both samples, with the **Ni/ACR–CeO_2** catalyst exhibiting a higher value. It is known that the oxygen vacancies can be formed in the transformation process of Ce^{4+} into Ce^{3+}; thus, the amount of oxygen vacancies is usually proportional to the Ce^{3+} amount [34]. Therefore, we can hypothesize that **Ni/ACR–CeO_2** catalyst may contain a higher amount of oxygen vacancies, which are known to be important in the methanation reaction, than does **Ni/CeO_2**. This hypothesis cannot be directly supported by the analysis of the O 1s spectra because the O 1s spectra of **Ni/ACR–CeO_2** contain components from the organic phase of ACR, in addition to the components related to CeO_2 (Fig. S7) [31,33,35,45].

After the stability experiment over a long TOS, the major modification was observed in **Ni/ACR–CeO_2**, in which the CeO_2 particles presented a needle-like shape. Most likely, the presence of steam, a subproduct of the reaction, leads to hydrothermal recrystallization of the initial CeO_2 nanoparticles into CeO_2 nanoneedles. This recrystallization is apparently templated by the presence of ACR, since carbon-free **Ni/CeO_2** did not exhibit the appearance of the CeO_2 needles after TOS testing (Fig. S8a). The carbon balance, that was close to zero, and the fact that our catalysts do not suffer deactivation over 90 h, indicate that carbon deposition should be minimal, if present at all, in these systems.

Our studies of CO_2 methanation over **Ni/CeO_2** and **Ni/ACR–CeO_2** have established that both catalysts demonstrated outstanding catalytic activity, selectivity, and stability in CO_2 methanation (Fig. 1). Notably, Ni catalysts supported on CeO_2 are among the materials exhibiting the highest methanation performance reported in the literature. To our gratification, the observed catalytic properties for our **Ni/CeO_2** and **Ni/ACR–CeO_2** catalysts compare favorably to the reported ones. Specifically, our catalysts achieved a maximum X_{CO2} of 86% and 87%, with $S_{CH4} \approx$ 100% at 370 °C, while having a T_{50} of 280 °C; this T_{50} is similar or even lower from most of the reported in the literature for similar catalytic systems (Table S3). For example, Rui *et al.* [20] prepared two different CeO_2 supports that were used for the preparation of two Ni-based catalysts, which could achieve $X_{CO2} \approx$ 85% with $S_{CH4} \approx$ 100% at 275 °C ($T_{50} \approx$ 260 °C) and 350 °C ($T_{50} \approx$ 280 °C). In another interesting report, which compares two differently synthesized Ni on CeO_2 catalysts, Ye *et al.* [24] observed X_{CO2} = 82.5% and S_{CH4} = 94.8% at 250 °C with Ni/CeO_2–SGM catalyst (synthesized via sol-gel method), as well as X_{CO2} = 69.8% and S_{CH4} = 84.8%, at 450 °C with Ni/CeO_2-IM (prepared by a simple impregnation method). They used conditions similar to those in the present study, albeit at a lower (10,000 cf. 60,000 cm^3 g^{-1} h^{-1}) weight hourly space velocity (*WHSV*); the catalysts exhibited a T_{50} of ≈ 240 °C and ≈ 330 °C, respectively. In another study

with two differently synthesized CeO_2 supports, with and without a g–C_3N_4 template, Yu *et al.* [25] obtained two Ni-based catalysts exhibiting T_{50} of 305 °C and 330 °C, with maximum $X_{CO2} \approx 75\%$ and $S_{CH4} \approx 100\%$, at 350 °C and 400 °C, for the catalyst prepared with g–C_3N_4 template and without, respectively, also at a lower *WHSV* (10,000 cf. 60,000 $cm^3\ g^{-1}\ h^{-1}$). Cárdenas-Arenas *et al.* [26] prepared a Ni/CeO_2 catalyst that reached ≈ 85% X_{CO2} with ≈ 100% S_{CH4} at 375 °C, with T_{50} of ≈ 280 °C.

The mechanism of the CO_2 methanation over Ni/CeO_2 catalysts has been a subject of intensive research. Zhang *et al.* [19] investigated the reaction mechanism on Ni/CeO_2 by first-principles calculations and concluded that the reaction on this catalyst follows the CO pathway through reverse water gas shift, rather than the formate (HCOO) formation or direct C–O bond cleavage pathways. Based on *in situ* DRIFTS study, Lee et al. [23] compared the mechanism of CO_2 methanation for Ni-based catalysts supported on different materials. They concluded that the Ni/CeO_2 catalyst, dissociates CO_2 into CO, which then participates in the CO_2 methanation reaction at high temperature. In another study with a Ni/CeO_2 catalyst synthesized by the sol-gel method, Ye *et al.* [24] suggested that the reaction occurred through a formate (HCOO) pathway with formyl (CHO) intermediate. Furthermore, the authors suggested that the good performance of the catalysts was related to the effective dissociation of H_2 by Ni and the strong adsorption/activation of CO_2 by CeO_2 support. Based on a DRIFTS study, Rui *et al.* [20] determined that the reaction proceeded through the CO pathway over Ni/CeO_2 catalyst, namely, by direct C–O bond cleavage via reverse water gas shift reaction followed by the methanation of the resultant CO.

Although some studies have indicated that CO_2 methanation over Ni/CeO_2 proceeds through the CO pathway [19,20,23], our results show that the methanation over our **Ni/CeO_2** follows a combination of CO pathway and the formate (HCOO) pathway, where CO forms through HCOO dissociation.

For **Ni/CeO_2**, we observed from steady-state *in situ* DRIFTs experiments (Fig. 5) that the CO_2 adsorption on the catalyst resulted in the formation of b–CO_3 and HCOO. When H_2 was added to the gas flow generating methanation conditions, another band attributed to CHO appeared, indicating that CHO is an important intermediate for the methanation over **Ni/CeO_2** catalyst.

The ME–PSD–DRIFT methodology improved the signal-to-noise ratio and allowed us to distinguish between the spectator and intermediate species. Now for **Ni/CeO_2**, it was possible to observe that the peak attributed to CHO in the steady-state *in situ* DRIFTS was in fact composed of two peaks out-of-phase with each other, namely, br–CO on Ni^0 and CHO [20,24].

Based on the collected experimental in situ ME–PSD–DRIFTS evidence (Fig. 6, S10, S12 and Table 2), Scheme 1 outlines the envisioned mechanism of the CO_2 methanation over synthesized **Ni/CeO_2**. There are two possibilities for the formation of br–CO on Ni^0: by direct dissociation of CO_2 over Ni, or dissociation of HCOO. In the second case, specifically, CO_2 is adsorbed on the CeO_2 surface as $CO_2^{\delta-}$, which then forms b–CO_3/p–CO_3 species [43]. These species are then hydrogenated by the hydrogen dissociated over Ni^0 to form HCOO, which is further dissociated forming br–CO on Ni^0. Next, the br–CO is firstly hydrogenated to CHO over the CeO_2 [24] and then to OCH_3, as observed in the respective in situ ME–PSD–DRIFTS spectra (Fig. 6, Table 2). It is difficult to access the phase delay of the methoxy species, due to a small signal being observed, but according to the literature, the presence of OCH_3 indicate that CHO should be hydrogenated to this species. Eventually, the as-formed OCH_3 is sequentially hydrogenated to CH_4 and released as the end-product.

There is an alternative pathway in which br–CO could be only involved in CO formation and not in the formation of the desired CH_4, and, accordingly, CHO would be formed through direct dissociation of HCOO. However, the fact that b–CO and CHO bands are 180° out-of-phase with each other (Fig. 6) strongly suggests that their transformation is directly correlated, which rules out this pathway.

When comparing the carbon-containing **$Ni/ACR–CeO_2$** to the carbon-free **Ni/CeO_2**, our characterization data indicate that the catalysts are quite different. **$Ni/ACR–CeO_2$** has a significantly higher surface area, porosity, and metallic Ni surface area, with smaller Ni nanoparticles size in comparison with **Ni/CeO_2**. At the same time, **Ni/CeO_2** is expected to have stronger metal–support interactions. The observation of similar methanation properties for such different catalysts leads to the hypothesis that the CO_2 methanation over **$Ni/ACR–CeO_2$** and **Ni/CeO_2** might proceed through different mechanisms.

The presence of CHO and especially the br–CO intermediates are less pronounced in **$Ni/ACR–CeO_2$** (Fig. 7), while the relative intensity of the HCOO, compared to the other species, appears to be higher (Fig. 7) than in the case of **Ni/CeO_2** (Fig. 6). Additionally, at higher temperature of 350 °C, the presence of the band from br–CO is not observed (Fig. 7). This could be explained by the fact that the consumption rate of CO on this catalyst is more favored by high temperatures than the formation rate, leading to less accumulation of this intermediate. However, if we consider that CO is hydrogenated to CHO, the instantaneous reaction (with lack of CO accumulation) would lead to a higher accumulation of CHO, if CHO is not hydrogenated at the same rate as CO, which is not observed. Therefore, the disappearance of the band from br–CO at high temperatures is related to desorption, instead of hydrogenation to CHO.

Thus, the data indicate that the br–CO does not play a significant role in the reaction pathway but may be related to the formation of the CO

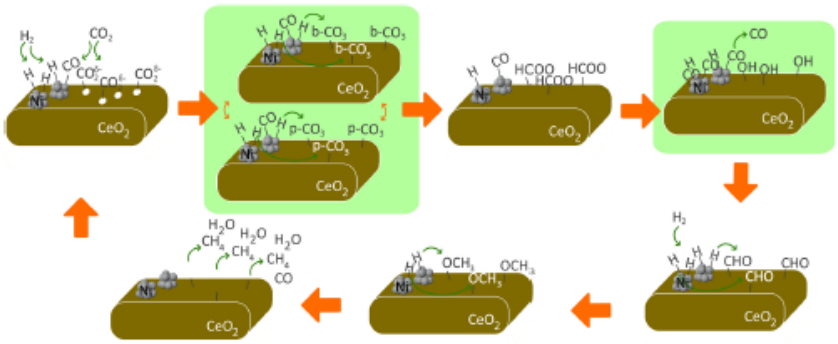

Scheme 1. Proposed mechanism for the CO_2 methanation over Ni/CeO_2 catalyst, displaying the formation/transformation of the reaction intermediates as elucidated by *in situ* ME–PSD–DRIFTS. The green boxes mark the differences in the mechanism between the two samples (Scheme 1 vs. Scheme 2).

byproduct (Scheme 2 (b)).

Regarding Ni catalysts supported on carbon materials, Hu *et al.* [17] concluded that the methanation over Ni catalyst supported on graphene aerogel followed the formate pathway, with carbonate intermediates being present, i.e., without the formation of CO. Consistently with this report, the CO_2 methanation over our carbon-containing **Ni/ACR–CeO$_2$** catalyst proceeds through the formate pathway, which is depicted on Scheme 2 (a). The methanation starts with the adsorption of CO_2 as $CO_2^{\delta-}$, followed by the formation of b–CO_3/p–CO_3 species [43]. Those are then hydrogenated to HCOO, similarly to what we observed for the carbon-free **Ni/CeO$_2$**. At the same time, in sharp contrast to **Ni/CeO$_2$**, br–CO was not detected for **Ni/ACR–CeO$_2$** at higher temperatures (350 °C). This fact indicates the significant difference between methanation over **Ni/CeO$_2$** and **Ni/ACR–CeO$_2$**, wherein over the composite catalyst, the formate (HCOO) is directly dissociated to formyl (CHO) [46], then following the same pathway as over the **Ni/CeO$_2$**. In particular, CHO is further hydrogenated to methoxy and finally to methane end product.

With regards to the proposed mechanisms (Schemes 1, 2), it is important to emphasize that some of the H_2 can be partially dissociated on the CeO_2 surface (i.e., not only on the Ni^0). This is suggested by *in situ* ME–PSD–DRIFTS of pure CeO_2 and composite ACR–CeO_2 supporting materials, revealing the presence of partially hydrogenated HCOO and OCH_3 species (Figs. S12, S13).

Interestingly, our detailed electron microscopy investigation of the microstructural changes, together with the XPS analysis, within the catalysts after 90 h of time-on-stream testing evidences that even though the catalysts did not lose their catalytic performance over 90 h (Fig. 1c, d), their fine microstructure and chemical composition were indeed affected.

The analysis of the Ni $2p_{3/2}$ and Ce 3d spectra of the fresh and TOS tested **Ni/CeO$_2$** and **Ni/ACR–CeO$_2$** revealed alterations in the Ni^0 content and the Ce^{3+}/Ce^{4+} ratios. The Ni^0 relative at% increase in **Ni/ACR–CeO$_{2\ TOS}$** indicating that the Ni nanoparticles likely undergo a further reduction under the reductive conditions of the CO_2 methanation reaction, probably due to the higher reducibility and weaker metal-support interactions in this sample (Fig. S4). On the contrary, an increase in the Ni^0 relative at% is observed in **Ni/CeO$_2$**. Regarding the CeO_2 support, Ce 3d spectra indicate that the relative at% of Ce^{3+}, and consequently the amount of oxygen vacancies remain similar in the **Ni/ACR–CeO$_{2\ TOS}$**, while, in contrast, increasing under reaction conditions in **Ni/CeO$_2$**.

The microstructural changes are mostly reflected by the preservation of the shell around Ni particles in both TOS-tested **Ni/CeO$_2$** and **Ni/ACR-CeO$_2$** materials (Fig. 4,S3). The catalytic functions of the observed NiO shells are not well understood and our future work underpinning the role of the shell in the CO_2 methanation over high-performing Ni catalysts is ongoing.

5. Conclusions

A set of Ni catalysts deposited either on pure CeO_2 or composite carbon–CeO_2 supporting materials have been synthesized and characterized. CO_2 methanation with excellent conversion, selectivity and stability at favorably low reaction temperature was achieved using the as-synthesized **Ni/CeO$_2$** and **Ni/ACR–CeO$_2$** catalysts.

Our work demonstrated that compositing carbon with CeO_2 within the supporting material afforded an effective reduction in the usage of the expensive rare-earth CeO_2 while providing access to not only a cost-effective but also a high-performing methanation catalyst operating at low temperature. The mechanism of the CO_2 methanation over the newly synthesized catalysts was investigated by means of in situ spectroscopy, using the emerging ME–PSD–DRIFTS technique. The collected insights uncovered that the methanation over **Ni/CeO$_2$** proceeded via a combination of the CO and formate pathways, while in **Ni/ACR–CeO$_2$** it proceeded exclusively via the formate pathway. The main underlying mechanistic difference between the catalysts is that, during methanation over carbon-free **Ni/CeO$_2$**, the reaction is mediated by CO from both CO_2 and formate dissociation, while carbon-containing **Ni/ACR–CeO$_2$** catalyst is producing CH_4 without intermediate CO formation. Overall, these results illustrated that even partial modification of the supporting material for Ni methanation catalysts can influence the reaction mechanism.

CRediT authorship contribution Statement

Liliana P.L. Gonçalves: Conceptualization, Methodology, Formal analysis, Investigation, Writing – original draft. **Jerrik Mielby:**

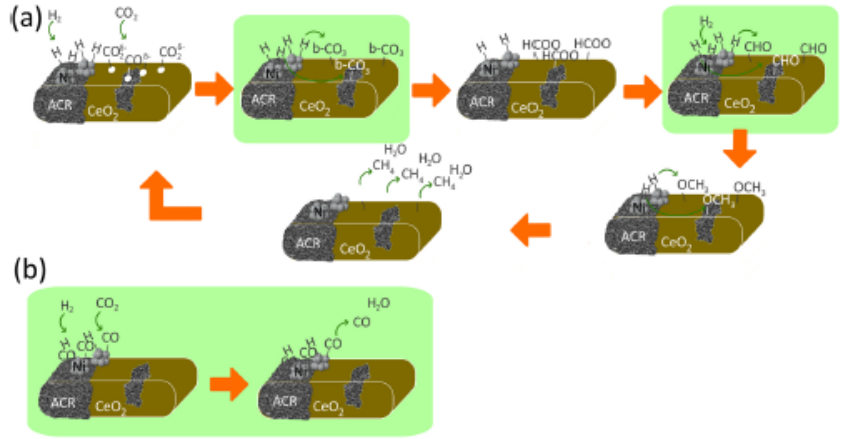

Scheme 2. Proposed mechanism for the CO_2 methanation over Ni/ARC–CeO_2 catalyst, displaying the formation/transformation of the reaction intermediates as elucidated by *in situ* ME–PSD–DRIFTS. (a) illustrates the mechanism of CH_4 formation while (b) depicts the mechanism of CO formation. The green boxes mark the differences in the mechanism between the two samples (Scheme 1 vs. Scheme 2).

Conceptualization, Methodology, Writing – review & editing. O. Salomé G.P. Soares: Methodology, Writing – review & editing, Supervision. **Juliana P.S. Sousa:** Writing – review & editing, Supervision. **Dmitri Y. Petrovykh:** Writing – review & editing. **Oleg I. Lebedev:** Writing – review & editing, Funding acquisition. **M. Fernando R. Pereira:** Writing – review & editing, Supervision, Funding acquisition. **Søren Kegnæs:** Conceptualization, Writing – review & editing, Funding acquisition. **Yury V. Kolen'ko:** Conceptualization, Writing – original draft, Supervision, Funding acquisition.

Declaration of Competing Interest

The authors declare that they have no known competing financial interests or personal relationships that could have appeared to influence the work reported in this paper.

Acknowledgments

L.P.L.G. thanks the Portuguese Foundation for Science and Technology (FCT) for the PhD grant (SFRH/BD/128936/2017). This work was financially supported by LA/P/0045/2020 (ALiCE), UIDB/50020/2020 and UIDP/50020/2020 (LSRE-LCM), funded by National Funds through FCT/MCTES (PIDDAC). O.S.G.P.S. acknowledges FCT funding under the Scientific Employment Stimulus - Institutional Call (CEECINST/00049/2018). S.K. thank the Independent Research Fund Denmark (grant no. 6111-00237 and 0217-00146B) and the Villum Foundation (grant no. 13158). Yu.V.K. thanks the FCT for support under the CritMag Project (PTDC/NAN-MAT/28745/2017).

Appendix A. Supporting information

Supplementary data associated with this article can be found in the online version at doi:10.1016/j.apcatb.2022.121376.

References

[1] J. Ashok, S. Pati, P. Hongmanorom, Z. Tianxi, C. Junmei, S. Kawi, A review of recent catalyst advances in CO_2 methanation processes, Catal. Today 356 (2020) 471–489, https://doi.org/10.1016/j.cattod.2020.07.023.

[2] L.P.L. Gonçalves, J.P.S. Sousa, O.S.G.P. Soares, O. Bondarchuk, O.I. Lebedev, Y. V. Kolen'ko, M.F.R. Pereira, The role of surface properties in CO_2 methanation over carbon-supported Ni catalysts and their promotion by Fe, Catal. Sci. Technol. 10 (2020) 7217, https://doi.org/10.1039/D0CY01254H.

[3] B. Miao, S.S.K. Ma, X. Wang, H. Su, S.H. Chan, Catalysis mechanisms of CO_2 and CO methanation, Catal. Sci. Technol. 6 (2016) 4048–4058, https://doi.org/10.1039/C6CY00478D.

[4] F. Goodarzi, L. Kang, F.R. Wang, F. Joensen, S. Kegnæs, J. Mielby, Methanation of carbon dioxide over zeolite-encapsulated nickel nanoparticles, ChemCatChem 10 (2018) 1566–1570, https://doi.org/10.1002/cctc.201701946.

[5] L.P.L. Gonçalves, A. Serov, G. McCool, M. Dicome, J.P.S. Sousa, O.S.G.P. Soares, O. Bondarchuk, D.Y. Petrovykh, O.I. Lebedev, M.F.R. Pereira, Y. Kolen'ko, New opportunity for carbon-supported Ni-based electrocatalysts: gas-phase CO_2 methanation, ChemCatChem 13 (2021) 1–11, https://doi.org/10.1002/cctc.202101284.

[6] Z. Zhang, Y. Tian, L. Zhang, S. Hu, J. Xiang, Impacts of nickel loading on properties, catalytic behaviors of $Ni/\gamma Al_2O_3$ catalysts and the reaction intermediates formed in methanation of CO_2, Int. J. Hydrog. Energy 44 (2019) 9291–9306, https://doi.org/10.1016/j.ijhydene.2019.02.129.

[7] T.A. Le, M.S. Kim, S.H. Lee, E.D. Park, CO and CO_2 methanation over supported cobalt catalysts, Top. Catal. 60 (2017) 714–720, https://doi.org/10.1007/s11244-017-0788-y.

[8] G. Zhou, T. Wu, H. Xie, X. Zheng, Effects of structure on the carbon dioxide methanation performance of Co-based catalysts, Int. J. Hydrog. Energy 38 (2013) 10012–10018, https://doi.org/10.1016/j.ijhydene.2013.05.130.

[9] D.L. Williamson, M.D. Jones, D. Mattia, Highly selective, iron-driven CO_2 methanation, Energy Technol. 7 (2019) 294–306, https://doi.org/10.1002/ente.201800923.

[10] F. Hemmingsson, A. Schaefer, M. Skoglundh, P.A. Carlsson, CO_2 methanation over Rh/CeO_2 studied with infrared modulation excitation spectroscopy and phase sensitive detection, Catalysts 10 (2020) 601, https://doi.org/10.3390/catal10060601.

[11] H. Chen, F. Goodarzi, Y. Mu, S. Chansai, J.J. Mielby, B. Mao, T. Sooknoi, C. Hardacre, S. Kegnæs, X. Fan, Effect of metal dispersion and support structure of Ni/silicalite-1 catalysts on non-thermal plasma (NTP) activated CO_2 hydrogenation, Appl. Catal. B Environ. 272 (2020), 119013, https://doi.org/10.1016/j.apcatb.2020.119013.

[12] K.H. Rasmussen, F. Goodarzi, D.B. Christensen, J. Mielby, S. Kegnæs, Stabilization of metal nanoparticle catalysts via encapsulation in mesoporous zeolites by steam-assisted recrystallization, ACS Appl. Nano Mater. 2 (2019) 8083–8091, https://doi.org/10.1021/acsanm.9b02205.

[13] I. Champon, A. Bengaouer, A. Chaise, S. Thomas, A.C. Roger, Carbon dioxide methanation kinetic model on a commercial Ni/Al_2O_3 catalyst, J. CO2 Util. 34 (2019) 256–265, https://doi.org/10.1016/j.jcou.2019.05.030.

[14] G. Garbarino, P. Riani, L. Magistri, G. Busca, A study of the methanation of carbon dioxide on Ni/Al_2O_3 catalysts at atmospheric pressure, Int. J. Hydrog. Energy 39 (2014) 11557–11565, https://doi.org/10.1016/j.ijhydene.2014.05.111.

[15] G.M. Shashidhara, M. Ravindram, A kinetic study of the methanation of CO_2 over $Ni-Al_2O_3$ catalyst, React. Kinet. Catal. Lett. 37 (1988) 451–456.

[16] W. Wang, C. Duong-Viet, H. Ba, W. Baaziz, G. Tuci, S. Caporali, L. Nguyen-Dinh, O. Ersen, G. Giambastiani, C. Pham-Huu, Nickel nanoparticles decorated nitrogen-doped carbon nanotubes (Ni/N-CNT): a robust catalyst for the efficient and selective CO_2 methanation, ACS Appl. Energy Mater. 2 (2019) 1111–1120, https://doi.org/10.1021/acsaem.8b01681.

[17] F. Hu, X. Chen, Z. Tu, Z.-H. Lu, G. Feng, R. Zhang, Graphene aerogel supported Ni for CO2 hydrogenation to methane, Ind. Eng. Chem. Res. 60 (2021) 12235–12243, https://doi.org/10.1021/acs.iecr.1c01953.

[18] J.L. Figueiredo, M.F.R. Pereira, M.M.A. Freitas, J.J.M. Órfão, Characterization of active sites on carbon catalysts, Ind. Eng. Chem. Res. 46 (2007) 4110–4115, https://doi.org/10.1021/ie061071v.

[19] J. Zhang, Y. Yang, J. Liu, B. Xiong, Mechanistic understanding of CO_2 hydrogenation to methane over Ni/CeO_2 catalyst, Appl. Surf. Sci. 558 (2021), 149866, https://doi.org/10.1016/j.apsusc.2021.149866.

[20] N. Rui, X. Zhang, F. Zhang, Z. Liu, X. Cao, Z. Xie, R. Zou, S.D. Senanayake, Y. Yang, J.A. Rodriguez, C.J. Liu, Highly active Ni/CeO_2 catalyst for CO_2 methanation: preparation and characterization, Appl. Catal. B Environ. 282 (2021), 119581, https://doi.org/10.1016/j.apcatb.2020.119581.

[21] P. Hongmanorom, J. Ashok, P. Chirawatkul, S. Kawi, Interfacial synergistic catalysis over Ni nanoparticles encapsulated in mesoporous ceria for CO_2 methanation, Appl. Catal. B Environ. 297 (2021), 120454, https://doi.org/10.1016/j.apcatb.2021.120454.

[22] S. Tada, T. Shimizu, H. Kameyama, T. Haneda, R. Kikuchi, Ni/CeO_2 catalysts with high CO_2 methanation activity and high CH_4 selectivity at low temperatures, Int. J. Hydrog. Energy 37 (2012) 5527–5531, https://doi.org/10.1016/j.ijhydene.2011.12.122.

[23] Y.H. Lee, J.Y. Ahn, D.D. Nguyen, S.W. Chang, S.S. Kim, S.M. Lee, Role of oxide support in Ni based catalysts for CO_2 methanation, RSC Adv. 11 (2021) 17648–17657, https://doi.org/10.1039/d1ra02327f.

[24] R.P. Ye, Q. Li, W. Gong, T. Wang, J.J. Razink, L. Lin, Y.Y. Qin, Z. Zhou, H. Adidharma, J. Tang, A.G. Russell, M. Fan, Y.G. Yao, High-performance of nanostructured Ni/CeO_2 catalyst on CO_2 methanation, Appl. Catal. B Environ. 268 (2020), 118474, https://doi.org/10.1016/j.apcatb.2019.118474.

[25] Y. Yu, Y.M. Chan, Z. Bian, F. Song, J. Wang, Q. Zhong, S. Kawi, Enhanced performance and selectivity of CO_2 methanation over $g\text{-}C_3N_4$ assisted synthesis of $Ni–CeO_2$ catalyst: kinetics and DRIFTS studies, Int. J. Hydrog. Energy 43 (2018) 15191–15204, https://doi.org/10.1016/j.ijhydene.2018.06.090.

[26] A. Cárdenas-Arenas, A. Quindimil, A. Davó-Quiñonero, E. Bailón-García, D. Lozano-Castelló, U. De-La-Torre, B. Pereda-Ayo, J.A. González-Marcos, J. R. González-Velasco, A. Bueno-López, Isotopic and in situ DRIFTS study of the CO_2 methanation mechanism using Ni/CeO_2 and Ni/Al_2O_3 catalysts, Appl. Catal. B Environ. 265 (2020), 118538, https://doi.org/10.1016/j.apcatb.2019.118538.

[27] P.C.C. Faria, J.J.M. Órfão, M.F.R. Pereira, A novel ceria – activated carbon composite for the catalytic ozonation of carboxylic acids, Catal. Commun. 9 (2008) 2121–2126, https://doi.org/10.1016/j.catcom.2008.04.009.

[28] B. Owens-Baird, J. Xu, D.Y. Petrovykh, O. Bondarchuk, Y. Ziouani, N. González-Ballesteros, P. Yox, F.M. Sapountzi, H. Niemantsverdriet, Y.V. Kolen'ko, K. Kovnir, NiP_2: a story of two divergent polymorphic multifunctional materials, Chem. Mater. 31 (2019) 3407–3418, https://doi.org/10.1021/acs.chemmater.9b00565.

[29] M.C. Biesinger, B.P. Payne, L.W.M. Lau, A. Gerson, R.S.C. Smart, X-ray photoelectron spectroscopic chemical state quantification of mixed nickel metal, oxide and hydroxide systems, Surf. Interface Anal. 41 (2009) 324–332, https://doi.org/10.1002/sia.3026.

[30] B. Owens-Baird, J.P.S. Sousa, Y. Ziouani, D.Y. Petrovykh, N.A. Zarkevich, D. D. Johnson, Y.V. Kolen'ko, K. Kovnir, Crystallographic facet selective HER catalysis: exemplified in FeP and NiP_2 single crystals, Chem. Sci. 11 (2020) 5007–5016, https://doi.org/10.1039/D0SC00676A.

[31] E. Bêche, P. Charvin, D. Perarnau, S. Abanades, G. Flamant, Ce 3d XPS investigation of cerium oxides and mixed cerium oxide ($Ce_xTi_yO_z$), Surf. Interface Anal. 40 (2008) 264–267, https://doi.org/10.1002/sia.2686.

[32] F. Zhang, P. Wang, J. Koberstein, S. Khalid, S.W. Chan, Cerium oxidation state in ceria nanoparticles studied with X-ray photoelectron spectroscopy and absorption near edge spectroscopy, Surf. Sci. 563 (2004) 74–82, https://doi.org/10.1016/j.susc.2004.05.138.

[33] D.R. Mullins, S.H. Overbury, D.R. Huntley, Electron spectroscopy of single crystal and polycrystalline cerium oxide surfaces, Surf. Sci. 409 (1998) 307–319, https://doi.org/10.1016/S0039-6028(98)00257-X.

[34] M. Nolan, J.E. Fearon, G.W. Watson, Oxygen vacancy formation and migration in ceria, Solid State Ion. 177 (2006) 3069–3074, https://doi.org/10.1016/j.ssi.2006.07.045.

[35] J.L. Figueiredo, M.F.R. Pereira, The role of surface chemistry in catalysis with carbons, Catal. Today 150 (2010) 2–7, https://doi.org/10.1016/j.cattod.2009.04.010.
[36] L.P.L. Gonçalves, D.B. Christensen, M. Meledina, L.M. Salonen, D.Y. Petrovykh, E. Carbó-Argibay, J.P.S. Sousa, O.S.G.P. Soares, M.F.R. Pereira, S. Kegnæs, Y. V. Kolen'Ko, Selective formic acid dehydrogenation at low temperature over a RuO_2/COF pre-catalyst synthesized on the gram scale, Catal. Sci. Technol. 10 (2020) 1991–1995, https://doi.org/10.1039/d0cy00145g.
[37] P.D. Srinivasan, B.S. Patil, H. Zhu, J.J. Bravo-Suárez, Application of modulation excitation-phase sensitive detection-DRIFTS for: in situ /operando characterization of heterogeneous catalysts, React. Chem. Eng. 4 (2019) 862–883, https://doi.org/10.1039/c9re00011a.
[38] A. Urakawa, T. Bürgi, A. Baiker, Sensitivity enhancement and dynamic behavior analysis by modulation excitation spectroscopy: principle and application in heterogeneous catalysis, Chem. Eng. Sci. 63 (2009) 4902–4909, https://doi.org/10.1016/j.ces.2007.06.009.
[39] A. Aguirre, S.E. Collins, Selective detection of reaction intermediates using concentration- modulation excitation DRIFT spectroscopy, Catal. Today 205 (2013) 34–40, https://doi.org/10.1016/j.cattod.2012.08.020.
[40] D. Baurecht, U.P. Fringeli, Quantitative modulated excitation Fourier transform infrared spectroscopy, Rev. Sci. Instrum. 72 (2001) 3782–3792, https://doi.org/10.1063/1.1400152.
[41] P.D. Srinivasan, K. Khivantsev, J.M.M. Tengco, H. Zhu, J.J. Bravo-Suárez, Enhanced ethanol dehydration on γ-Al_2O_3 supported cobalt catalyst, J. Catal. 373 (2019) 276–296, https://doi.org/10.1016/j.jcat.2019.03.024.
[42] S.M. Fehr, L. Krossing, Spectroscopic signatures of pressurized carbon dioxide in diffuse reflectance infrared spectroscopy of heterogeneous catalysts, ChemCatChem 12 (2020) 2622–2629, https://doi.org/10.1002/cctc.201902038.
[43] Y. Yu, Z. Bian, Z. Wang, J. Wang, W. Tan, Q. Zhong, S. Kawi, CO_2 methanation on Ni-$Ce_{0.8}$ $M_{0.2}$ O_2 (M=Zr, Sn or Ti) catalyst: suppression of CO via formation of bridging carbonyls on nickel, Catal. Today 2 (2020), https://doi.org/10.1016/j.cattod.2020.07.049. (https://doi.org/10.1016/j.cattod.2020.07.049).
[44] R. Tang, N. Ullah, Y. Hui, X. Li, Z. Li, Enhanced CO_2 methanation activity over Ni/CeO_2 catalyst by one-pot method, Mol. Catal. 508 (2021), 111602, https://doi.org/10.1016/j.mcat.2021.111602.
[45] X. Liao, Y. Zhang, M. Hill, X. Xia, Y. Zhao, Z. Jiang, Highly efficient Ni/CeO2 catalyst for the liquid phase hydrogenation of maleic anhydride, Appl. Catal. A Gen. 488 (2014) 256–264, https://doi.org/10.1016/j.apcata.2014.09.042.
[46] H.L. Huynh, J. Zhu, G. Zhang, Y. Shen, W.M. Tucho, Y. Ding, Z. Yu, Promoting effect of Fe on supported Ni catalysts in CO_2 methanation by in situ DRIFTS and DFT study, J. Catal. 392 (2020) 266–277, https://doi.org/10.1016/j.jcat.2020.10.018.